Government of Western Australia

Department of
Mines and Petroleum

REPORT
156

INTEGRATED SPECTRAL MAPPING OF PRECIOUS AND BASE METAL RELATED MINERAL FOOTPRINTS, NANJILGARDY FAULT, WESTERN AUSTRALIA

by M Wells, C Laukamp, and E Hancock

EXPLORATION
INCENTIVE SCHEME

CSIRO

Geological Survey of Western Australia

Government of **Western Australia**
Department of **Mines and Petroleum**

REPORT 156

INTEGRATED SPECTRAL MAPPING OF PRECIOUS AND BASE METAL RELATED MINERAL FOOTPRINTS, NANJILGARDY FAULT, WESTERN AUSTRALIA

by
M Wells, C Laukamp, and E Hancock

Perth 2016

Geological Survey of Western Australia

REFERENCE
The recommended reference for this publication is:
Wells, M, Laukamp, C and Hancock, E 2016, Integrated spectral mapping of precious and base metal related mineral footprints, Nanjilgardy Fault, Western Australia: Geological Survey of Western Australia, Report 156, 90p.

National Library of Australia Cataloguing-in-Publication entry:

Creator:	Wells, M. R., author.
Title:	Integrated spectral mapping of precious and base metal related mineral footprints, Nanjilgardy Fault, WA / Martin Wells, Carsten Laukamp and Elena Hancock.
ISBN:	9781741686616 (ebook)
Subjects:	Mines and mineral resources--Western Australia. Geological mapping--Western Australia.
Other Creators/Contributors:	Laukamp, Carsten, author. Hancock, Elena, author.
Dewey Decimal Classification:	559.41

ISSN 1834–2280

Grid references in this publication refer to the Geocentric Datum of Australia 1994 (GDA94). Locations mentioned in the text are referenced using Map Grid Australia (MGA) coordinates, Zone 50. All locations are quoted to at least the nearest 100 m.

About this publication
This Report presents the results of a study by CSIRO and GSWA, with funding support for CSIRO from GSWA via the Exploration Incentive Scheme (EIS). GSWA is releasing the information as part of its Report Series to ensure a wider distribution of the results. CSIRO is responsible for the scientific content of the Report and the drafting of figures. No editing has been undertaken by GSWA.

CSIRO

EXPLORATION INCENTIVE SCHEME

Published 2016 by Geological Survey of Western Australia
This Report is published in digital format (PDF) and is available online at <www.dmp.wa.gov.au/GSWApublications>.

Further details of geological publications and maps produced by the Geological Survey of Western Australia are available from:
Information Centre | Department of Mines and Petroleum | 100 Plain Street | EAST PERTH | WESTERN AUSTRALIA 6004
Telephone: +61 8 9222 3459 Facsimile: +61 8 9222 3444 **www.dmp.wa.gov.au/GSWApublications**

Cover photograph: The Mt Olympus gold deposit and study area along the Nanjilgardy Fault, Capricorn Orogen

MINERALS DOWN UNDER
www.csiro.au

Integrated Spectral Mapping of Precious and Base Metal Related Mineral Footprints, Nanjilgardy Fault, WA.

Final Report: December 2015

Martin Wells, Carsten Laukamp and Lena Hancock

CSIRO Mineral Resources

18th December 2015

Department of Mines and Petroleum (Acting through the Geological Survey of Western Australia, GSWA)
Dr. Ian Tyler (Assistant Director, Geoscience Mapping)

CESRE/Mineral Resources

Citation

Wells, M., Laukamp, C. and Hancock, L. (2015). Integrated Spectral Mapping of Precious and Base Metal Related Mineral Footprints, Nanjilgardy Fault, WA.

Final Report, EP155294, CSIRO, Australia, p90.

Copyright and disclaimer

Important disclaimer

Contents

Contents ii

Figures v

Tables ix

Acknowledgments x

Executive summary xi

1 Introduction 16

1.1 Scope 18
Other Geophysical data-sets 18

1.2 Regional Geology 18

1.3 Mineral Systems 19

1.4 Minerals as indicators for diagenesis, metamorphism, hydrothermal alteration and weathering 21
Di-octahedral Al-Clay minerals 21
Sulphates 23

2 Methods (Applied Technology and Software) 25

2.1 HyLogging™ (Proximal Sensing) 25

2.2 TSA 27

2.3 MFEM 28

2.4 ASTER (Remote Sensing) 31

2.5 Field Sampling and Diamond Drill Core Sampling 32
Drill core Data integration 36

2.6 FieldSpec3 (ASD) 37
Field measurements 37
Laboratory measurements 37

2.7 Whole Rock Geochemistry 37
Gold analysis 38
Base and Trace Metals by Microwave-Assisted Multi-Acid Digestion 38
Major Oxides (Whole Rock) by Alkaline Fusion 38

2.8 Element Distribution Mapping 38

2.9 X-ray Diffraction (XRD) analysis 39

2.10 GSWA surface sample geochemistry 40

2.11 Leapfrog Geo and 3D modelling 40

2.12 Geophyscial Data 42

3 Results and Discussion 43

3.1 Drill Core Analyses....43
XRD, Geochemcial & HyLogging associations....43
Element mapping....47
Drill Core Deterioration (Atmospheric Oxidation)....51
3.2 Field Work....53
XRD and Geochemical validation....53
Spectral-geochemical associations....54
3.3 Mineral identification: TSA vs. XRD....55
3.4 Au -related mineral footprints at Mount Olympus....57
Oxidised high-grade gold mineralization....58
Primary oxidized mineralization (low-grade)....58
Primary mineralization (un-oxidized)....59
Distal and Proximal low-grade mineralization....59
3.5 Leapfrog modelling....64
3.6 Comparison of ASTER with surface data....67
Discussion of Mineral Footprints observed in Samples....67
ASTER68
ASTER and AEM data Comparison....71
GSWA Regolith Samples....74

4 Summary and Conclusions 78

4.1 Alteration Mineralogical Assemblages....78
4.2 Efficacy of TSA Mineral identification....79
4.3 Remotely Sensed Data: Applications for Industry Exploration....80
4.4 Recommendations for future work....81

References 82

Appendices 86

Report Appendices are presented as a supplement to the main report and full details are described therein. The following lists only the title heading of each Appendix....86
Appendix 1 Table of MFEM scripts....86
Appendix 2 Bulk Geochemistry (Drill hole-Transect samples)....86
Appendix 3 Bulk XRD Mineralogy....86
Appendix 4 XRD patterns....86
Appendix 5 Regolith geochemistry and related data....86
Appendix 6 Tornado mapping....86
Appendix 7 Drill core logs....86
Appendix 8 AEM flight line profiles, Electric Dingo Area....86

Figures

Figure 1 Location of the Capricorn Orogen and major elements of surrounding cratons and basins, with general age of the main rock types. Paleoproterozoic crustal elements are shown (see inset) for the western part of the Capricorn Orogen (KC = Kimberley Craton; NAC = North Australian Craton; SAC = South Australian Craton; WAC = Western Australian Craton), and Archean cratons (YC = Yilgarn Craton; PC = Pilbara Craton; GC = Gawler Craton). Figure modified from Johnson et al. (2013). 17

Figure 2 Regional geological setting of the Capricorn Orogen, location of the Nanjilgardy Fault and the Paulsens and Mt Olympus gold deposits. Location of one of the Capricorn Orogen seismic lines, 10GA-CP1 (orange line) across the Nanjilgardy fault is also shown. 17

Figure 3 General stratigraphic sequence and major orogenic events of the Capricorn Orogeny; modified from Johnson et al. (2013). Regional stratigraphy of the Wyloo Group showing gold mineralisation at Mt Olympus is hosted mainly by meta-sediments of the McGrath Formation but also by the Duck Creek Dolomite; modified from Tyler and Thorne (1990). 19

Figure 4 Commodities according to Minedex over the regional bedrock, geological map (500K) of the project area, with the WNW-trending Nanjilgardy Fault separating the Hamersley Basin in the Northeast from the Ashburton Basin in the Southwest. Black frame 'A' highlights the Mount Olympus case study area. Numbered circles in yellow are HyLogging™ data available for this project (1 – MD003; 2 – PDU3000, PDU3001, PDU3002, PDU3003; 3 – AWD003; 4 – NMD001; 5 – EDD005; 6 – ID001; 7 – LD004; 8 – MOD3 - MOD8, MOD11 - MOD14, MT090, NMOD001, NMOD002, NMOD004, NMOD005; 9 – SPD001). 20

Figure 5 Hydrothermal alteration mineralogy as controlled by cation activity and temperature in hydrothermal systems; modified from Utada (1980). 23

Figure 6 Location of drill holes in the study area, acquired through the EIS program or donated by Sipa Resources to the GSWA Perth Core Library. 26

Figure 7 TSG summary logs showing user TSA mineral distribution and relative abundance in the SWIR (top) and TIR (bottom) wavelength regions. Drill hole MTO90 was used as the example. 27

Figure 8 MFEM white mica parameters: a) relative white mica abundance; b) white mica composition: short wavelength values – Al-rich white mica (e.g., paragonite, muscovite), long wavelength values – Al-poor white mica (e.g., phengite); c) relative white mica abundance coloured up by white mica composition; d) detail of 109.5 to 110.5 m of plot c). Colour scale for b), c) and d) bottom right. 28

Figure 9 Scatter plots showing the application of the MFEM 2160D (y-axis) and 2250D (x-axis) scripts to aid in the discrimination of alumina-silicates (kaolinite, muscovite) and sulphates (jarosite, alunite). Data points are coloured by (A) TSA mineralogy, and (B) assayed Au values (ppm). The smaller boxed plots show the reflectance spectrum for each of the arrowed points, representative of the main mineral/s group identified, and a digital image of the location for each reflectance spectrum. Drill hole MOD4 was used as the example. 30

Figure 10 Band coverage of ASTER and Landsat TM across the visible and infrared wavelength regions. Collected bands are located in atmospheric windows, indicated by the generalised atmospheric transmission spectrum at the bottom of this diagram. Generalized atmospheric transmission spectrum of 1 km horizontal air path at sea level conditions of 15° C air temperature, 46 % relative humidity, 1013 mb atmospheric pressure (Laukamp et al., 2013). 31

Figure 11 Location of fieldwork transects and GSWA Regolith samples in the Mount Olympus area on a 500K surface geology map 33

Figure 12 Location of GSWA transects and drill core EDD005 in the Electric Dingo area on a 1 s DEM, blue = 250 m, red = 450 m. For the location of EDD005 see Figure 6. 33

Figure 13 Stacked, down-hole plots (i.e., x-axis = depth) for drill hole NMOD001 showing the variation (i.e., y-axis) with depth in: a) lithology, b) Au assay (ppm), c) As assay (ppm); and spectral mineralogy

scalars for, d) Kaolin/palygorskite spectral abundance. The inset view of the drill core shows the location from which sample #35 was taken for validation XRD and bulk geochemical analysis. 36

Figure 14 Location of drill holes used for Leapfrog modelling. Only those holes within the vicinity of Mt Olympus were used. For example, drill holes LD004 and SPD001 (not plotted) were considered too far removed from the 'cluster' of drill holes in the immediate vicinity of Mt Olympus (box outlined in red) and were not included in the 3D modelling. Drill hole key: 1 = MOD04, 2 = MOD08, 3 = MOD07, 4 = MOD05, 5 = MOD06, 6 = MOD12, 7 = MOD13, 8 = MOD03, 9 = MTO90, 10 = MOD11, 11 = MOD14, 12 = NMOD001/NMOD002, 13 = NMOD004, 14 = NMOD005, 15 = AMMOD0026, 16 = AMMOD0028..... 41

Figure 15 Plots of major and minor elements highlighting various element-mineral associations: (A) wt% K_2O *vs*. wt% Al_2O_3; (B) wt% S *vs*. wt% Fe; (C) wt% MgO *vs*. wt% CaO; and (D) XRD pattern of an Fe-bearing sample (Fe-chlorite) representative of the S-free, Fe-bearing phases (circled in red in B). These samples contain other Fe(II)- or Fe(III)-bearing phases, such as siderite or Fe-chlorite. The sample arrowed in the plot contains both pyrite and the ferrous sulphate, szomolnokite. The black dashed line in plots A, B and C represent the oxide or element ratio expected for pure muscovite, pyrite or dolomite, respectively. 44

Figure 16 Illustration of the effect Fe substitution on the basal peak intensity of chlorite, for sample SPD001_2. Where Fe is symmetrically distributed between the 'interlayer sheet', octahedral co-ordinated by hydroxyl groups (hydroxyl sheet), and the octahedral co-ordinated 'silicate' sheet, odd-numbered (001, 003) basal peaks have a weaker intensity than even-numbered (002, 004) basal peaks. 45

Figure 17 Plot of the XRD peak intensity ratio for the 002 and 003 lines (I002/003) of chlorite *vs*. the bulk wt% MgO content for drill core samples containing only chlorite as the main Mg-bearing phase, as detected by XRD analysis. The I002/003 ratio decreases with increasing Mg content in response to the decreased influence of Fe on peak intensity (refer to text for a more detailed discussion). 45

Figure 18 Chlorite composition script (chlepci3pfit) *vs*. the bulk MgO content (wt%), with sample points coloured by (A) the wavelength of the 2250 absorption feature, and (B) the TSA mineral1 designation. Samples arrowed in (B) identified to TSA Min1 as 'Muscovite' were identified to TSA Min2 level as 'Chlorite' (data not shown) as confirmed by XRD analysis. 46

Figure 19 Plot of the 001 d-spacing for muscovite *vs*. the bulk wt% Na_2O content, with samples coloured by; (A) the wavelength (nm) of the 2200 "white-mica" absorption feature, and (B) the TSA Grp1 designation. Samples with a TSA Min1 "NULL" designation, were spectrally noisy due to the presence of pyrite as detected by XRD analysis. 47

Figure 20 Optical (top left) and false-colour element distribution maps of siltstone MOD13_29 (139.20–139.27 m; @ 2 ppb Au) showing (A) a composite (Fe – red, Si – green, K – blue) and Al map images. The sample mineralogy comprising: siderite, quartz, muscovite (maj); Fe-chlorite (min); Rutile (tr) as detected by XRD analysis, is consistent with that expected of a siltstone. 48

Figure 21 Optical (top left) and false-colour element distribution maps for Fe, S and Mg of dolomitic sample SPD001_7 (386.00–386.25 m; Au BD). The Fe distribution map highlights the compositional zonation of dolomite and indicates carbonate formation occurred in two stages. Mineralogy comprised dolomite as the major phase with trace amounts of quartz and muscovite (Appendix 3). 49

Figure 22 Optical (top left) and false-colour element distribution maps of Dolomite SPD001_13 (445.68–445.82 m): (A) Optical imagery of grey dolomite with greenish colour variations and crosscutting veins. (B) False colour element distribution map (Si – red, K – green, Mg – blue). (C) Drill core image acquired with HyLogging™-3 system of same drill core interval as (A) and (B) (Note that the thin section and HyLogging™-3 scans are mirror images). (D) Tornado XRF values for two sample points (Carb1 and Alter1) shown in (B). SWIR (E) and TIR (F) reflectance spectra, offset for clarity, for sampling points #1-10 across the alteration zone shown in (C). 50

Figure 23 Optical (top left) and false-colour element distribution maps of shale from the Mt Olympus pit (reflected light, RL) showing composite images (top right) of Si (yellow), Fe (orange) and S (green),

and (bottom right) of Al (orange), S (green) and K (red). High levels of As, to 1.2–1.8 wt%, are associated with pyrite. The bulk mineralogy comprises quartz (maj); muscovite (min); pyrite (tr), as detected by XRD analysis (Appendix 3 and 4). 51

Figure 24 XRD diffraction pattern of MOD13_23 showing the presence of abundant ferrous sulphates as secondary alteration products of pyrite oxidation formed upon exposure of the drill core to the atmosphere while the drill core has been sitting in storage. Mineral key of the main phases follows the abbreviation convention of Whitney and Evans (2010): Roz = rozenite, Py = pyrite, Szk = szmolnokite. 52

Figure 25 Plots of major and minor element-element relationships that highlight various element-mineral associations: (A) wt% K_2O *vs*. wt% Al_2O_3; (B) wt% S *vs*. wt% Fe, and (C) wt% MgO *vs*. wt% CaO. The dashed line in the plots A and C, represent the K_2O:Al_2O_3 and MgO:CaO ratio expected for pure muscovite and dolomite, respectively. Samples lying above or falling below the dolomite MgO:CaO ratio indicate the presence of other Mg or Ca-bearing phases, respectively (refer to text for further explanation). 53

Figure 26 Plots of, (A) XRD peak intensity ratio for the 002 and 003 lines (I002/003) of chlorite, and (B) the MFEM chlorite composition script (chlepci3pfit) *vs*. the bulk Mg content, for field samples collected in the Electric Dingo vicinity and at Mt Olympus. XRD I002/003 values suggest that chlorite at Mt. Olympus was compositionally more variable whereas chlorite at Electric Dingo is more Mg-rich and has a relatively constant Fe/Mg composition, as confirmed by the shift to shorter wavelengths of the MFEM chlorite composition index for chlorite at Mt Olympus. The samples arrowed do not contain chlorite but gibbsite, as detected by XRD analysis and identified to TSA Min1 level, and suggest that further refinement of the chlorite composition script is needed. 54

Figure 27 Plots of, (A) the 001 *d*-spacing for muscovite, and (B) the wavelength (nm) of the 2200 "white-mica" absorption feature (2200W3pfit), *vs*. the bulk wt.% Na_2O content for field samples collected in the vicinity of the Electric Dingo drill hole and at Mt Olympus, that only contain muscovite as the predominant Al/K/Na-bearing phase. 55

Figure 28 Downhole plots for drill core MOD13 over the depth interval 83.5 to 142.0 m. The zone of the highest Au grade is highlighted in pink. A: Sulphate abundance index coloured by Au (ppm) values. B: Sulphate abundance index coloured by the sulphate species index. C: Al-clay abundance index coloured by Al-clay species index. D: alunite and/or kaolin group abundance index coloured by the related mineral species index. 60

Figure 29 Downhole plots for drill core MOD4 over the depth interval 70 to 95 m. A: Sulphate abundance index coloured by Au (ppm) values. B: Sulphate abundance index coloured by the sulphate species index. C: Al-clay abundance index coloured by Al-clay species index. D: alunite and/or kaolin group abundance index coloured by the related mineral species index. 62

Figure 30 Sulphate species variations in MOD4. A. Plot of the relative absorption depth of the hydroxyl-related overtones in sulphates located at around 1480 nm (y-axis) and at 1760 nm (x-axis). Data points are coloured by the wavelength (nm) of the 1480 nm absorption feature. B. Overlay plot of representative examples of VNIR-SWIR reflectance spectra for K-alunite, Na-alunite and jarosite. 62

Figure 31 Downhole plots for drill core NMOD001 over the depth interval 180 to 481 m. The zone of the highest Au grade is highlighted in pink. A: Sulphate abundance index coloured by Au (ppm) values. B: Sulphate abundance index coloured by the sulphate species index. C: Al-clay abundance index coloured by Al-clay species index. D: alunite and/or kaolin group abundance index coloured by the related mineral species index. Based on the available scanning data (Appendix 7), core trays 17–18 (interval 255.78–265.3 m) and tray 21 (interval 274.25–278.91 m) were either missing or were not scanned with the HyLogger™-3 system. 64

Figure 32 Elevated perspective, near westerly views of (A): Mt Olympus, with the digital terrain model (DTM-brown) showing the Mt Olympus pit outline and the steeply inclined, NW-SE striking Zoe Fault (lilac). The modelled isovolume defines the highest sulphate abundance (yellow) detected spectrally (plunge +20°, azimuth 073°), and, (B) similar view of Mt Olympus with DTM removed to show

modelled Au zones (>0.5 ppm) and occurrence of sulphate (plunge +44°, azimuth 075°). Drill core strings, with labelled collars, are coloured according to the assayed Au grade (ppm). Image scale (metres) are shown in the bottom right-hand corner. 65

Figure 33 Elevated perspective, near westerly (azimuth 073) view of Mt Olympus, without the DTM overlay (same view as in Figure 32), with the location of Mt Olympus (arrowed) and the Zoe Fault (lilac) shown. The modelled isovolumes define (A): Fe-chlorite (dark green), Al-poor mica (blue), sulphate abundance (yellow), and gold (gold at >0.5 ppm), and, (B): cross-section view orthogonal to the Zoe Fault (dip 90°, dip azimuth 300°) with Mg-chlorite (light green), Fe-chlorite (dark green), sulphate abundance (yellow) and gold. Drill core strings, with labelled collars, are coloured according to the assayed Au grade (ppm). Both views at plunge (+020°), azimuth (073°) and image scale (metres) are shown. 66

Figure 34 Au-related mineral alteration patterns and indicator minerals identified in the Mount Olympus area. A - Sandstone (Type-A), B – siltstone (Type-B). A comparison of Hyperspectral (C) and multispectral or ASTER (D) reflectance spectra is shown for indicator minerals associated with sandstone Type-A alteration..... 69

Figure 35 Mt Olympus field ASD spectroradiometer transects E and F compared with ASTER Geoscience Products. A - 1480D field data over the 500K Geological Map; B - 2160D field data over DEM; C - 1480D field data over the ASTER Kaolin Group Index over DEM. D - 2160D field data over ASTER Kaolin Group Index over DEM. 70

Figure 36 False colour ASTER Geoscience products overlaying the DEM (black-white image) of the Mt Olympus area. (A) MgOH Group Content, (B) Opaques Index. Elevated MgOH contents west of My Olympus (white arrow) may be related to pervasive white mica+chlorite assemblages. 71

Figure 37 Comparison of AEM and ASTER Geoscience Products, Mount Olympus area: (A) Bedrock geology (grey - lower Wyloo Group, pink - upper Wyloo Group), locations of HyLogging data (e.g., NMD004) and location of AEM lines FID59 and FID60 showing intersections with major structural/lithological boundaries (NF - Nanjilgardy Fault, OF1 - Fault at southern contact between lower and upper Wyloo Grp., LCN - Fault at northern contact between lower and upper Wyloo Grp.). (B) and (C) MgOH Group Content product (blue - low content, red - high content) over greyscale DEM. The red box outline in (B) shows the MgOH Group content mapped in (C). (D) Conductivity-depth sections from a smooth model (30-layer) inversion of TEMPEST data along AEM line FID59. Solid, vertical black lines (not arrowed) show locations of the Nanjilgardy Fault and the contacts between lower and upper Wyloo Group (OF1, LCN) in AEM and ASTER Geoscience Product. 72

Figure 38 Comparison of AEM and ASTER Geoscience Products, Mount Olympus area, along AEM flight line FID59 showing intersections with major structural/lithological boundaries (NF - Nanjilgardy Fault, OF1 - Fault at southern contact between lower and upper Wyloo Grp., LCN - Fault at northern contact between lower and upper Wyloo Grp.). False-colour ASTER Geoscience Products (A to G), stacked vertically, overlay DEM data (background grey image) in each image strip. Hot or red colours for each ASTER Geoscience Content Product indicate a relatively high content for each Product, whereas cool or blue colours indicate a low content. Hot colours for the AlOH group composition (B) indicate well-ordered kaolinite, and cool colours the presence of dickite. 73

Figure 39 Regolith geochemical data from GSWA's 1994–2001 regional regolith geochemistry dataset: a) SiO_2, b) Fe_2O_3, c) MgO, d) As which shows localised elevated contents (circled in red). 74

Figure 40 False-colour maps of: a) the ASTER Silica Index, and b) modelled SiO_2 distribution using the GSWA regolith geochemistry of WA (GSWA, 2012). Small coloured circles define regolith sample locations. White triangles in the ASTER Silica Index map show the locations of drill cores scanned using the HyLogging system. Pink lines, A, E and F represent transects conducted during fieldwork in July 2014. The SiO_2 interpolation plot (B) was modelled using the kriging method in ArcGIS Spatial Analyst Toolbox, histogram equalized, based on the regolith sample points shown as circles (a and b). The interpolated SiO_2 distribution map (b) shows high wt% SiO_2 values in hot colours (red) and low

wt% SiO_2 values in blue. The red box outline shows the location of the MgOH Group content area mapped in Figure 35. 75

Figure 41 Location of GSWA Regolith samples scanned at GSWA's drill core library, in Carlisle, using an ASD FieldSpec3 spectroradiometer (NF – Nanjilgardy Fault). 76

Figure 42 Mineralogical interpretation of reflectance spectra acquired from 154 of GSWA's regolith sample set based on application of CSIRO's "MFEM" scripts. A: white mica abundance, B: chlorite abundance, C: kaolin abundance, D: kaolin crystallinity. Refer to section 2.3 for a more detailed description of the MFEM scripts. 77

Tables

Table 1. Spectrally determined parameters that relate to 'indicator' mineral groups and their associated geological environment. 21

Table 2 Available diamond drill holes along the Nanjilgardy Fault zone scanned using the HyLogging™-3 system and archived at the GSWA core library (MTO – Mount Olympus area; NF – Nanjilgardy Fault). 26

Table 3 VNIR-SWIR based mineral maps of the 2011 precompetitive WA ASTER Geoscience Products (Cudahy, 2011) and TIR based mineral maps of the 2012 continental scale Geoscience Products (Cudahy, 2012). A rainbow colour look up table was applied to all mineral group content and composition products. In the mineral group content yellow to red colours indicate a high relative content of the respective mineral group. 32

Table 4 Sampling intervals, sample media type and analytical methods applied to selected drill core samples 34

Table 5 Selected drill core samples collected for follow-up mineralogical and composition validation analysis and general observations for each sample 35

Table 6 Geochemical analysis suite and associated analyte detection limits 38

Table 7 COD mineral standards used for mineral identification in X-ray powder diffraction patterns of all drill hole and field-collected samples. 39

Table 8 XRD mineralogy of pulverulent and white, efflorescent coatings observed in sections of deteriorated drill core. 52

Table 9 Comparison of XRD mineralogy and mineralogy identified spectrally from the TSA spectral library for drill core validation samples. 57

Table 10 Classification of drill holes based on Au grade, host rock and alteration mineralogy from both XRD and HyLogging data 58

Table 11 Presence of potential indicator minerals (Quartz vein and fault zone were not adopted as lithological description; Black Shale = Siltstone 2; *not analysed for Au) 66

Table 12 Potential ASTER Geoscience Products for mapping indicator minerals and potential host rocks 70

Acknowledgments

The first two authors (MW and CL) would like to acknowledge funding support of this work by the GSWA through the Exploration Incentive Scheme (EIS)-2 and, in particular to Ian Tyler for supporting this work. Thanks are also given to the helpful GSWA staff at the Perth Core Library for enabling access to drill core and for their assistance in sampling of drill core when required. Sidy Morin (GSWA) assisted in collecting field samples in the Electric Dingo area. All report authors would like to thank Northern Star Ltd, particularly Greg Mills, Dale Annison, Matthew Rolfe and Imogen Fielding for their hospitality and help in the field during a visit to the Mt Olympus mine site and camp during the field campaign undertaken in June/July 2014. In addition, Dale Annison kindly provided the dxf files of the Zoe Fault and DTM of Mt Olympus used in the 3D Leapfrog modelling. Tom Cudahy (CSIRO MRF) provided expert advice and guidance throughout the project, particularly in the early stages of project development. Yusen Ley-Cooper (CSIRO MR) processed the airborne electromagnetic (AEM) data for three Tempest flight lines over the Electric Dingo and Mt Olympus areas. Treavor Beardsmore (GSWA) and Tom Cuday (CSIRO) are thanked for their helpful comments in reviewing an earlier draft of the report.

Executive summary

The Nanjilgardy Fault juxtaposes an inlier of the Proterozoic Lower Wyloo Group and older meta-sedimentary units against the Upper Wyloo Group at the Mt Olympus Au deposit. This fault and related structures are possibly deep-rooted, suture zones that may have provided conduits for mineralising fluids and, hence, define a potentially highly prospective, NW-SE trending corridor for Au mineralisation.

Four Au mineralisation types or associated alteration patterns were identified after comparing the most abundant mineral groups detected by the HyLogger™-3 (white mica, chlorite, kaolin, sulphates, quartz, and carbonate; validated using X-ray diffraction, XRD, and compositional analyses) against lithological logging and gold assay data. Potential hydrothermal alteration phases in common rock types along the Nanjilgardy Fault are Na/K-alunite, kaolin phases (kaolinite, dickite), pyrophyllite, white mica and chlorite.

White mica and chlorite were widespread. White mica has a characteristic hydrothermal spectral signature and occurred throughout alteration footprints for all mineralisation types. Chlorite abundance increased away from mineralisation, but it was difficult to differentiate between regional metamorphic and later hydrothermal varieties. Kaolinite and dickite appeared to occur proximally to all four mineralisation types, but their distribution was restricted to certain intervals in drill cores. Jarosite probably formed during sulphide oxidation.

XRD-determined mineralogy was consistent with that identified using “The Spectral Geologist” TSA_SWIR and TSA_TIR scalars, but only at the mineral group level, such as quartz, kaolin, white mica, and carbonate. TSA mineral identification should, therefore, be limited to the mineral group level.

A 3D model was created of the gold distribution and associated alteration within and around Mt Olympus and, though limited by the small number of drill holes used in the study, revealed: (i) several irregular, poddy, SE-plunging zones of > 0.5 ppm Au (including the largest, now depleted by mining) that are intersected by the Zoe Fault (the most significant structural feature in the area); (ii) that sulphate alteration was proximal to mineralisation on the northern side of the open pit; (iii) that white-mica composition varied with proximity to gold mineralization; and (iv) that chlorite was distally developed.

Comparison of HyLogger™-3 data with ASTER surficial data for Mount Olympus suggests that potential gold-related alteration or structural indicators might be identifiable in the latter. The “Kaolin Group”, “MgOH Group Content” and “Opaques” Indices showed patterns that could be correlated with pervasive chlorite±white mica assemblages or major structures.

The utility of ASTER data for mapping alteration mineralogy and structure at a regional scale was tested, constrained by GSWA regolith geochemistry and inversion modelling of airborne EM data along selected TEMPEST flight lines. At Mt Olympus, ASTER mineral footprints were associated with distinct, conductive, sub-surface geological domains potentially separated by faults. A number of sharp, east-trending conductivity highs occur between larger structures (e.g., the NF and OF1 faults). These coincided with increased ASTER “MgOH Group Content” index values, and may be smaller structures not previously identified in geological mapping (e.g., faults, lithological contacts, bedding-parallel shear zones). There is also a well-defined conductivity contrast south of the NF fault that may indicate another large structure not recognised in 1:500 geological mapping, although there were no corresponding changes in the ASTER “MgOH Group content” index. Correlation of ASTER Geoscience Products with surface geochemical data was only evident using the relatively coarsely spaced, GSWA regional regolith sampling. For example, peaks

in the ASTER “Silica Index” broadly coincided with elevated wt% SiO_2 contents in the GSWA regolith geochemistry data, and were related to distinct lithologies.

Mineralogical variations associated with large and small-scale structures can be defined using remotely sensed AEM and ASTER data, and, therefore, could be used to provide a more robust, first-pass compositional characterisation of the landscape at the regional and/or district scale. Hence, this would help focus regolith geochemical sampling regimes to better target anomalies that may be associated with metalliferous mineralization.

1 Introduction

The northern Capricorn Orogen, encompassing the northern margin of the Ashburton Province, represents one of the major Palaeoproterozoic gold provinces within Australia (Sener et al., 2005) (Figure 1). Along the northern margin of the province, located west and south of the Pilbara craton, a number of gold deposits are situated nearby to major, possibly mantle-tapping, regional structures. The two largest gold deposits occur at Mt Olympus (1.7Moz), hosted by low-grade, metasediments of the Mt McGrath formation, and the Paulsens Mine (1.1Moz), hosted by folded metasediments of the Fortescue Group at the Wyloo Dome (Tyler et al., 2011). The Paulsens and Mt Olympus deposits occur in close proximity to the NW and SE extremities of the Nanjilgardy Fault (NF) (Figure 2), a major NW-SE trending, deep-seated structure that defines a potentially highly prospective corridor for Au mineralisation (NorthernStar, 2013a).

Another major, deep-seated regional structure, the Baring Downs Fault (BDF) located approximately 25 km south of and running sub-parallel to the NF, has recently been recognised and may define another pathway for mineralising fluids (NorthernStar, 2013b) extending the prospective area to the South.

As part of the Exploration Incentive Scheme (EIS) and through exploration company donations a number of diamond cores drilled essentially along strike of the NW-SE trending NF and submitted to the DMP core library, were scanned using the HyLogger™-3 system. Furthermore, preliminary evaluation of available remotely-sensed, WA ASTER mineral data (Cudahy, 2011), and in part processed over the Rocklea Dome (Haest et al., 2012), along the NF showed some regional variation for a number of spectral mineral products (e.g., MgOH, AlOH) that varied along strike from Mt Olympus to Paulsens (Wells et al., 2014).

Thus, the HyLogger™-3 and remote sensing data, such as ASTER, provides a strong platform to develop a spectrally-derived, 3D mineral mapping approach to add value to GSWA's precompetitive spectral data. Therefore, by combining remotely-sensed ASTER mineral map data with proximally derived HyLogging™-3 data, with the mineralogy identified spectrally validated through use of independent techniques (e.g., X-ray diffraction and geochemical analyses), this project presents an opportunity to provide 3D mineral characterisation to enhance our understanding of potential, structurally related alteration footprints that may be associated with Au-mineralisation along the NF corridor.

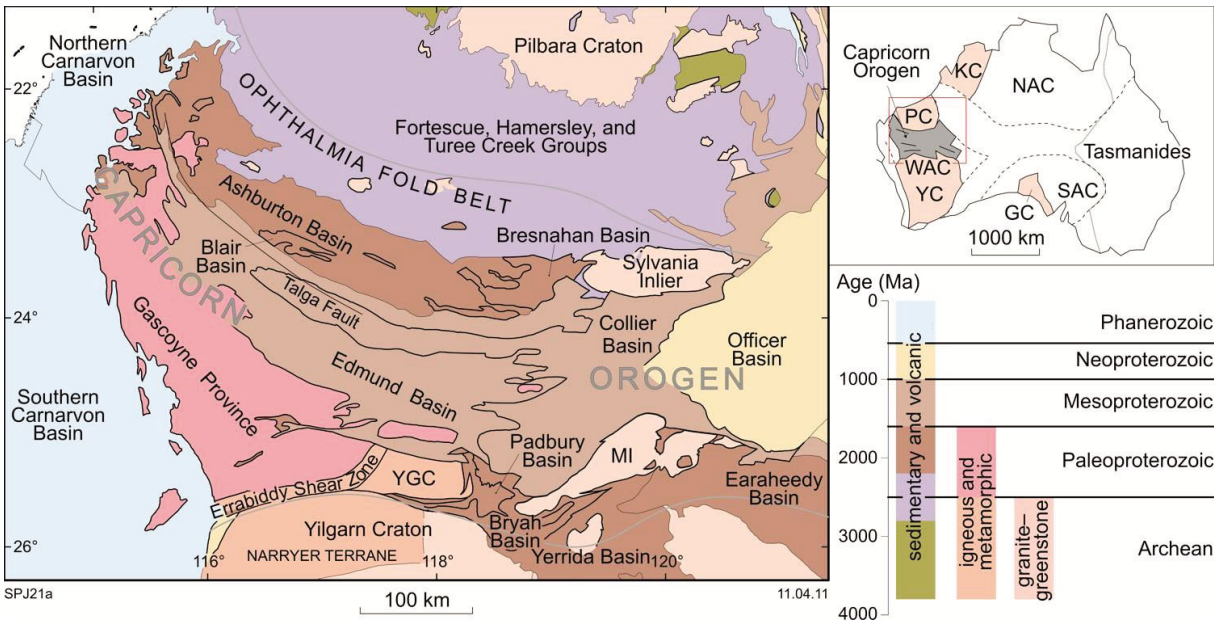

Figure 1 Location of the Capricorn Orogen and major elements of surrounding cratons and basins, with general age of the main rock types. Paleoproterozoic crustal elements are shown (see inset) for the western part of the Capricorn Orogen (KC = Kimberley Craton; NAC = North Australian Craton; SAC = South Australian Craton; WAC = Western Australian Craton), and Archean cratons (YC = Yilgarn Craton; PC = Pilbara Craton; GC = Gawler Craton). Figure modified from Johnson et al. (2013).

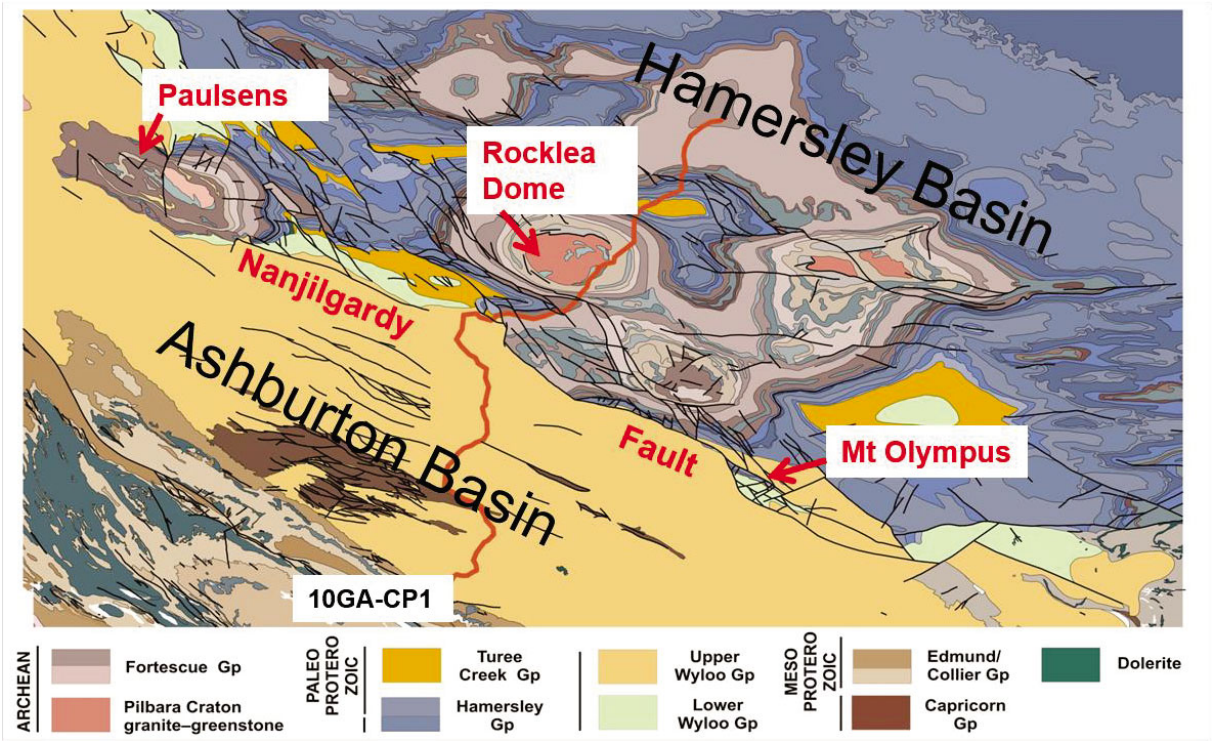

Figure 2 Regional geological setting of the Capricorn Orogen, location of the Nanjilgardy Fault and the Paulsens and Mt Olympus gold deposits. Location of one of the Capricorn Orogen seismic lines, 10GA-CP1 (orange line) across the Nanjilgardy fault is also shown.

1.1 Scope

The findings and conclusions of this study present an integrated, proximal and remote spectral reflectance evaluation of potentially Au-related mineral footprints within the vicinity of the Mt Olympus Au-deposit. This was principally because of the greater drilling density of drill holes in close proximity to Mt Olympus. Of a total of 24 drill holes scanned by the HyLogging™ system, two were drilled as part of the EIS program and the remainder donated to the Perth Core Library by Sipa Resources. A majority (14) of the drill holes fall within the Mt Olympus project, with the ten remaining holes occurring within Northern Star Resources (NSR) tenements along the NF.

Primarily, HyLogging-3™ drill-core data (Section 2.1) and ASTER (Section 2.4) data were integrated within a validated mineralogical framework on the basis of the X-ray diffraction (XRD) and compositional analysis of surface regolith and outcrop material, and selected drill core samples from key drill holes. This approach was used to aid refinement of the alteration mineralogy at Mt Olympus by:

1) Characterising the surface expression of mineral assemblages found in the drill core data, and

2) Evaluating any broad-scale changes indicative of alteration footprints that may be associated with gold or base metal mineralisation along the NF corridor.

Close collaboration with GSWA staff was key to the assembly, assessment, processing and interpretation of the HyLogger™-3 (VNIR, SWIR and TIR) data.

OTHER GEOPHYSICAL DATA-SETS

Initial definition of the project scope, as outlined in the June 2014 preliminary report, described the integration of other data sets, such as seismic, radiometric and AMS data, depending on their availability. Proprietary issues with the airborne, multispectral (AMS) data and uncertainties regarding their quality precluded this data set from being integrated within the current study. Seismic data from the 10GA-CP seismic traverse line (Figure 2), though suitable for probing to Moho depths, is unsuitable (noisy) for evaluating shallow (<500 m depth) changes in lithology. Airborne electromagnetic (AEM) data, acquired by GSWA in 2013–2014, was accessed and inversion modelling conducted for several flight lines over the Mt Olympus area with the goal of defining shallow (<400–500 m) structural features and their relationship to mineral spectral distribution patterns (refer to section 2.9 for a more detailed discussion).

1.2 Regional Geology

The regional geology of the Capricorn Orogeny has been extensively investigated in the past (e.g., Morant and Doepel, 1997; Piranjo, 2004; Sener et al., 2005; Tyler et al., 2011), and recently Johnson et al. (2013) provided a regional overview of the crustal architecture and associated metallogeny of the Capricorn Orogeny. Hence, in view of previous work, the geological setting of the Capricorn Orogeny, stratigraphy and the general mineralisation characteristics at Mt. Olympus are only summarily discussed.

The study area is located near the northern margin of the Ashburton Basin, an arcuate belt of meta-sedimentary and volcanic Proterozoic rocks, which abuts the southern margin of the Hamersley Basin, representing an Archaean to early Proterozoic basinal system (Morant and Doepel, 1997). A generalised stratigraphy and timing of Au mineralisation events at Mt Olympus is shown in Figure 3.

Deposition of the upper Hamersley Basin (Turee Creek Group) and lower unit of the Ashburton Basin (lower Wyloo Group) took place during the 2215–2145 Ma Ophthalmia Orogeny when the Pilbara Craton collided with the Glenburgh Terrane of the Gascoyne Province (Johnson et al., 2013). Formation of the upper Wyloo Group, thought to be a foreland basin, occurred with the onset of early deformation of the 1820–1770 Ma Capricorn Orogeny (Johnson et al., 2013).

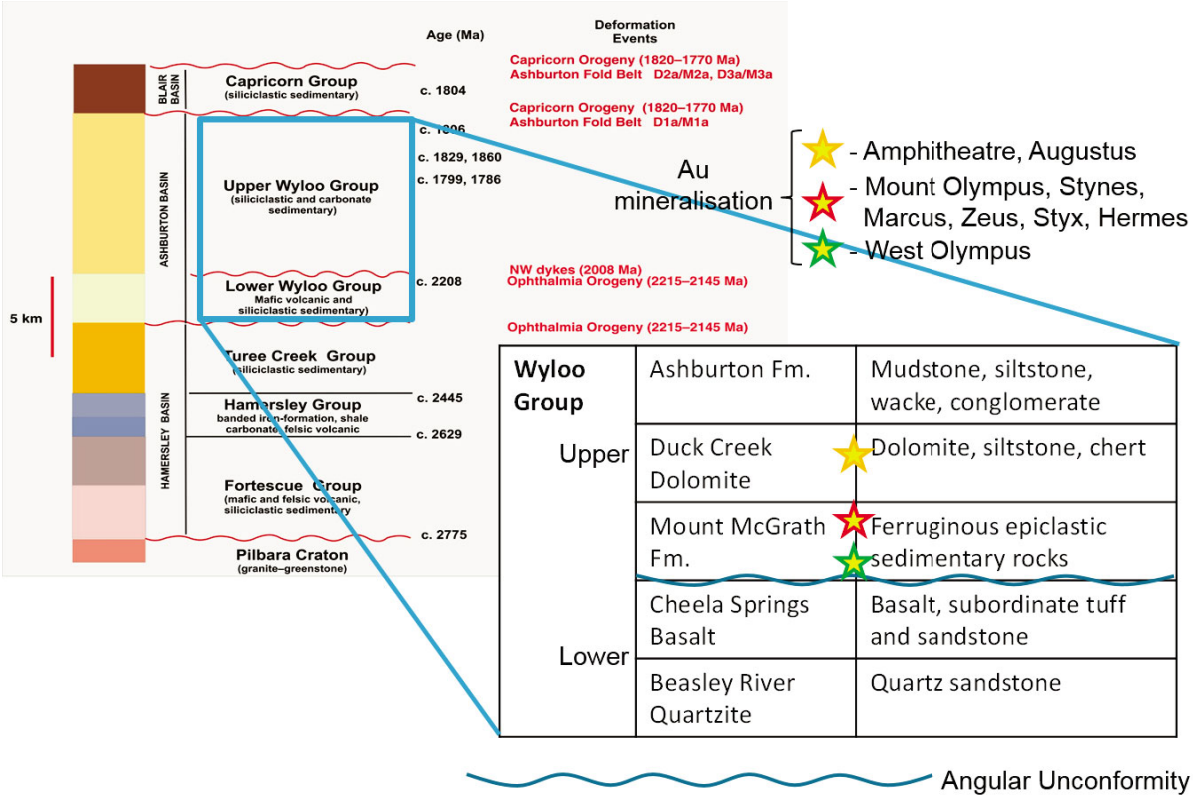

Figure 3 General stratigraphic sequence and major orogenic events of the Capricorn Orogeny; modified from Johnson et al. (2013). Regional stratigraphy of the Wyloo Group showing gold mineralisation at Mt Olympus is hosted mainly by meta-sediments of the McGrath Formation but also by the Duck Creek Dolomite; modified from Tyler and Thorne (1990).

The Lower Wyloo Group has a maximum thickness of ≈3 km (near the southern Pilbara margin) and comprises conglomerate, sandstone, mudstone, basalt, chert and, locally, stromatolitic dolomite of the Beasley River Quartzite and Cheela Springs Basalt, later intruded by dolerite dykes and sills (Figure 3). The overlying Upper Wyloo Group is an ≈7.5 km thick, meta-sedimentary sequence of wacke, mudstone, ferruginous mudstone, BIF, chert, sandstone, conglomerate, felsic and mafic volcanic rocks and, locally, stromatolitic dolomite, that form the Mt McGrath Formation, Duck Creek Dolomite and Ashburton Formation units (Figure 3).

1.3 Mineral Systems

In a recent review of the crustal architecture and associated metallogeny of the Capricorn Orogeny, Johnson et al. (2013) provided a broad overview of the mineral prospectivity of the region. In noting the presence of a range of deposit types, such as world-class iron ore deposits in the Hamersley Basin, Cu-Au volcanic-hosted massive sulphides (VHMS) in the Bryah Basin, orogenic lode-gold deposits (e.g., Paulsens and Mt Olympus) and various intrusion and shear-zone related, small base metal-W-REE-U occurrences

(e.g., Tyler et al., 2011), Johnson et al. (2013) emphasized the importance of large, crustal-scale structures, such as the Nanjilgardy Fault, as key to the regions mineral prospectivity. These large-scale structures are considered to provide a deep-seated plumbing system, focussing fluid flow and energy flux of the mineral system from the mantle into the upper crust (Johnson et al., 2013).

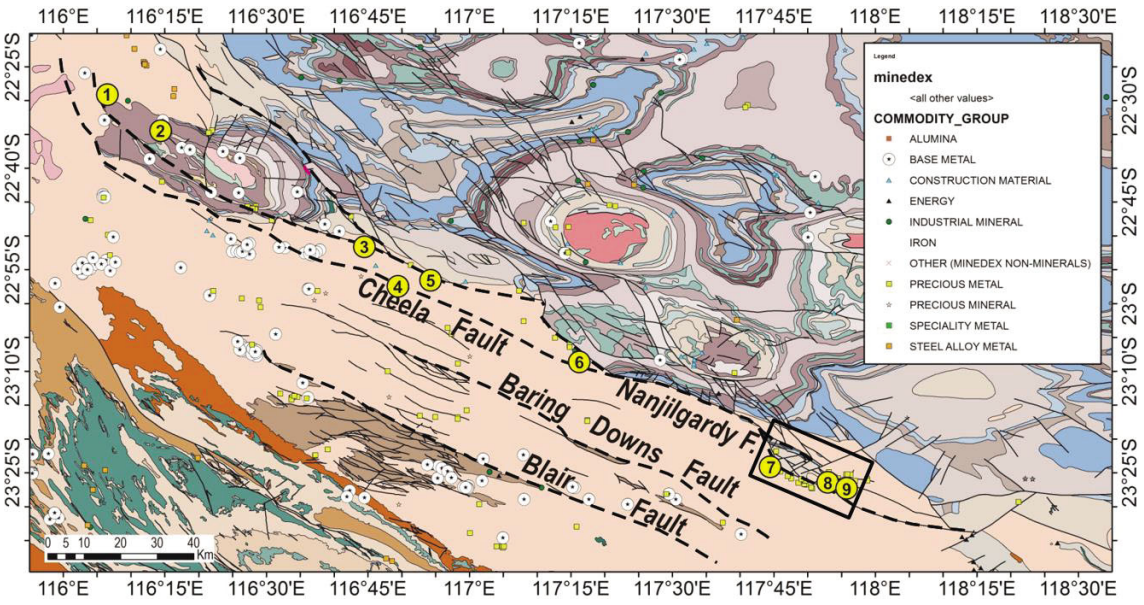

Figure 4 Commodities according to Minedex over the regional bedrock, geological map (500K) of the project area, with the WNW-trending Nanjilgardy Fault separating the Hamersley Basin in the Northeast from the Ashburton Basin in the Southwest. Black frame 'A' highlights the Mount Olympus case study area. Numbered circles in yellow are HyLogging™ data available for this project (1 – MD003; 2 – PDU3000, PDU3001, PDU3002, PDU3003; 3 – AWD003; 4 – NMD001; 5 – EDD005; 6 – ID001; 7 – LD004; 8 – MOD3 - MOD8, MOD11 - MOD14, MT090, NMOD001, NMOD002, NMOD004, NMOD005; 9 – SPD001).

At Mt Olympus, which lies along the Nanjilgardy Fault, gold mineralisation is hosted about equally by coarse and fine-grained, epiclastic sedimentary rocks (sandstone/siltstone) of mainly the Mt McGrath Formation but also by the Duck Creek Dolomite (Figure 3) (Sener et al., 2005). The Mount Olympus area (i.e., Xanadu-Mount Olympus Au field (Piranjo, 2004) comprises structurally-controlled, precious metal lodes and polymetallic veins, associated with the regional scale, NW-trending, dextral Nanjilgardy Fault (NF) system. The Nanjilgardy Fault, juxtaposing an inlier of Lower Wyloo Group and older sedimentary units against the Upper Wyloo Group, represents a possibly deeply rooted, suture zone and is discussed as pathway for mineralising fluids (Tyler et al., 2011; Johnson et al., 2013).

Gold mineralisation at Mt Olympus is dated at 1738 ± 5 Ma based on analysis of xenotime grains and formed at up to 350°C between 1–2 kbar (Young et al., 2003). The period 1740–1730 Ma represents a major, wide spread Au mineralisation episode in northern Australia, involving major hydrothermal gold events linked to continental-scale tectonism, associated with near-final(?) amalgamation of Archean and Proterozoic crustal domains, involving the Ashburton Province, Northern Yilgarn margin and Southern Pilbara cratonic margin (Sener et al., 2005; Johnson et al., 2013).

Gold mineralisation at Mt Olympus is associated with strong sulphide alteration, with As-pyrite and/or pyrite as the main sulphide mineral. Gold occurs as microscopic inclusions or particles in As-pyrite or as fracture fillings in pyrite, and as macroscopic Au with quartz-veins (Morant and Doepel, 1997; Tyler et al., 2011). Gold is not strongly correlated with either sulphide content or quartz veining but appears associated with silica, sericite and carbonate alteration (Morant and Doepel, 1997). These mineralisation

characteristics are typical of Carlin-style Au mineralisation, although Young et al. (2003) argued that mineralisation associated with transpressional deformation also shows similarities with orogenic gold. (Piranjo, 2004) suggested that the (Xanadu)-Mt Olympus mineralisation style be classed as epigenetic, with quartz as the alteration mineral/s.

1.4 Minerals as indicators for diagenesis, metamorphism, hydrothermal alteration and weathering

Certain mineral groups and phases have been described in the literature as indicators for, 1) diagenetic and metamorphic overprinting, 2) hydrothermal alteration potentially associated with mineralisation, and 3) weathering processes. All of these processes and resulting mineral assemblages have to be differentiated from the primary mineral assemblage. Many indicator minerals can form in more than one of the above geological environments, requiring the consideration of the impact of all related processes on the resulting mineral assemblage. In the following discussion, the diagenetic, metamorphic and hydrothermal formation processes of two mineral groups of major importance, namely the Al-clay minerals and the sulphates, for the quest for hydrothermal mineral footprints along the Nanjilgardy Fault are summarised. Some indicative spectral mineral parameters or indices, useful for the identification of Al-clay and sulphate minerals, are listed in Table 1.

Table 1. Spectrally determined parameters that relate to 'indicator' mineral groups and their associated geological environment.

Parameter	Mineral Group	Geological environment	Active wavelength range [nm]
Advanced argillic alteration	Pyrophyllite	Porphyry	~ 2160
Advanced argillic alteration	Alunite	Epithermal	~ 1480, ~ 1760
(Advanced) argillic alteration	Kaolinit/Dickite	Epithermal	~ 2160/2180, ~ 2200
Tschermak exchange due to pH and/or T	White mica, Al-smectites	Hydrothermal (metamorphic?)	~ 2200

DI-OCTAHEDRAL AL-CLAY MINERALS

Di-octahedral Al-clay minerals comprise four mineral groups:

1) kaolin group (also called kandites), comprising kaolinite, halloysite, dickite and nacrite,

2) pyrophyllite

3) white micas, including the muscovite-celadonite series and paragonite, as well as illitic types

4) Al-smectites, including the beidellite-montmorillonite series

Kaolin-group minerals

Kaolin group minerals (1:1 phyllosilicate, "7Å phase") can be formed during diagenesis, in hydrothermal systems and during weathering processes. Kaolin group minerals that form in soils and laterites are readily transformed during diagenesis. This process involves the recrystallisation of kaolinite and the loss of ferric iron (Meunier, 2005), which can often be found in soils. Dickite is the more stable polymorph of the kaolin

group minerals, which explains the replacement of kaolinite by dickite with increasing diagenetic grade. The transformation from kaolinite to dickite occurs between 100° and 160°C at 0.5 to 0.8 kbar (Ehrenberg et al., 1993; Fialips et al., 2003). However, these authors noted that the thermodynamic properties of kaolinite and dickite were very close, such that the presence of impurities may influence the specific transformation pathway. An example of this is the earlier work by Zotov et al. (1998) which suggested that kaolinite was metastable to dickite to temperatures of at least 350°C. Nacrite rarely forms during diagenesis, but was described in sediments containing bitumen or coal (Meunier, 2005).

In hydrothermal systems, such as porphyry and epithermal systems, kaolin group minerals are major indicators for argillic and advanced argillic alteration, formed during extended acidic leaching (Tosdal et al., 2009). In acidic conditions, aluminium becomes more soluble when compared to silica, resulting in siliceous domains that are surrounded by argillic alteration, which can comprise kaolinite, dickite and nacrite. In weathering environments (e.g., regolith systems) kaolinite (and halloysite), for example, are typical weathering products of feldspars (± muscovite) and are more abundant in regolith formed on mafic and felsic rocks than on ultramafic rocks (Anand and Paine, 2002). Other environments where kaolin group minerals can be formed include, for example, acid lakes (Anand and Paine, 2002).

Al-smectites

Al-smectites (2:1 phyllosilicate, “10Å phase”, with interlayer cations, swelling) can be formed during diagenesis, hydrothermal alteration and during weathering processes. Diagenesis of sedimentary rocks causes the transformation of clay-minerals into low-charge montmorillonite at temperatures from 50° to 80°C. With increasing diagenesis and depending on availability of K, smectite is transformed into illite, beginning with interlayered I/S minerals and, finally, well ordered illite (Meunier, 2005) (Figure 5). The most common smectites in sedimentary rocks are bentonites, which are nearly monomineralic montmorillonite with very low porosity and permeability (Sucha et al., 1993). A closed system results from each clay bed experiencing diagenesis independently from other layers (Meunier, 2005), with important implications for the composition of such rocks and fluid flow in sedimentary systems.

In hydrothermal systems, smectites are formed between the inner argillic alteration halo and the outer propyllitic alteration, reflecting the more intermediary pH conditions and lower temperature away from the acidic hydrothermal fluids in the centre of the mineral system (e.g., Figure 5). Intermediate beidellite-montmorillonites can form together with other smectites (e.g., saponite) and in the clay caps of hydrothermal systems at temperatures < 130°C (Meunier, 2005). The Al-smectites are represented by beidellite at higher temperature (185–210°C), formed along permeable, unsealed fractures (Meunier, 2005), and references therein). Along hydrothermal veins, a zoning of low charge smectites associated with illite to an outward increase of high charge smectite was described by Bouchet et al. (1988).

Pyrophyllite

Pyrophyllite (2:1 phyllosilicate, “9Å phase”, without an interlayer sheet) forms mainly due to hydrothermal alteration of feldspar. Together with alunite, pyrophyllite forms in the vicinity of hydrothermal systems as a result of acidic leaching in the central part of the mineral system.

White mica

White micas (2:1 phyllosilicate, “10Å phase”, with interlayer sheet, non-swelling) form during diagenetic and metamorphic conditions and are important indicator minerals in hydrothermal systems (Doublier et al., 2010). Illite may form during diagenesis by the transformation of smectite, but may also form directly on, for example, kaolinite or quartz. The driver for the formation of illite during diagenesis can be the dissolution of K-feldspars or the invasion of K-rich brines, possibly originating from evaporitic deposits

(Meunier, 2005). Notably, during the diagenesis of shales, illite mainly results from the transformation of smectite via interlayered I/S. Interlayer cations may provide important information about the formation of white micas. According to Velde and Meunier (2008), no Na or Ca micas are formed below 250°C, which excludes the possibility of Na- or Ca-micas being formed under diagenetic conditions.

In porphyry systems, white mica forms via hydrolytic alteration of feldspar initially between 300 to 550°C above the higher T potassic alteration zone (i.e., dark micas and K-feldspar) and below the advanced argillic alteration zone (i.e., alunite ± pyrophyllite ± dickite/kaolinite), reflecting an upwards decreasing T gradient. However, the collapse of the hydrothermal system can lead to a superposition of white mica alteration on earlier formed potassic alteration (Gustafson and Hunt, 1975). Ruitenbeek et al. (2005) described the growth of white micas in the VHMS system of Panorama (Western Australia) as result of upwelling hydrothermal fluids at temperatures of 175 to 325°C.

Often, a zoning of the composition of white micas is observed in hydrothermal deposits, is manifested in a change of the Tschermak composition ($Al^{IV}Al^{VI}Si^{IV}_{-1}(Fe,Mg)^{VI}_{-1}$) (Duke, 1994). This trend can be from distal high-Al/low-Si micas (e.g., muscovite) to low-Al/high-Si micas (e.g., phengite) proximal to the ore (e.g., Kanowna Belle, WA, Neumayr et al. (2004) or the opposite (e.g., Ann Mason porphyry Cu-Mo deposit, Halley et al. (2015); Sunrise Dam, Blenkinsop et al. (2007)). Numerous reasons for the zoning of white micas in different hydrothermal systems are discussed in literature, such as pH and concentration of ferrous iron and potassium in the hydrothermal fluids (Porphyry Cu, Halley Halley et al. (2015); muscovite = more acidic vs. phengite = less acidic; Panorama VHMS, van Ruitenbeek et al. (2012) and temperature (e.g., muscovite = low-T recharge zones *vs.* phengite = high T hydrothermal fluids). For comparison, Duke (1994) and Duke and Lewis (2010) described for metamorphic sedimentary rocks the correlation of high-Al micas with higher T. Below 300°C, illite grows as the K-deficient variety of white micas.

Weathering of sulphide-rich rocks can generate sulphuric acid and supergene leaching, which ultimately destroys white micas and produces kaolin-group minerals.

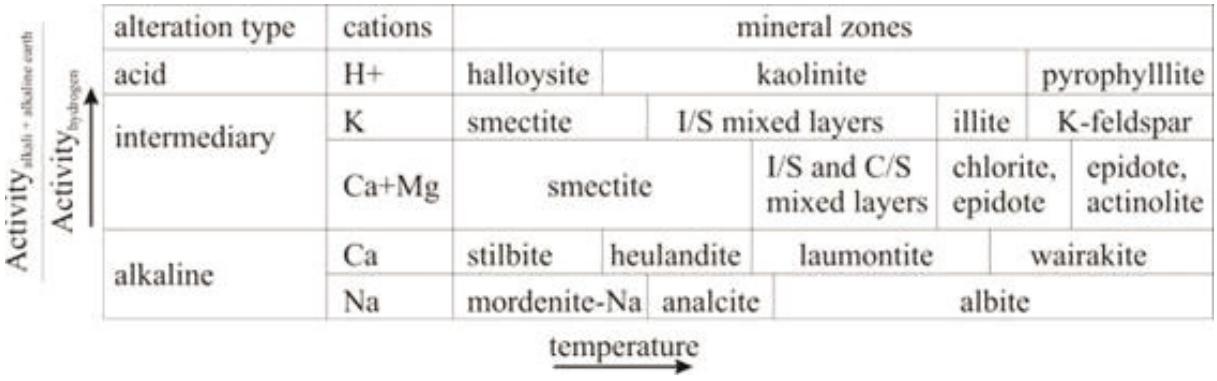

Figure 5 Hydrothermal alteration mineralogy as controlled by cation activity and temperature in hydrothermal systems; modified from Utada (1980).

SULPHATES

The main sulphates of relevance in relation to hydrothermal systems are alunite, $KAl_3(SO_4)_2(OH)_6$ and jarosite, $KFe^{3+}_3(SO_4)_2(OH)_6$. Jarosite comprises a sub-group within the alunite group of minerals, all of which are isostructural and have the following general formula, $AB^{3+}_3(TO_4)_2(OH)_6$, where A may be occupied by K, Na, Tl, H_3O, NH_4, Ag, Pb, Ca and Ba. The B site is occupied by Al, Fe^{3+} or Cu, and T is mainly occupied by S but

P, As, V and Si may occur (Gaines et al., 1997). For alunite, replacement of K by Na may occur up to Na/K ratios of 9:2 (Gaines et al., 1997). Similarly, Na-K exchange in jarosite has been reported to Na:K ratios of 1:2.4 but a complete solid solution series between jarosite and the Na-form has not been demonstrated (Gaines et al., 1997).

Alunite and jarosite are both formed by the action of H_2SO_4, derived from the oxidation of pyrite and other sulphides, on nearby rocks, where 'alunitization' is usually accompanied by kaolinization and silicification, and the formation of jarosite is usually associated with the formation of goethite (Gaines et al., 1997).

Experimental studies have helped to establish the stability ranges of alunite and jarosite under hydrothermal conditions (Stoffregen, 2006). The findings of Stoffregen (2006) demonstrated that natrojarosite was stable relative to hematite at 200°C with an H_2SO_4 concentration equivalent to 0.68 m (molality), whereas natrojarosite is unstable relative to hematite at 250°C (Stoffregen, 1993). These extreme concentrations of H_2SO_4 required for the stability of jarosite are consistent with its rare occurrence in hydrothermal systems. Indeed, decreasing temperature increases the stability field of jarosite consistent with the common occurrence of jarosite in surficial terrestrial environments (Arslan and Arslan, 2003; Stoffregen, 2006).

Evaluation of the alkalie exchange rate between alunite and jarosite indicated that the partitioning of Na and K was similar but that increasing temperature favoured the Na end-member for both phases (Stoffregen, 2006). A complete solid solution was demonstrated between alunite and natro-alunite for temperatures in the range 350–450°C though a solvus was suggested to extend to as low as 250°C (Stoffregen and Cygan, 1990). In the case of jarosite, a solid solution between jarosite and natro-jarosite was shown to occur at 200–250°C (Stoffregen, 1993).

2 Methods (Applied Technology and Software)

2.1 HyLogging™ (Proximal Sensing)

The HyLogger™-3 system at GSWA's core library in Carlisle was developed by CSIRO to enable the rapid acquisition of reflectance spectra from drill cores, covering the VNIR (0.39 to 1.0 μm), SWIR (1.0 to 2.5 μm) and TIR (6.5 to 14.5 μm) wavelength regions of the electromagnetic spectrum to determine the presence, abundance, composition and other characteristics of minerals in drill core samples. Reflectance spectroscopy is a non-invasive technology that, depending on the wavelength region, penetrates the upper few microns or only reflects from the surface of the analysed material. The HyLogging™-3 system uses a computer-controlled, X-Y table moving in a serpentine path under a fixed spectrometer and illumination system to log contiguous reflectance spectra in the VNIR, SWIR and TIR wavelength ranges along the drill core. High resolution (0.1 mm resolution) visible colour images of the drill core were collected during scanning using an in-built, line-scan camera. The reflectance spectra were resampled to 8 nm spectral resolution and 1 cm spatial resolution in The Spectral Geologist software (TSG™).

Raw HyLogging™ spectral data for the 24 drill holes (Table 2; Figure 6) were evaluated and processed using The Spectral Geologist (TSG)–Core version software version 7.1.0.062 developed by CSIRO (http://www.thespectralgeologist.com , and refer to Berman et al. (1999) and Yang et al. (2005) using the method of Cudahy et al. (2008). Initial spectral processing involved generation of Level 2 spectral products (Hancock and Huntington, 2010), including:

- Final masks to hide non-geological materials (i.e., removal of 'artificial spectral signatures, such as those arising from plastic or wood, or from empty core tray sections).
- Depth logging
- Trays and mosaic imageries
- User TSA minerals for VNIR, SWIR and TIR (see TSA chapter)
- New numeric scalars (see MFEM scripts chapter)
- Importing geological logs and assay data (mainly Au values)

Subsequent spectral analysis and extraction of mineral related, spectral products or indices was undertaken using two approaches: The spectral interpretation algorithm, The Spectral Assistant (TSA™) (Berman et al., 1999), and the CSIRO multiple feature extraction method, MFEM. Each spectral processing method is discussed more fully in the following sections (Cudahy et al., 2008; Laukamp et al., 2010).

Table 2 Available diamond drill holes along the Nanjilgardy Fault zone scanned using the HyLogging™-3 system and archived at the GSWA core library (MTO – Mount Olympus area; NF – Nanjilgardy Fault).

Well Name	Archived	Scanned with VNIR-SWIR	Scanned with TIR	Project (GSWA)	Area	Confidential
AMODD0026	Carlisle	30-Jul-13	30-Jul-13	MTO	MTO	open file
AMODD0028	Carlisle	6-Aug-13	6-Aug-13	MTO	MTO	open file
AWD003	Carlisle	30-Jan-12	30-Jan-12	NF (Ashburton)		open file
EDD005	Carlisle	25-May-12	25-May-12	NF (Ashburton)		open file
ID001	Carlisle	5-Jun-12	5-Jun-12	Nanjilgardy (Ibex/Bacome)		open file
LD004	Carlisle	8-Jun-12	8-Jun-12	Nanjilgardy (Romulus)		open file
MD03	Carlisle	17-Jan-12	17-Jan-12	NF (Ashburton)	MTO	open file
MOD3	Carlisle	18-Jun-12	18-Jun-12	Nanjilgardy (MTO)	MTO	open file
MOD4	Carlisle	7-Jun-12	7-Jun-12	Nanjilgardy (MTO)	MTO	open file
MOD5	Carlisle	22-May-13	22-May-13	Nanjilgardy (MTO)	MTO	open file
MOD6	Carlisle	23-May-13	23-May-13	Nanjilgardy (MTO)	MTO	open file
MOD7	Carlisle	24-May-13	24-May-13	Nanjilgardy (MTO)	MTO	open file
MOD8	Carlisle	27-May-13	27-May-13	Nanjilgardy (MTO)	MTO	open file
MOD11	Carlisle	21-Jun-12	21-Jun-12	Nanjilgardy (MTO)	MTO	open file
MOD12	Carlisle	28-May-13	28-May-13	Nanjilgardy (MTO)	MTO	open file
MOD13	Carlisle	14-Jun-12	14-Jun-12	Nanjilgardy (MTO)	MTO	open file
MOD14	Carlisle	29-May-13	29-May-13	Nanjilgardy (MTO)	MTO	open file
MTO90	Carlisle	21-May-13	21-May-13	Nanjilgardy (MTO)	MTO	open file
NMD001	Carlisle	4-Jun-13	4-Jun-13	Nanjilgardy (MTO)		open file
NMOD001	Carlisle	25-Jun-12	25-Jun-12	NF (Olympus-Zeus)		open file
NMOD002	Carlisle	6-Jun-13	6-Jun-13	NF (Olympus-Zeus)		open file
NMOD004	Carlisle	4-Jul-12	4-Jul-12	NF (Olympus-Zeus)		open file
NMOD005	Carlisle	10-Jul-12	10-Jul-12	NF (Olympus-Zeus)		open file
SPD001	Carlisle	18-Jul-12	18-Jul-12	NF (Olympus-Zeus)		open file

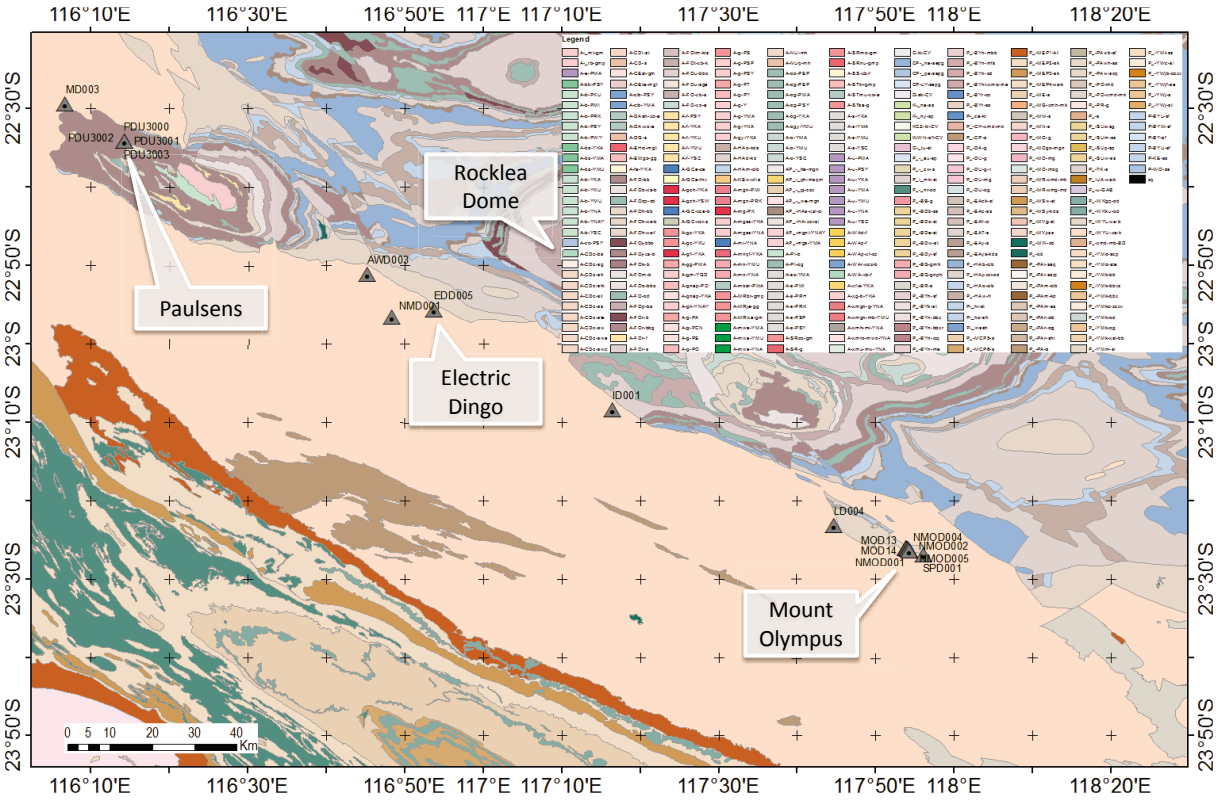

Figure 6 Location of drill holes in the study area, acquired through the EIS program or donated by Sipa Resources to the GSWA Perth Core Library.

2.2 TSA

The Spectral Assistant (TSA™) method of hyperspectral data interpretation is an algorithm built into TSG™ software package for rapid, automated identification of mineral assemblages in drill core, chips and rock or mineral powders (Berman et al., 1999).

TSA™ is designed to un-mix spectra by using a reference mineral spectral library with currently 12 minerals in the visible to near-infrared (VNIR) wavelength range (14 spectra), 47 minerals in the shortwave infrared (SWIR) wavelength range (53 spectra) and 110 minerals (157 spectra) in the thermal infrared (TIR) wavelength range. Each spectrum is calculated using a canonical variants analysis method or, in other words, each measured spectrum is modelled against the spectra database and extracts either two (for VNIR and SWIR) or three (for TIR) best matched minerals along with estimates of their relative proportions and fitting errors. However, as with any automated interpretation system, the TSA scalars should be checked by the user (geologist) to avoid obvious, erroneous mineral identification, such as modelling unusual minerals to the noisy spectra of dark rocks or un-mixing spectra with geologically ambiguous results. Thus, the user may personalise or refine the TSA matching scalars (Figure 7) (uTSAV, uTSAS and uTSAT), and together with depth logging, final mask generation and tray images define a minimum level of processing referred to as Level 2 HyLogging™ data processing, which can be made available to the public domain (Hancock and Huntington, 2010).

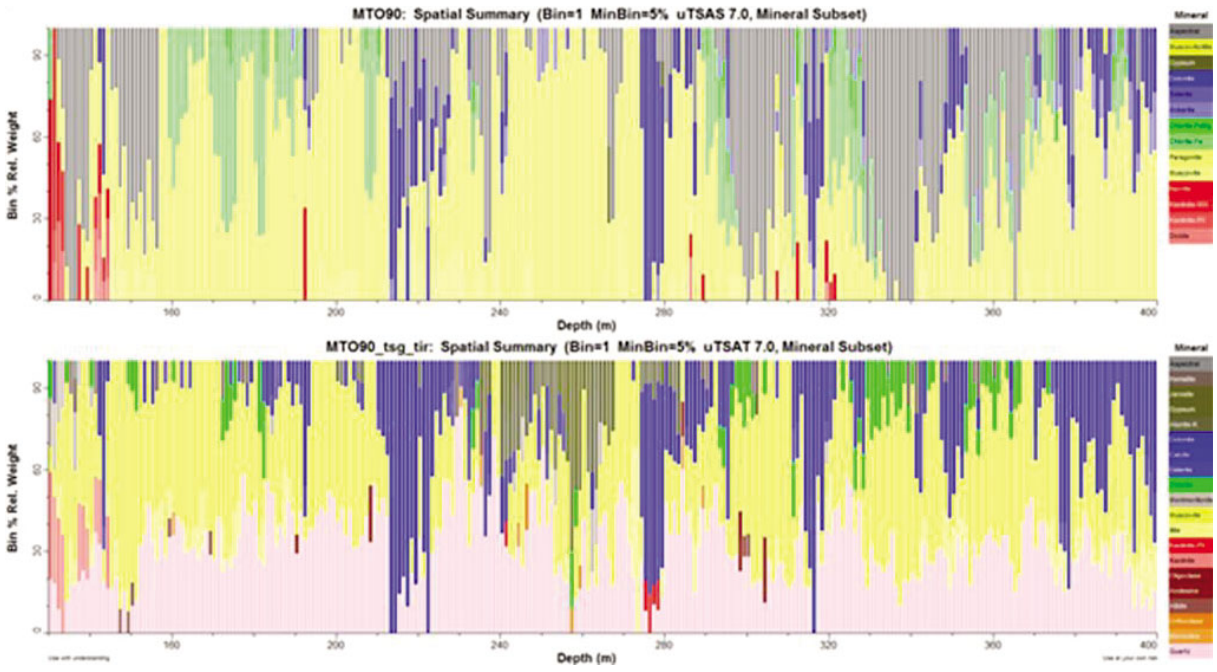

Figure 7 TSG summary logs showing user TSA mineral distribution and relative abundance in the SWIR (top) and TIR (bottom) wavelength regions. Drill hole MTO90 was used as the example.

Overall, the TSA™ mineral identification method provides very rapid characterization of drillhole mineralogy and alteration trends. However, it is always recommended to validate any results using alternative spectroscopic methods, such as parameterizing the spectral shapes with indices or scalars, or other independent techniques, such as XRD and scanning electron microscopy analysis methods (SEM-EDX).

2.3 MFEM

The relative abundance and composition of mineral species derived from HyLogging™ data using the MFEM scripts are displayed in this report as landscape-style plots. Figure 8 demonstrates the strategy behind this visualisation. Figure 8A shows the abundance of white mica (y-axis) in a drill core from 105 to 120 m depth (x-axis). Every black spot represents one measurement. Figure 8B shows the composition of white mica (y-axis and colour scale) in the same drill core interval, with the values representing the wavelength position of the 2200 nm feature diagnostic for white mica. Short wavelengths (ca. 2195 nm) indicate Al-rich white micas (e.g., paragonite, muscovite), whereas longer wavelength values (ca. 2220 nm) represent Al-poor white micas (e.g., phengite). Figure 8C is the combination of plots A and B, with the white mica abundance displayed on the y-axis and the white mica composition represented by the colour scale. Due to the high sample density (1 cm steps) a number of measurements seem to be from the same sample. Figure 8D displays detail for the 109.5 and 110.5 m interval, and confirms that the data points are individual samples.

Most of the remaining MFEM scripts are displayed in the same way with the relative abundance values on the y-axis and compositional parameters in the colour scale. An exemption to this is, for example, the quartz abundance, coloured by the “Reststrahlen feature position”, which provides an estimate of accuracy of the quartz abundance script as well as the degree of mixing with other silicates. MFEM scripts applied in this project are tabulated in Appendix 1.

The VNIR, SWIR and TIR derived mineral abundance and composition information of the drill cores were also stored in TSG-files that are available from the report authors. A free TSG viewer to query the data in detail can be downloaded from: http://www.thespectralgeologist.com/tsg_viewer.htm.

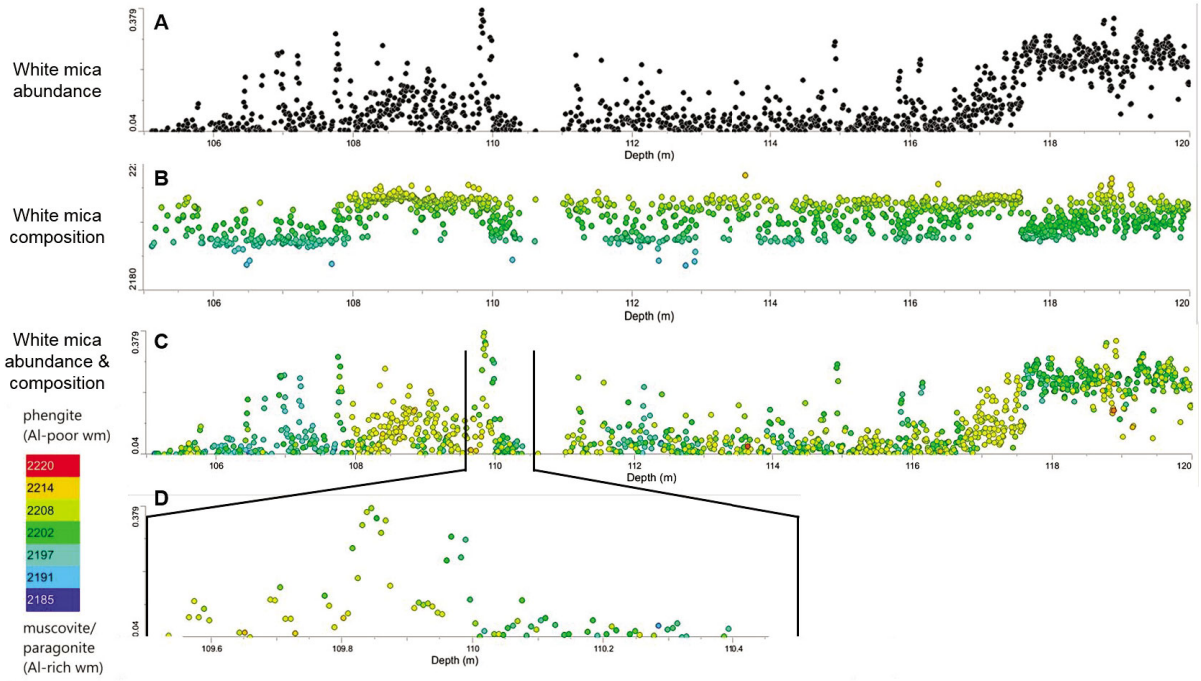

Figure 8 MFEM white mica parameters: a) relative white mica abundance; b) white mica composition: short wavelength values – Al-rich white mica (e.g., paragonite, muscovite), long wavelength values – Al-poor white mica (e.g., phengite); c) relative white mica abundance coloured up by white mica composition; d) detail of 109.5 to 110.5 m of plot c). Colour scale for b), c) and d) bottom right.

The above described MFEM scripts (e.g., white mica abundance) and their subordinate base scripts (e.g., 2160D, 2200D and 2250D) can also be used to establish an overview over the general mineral assemblages in a given data set. An example of this approach is provided in Figure 9, where two scalars were used to investigate the occurrence of kaolinite, alunite, jarosite, muscovite and chlorite using the 2160D and 2250D scalars in drill hole MOD04. For comparison, Figure 9A is coloured by the most dominant SWIR active mineral according to TSA ("Min1 uTSAS"). Kaolinite and alunite plot in the area of high 2160D values along the upper y-axis, as both of these minerals exhibit a major absorption feature at around 2160 nm. In contrast, chlorite and most of the jarosites plot along the x-axis, related to a major absorption feature at around 2250 nm in those minerals. Chlorites plot largely below a 2160D value of 1, as chlorite does not show an absorption feature in the respective wavelength region. Chlorite-bearing samples that plot above a y-axis value of 1 contain probably also kaolinite and/or alunite.

Apart from a quick characterisation of mineral assemblages, these base scripts scatter plots can also be used to investigate the mineral assemblage and associated geochemistry. For example, Figure 9B uses the same spectral indices as Figure 9A, but shows the complete HyLogging data set of the Mount Olympus area and is coloured by the Au content. It is evident from in Figure 9B that Au can be associated with jarosite.

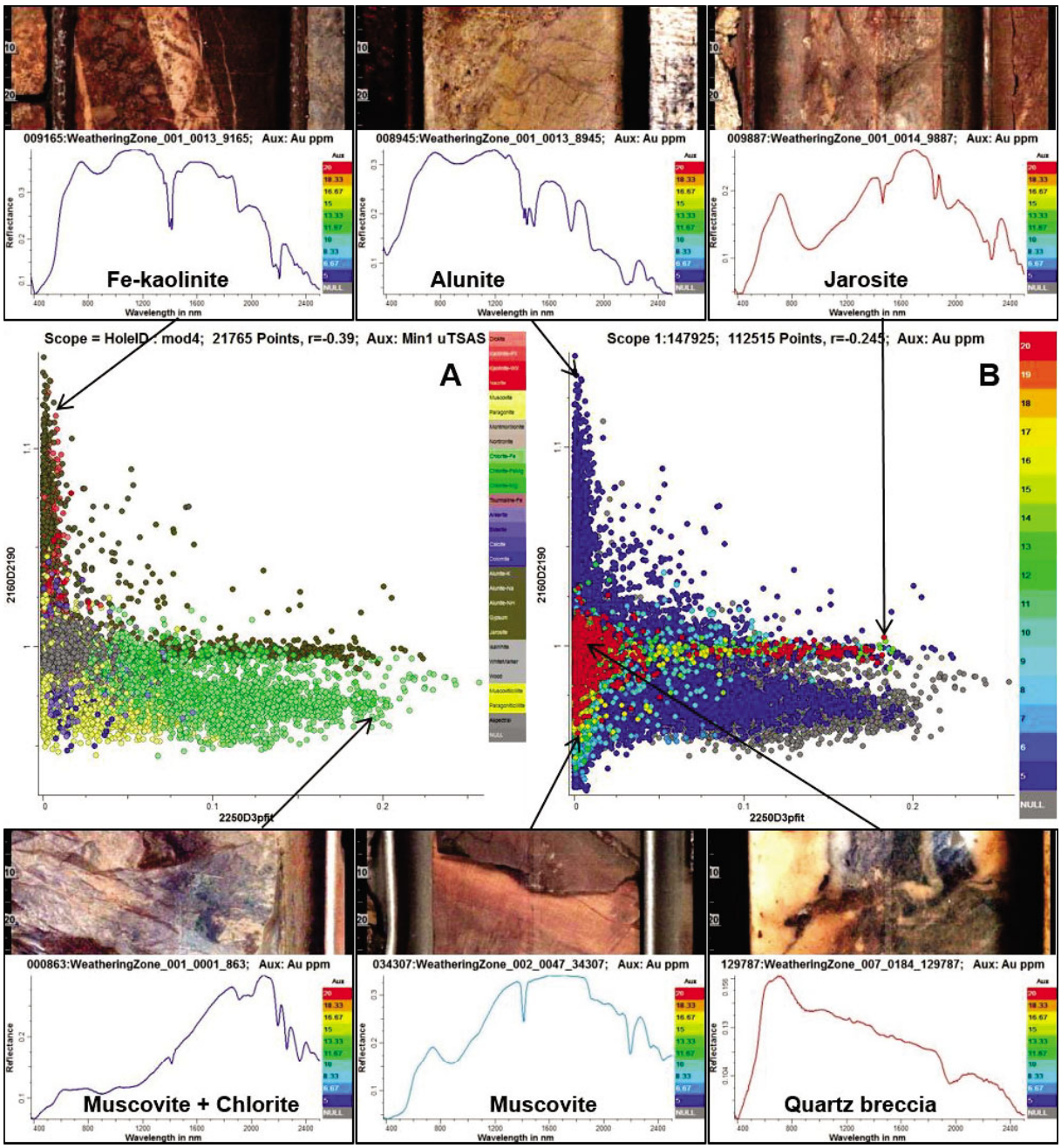

Figure 9 Scatter plots showing the application of the MFEM 2160D (y-axis) and 2250D (x-axis) scripts to aid in the discrimination of alumina-silicates (kaolinite, muscovite) and sulphates (jarosite, alunite). Data points are coloured by (A) TSA mineralogy, and (B) assayed Au values (ppm). The smaller boxed plots show the reflectance spectrum for each of the arrowed points, representative of the main mineral/s group identified, and a digital image of the location for each reflectance spectrum. Drill hole MOD4 was used as the example.

From evaluating the external lithology log and gold assay values and extracting the most abundant mineral groups (e.g., white mica, chlorite, kaolin, quartz, and carbonate abundances), using MFEM scalars (refer to Appendix 1), and TSA summary mineralogical data, the scanned drill holes were classed into groups (Section 4.4). These groups represent varying Au mineralisation types or associated alteration at Mt Olympus and show some lithological, lateral and vertical variation in the alteration mineralogy.

2.4 ASTER (Remote Sensing)

ASTER (Advanced Spaceborne Thermal Emission and Reflection Radiometer) collects 14 spectral bands in the visible-near (VNIR), shortwave (SWIR) and thermal infrared (TIR) that are positioned in “atmospheric windows” (Figure 10) to minimise the impact of atmospheric effects, such as absorption by water vapour and scattering by aerosols (Yamaguchi et al., 1999). The spatial resolution of the ASTER is 15m/pixel in the VNIR, 30m/pixel in the SWIR and 90m/pixel in the TIR with a total swath width of about 60km for all wavelength regions. The single bands cover important wavelength regions, where most of the major rock forming minerals have characteristic absorption bands (e.g., Bands 3 and 4 – ferric oxides; Bands 5 to 9 – AlOH-, FeOH- and MgOH-bearing silicates as well as carbonates; Bands 10 to 12 – quartz and other silicates). This is a major advantage over other multispectral systems, such as the Landsat Thematic Mapper (TM) (Short, 1982), which don't have an appropriate position of their collected bands for distinguishing major mineral groups (Figure 10). However, as a multispectral system, ASTER can only be used to identify the abundance and the composition of mineral groups, whereas hyperspectral remote sensing data can be applied for identifying mineral species and changes in their chemical composition or crystalline order (Hewson et al., 2005; Cudahy et al., 2005). Unfortunately, high quality, space-borne hyperspectral data are not yet commercially available and ASTER remains the only "Geoscience-tuned" satellite sensor to this date, providing spatial mineralogical information from the continental to deposit scale.

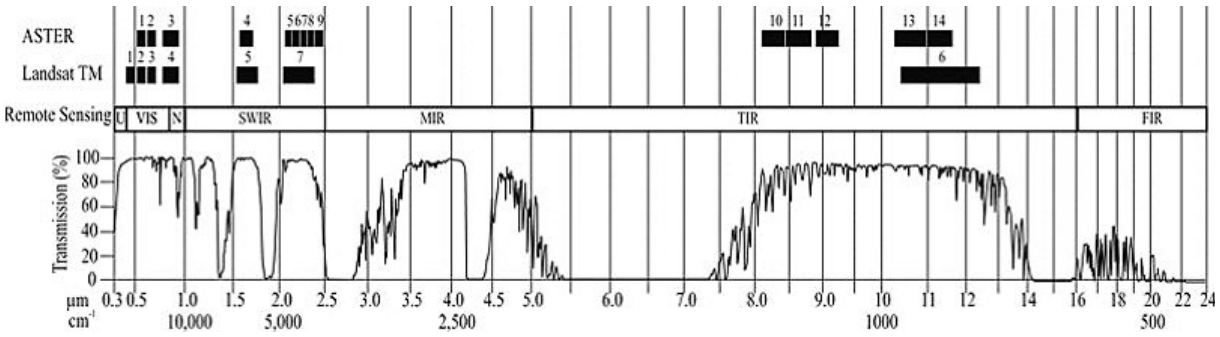

Figure 10 Band coverage of ASTER and Landsat TM across the visible and infrared wavelength regions. Collected bands are located in atmospheric windows, indicated by the generalised atmospheric transmission spectrum at the bottom of this diagram. Generalized atmospheric transmission spectrum of 1 km horizontal air path at sea level conditions of 15° C air temperature, 46 % relative humidity, 1013 mb atmospheric pressure (Laukamp et al., 2013).

For the current project, a suite of precompetitive ASTER Geoscience Products (Cudahy, 2011, 2012) were evaluated for the surface characterisation of rock forming minerals (Table 3). The publically available ASTER Geoscience Products comprise 14 mineral group content and composition maps, such as the AlOH group mineral maps, which show the relative abundance and composition of major Al-bearing clay minerals (i.e., kaolinite group, Al-smectites, white micas), as well as a green vegetation and false colour image. In addition, 3D versions of the Australian continental scale Geoscience Products can be generated. These 3D images are accessible online using NASA's World Wind Java Software Development Kit, displaying Australia's continental data sets (http://www.ga.gov.au/resources/multimedia/world-wind.jsp). It should be noted that the continental Australian Geoscience Products can vary from the Western Australian Geoscience Products, due to different thresholds or stretching limits. Refer to Caccetta et al. (2013) and Cudahy (2011, 2012) for further details.

Table 3 VNIR-SWIR based mineral maps of the 2011 precompetitive WA ASTER Geoscience Products (Cudahy, 2011) and TIR based mineral maps of the 2012 continental scale Geoscience Products (Cudahy, 2012). A rainbow colour look up table was applied to all mineral group content and composition products. In the mineral group content yellow to red colours indicate a high relative content of the respective mineral group.

GEOSCIENCE PRODUCT	BASE ALGORITHM[1)]	MATERIAL/MINERAL GROUP (EXAMPLES)	REFERENCES
False Colour RGB	R: B3, G: B2, B: B1	Red = green vegetation	Cudahy et al. (2008)
Ferric Oxide content	B4/B3	Hematite, goethite, jarosite	Cudahy et al. (2008)
Ferric Oxide composition	B2/B1	Blue is goethite-rich, green is hematite-goethite, red/yellow is hematite-rich	Cudahy et al. (2008)
AlOH group content	(B5+B7)/B6	Phengite, muscovite, paragonite, lepidolite, illite, brammalite, montmorillonite, beidellite, kaolinite, dickite	Rowan and Mars (2003)
AlOH group composition	B5/B7	Blue is well ordered kaolinite, Al-rich muscovite/ illite, paragonite, pyrophyllite; Red is Al-poor (Si-rich) muscovite (phengite)	Cudahy et al. (2008)
Kaolin Group Index	B6/B5	Pyrophyllite, alunite, well-ordered kaolinite	Cudahy et al. (2012)
Ferrous Iron Index	B5/B4	Ferrous iron in silicates and carbonates	Cudahy et al. (2008)
MgOH/Carbonate group content	(B6+B9)/(B7+B8)	Calcite, dolomite, magnesite, chlorite, epidote, amphibole, talc, serpentine	Cudahy et al. (2008)
MgOH/Carbonate group composition	B7/B8	Blue-cyan is magnesite, dolomite, amphibole, chlorite; Red is calcite, epidote, amphibole	Cudahy et al. (2008)
Ferrous iron in MgOH/carbonate index	B5/B4	Blue is low ferrous iron content in carbonate and MgOH minerals like talc and tremolite; Red is high ferrous iron content in carbonate and MgOH minerals like chlorite and actinolite.	Cudahy et al. (2008)
FeOH group content	(B6+B8)/B7	Chlorite, epidote, jarosite, nontronite, gibbsite, gypsum, opal-chalcedony	Cudahy et al. (2008)
Opaques Index	B1/B4	Carbon black (e.g. ash), magnetite, Mn oxides, sulphides in unoxidised environments	Cudahy et al. (2008)
Green vegetation content	B3/B2	Green Vegetation	Cudahy et al. (2008)
Silica Index	B13/B10	Si-rich minerals (e.g. quartz, feldspars, Al-clays)	Cudahy et al. (2012)
Quartz Index	B11/(B10+B12)	Quartz	Cudahy et al. (2012)
Gypsum Index	(B10+B12)/B11	Gypsum	Cudahy et al. (2012)

[1)] For the full table with detailed explanations of applied masks to the base algorithms provided below see Cudahy (2011, 2012).

2.5 Field Sampling and Diamond Drill Core Sampling

On the basis of the variations shown in the ASTER data and considering the proximity of some of the drill holes in the Mt Olympus area, several transects were delineated (Figure 11) and a field campaign was conducted in July 2014 where bulk samples representative of the main lithological units were collected for the purposes of compositional and mineralogical validation. Bulk regolith and outcrop samples were collected approximately every 300 m along each transect or whenever a change in lithology was noted. Due to time constraints and the limited accessibility to some areas sampling was completed only for transects A, E and F.

Additional bulk, regolith material was collected by GSWA staff Sidy Morin-Ka and report author (LH) along two additional transects to the north-west of Mt Olympus in the vicinity of drill hole “Electric Dingo” ED005 (Figure 12). Table 4 lists the location (eastings/northings), sample media type and proposed follow-up methods of analysis of the collected transect samples.

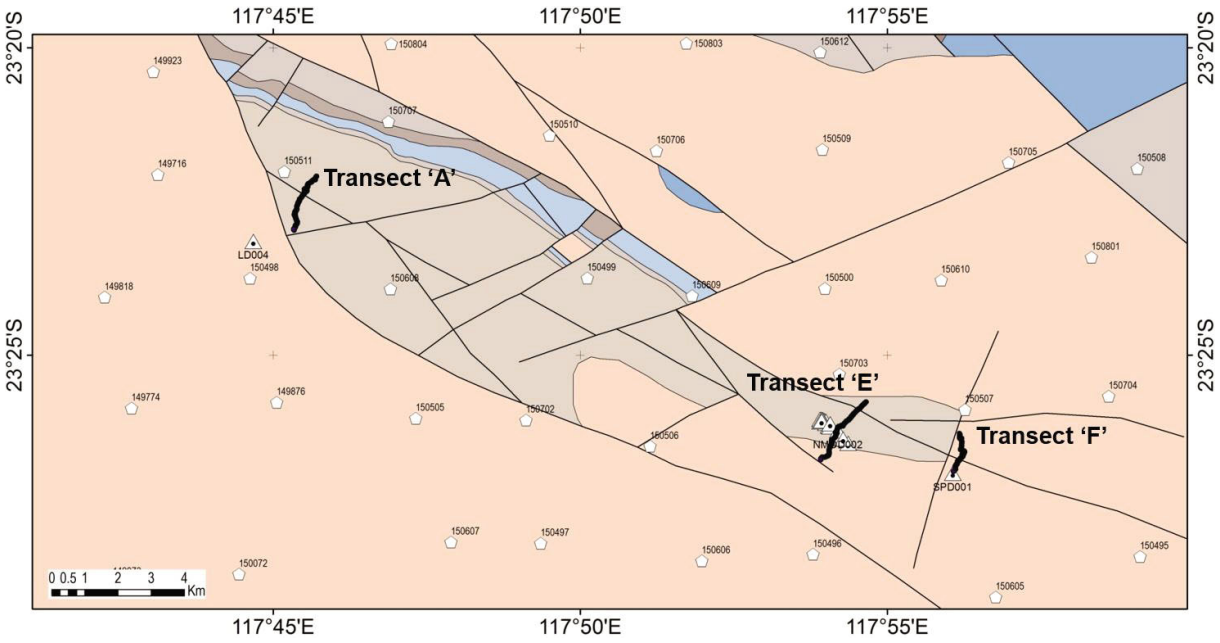

Figure 11 Location of fieldwork transects and GSWA Regolith samples in the Mount Olympus area on a 500K surface geology map

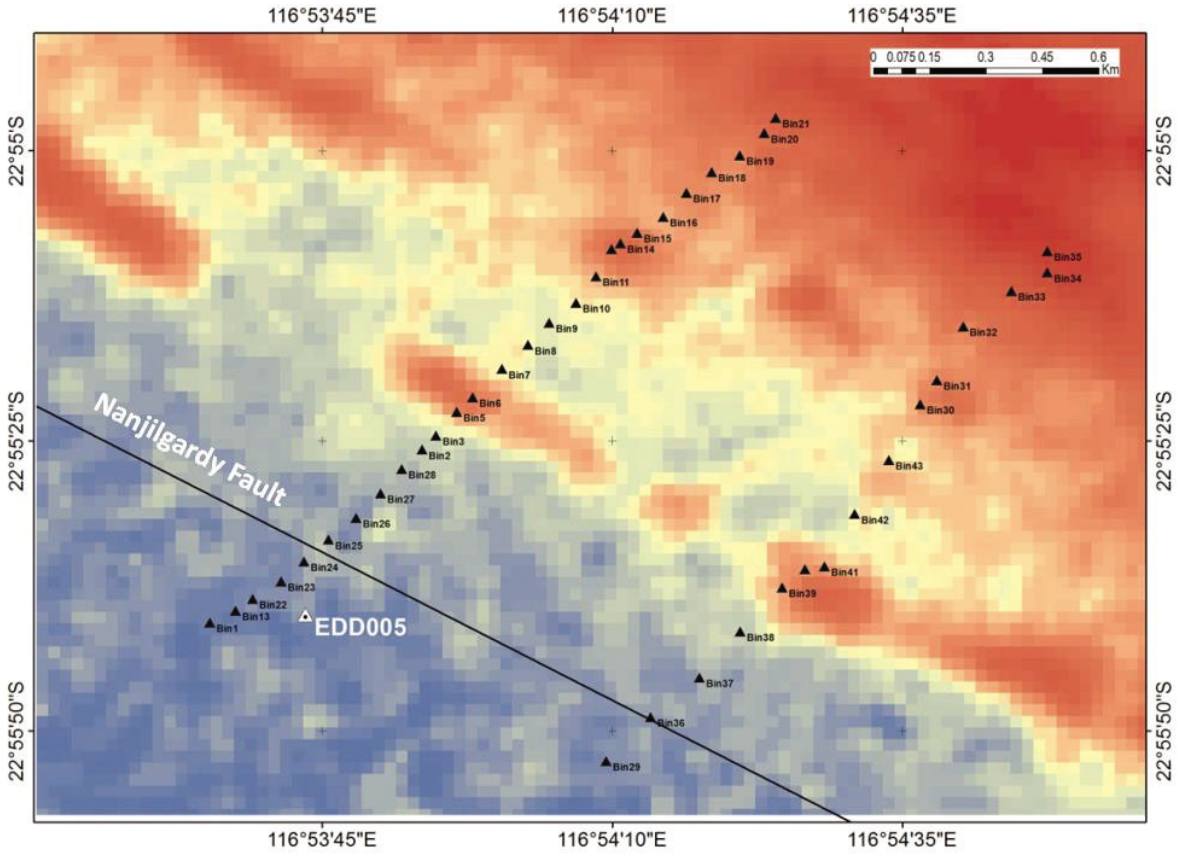

Figure 12 Location of GSWA transects and drill core EDD005 in the Electric Dingo area on a 1 s DEM, blue = 250 m, red = 450 m. For the location of EDD005 see Figure 6.

Table 4 Sampling intervals, sample media type and analytical methods applied to selected drill core samples

Transect/pit	Sample#	Eastings	Northings	Sample Size/Type	Cut	XRF	XRD	ASD (pulp)	Description and Comments
Mount Olympus Pit	MT01			grab sample	Y	Y	Y	Y	conglomerate, C-rich; quartz (pebbles, veins), +- sulphides
Mount Olympus Pit	MT02*			grab sample	Y	Y	Y	Y	conglomerate, C-rich; quartz (pebbles), +- sulphides
Mount Olympus Pit	MT03			grab sample	Y	Y	Y	Y	schist, C-rich
Mount Olympus Pit	MT04			grab sample	Y	Y	Y	Y	conglomerate, C-rich; quartz (pebbles), ++ sulphides
Waugh Pit	W1			grab sample	Y	Y	Y	Y	basalt (amygdales). Cheelah Springs Basalt (fresh)
Waugh Pit	W2			grab sample	Y	Y	Y	Y	basalt (Cheelah Springs Basalt - weathered). Outcrop S of Pit
Waugh Pit	W3	594693	7409759	grab sample	Y	Y	Y	Y	ore zone, iron oxide-rich, quartz
Waugh Pit	W4	594693	7409759	grab sample	Y	Y	Y	Y	ore zone (qtz veining); iron oxide-rich, quartz
A	A1	577863	7415491	grab sample	Y	Y	Y	Y	Fe-carbonate (sheet-wash, scree)
A	A2	577818	7415478	grab sample	Y	Y	Y	Y	Si-carbonate
A	A3	577812	7415434	grab sample	Y	Y	Y	Y	Calcrete exposure over carbonate
A	A4	577748	7415307	grab sample	Y	Y	Y	Y	Duricrust over siltstone
A	A5	577628	7415244	grab sample	Y	Y	Y	Y	Siltstone
A	A6			grab sample	Y	Y	Y	Y	Fe-siltstone
A	A7	577520	7415174	grab sample	N	Y	Y	Y	Fe-siltstone (duricrust ridge)
A	A8	577513	7415047	grab sample	N	Y	Y	Y	Basalt (highly foliated)
A	A9	577444	7414920	grab sample	Y	Y	Y	Y	Basalt (foliated)
A	A10	577361	7414716	grab sample	Y	Y	Y	Y	Basalt
A	A11	577234	7414386	grab sample	N	Y	Y	Y	Colluvium
A	A12	577183	7413980	grab sample	N	Y	Y	Y	Cobble field
E	E1	592704	7408307	grab sample	N	Y	Y	Y	Fe-shale
E	E2			grab sample	Y	Y	Y	Y	Carbonate-rich, Fe-shale (brecciated)
E	E3	593257	7407520	grab sample	Y	Y	Y	Y	Duricrust of conglomerate unit
E	E4			grab sample	N	Y	Y	Y	Fe-siltstone
E	E5	592596	7407876	grab sample	N	Y	Y	Y	Silicified, fine-grained sandstone
E	E6	591726	7409908	grab sample	N	Y	Y	Y	Dolomitic siltstone
E	E7	592217	7407755	grab sample	N	Y	Y	Y	(chloritic) siltstone
E	E8	592091	7407515	grab sample	N	Y	Y	Y	Fe-siltstone+conglomerate
E	E9	592043	7407328	grab sample	N	Y	Y	Y	Fe-siltstone
E	E10	591971	7407040	grab sample	N	Y	Y	Y	Fe/Si-siltstone
E	E11			grab sample	N	Y	Y	Y	Fe-siltstone
E	E12	592422	7407522	grab sample	N	Y	Y	Y	Mn(?)-siltstone
F	F1	595670	7407640	grab sample	N	Y	Y	Y	(chloritic) siltstone
F	F2	595676	7407513	grab sample	N	Y	Y	Y	Fe-siltstone
F	F3A	595721	7407342	grab sample	N	Y	Y	Y	Fe-siltstone
F	F3B	595721	7407342	grab sample	Y	Y	Y	Y	Ochreous/Vitreous goethite
F	F4	595689	7407246	grab sample	N	Y	Y	Y	Silicified, conglomerate
F	F5	595708	7407088	grab sample	Y	Y	Y	Y	Fe-siltstone
F	F6	595619	7406967	grab sample	Y	Y	Y	Y	Fe-conglomerate
F	F7	595607	7406891	grab sample	Y	Y	Y	Y	Quartzite?
F	F8	595384	7406669	grab sample	N	Y	Y	Y	Talcose siltstone
(Electric Dingo Area)									
1	001-1	489043	7464451	grab sample	N	Y	Y	Y	
1	001-2	489106	7464482	grab sample	N	Y	Y	Y	
1	001-3	489148	7464514	grab sample	N	Y	Y	Y	
1	001-4	489218	7464560	grab sample	N	Y	Y	Y	
1	001-5	489274	7464613	grab sample	N	Y	Y	Y	
1	001-6	489334	7464671	grab sample	N	Y	Y	Y	
1	001-7	489402	7464729	grab sample	N	Y	Y	Y	
1	001-8	489462	7464794	grab sample	N	Y	Y	Y	
1	001-9	489514	7464859	grab sample	N	Y	Y	Y	
1	001-10	489564	7464910	grab sample	N	Y	Y	Y	
1	001-11	489598	7464947	grab sample	N	Y	Y	Y	
1	001-12A	489649	7465010	grab sample	N	Y	Y	Y	'Fines'
1	001-12B	489649	7465010	grab sample	N	Y	Y	Y	Conglomerate
1	001-13	489688	7465049	grab sample	N	Y	Y	Y	
1	001-14	489760	7465124	grab sample	N	Y	Y	Y	
1	001-15	489824	7465188	grab sample	N	Y	Y	Y	
1	001-16	489876	7465247	grab sample	N	Y	Y	Y	
1	001-17	489942	7465300	grab sample	N	Y	Y	Y	
1	001-18	489991	7465370	grab sample	N	Y	Y	Y	
1	001-19	490029	7465442	grab sample	N	Y	Y	Y	
1	001-20	490051	7465458	grab sample	Y	Y	Y	Y	
1	001-21	490092	7465486	grab sample	N	Y	Y	Y	
1	001-22	490156	7465528	grab sample	N	Y	Y	Y	
1	001-23	490213	7465592	grab sample	N	Y	Y	Y	
1	001-24	490275	7465647	grab sample	N	Y	Y	Y	
1	001-25	490344	7465691	grab sample	N	Y	Y	Y	
1	001-26	490404	7465750	grab sample	N	Y	Y	Y	
1	001-27	490432	7465791	grab sample	Y	Y	Y	Y	
2	002-1	490017	7464084	grab sample	N	Y	Y	Y	
2	002-2	490126	7464201	grab sample	N	Y	Y	Y	
2	002-3	490246	7464306	grab sample	N	Y	Y	Y	
2	002-4	490346	7464428	grab sample	N	Y	Y	Y	
2	002-5	490449	7464545	grab sample	N	Y	Y	Y	
2	002-6	490505	7464593	grab sample	N	Y	Y	Y	
2	002-7	490553	7464601	grab sample	Y	Y	Y	Y	
2	002-8	490627	7464740	grab sample	N	Y	Y	Y	
2	002-9	490711	7464883	grab sample	N	Y	Y	Y	
2	002-10	490788	7465031	grab sample	N	Y	Y	Y	
2	002-11	490829	7465095	grab sample	Y	Y	Y	Y	
2	002-12	490893	7465238	grab sample	N	Y	Y	Y	
2	002-13	491012	7465332	grab sample	Y	Y	Y	Y	
2	002-14	491100	7465381	grab sample	Y	Y	Y	Y	
2	002-15	491100	7465438	grab sample	N	Y	Y	Y	

*Sample MOT2 was further analysed for TOC, thin-section and element distribution mapping

Table 5 Selected drill core samples collected for follow-up mineralogical and composition validation analysis and general observations for each sample

Sample No.	Well Name	Tray Box No.	Depth From	Depth To	Sample Size	Sample Type	XRD	XRF	TOC	Thin Section Tornado mapping	ASD (pulp)	Description and Comments
1	SPD001	55	323.03	323.12	¼	core	Y	Y			Y	Boundary between hematite-quartz siltstone and bleached white mica-chlorite alteration
2	SPD001	55	324.14	324.27	¼	core	Y	Y			Y	Altered white mica-chlorite with highest gold content (up to 0.95 ppm)
3	SPD001	59	345.33	345.44	¼	core	Y	Y			Y	Chlorite-sericite silicified siltstone
4	SPD001	58	340.7	341	¼	core	Y	Y			Y	Chlorite-sericite silicified siltstone with disseminated sulphides surrounded by alteration rims
5	SPD001	60	354.41	354.6	¼	core	Y	Y			Y	Carbonate veins and dissem.sulphides lenses along stylolites in light grey siltstone
6	SPD001	62	365.89	366	¼	core	Y	Y			Y	Boundary between silicified carbonate-rich grey sediment and white mica alteration
7	SPD001	66	386	386.25	¼	core	Y	Y		Y	Y	Bleached dolomite-rich zone (3.5 m)
8	SPD001	67	395.2	395.34	¼	core	Y	Y			Y	Red-grey sediment with dissem.sulphides along fractures and fissures. Elevated Au (0.35 ppm) and high As (800 ppm)
9	SPD001	68	400.55	400.72	¼	core	Y	Y			Y	Carbonate veining in light grey siltstone
10	SPD001	71	417.44	417.62	¼	core	Y	Y			Y	Changing of carbonate composition in silicified siltstone
11	SPD001	74	431.26	431.44	¼	core	Y	Y			Y	Carbonate-quartz breccia with slightly elevated level of Au (0.1 ppm)
12	SPD001	66	389.65	389.85	¼	core	Y	Y			Y	High Sb (124 ppm) in silicified siltstone
13	SPD001	76	445.68	445.82	¼	core	Y	Y		Y	Y	Hanging wall of high Au (0.95 ppm): white mica alteration and disseminated pyrite
14	SPD001	76	446.76	446.9	¼	core	Y	Y			Y	Gold mineralization (0.95 ppm, but lack of As) in sulphides lenses along veinlets in light grey silicified siltstone. White mica alteration
15	SPD001	79	462.62	462.8	¼	core	Y	Y			Y	Footwall: changing white mica composition from 2200 to 2193 nm in bleached core interval
16	SPD001	80	464.56	464.7	¼	core	Y	Y			Y	Hematite-quartz sediment with calcite veins; elevated Cu (465 ppm)
17	SPD001	125	727.6	727.76	¼	core	Y	Y			Y	Boundary between carbonate-rich conglomerate and hematite-quartz-carbon sediment; high Cu (700 ppm)
											Y	
18	MOD13	1	88.25	88.3	¼	core	Y	Y			Y	Quartz-sericite sediment in hanging wall of first high Au
19	MOD13	2	90.6	90.7	¼	core	Y	Y			Y	Oxidazed zone with high Au (58.7 ppm)
20	MOD13	2	92	92	powder	powder	Y	Y			Y	Grey powder; Au - 2 ppm
21	MOD13	2	92.3	92.4	¼	core		Y			Y	Quartz-sericite sediment in hanging wall of first high Au
22	MOD13	2	92.75	92.8	powder	powder	Y	Y			Y	White-grey powder; Au - 6.6 ppm
23	MOD13	8	118.4	118.4	powder	powder	Y	Y			Y	White powder in quartz-sericite-sulphate(?) hanging wall zone of highest Au
24	MOD13	8	118.8	118.8	powder	powder	Y	Y			Y	Grey powder in quartz-sericite-sulphate(?) hanging wall zone of highest Au
25	MOD13	9	121.9	121.97	¼	core	Y	Y			Y	Ore zone: highest Au (124 ppm); oxidized silicified carbon-rich sediment, lack of white mica
26	MOD13	9	123.4	123.5	grab sample	grab sample	Y	Y	Y		Y	Ore zone: organic-rich sample for TOC
27	MOD13	9	123.68	123.77	grab sample	grab sample	Y	Y			Y	Ore zone: Au - 97 ppm; oxidized silicified carbon-rich sediment
28	MOD13	10	127.8	127.85	¼	core	Y	Y		Y	Y	Au - 7.3 ppm; light grey white mica-quartz siltstone
29	MOD13	13	139.2	139.27	¼	core	Y	Y		Y	Y	Footwall: sericite-rich light brown siltstone
30	MOD13	6	110.1	110.15	grab sample	grab sample	Y	Y			Y	White mica-quartz zone with Au - 15 ppm
											Y	
31	NMOD001	7	210.4	210.5	¼	core	Y	Y	Y		Y	Hematite and organic-rich (flat SWIR) sediment for TOC
32	NMOD001	15	250.3	250.37	¼	core	Y	Y			Y	Bleached zone: white mica-chlorite alteration
33	NMOD001	16	255.27	255.35	¼	core	Y	Y			Y	Hanging wall: light white mica-rich siltstone
34	NMOD001	19	266.3	266.35	grab sample	grab sample	Y	Y			Y	Above fault zone with Au mineralization: light white-mica-rich siltstone
35	NMOD001	19	267.4	267.46	grab sample	grab sample	Y	Y			Y	Ore zone: Au - 4 ppm; As - 750 ppm; chiped and powered light grey and cream sericite-rich siltstone
36	NMOD001	20	270.3	270.35	grab sample	grab sample	Y	Y		Y	Y	Ore zone: Au - 1.54 ppm; As - 4000 ppm; cluster of arsenopyrite crystals
37	NMOD001	27	303.1	303.23	¼	core	Y	Y	Y		Y	Background brown organic-rich (flat SWIR) sediment for TOC; small bleached white mica interval
38	NMOD001	29	314.85	314.9	grab sample	grab sample	Y	Y			Y	Light grey altered sediment: high Cu - 2517 ppm, As - 4600 ppm, Sb - 663 ppm, Zn - 336 ppm, but no gold
39	NMOD001	37	349.74	349.8	¼	core	Y	Y			Y	Ore zone: Au - 3.16 ppm; As - 2775 ppm; light grey white mica-rich sediment
40	NMOD001	37	349.9	349.95	grab sample	grab sample	Y	Y			Y	Ore zone: Au - 3.16 ppm; As - 2775 ppm; grey white mica-rich chips and powder
41	NMOD001	40	362.64	362.76	¼	core	Y	Y		Y	Y	Highest As - 11612 ppm, no Au; grey powder and light brown sediment
42	NMOD001	41	367.75	367.85	powder	powder	Y	Y			Y	High As - 1019 ppm, no Au; light grey powder
43	NMOD001	56	438.1	438.29	¼	core	Y	Y		Y	Y	Background quartz-rich conglomerate
44	NMOD001	57	442.9	443.05	grab sample	grab sample	Y	Y			Y	High Au - 2.15 ppm; As - 4407 ppm; brecciated and altered brown-grey conglomerate

DRILL CORE DATA INTEGRATION

Extraction and digitisation of historical drill hole lithological logs and compositional data, mainly Au assay values, were extracted from Sipa Resources reports and imported into TSG™, and integrated with HyLogging™-3 data to aid initial evaluation of spectral-compositional associations, particularly where gold mineralisation (i.e., elevated Au values) were reported. On this basis, two mineralised drill holes (MOD13 and NM0D001) located at Mt Olympus, as part of the eastern extension of the Lower Wyloo Group inlier and, for comparative purposes, one unmineralised drill hole (SPD001) east of Mt Olympus in the Upper Wyloo Group (refer to Figure 11) were selected for validation sampling. Table 5 lists the sampling intervals, sample media type and proposed follow-up methods of analysis of the samples selected for study.

Sample selection for each drill hole was aided by evaluating down-hole variations of, primarily, Au composition in relation to changes in the dominant mineralogy detected spectrally. For example, Figure 13 presents a series of stacked, down-holes plots for drill core NMOD001 that shows the main lithological units logged for the drill hole, along with assayed values for Au and As, and variations in some spectral (MFEM) mineral index values. The drill hole presented as a siltstone package overlying an alternating sequence of arenite and conglomerate (Figure 13). Elevated Au contents, to about 4 ppm, were assayed for the interval 266–268 m, associated with elevated As contents (750 ppm); sample #35 was selected as representative for this interval (refer to Table 5). Locations with higher As contents (11,000 ppm) but showing no Au mineralisation were also sampled (Figure 13).

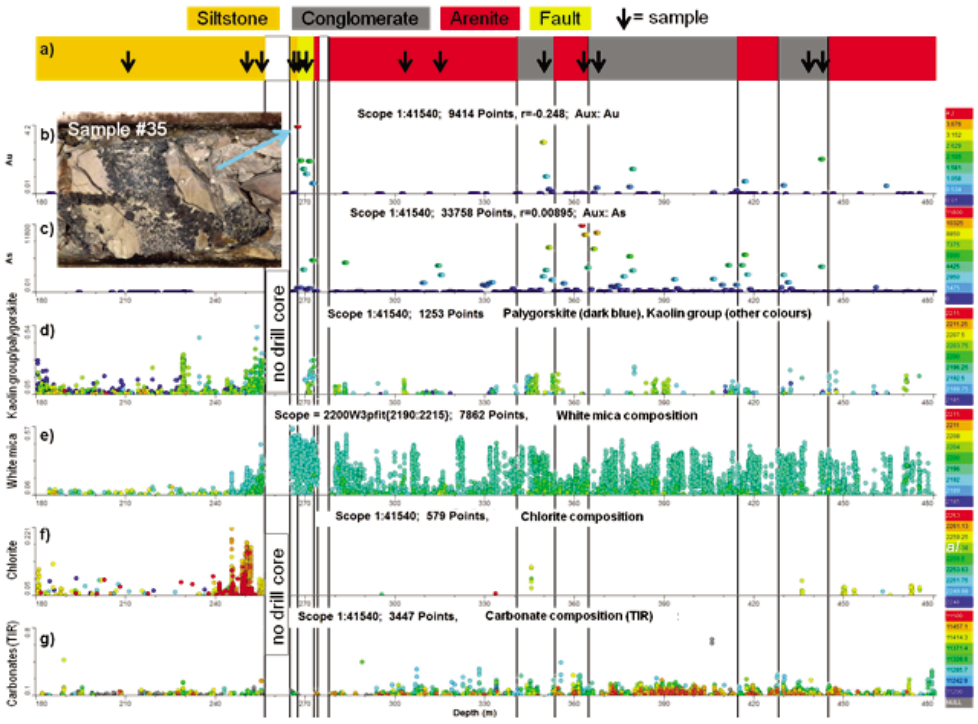

Figure 13 Stacked, down-hole plots (i.e., x-axis = depth) for drill hole NMOD001 showing the variation (i.e., y-axis) with depth in: a) lithology, b) Au assay (ppm), c) As assay (ppm); and spectral mineralogy scalars for, d) Kaolin/palygorskite spectral abundance. The inset view of the drill core shows the location from which sample #35 was taken for validation XRD and bulk geochemical analysis.

In addition, selected intervals along other drill holes (MOD4, MOD11, MOD5, AMODD026) were sampled to corroborate initial TSA mineral identification, which indicated the presence of jarosite/alunite (MOD4), dickite (MOD5), pyrophyllite/kaolinite (MOD11), and dickite/paragonite (AMODD026).

2.6 FieldSpec3 (ASD)

FIELD MEASUREMENTS

Hemi-spherical, reflectance spectroscopic measurements covering the visible to near-infrared to shortwave infrared wavelength range, 400–2500 nm, were measured using a field-portable, Analytical Spectral Devices (ASD) FieldSpec Pro 3 (unit #16446) spectrometer. This was to enable a comparative evaluation and calibration against the remote sensing (i.e., ASTER) data. Measurements were taken approximately every 10 m only along transects A, E and F (Figure 11) approximately 1 m above the ground surface. Instrument standardisation and optimisation was performed by measurement approximately 1 m above a 99 % reflectance Spectralon™ panel (30 x 30 cm) as the reflectance standard, using sunlight as the illumination source. Reflectance spectra along transects conducted by GSWA staff in the vicinity of drill hole EDD05 (Electric Dingo) were not measured.

LABORATORY MEASUREMENTS

Bi-directional reflectance spectra covering the full visible and near-infrared to shortwave infrared wavelength range, 400–2500 nm, were measured using an Analytical Spectral Devices (ASD) FieldSpec Pro 3 (unit #16446) spectrometer. Constant illumination was achieved using the internal lamp of the ASD spectrometer sensing-head. Powdered material of XRD validation samples were loaded into a custom-made sample holder with a sapphire-window (25 mm diameter), permitting ≈100 % transmittance of the incident light, tapped lightly on the bench to pack the sample and cover the window and placed onto the viewing port of the ASD sensor-head fixed in a vertical position. Two reflectance measurements were collected with the powdered material re-loaded prior to measurement.

Spectra were processed using The Spectral Geologist™ Core (TSG)-Core version 7.1.0.062 Software (Berman et al., 1999; Yang et al., 2005) using the method of Cudahy et al. (2008).

2.7 Whole Rock Geochemistry

Compositional analysis of both diamond drill core samples and outcrop samples collected in the field, along all transects (refer to section 2.3), was undertaken by the commercial mineral analysis laboratory, Lab West Minerals Analysis Pty Ltd, Malaga. Samples were dried, crushed to 2 mm where required and a 500–700 g split taken by rotary-division for pulverisation to 75 µm in an LM1 pulveriser. A split of 50 g of the pulp was separated for bulk mineralogical characterisation using X-ray diffraction (XRD) analysis.

A 36-element analysis suite was assayed for all collected samples and Table 6 lists the method of analysis for each element as well as the associated detection limits. Geochemical data for all assayed samples are presented in Appendix 2. Weight percentage values of Fe were recalculated as either wt% FeO or wt% Fe_2O_3 values depending on whether the dominant Fe-bearing mineralogy, as detected by XRD analysis, were ferrous (e.g., Fe-chlorite) or ferric (e.g., goethite, hematite) bearing phases. For example, where pyrite

and/or Fe-chlorite was detected as the only Fe(II)-bearing phase, iron contents were recalculated as wt% FeO. A minority of samples comprised both ferrous and ferric-bearing phases and these samples are highlighted in blue (Appendix 2).

Table 6 Geochemical analysis suite and associated analyte detection limits

Element/oxide	DL (units)	Element/oxide	DL (units)	Element/oxide	DL (units)	Element/oxide	DL (units)
Au	0.5 (ppb)	Er	0.05 (ppm)	MgO	0.01 (%)	S	0.01 (p)pm
Ag	0.01 (ppm)	Eu	0.02 (ppm)	MnO	0.01 (%)	Sb	0.1 ppm
Al2O3	0.01 (%)	Fe	0.01 (%)	Mo	0.1 ppm	SiO2	0.01 (%)
As	0.5 (ppm)	Gd	0.05 (ppm)	Na2O	0.01 (%)	Sm	0.02 (ppm)
CaO	0.01 (%)	Hg	0.05 ppm	Nd	0.02 (ppm)	Tb	0.02 (ppm)
Co	0.2 ppm	Ho	0.02 (ppm)	Ni	2 ppm	TiO2	0.01 (%)
Cr	2 ppm	K2O	0.01 (%)	P2O5	0.01 (%)	Tm	0.05 (ppm)
Cu	0.2 ppm	LOI	0.01 (%)	Pb	0.2 ppm	Yb	0.05 (ppm)
Dy	0.02 (ppm)	Lu	0.02 (ppm)	Pr	0.05 (ppm)	Zn	0.2 ppm

Aqua-regia digest
MMA analysis (ICP-MS)
MMA analysis (ICP-OES)

The following provides a brief description of the analysis methods used for each element.

GOLD ANALYSIS

A portion of pulverised sample was analysed for gold using aqua-regia digestion, with determination by Inductively Coupled Plasma-Mass Spectrometry (ICP-MS).

BASE AND TRACE METALS BY MICROWAVE-ASSISTED MULTI-ACID DIGESTION

Base and trace elements (Table 6) were analysed using a microwave-assisted, multi-acid (MMA) digestion method where a portion of sample was digested in an HF-based acid mixture under high pressure and temperature in microwave apparatus to assist digestion. Analytes, including Rare-Earths, were measured using Inductively Coupled Plasma- Mass Spectrometry (ICP-MS).

MAJOR OXIDES (WHOLE ROCK) BY ALKALINE FUSION

Major elements (Table 6) were analysed using an alkaline fusion technique which yields total recovery for major rock-forming elements. A portion of sample was fused at high temperature with an alkaline flux then dissolved into an acidic solution. Major elemental concentrations were determined by Inductively Coupled Plasma-Optical Emission Spectroscopy (ICP-OES).

2.8 Element Distribution Mapping

Selected drill core samples were prepared as polished, 50 x 25 mm, thin-sections to enable mapping of the element-mineral association at the macroscopic scale (refer to section 3.1). Uncoated (i.e., not carbon-

coated) thin-sections were scanned using a Bruker M4 Tornado XRF instrument and mapped with a spatial resolution of 25 μm. Area maps were processed using the Bruker M4 software and spot analyses obtained using a standard-less quantification routine with a 0.5 wt% element cut-off, that is, elements detected at <0.5 wt% were not reported. As a standard-less routine was used, the reported compositions provide only a semi-quantitative (at best) analysis of element abundance. However, the derived element distribution maps provide important information to changes in the relative element composition.

2.9 X-ray Diffraction (XRD) analysis

Bulk, random powder diffraction patterns were collected using a Bruker D4 Endeavour diffractometer using CoKα radiation. Pulverised samples were back-loaded into steel mounts and diffraction patterns collected by scanning from 5 to 90° 2θ in 0.02° 2θ steps and counting for ≈1.0 s/step for a total scan time of ≈7 minutes/scan. Diffraction patterns were evaluated using the Bruker Diffrac.Suite EVA V2.1, release 2011, software. Each diffraction pattern was background corrected and the Co $K\alpha_2$ component stripped assuming a $K\alpha_1/\alpha_2$ ratio of 0.5. Instrumental shifts in 2θ were corrected by reference to the 100% intensity (101) peak of quartz at 31.034° 2θ, *d*-spacing of 3.344 Å. The 2θ-position of the quartz (101) peak was measured by using the feature extraction method in TSG applied as a batch routine to all imported diffraction patterns. Quartz was detected in all samples submitted for XRD analysis, with the exception of sample A4, which comprised essentially 100% goethite.

Mineralogical identification was facilitated by using the Crystallography Open Database (COD), REV 30738 2011.11.2 software, and the International Centre of Diffraction Data (ICDD) data base. Table 7 lists the COD and ICDD mineral standards and their associated database numbers used for mineral matching and identification purposes. Bulk mineralogical descriptions are presented in Appendix 3, with qualitative mineral abundances listed in approximate decreasing order as major (maj), minor (min) and trace (tr) quantities. XRD patterns for all measured samples are presented in Appendix 4.

Table 7 COD mineral standards used for mineral identification in X-ray powder diffraction patterns of all drill hole and field-collected samples.

Oxides	COD#	Min. Abb.*	Silicates	COD#	Min. Abb.*	Carbonates	COD#	Min. Abb.*	Sulfides/sulfates/chlorides	COD#	Min. Abb.*
hematite	9000139	Hem	quartz	1011172	Qtz	siderite	2104746	Sd	pyrite	5000115	Py
goethite	1008766	Gth	muscovite-2M1	1000042	Ms	dolomite	9001006	Dol	As-pyrite	5000115	As-Py
			(Fe)-chlorite	9010165	Fe-Chl	calcite	1010928	Cal	halite	9003308	Hl
rutile	9004141	Rt	pyrophyllite	9000809	Prl						
anatase	9008213	Ant								ICDD Card #	
			kaolinite	1011045	Kln				szomolnokite	45-1365	Szk
gibbsite	1011081	Gbs	dickite	9000122	Dck				alunite	14-136	Alu
			cronstedtite	9005752	Crd				jarosite	22-827	Jar
			amesite	9001331	Ame				melanterite	22-663	Mlt
			sepiolite	9011946	Sep				rozenite	16-699	Roz
			palygorskite	9005565	Plg				gypsum	21-816	Gp
			orthoclase	1011205	Or						
			albite	9000783	Am						
			microcline	9000189	Mc						
			amphibole (actinolite)	9001927	Amp						

*Min. Abb. Mineral abbreviations follow the mineral key recommended by Whitney and Evans (2010).
COD# Crystallography Open Database (Rev 30738 2011.11.1)
ICDD Card # International Centre of Diffraction Data

Where selected sheet-silicates, such as chlorite and white-mica (muscovite), were identified in diffraction patterns, peak parameters including the peak position (*d*-space) and peak full width at half maximum, FWHM, values were measured using the Diffrac.Suite EVA V2.1 software. These diffraction peak parameters were used to evaluate, in the case of chlorite, if changes in the relative diffraction peak

intensity may be related to chlorite composition (e.g., wt% Mg content) and to validate identification of the TSA chlorite type whether as Fe-chlorite, FeMg-chlorite or Mg-chlorite (refer to section 3.1 for a more detailed discussion). Peak position and FWHM parameters of only the 002, 003, 004 and 005 reflections of chlorite and the 001 and 002 reflections of muscovite were measured, partly because of interference or overlap with other mineral peaks but also because of errors in peak intensity for low 2θ peaks, such as the 001 reflection of chlorite, which can arise from sample-length problems (i.e., the area of the sample irradiated by the XRD beam) and uncertainties in the Lorentz factor (Moore and Reynolds, 1997).

2.10 GSWA surface sample geochemistry

Regolith geochemical data from the project area were extracted from GSWA's 1994–2001 regional regolith geochemistry data set and compared with the multispectral surface (i.e., ASTER) and hyperspectral surface (i.e., field spectroradiometer) data. In addition, VNIR-SWIR reflectance spectra were acquired from 154 pulps of GSWA's regolith sample set using a field-portable, Analytical Spectral Devices (ASD) FieldSpec Pro 3 (unit #16446) spectrometer. The locations and geochemistry results of scanned regolith samples are summarised in Appendix 5.

2.11 Leapfrog Geo and 3D modelling

A plot of the location of drill holes available for the current study, as listed in Table 2, highlights their widely spaced occurrence, with drill holes essentially following along strike of the Nanjilgardy Fault and having little lateral distribution orthogonal or away from the NF (see Figure 6 and Figure 14). Hence, it is reasonable to assume that modelling of the spectral and geochemical characteristics of such widely separated drill holes would likely yield geologically meaningless results. Therefore, only drill holes with the greatest spatial density within the immediate vicinity of Mt Olympus were used for 3D modelling (Figure 14B). The boxed area outline in Figure 14B excludes drill holes LD004 and SPD001.

3D modelling of the combined geochemistry (extracted Au assay values) and calculated spectral mineral indices for drill holes in the Mt Olympus area was performed using Leapfrog Geo™ version 1.3.1 software (build #0.0.6.5432). On the basis of the mineral spectral evaluation results, the following MFEM products were included in the 3D modelling:

- '2160D2190' – Relative abundance of AlOH-bearing phases, e.g., kaolin/white-mica (SWIR)
- '1480Dpoly' – Relative sulphate abundance (SWIR)
- 'wmAlsmci_prof' – White-mica composition (SWIR)
- 'chlepci3pfit' – Chlorite composition (SWIR)
- 'Quartz_ai2' – Relative quartz abundance (TIR)

Other MFEM spectral mineral products may be extracted and incorporated into the 3D model evaluation of Mt Olympus, such as an attempt to better discriminate the kaolin minerals (kaolinite vs. dickite) using SWIR defined indices, 'FeatEx2180_50' and 'FeatEx2180_50_2'.

For modelling purposes, drill hole collar locations, geochemical data (reported Au ppm assay values) and the above described mineral spectral (MFEM) indices were imported into Leapfrog as separate .csv files. Drill hole collar easting and northing co-ordinates were given as the equivalent AMG84 projection values. In addition, Northern Star kindly provided surface or mesh files (in .dxf format) in AMG84 projection, for the Mt Olympus digital terrain model (DTM) and mine pit outline, and for the Zoe Fault. These were

incorporated into the Leapfrog model to provide an upper or surface boundary (i.e., DTM) for modelling and to assess any structural control to the modelled spectral-geochemical associations at Mt. Olympus.

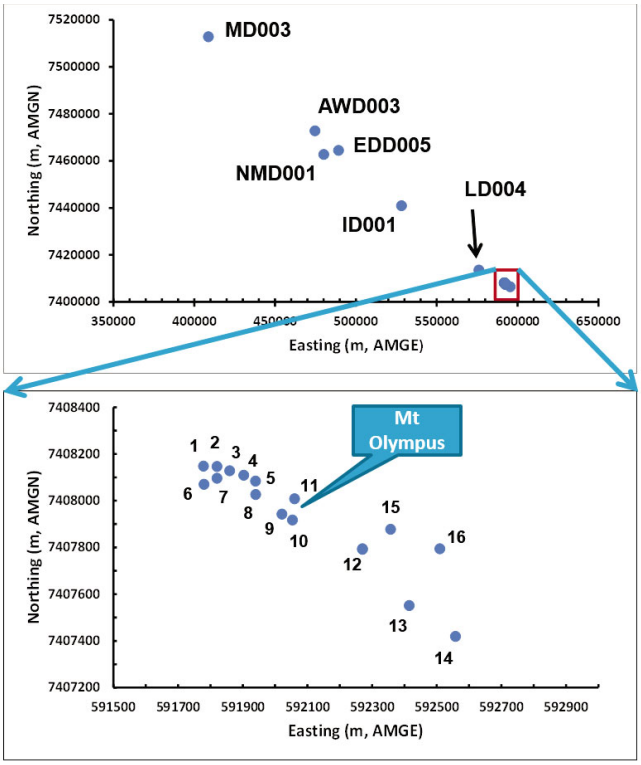

Figure 14 Location of drill holes used for Leapfrog modelling. Only those holes within the vicinity of Mt Olympus were used. For example, drill holes LD004 and SPD001 (not plotted) were considered too far removed from the 'cluster' of drill holes in the immediate vicinity of Mt Olympus (box outlined in red) and were not included in the 3D modelling. Drill hole key: 1 = MOD04, 2 = MOD08, 3 = MOD07, 4 = MOD05, 5 = MOD06, 6 = MOD12, 7 = MOD13, 8 = MOD03, 9 = MTO90, 10 = MOD11, 11 = MOD14, 12 = NMOD001/NMOD002, 13 = NMOD004, 14 = NMOD005, 15 = AMMOD0026, 16 = AMMOD0028.

In addition, the following pre-processing and modelling protocols were used:

- A 'NULL' descriptor was reported in TSG where application of the MFEM scripts failed to return a value for the absorption feature targeted. Any returned NULL designations were removed and were left as blank cells in the .csv files.
- Gold assay values for extended intervals within a number of drill holes reported Au contents of '0' ppm. It was unclear whether this indicated that Au was below detection or that, indeed, the assayed Au content was 0 ppm. Reported Au values of '0' were changed to a more realistic, low value of 0.005 ppm to enable Leapfrog to better model low levels of Au.
- Many drill holes contained long sections or intervals for which no Au assay values were reported. For example, in EIS hole AMOD0026, for the intervals 322–338 m (length = 16 m), 344–376 m (length = 32 m) and 418.4–428.5 m (length = 10.1 m) no Au values were reported. Similarly, in drill hole MOD14 no Au values were reported for the interval 185–205 m. It was unclear for such intervals whether these represented zones that were not assayed or that Au assay values were 'missing': such intervals in the .csv files were left blank. In addition, Au assay data was absent, that is, could not be retrieved for several drill holes (MOD3, MOD11 and MTO90) near Mt Olympus.

- A buffer distance of radius 100 m about each drill hole was used to constrain the lateral extent of modelling to avoid or limit 'over modelling' of the spatial distribution of spectral-geochemical associations at too great a distance away from each drill hole.
- A surface boundary defined by drill hole collar RL's was used as an upper surface limit to constrain modelling in the vertical direction.

2.12 Geophyscial Data

Airborne electromagnetic (AEM) data, acquired by GSWA in 2013–2014 and released in June 2014, were compared with multispectral surface (i.e., ASTER) and subsurface (i.e., HyLogging) data to, 1) better understand lithological and mineralogical changes that are indicated by the AEM profiles, and 2) to evaluate whether spectral sensing data can be extrapolated subsurface using AEM data. The Capricorn 2013 AEM fixed-wing survey was collected using a TEMPEST® system and covers over 146 300 km^2 (Costello, 2014). A total of 190 flight lines were acquired at a 5 km spacing. Not all of the acquired flight line were processed for this work. AEM inversion processing was only conducted for flight lines FID39 (Electric Dingo area) and FID59 and FID60 (Mt Olympus area). Inversion was based on Geoscience Australia's Layered Earth Inversion algorithm (Lane et al., 2004; Brodie, 2012), with variations of parameters, such as reference and noise models, numbers of layers, constraints and regularisation values, resulting in a wide range of models that fit the data (Ley-Cooper et al., 2015). The results presented here should be viewed as preliminary and further evaluation is required.

3 Results and Discussion

3.1 Drill Core Analyses

Evaluation of drill core data initially focussed on assessing major and minor element associations, in conjunction with bulk powder XRD analysis, so that any element-element relationships may be discussed and explained within a validated, mineralogical framework.

XRD, GEOCHEMCIAL & HYLOGGING ASSOCIATIONS

Orthogonal plots of general element-element associations are shown in Figure 15. The black dashed line in the wt% K_2O *vs*. wt% Al_2O_3 plot (Figure 12A), the wt% S *vs*. wt% Fe plot (Figure 15B) and the wt% MgO *vs*. wt% CaO plot (Figure 15C) represents the expected element ratios for the pure, end-member phases, muscovite, pyrite and dolomite, respectively. Most sample points in the K_2O-Al_2O_3 association were highly correlated and lie close to the K_2O-Al_2O_3 ratio expected for muscovite (Figure 15A). Scatter about the regression line, particularly of samples below the correlation line is due to the presence of other Al-bearing phases, such as pyrophyllite, as confirmed by XRD analysis (Figure 15A arrowed; sample NMOD1-31 Appendix 3).

Similarly, sample points for the S-Fe association lying close to the S:Fe ratio expected for stoichiometric pyrite and are consistent with the presence of this ferrous sulphide as the only Fe-bearing phase. Low-S, high-Fe bearing samples comprise a varied Fe-bearing mineralogy of either Fe(II)-bearing phases (e.g., siderite or Fe-chlorite, Figure 15D) or Fe(III)-bearing phases, such as goethite and hematite.

The line of regression for the CaO-MgO association was almost co-incidental to the CaO-MgO ratio expected for dolomite, as confirmed by XRD analysis as the main Ca/Mg-bearing phase, in the absence of Fe-chlorite (Figure 15C).

Scatter in the trends for the K_2O-Al_2O_3 and MgO-CaO associations are likely due, in part, to compositional changes not accounted in the present plots. For example, solid solution of Na for K along the muscovite-paragonite solid solution, and in the case of dolomite, compositional variations due to the incorporation of low levels of Fe (refer to Tornado mapping section).

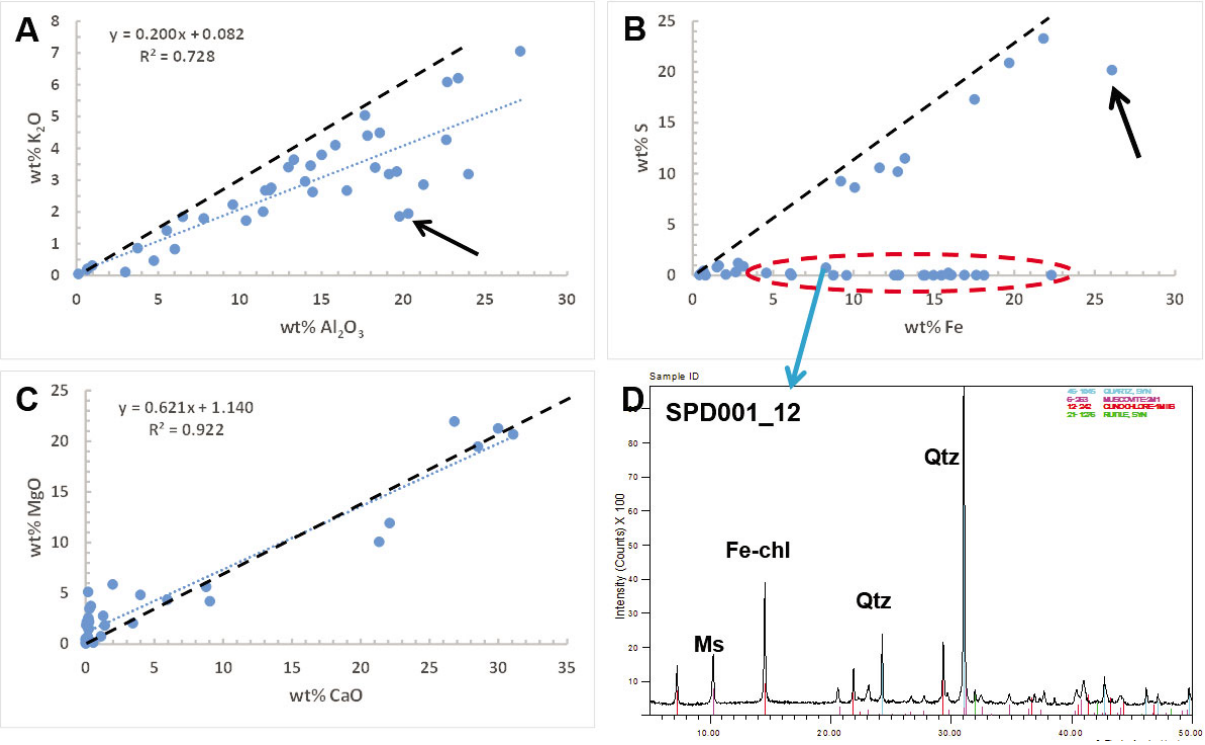

Figure 15 Plots of major and minor elements highlighting various element-mineral associations: (A) wt% K_2O *vs*. wt% Al_2O_3; (B) wt% S *vs*. wt% Fe; (C) wt% MgO *vs*. wt% CaO; and (D) XRD pattern of an Fe-bearing sample (Fe-chlorite) representative of the S-free, Fe-bearing phases (circled in red in B). These samples contain other Fe(II)- or Fe(III)-bearing phases, such as siderite or Fe-chlorite. The sample arrowed in the plot contains both pyrite and the ferrous sulphate, szomolnokite. The black dashed line in plots A, B and C represent the oxide or element ratio expected for pure muscovite, pyrite or dolomite, respectively.

Chlorite

It is well known that variations in chlorite composition (e.g., Al, Ni, Fe) are manifested as differences in the relative intensity of the chlorite basal diffraction peaks (Moore and Reynolds, 1997). In the case of Fe as the most common 'heavy' element that can replace Mg in the chlorite structure, the Fe content and relative cation occupancy of Fe (i.e., hydroxyl sheet vs. silicate sheet) may be determined by measurement of the relative peak intensities of the basal reflections of chlorite. For example, for Fe-bearing chlorite where Fe is symmetrically distributed across octahedral sites in the hydroxyl sheet and silicate sheets, odd-numbered basal peaks (001 and 003) are weaker compared to even-numbered peaks (002 and 004) (Moore and Reynolds, 1997). Chlorite identified in XRD patterns of drill core validation samples consistently demonstrated odd-numbered (001 and 003), basal peaks of a weaker intensity compared to the stronger intensity of even-numbered (002 and 004), basal spacing peaks indicating the presence of Fe-bearing chlorite with a typically symmetrical distribution of Fe (Figure 16).

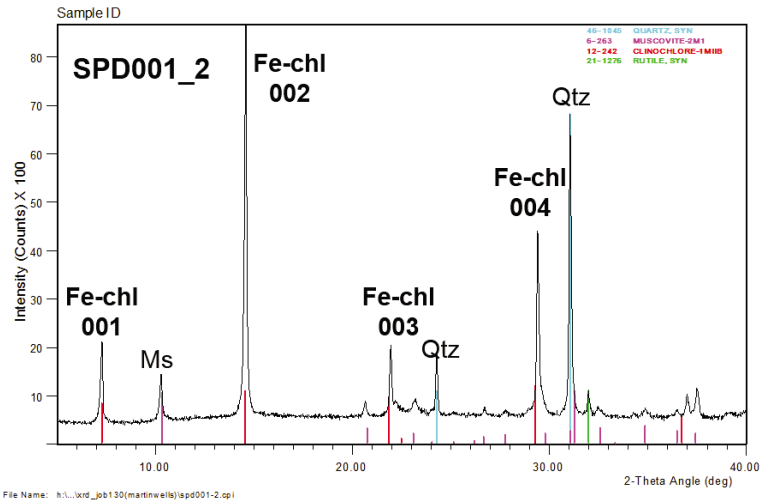

Figure 16 Illustration of the effect Fe substitution on the basal peak intensity of chlorite, for sample SPD001_2. Where Fe is symmetrically distributed between the 'interlayer sheet', octahedral co-ordinated by hydroxyl groups (hydroxyl sheet), and the octahedral co-ordinated 'silicate' sheet, odd-numbered (001, 003) basal peaks have a weaker intensity than even-numbered (002, 004) basal peaks.

Despite the small sample population, changes in the relative intensity of the chlorite 002 and 003 peaks (I002/003) decreased with increasing Mg content (Figure 17). That is, as the Mg content of chlorite increased, the difference in the relative intensity of the 002 and 003 reflections decreased. Compositional variations in the Fe:Mg ratio of chlorite are also manifested as shift in the wavelength of a major absorption feature at around 2250 nm (McLeod et al., 1987). Absorption features at this wavelength range shift to longer wavelengths as the iron content increases. A plot of the chlorite composition script (Sonntag et al., 2012) as a function of the bulk Mg content, with data points coloured by the wavelength of the chlorite 2250 nm feature, highlights the shift to shorter wavelengths as the Mg content increases (Figure 18A). The relationship described in Figure 18A extends over a greater range of Mg content when both drill core and field samples are considered (data not shown; refer to section 4.2 for a more detailed discussion). Colouring of sample points in Figure 18A by the TSA mineralogy demonstrated that chlorite was correctly identified to the TSA Mineral 1 (Figure 18B) and TSA Mineral 2 level (data not shown), as confirmed by XRD analysis. Refer to section 4.3 for a more detailed discussion comparing mineralogy identified using TSA™ and XRD methods.

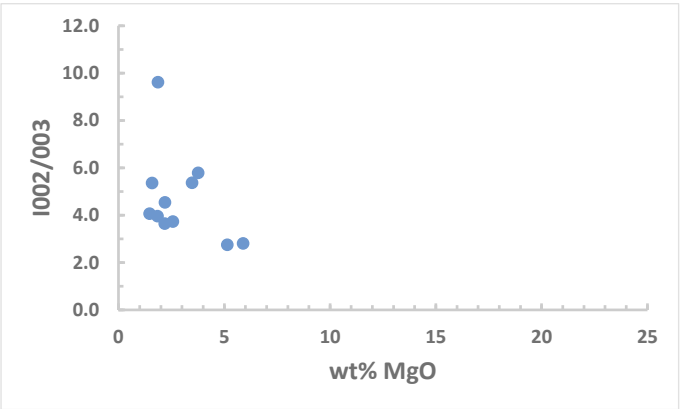

Figure 17 Plot of the XRD peak intensity ratio for the 002 and 003 lines (I002/003) of chlorite *vs*. the bulk wt% MgO content for drill core samples containing only chlorite as the main Mg-bearing phase, as detected by XRD analysis. The I002/003 ratio decreases with increasing Mg content in response to the decreased influence of Fe on peak intensity (refer to text for a more detailed discussion).

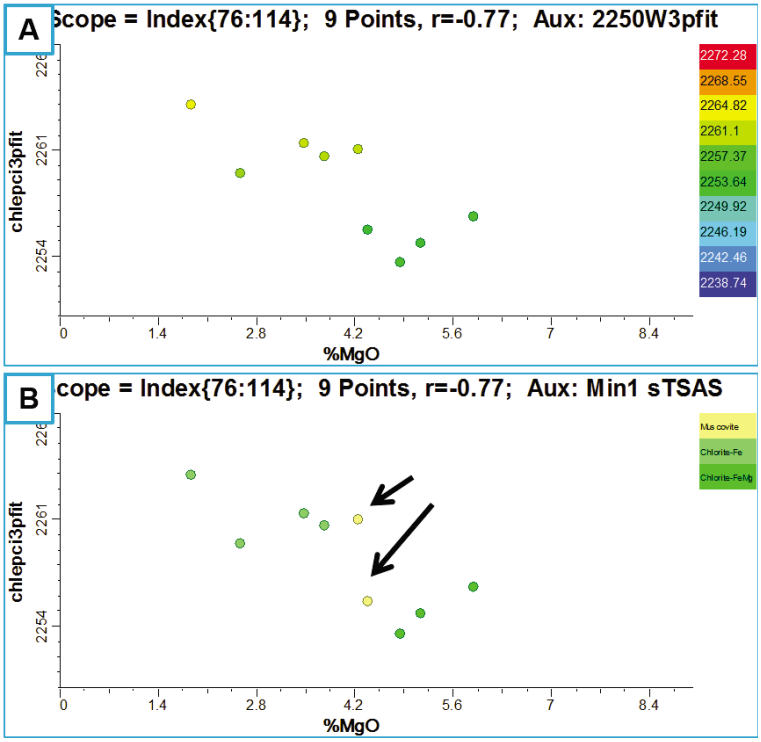

Figure 18 Chlorite composition script (chlepci3pfit) *vs*. the bulk MgO content (wt%), with sample points coloured by (A) the wavelength of the 2250 absorption feature, and (B) the TSA mineral1 designation. Samples arrowed in (B) identified to TSA Min1 as 'Muscovite' were identified to TSA Min2 level as 'Chlorite' (data not shown) as confirmed by XRD analysis.

Muscovite

As demonstrated for chlorite, compositional changes in muscovite associated with Na-K exchange along the muscovite-paragonite, $KAl_3Si_3O_{10}(OH)_2$—$NaAl_3Si_3O_{10}(OH)_2$, series are also manifested as a decrease in the *d*-spacing of the basal 00l reflections. Muscovite-1M has a 001 basal spacing of 10.077 Å compared to the basal 001 spacing of 9.665 Å for paragonite-1M (Bailey, 1980). Muscovite 001 *d*-spacings were negatively related to increasing Na content and showed a shift in the white-mica 2200 nm absorption feature (2200W3pfit) to shorter wavelengths consistent with the exchange of K by Na (Figure 19A).

Colouring of sample points at the TSA Group level correctly identified the presence of white-mica to the Group1 (Grp1) level (Figure 19B) and Group2 level (data not shown). Samples in Figure 16B designated at the TSA Group1 level as "Chlorite" and "Carbonate" did, indeed, contain these phases but muscovite was also present as confirmed by XRD analysis. Samples for which a TSA™ Grp1 "NULL" designation was returned (arrowed in Figure 19B) were spectrally noisy due to the presence of pyrite as either a major or minor phase, as identified by XRD analysis. Refer to section 3.3 for a more detailed discussion comparing mineralogy identified using TSA™ and XRD methods.

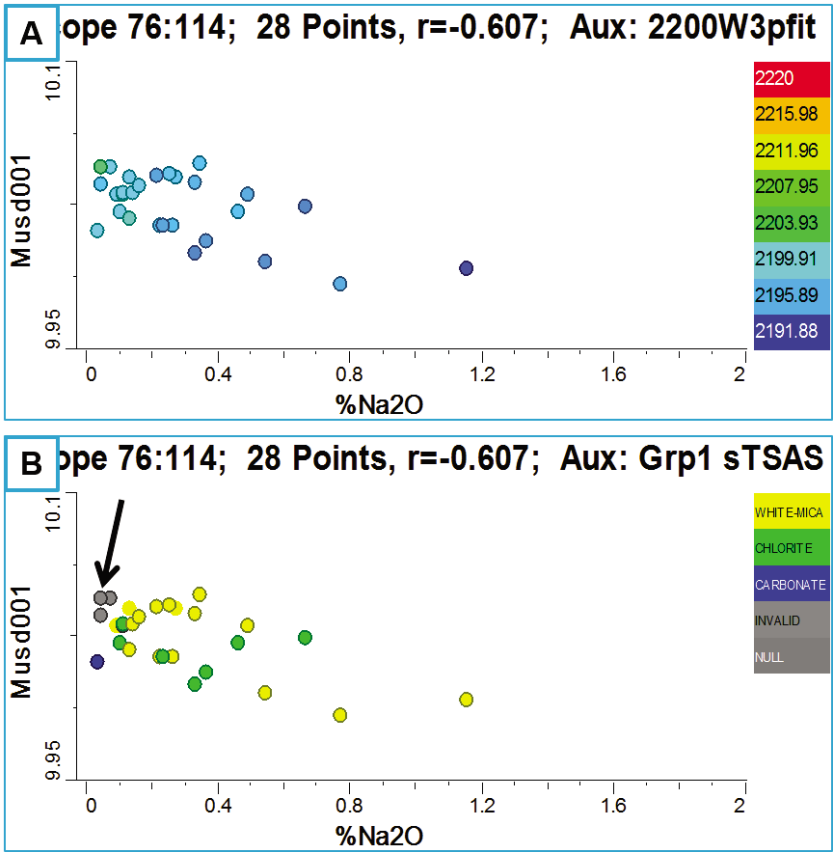

Figure 19 Plot of the 001 d-spacing for muscovite *vs*. the bulk wt% Na_2O content, with samples coloured by; (A) the wavelength (nm) of the 2200 "white-mica" absorption feature, and (B) the TSA Grp1 designation. Samples with a TSA Min1 "NULL" designation, were spectrally noisy due to the presence of pyrite as detected by XRD analysis.

ELEMENT MAPPING

Larger-scale changes in composition and characterisation of element-mineral associations at the scale of the thin-section may be elucidated from element distribution mapping using a Tornado M4 instrument. False-colour element distribution maps of selected drill core samples are presented in Figures 20–23, with element distribution maps for all drill samples scanned using the M4 Tornado instrument presented in Appendix 6.

Optical and false-colour, element distribution maps of MOD13_29 (siltstone) show alternating bands of Fe and K, coincident with high alumina values, consistent with the presence of carbonate (siderite) and muscovite as the major mineralogy, stained by free ferric oxides (hematite) (Figure 20). Optical scanning imagery indicated removal or bleaching (Fe-reduction) of iron oxides along cracks and internal fractures. For the muscovite-rich band containing analysis spots #2 and #3, the composition remained essentially constant, with a slight reduction in Fe content from 9.5 to 8.0%. For analysis spots #4 and #5, bleaching or whitening of the band closest to the fracture was associated with a slight decrease in Fe content from 18.4 to 17.7% (Figure 20). Reduction of free ferric oxides (hematite) resulted in a lightening or bleaching effect. Ferric iron oxides need only be present in small amounts (<1–2 %) to cause a red colouration. HyLogging data over the same sample interval didn't show any changes in the abundance of minerals that could be associated with bleaching, such as muscovite, dickite or alunite. Of those three minerals only muscovite was detected, however, without any changes in the spectral signature across the investigated drill core interval.

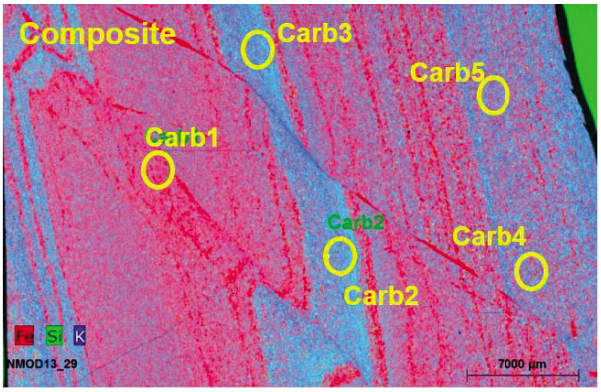

Element	Carb1	Carb2	Carb3	Carb4	Carb5
Fe	35.1	9.53	8.03	17.7	18.4
Si	34.5	48.0	48.0	46.1	45.0
Al	20.9	22.0	22.8	23.2	23.5
K	6.73	16.4	16.8	9.23	9.32
Ti	2.24	4.08	4.37	3.79	3.85
Mg	0.61				

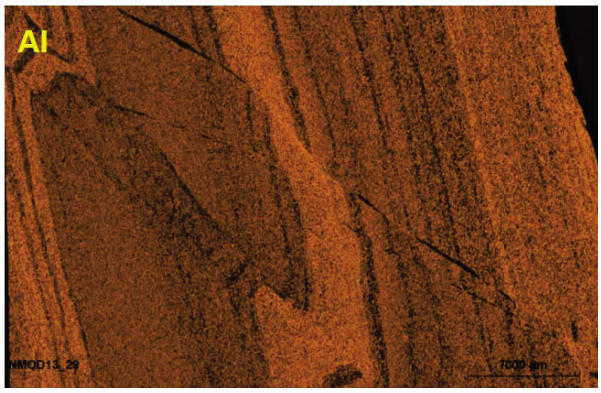

Figure 20 Optical (top left) and false-colour element distribution maps of siltstone MOD13_29 (139.20–139.27 m; @ 2 ppb Au) showing (A) a composite (Fe – red, Si – green, K – blue) and Al map images. The sample mineralogy comprising: siderite, quartz, muscovite (maj); Fe-chlorite (min); Rutile (tr) as detected by XRD analysis, is consistent with that expected of a siltstone.

Optical imagery for dolomitic sample SPD001_7 showed only very subtle changes in mineralogy based on differences in contrast (Figure 21). This was reflected in the Mg distribution map and confirmed by spot analysis at two locations where only small differences in the Mg content were measured (20.3% Mg at Dol_1 and 28.0 % Mg at Dol_2) (Figure 21). However, distribution mapping of the Fe content highlighted distinct compositional zonation with the Fe content at Dol_1 (about 23% Fe) nearly 3 times greater than the Fe content (7.6 %) measured at spot Dol_2. Changes in the Fe composition, suggest two stages of carbonate formation with an initial stage of euhedral (cm-sized), low-Fe dolomite followed by high-Fe dolomite, with a slight, concomitant reduction in the Ca/Mg content that has infilled void space (Figure 21).

The S distribution image maps the presence of pyrite, which may also represent two generations. The first generation, of generally finer-sized pyrite, appears parallel to bedding associated with the first-stage, low-Fe carbonate mineralisation, whereas larger, disseminated pyrite appears associated with second stage, high-Fe dolomite formation (Figure 21).

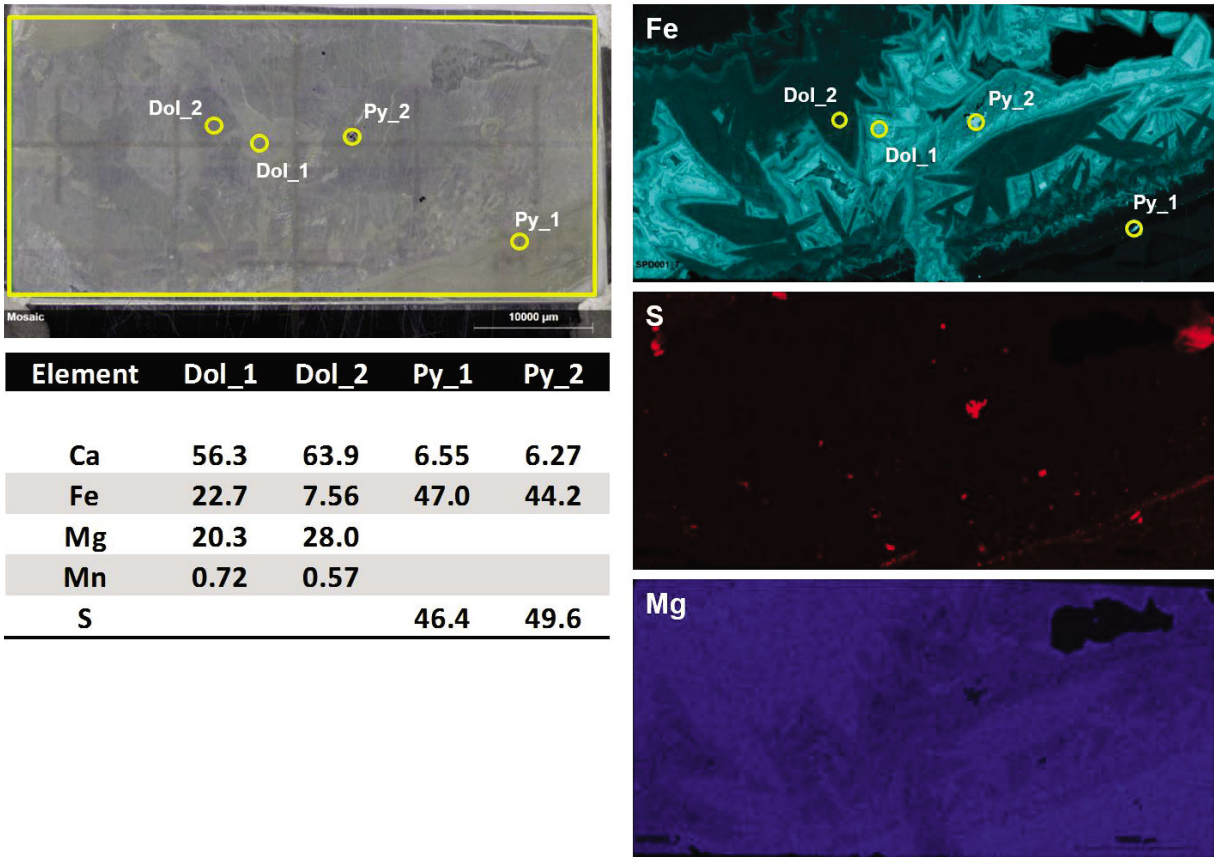

Element	Dol_1	Dol_2	Py_1	Py_2
Ca	56.3	63.9	6.55	6.27
Fe	22.7	7.56	47.0	44.2
Mg	20.3	28.0		
Mn	0.72	0.57		
S			46.4	49.6

Figure 21 Optical (top left) and false-colour element distribution maps for Fe, S and Mg of dolomitic sample SPD001_7 (386.00–386.25 m; Au BD). The Fe distribution map highlights the compositional zonation of dolomite and indicates carbonate formation occurred in two stages. Mineralogy comprised dolomite as the major phase with trace amounts of quartz and muscovite (Appendix 3).

Optical scanning imagery for another dolomitic sample, SPD001_13, showed a more defined colour variation associated with changes in mineralogy as confirmed by the elemental mapping imagery (Figure 22B). The false-colour, composite element map (Si = red, Mg = blue, K = green) clearly shows changes in white-mica and quartz distribution within the host dolomite, and provides a clue to the relative timing of alteration. The cross-cutting nature of the quartz veining indicates that veining occurred following potassic alteration (Figure 22D) of the dolomite (Figure 22B). Sulphide (i.e., pyrite) mineralisation does not appear associated with timing of the quartz veining but was associated with dolomite formation, that is, was present prior to the K-alteration.

Changes in the SWIR and TIR spectral signatures across the alteration zone are consistent with compositional changes that reflect the alteration mineralogy (Figure 22E, F). SWIR spectra measured for location points #4-7 (Figure 22E) show the development of a strong 2200 nm muscovite absorption feature, whereas at the same time TIR spectra for the same measurement locations record a concomitant decrease in intensity of the characteristic carbonate peaks at about 6500 and 11400 nm (Figure 22F).

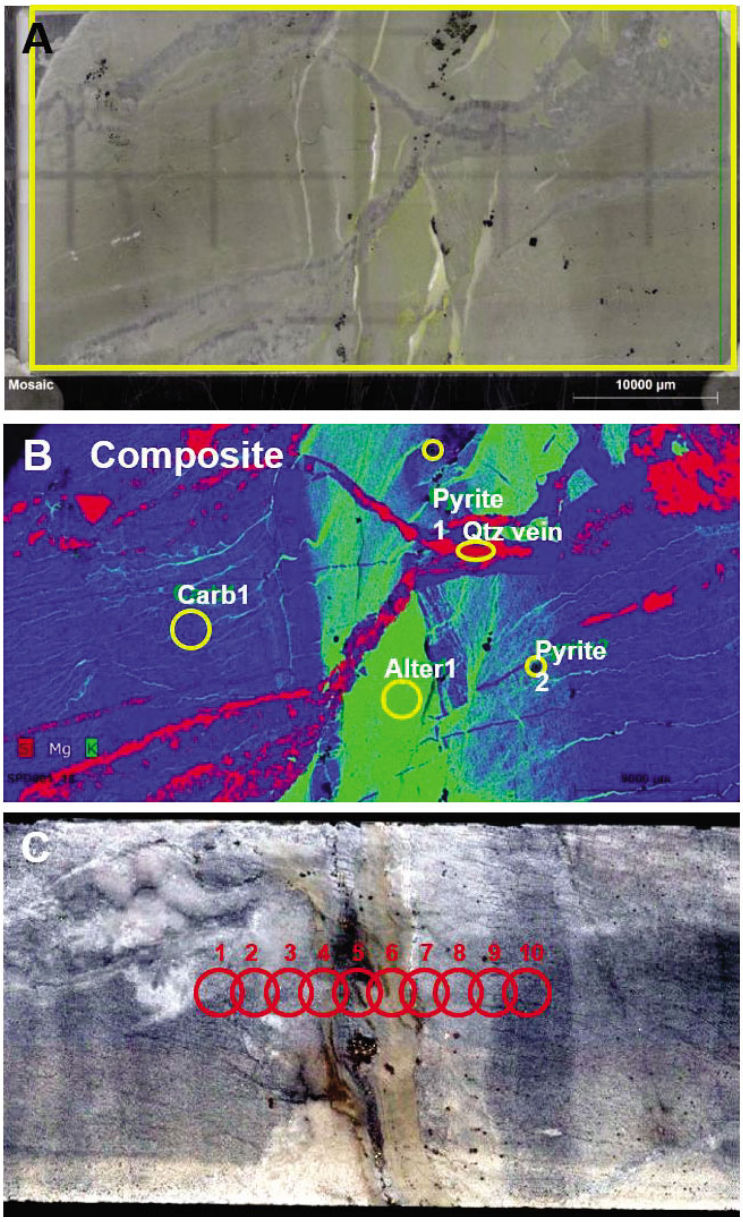

Element	Alter1	Carb1
Si	38.8	5.80
Al	28.7	4.58
K	22.9	2.55
Ti	5.59	0.57
Ca	2.43	55.2
Fe	0.92	10.5
Mg	0.69	20.0
Mn		0.67
P		0.06
Ni		0.04
S		0.00

Figure 22 Optical (top left) and false-colour element distribution maps of Dolomite SPD001_13 (445.68–445.82 m): (A) Optical imagery of grey dolomite with greenish colour variations and crosscutting veins. (B) False colour element distribution map (Si – red, K – green, Mg – blue). (C) Drill core image acquired with HyLogging™-3 system of same drill core interval as (A) and (B) (Note that the thin section and HyLogging™-3 scans are mirror images). (D) Tornado XRF values for two sample points (Carb1 and Alter1) shown in (B). SWIR (E) and TIR (F) reflectance spectra, offset for clarity, for sampling points #1-10 across the alteration zone shown in (C).

Scanning of a siltstone MTO2 from the mineralised zone at the Mt Olympus pit mapped the extent of sulphide alteration through the presence of compositionally variable sulphates, such as alunite (jarosite?) (Figure 23). The false-colour, composite image map of the Si (yellow), Fe (orange) and S (green) distribution, clearly defined the presence of primary sulphides (Figure 23), which showed S contents (51.6–52.3 wt%) close to S values for pyrite, FeS_2 (53. 4 wt%). Measurements of the Fe content (42.6–44.2 wt%) were slightly less than expected for pure pyrite (46.6 wt%) due to the presence of several weight % Si and As (Figure 23). Areas of sulphate alteration (Sulf1—Sulf5) were clearly mapped in the false-colour composite Al (orange), S (green) and K (red) map, with compositionally variable sulphates adjacent to grains of As-pyrite (Figure 23).

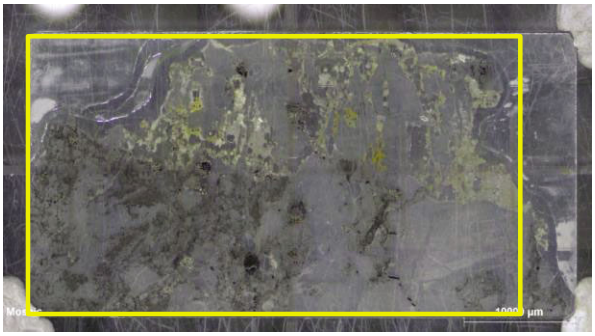

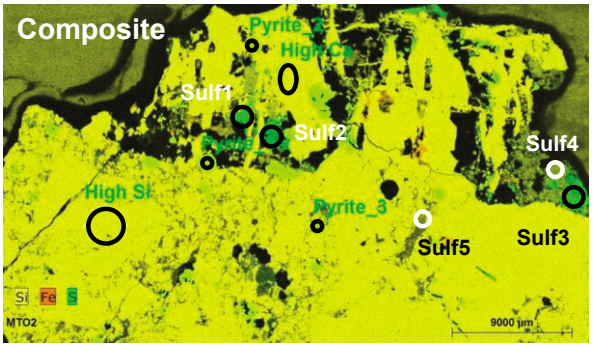

Element	Py1	Py2	Py3	Sulf1	Sulf2	Sulf3	Sulf4	Sulf5
S	52.0	52.3	51.6	34.5	28.5	31.1	6.77	4.49
Fe	43.2	44.2	42.6	2.02	1.47	4.86	2.10	3.96
Si	2.96	2.23	3.02	4.12	24.49	11.19	74.9	44.0
As	1.81	1.32	1.21					
Al			0.94	30.2	19.3	24.6		23.0
K			0.67	25.7	20.6	18.8	2.03	18.9
Ca				3.42	5.62	9.42	14.2	4.23
Ti								1.36

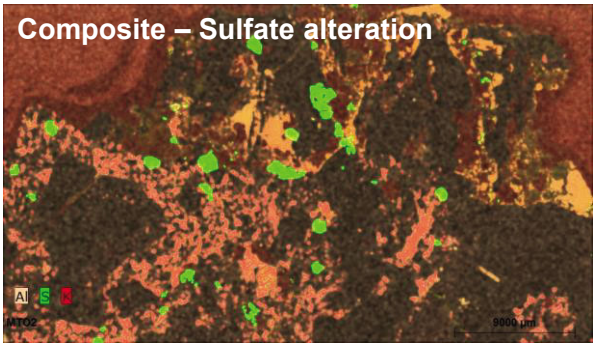

Figure 23 Optical (top left) and false-colour element distribution maps of shale from the Mt Olympus pit (reflected light, RL) showing composite images (top right) of Si (yellow), Fe (orange) and S (green), and (bottom right) of Al (orange), S (green) and K (red). High levels of As, to 1.2–1.8 wt%, are associated with pyrite. The bulk mineralogy comprises quartz (maj); muscovite (min); pyrite (tr), as detected by XRD analysis (Appendix 3 and 4).

DRILL CORE DETERIORATION (ATMOSPHERIC OXIDATION)

During sampling of drill core for XRD validation material it was observed that some sections of drill core had deteriorated to a collapsed, slaked state with abundant conspicuous, white earthy material or as fine, efflorescent coatings. A representative example is shown in Figure 24 from drill core MOD13 (118.4–118.4 m) denoted as sample #23 in Table 4. Similar examples were observed for other sections in drill core MOD13, and in other drill holes (e.g., NMOD-001: 367.75–367.85 (sample #42), and NMOD-002, @ 362.1–366.3 m). The mineralogy of material collected from the zones in core MOD13 is summarised in Table 8.

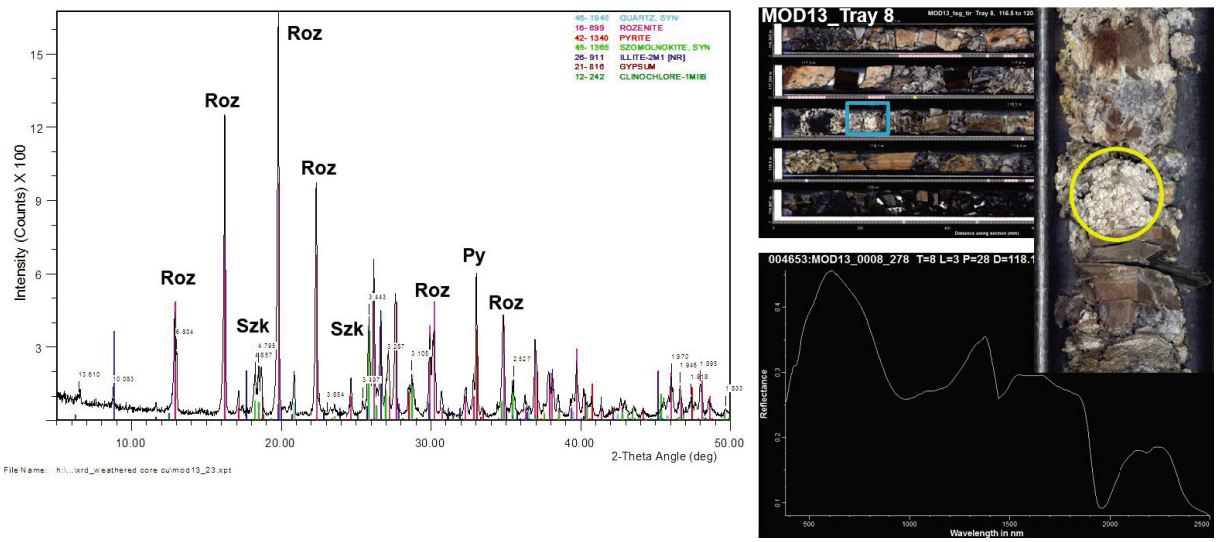

Figure 24 XRD diffraction pattern of MOD13_23 showing the presence of abundant ferrous sulphates as secondary alteration products of pyrite oxidation formed upon exposure of the drill core to the atmosphere while the drill core has been sitting in storage. Mineral key of the main phases follows the abbreviation convention of Whitney and Evans (2010): Roz = rozenite, Py = pyrite, Szk = szmolnokite.

Table 8 XRD mineralogy of pulverulent and white, efflorescent coatings observed in sections of deteriorated drill core.

Core	Sample type	Depth (m)	Mineralogy
MOD13-20	Drill core (Grab Sample)	92-92	Pyrite (maj); szomolnokite, illite, quartz, melanterite (min); sulfur? (tr)
MOD13-22	Drill core (Grab Sample)	92.75-92.8	Melanterite (maj); rozenite, szomolnokite, illite, quartz (min); chlorite, jarosite? (tr)
MOD13-23	Drill core (Grab Sample)	118.4-118.4	Rozenite, pyrite (maj); szomolnokite, illite, quartz (min); chlorite, gypsum(tr)
MOD13-24	Drill core (Grab Sample)	118.8-118.8	Pyrite, szomolnokite, illite (maj); rozenite, quartz (min); chlorite, gypsum, jarosite, As-pyrite? (tr)
NMOD1-42	Drill core (Grab Sample)	367.75-367.85	Illite, szomolnokite, pyrite, quartz (maj); halite?, chlorite, rozenite, (min); gypsum, As-pyrite? (tr)

Melanterite, $FeSO_4.7H_2O$; sidertil, $(Fe,Cu)SO_4.5H_2O$; rozenite $FeSO_4.4H_2O$ and szomolnokite, $FeSO_4.H_2O$, are variably hydrated ferrous sulphates formed as secondary alteration or oxidation products of pyrite, marcasite or other Fe-sulphides (Gaines et al., 1997). They occur as fibrous crusts and splays of needle-like crystals or as feathery efflorescences typically on the exposed walls and timbers of mine workings (Gaines et al., 1997). Melanterite alters in air by dehydration to siderotil or other ferrous sulphates depending on the temperature and relative humidity (Gaines et al., 1997). The occurrence of these phases, likely formed by atmospheric oxidation of fine-grained, mainly, pyrite in drill core exposed for long periods (+10 years) whilst in core trays, is distinct from the occurrence of jarosite as a primary, low temperature alteration of pyrite or to the occurrence of alunite as detected by XRD analysis. Refer to section 1.4.1 for a more detailed discussion.

3.2 Field Work

XRD AND GEOCHEMICAL VALIDATION

As for the validation drill core samples, general element-element associations were evaluated against the bulk XRD mineralogy (Appendix 3). Plots of the K_2O-Al_2O_3, S-Fe and CaO-MgO associations are shown in Figure 25. Samples lying on or close to the expected K_2O:Al_2O_3 ratio expected for muscovite indicate the presence of the white mica as the main K/Al-bearing phase, as confirmed by XRD analysis for these samples (data not shown). However, a majority of the samples fall below this line indicating the presence of other K-free, Al-bearing samples, such as kaolinite and gibbsite, as confirmed spectrally and by XRD analysis.

All field samples contained very little S, with the highest measured S content of 0.35 wt% (sample G1-17) (Figure 25B). However, this amount of S was too low for any free S-bearing phases to be detected by XRD analysis. The Fe-bearing mineralogy of these samples comprised both free iron oxides (goethite and hematite) and Fe-bearing silicates, such as Fe-chlorite.

Samples lying on or very close to the MgO:CaO ratio line expected for pure dolomite indicate the presence of the carbonate as the main Ca/Mg-bearing phase, as confirmed by XRD analysis (Figure 25C). Samples lying above the expected MgO:CaO ratio for dolomite (circled in red, Figure 25C) indicate the presence of other Mg-bearing phases. Iron-bearing chlorite was confirmed by XRD analysis as the main Mg-bearing phase in these cases. For the single sample falling below the MgO:CaO ration line (arrowed), the presence of calcite was confirmed as detected by XRD analysis (Figure 25C).

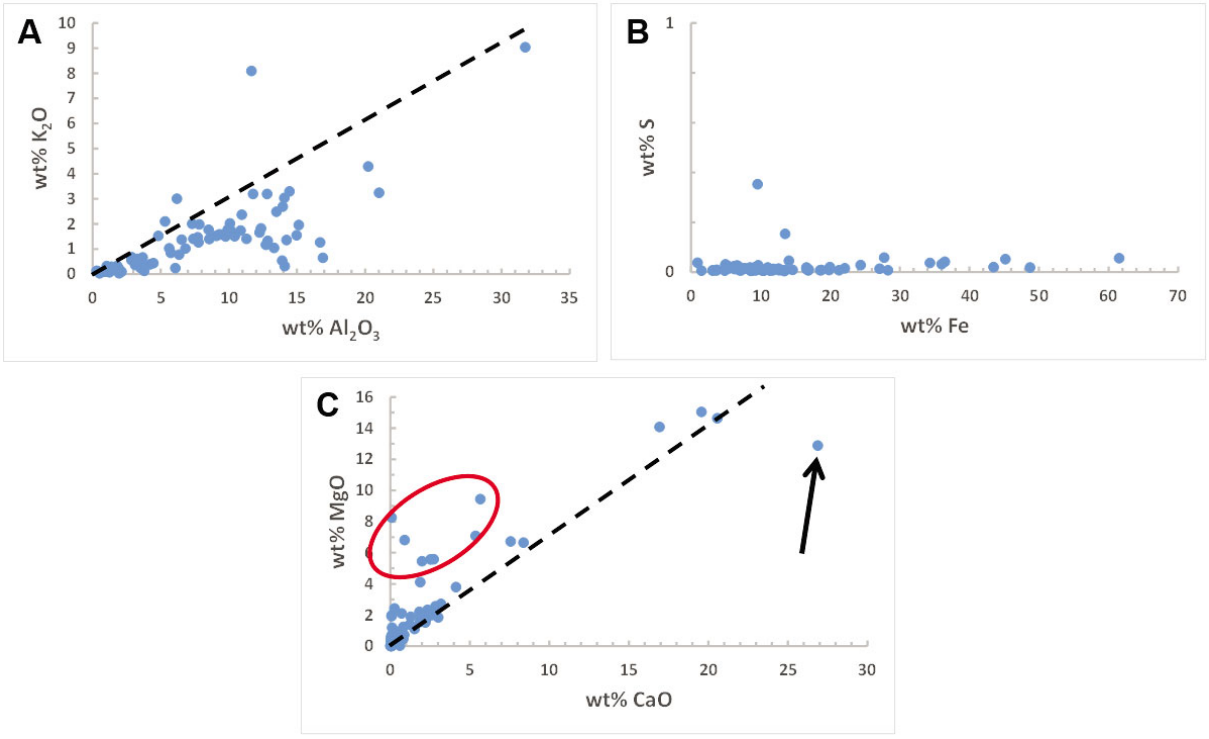

Figure 25 Plots of major and minor element-element relationships that highlight various element-mineral associations: (A) wt% K_2O *vs.* wt% Al_2O_3; (B) wt% S *vs.* wt% Fe, and (C) wt% MgO *vs.* wt% CaO. The dashed line in the plots A and C, represent the K_2O:Al_2O_3 and MgO:CaO ratio expected for pure muscovite and dolomite, respectively. Samples lying above or falling below the dolomite MgO:CaO ratio indicate the presence of other Mg or Ca-bearing phases, respectively (refer to text for further explanation).

SPECTRAL-GEOCHEMICAL ASSOCIATIONS

Chlorite

Changes in the chlorite composition in field samples collected in the vicinity of the Electric Dingo drill hole (refer to Figure 12) and from transects near My Olympus, were characterised by relative changes in the XRD peak intensity (Figure 26A). XRD peak intensity I002/003 values suggest that near-surface chlorite at Mt. Olympus was compositionally more variable than chlorite at Electric Dingo which was more Mg-rich and had a relatively constant Fe/Mg composition. This was confirmed by measurement of the MFEM chlorite composition index (chlepci3pfit) which shifted to shorter wavelengths with increasing Mg content (Figure 26B). The same trend was shown for chlorite detected in validation core samples (refer to Figure 17). The two Electric Dingo samples arrowed in Figure 26B do not contain chlorite but gibbsite as confirmed by XRD analysis. Gibbsite shows a very strong absorption feature at about 2266–2267 nm, which suggests that application of the MFEM chlorite composition index should have an upper limit of 2264 nm (Figure 26B).

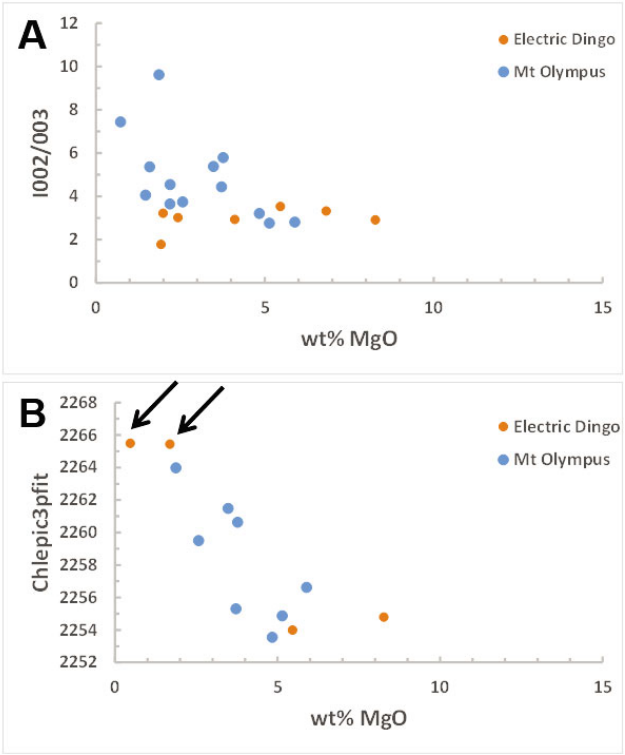

Figure 26 Plots of, (A) XRD peak intensity ratio for the 002 and 003 lines (I002/003) of chlorite, and (B) the MFEM chlorite composition script (chlepci3pfit) *vs*. the bulk Mg content, for field samples collected in the Electric Dingo vicinity and at Mt Olympus. XRD I002/003 values suggest that chlorite at Mt. Olympus was compositionally more variable whereas chlorite at Electric Dingo is more Mg-rich and has a relatively constant Fe/Mg composition, as confirmed by the shift to shorter wavelengths of the MFEM chlorite composition index for chlorite at Mt Olympus. The samples arrowed do not contain chlorite but gibbsite, as detected by XRD analysis and identified to TSA Min1 level, and suggest that further refinement of the chlorite composition script is needed.

Muscovite

Unlike muscovite characterised in validation drill core, changes in the 001 *d*-spacing were unrelated to the bulk Na_2O content for muscovite detected in field samples near Electric Dingo or at Mt. Olympus (Figure 27A). Similarly, changes in the white-mica 2200 nm absorption feature (2200W3pfit) were unrelated to

increasing Na_2O content (Figure 27B) in contrast to muscovite detected in the XRD validation samples (refer to Figure 15). However, grouping of muscovite on the basis of the magnitude of the wavelength of the 2200 nm absorption feature was suggested with muscovite in the Electric Dingo samples tending to have 2200W3pfit values >2202 nm compared to muscovite detected at Mt. Olympus, which showed 2200W3pfit values of <2202 nm (Figure 27B).

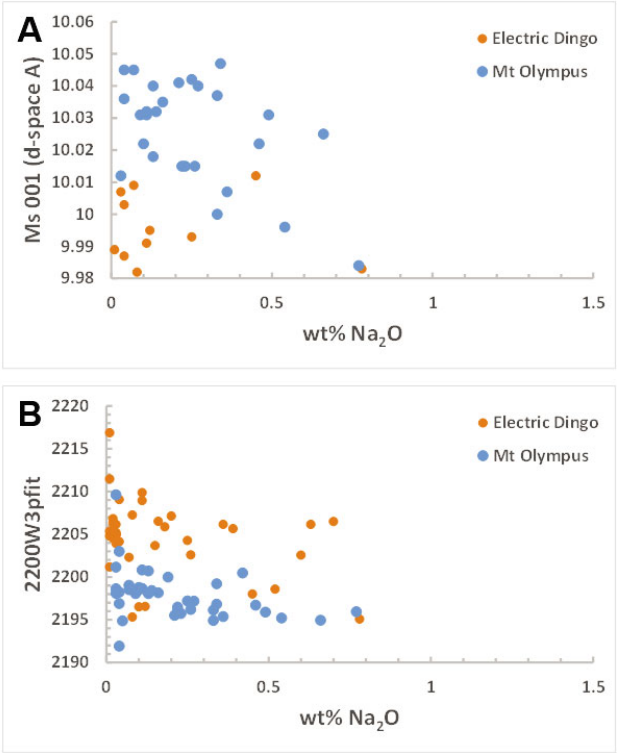

Figure 27 Plots of, (A) the 001 *d*-spacing for muscovite, and (B) the wavelength (nm) of the 2200 "white-mica" absorption feature (2200W3pfit), *vs*. the bulk wt.% Na_2O content for field samples collected in the vicinity of the Electric Dingo drill hole and at Mt Olympus, that only contain muscovite as the predominant Al/K/Na-bearing phase.

3.3 Mineral identification: TSA vs. XRD

Initial comparisons between the mineralogy identified by XRD analysis to that identified using TSA™ were described in section 3.1 for some drill core. A more detailed evaluation was undertaken comparing the HyLogger™-3 results, automatically processed using the TSA spectral reference libraries built in TSG HotCore™ software (see section 2.1), and the XRD mineralogy for all drill core validation samples. TSA_SWIR and TIR user scalars were created, and data for selected drill holes were compared against the identified XRD mineralogy (see section 2.9) (Appendix 3).

Forty one samples were collected from drill holes MOD5, MOD11, MOD13, NMOD001, and SPD001, which represent:

- Oxidised high grade mineralized zone (e.g., MOD13)
- Oxidized low grade ore (e.g., MOD11 and NMOD001)
- Poorly oxidised, unmineralized or very low grade mineralisation (e.g., SPD001).

The mineralisation types identified are discussed in more detail in the following section. However, the XRD validation samples provided were mineralogically varied enough to enable an evaluation of the spectral efficacy for mineral identification compared to that enabled by XRD analysis (Table 9).

Irrespective of the Au mineralisation type, minerals identified at the TSAUser_SWIR group level (e.g, quartz, kaolin, white mica group, carbonate group) were generally consistent to the mineralogy identified using XRD analysis (Table 9). The mineral group with the least congruency between the two characterisation techniques was the chlorite group (Table 9).

For the selected validation XRD samples analysed, kaolin group minerals occurred mainly within low-grade oxidised core (Table 9). Pyrophyllite and kaolinite were reported by TSA_TIR in good agreement with XRD results, although TSA_SWIR results returned only paragonite and occasional pyrophyllite and dickite (Table 9). It was difficult to distinguish between kaolinite and dickite in diffraction patterns and, hence, spectral SWIR data is, in this case, the better tool for identifying these phases at the mineral level.

A less defined, consistent spectrum of paragonite in the SWIR for the same samples was different to muscovite or 'white mica'. In the TSA_SWIR region, the muscovite-paragonite solid solution boundary was determined by an AlOH absorption feature measured at 2195 nm, whereas for shorter wavelengths the Al-rich white mica designation refers to paragonite and at longer wavelengths the designation refers to muscovite. However, pure paragonite has an AlOH absorption feature at 2184 nm, and in this case, where both XRD analysis and TIR spectrum verified the presence of muscovite, it is suggested that high-grade siltstones samples contain white mica of muscovite composition in transition to a paragonitic, more Al-rich member.

Drill core from which the validation samples were selected was often highly fractured and fragmented. During scanning, the fractured surfaces may have increased light scattering producing noisy, low albedo spectra resulting in 'Null' or aspectral results for the TSA mineralogy, especially for the SWIR region (Table 9). In addition, sulphide/sulphate-rich, oxidized core is friable (section 4.1.4) and showed noisy, low reflectance spectra in 50 % samples for both spectrometers, again resulting in 'Null' or aspectral TSA results.

Table 9 Comparison of XRD mineralogy and mineralogy identified spectrally from the TSA spectral library for drill core validation samples.

Sample ID	Kaolin Group			White Mica Group		Chlorite Group		Carbonate Group			Quartz	Feldspar Group			Sulphate/Sulphide Group				
	Kaolinite	Dickite	Pyrophillite	Muscovite	Paragonite	Fe chlorite	Fe/Mg chlorite	Dolomite	Ankerite	Siderite		Albite	Oligoclase	Orthoclase	Gypsum	Fe sulphate	Pyrite	Aspectral	Null
MOD13-18				XT	S						XT								
MOD13-19				X	S						XT			T					
MOD13-21				X	S						X								T
MOD13-25				X							XT							S	
MOD13-26				XT							XT							S	
MOD13-27				X							XT			T		T		S	
MOD13-28				XT	S						XT								
MOD13-29				XT	S					XT	XT								
MOD5-7	XT	S		XS							XT								
MOD11-1			XST	T		X					X								
MOD11-2			XT	T		X					X							S	
MOD11-3	XT	XS	T							X	X								
MOD11-4	ST			X	S						XT								
MOD11-5	X	X		X	S						X								T
MOD11-6	S		XS								XT								
NMOD1-31			XT	XT		X					X							S	
NMOD1-32				X	ST	XS					XT								
NMOD1-33				XT	S	X			S	XT	XT								
NMOD1-34				X	S					X	X								T
NMOD1-35				X	S						X					X	X		T
NMOD1-37				XT	S					XT	XT								
NMOD1-41											X						X	S	T
NMOD1-42											X					X	X	S	T
NMOD1-43										XT	XT							S	
NMOD1-44				T	S						XT				T				
SPD001-1				XT		XT					XT							S	
SPD001-10				S		X	S				X								T
SPD001-11								S	T								X		
SPD001-12				X	T	X	S				XT	T							
SPD001-14				S		X	S	X			X								T
SPD001-15				X	S	XS		X			X								T
SPD001-16						X					X							S	T
SPD001-17						X					X							S	T
SPD001-2					ST	XS							T						
SPD001-3				XT	S	XS					XT			T					
SPD001-4				X		X				X	X								T
SPD001-5								XS	T										
SPD001-6				S				X											T
SPD001-7								XS	T										
SPD001-8				XS				X			X								T
SPD001-9								XS	T										

X - XRD dominant mineralogy
S - SWIR user
T- TIR user

Oxidised high-grade
Primary oxidised (low-grade)
Unmineralised (Distal)

Trace amounts of disseminated pyrite and rutile detected by XRD analysis are not resolvable by the TSA method in these samples. However, there are some options to extract massive sulphides and oxides from TIR spectra. Two samples were mistakenly modelled by TSA_TIR as orthoclase instead of muscovite and the mis-identification of some carbonate species (i.e., ankerite) and some feldspar minerals in TIR data for SPD001 samples may be attributed to very noisy spectra (fine-grained core?) observed for these samples. TSA_TIR data for drill core from this zone were characterised by very noisy spectra (fine-grained core?) which may have contributed to the mis-identification.

3.4 Au -related mineral footprints at Mount Olympus

This section aims to describe some examples of mineral patterns found in the HyLogging data that may be associated with the occurrence of Au at Mount Olympus. First, from evaluating the TSA summary mineralogical data, external lithology log and gold assay values and extracting the most abundant mineral groups (white mica, chlorite, kaolin, quartz, and carbonate abundances), using MFEM scalars (refer to Appendix 1), the scanned drill holes were classed into four groups (Table 10). These groups represent varying Au mineralisation types or associated alteration at Mt Olympus and show some lithological, lateral and vertical variation in the alteration mineralogy.

A summary evaluation, integrating both HyLogging, geochemistry (mainly Au grades) and lithological data, where available, is provided in Appendix 7 for all drill holes examined in the present study.

Table 10 Classification of drill holes based on Au grade, host rock and alteration mineralogy from both XRD and HyLogging data.

Drill hole example	Depth (m)	Au grade (ppm)	Host rock	Alteration	Geochemistry
Weathering zone					
MOD4*, MOD5, MOD6,MOD7,MOD8, MOD12*,MOD13, MOD14	0–140	5–124	**Ferruginous conglomerate** and brecciated silicified siltstone/sandstone	**Hematite**, muscovite, Fe-rich sulphates, patchy kaolinite within sandstone	No data
Primary mineralization (oxidized)					
MOD3**, MOD11**, NMOD001, NMOD002, NMOD005, MTO90	140–570	1–23	Sheared **bleached** and silicified siltstone with disseminated oxidized pyrite	Muscovite, Fe-rich sulphates and **carbonates**, patchy **Fe chlorite**	As, +/-(Pb, Sb, Cu)
Primary mineralization (fresh)					
AMODD0026, AMODD0028	60–450	4–36	Brecciated **quartz-pyrite veins**; bleached sandstone and conglomerate with veinlets and concretions of **pyrite**	Muscovite, **Fe-rich carbonate**, patchy **Fe chlorite**	**S, As, Hg**, +/-(Pb, Sb, Cu, W)
Poorly/unmineralized					
NMOD004, SPD001, **AWD003, EDD005**, NMD001, ID001, LD004	215–860	0.1–2	**Dolomite/siltstone** with pyrite disseminated and veinlets, arenite	**Fe-Mg carbonate and/or chlorite**, muscovite, actinolite	**As**, +/-(Pb, Sb, Cu)

*Au assay available only for the weathering zone
**Au assay available only for the deeper core
Highlighted and underlined holes are not proximal to the Mt Olympus deposit

OXIDISED HIGH-GRADE GOLD MINERALIZATION

High-grade gold mineralization occurs in the oxidised (weathering) zone of ferruginous brecciated siltstones/sandstones, conglomerates and/or black shales in association with quartz-muscovite-pyrite and minor hematite alteration (drill holes MOD4, MOD5, MOD6, MOD7, MOD8, MOD12, MOD13, and MOD14). The zone is traced down to about 140–160 m, where carbonate alteration is dominant, and characterised by high-grade gold located in disseminated pyrite. However, the highest gold value of 124 ppm is hosted by black shales in a strongly brecciated and sheared quartz vein with massive sulphides at depth of 121.4 m in drill hole MOD13 (Table 10). Widespread quartz-muscovite alteration is accompanied by unevenly distributed kaolinite and hematite in sandstones and conglomerates, and minor Fe-chlorite in siltstones. The white mica composition tends to be slightly more Al-rich than for a pure muscovite member and shows a shift in the wavelength position for the Al-OH absorption feature from 2202 nm to 2194 nm. Friable, oxidized and highly mineralized core also show spectra of sulphate minerals, such as alunite and jarosite derived from sulphide oxidation. There wasn't any significant carbonate and chlorite alteration in this zone. Geochemical data was not available.

Simple quartz-white mica composition of the core without widespread kaolinite is not typical for a surface weathering environment and illustrates the strong influence of both hydrothermal alteration and weathering leaching processes on the formation of high-grade ore.

PRIMARY OXIDIZED MINERALIZATION (LOW-GRADE)

Weakly oxidized, low grade gold mineralization is widespread throughout bleached siltstone, minor conglomerates and sandstone rocks in drill holes of this group, and consists of disseminated, oxidized pyrite

in association with quartz, muscovite, graphite, kaolinite/dickite, Fe-chlorite, Fe-carbonate and pyrophyllite (drill holes MOD3, MOD11, NMOD001, NMOD002, NMOD005, MTO90) (Table 10). The highest gold value of 23 ppm refers to a brecciated, quartz-graphite vein at a depth of 260.5 m (drill hole MTO90). Low temperature, hydrothermal mineral assemblages detected by HyLogging were positively validated by XRD analysis (section 4.3, Table 9). Geochemistry shows elevated concentrations of As, Pb, Sb, and Cu in gold-bearing core.

PRIMARY MINERALIZATION (UN-OXIDIZED)

Two recent diamond core holes, AMODD0026 and AMODD0028, drilled under the EIS drilling program intersected fresh (non-oxidized), gold mineralization of 4–36 ppm at a range of depths. Gold-bearing mineralization was associated with:

- brecciated quartz-pyrite-graphite veins
- disseminated in bleached, brecciated graphite-rich sandstones and conglomerates
- veinlets and concretions of pyrite in siltstones.

Widespread Al-rich muscovite, Fe-carbonates, and minor Fe-chlorite accompanied non-oxidized gold mineralization in these drill holes. Geochemical data showed high concentrations of S, As and Hg (Table 10).

DISTAL AND PROXIMAL LOW-GRADE MINERALIZATION

Distal, low-grade mineralization (drill holes NMOD004, SPD001, AWD003, EDD005, NMD001, ID001, LD004) is characterised by widespread dolomite, Fe- and Fe/Mg chlorites, quartz and subsidiary muscovite (Table 10). The highest gold content in core associated with Fe-rich dolomites did not exceed 2 ppm and was confined to only bedrock mineralization (a surface weathering zone was not available). There was a tendency for Al-poor or longer wavelength muscovite to occur in this zone compared to abundant Al-rich muscovite occurring in mineralized core. In addition, the composition of chlorite changed from a pure Fe-rich, associated with gold mineralization, to slightly Fe/Mg-rich in the distal zone.

The following provides a general description of the main lithological logging and spectroscopic characterisation of selected drill cores representative of oxidised lithologies hosting low-grade (e.g., drill hole NMOD001) and high-grade (e.g., drill holes MOD4 and MOD13) Au-mineralisation. Of the drill holes evaluated within the present study, drill hole MOD13 contained the greatest reported Au values amongst the Hylogged™ data set.

MOD13 (high-grade mineralisation)

Drill core MOD13 is comparatively short, from 83.5 to 142 m, for a total length of only 58.5 m and comprises predominantly siltstone as the major logged lithology. Based on the associated logging data, an upper siltstone unit (83.5 to 94.9 m) includes a fault zone (83.5 to 90.6 m) overlying a quartz vein zone (94–103.49 m) that separates the remaining lower siltstone (103.49 to 142 m). The base of the quartz vein zone is marked by an approximately 2 m-thick, massive siliceous (i.e., quartz) vein. The highest Au grades, vary

between 97 and 124 ppm, are hosted by siltstone over the interval 121–124 m. Numerous other mineralised zones (i.e., > 8 ppm) are reported within the siltstone unit at depths of 90–90.8 m, 92.1–94.1 m, 105.1–105.8 m, 109–111.7 and 135.2–136.2 m. The highest gold grades appear associated with sulphidic, black shales with coarse quartz veining.

Inspection of the visual logging data and TIR measurements of the lower siltstone unit confirmed the presence of massive quartz veining associated with pulverulent, sulphidic black shale interspersed throughout the main siltstone unit. These earthy, disintegrated zones displayed white-pale gray, feathery, efflorescent coatings of likely secondary Fe-sulphates, similar to that described in section 4.1.3.

As expected, based on lithological logging, white-mica (e.g., muscovite) with a largely Al-rich composition comprised the main VNIR_SWIR active phase in the drill core (Figure 28C). However, hyperspectral data confirmed the absence of carbonates and chlorite in drill hole MDO13 (data not shown). Coincident with the interval of highest Au mineralisation (121–124 m), white-mica was conspicuously absent and was, instead, associated with the occurrence of kaolin group+alunite (Figure 28D). Though unmineralised, another shallower kaolin group zone at 101.7–103.8 m was also comparatively free of white-mica (Figure 28C).

Two, narrow zones of approximately 20 cm in width, at approximately 95 m and 137.4 m depth showed the presence of sulphates, as K-alunite and possibly gypsum, respectively (Figure 28A and B).

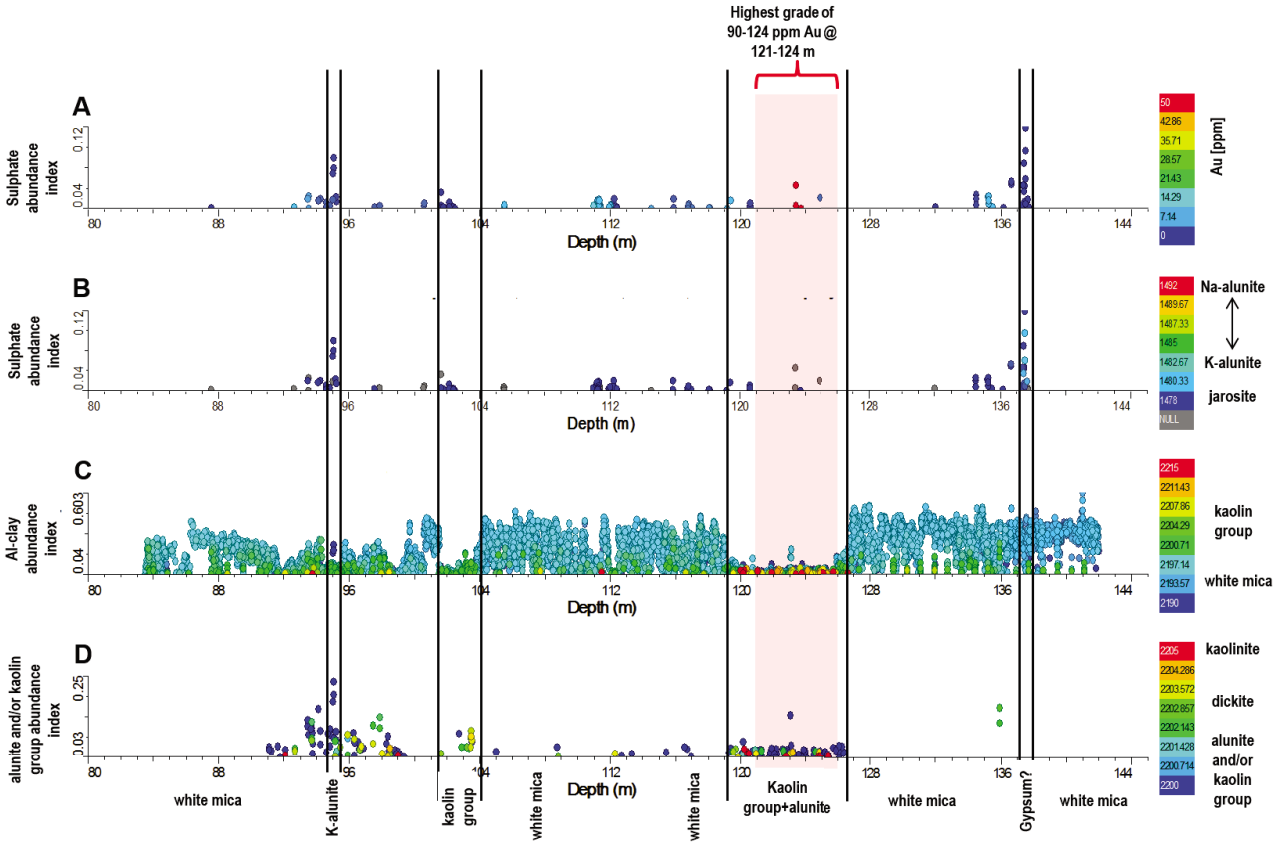

Figure 28 Downhole plots for drill core MOD13 over the depth interval 83.5 to 142.0 m. The zone of the highest Au grade is highlighted in pink. A: Sulphate abundance index coloured by Au (ppm) values. B: Sulphate abundance index coloured by the sulphate species index. C: Al-clay abundance index coloured by Al-clay species index. D: alunite and/or kaolin group abundance index coloured by the related mineral species index.

MOD4 (high-grade mineralisation)

Drill Core MOD4 comprises 190.6 m of drill core (from 11.7 to 202.3 m), which intersects mainly siltstones that are interbedded with carbonates (ca. 192 m depth), dolomites (ca. 140 to 175 m depth) and sandstones (ca. 45 to 92 m depth) according to the supporting drill core logs (Appendix 7). Intense quartz veining occurs between 93 to 97 m depth and a fault zone was described at 40 to 45 m depth. Au is hosted mainly by sandstones and siltstones, recorded at ca. 115, 95, 82 and 54 m depth. Highest Au values of up to 33 ppm occur at 54 m and the mineralised interval at a depth of 82 m coincides with intense quartz veining.

Visual logging and TIR data revealed conglomerate intervals at around 78, 60 and 48 m depth. Hyperspectral data indicate distinct variations in the presence of white mica, chlorite and kaolin group minerals in the siliciclastics. White micas have a largely Al-rich composition in the sandstones and siltstones of MOD4. The chlorite composition ranges from intermediate Fe/Mg ratios to Fe-rich chlorites (e.g., at around 105 m depth). Kaolin group minerals comprise kaolinite and dickite. According to the hyperspectral data, the carbonate rocks are interbedded with siliciclastics in 2–4 m intervals, highlighting a more frequent occurrence of siliciclastics in this interval than suggested by the earlier drill core logs. Shifts of a carbonate-related absorption feature in the SWIR at around 2340 nm suggest that the carbonate composition ranges from Mg-rich calcite to dolomite from bottom to top.

A more detailed view of sandstones between 70 and 95 m depth of MOD4 is shown in Figure 29.This interval surrounds the highest gold values in MOD4 (i.e., up to 33 ppm Au) from 82 to 83 m depth (Figure 29A). No carbonates or chlorites were detected in this interval and there were no major changes in the quartz abundance. The relative abundance of sulphates, such as alunite and jarosite, increased around the mineralised interval, with the highest abundances detected between 76 to 77 m depth. The sulphate species changed from jarosite proximal to the mineralised section to more distal alunite (Figure 29B). A wavelength shift of the hydroxyl-related overtone in sulphates (Figure 30) indicates variations of the Na/K ratio in detected alunites (Bishop and Murad, 2005). Chang et al. (2011) proposed an increase of the Na/K ratio in alunite with increasing temperature and proximity to an intrusive centre in the Mankayan Cu-Au district, Luzon, Philippines. In MOD4, a similar increase of the Na/K ratio towards the mineralised interval at 82 m can be observed only above the gold mineralisation. In fact, the lower half of this interval shows the opposite trend.

The relative abundance of Al-clays, including white mica and kaolin group minerals, in the mineralised interval is highly variable (Figure 29C). However, the abundance of Al-clays, in general, increases more distal from the Au mineralisation. Kaolinite occurs with alunite or is the dominant SWIR-active mineral between sulphate-rich layers (e.g., Figure 29C at 77.5 m depth). More distally, kaolinite is replaced by dickite and muscovite (Figure 29D). Al-clays and sulphates inferred from the SWIR data are presented at the bottom of Figure 29, summarising a mineral footprint that is spatially related to Au mineralisation in MOD4. Similar patterns were observed in HyLogging™ data from drill cores MOD5, 6 and 7.

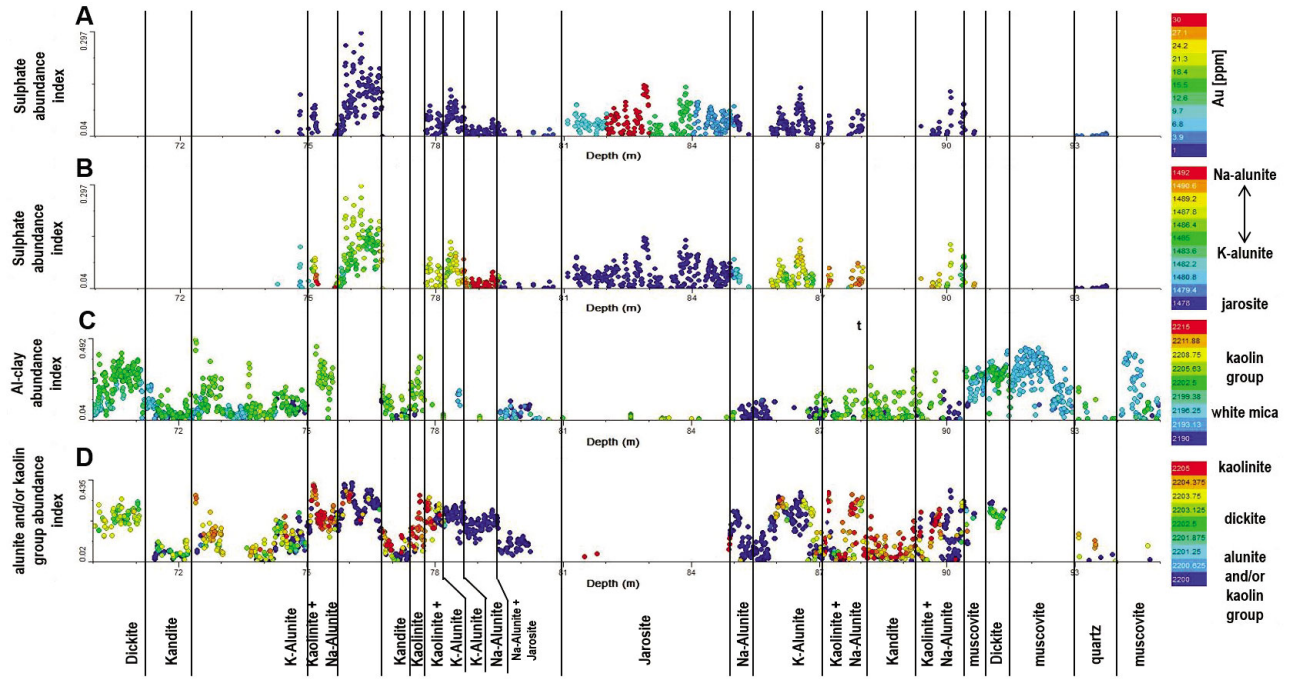

Figure 29 Downhole plots for drill core MOD4 over the depth interval 70 to 95 m. A: Sulphate abundance index coloured by Au (ppm) values. B: Sulphate abundance index coloured by the sulphate species index. C: Al-clay abundance index coloured by Al-clay species index. D: alunite and/or kaolin group abundance index coloured by the related mineral species index.

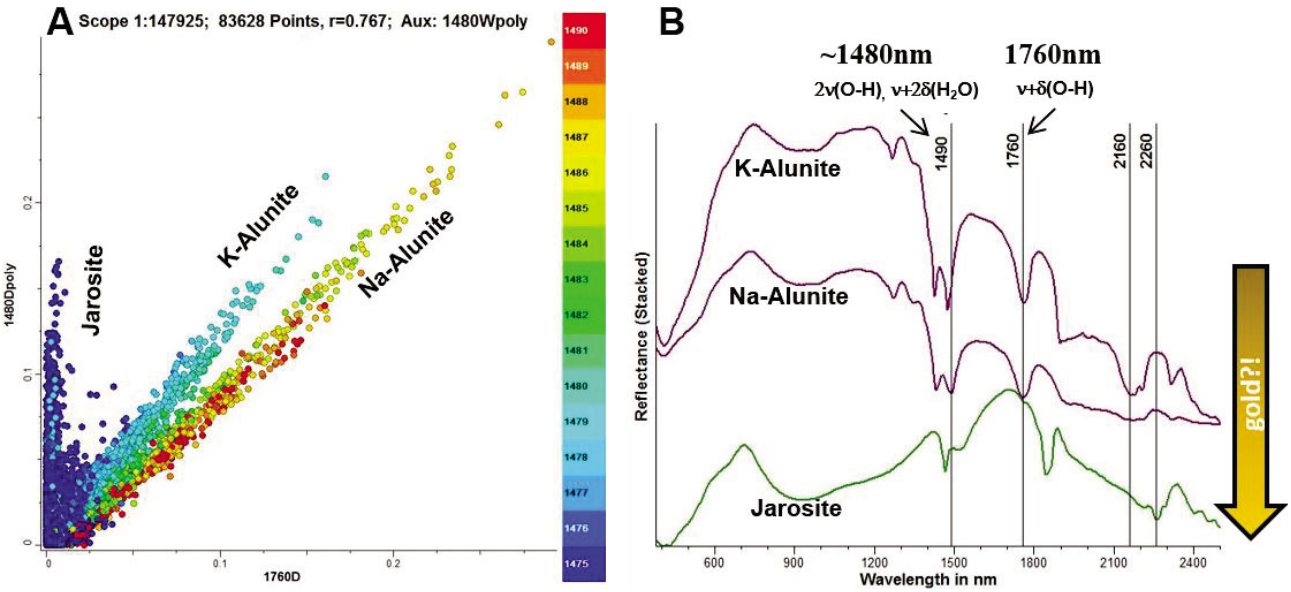

Figure 30 Sulphate species variations in MOD4. A. Plot of the relative absorption depth of the hydroxyl-related overtones in sulphates located at around 1480 nm (y-axis) and at 1760 nm (x-axis). Data points are coloured by the wavelength (nm) of the 1480 nm absorption feature. B. Overlay plot of representative examples of VNIR-SWIR reflectance spectra for K-alunite, Na-alunite and jarosite.

NMOD001 (low-grade mineralisation)

Drill core NMOD001 comprises a total length of 301.3 m (from 179.7 to 481 m) with an upper siltstone sequence (179.7–267 m) overlying a bleached, sheared siltstone zone (267–273 m) hosting quartz veining and pulverulent grey sulphate (e.g., Appendix 7, tray 19), similar to previously described zones, for example in drill core MOD13. These sequences, in turn, overlay an alternating package of arenite (sandstone) and conglomerate. However, inspection of the HyLogging visual imagery shows some level of interbedding between the sandstone and conglomerate units. The highest assayed gold grades, to 4.13 ppm, occur in the faulted siltstone zone (Appendix 7). Two other occurrences with elevated Au grades > 2 ppm occurred at 349.55 m (3.16 ppm Au) and at 442.47 m (2.15 ppm Au) hosted towards the base of the respective conglomerate units (Appendix 7). All three mineralised zones occur within disintegrated (and pulverulent?), bleached siltstone with grey-black sulphides (i.e., sulphidic shale?) (e.g., Tray 19, Appendix 7).

TIR data showed that there were no major changes in the quartz content throughout the drill hole. However, hyperspectral data indicated that the presence of Fe-chlorite was primarily confined to the siltstone unit where the drill hole first intersects this unit (ca. 181 m) and in variable occurrences over the interval 245–255 m (e.g., Appendix 7). Chlorite was essentially absent from the underlying arenite-conglomerate sequence with the exception of two isolated occurrences of Fe-rich chlorite at 345.6 m and 436.1 m in conglomerate that are associated with thin siltstone zones.

Compared to drill holes MOD4 and MOD13, only sporadic, low level occurrences of sulphate alteration (alunite-jarosite) were detected in NMOD001 (Figure 31A and B). Changes in the relative abundance of AlOH-bearing clays (kaolin+white mica) are quite varied throughout NMOD001 (Figure 31C and D). Generally, within the upper siltstone unit, relative abundances of kaolin+white mica were low, with the exception of a thin band at about 229.2 m with a relatively high abundance of kaolin (i.e., dickite) and an increase in the kaolin+white mica abundance towards the end of the siltstone unit for which continuous HyLogging data was measured (Figure 31C). Within the bleached, high-grade sheared siltstone zone, kaolin was essentially absent with the main SWIR-active AlOH phase comprising largely, abundant Al-rich, white mica (Figure 31C). Similarly, the occurrence of Al-rich, white-mica was highly variable throughout the sandstone-conglomerate sequence (Figure 31C) and was essentially free of kaolin, with the exception of localised occurrences of thin, 5–10 cm wide, dickite-bearing bands (Figure 31D).

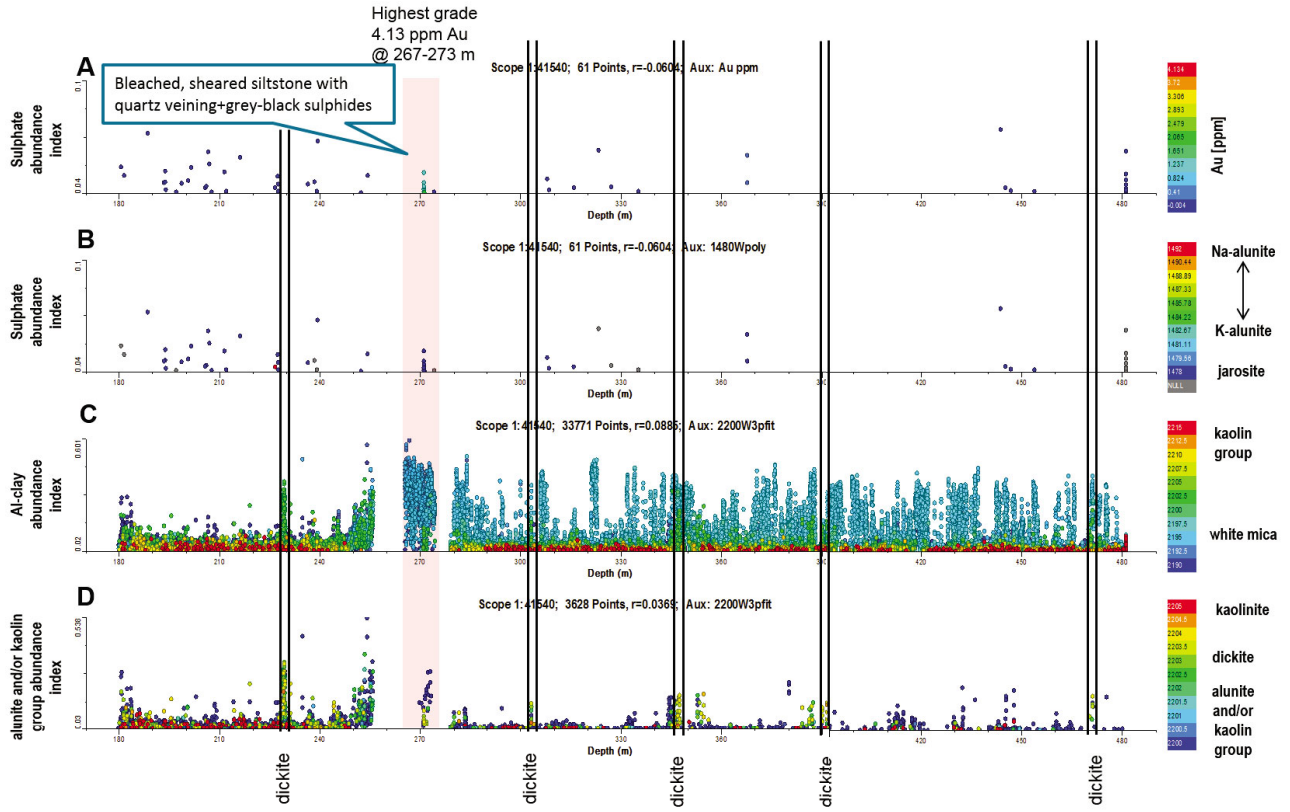

Figure 31 Downhole plots for drill core NMOD001 over the depth interval 180 to 481 m. The zone of the highest Au grade is highlighted in pink. A: Sulphate abundance index coloured by Au (ppm) values. B: Sulphate abundance index coloured by the sulphate species index. C: Al-clay abundance index coloured by Al-clay species index. D: alunite and/or kaolin group abundance index coloured by the related mineral species index. Based on the available scanning data (Appendix 7), core trays 17–18 (interval 255.78–265.3 m) and tray 21 (interval 274.25–278.91 m) were either missing or were not scanned with the HyLogger™-3 system.

3.5 Leapfrog modelling

Visualisation of the main alteration mineralogy in 3D helps to establish the spatial relationships to known (i.e., measured) Au mineralisation. 3D-modelling focussed on the area within the immediate vicinity of Mt Olympus due to the greater number and density of drill holes, as previously discussed (see section 2.11). The Leapfrog model constructed in the course of this project is available from the first author.

The largest zone of Au mineralisation, now exhausted by mining as defined by the Mt Olympus pit, is intersected to the NW by the Zoe Fault, the most significant structural feature mapped in the area (Figure 32). Proximal to this is a zone of sulphate alteration on the northern side of the Zoe Fault within the Mt Olympus pit. 3D modelling revealed irregular, discrete (poddy) zones of Au mineralisation plunging to the SE and intersected by the Zoe Fault plane surface, for example in drill holes AMODD0026 and AMODD0028 intersected by the Zoe Fault (Figure 32). Similar ‘poddy’ zones of sulphate alteration followed the same SE-plunging trend as the Au mineralisation (> 0.5 ppm) but were sub-parallel to the Zoe Fault surface.

In the 3D model, Al-poor white-mica can be observed proximal to and following a similar, plunging trend as the Au mineralisation and sulphate alteration pattern (Figure 33), with the exception of Al-rich white mica occurring within the Mt Olympus pit associated with the main zone of Au mineralisation (Figure 33). Generally coincident with the enveloping zone of Al-poor white mica are Fe-rich chlorites (Figure 33). The exception again, as similarly described for changes in the mica composition, occurs within the area of the

Mt Olympus pit, where proximal to the main zone of Au mineralisation, the chlorite composition changes from Fe-rich in the upper part of the ore zone to an underlying Mg-rich chlorite (Figure 33).

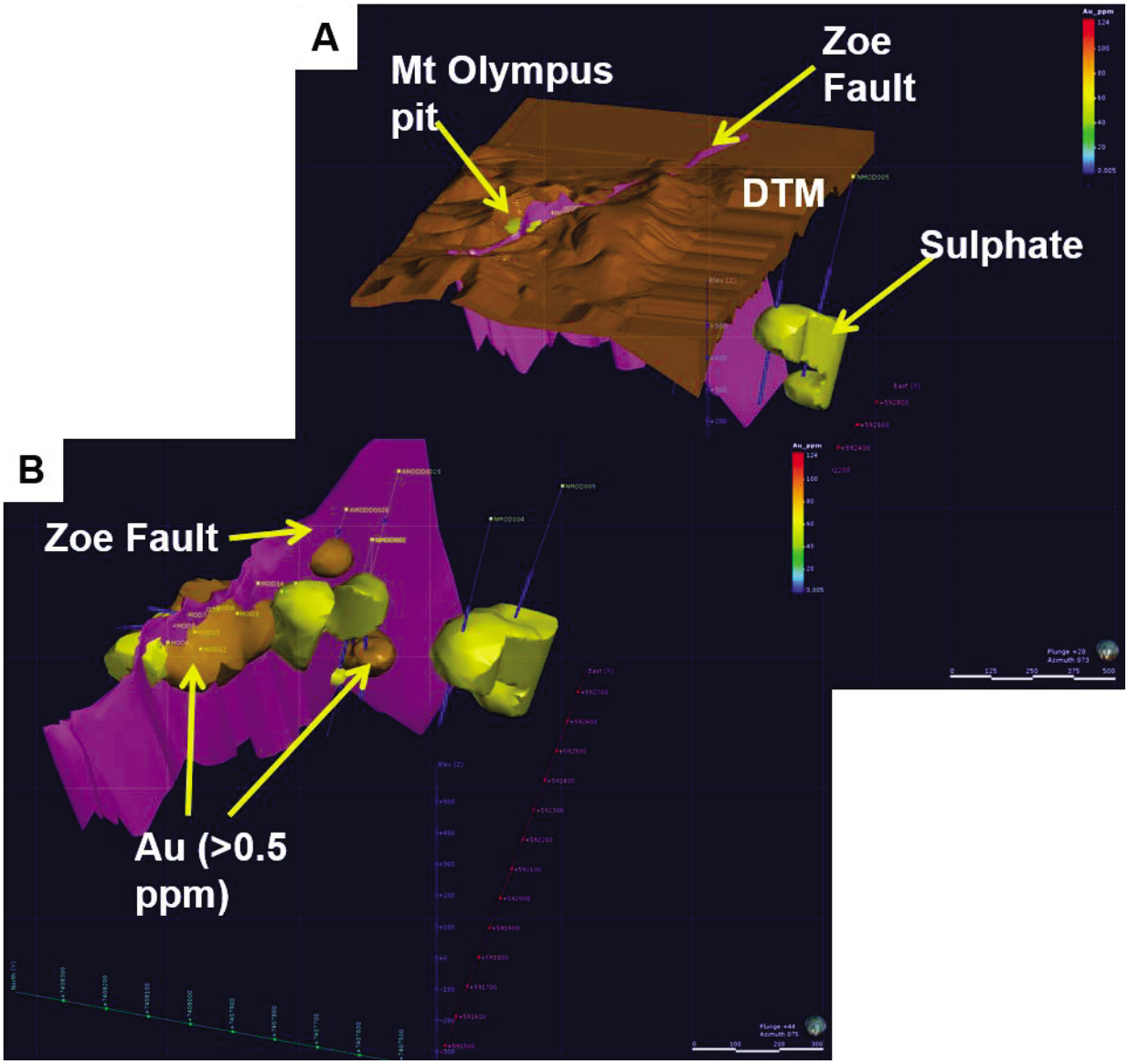

Figure 32 Elevated perspective, near westerly views of (A): Mt Olympus, with the digital terrain model (DTM-brown) showing the Mt Olympus pit outline and the steeply inclined, NW-SE striking Zoe Fault (lilac). The modelled isovolume defines the highest sulphate abundance (yellow) detected spectrally (plunge +20°, azimuth 073°), and, (B) similar view of Mt Olympus with DTM removed to show modelled Au zones (>0.5 ppm) and occurrence of sulphate (plunge +44°, azimuth 075°). Drill core strings, with labelled collars, are coloured according to the assayed Au grade (ppm). Image scale (metres) are shown in the bottom right-hand corner.

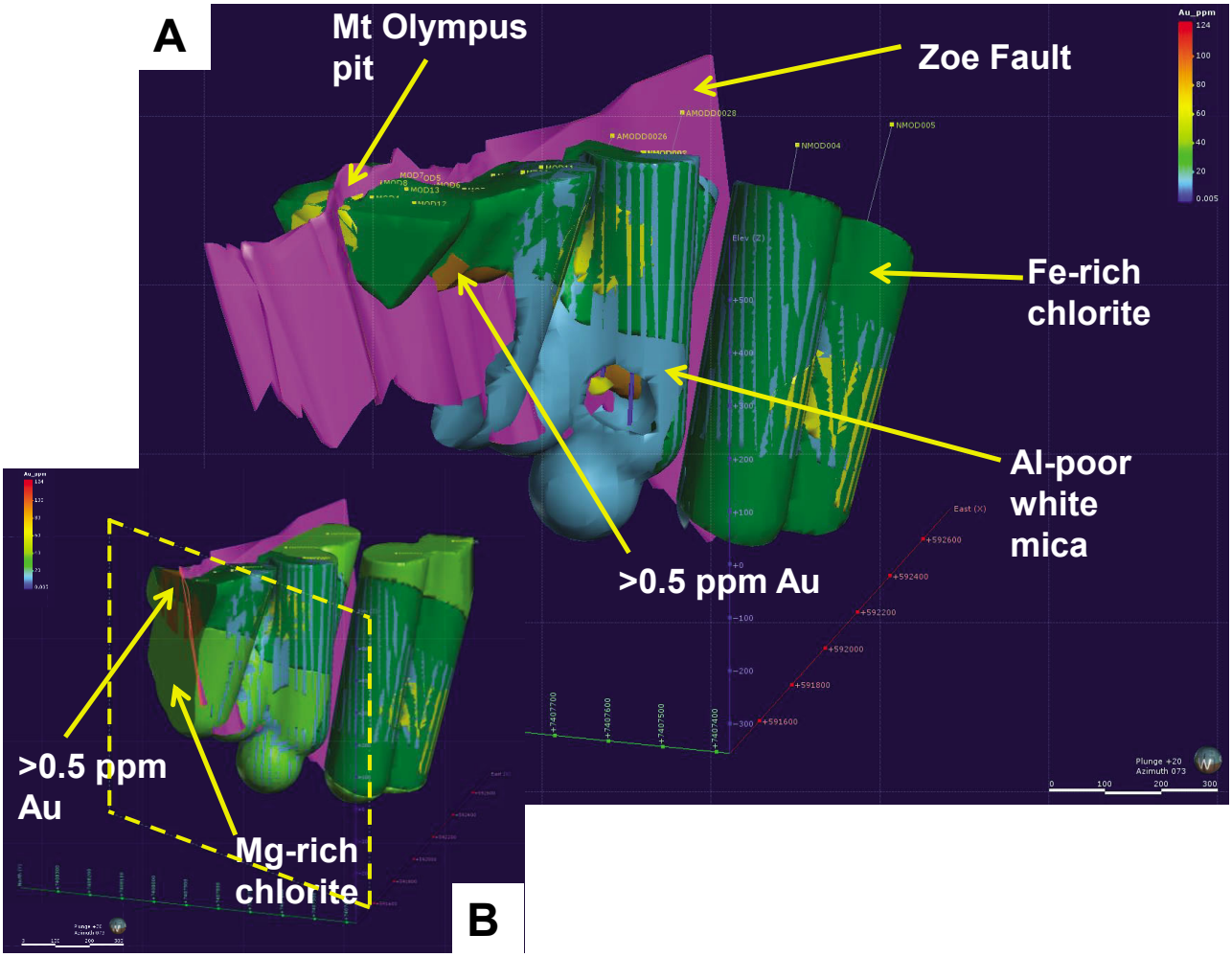

Figure 33 Elevated perspective, near westerly (azimuth 073) view of Mt Olympus, without the DTM overlay (same view as in Figure 32), with the location of Mt Olympus (arrowed) and the Zoe Fault (lilac) shown. The modelled isovolumes define (A): Fe-chlorite (dark green), Al-poor mica (blue), sulphate abundance (yellow), and gold (gold at >0.5 ppm), and, (B): cross-section view orthogonal to the Zoe Fault (dip 90°, dip azimuth 300°) with Mg-chlorite (light green), Fe-chlorite (dark green), sulphate abundance (yellow) and gold. Drill core strings, with labelled collars, are coloured according to the assayed Au grade (ppm). Both views at plunge (+020°), azimuth (073°) and image scale (metres) are shown.

Such spatial changes in the white mica and chlorite composition may reflect hydrothermal alteration overprinting of earlier metamorphic patterns in relation to associated changes in lithology (e.g., siltstone, conglomerate, sandstone) within proximity to the Zoe Fault. In addition, the presence of other fault surfaces not mapped or recognized within the vicinity may also play a role. For example, AEM modelling indicates the presence of other conductive domains sub-parallel to the Nanjilgardy Fault (refer to section 3.6 for a more detailed discussion). However, given the small number of drill holes and, perhaps more importantly, the restricted distribution of the drill holes, which occur essentially along strike of the Zoe Fault and the incomplete nature of the Au geochemical data set evaluated within the 3D model, care should be exercised in attaching too great a significance to the modelled mineral-compositional changes as being geologically meaningful. Inclusion of a larger number of drill holes, of a greater lateral extent with a more complete geochemical data set (i.e., Au assays) would enable a more robust visualisation of the alteration mineralogy at Mt Olympus.

Table 11 Presence of potential indicator minerals (Quartz vein and fault zone were not adopted as lithological description; Black Shale = Siltstone 2; *not analysed for Au)

Mineralisation Style	Mineral Potential origin	K-alunite hydrotherm.	Na-alunite hydrotherm.	Jarosite oxidation	Other sulphates weathering (core)	kaolinite hydrotherm., weathering	dickite diag., hydrotherm.	pyrophyllite hydrotherm	white mica lithic, metamorph., hydrotherm.	chlorite metamorph., hydrotherm.	Host rocks	Barren Lithologies
Oxidation Zone (strongly)	MOD4	Y	Y	Y	-	Y	Y	-	Y	Y	Siltstone 1, sandstone	dolomite, carbonate
	MOD5	Y	Y	Y	-	Y	Y	-	Y	Y	sandstone, conglomerate	ironstone, siltstone
	MOD6	Y	Y	Y	-	Y	Y	-	Y	Y	sandstone, conglomerate	siltstone
	MOD7	Y	Y	Y	-	Y	-	-	Y	-	sandstone, conglomerate	siltstone
	MOD8	Y	-	-	-	Y	Y	-	Y	-	Siltstone 1, sandstone, conglomerate	-
	MOD12	-	-	-	-	Y	-	-	Y	Y	Black shale	carbonate*
	MOD13	Y	-	-	-	Y	Y	-	Y	Y	Black shale	-
	MOD14	-	-	-	Y	-	Y	-	Y	Y	sandstone, (conglomerate)	siltstone
(weakly)	MOD3	-	-	-	Y	Y	y	-	Y	Y	Siltstone 1	Shale, dolomite
	MOD11	-	-	-	Y	Y	y	Y	Y	Y	Siltstone 1	marl, dolomite
	MT090	-	-	-	Y	Y	y	-	Y	Y	Siltstone 1	-
	NMOD001	-	-	-	-	-	Y	Y	Y	Y	Siltstone 1, conglomerate	arenite
	NMOD002	-	-	-	Y	-	Y	_	Y	Y	Black shale	dolomite, siltstone
	NMOD005										Siltstone 1	dolomite, arenite
Primary Mineralisation	AMODD0026	-	-	-	Y	Y	Y	-	Y	Y	Black shale, sandstone (conglom., dol.)	Ltihic sandstone, breccia
	AMODD0028	-	-	-	-	Y	Y	-	Y	Y	conglomerate (sandstone, siltstone)	dolomite, carbonate
Un/Poorly Miner. (Prox)	NMOD004	-	-	-	-	Y	Y	Y	Y	Y	(Black shale)	
(Distal)	NMD001	-	-	-	-	-	-	-			(carbonate)	
	AWD003	-	-	-	-	-	-	-	Y	Y	(Black shale)	
	EDD005	-	-	-	-	-	-	-	Y	Y	(carbonate)	
	ID001	-	-	-	-	-	(?)	-	Y	Y	(carbonate)	
	LD004	-	-	-	-	Y	-	-	Y	-	(Black shale)	
	SPD001	-	?	?	-	-	Y	-	Y	Y	(carbonate)	

3.6 Comparison of ASTER with surface data

DISCUSSION OF MINERAL FOOTPRINTS OBSERVED IN SAMPLES

Before tracing mineral footprints potentially associated with Au by means of remote sensing data, the respective mineral footprints and their characteristics in terms of mineral assemblage and radius around the mineralisation are discussed. Mineral footprints along the Nanjilgardy Fault can be classified in the following categories: 1) igneous, 2) diagenetic to metamorphic, 3) hydrothermal, 4) oxidation of primary mineralisation, 5) regolith. Potential indicator minerals for these five categories of mineral footprints along the central and eastern Nanjilgardy Fault comprise sheetsilicates (i.e., kaolinite, dickite, pyrophyllite, white mica, chlorite), sulphates (alunite, jarosite), iron oxides, quartz and carbonates. Table 11 lists the occurrence of selected indicator minerals in the investigated drill cores, grouped according to the respective zones (see section 4.4 for description of zones).

Diagenetic and metamorphic footprints: Diagenetic and metamorphic footprints can be assigned to burial diagenesis and regional metamorphism, respectively. Both will create regional mineral footprints that can, however, vary strongly depending on the respective affected lithology. The northern Ashburton Basin has been exposed to up to sub-greenshist facies metamorphism (Wilson et al., 2010). Depending on the respective metamorphosed rocks and local PT-variations this may have caused a regional transformation of kaolin group minerals and smectites to white mica and chlorite. Wilson et al. (2010) described chlorite, berthierine and 1M illite as well as glauconite in carbonates of the Duck Creek Dolomite to the West of the Wyloo Dome. Potential glauconite was detected in some of the HyLogged™ drill cores that intersected the Duck Creek Dolomite (e.g., LD0004). Siliclastics of the Mount McGrath Formation, including siltstone, sandstone and conglomerate, and tholeiites of the Cheelah Springs Basalt also show metamorphic chlorite.

Hydrothermal: Hydrothermal footprints comprise local veining and bleaching, but also extensive pervasive alteration of earlier formed mineral assemblages. Veins are mainly composed of quartz. Single quartz veins are usually less than 0.5 m thick, but can accumulate in certain areas, which could represent footprints of considerable size. However, sandstones and conglomerates contain, originally, high abundances of silicates, creating an already elevated “background” of silica. In addition, removal of quartz in mineralised intervals was observed in, for example, MOD7 and MOD14. In summary, the tracking of silicification in the Mount Olympus area using remote sensing data is not recommended.

Bleaching of metasediments is used by local geologists as a vector towards mineralisation (Dale Annison pers. comm.) and was observed in drill cores from all four zones (see section 4.4 for a description of zones). Young et al. (2003) associated illitic sericite and silicification with the bleached appearance of alteration zones. Hyperspectral data suggest that bleached intervals mainly, indeed, contain white mica (potentially illitic), but also dickite and/or alunite or simply may be related to variations in surface iron oxide staining (section 3.1). However, no distinct correlation between bleaching and Au mineralisation was found in the sandstones or siltstones.

Minerals that could be attributed to pervasive hydrothermal alteration in common lithologies along the Nanjilgardy Fault comprise sodic and potassic alunite, kaolinite, dickite, pyrophyllite, white mica and chlorite. White mica was present across all four zones, including almost all four drill cores of the distal zone. At this stage, it is difficult to differentiate between metamorphic and hydrothermal chlorites along the Nanjilgardy Fault. However, white micas that were found along potential pathways for hydrothermal fluids potentially bear a characteristic spectral signature. The kaolin group minerals kaolinite and dickite were

observed in all four zones as well. However, their distribution was more restricted to certain intervals in the drill cores, when compared to the widespread occurrence of white mica and chlorite. Pyrophyllite was only observed in drill cores MOD11, NMOD001 (both zone "primary mineralisation, oxidised") as well as NMOD004 ("proximal"). Validated by XRD, the HyLogging data showed that chlorite contains variable amounts of Mg/Fe in siliciclastics of the Mt Olympus area, whereas the composition as more Mg-rich atop mafic rocks, such as around Electric Dingo (e.g., see Figure 26). No systematic variation of the chlorite composition in respect to Au mineralisation was found, with drill core HyLogging data showing a low chlorite abundance in Au-bearing intervals. Pervasive sulphate alteration was only recorded in the "weathering" zone, with potassic alunite dominant over sodic alunite. The presence of potassic alunite proximal to mineralisation was confirmed by Tornado element mapping (e.g., Figure 23).

A number of drill cores showed a characteristic spatial distribution of indicator minerals with respect to the presence of Au. These possible Au-related mineral footprints can be summarised as follows:

1) Siltstones 1 (bright shales): muscovite ± quartz veining ± post quartz removal? > muscovite + chlorite

2) Siltstones 2 (black shales): white mica ± kaolinite > white mica > white mica + chlorite (e.g., Figure 28 for details)

3) Sandstone:

Type-A): jarosite > alunite (K/Na) > alunite + kln > dickite > white mica > chlorite (e.g., Figure 29 "MOD4" for details)

Type-B): white mica > white mica + kaolinite > white mica?!

4) Conglomerate: white mica ± dickite > kaolinite/dickite

In addition to those four major mineral footprints possibly related to Au mineralisation it was observed that quartz veining can increase in the mineralised zone. It was evident from a number of drill cores (e.g., MOD7, MOD11, MOD14) that primary quartz was often removed from the background mineral assemblage.

Oxidation: Main indicator mineral groups for oxidation of primary sulphides in the Mount Olympus area are jarosite and, to a lesser degree, iron oxides, such as hematite.

Regolith: Mineral footprints due to regolith formation along the Nanjilgardy Fault were mainly related to the formation of kaolin group minerals and iron oxides. Other minerals that are typically formed in the regolith, such as smectites, were not detected in the HyLogger™-3 data set to any large extent.

ASTER

Based on the above discussion of mineral footprints in the surface and subsurface data sets, a suite of indicator minerals was selected for the corresponding mineral assemblages that point, potentially towards Au mineralisation in the Mount Olympus area using the ASTER Geoscience Products. The indicator minerals for sandstone, such as observed in MOD4, and siltstone hosted Au mineralisation, such as in MOD13, are summarised in Figure 34A and Figure 34B, respectively. The respective minerals show a number of diagnostic absorption features in the hyperspectral SWIR, but also VNIR wavelength regions as in the case of jarosite (Figure 34C). For example, both sulphate minerals, jarosite and alunite, which occurred proximal to Au mineralisation in sandstones, display a distinct absorption feature at around 1480 nm (see also Figure 29 and Figure 30). In addition, alunite shows a strong absorption feature in the 2160 nm wavelength region, which can also be observed in kaolinite. Both the 1480 and 2160 nm absorption feature could be traced in field surface spectroradiometer data acquired in transects E and F (Figure 35A, B). However, ASTER

provides only a multispectral resolution of the 2160 nm wavelength region (see also section 2.1) and does not record the 1480 nm wavelength region. Therefore, only the 2160 nm absorption feature can be used to map alunite and/or kaolinite, using, for example, the Kaolin Group Index (Figure 35C), where a moderate correlation between the surface hyperspectral and remote multispectral data was evident. The Ferrous Iron Index and FeOH Group Content products were evaluated for mapping jarosite in the study area, based on the potential absorptions at bands 3 and 6, respectively (Figure 34), but without success.

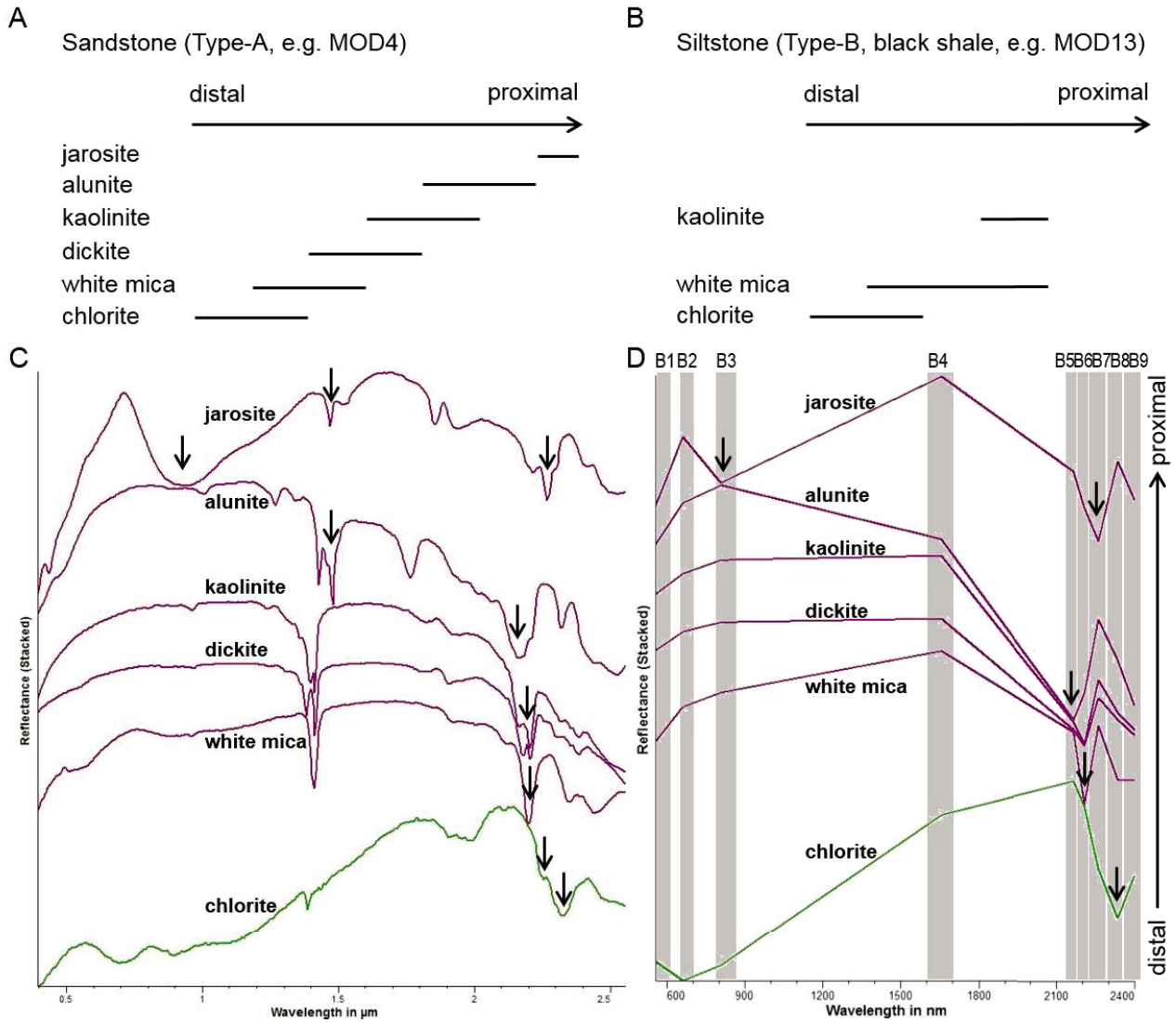

Figure 34 Au-related mineral alteration patterns and indicator minerals identified in the Mount Olympus area. A - Sandstone (Type-A), B – siltstone (Type-B). A comparison of Hyperspectral (C) and multispectral or ASTER (D) reflectance spectra is shown for indicator minerals associated with sandstone Type-A alteration.

A summary of ASTER Geoscience Products with potential for use in mapping the indicator minerals described above is provided in Table 12. At the scale of transects E and F, only the Kaolin Group Index (Figure 35), MgOH Group Content (Figure 36A) and Opaques Index (Figure 36B), showed patterns that could be correlated with major structures or with the HyLogged drill cores around Mount Olympus. A widespread, elevated MgOH content around Mount Olympus (Figure 36A, left white arrow), for example, could be related to pervasive white mica+chlorite assemblages. A similar sized footprint is located to the northeast of SPD001 close to the intersection of a northeast trending fault and north-northwest trending faults, parallel to the Nanjilgardy Fault (Figure 36, black arrowed location). The centres of both areas are also highlighted by elevated values in the Opaques Index, and other areas along the NNW trending fault

(Figure 36B, black arrows), potentially pointing to the occurrence of black shales, such as described in MOD13.

Table 12 Potential ASTER Geoscience Products for mapping indicator minerals and potential host rocks

Indicator material	Possible origin	ASTER Geoscience Product
jarosite	oxidation	FeOH Group Content, Ferrous Iron Index
alunite	hydrothermal	Kaolin Group Index
kaolinite	hydrothermal, weathering	Kaolin Group Index, AlOH Group Content & Composition
dickite	hydrothermal	Kaolin Group Index, AlOH Group Content & Composition
white mica	metamorphic, hydrothermal	AlOH Group Content & Composition
chlorite	metamorphic	MgOH Group Content, FeOH Group Content
White mica + chlorite	metamorphic, hydrothermal	MgOH Group Content
black shale	Host rock	Opaques Index

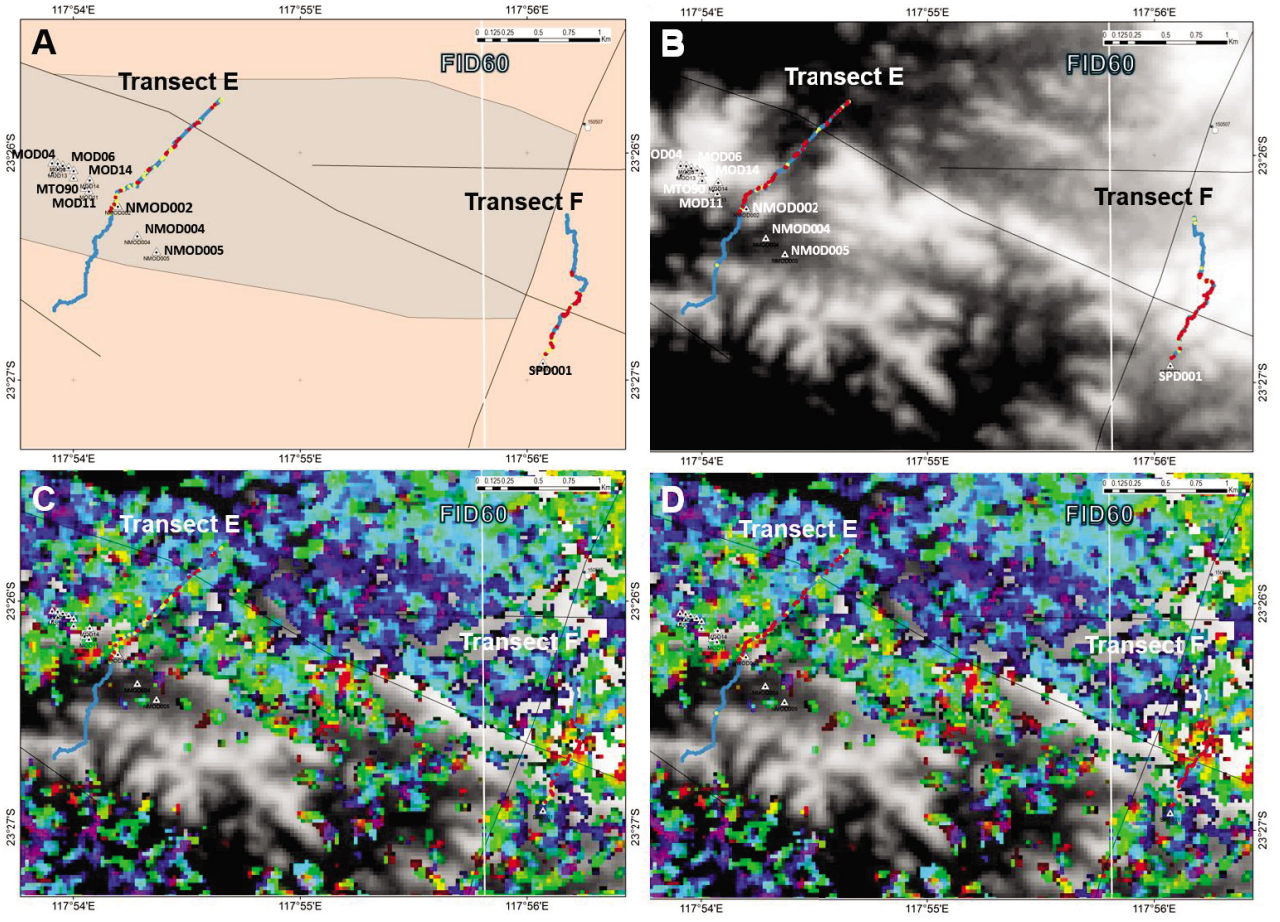

Figure 35 Mt Olympus field ASD spectroradiometer transects E and F compared with ASTER Geoscience Products. A - 1480D field data over the 500K Geological Map; B - 2160D field data over DEM; C - 1480D field data over the ASTER Kaolin Group Index over DEM. D - 2160D field data over ASTER Kaolin Group Index over DEM.

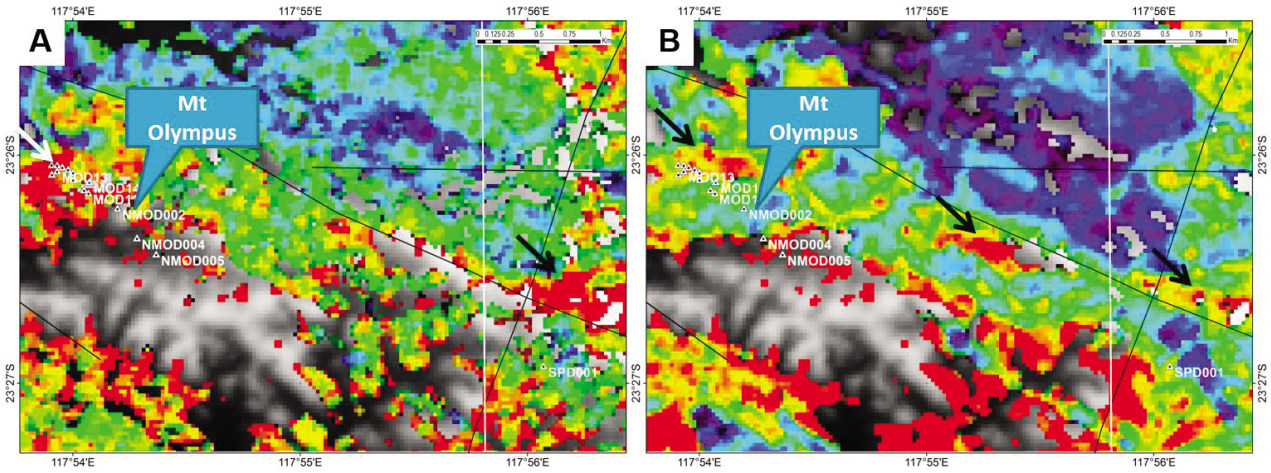

Figure 36 False colour ASTER Geoscience products overlaying the DEM (black-white image) of the Mt Olympus area. (A) MgOH Group Content, (B) Opaques Index. Elevated MgOH contents west of My Olympus (white arrow) may be related to pervasive white mica+chlorite assemblages.

ASTER AND AEM DATA COMPARISON

The previously selected ASTER Geoscience Products (Table 12) were compared with AEM data to find potential relationships between surface mineral footprints and geological subsurface domains of different conductivity that are potentially separated by significant fault systems. As a first example, the MgOH Group Content was used for this comparison, as preliminary results showed a NNW-trending pattern, parallel to the Nanjilgardy Fault with significant, non-fault related changes in the chlorite+white mica content along strike (e.g., white arrow in Figure 37B). The cross cutting points of the AEM profile FID59 with major geological boundaries are shown in the geological map (Figure 37A) and the AEM profile (Figure 37D) for orientation. The Nanjilgardy Fault (NF) shows no significant change in the MgOH Group Content, but separates a high conductivity domain in the South from a low conductivity domain in the North. The northern fault between the lower and upper Wyloo Groups (LCN) is neither evident from the MgOH Group Content nor the AEM profile. In contrast, the southern fault (OF1) between the lower and upper Wyloo Groups, coincides with a marked change in the MgOH Group content and also the surface expression of a south dipping fault line or lithological contact. However, the MgOH Group Content clearly shows that this structure is not parallel to the NW-trending fault described in the geological map, but rather trends EW and can be followed further to the West and East of FID59. In addition, three more sharp, conductivity highs are evident between OF1 and NF (pink arrows), which all can be extrapolated to the East and West using the MgOH Group Content image. In fact, other ASTER Geoscience Products (Figure 38), such as the Opaques Index, trace the same features (Figure 38D). It is unclear, if these features are fault lines, lithological contacts or bedding parallel shear zones, but they may resemble smaller scale structures that can also be observed in Mount Olympus.

The AEM profile exhibits additional sharp, conductivity contrasts that may be related to fault zones, but are not displayed in the bedrock geological map. For example, a distinct south dipping, high conductivity layer (black arrow) is located to the South of the Nanjilgardy Fault at approximately 7404400 mN but was not mapped on the geological bedrock map (Figure 37 and Figure 38). Similarly, shallow, South dipping zones were identified in AEM profiles to the West, such as in the Electric Dingo area (Appendix 8).

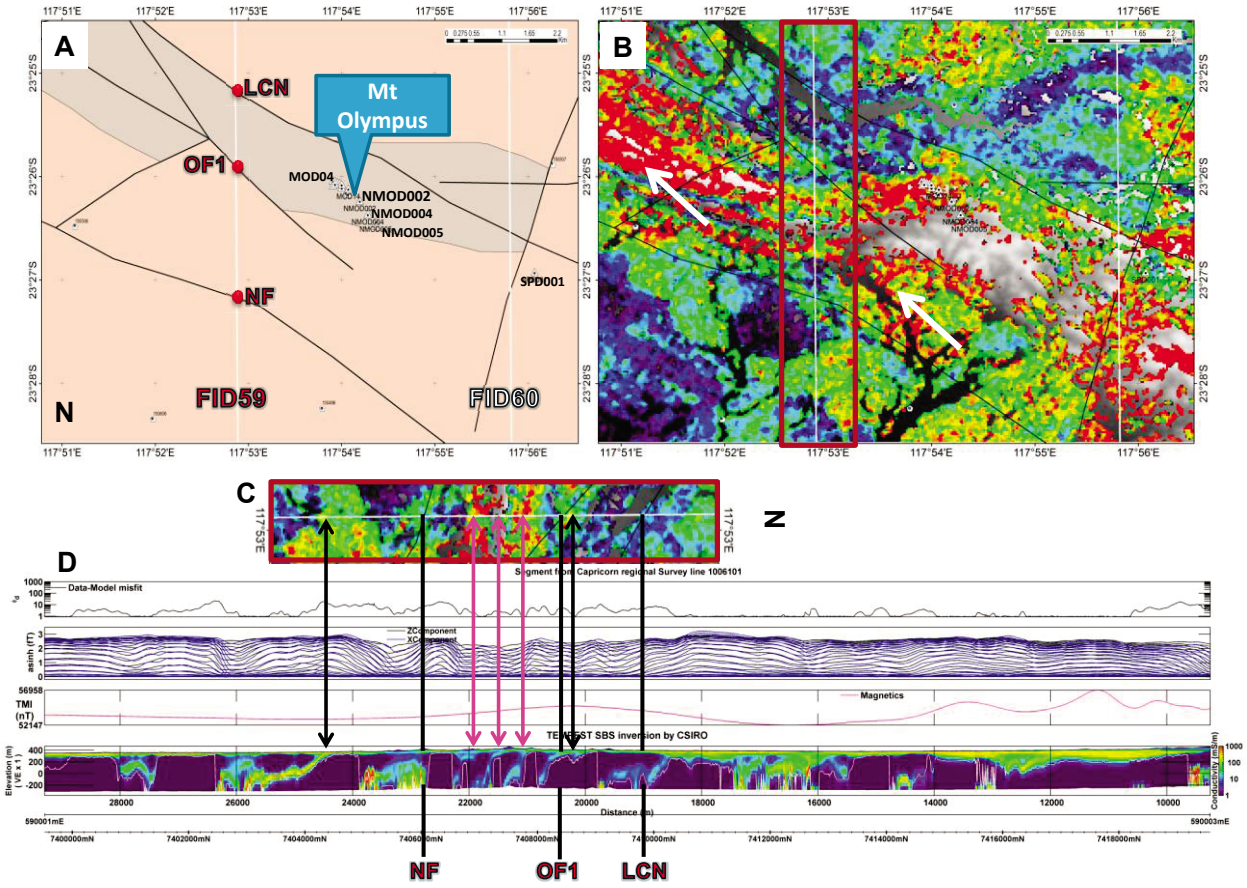

Figure 37 Comparison of AEM and ASTER Geoscience Products, Mount Olympus area: (A) Bedrock geology (grey - lower Wyloo Group, pink - upper Wyloo Group), locations of HyLogging data (e.g., NMD004) and location of AEM lines FID59 and FID60 showing intersections with major structural/lithological boundaries (NF - Nanjilgardy Fault, OF1 - Fault at southern contact between lower and upper Wyloo Grp., LCN - Fault at northern contact between lower and upper Wyloo Grp.). (B) and (C) MgOH Group Content product (blue - low content, red - high content) over greyscale DEM. The red box outline in (B) shows the MgOH Group content mapped in (C). (D) Conductivity-depth sections from a smooth model (30-layer) inversion of TEMPEST data along AEM line FID59. Solid, vertical black lines (not arrowed) show locations of the Nanjilgardy Fault and the contacts between lower and upper Wyloo Group (OF1, LCN) in AEM and ASTER Geoscience Product.

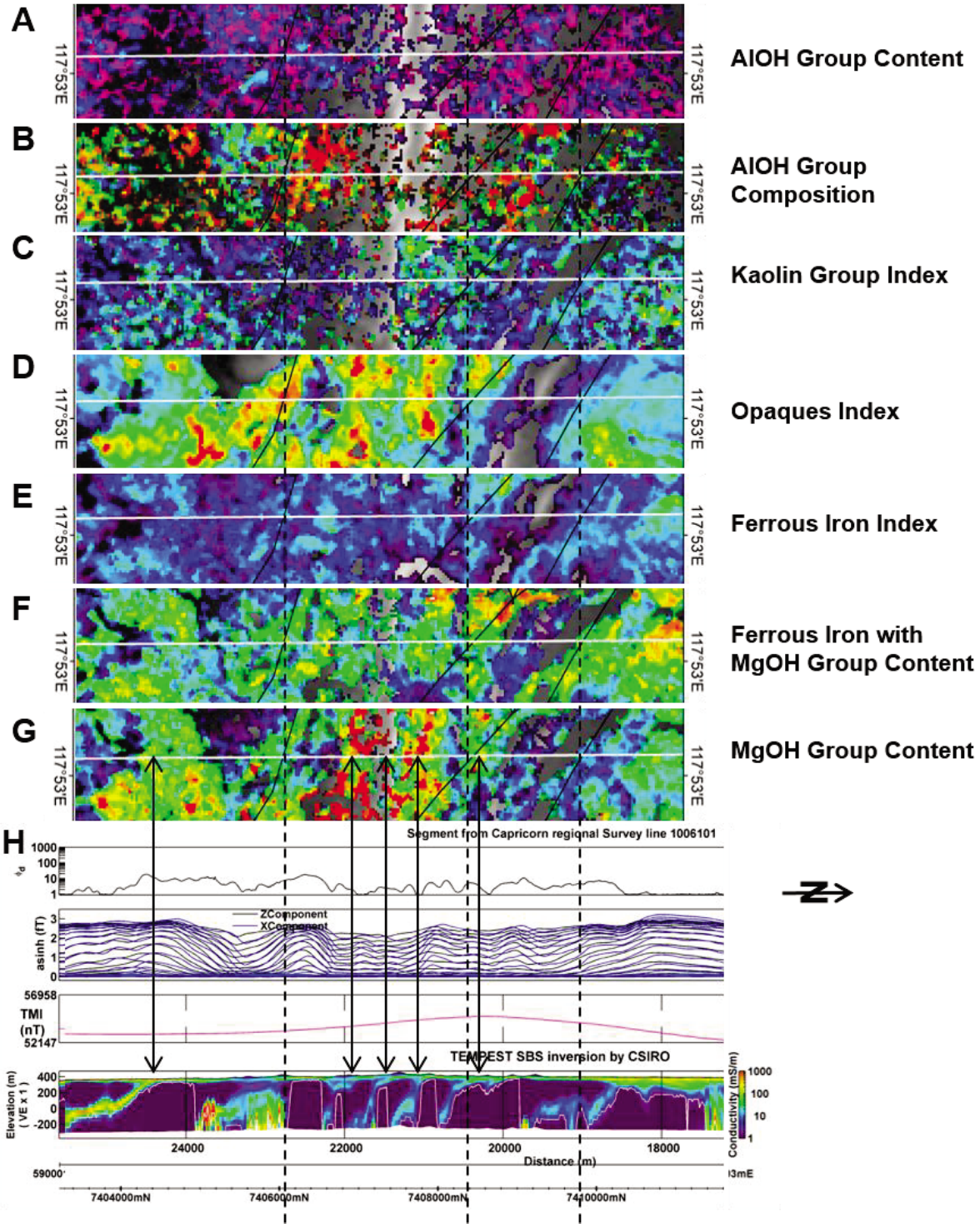

Figure 38 Comparison of AEM and ASTER Geoscience Products, Mount Olympus area, along AEM flight line FID59 showing intersections with major structural/lithological boundaries (NF - Nanjilgardy Fault, OF1 - Fault at southern contact between lower and upper Wyloo Grp., LCN - Fault at northern contact between lower and upper Wyloo Grp.). False-colour ASTER Geoscience Products (A to G), stacked vertically, overlay DEM data (background grey image) in each image strip. Hot or red colours for each ASTER Geoscience Content Product indicate a relatively high content for each Product, whereas cool or blue colours indicate a low content. Hot colours for the AlOH group composition (B) indicate well-ordered kaolinite, and cool colours the presence of dickite.

GSWA REGOLITH SAMPLES

Regional Regolith Geochemistry

GSWA's regolith geochemical data set (Morris, 2005) was investigated for regional to district scale patterns and evaluated against the ASTER Geoscience Products. A number of major elements trace regional scale geological provinces. For example, the Ashburton Basin is characterised by elevated SiO_2 values when compared to low silica values in the Hamersley Basin and low to intermediate values in the Edmund-Collier Basins (Figure 39a). In contrast, the Fe_2O_3 and MgO values of the Ashburton Basin are lower than for the adjacent basins (Figure 39b and c). Selected trace elements, such as As, don't show these regional scale changes (Figure 39d). However, As was locally elevated, as in the area to the west of Mount Olympus and immediately north of drill hole LD004 (red circles in Figure 39d). Distinct local changes of the major elements, as highlighted by black circles in Figure 39a and b were sparse.

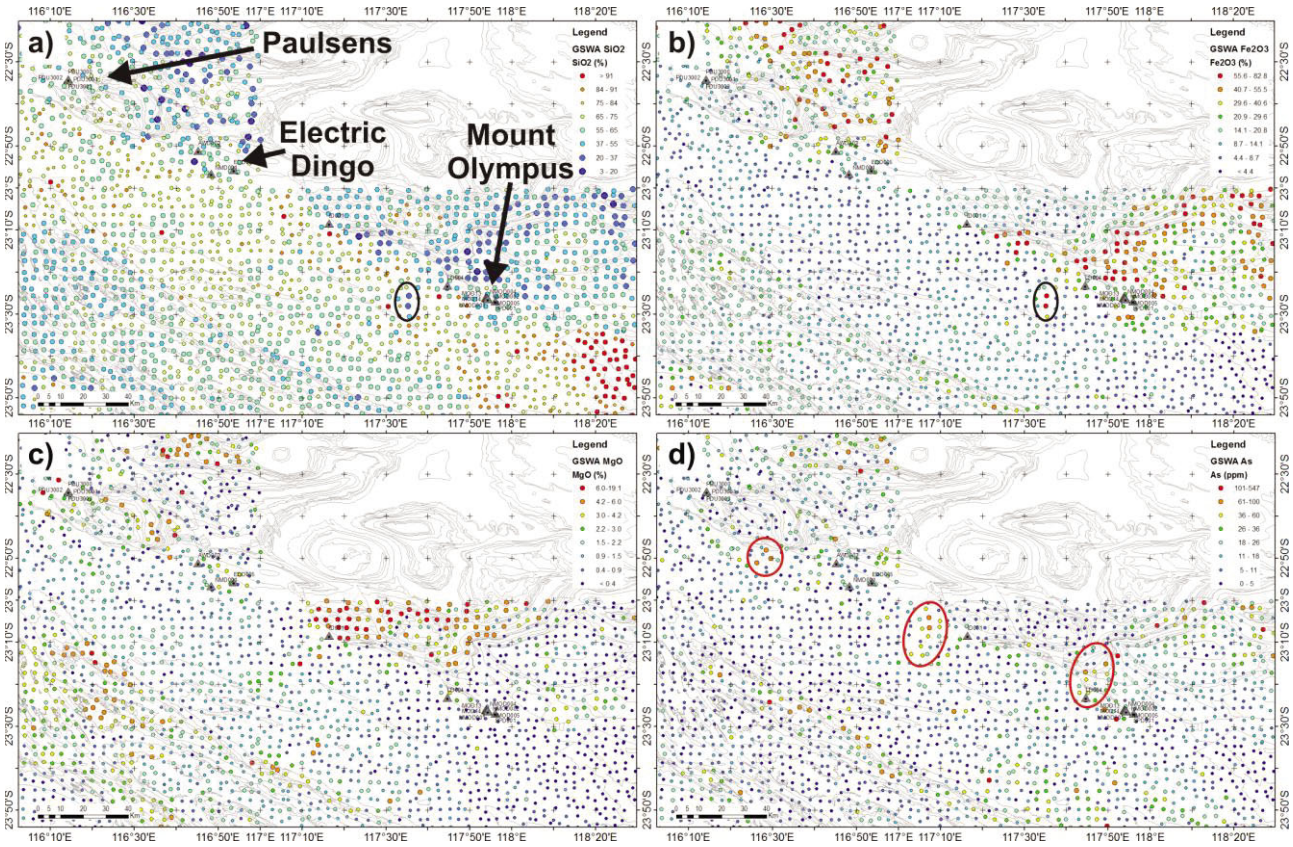

Figure 39 Regolith geochemical data from GSWA's 1994–2001 regional regolith geochemistry dataset: a) SiO_2, b) Fe_2O_3, c) MgO, d) As which shows localised elevated contents (circled in red).

Regolith Geochemistry and ASTER

As outlined in the progress report (Wells et al., 2014), the ASTER Geoscience Products allow regional scale mineralogical characterisation of major geological provinces. However, due to the finer spatial resolution of the ASTER data when compared to the regolith geochemistry dataset, coherent mineralogical patterns become evident mainly at the sub-province scale. For example, the Ferric Oxide Content, AlOH Group Content and Silica Index products showed elevated values in various parts of the Ashburton Basin, related to distinct lithologies. At a district scale over the southwestern part of the Mount Olympus area, the ASTER-derived Silica Index (a) identifies a high silica abundance, resembling siliceous, WNW-trending lithologies of

the Upper Wyloo Group, which seem to constitute a major part of the latter group (Figure 40a). In contrast, to the North of the Nanjilgardy Fault the Silica Index decreases considerably in, not only, both the Lower and Upper Wyloo Groups, but also in the Hamersley Basin to the North. Silica-void lithologies of the Lower Wyloo Group were largely matched with high values in the MgOH/Carbonate abundance image (Figure 37a). However, along-strike variations in the Lower Wyloo Group are evident (Wells et al., 2014). The general trends of the ASTER derived Silica Index were confirmed by the regolith geochemistry data (Figure 40b). However, the Lower Wyloo Group inlier is characterised by 55 to 84 weight % SiO_2, which is significantly higher than results reported from the Hamersley Basin.

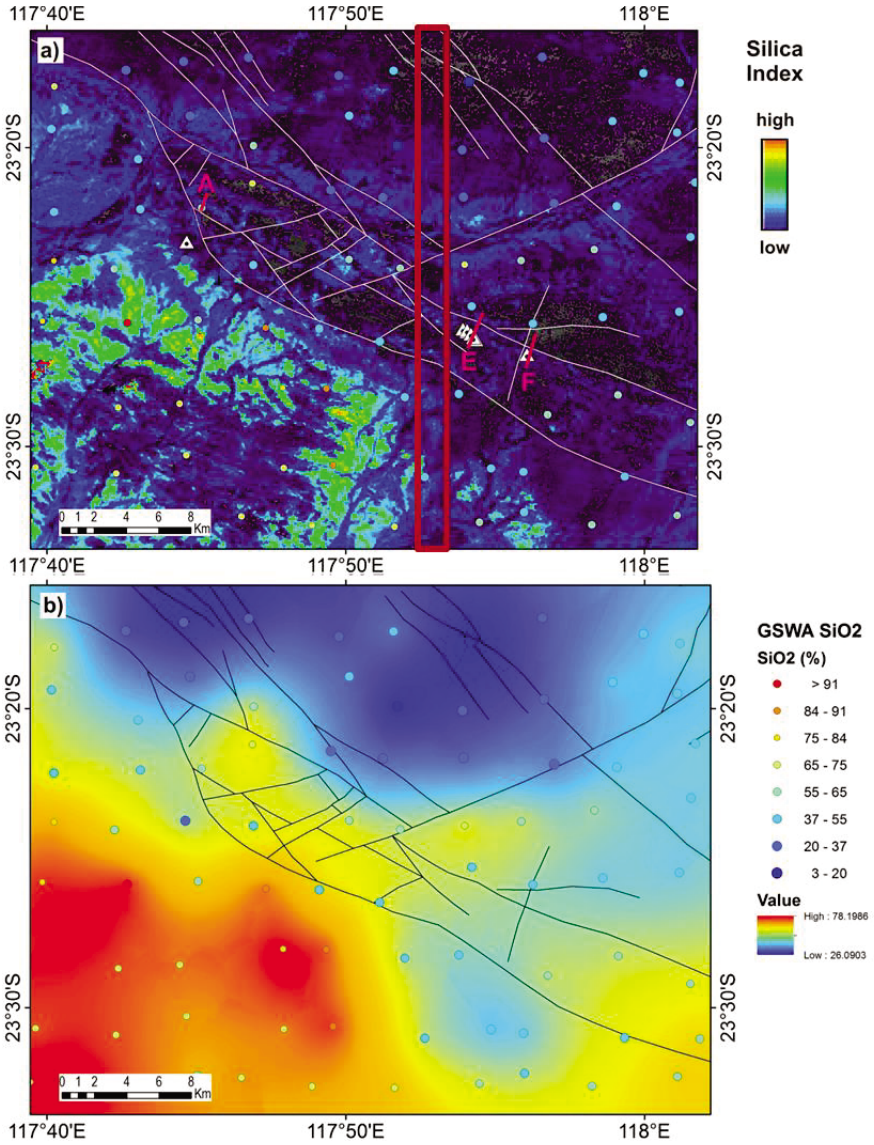

Figure 40 False-colour maps of: a) the ASTER Silica Index, and b) modelled SiO_2 distribution using the GSWA regolith geochemistry of WA (GSWA, 2012). Small coloured circles define regolith sample locations. White triangles in the ASTER Silica Index map show the locations of drill cores scanned using the HyLogging system. Pink lines, A, E and F represent transects conducted during fieldwork in July 2014. The SiO_2 interpolation plot (B) was modelled using the kriging method in ArcGIS Spatial Analyst Toolbox, histogram equalized, based on the regolith sample points shown as circles (a and b). The interpolated SiO_2 distribution map (b) shows high wt% SiO_2 values in hot colours (red) and low wt% SiO_2 values in blue. The red box outline shows the location of the MgOH Group content area mapped in Figure 35.

Regolith Geochemistry and ASD

VNIR-SWIR reflectance spectra were acquired for 154 samples from the GSWA's regolith sample set (Figure 41) for comparison with hyper- and multi-spectral data in the Mount Olympus area (related data collated in Appendix 5: "GSWA_RegolithSamples_MtOlympus_ASDtsgexport.xlsx" and "GSWA_RegolithSamples_MtOlympus_ASD.tsg"). As for the field transects and the ASTER data, the main mineral groups that were targeted in the hyperspectral data collected from the regolith sample pulps included jarosite, alunite, kaolinite, dickite, muscovite and chlorite. The relative abundance of white mica, chlorite and kaolin group minerals across the 154 samples (Figure 42) indicates that the southwestern part around Mount Olympus is dominated by kaolin group minerals, whereas to the north and northwest white mica and chlorite are more common. The Mount Olympus area also shows the highest density of well crystalline kaolinite (Figure 42D). The hyperspectral data didn't provide any clear indication for sulphates in the tested samples.

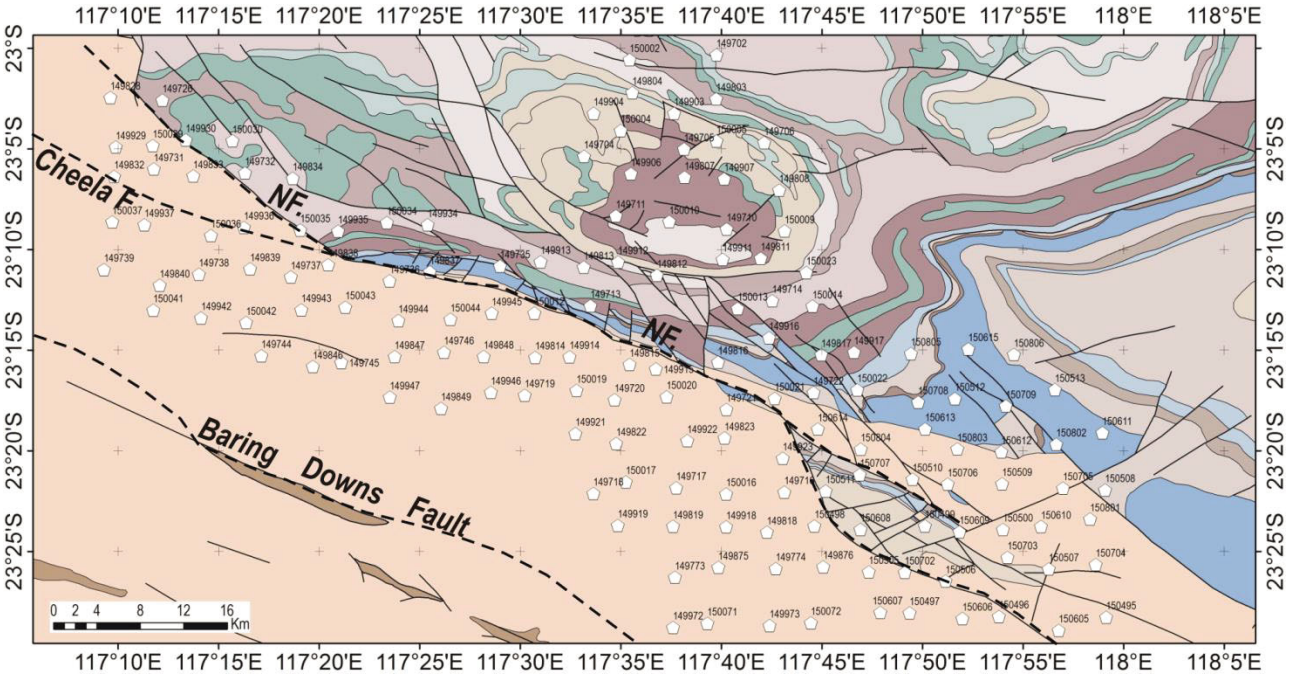

Figure 41 Location of GSWA Regolith samples scanned at GSWA's drill core library, in Carlisle, using an ASD FieldSpec3 spectroradiometer (NF – Nanjilgardy Fault).

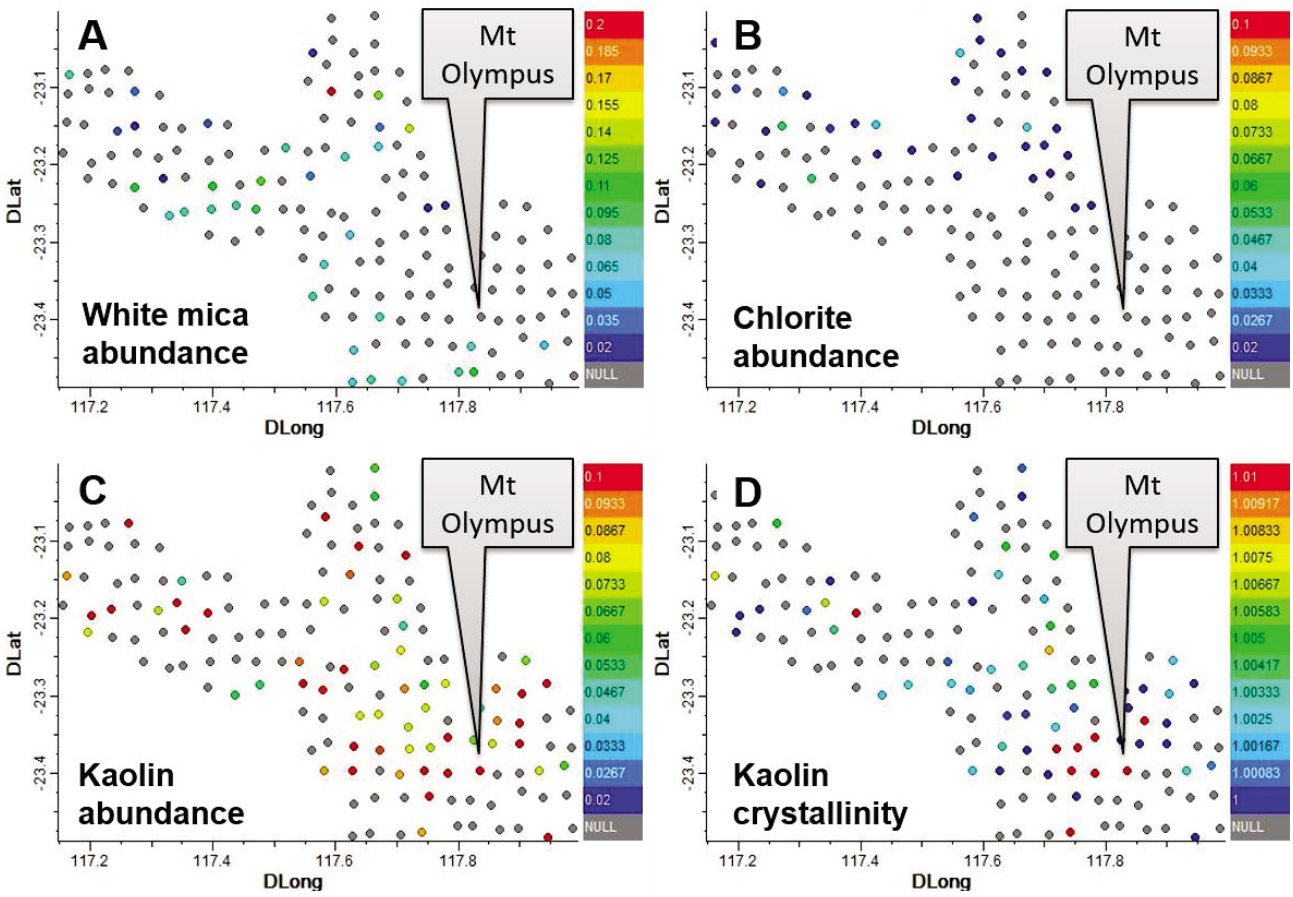

Figure 42 Mineralogical interpretation of reflectance spectra acquired from 154 of GSWA's regolith sample set based on application of CSIRO's "MFEM" scripts. A: white mica abundance, B: chlorite abundance, C: kaolin abundance, D: kaolin crystallinity. Refer to section 2.3 for a more detailed description of the MFEM scripts.

4 Summary and Conclusions

Proximal and remote sensing data analysis platforms, such as the HyLogger™-3 and ASTER mapping systems, provide a multi-scale approach for developing a spectrally-derived, 3D mineral mapping workflow to add value to GSWA's precompetitive spectral data. This project combined remotely-sensed ASTER mineral map data and proximally derived HyLogging™-3 data, validated through means of independent techniques to provide 3D mineral characterisation of structurally(?) related alteration footprints that may be associated with Au-mineralisation along the Nanjilgardy Fault (NF) corridor. The NF and parallel structures, such as the Baring Downs Fault, are possibly deeply rooted, remanent suture zones that may have acted as conduits for mineralising fluids and define a potentially highly prospective corridor for Au mineralisation.

GSWA HyLogging-3™ drill-core data and ASTER data were integrated within a validated mineralogical framework on the basis of the X-ray diffraction (XRD) and compositional analysis of surface regolith and outcrop material, and selected samples from key EIS and Sipa Resources drill core. This was used to aid refinement of the alteration pattern within close proximity to the Mt Olympus Au deposit leading to the development of a 3D model of the alteration mineralogy focussed on Mt Olympus.

As part of the multi-scale approach for characterising alteration mineralogy associated with the NF, a parallel evaluation of the TSA, automated spectral mineral identification routine against the more traditional method of mineralogical identification by XRD analysis was made. Whilst at a more regional scale, application of ASTER data was tested to map alteration mineralogy identified from the HyLogging-3 data, in conjunction with AEM data and the GSWA regolith geochemical data set.

4.1 Alteration Mineralogical Assemblages

A combined evaluation of the TSA summary mineralogical data, external lithology log and gold assay values in conjunction with the most abundant mineral groups (white mica, chlorite, kaolin, quartz, and carbonate abundances) described using the MFEM scalars, identified four Au mineralisation types or associated alteration patterns with lithological, lateral and vertical variations in the alteration mineralogy from the drill cores examined in the present study:

- Oxidised, high-grade gold mineralization (drill holes MOD4, MOD5, MOD6, MOD7, MOD8, MOD12, MOD13, and MOD14): occurring in the oxidised (weathering) zone of ferruginous brecciated siltstones/sandstones, conglomerates and/or black shales in association with quartz-muscovite-pyrite and minor hematite alteration.
- Oxidised, low-grade gold mineralization (drill holes MOD3, MOD11, NMOD001, NMOD002, NMOD005, MTO90): being widespread throughout bleached siltstone, minor conglomerates and sandstone rocks in drill holes of this group, consisting of disseminated, oxidized pyrite in association with quartz, muscovite, kaolinite/dickite, Fe-chlorite, Fe-carbonate and pyrophyllite.
- Un-oxidised (fresh), primary Au mineralisation (drill holes AMODD0026 and AMODD0028): associated with widespread Al-rich muscovite, Fe-carbonates, and minor Fe-chlorite accompanied non-oxidized gold mineralization occurring in brecciated quartz-pyrite veins, disseminated in bleached, brecciated sandstones with intercalated black shales and conglomerates veinlets and pyrite concretions in siltstones.

- Un-oxidised (fresh) poor or low-grade mineralisation: both distal and proximal occurrences (drill holes NMOD004, SPD001, AWD003, EDD005, NMD001, ID001, LD004), characterised by widespread dolomite, Fe- and Fe/Mg-chlorite, quartz and subsidiary muscovite.

Of the EIS and Sipa Resources drill holes investigated, some cores exhibited characteristic indicator minerals, spatially distributed in relation to the presence of Au, summarised as:

1) Siltstones 1 (bright shales): muscovite ± quartz veining ± post quartz removal? > muscovite + chlorite

2) Siltstones 2 (black shales): White mica ± kaolinite > white mica > white mica + chlorite (e.g., MOD13)

3) Sandstone:

Type-A): jarosite > alunite (K/Na) > alunite + kln > dickite > white mica > chlorite (e.g., MOD4)

Type-B): White mica > white mica + kaolinite > white mica(?)

4) Conglomerate: White mica ± dickite > kaolinite/dickite

In addition to these four major mineral footprints, possibly related to Au mineralisation, it was observed that quartz veining increased in the mineralised zone, as evidenced in a number of drill cores (e.g., MOD7, MOD11, MOD14), whereas primary quartz was often removed from the background mineral assemblage.

Minerals attributed to pervasive hydrothermal alteration in common lithologies along the Nanjilgardy Fault comprised sodic and potassic alunite, kaolinite, dickite, pyrophyllite, white mica and chlorite. The presence of sulphates, such as jarosite and, in particular, alunite were considered to have formed as primary alteration phases. These are distinct from the formation of variably hydrated, ferrous sulphates, such as melanterite, siderotil and rozenite, which formed as a result of 'in situ', atmospheric oxidation of sulphides in some core sections whilst the core was in storage.

White mica was present across all four zones, including almost all four drill cores of the distal zone. It was difficult to differentiate between metamorphic and hydrothermal chlorite along the Nanjilgardy Fault. However, white micas identified along potential pathways for hydrothermal fluids bore a characteristic spectral signature. The kaolin group minerals, kaolinite and dickite, were observed in all four zones as well. However, their distribution was more restricted to certain intervals in the drill cores when compared to the widespread occurrence of white mica and chlorite.

4.2 Efficacy of TSA Mineral identification

Comparison of The Spectral Geologist TSA_SWIR and TSA_TIR user scalars against the identified XRD mineralogy demonstrated that, irrespective of the Au mineralisation type identified at Mt Olympus, minerals identified at the TSAUser_SWIR group level, such as quartz, kaolin, white mica group, and the carbonate group, were generally consistent to the mineralogy identified by XRD analysis. This was despite the low quality spectra measured for dark carbonaceous, sulphidic black shales and the friable and fine-grained nature of some of the drill core scanned.

The mineral group with the least congruency between the two characterisation techniques was the chlorite group. This was despite spectral distinction of Fe/Mg variations in chlorite being supported by XRD analysis. At a mineral species level, it was difficult to distinguish between kaolinite and dickite in diffraction patterns, which prevented a full evaluation of TSA user scalars at the mineral level. Hence, it is recommended that TSA mineral analysis should be limited to, at most, mineral identification down to the group level.

Visualisation of the main alteration mineralogy patterns in 3D focussed on their distribution within closest proximity to the Mt Olympus Au deposit due to the greater drilling density in the area. The largest zone of Au mineralisation, now exhausted by mining as defined by the Mt Olympus pit, was intersected to the NW by the Zoe Fault, the most significant structural feature mapped in the area. Proximal to this is a zone of sulphate alteration on the northern side of the Mt Olympus pit. Visualisation revealed irregular, poddy Au mineralisation plunging to the SE and intersected by the Zoe Fault plane surface with irregular, proximal zones of sulphate alteration sub-parallel to the main fault. Locally, changes in the white-mica composition were observed with chlorite more distally developed. Whilst 3D visualisation was useful for defining potential pathways for hydrothermal fluids and mineral footprints at Mt Olympus, these results must be considered in relation to the restricted lateral distribution of the small number of drill holes modelled in the area and the potential influence that local structural features may play in defining fluid pathways.

4.3 Remotely Sensed Data: Applications for Industry Exploration

Evaluation of HyLogger™-3 data, validated by XRD analysis, identified a suite of mineral groups that may be traced using CSIRO's ASTER Geoscience Products to find potential indicators towards Au mineralisation in the Mount Olympus area. At the local transect scale the ASTER Kaolin Group Index, MgOH Group Content and Opaques Index showed patterns that could be correlated with major structures or with mineral footprints identified in the HyLogged drill cores around Mount Olympus.

Comparison of ASTER Geoscience Products and AEM data along selected TEMPEST flight lines in proximity to Mt Olympus identified surface mineral footprints associated with distinct sub-surface (< 400 m deep), conductive geological domains separated by potential fault systems. Inversion modelling identified a number of sharp, conductivity highs, not shown in previous geological mapping, evident between larger scale structures (e.g., the NF and OF1 faults as shown in Figure 37), of which an East-West extrapolation could be made with the ASTER MgOH Group Content and other products, such as the Opaques Index. These may resemble smaller scale structures (e.g., fault lines, lithological contacts, bedding parallel shear zones) not previously identified. An additional, well defined conductivity contrast, also not marked on the 1:500 geological bedrock map, was identified south of the NF but no distinct changes in the ASTER MgOH Group content were noted for this larger-scale structure.

Correlation of the ASTER Geoscience Products to geochemical trends in the GSWA regolith geochemical data was only evident at the regional scale, due to the finer spatial resolution of the ASTER data compared to the coarser spatial sampling used in the regolith data set. For example, general trends of the ASTER derived Silica Index were confirmed by the regolith geochemistry data, with elevated wt% SiO_2 contents generally consistent to elevated ASTER Silica Index values related to distinct lithologies. Silica-void lithologies, for example, of the Lower Wyloo Group largely matched high values of the MgOH and Carbonate Geoscience products. However, along-strike variations in the Wyloo Group were evident, particularly in the MgOH ASTER Geoscience Product.

Hence, the application of integrated, remotely sensed data platforms can define mineralogical variations associated with both large and small-scale structures. Such associations could, in turn, be used to help focus regolith geochemical sampling regimes to better target and, thus, characterise compositional changes detected remotely within the landscape. Such an approach may prove a useful exploration tool, and provide for a more robust, first-pass mineralogical characterisation at the regional and/or district scale.

4.4 Recommendations for future work

On the findings of the current work, the following are recommendations for a continuation of the work, for example, as a second stage of this project:

1. Further validation analysis, by use of HyLogger™-3 data integrated with independent methods (e.g., XRD analysis, XRF mapping) of the mineralogy and geochemistry of drill holes intersected by AEM modelling, which indicated strong conductors near or in the vicinity of the Nanjilgardy fault, such as those described in the Electric Dingo area.
2. HyLogger™-3 scanning of targeted drill cores that intersect “fresh” rock levels, below the largely oxidised/weathered overprinted system of the current study.
3. Extension of the current study along strike of the Nanjilgardy Fault to include drill holes in the Paulsens areas, particularly of any recently drilled holes, for a comparative evaluation of the alteration-related mineralogy between Mt Olympus and Paulsens.
4. Inclusion of a study similar to the Nanjilgardy Fault Project along the Baring Downs Fault to the southwest and/or along the Blair Fault further to the southwest towards the southern margin of the Ashburton Basin. These may be undertaken as a combined study or individually as separate studies depending on the regional focus of interest. Consideration should be given to the inclusion of airborne hyperspectral data (e.g., AMS), which would enable a distinction of key alteration minerals (e.g., alunite vs. kaolinite).
5. C-isotope analysis in conjunction with S-isotope analysis. Preliminary Total Organic Carbon (TOC) and C-isotope measurements, of a very limited sample suite, indicated an organic source for the carbon in sulphidic, black shales.

References

Anand, R. R. and Paine, M. (2002). Regolith geology of the Yilgarn Craton, Western Australia: Implications for exploration. *Australian Journal of Earth Sciences,* **49,** 3-162.

Arslan, C. and Arslan, F. (2003). Thermochemical review of Jarosite and Goethite stability regions at 25 and 95C. *Turkish Journal of Engineering and Environmental Science,* **27,** 45-52.

Bailey, S. W. (1980). Structures of layer silicates. *In:* BRINDLEY, G. W. & BROWN, G. E. J. (eds.) *Crystal structures of clay minerals and their X-Ray identification.* Mineralogical Society Monographs 5.

Berman, M., Bischof, L. and Hungtington, J. (1999). Algorithms and software for the automated identification of minerals using field spectra or hyperspectral imagery. Proceedings of the Thirteenth International Conference on Applied Geologic Remote Sensing, 1999 Vancouver., BC., Canada., Ann Arbor. Environmental research institute of Michigan, 222-232.

Bishop, J. L. and Murad, E. (2005). The visible and infrared spectral properties of jarosite and alunite. *American Mineralogist,* **90,** 1100-1107.

Blenkinsop, T., Baker, T., McLellan, J., Cleverley, J. and Nugus, M. (2007). Sunrise Dam Gold Mine Geological Study Project – Final Report Project G15. Perth: CSIRO.

Bouchet, A., Proust, D., Meunier, A. and Beaufort, D. (1988). High-charge to los-charge smectite rectioin in hydtrothermal alteration processes. *Clay Minerals,* **23,** 133-146.

Brodie, R. C. (2012). Appendix 3: GA-LEI Inversion of TEMPEST Data. *In:* ROACHE, A. (ed.) *The Frome airborne electromagnetic survey, South Australia: implications for energy, minerals and regional geology.* Geoscience Australia.

Caccetta, M., Collings, S. and Cudahy, T. (2013). A calibration methodology for continental scale mapping using ASTER imagery. *Remote Sensing of Environment,* **139,** 306-317.

Chang, Z., Hedenquist, J. W., White, N. C., Cooke, D. R., Roach, M., Deyell, C. L., Garcia, J. J., Gemmell, J. B., McKnight, S. and Cuison, A. L. (2011). Exploration tools for linked porhyry and epithermal deposits: Example from the Mankayan intrusion-centered Cu-Au district, Luzon, Philippines. *Economic Geology,* **106,** 1365-1398.

Costello, M. (2014). The Capricorn 2013 AEM TEMPEST survey. Perth, WA: Geological Survey of Western Australia.

Cudahy, T. (2011). Satellite ASTER Geoscience Product Notes Western Australia.

Cudahy, T. (2012). Geoscience Product Notes Australia.

Cudahy, T., Jones, M., Thomas, M., Laukamp, C., Caccetta, M., Hewson, R., Rodger, A. and Verrall, M. (2008). Next Generation Mineral Mapping: Queensland airborne HyMap and satellite ASTER surveys 2006-2008. Perth, WA: CSIRO.

Cudahy, T. J., Caccetta, M., Cornelius, A., Hewson, R. D., Wells, M., Skwarnecki, M., Halley, S., Hausknecht, P., Mason, P. and Quigley, M. A. (2005). Regolith geology and alteration mineral maps from new generation airborne and satellite remote sensing technologies and Explanatory Notes for the Kalgoorlie-Kanowna 1:100,000 scale map sheet, remote sensing mineral maps. Perth, WA: MERIWA.

Doublier, M. P., Roache, T. and Potel, S. (2010). Short-wavelength infrared spectroscopy: A new petrological tool in low-grade to very low-grade pelites. *Geology,* **38,** 1031-1034.

Duke, E. F. (1994). Near infrared spectra of muscovite, Tschermak substitution, and metamorphic reaction progress: Implications for remote sensing. *Geology,* **22,** 621-624.

Duke, E. F. and Lewis, R. S. (2010). Near infrared spectra of white mica in the Belt Supergroup and implications for metamorphism. *American Mineralogist,* **95,** 908-920.

Ehrenberg, S. N., Aagaard, P., Wilson, M. J., Fraser, A. R. and Duthie, D. M. L. (1993). Depth-dependent transformation of kaolinite to dickite in sandstones of the Norwegian continental shelf. *Clay Minerals,* **28,** 325-352.

Fialips, C.-I., Majzlan, J., Beaufort, D. and Navrotsky, A. (2003). New thermochemical evidence on the stability of dickite vs. kaolinite. *American Mineralogist,* **88,** 837-845.

Gaines, R. V., Skinner, H. C. W., Foord, E. E., Mason, B. and Rosenzweig, A. (1997). *Dana's new mineralogy,* New York, John Wiley and Sons.

GSWA (2012). Regolith Geochemistry of Western Australia 2012. *In:* AUSTRALIA, G. S. O. W. (ed.). East Perth, WA.

Gustafson, L. B. and Hunt, J. P. (1975). The porphyry copper deposit at El Salvador, Chile. *Economic Geology,* **70,** 857-912.

Haest, M., Cudahy, T., Laukamp, C. and Gregory, S. (2012). Quantitative mineralogy from infrared spectroscopic data. II. Three-dimensional mineralogical characterisation of the Rocklea channel iron deposit, Western Australia. *Economic Geology,* **107,** 229-249.

Halley, S., Dilles, J. H. and Tosdal, R. M. (2015). Footprints: Hydrothermal alteration and geochemical dispersion around porphyry copper deposits. *SEG Newsletter.* Society of Economic Geologists.

Hancock, E. A. and Huntington, J. F. (2010). The GSWA NVCL HyLogger: rapid mineralogical analysis for characterizing mineral and petroleum core. East Perth, WA: GSWA.

Hewson, R., Cudahy, T. J., Mizuhiko, S., Ueda, K. and Mauger, A. J. (2005). Seamless geological map generation using ASTER in the Borken Hill-Curnamona province of Australia. *Remote Sensing of Environment,* **99,** 159-172.

Johnson, S. P., Thorne, A. M., Tyler, I. M., Korsch, R. J., Kennett, B. L. N., Cutten, H. N., Goodwin, J., Blay, O., Blewett, R. S., Joly, A., Dentith, M. C., Aitken, A. R. A., Holzschuh, J., Salmon, M., Reading, A., Heinson, G., Boren, G., Ross, J., Costello, R. D. and Fomin, T. (2013). Crustal architecture of the Capricorn Orogen, Western Australia and associated metallogeny. *Australian Journal of Earth Sciences,* **60,** 681-705.

Lane, R., Brodie, R. C. and Fitzpatrick, A. (2004). Constrained inversion of AEM data from the Lower Balonne area, Southern Queensland, Australia. CSIRO.

Laukamp, C., Cudahy, T., Caccetta, M., Chia, J., Gessner, K., Haest, M., Liu, Y. C. and Rodger, A. (2010). The uses, abuses and opportunities for hyperspectral technologies and derived geoscience information. *AIG 'Geo-Computing 2010 Conference'.* Brisbane.

Laukamp, C., Ramanaidou, E., Wells, M. and Yang, K. (2013). Kaolin and smectite group minerals in exploration and discovery. *In:* GRÄFE, M., KLAUBER, C. & MCFARLANE, A. (eds.) *Clays in the Mineral Resources Value Chain: A Literature Survey.* Perth: CSIRO.

Ley-Cooper, A. Y., Munday, T. and Ibrahimi, T. (2015). Determining cover variability in the Capricorn Orogen with airborne EM. *ASEG-PESA2015 Geophysics and Geology together for Discovery.* Perth.

McLeod, R. L., Gabell, A. R., Green, A. A. and Gardavsky, V. (1987). Chlorite infrared spectral data as proximity indicators of volcanogenic massive sulphide mineralisation. *Pacific Rim Congress 87, The Geology, Structure, Mineralisation and Economics of the Pacific Rim.* Gold Coast, Australia.

Meunier, A. (2005). *Clays,* Germany, Springer.

Moore, D. M. and Reynolds, R. C. J. (1997). *X-ray diffraction and the identification and analysis of clay minerals*, Oxford University Press.

Morant, P. and Doepel, M. G. (1997). The Mount Olympus gold deposit. Perth, WA.

Morris, P. A. (2005). GSWA's regional regolith goechemistry program: An overview. East Perth, WA: Geological Survery of Western Australia.

Neumayr, P., Walshe, J., Connors, K., Cox, S., Morrison, R. S. and Stolz, E. (2004). Gold mineralization in the St Ives camp near Kambalda. East Perth, WA: Geological Survey of Western Australia.

NorthernStar (2013a). ASX Announcement. *March Quarter Activities Report.* Norther Star.

NorthernStar (2013b). ASX Announcement. *Norther Star set for exploration blitz after acquiring JV interest over Fortescue ground.* Perth: Norther Star.

Piranjo, F. (2004). Metallogeny in the Capricorn Orogen, Western Australia, the result of multiple ore-forming processes. *Precambrian Research,* **128,** 411-439.

Ruitenbeek, F. J. A. v., Cudahy, T., Hale, M. and van der Meer, F. (2005). Tracing fluid pathways in fossil hydrothermal systems with near-infrared spectroscopy. *Geology,* **33,** 597-600.

Sener, A. K., Young, C., Groves, D. I., Krapez, B. and Fletcher, I. R. (2005). Major orogenic gold episode associated with Cordilleran-sty;e tectonis realted to the assembly of Paleoproterozoic Australia. *Geology,* **33,** 225-228.

Short, N. M. (1982). *The Landsat tutorial wookbook - Basics of satellite remote sensing,* Washington, DC, Goddard Space Flight Center United States, National Aeronautics and Space Administration. Scientific and Technical Information Branch.

Sonntag, I., Laukamp, C. and Hagemann, S. G. (2012). Low potassium hydrothermal alteration in low sulfication epithermal systems as detected by IRS and XRD: An example from the Co-O mine, Eastern Mindano, Philippines. *Ore Geology Reviews,* **45,** 47-60.

Stoffregen, R. E. (1993). Stability relations of jarosite and natrojarosite at 150-250C. *Geochimica et Cosmochimica Acta,* **57,** 2417-2429.

Stoffregen, R. E. (2006). Experimental studies of jarosite and alunite at hydrothermal conditions. Workshop on Sulfates as Recorders of Atmospheric-Fluid-Rock Interactions, 2006 Lunar and Planetary Institute. 1.

Stoffregen, R. E. and Cygan, G. L. (1990). An experimental study of Na-K exchange between alunite and aqueous sulfate solutions. *American Mineralogist,* **75,** 209-220.

Sucha, V., Kraus, I., Gerthofferova, H., Petes, J. and Serekova, M. (1993). Smectite to illite conversion in bentonites and shales of the East Slovak Basin. *Clay Minerals,* **28,** 243-253.

Tosdal, R. M., Dilles, J. H. and Cooke, D. R. (2009). From Source to Sinks in Auriferous Magmatic-Hydrothermal Porphyry and Epithermal Deposits. *Elements,* **5,** 289-295.

Tyler, I. M., Johnson, S. P., Thorne, A. M. and Cutten, H. N. (2011). Implications of the Capricorn deep seismic survey for mineral systems. *In:* JOHNSON, S. P., THORNE, A. M. & TYLER, I. M. (eds.) *Capricorn Orogen Seismic and Magnetotelluric (MT) Workshop.* Perth, WA: Geological Survey of Western Australia.

Tyler, I. M. and Thorne, A. M. (1990). The northern margin of the Capricorn Orogen, Western Australia - an example of an Early Proterozoic collision. *Journal of Structural Geology,* **12,** 685-701.

Utada, M. (1980). Hydrothermal alterations related to igneous activity in Cretaceous and Neogene formations of Japan. *Mining Geology Special Issue,* **8,** 67-83.

van Ruitenbeek, F. J. A., Cudahy, T., van der Meer, F. D. and Hale, M. (2012). Characterization of the hydrothermal systems associated with Archean VMS-mineralization at Panorama, Western Australia, using hyperspectral, geochemical and goethermometric data. *Ore Geology Reviews,* **45,** 33-46.

Velde, B. B. and Meunier, A. (2008). *The origin of clay minerals in soils and weathered rocks*, Springer, Berlin Heidelberg.

Wells, M. A., Laukamp, C. and Hancock, L. (2014). Integrated Spectral Mapping of Precious and Base Metal Related Mineral Footprints, Nanjilgardy Fault, WA: Mid-Term Progress Report. Perth, WA: CSIRO.

Whitney, D. L. and Evans, B. W. (2010). Abbreviations for names of rock-forming minerals. *American Mineralogist,* **95,** 185-187.

Wilson, J. P., Fischer, W. W., Johnston, D. T., Knoll, A. H., Grotzinger, J. P., Walter, M. P., McNaughton, N. J., Simon, M., Abelson, J., Schrag, D. P., Summons, R., Allwood, A., Andres, M., Gammon, C., Garvin, J., Rashby, S., Schweizer, M. and Watters, W. A. (2010). Geology of the late Paleoproterozoic Duck Creek Formation, Western Australia. *Precambrian Research,* **179,** 135-149.

Yamaguchi, Y., Fujisada, H., Kudoh, M., Kawakami, T., Tsu, H., Kahle, A. B. and Pniel, M. (1999). ASTER instrument characterisation and operation scenario. *Advances in Space Research,* **23,** 1415-1424.

Yang, K., Lian, C., Huntington, J. F., Peng, Q. and Wang, Q. (2005). Infrared spectral reflectance characterization of the hydrothermal alteration at the Tuwu Cu-Au deposit, Xinjiang, China. *Mineralium Deposita,* **40,** 324-336.

Young, C., Groves, D. I. and Morant, P. (2003). Sediment-hosted disseminated gold mineralization in the Palaeoproterozoic Ashburton Province, Western Australia: A new epizonal orogenic gold province related to Capricorn orogeny? *In:* ELIOPOULOS, D., ET AL. (ed.) *Mineral exploration and sustainable development.* Rotterdam: Balkema.

Zotov, A., Galeev-Mukhamet, A. and CSchott, J. (1998). An experimental study of kaolinite and dickite relative stability at 150-300C and the thermodynamic properties of kaolinite. *American Mineralogist,* **83,** 516-524.

Appendices

Report Appendices are presented as a supplement to the main report and full details are described therein. The following lists only the title heading of each Appendix.

Appendix 1 Table of MFEM scripts

The MFEM (Multiple feature extraction method) scripts (01-01-2013) are based on a method for extracting the relative abundance and composition of mineral groups based on their diagnostic absorption features developed by Tom Cudahy and co-workers (Cudahy et al., 2008; Laukamp et al., 2010). Note: stretch limits can be adjusted for the respective deposit type. Lower stretches in abundance scripts are conservative to avoid influence of other mineral species. The given stretches of the wavelength scripts (e.g., 2250W) are developed however based on the physico-chemistry of the respective minerals. Mineral mixtures will have a great influence. Note: stretches are linear if not otherwise stated.

Appendix 2 Bulk Geochemistry (Drill hole-Transect samples)

Appendix 3 Bulk XRD Mineralogy

Appendix 4 XRD patterns

Appendix 5 Regolith geochemistry and related data

Appendix 6 Tornado mapping

Appendix 7 Drill core logs

Appendix 8 AEM flight line profiles, Electric Dingo Area

MINERALS DOWN UNDER
www.csiro.au

Integrated Spectral Mapping of Precious and Base Metal Related Mineral Footprints, Nanjilgardy Fault, WA: Appendices

Final Report: December 2015

Martin Wells, Carsten Laukamp and Lena Hancock

CSIRO Mineral Resources

18th December 2015

Department of Mines and Petroleum (Acting through the Geological Survey of Western Australia, GSWA)
Dr. Ian Tyler (Assistant Director, Geoscience Mapping)

Commercial-in-confidence, EP155294

CESRE/Mineral Resources

Citation

Wells, M., Laukamp, C. and Hancock, L. (2015). Integrated Spectral Mapping of Precious and Base Metal Related Mineral Footprints, Nanjilgardy Fault, WA: Appendices, p126.

Final Report, EP#155294, CSIRO, Australia

Copyright and disclaimer

Important disclaimer

Appendices

Appendix 1 Table of MFEM scripts

The MFEM (Multiple feature extraction method) scripts (01-01-2013) are based on a method for extracting the relative abundance and composition of mineral groups based on their diagnostic absorption features developed by Tom Cudahy and co-workers (Cudahy et al., 2008, Laukamp et al., 2010). Note: stretch limits can be adjusted for the respective deposit type. Lower stretches in abundance scripts are conservative to avoid influence of other mineral species. The given stretches of the wavelength scripts (e.g. 2250W) are developed however based on the physico-chemistry of the respective minerals. Mineral mixtures will have a great influence. Note: stretches are linear, if not otherwise stated - **Note: Use the scripts in this list at your own risk!**

Product name	Minerals detected	Base algorithm	Filters/Masks	Lower stretch limit	Upper stretch limit (based on UGD1683)	Related publication	Comments on general accuracy
Ferric oxide abundance (Ferric_oxide_abundance.txt)	Hematite, goethite, jarosite, "limonite"	Continuum removed depth of the 900 nm absorption calculated using a fitted 2nd order polynomial between 776 and 1050 nm ***900D***	R450 > R1650	0.04: low content	not specified yet - depending on results from other drill cores	further developed on the basis of Haest et al, (2012a,b), which used a 4th order polynomial or 4 band ratio approach	High: Complicated by (1) water vapour residuals; (2) mixing with green and dry vegetation, carbon black (e.g. soil carbon); and (3) ferrous iron in silicates/carbonates. Rocklea case study: RMSE = 9.7%
Ferrous iron abundance (Ferrous iron abundance.txt)	Fe^{2+} in silicates & carbonates. (Fe-chlorites, Fe-amphibole, Fe-pyroxene, Fe-olivine, Fe-carbonate)	$(R_{950}+R_{1650})/(R_{1020}+R_{1235})$ ***Ferrous***		~1.005: low content	not specified yet - depending on results from other drill cores	Laukamp et al. (2012)	Moderate. Broad absorption centred at ~1100nm can be influenced by ferrous iron in a range of silicates and carbonates. Including non-OH-bearing minerals like pyroxenes and garnets, as well as ferric iron.
Opaques 1 (greybody) (Opaques_1.txt)	"Reduced" materials such as carbon black, sulphides and magnetite as well as Mn oxides. Note sulphides and magnetite are expected to easily oxidise in the regolith to other minerals.	(R456)/(R1650) ***OPAQUES_450D1650***	albedo @ 1650 nm <30%	0.25: low content	not specified yet - depending on results from other drill cores		Moderate: Errors introduced by a lack of Fe3+ absorption in the visible, e.g. iron oxide poor clays that in theory would be masked by the <30% albedo but may be in partial "shadow".
opaques2 (opaques2inv.txt)	"Reduced" materials such as carbon black, sulphides and magnetite as well as Mn oxides.	albedo @ 1650 nm ***1650***	**OPAQUES_450D1650** >0.25; albedo @ 1650 nm 1650 <30%	2: low content	not specified - depending on samples		
White mica and Al-smectite abundance (wmAlsmai.txt)	Abundance of white micas (e.g. illite, muscovite, paragonite, brammalite, phengite, lepidolite, margarite) and smectites (montmorillonite, beidellite)	Relative absorption depth of the 2200 nm absorption for which the continuum is removed between 2120 and 2245, determined using a 3 band polynomial fit around the band with the lowest reflectance. ***2200D3pfit***	(R2326+R2376)/(R2343+R2359) **2350DE** >0.035) + $((R_{2138}+R_{2150})/(R_{2156}+R_{2179})$ **2160D2190** <1.063	0.02: low content	not specified yet - depending on results from other drill cores	further developed on the basis of Sonntag et al. (2012), which used a 4th order polynomial or 4 band ratio approach	Moderate: Inherent errors related to the process of masking rather than unmixing. That is, the threshold levels on mask parameters could exclude/include other materials especially for "lower" levels.
White mica and Al-smectite composition (wmAlsmci.txt)	Tschermak substitution of white micas, ranging from paragonite, brammalite, to illite, muscovite to phengite, and smectites, ranging from beidellite to montmorillonite.	Minimum wavelength of the 2200 nm absorption for which the continuum is removed between 2120 and 2245, determined using a 3 band polynomial fit around the band with the lowest reflectance. ***2200W3pfit***	(R2326+R2376)/(R2343+R2359) **2350DE** >0.035) + $((R_{2138}+R_{2150})/(R_{2156}+R_{2179})$ **2160D2190** <1.063	**2180** nm: Al-rich mica (muscovite, illite, paragonite, brammalite, lepidolite)	**2220** nm: Al-poor mica (~phengite)	further developed on the basis of Sonntag et al. (2012), which used a 4th order polynomila or 4 band ratio approach	High:
Kaolin abundance index	Kaolin group minerals, namely kaolinite halloysite, dickite and nacrite	2200D (Normalized depth of a fitted 4th order polynomial between 2120 and 2245 nm)	2160D ((R2138+R2190)/(R2156+R2179))>1.005			**Sonntag et al. (2012)**	
Kaolin composition index	Composition and crystallinity of kaolin group minerals ranging from well-ordered kaolinite to halloysite to dickite (and nacrite)	[(R2138+R2173)/R2156)/[(R2156+R2190)/R2173]	2200D>0.005			**Sonntag et al. (2012)**	
chlorite-epidote(-biotite) abundance (chlepai3pfit.txt)	Chlorite, epidote, biotite	Relative absorption depth of the 2250 nm absorption for which the continuum is removed between 2230 and 2270, determined using a 3 band polynomial fit around the band with the lowest reflectance. **2250D3pfit**	**2250D3pfit**>0.01, 2230nm<**2250wvl**<2270nm;	**0.02:** low content	not specified yet - depending on results from other drill cores	further developed on the basis of Sonntag et al. (2012), which used a 4th order polynomial or 4 band ratio approach	probably some correlation with Ferrous iron abundance!
chlorite(-biotite) abundance (chlai.txt)	Chlorite, biotite	Relative absorption depth of the 2250 nm absorption for which the continuum is removed between 2230 and 2270, determined using a 3 band polynomial fit around the band with the lowest reflectance. **2250D3pfit**	**2250D3pfit**>0.01, 2230nm<**2250wvl**<2270nm; **1550Dpoly** < 0.01	**0.02:** low content	not specified yet - depending on results from other drill cores	further developed on the basis of Sonntag et al. (2012), which used a 4th order polynomila or 4 band ratio approach	probably some correlation with Ferrous iron abundance!
Chlorite composition (chlepo3pfit.txt)	estimation of the Mg/Fe-ratio (~Mg#) of Chlorites	Minimum wavelength of the 2250 nm absorption for which the continuum is removed between 2230 and 2270, determined using a 3 band polynomial fit around the band with the lowest reflectance. ***2250W3pfit***	**2250D3pfit**>0.01, 2230nm<**2250wvl**<2270nm; **1550Dpoly** < 0.01	**2248nm**: Mg-rich (Bishop et al., 2008)	**2261nm**: Fe-rich (Bishop et al., 2008)		Medium: high influence of abundance of epidote and biotite!
epidote abundance (epai.txt)	epidote	Relative absorption depth of the 2250 nm absorption for which the continuum is removed between 2230 and 2270, determined using a 3 band polynomial fit around the band with the lowest reflectance. **2250D3pfit**	**2250D3pfit**>0.01, 2230nm<**2250wvl**<2270nm; **1550Dpoly** > 0.01	**0.02:** low content	not specified yet - depending on results from other drill cores		probably some correlation with Ferrous iron abundance!
Amphibole & Talc abundance (Amph_Talc_abundance.txt and Amph_Talc_abundance_without_kaolinmask.txt)	Abundance of amphibole and talc	***2380D*** ((R2365+R2415)/(R2381+R2390))	Composite mask* + **MgOH abundance** > 1.01 (+ **2160D2190** < 1.005)	**1.005:** low content	not specified yet - depending on results from other drill cores	Laukamp et al. (2012)	
Carbonates abundance (carbai3pfit.txt)	carbonates vs. MgOH-bearing silicates, based on left-asymmetry of CO3 feature @ 2340	Relative absorption depth of the 2340 nm absorption for which the continuum is removed between 2270 and 2370, determined using a 3 band polynomial fit around the band with the lowest reflectance. **2340D**	**2340D**>0.04, 2295nm<**2340W**<2360nm, **2250D** < 0.025, **2380D**<0.1117*(**2340D**+0.0002, Asymmetry of the 2340 absorption using a fitted 4th order polynomial between 2120 and 2370: **2340_left_asym** > 1.13	**0.05:** low content	not specified yet - depending on results from other drill cores	further developed on the basis of Sonntag et al. (2012), which used a 4th order polynomila or 4 band ratio approach	
Carbonate composition (carbci3pfit.txt)	separating calcite, dolomite, siderite, ...	Minimum wavelength of the 2340 nm absorption for which the continuum is removed between 2270 and 2370, determined using a 3 band polynomial fit around the band with the lowest reflectance. **2340W**	**2340D**>0.04, 2295nm<**2340W**<2360nm, **2250D** < 0.025, **2380D**<0.1117*(**2340D**+0.0002, Asymmetry of the 2340 absorption using a fitted 4th order polynomial between 2120 and 2370: **2340_left_asym** > 1.13	2303 nm: magnesite; 2326 nm: dolomite	2343 nm: calcite	further developed on the basis of Sonntag et al. (2012), which used a 4th order polynomila or 4 band ratio approach	Moderate: works well for those carbonates, which are not masked out

Appendix 1 continued…

Base scripts						
650D	Yellowness	Continuum removed depth of 650 nm CFA,1 calculated using a fourth-order polynomial between 600 and 740 nm			Haest et al, (2012a,b)	
900D	Fe (oxyhydr-)oxides	Continuum removed depth of 900 nm CFA,2, calculated using a second-order polynomial between 776 and 1,050 nm			Haest et al, (2012a,b)	
900wvl	Fe (oxyhydr-)oxides	Continuum removed wavelength of 900 nm CFA,2 calculated using a fourth-order polynomial between 776 and 1,150 nm			Haest et al, (2012a,b)	
1300wvl	Fe oxyhydroxide type	Position of maximum reflectance between 1,260 and 1,420 nm			Haest et al, (2012a,b)	
1300R/1800R	~vitreous index	Ratio of maximum reflectance at 1,340 ± 80 nm over the minimum reflectance at 1,780 ± 40 nm			Haest et al, (2012a,b)	
1300R/2500R	~water index	Ratio of maximum reflectance at 1,340 ± 80 nm over the minimum reflectance at 2,500 nm			Haest et al, (2012a,b)	
1480D	prehnite	Relative absorption depth of the 1480 nm absorption for which the continuum is removed between 1450 and 1500, determined using a 3 band polynomial fit around the band with the lowest reflectance. **1480D**			Slam et al. (in prep)	
1550D (1550Dpoly.txt)	epidote, clinozoisite (minor in chlorite)	Relative absorption depth of the 1550 nm absorption for which the continuum is removed between 1500 and 1610, determined using a 3 band polynomial fit around the band with the lowest reflectance. **1550D**				conflict with gypsum, when used for identification of epidote series minerals
1550W	epidote, clinozoisite	Minimum wavelength of the 1550 nm absorption for which the continuum is removed between 1500 and 1610, determined using a 3 band polynomial fit around the band with the lowest reflectance. **1550W**	epidote (in Yilgarn study by Roache et al., 2010: 1550W < 1552.5)	clinozoisite (in Yilgarn study by Roache et al., 2010: 1550W > 1552.5)		conflict with gypsum, when used for identification of epidote series minerals
N1650R	Albedo	Normalized reflectance at 1,650 ± 100 nm				
1760D	sulphates (e.g. gyspum and alunite, but not jarosite)	(R1730+R1790)/(R1740+R1780) ***1760D***				
2080D3pfit	Depth of the 2080 feature, evident in talc. Useful for separating talc from Amphiboles, the latter ones in general not showing this absorption feature.	Depth of the 2080 nm absorption feature, for which the continuum is removed between 2060 and 2100, determined using a second order polynomial fitted through the 3 bands with the lowest reflectance. **2080D**			Laukamp et al. (2012)	
2200D3pfit (2200D3pfit.txt)	Abundance of Al-clays	Relative absorption depth of the 2200 nm absorption for which the continuum is removed between 2120 and 2245, determined using a 3 band polynomial fit around the band with the lowest reflectance. **2200D**				
2200W3pfit (2200W3pfit.txt)	Tschermak substitution of Al-clays	Minimum wavelength of the 2200 nm absorption for which the continuum is removed between 2120 and 2245, determined using a 3 band polynomial fit around the band with the lowest reflectance. **2200W**	**~2180** nm: Al-rich	**~2215** nm: Al-poor		
2250D3pfit (2250D3pfit.txt)	Chlorite, epidote, biotite	Relative absorption depth of the 2250 nm absorption for which the continuum is removed between 2230 and 2280, determined using a 3 band polynomial fit around the band with the lowest reflectance. **2250D**				
2250W3pfit (2250W3pfit.txt)	estimation of the Mg/Fe-ratio (~Mg#) in chlorite, but alos the shift of an coinciding absorption feature in epidote and bitotite, where the wavelength position is not necessarily only due to the Mg#, but possibly more due to the relative Al, Fe3+ or Ca content.	Minimum wavelength of the 2250 nm absorption for which the continuum is removed between 2230 and 2280, determined using a 3 band polynomial fit around the band with the lowest reflectance. **2250W**	**2248nm**: Mg-rich (Bishop et al., 2008)	**2261nm**: Fe-rich (Bishop et al., 2008)		
2290D	Fe smectite	Continuum removed depth of fourth-order polynomial between 2,270 and 2,330 nm			Haest et al, (2012a,b)	
2290wvl	Fe smectite	Continuum removed wavelength of fourth-order polynomial, fitted between 2,270 and 2,330 nm			Haest et al, (2012a,b)	
2320W	In carbonates: wavelength position of the 2320 feature relates to Mg and/or Fe content of carbonates	Wavelength of absorption minimum calculated using a fitted fourth order polynomial between 2300 and 2345 nm, focused between 2310 and 2340 nm. **2320W**			Laukamp et al. (2012)	
2330Asym	Carbonates	Continuum removed asymmetry of fourth-order polynomial, fitted between 2,120 and 2,370 nm			Haest et al, (2012a,b)	
2350De	Depth of the 2350 feature, evident in white mica. Used to separate white mica from Al-smectites.	(R2326+R2359)/(R2343+R2359) ***2350De***	<1.025: Al-smectite (when 2200D present) < not applied in this project	>1.035: white mica (when 2200D present) < not applied in this project	Haest et al, (2012a,b)	
2380D	Depth of the 2380 feature, evident in for example amphiboles and talc	(R2365+R2415)/(R2381+R2390) **2380D**			Haest et al, (2012a,b)	
2390W3pfit (2390W3pfit.txt)	estimation of the Mg/Fe-ratio (~Mg#) in for example amphiboles and talc	Wavelength of absorption minimum calculated using a fitted fourth order polynomial between 2365 and 2430 nm, focused between 2380 and 2410 nm. **2390W**	**2382nm**: Mg-rich (Laukamp et al., 2012)	**2406nm**: Fe-rich (Laukamp et al., 2012)	Laukamp et al. (2012)	
2160D2190	intensity of the 2160 fetaure, indicative for Kaolin abundance. Used to sperate Kaolin from non Kaolin Al-silicates (i.e. Al-smectite & white mica)	(R2136+R2188)/(R2153+2171) **2160D2190**	<1.005: no kaolin	>1.005: kaolin	Haest et al, (2012a,b)	

Cudahy, T., Jones, M., Thomas, M., Laukamp, C., Caccetta, M., Hewson, R., Rodger, A., Verrall, M. (2008).CSIRO report P2007/364, 161pp.
Haest, M., Cudahy, T., Laukamp, C., Gregrory, S. (2012a). Economic Geology, 107, 209 - 228. (IF10: 2.021, 5yearIF10: 2.761; citations: 1)
Haest, M., Cudahy, T., Laukamp, C., Gregrory, S. (2012b). Economic Geology, 107, 229 - 249. (IF10: 2.021, 5yearIF10: 2.761; citations: 1)
Laukamp, C., Termin, K.A., Pejcic, B., Haest, M., Cudahy, T. (2012). European Journal of Mineralogy. 24, 863-878. (IF10: 1.469, 5yearIF10: 1.487)
Laukamp, C., Cudahy, T., Caccetta, M., Chia, J., Gessner, K., Haest, M., Liu, Y.C., Rodger, A. (2010). AIG Bulletin, 51(Geo-Computing 2010 Conference, Brisbane, September 2010): 73-76.
Roache, T.J., Walshe, J.L., Huntington, J.F., Quigley, M.A., Yang, K., Bil, B.W., Blake, K.L., Hyvaerinen, T. (2011). Australian Journal of Earth Sciences, 58 (7), 813-822.
Sonntag, I., Laukamp, C., Hagemann, S. (2012). Ore Geology Reviews, 45, 47-60. (IF10: 2.079, 5yearIF10: 2.2; citations: 1)

Appendix 2 Bulk Geochemistry (Drill hole-Transect samples)

Sample# (Traverse)	Au (ppb)	Ag	As	Co	Cr	Cu	Dy	Er	Eu	Gd	Hg	Ho	Lu	Mo	Nd	Ni	Pb	Pr	Sb	Sm	Tb	Tm	Yb	Zn
													(ppm)											
MT01	4.6	0.12	633	8.3	34	42.5	3.01	1.33	1.12	3.99	0.87	0.5	0.21	1.1	21.5	9	5.4	5.29	28.6	4.54	0.49	0.19	1.37	5.6
MT02	0.9	0.07	209	5.6	26	55.3	2.23	1.27	0.97	3.66	0.31	0.42	0.18	1.3	21.8	4	3	5.37	27	4.39	0.38	0.18	1.15	3.5
MT03	2.3	0.1	1370	41	60	246	16.6	6.5	3.08	12.6	0.94	2.73	0.67	1.7	26.3	22	2.7	6.52	202	7.65	2.49	0.78	4.69	5.9
MT04	19.6	0.26	4260	17.2	12	52.8	1.66	0.93	0.71	2.63	1.03	0.3	0.15	1.1	14.9	22	10.6	3.79	30	2.89	0.28	0.13	0.95	1.7
W1	14.4	0.1	15	35.7	40	144	3.66	1.85	1.01	3.71	0.06	0.67	0.22	0.2	14.6	47	5.3	3.56	0.6	3.46	0.59	0.24	1.53	75.2
W2	8.5	0.11	13.6	58.1	17	156	3.2	1.59	0.84	3.44	0.2	0.58	0.16	1.1	12.9	65	8.4	3.06	0.9	3.02	0.55	0.2	1.22	93.1
W3	15.4	0.06	339	46.1	4	208	1.11	0.57	0.36	1	0.09	0.2	0.05	7	4.77	45	19.1	1.01	57.1	1.04	0.18	0.08	0.42	155
W4	58	0.05	206	19.7	3	50.8	0.55	0.31	0.18	0.47		0.11	0.03	1	1.51	29	6.1	0.29	9.9	0.46	0.09		0.26	73.4
A1	3.5	0.06	54	53.2		385	1.3	0.55	0.42	1.06	0.14	0.21	0.06	1	2.78	54	3.9	0.46	0.4	1.13	0.22	0.07	0.41	136
A2	1.6	0.16	11.7	0.7	8	12.8	3.26	2.48	0.36	1.51		0.75	0.37	2	3.29	2	42.2	0.85	22.5	0.96	0.38	0.36	2.46	7.4
A3	3.5	0.32	90.7	3.9	12	9.7	4.88	3.05	1.25	5.57	0.52	0.97	0.42	1.7	27.6	8	68.2	8.25	36.2	5.03	0.73	0.44	2.94	6.8
A4	1.2	0.19	250	39.4	5	148	3.52	1.89	0.63	2.85	0.31	0.7	0.17	2.8	7.08	82	45.9	1.47	19.5	1.89	0.52	0.21	1.19	1050
A5	1.8	0.03	53	72.1	68	167	7.05	3.68	1.5	5.01	1.1	1.31	0.47	1.4	9.45	84	70.8	1.79	6.4	3.79	1.1	0.49	3.16	380
A6	0.6	0.05	2.7	5.3	22	103	1.85	1	0.45	2.51		0.35	0.13	0.7	8.47	20	5.2	2.58	0.3	1.58	0.29	0.14	0.94	18
A7	4.9	1.76	273	7.5	14	58.1	3.34	2.24	0.52	2.11	0.29	0.7	0.34	4	6.83	8	61.8	1.58	39.7	1.66	0.44	0.33	2.31	116
A8	2.4	0.11	3.4	48.8	85	188	4.13	2.18	1.51	5.49		0.76	0.28	0.4	23.1	73	6.2	5.75	0.5	4.96	0.76	0.3	1.94	114
A9	0.5	0.1	2.1	46.7	37	142	4.61	2.37	1.64	5.3		0.84	0.3	1.5	21.3	62	9.8	5.39	0.4	4.65	0.77	0.31	2.02	113
A10		0.08	1.8	37.2	51	145	4.8	2.5	1.44	5.56	0.38	0.88	0.32	0.2	22.2	71	5.5	5.64	0.9	4.8	0.79	0.34	2.21	82.7
A11	4.7	0.08	16.3	22.5	47	97.9	3.56	1.82	1.1	4.33	0.09	0.64	0.24	1	19.1	35	16	4.95	4.8	3.98	0.59	0.25	1.6	63.9
A12	1.2	0.25	45.3	15	105	138	3.02	1.61	0.84	3.16		0.56	0.24	3	12.3	36	38.6	3.13	12	2.83	0.48	0.23	1.58	118
E1	2.1	0.09	12.6	61.8	33	29.1	4.84	2.58	1.86	5.95	0.07	0.89	0.36	0.3	28.2	99	10.3	7.08	5.2	5.91	0.81	0.36	2.4	300
E2	1.1	0.03	4.5	43.5	6	146	2.36	1.21	0.69	2.54	0.11	0.42	0.13	0.2	9.89	27	4.2	2.4	1.2	2.26	0.39	0.16	0.97	83.8
E3	0.5	0.16	3.7	50.3	15	73	1.86	0.91	0.65	2.61	0.1	0.33	0.11	0.6	12.8	25	2.4	3.29	5.5	2.54	0.33	0.13	0.8	172
E4	3.2	0.08	8.4	58.4	37	241	5.22	3.04	1.64	5.89		1	0.41	0.6	26.7	90	11.8	6.93	1.6	5.67	0.82	0.44	2.86	285
E5		0.04	2.1	2.6	16	12.4	0.85	0.46	0.46	1.97		0.14	0.08	0.3	12.6	5	1.7	3.36	0.8	2.23	0.15	0.07	0.49	11
E6	0.7	0.03	5.5	58.9	6	21.8	4.31	1.92	1.22	4.38		0.73	0.23	0.5	12.5	34	3.6	2.77	0.8	3.73	0.75	0.25	1.59	97.4
E7		0.07	3.9	57.7	43	157	2.33	1.2	0.76	2.76		0.42	0.15	0.1	11.8	55	10	3.04	3.7	2.83	0.4	0.17	1.13	141
E8		0.03	2.5	1.7	29	29.1	1.19	0.55	0.56	2.02		0.19	0.07	0.4	10.5	6	2.9	2.69	2	2.22	0.23	0.08	0.55	6.6
E9		0.1	2.6	50.8	39	84.1	2.86	1.41	1.06	3.73		0.51	0.18	1.7	17.3	41	8.5	4.3	2.4	3.85	0.5	0.19	1.31	101
E10	2.3	0.1	1.1	51.4	19	184	3.69	2.1	0.88	3.44		0.7	0.29	1.2	9.53	29	4.4	2.23	0.8	2.52	0.59	0.29	1.9	164
E11		0.06	3.3	3.6	55	74	3.75	1.79	1.25	4.66		0.65	0.25	1.3	19.8	18	5.9	4.76	1.9	4.48	0.66	0.25	1.67	17.9
E12	1.1	0.05	4.8	2.8	64	44.9	3.79	1.47	1.86	6.43		0.58	0.17	0.8	33	21	7.2	8.26	3.3	7.3	0.78	0.2	1.31	14.5
F1		0.04	1.6	61.7	19	40.8	4.76	2.5	1.54	6.1	0.48	0.87	0.33	0.3	27	59	3	6.76	1.3	5.94	0.82	0.34	2.24	527
F2	0.7	0.02	4.7	28.7	27	13.3	2.48	1.22	0.77	2.64		0.43	0.16	0.3	8.36	65	9.8	2	9.6	2.72	0.44	0.17	1.15	84.5
F3A	0.6	0.03	21.8	23.4	45	19.6	5.83	3.38	0.98	5.58		1.19	0.38	0.4	19.8	27	29.2	5.54	39.4	3.98	0.87	0.42	2.44	67.4
F3B		0.01	41.6	152		115	4.07	1.76	1.36	4.22		0.71	0.17	1.2	12.2	222	102	2.56	78.2	3.61	0.78	0.21	1.18	383
F4		0.03	10	3.7	60	18.9	4.45	1.98	1.59	5.6		0.71	0.27	0.9	27.3	9	9.2	6.59	6.8	6.23	0.81	0.27	1.83	11.3
F5			71.2	29	10	259	2.78	1.63	1.12	3.76		0.53	0.21	1.3	18.2	70	2.8	4.5	37.7	4.1	0.46	0.22	1.5	70.8
F6		0.05	3.6	39.8	23	122	2.8	1.39	1.4	5		0.49	0.19	0.4	24.6	55	3.9	6.23	7	5.17	0.51	0.2	1.3	146
F7	1.3	0.05	4.6	1.5	12	27.1	0.48	0.24	0.16	0.89		0.09	0.03	0.5	4.21	4	1.1	1.16	7.3	0.77	0.08		0.24	4.7
F8	1.9	0.16	9.3	6.1	146	26.8	3.99	2.38	1.22	6.51		0.78	0.4	0.3	28.4	22	26.2	8.06	13.2	5.5	0.77	0.39	2.63	46.7
001-1	1.2	0.08	7.6	21.7	70	64	3.79	2.3	1.11	4.85		0.77	0.32	0.8	18.6	45	15.5	4.83	1.3	4.05	0.72	0.36	2.31	75.1
001-2	0.8	0.08	7.7	23.7	63	69.3	4.03	2.4	1.19	4.98		0.8	0.33	0.7	19	47	14.4	4.85	1.2	4.22	0.77	0.38	2.38	77.9
001-3	1.4	0.12	34.7	23.9	66	92.3	4.97	3.09	1.24	6.95	0.07	1.02	0.43	3.2	27.7	45	17.6	7.35	2.1	5.56	0.95	0.48	3.05	84.5
001-4	1.8	0.09	7.8	25.8	65	76.4	4.63	2.8	1.36	5.8		0.94	0.39	0.8	21.7	52	16.2	5.52	1.3	4.87	0.89	0.43	2.79	90.4
001-5	1.7	0.08	7.8	29.1	67	81.5	3.99	2.41	1.14	5.2		0.8	0.32	0.8	20.4	54	14.6	5.38	1.2	4.37	0.75	0.38	2.38	87
001-6	3.7	0.09	8.8	27.8	67	79	4.15	2.5	1.19	5		0.83	0.34	0.7	18.8	54	14.2	4.79	1.2	4.17	0.77	0.39	2.47	100
001-7	0.9	0.08	8.6	27.5	71	79.4	4.07	2.49	1.17	5.06		0.83	0.34	0.8	19	52	14.7	4.91	1.4	4.22	0.77	0.39	2.42	86.9
001-8	0.6	0.09	9.4	25.2	76	71.4	4	2.43	1.11	4.71		0.79	0.32	0.7	17.1	50	13.9	4.4	1.4	3.83	0.73	0.38	2.43	86
001-9	0.5	0.14	13.6	10.9	189	33.7	2.07	1.48	0.45	2.14		0.46	0.24	0.9	7.62	30	10.9	2.04	3.5	1.71	0.35	0.24	1.65	44.9
001-10	0.8	0.1	7.2	34.8	70	82.6	4.19	2.53	1.24	5.33		0.84	0.35	0.8	20.6	58	13.8	5.3	1.2	4.5	0.79	0.4	2.59	88.5
001-11	2.4	0.06	5.5	9.6	18	40.2	8.14	3.86	3.7	13.9		1.42	0.41	1.3	68.8	22	3.7	14.8	1	15.1	1.88	0.53	3.06	15.7
001-12A	0.9	0.07	9	40.6	109	69.9	3.6	2.23	1.08	4.73		0.73	0.33	0.9	18.8	68	10.8	4.75	1.4	4.24	0.7	0.35	2.28	89.3
001-12B	0.5	0.04	5.5	8.9	24	30.9	3.79	1.69	1.74	7.19		0.63	0.2	1.1	34.6	21	2.3	8.62	1.5	7.14	0.87	0.25	1.57	16.5
001-13		0.04	4.3	5.1	25	18.4	2.68	1.3	1.2	4.83		0.46	0.19	0.7	25	8	2.6	6.13	1.3	5.02	0.59	0.21	1.4	10.8
001-14	0.6	0.03	5.6	12.6	40	24.7	9.14	4.72	4.05	15.4		1.67	0.55	0.7	79	15	4.6	17.4	1.3	17.2	2.01	0.68	4.12	17.8
001-15		0.14	12	9.7	235	30	3.65	2.52	0.85	3.89	0.09	0.77	0.4	1.1	14.6	26	11.9	3.82	2.9	3.24	0.64	0.42	2.81	46.2
001-16	0.8	0.06	6.3	22	63	75.7	4.06	2.36	1.23	5.66		0.8	0.31	0.7	22.3	42	12.8	5.51	0.9	4.84	0.79	0.36	2.24	61.2
001-17	1.1	0.07	10.7	21.5	85	65.6	3.35	1.96	1.01	5.02		0.65	0.28	1.1	22.4	39	12.7	5.97	1.3	4.4	0.65	0.32	2.05	53.2
001-18	0.7	0.07	11	23.3	62	86.9	3.67	1.97	1.24	5.9		0.66	0.27	0.9	27.2	27	8.5	7.07	0.9	5.56	0.74	0.31	2.03	35.8
001-19	1.6	0.06	5.7	14.3	41	68.4	1.78	1.06	0.51	2.48		0.35	0.16	0.8	11.6	16	1.4	3	0.4	2.25	0.35	0.17	1.13	17.5
001-20		0.09	2.3	7.4	13	81.6	2.2	1.08	0.91	4.3	0.12	0.37	0.16	0.5	22.2	13	7.4	5.73	0.6	4.12	0.47	0.17	1.15	43.9
001-21	1	0.03	10.4	63.3	25	290	6.01	3.22	2.21	10.1		1.11	0.44	1.5	46.3	75	5.1	12.8	1.8	9.58	1.24	0.49	3.21	156
001-22	0.6	0.11	5.3	35.4	64	81.3	3.37	2.14	0.89	3.94		0.71	0.3	0.5	14.7	70	17	3.78	1	3.27	0.63	0.33	2.18	107
001-23	0.7	0.1	6	31.1	56	81.1	3.1	2.02	0.8	3.54		0.65	0.28	0.7	12.6	57	13.3	3.28	1	2.91	0.56	0.33	2.1	93.6
001-24	1.7	0.07	3.5	44.5	55	81.8	3.79	2.44	0.99	3.89		0.8	0.34	0.6	12.6	77	8.6	3.1	1	3.12	0.68	0.38	2.49	121
001-25	3.4	0.18	8.8	11.6	20	78.4	4.21	2.72	1.1	5.74		0.88	0.39	0.5	22	16	11.1	5.93	0.8	4.51	0.79	0.44	2.85	93.2
001-26	0.9	0.09	6.5	31.4	92	83.8	3.6	2.34	0.91	4.29		0.75	0.32	0.7	15.5	69	11.2	4.07	1	3.46	0.65	0.38	2.37	99.5
001-27	3.8	0.11	1.5	23.1	5	97.1	5.09	3.2	0.89	5.31		1.05	0.45	0.4	17.9	17	5.9	4.38	0.5	4.39	0.93	0.5	3.18	91.9
002-1		0.08	14.5	28.7	78	69.5	3.84	2.31	1.11	5.21		0.76	0.3	0.9	20.1	44	14.6	5.27	1.6	4.33	0.73	0.35	2.27	66.9
002-2	0.6	0.09	17.3	34.5	71	88.1	3.68	2.22	1.09	4.99		0.74	0.3	0.8	18.9	43	13.5	4.85	1.5	4.25	0.73	0.34	2.18	70.8
002-3		0.07	14	25.2	78	69.3	3.69	2.23	1.05	4.86		0.72	0.3	0.7	18.9	47	13.6	4.95	1.5	4.07	0.7	0.35	2.24	69.5
002-4		0.07	23	28	81	65.1	3.46	2.01	1.12	5.48		0.66	0.28	0.8	23.4	45	15.8	6.24	1.5	4.78	0.7	0.32	2.03	71
002-5		0.03	2.4	1.6	22	19.8	1.27	0.79	0.42	2.35		0.25	0.11	0.4	10.1	12	2.2	2.83	0.5	1.84	0.25	0.12	0.85	6.4
002-6		0.07	5.7	24.6	23	20.5	5.89	2.65	3.12	12.3		0.98	0.36	0.4	55.4	24	11.8	13.7	1.6	11.6	1.43	0.4	2.62	38.1
002-7		0.02	2.5	5.6	10	19.3	1.75	0.8	0.83	3.71		0.3	0.1	0.4	17.2	8	2.2	4.35	0.7	3.47	0.41	0.12	0.76	6.2
002-8	0.7	0.08	9.4	22.8	83	66.8	3.69	2.31	1	4.92		0.74	0.32	0.9	19.1	50	14.5	5.1	1.4	4.01	0.7	0.37	2.34	74.2
002-9	0.6	0.07	8.1	22.2	71	68	3.17	1.95	0.89	4.31		0.63	0.27	0.7	16.9	49	14	4.52	1.3	3.54	0.61	0.31	1.95	75.9
002-10	0.7	0.28	31.7	672	63	358	5.78	3.24	2.47	10.9	0.33	1.1	0.47	1.6	37.4	50	38.7	10.7	2.7	7.77	1.17	0.52	3.58	156
002-11	0.9	0.04	5.7	5.4	16	32.5	0.81	0.37	0.34	1.53	0.07	0.14	0.05	0.4	8.2	7	2.5	2.17	0.5	1.66	0.18	0.06	0.39	14.4
002-12	0.7	0.07	9	31.3	120	74.3	3.83	2.25	0.98	3.99		0.78	0.36	0.8	18.3	59	15.1	4.75	1.3	3.93	0.66	0.34	2.11	83.8
002-13	1.8	0.06	1.7	44.5	152	92.7	2.79	1.65	0.68	2.33		0.59	0.19	0.3	8.9	101	5.1	2.16	0.2	2.23	0.46	0.23	1.37	84.4
002-14	1.2	0.05		43.7	144	85.9	2.48	1.46	0.54	2.06		0.51	0.17	0.3	7.94	95	4.1	1.9	0.1	2.01	0.41	0.2	1.26	73.9
002-15	1.7	0.05	2.5	43.4	144	92.8	2.98	1.81	0.66	2.48		0.62	0.22	0.5	9.25	96	4.7	2.23	0.2	2.26	0.48	0.26	1.58	76.6

Appendix 2 continued…

Sample# (Traverse)	Au (ppb)	Ag	As	Co	Cr	Cu	Dy	Er	Eu	Gd	Hg	Ho	Lu	Mo	Nd	Ni	Pb	Pr	Sb	Sm	Tb	Tm	Yb	Zn
(Drill Core)												(ppm)												
SPD001-1		0.03	3.8	42.2	47	7.2	2.35	1.37	0.78	3.03		0.48	0.19	0.2	16.1	48	12.4	4.36	1.5	3.45	0.42	0.21	1.41	145
SPD001-2	0.6	0.07	6.5	60.9	54	870	2.84	1.52	1.21	3.74	0.38	0.54	0.23	0.2	19.3	70	11.9	4.93	1.8	4.55	0.54	0.23	1.59	213
SPD001-3	0.5	0.04	42.6	41.2	60	77	1.94	1.16	0.56	2.57		0.39	0.18	0.3	15.2	65	5.4	4.21	4.2	2.9	0.35	0.18	1.21	106
SPD001-4		0.04	6.9	29.9	50	9.4	1.81	1.06	0.55	2.04		0.36	0.15		11	37	6.3	3.04	3.1	2.27	0.31	0.16	1.09	93.8
SPD001-5	17.1	0.03	16.5	19.2	2	3.2	0.27	0.15	0.1	0.35	0.07	0.06		0.4	1.52	14	2.4	0.35	3.4	0.41	0.06		0.12	17.6
SPD001-6		0.04	34.3	22.1	36	19.9	2.43	1.33	0.61	2.86	0.09	0.48	0.16		16.1	20	4.6	4.32	24	3.1	0.43	0.19	1.2	34.1
SPD001-7				10.5	2	0.5	0.15	0.1	0.07	0.21		0.03			0.79	10	0.7	0.21	0.7	0.18	0.03		0.08	13.4
SPD001-8	2.4	0.03	162	22.1	42	4.4	2.6	1.39	0.53	2.82	0.08	0.51	0.19	0.1	14.4	25	3.1	3.92	13.7	2.9	0.45	0.21	1.36	44.5
SPD001-9	2.8	0.04	5.8	12.7	3	2.7	0.35	0.2	0.14	0.47	0.1	0.07			2.23	12	1.3	0.59	3.3	0.45	0.07		0.17	14.6
SPD001-10		0.03	29.7	18.2	52	7.7	1.84	1.14	0.39	2.6		0.38	0.17		15.2	43	1.5	4.3	19.7	2.56	0.32	0.18	1.17	76.8
SPD001-11	121	1.07	264	94.3		14.2	0.1	0.07	0.05	0.14	1.6	0.02		2.6	0.63	60	42	0.17	46.1	0.11	0.02		0.05	14.3
SPD001-12	1.9	0.05	48.4	35.4	51	19.8	2.88	1.68	0.67	3.87	0.14	0.58	0.23	0.2	21.8	53	4.5	6.17	34.9	3.93	0.5	0.26	1.66	104
SPD001-13	5.1	0.05	70.9	17.5	25	2.7	2.66	1.5	0.65	3.3	0.06	0.54	0.18	0.2	16.9	21	3.1	4.13	3.9	3.31	0.48	0.21	1.22	32.4
SPD001-14	1420	0.07	72.8	22.3	66	49.3	1.31	0.92	0.36	1.54	0.23	0.3	0.14	0.2	8.89	35	4.9	2.54	6.9	1.47	0.21	0.15	0.98	38.9
SPD001-15	16.7	0.05	3.2	31.1	46	4.2	3.36	1.9	0.85	3.74	0.06	0.68	0.25		19.6	41	5.9	5.13	0.8	4.01	0.6	0.28	1.76	90.3
SPD001-16	3.8	0.06	7.8	63.1	50	16.1	2.12	1.26	0.62	2.44	0.09	0.44	0.18	0.3	11.8	83	15.6	2.97	2.3	2.72	0.39	0.19	1.27	129
SPD001-17	11.5	0.22	2.4	75.1	8	1150	3.67	1.56	1.46	4.17	0.25	0.65	0.17	0.3	13.6	50	5.9	2.97	0.3	4.81	0.76	0.21	1.23	135
MOD13-18	1.2	0.1	1320	67.4	78	23.5	2.82	1.95	0.64	3.7		0.61	0.31	1.1	20.8	64	44.8	5.87	508	3.62	0.44	0.31	2.15	122
MOD13-19	3200	0.5	2030	33.8	12	31.2	1.1	0.65	0.3	1.55	0.42	0.23	0.08	0.3	6.45	49	1.1	1.67	27.2	1.56	0.2	0.09	0.6	177
MOD13-21		0.05	126	0.6	63	11.3	2.53	1.92	0.65	4.47	0.12	0.58	0.34	0.1	27.2	3	3.2	7.95	26.5	4.63	0.4	0.32	2.3	146
MOD13-25	32	0.07	394	5.6	11	33.6	0.5	0.31	0.09	0.7	1.13	0.1	0.04	0.4	4.03	10	1.7	1.15	28.5	0.57	0.08	0.05	0.31	79.5
MOD13-26	6.5	0.06	147	21.8	72	10.5	1.59	1.21	0.37	2.55	0.17	0.36	0.21	0.3	16.5	17	3.5	4.76	21.7	2.44	0.25	0.2	1.41	1110
MOD13-27	13.4	0.05	358	21.1	16	12.5	1.45	0.83	0.22	1.67	0.12	0.29	0.11	0.2	10.4	29	3.1	2.88	15.8	1.5	0.25	0.12	0.74	184
MOD13-28	13.4	0.03	273	65.1	50	10.7	3.21	2.29	0.79	3.99	0.44	0.72	0.41	0.3	27.9	84	3.4	7.21	22.2	4.87	0.5	0.38	2.67	293
MOD13-29	1.9	0.14	209	38.4	44	35.8	5.03	2.93	1.78	6.23	0.14	1.02	0.41	0.5	33.6	57	9.2	8.3	38.8	7.36	0.87	0.44	2.89	135
MOD13-30	11700	0.91	4590	55.5	28	114	2.11	1.35	0.65	2.7	6.95	0.44	0.23	1.2	17.3	64	8.4	4.44	63.5	3.38	0.36	0.22	1.53	3120
NMOD-001-31	1.4	0.05	35.1	45.1	42	72.4	4.48	2.48	1.66	5.82	0.12	0.87	0.35	0.6	31.3	56	16.7	7.96	19.1	6.77	0.81	0.37	2.46	108
NMOD-001-32	10.5	0.05	11.9	64.5	49	19	5.27	3.1	1.91	6.7	0.23	1.07	0.46	0.4	40.3	63	8.5	10.1	15.1	8.61	0.93	0.48	3.1	258
NMOD-001-33	6.9	0.17	34.6	68.3	40	880	4.36	2.63	1.43	4.97	1	0.91	0.37	0.4	26.9	69	8.4	6.9	47.5	5.7	0.72	0.4	2.62	189
NMOD-001-34	20.9	0.11	107	57.5	42	69.6	5.34	3.04	1.76	6.13	1.74	1.06	0.43	0.6	34.5	47	5	8.65	61.1	7.52	0.94	0.46	3.01	76.4
NMOD-001-35	288	0.3	691	88.4	33	169	5.74	2.66	2.2	7.03	11.1	1.02	0.32	0.5	30.3	101	18.5	6.99	131	8.17	1.18	0.37	2.36	25.1
NMOD-001-37	12.7	0.05	37.3	60.4	34	13.9	4.16	2.31	1.43	4.48	0.37	0.82	0.31	0.4	23.4	53	7.3	5.51	31.1	5.42	0.74	0.35	2.23	133
NMOD-001-38	6.5	2.92	5990	77.8	34	1510	4.87	2.9	2.03	6.52	106	0.99	0.42	0.9	38.1	43	85.7	9.14	1040	8.93	0.87	0.44	2.97	186
NMOD-001-39	3400	0.18	3740	37.7	44	81.9	4.23	2.33	1.45	5.3	10.6	0.83	0.34	0.3	28.4	31	8	6.99	55.7	6.19	0.78	0.35	2.29	36.3
NMOD-001-40	1920	0.4	8790	60.7	30	78.4	3.78	2.46	1.09	3.97	8.41	0.82	0.36	0.3	20.3	68	22	5.04	77.8	4.68	0.64	0.38	2.49	16.1
NMOD-001-41	128	1.25	20300	76.8	28	672	2.54	1.36	1.53	4.91	55.8	0.47	0.21	0.3	35.7	73	31.4	8.74	384	7.45	0.52	0.21	1.47	130
NMOD-001-42	354	1.69	27600	89.9	27	258	3.37	2.07	1.71	5.06	25.8	0.68	0.3	0.5	31.6	87	93.1	7.7	120	7.18	0.65	0.31	2.08	896
NMOD-001-43	18.9	0.04	127	38.4	28	17.1	3.79	1.99	1.52	5.24	0.61	0.75	0.26	0.3	32.6	28	4	7.92	21	6.9	0.72	0.3	1.87	102
NMOD-001-44	2980	1.57	4380	93	51	425	5.05	2.95	2.87	8.71	22.3	0.98	0.41	1	68.9	68	50.4	16.9	208	13.8	0.97	0.44	3.01	83.9

Appendix 3 Bulk XRD Mineralogy

SampleID	Sample Type	Tray/Depth	Powder Mineralogy
(Transects)			
G001-1	Surface (Transect)	N/A	Quartz (maj); albite, amphibole, kaolinite, chlorite, muscovite, hematite (min); rutile (tr)
G001-2	Surface (Transect)	N/A	Quartz (maj); albite, amphibole, kaolinite, chlorite, muscovite, hematite (min); rutile (tr)
G001-3	Surface (Transect)	N/A	Quartz (maj); albite, muscovite, kaolinite (min); amphibole, goethite, chlorite, sepiolite?, rutile (tr)
G001-4	Surface (Transect)	N/A	Quartz, albite, microcline (maj); amphibole (min); kaolinite, muscovite, chlorite, sepiolite?, rutile (tr)
G001-5	Surface (Transect)	N/A	Quartz (maj); albite, microcline (min); amphibole, hematite, kaolinite,, muscovite, chlorite, rutile (tr)
G001-6	Surface (Transect)	N/A	Quartz (maj); albite, microcline (min); amphibole, hematite, kaolinite,, muscovite, chlorite (tr)
G001-7	Surface (Transect)	N/A	Quartz (maj); albite, microcline (min); amphibole, hematite, kaolinite,, muscovite, chlorite, rutile (tr)
G001-8	Surface (Transect)	N/A	Quartz (maj); albite, microcline (min); amphibole, hematite, kaolinite,, muscovite, gibbsite, chlorite (tr)
G001-9	Surface (Transect)	N/A	Quartz, hematite (maj); gibbsite (min); kaolinite, dolomite, rutile (tr)
G001-10	Surface (Transect)	N/A	Quartz (maj); albite, microcline, amphibole, hematite, chlorite, muscovite (min); rutile (tr)
G001-11	Surface (Transect)	N/A	Quartz (maj); hematite (min); kaolinite (tr)
G001-12A	Surface (Transect)	N/A	Quartz (maj); muscovite, kaolinite, hematite, palygorskite, microcline, goethite (min); rutile (tr)
G001-12B	Surface (Transect)	N/A	Quartz (maj); hematite (min); kaolinite (tr)
G001-13	Surface (Transect)	N/A	Quartz (maj); hematite (min); kaolinite, muscovite (tr)
G001-14	Surface (Transect)	N/A	Quartz (maj); hematite (min); kaolinite, muscovite (tr)
G001-15	Surface (Transect)	N/A	Quartz, hematite, gibbsite (maj); goethite, kaolinite, rutile (tr)
G001-16	Surface (Transect)	N/A	Quartz (maj); albite, microcline, Fe-chlorite, amphibole, goethite (min); rutile? (tr)
G001-17	Surface (Transect)	N/A	Quartz (maj); albite, microcline, goethite, hematite, kaolinite, amphibole (min); rutile? (tr)
G001-18	Surface (Transect)	N/A	Quartz (maj); hematite, goethite, kaolinite, albite, dolomite, muscovite (min)
G001-19	Surface (Transect)	N/A	Quartz (maj); goethite (min)
G001-20	Surface (Transect)	N/A	Quartz (maj); goethite, kaolinite, muscovite (min)
G001-21	Surface (Transect)	N/A	Quartz, goethite (maj); muscovite (min); hematite (tr)
G001-22	Surface (Transect)	N/A	Quartz, albite, amphibole, Fe-chlorite (maj); orthoclase, dolomite (min); muscovite, rutile (tr)
G001-23	Surface (Transect)	N/A	Quartz, albite, amphibole, Fe-chlorite (maj); orthoclase, dolomite (min); hematite, muscovite, rutile (tr)
G001-24	Surface (Transect)	N/A	Amphibole, quartz, Fe-chlorite, albite, orthoclase (maj); dolomite (min); rutile (tr)
G001-25	Surface (Transect)	N/A	Quartz, microcline (maj); kaolinite, muscovite (min); rutile (tr)
G001-26	Surface (Transect)	N/A	Quartz, albite, amphibole, Fe-chlorite (maj); microcline, dolomite (min); muscovite, rutile (tr)
G001-27	Surface (Transect)	N/A	Quartz, Fe-chlorite, albite (maj); microcline, calcite (min); rutile (tr)
H002-1	Surface (Transect)	N/A	Quartz (maj); albite, microcline, goethite, hematite, kaolinite, muscovite, Fe-chlorite, amphibole (min); rutile (tr)
H002-2	Surface (Transect)	N/A	Quartz (maj); albite, microcline, goethite, hematite, kaolinite, muscovite, actinolite, Fe-chlorite (min)
H002-3	Surface (Transect)	N/A	Quartz (maj); albite, microcline, goethite, hematite, kaolinite, muscovite, actinolite, Fe-chlorite? (min)
H002-4	Surface (Transect)	N/A	Quartz (maj); goethite, hematite, muscovite, kaolinite, microcline, albite (min)
H002-5	Surface (Transect)	N/A	Quartz (maj); muscovite, kaolinite (min)
H002-6	Surface (Transect)	N/A	Quartz, hematite, muscovite (maj); kaolinite, rutile (tr)
H002-7	Surface (Transect)	N/A	Quartz (maj); hematite (min); muscovite (tr)
H002-8	Surface (Transect)	N/A	Quartz (maj); albite, microcline, actinolite, kaolinite, Fe-chlorite?, goethite, hematite, muscovite (min); rutile (tr)
H002-9	Surface (Transect)	N/A	Quartz (maj); albite, microcline, actinolite, kaolinite, Fe-chlorite?, goethite, hematite, muscovite (min); rutile (tr)
H002-10	Surface (Transect)	N/A	Quartz, goethite (maj); kaolinite, muscovite (tr)
H002-11	Surface (Transect)	N/A	Quartz (maj); kaolinite, goethite (tr)
H002-12	Surface (Transect)	N/A	Quartz (maj); albite, microcline, kaolinite, muscovite, Fe-chlorite?, goethite, hematite, actinolite, rutile (tr)
H002-13	Surface (Transect)	N/A	Fe-chlorite, actinolite, albite, microcline, quartz (maj)
H002-14	Surface (Transect)	N/A	Albite, Fe-chlorite, quartz, actinolite, K-feldspar (maj); microcline (min); rutile (tr)
H002-15	Surface (Transect)	N/A	Quartz, albite, Fe-chlorite, actinolite (maj); microcline (min); muscovite (tr)
A1	Surface (Transect)	N/A	Quartz, goethite (maj)
A2	Surface (Transect)	N/A	Quartz (maj); anatase, rutile (tr)
A3	Surface (Transect)	N/A	Dolomite, muscovite, quartz (maj); K-feldspar?, hematite (min); rutile, anatase? (tr)
A4	Surface (Transect)	N/A	Goethite (maj); hematite (min)
A5	Surface (Transect)	N/A	Goethite, muscovite (maj); quartz, K-feldspar? (min); rutile (tr)
A6	Surface (Transect)	N/A	Quartz (maj); kaolinite, illite, goethite (min)
A7	Surface (Transect)	N/A	Quartz (maj); goethite (min); rutile (tr)
A8	Surface (Transect)	N/A	Quartz, Na-feldspar, Fe-chlorite, muscovite (maj); calcite, rutile (tr)
A9	Surface (Transect)	N/A	Quartz, Fe-chlorite, Na-feldspar (maj); K-feldspar (min), calcite (tr)
A10	Surface (Transect)	N/A	Na-feldspar, quartz, K-feldspar, Fe-chlorite, dolomite (maj); rutile (tr)
A11	Surface (Transect)	N/A	Quartz (maj); kaolinite, goethite, muscovite, Na-feldspar (min), rutile (tr)
A12	Surface (Transect)	N/A	Quartz, goethite (maj); hematite, kaolinite (min); rutile (tr)
E1	Surface (Transect)	N/A	Quartz, Fe-chlorite (maj); hematite, muscovite (min); rutile (tr)
E2	Surface (Transect)	N/A	Dolomite, quartz (maj); goethite, kaolinite, muscovite (min)
E3	Surface (Transect)	N/A	Quartz (maj); muscovite, goethite (min); hematite (tr)
E4	Surface (Transect)	N/A	Quartz, Fe-chlorite, hematite (maj); muscovite (min); rutile (tr)
E5	Surface (Transect)	N/A	Quartz (maj); hematite (min); kaolinite (tr)
E6	Surface (Transect)	N/A	Dolomite, calcite, quartz (maj); Fe-chlorite, muscovite, hematite (min)
E7	Surface (Transect)	N/A	Quartz, muscovite, Fe-chlorite (maj); hematite (min); rutile (tr)
E8	Surface (Transect)	N/A	Quartz (maj); hematite, kaolinite (tr)
E9	Surface (Transect)	N/A	Quartz (maj); hematite, muscovite, kaolinite (min); rutile (tr)
E10	Surface (Transect)	N/A	Dolomite, quartz, Fe-chlorite (maj); muscovite, goethite (min); calcite (tr)
E11	Surface (Transect)	N/A	Quartz (maj); muscovite, hemaite, kaolinite (min)
E12	Surface (Transect)	N/A	Quartz, hematite (maj); kaolinite (min)
F1	Surface (Transect)	N/A	Quartz, Fe-chlorite (maj); muscovite, rutile (tr)
F2	Surface (Transect)	N/A	Quartz, muscovite (maj); hematite, kaolinite, unknown? (min)
F3	Surface (Transect)	N/A	Quartz, muscovite, goethite (maj); kaolinite (min); rutile (tr)
F3	Surface (Transect)	N/A	Goethite, quartz (maj); muscovite (min)
F4	Surface (Transect)	N/A	Quartz, hematite (maj); kaolinite (tr)
F5	Surface (Transect)	N/A	Goethite, quartz (maj); hematite (min)
F6	Surface (Transect)	N/A	Quartz (maj); hematite (min); kaolinite (tr)
F7	Surface (Transect)	N/A	Quartz (maj); muscovite? (tr)
F8	Surface (Transect)	No sample for XRD	(NOT SCANNED)
(PIT Samples)			
W1	Pit	N/A	Quartz, Fe-chlorite, albite, calcite (maj); microcline (min)
W2	Pit	N/A	Albite, Fe-chlorite, quartz (maj); microcline, calcite, dolomite (min); rutile (tr)
W3	Pit	N/A	Quartz (maj); goethite (min); halite? (tr)
W4	Pit	N/A	Quartz (maj); goethite (min); halite? (tr)
MT01	Pit	N/A	Quartz (maj); muscovite, pyrite (min), jarosite (tr)
MT02	Pit	N/A	Quartz (maj); muscovite (min); pyrite (tr)
MT03	Pit	N/A	Quartz, muscovite (maj); alunite, kaolinite (min); rutile (tr)
MT04	Pit	N/A	Quartz, pyrite (maj); muscovite, rozenite (tr)

Appendix 3 continued..

SampleID	Sample Type	Tray/Depth	Powder Mineralogy
(DRILL CORE)			
MOD13-18	Drill core	88.25-88.3	Quartz, muscovite (maj); hematite (min)
MOD13-19	Drill core	90.6-90.7	Quartz (maj); muscovite, goethite, hematite (min)
MOD13-20	Drill core (Grab Sample)	92-92	Pyrite (maj); szomolnokite, illite, quartz, melanterite (min); sulfur? (tr)
MOD13-21	Drill core	92.3-92.4	Quartz, muscovite (maj); rutile (tr)
MOD13-22	Drill core (Grab Sample)	92.75-92.8	Melanterite (maj); rozenite, szomolnokite, illite, quartz (min); chlorite, jarosite? (tr)
MOD13-23	Drill core (Grab Sample)	118.4-118.4	Rozenite, pyrite (maj); szomolnokite, illite, quartz (min); chlorite, gypsum(tr)
MOD13-24	Drill core (Grab Sample)	118.8-118.8	Pyrite, szomolnokite, illite (maj); rozenite, quartz (min); chlorite, gypsum, jarosite, arsenopyrite? (tr)
MOD13-25	Drill core	121.9-121.97	Quartz (maj); muscovite, pyrite (tr)
MOD13-26	Drill core	123.4-123.5	Muscovite, quartz (maj); rutile (tr)
MOD13-27	Drill core	123.68-123.77	Muscovite, quartz (maj); pyrite, rutile (tr)
MOD13-28	Drill core	127.8-127.85	Quartz, muscovite (maj); rutile (tr)
MOD13-29	Drill core	139.2-139.27	Siderite, quartz, muscovite (maj); chlorite (min); rutile (tr)
MOD13-30	Drill core (Grab Sample)	110.1-110.15	(NOT SCANNED)
NMOD1-31	Drill core	210.4-210.5	Quartz, hematite, Fe-chlorite, muscovite, pyrophyllite (maj); rutile (tr)
NMOD1-32	Drill core	250.3-250.37	Fe-Chlorite, quartz, muscovite (maj); rutile (tr)
NMOD1-33	Drill core	255.27-255.35	Siderite, quartz, Fe-chlorite, muscovite (maj); kaolinite (min); rutile, hematite (tr)
NMOD1-34	Drill core (Grab Sample)	266.3-266.35	Siderite, muscovite, quartz (maj); rutile (tr)
NMOD1-35	Drill core (Grab Sample)	267.4-267.46	Pyrite, quartz, muscovite (maj); jarosite (min); rutile (tr)
NMOD1-36	Drill core (Grab Sample)	270.3-270.35	(NOT SCANNED)
NMOD1-37	Drill core	303.1-303.23	Quartz, siderite, muscovite (maj); hematite (min); rutile, amesite (tr)
NMOD1-38	Drill core (Grab Sample)	314.85-314.9	(NOT SCANNED)
NMOD1-39		349.74-349.8	(NOT SCANNED)
NMOD1-40	Drill core (Grab Sample)	349.9-349.95	(NOT SCANNED)
NMOD1-41	Drill core	362.64-362.76	Quartz (maj); As-pyrite?, dolomite (min); muscovite, chlorite, rutile (tr)
NMOD1-42	Drill core (Grab Sample)	367.75-367.85	Illite, szomolnokite, pyrite, quartz (maj); halite?, chlorite, rozenite, (min); gypsum, arsenopyrite? (tr)
NMOD1-43	Drill core	438.1-438.29	Quartz (maj); hematite, siderite, Fe-chlorite, dolomite, muscovite (min)
NMOD1-44	Drill core (Grab Sample)	442.9-443.05	Quartz (maj); pyrite, muscovite, chlorite (min); rutile (tr)
SPD001-1	Drill core	323.03-323.12	Quartz, Fe-chlorite, muscovite (maj); hematite (min); rutile (tr)
SPD001-2	Drill core	324.14-324.27	Fe-Chlorite, quartz (maj); muscovite (min); rutile (tr)
SPD001-3	Drill core	345.33-345.44	Quartz, Fe-chlorite, muscovite (maj); rutile (tr)
SPD001-4	Drill core	340.7-341	Quartz, siderite, Fe-chlorite, muscovite (maj)
SPD001-5	Drill core	354.41-354.6	Dolomite (maj); quartz, muscovite, pyrite (tr)
SPD001-6	Drill core	365.89-366	Dolomite (maj); quartz, muscovite (tr)
SPD001-7	Drill core	386-386.25	Dolomite (maj); quartz, muscovite (tr)
SPD001-8	Drill core	395.2-395.34	Quartz, dolomite, muscovite (maj); rutile, pyrite (tr)
SPD001-9	Drill core	400.55-400.72	Dolomite (maj); quartz, muscovite (tr)
SPD001-10	Drill core	417.44-417.62	Quartz, Fe-chlorite (maj); muscovite (min) rutile (tr)
SPD001-11	Drill core	431.26-431.44	Dolomite (maj); pyrite (min); quartz (tr)
SPD001-12	Drill core	389.65-389.85	Quartz, Fe-chlorite, muscovite (maj); rutile (tr)
SPD001-13	Not scanned	445.68-445.82	(NOT SCANNED)
SPD001-14	Drill core	446.76-446.9	Quartz, dolomite (maj); Fe-chlorite, muscovite (min); rutile (tr)
SPD001-15	Drill core	462.62-462.8	Quartz, dolomite, Fe-chlorite, muscovite (maj); rutile (tr)
SPD001-16	Drill core	464.56-464.7	Quartz, Fe-chlorite, muscovite (maj); hematite (min); rutile (tr)
SPD001-17	Drill core	726.6-727.76	Dolomite, quartz, Fe-chlorite (maj); siderite? (min)
MOD11-1	Drill core	Tray 9 (130.51-130.52)	Quartz, hematite, Fe-chlorite, pyrophyllite, muscovite (maj); rutile (tr)
MOD11-2	Drill core	Tray 9 (132.88-132.89)	Quartz, hematite, Fe-chlorite, pyrophyllite, muscovite (maj); rutile (tr)
MOD11-3	Drill core	Tray 16 (166.54-166.56)	Quartz, kaolinite/dickite, siderite?, hematite, muscovite (maj); rutile? (tr)
MOD11-4	Drill core	Trya 42 (306.88-306.90)	Quartz, muscovite (maj); kaolinite/dickite (min); rutile (tr)
MOD11-5	Drill core	Tray 42 (308.50-308.52)	Quartz, muscovite, kaolinite/dickite (maj); rutile (tr)
MOD11-6Green	Drill core	Tray 64 (421.58-421.60)	Pyrophyllite, quartz (maj); dolomite?, kaolinite, cronstedtite, muscovite (min)
MOD11-6White	Drill core	Tray 64 (421.58-421.60)	Dolomite, quartz (maj); pyrophyllite (min); muscovite, kaolinite (tr)
MOD5-7Red	Drill core	Tray 23 (110.15-110.18)	Quartz (maj); muscovite, goethite, hematite, kaolinite (min)
MOD5-7White	Drill core	Tray 23 (110.15-110.18)	Quartz (maj)

Appendix 4 XRD patterns

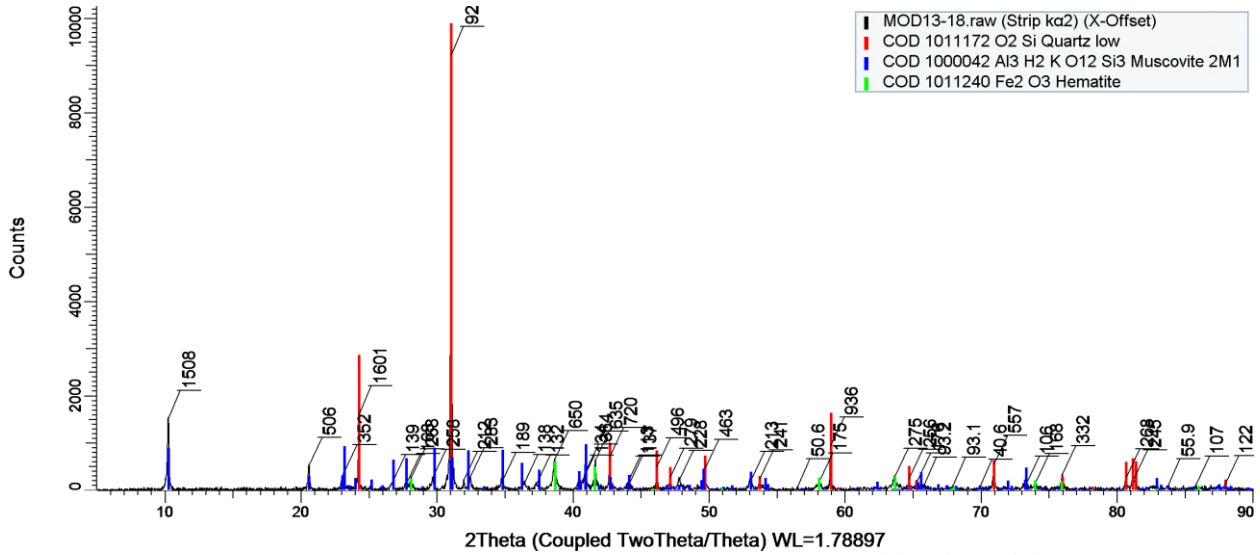

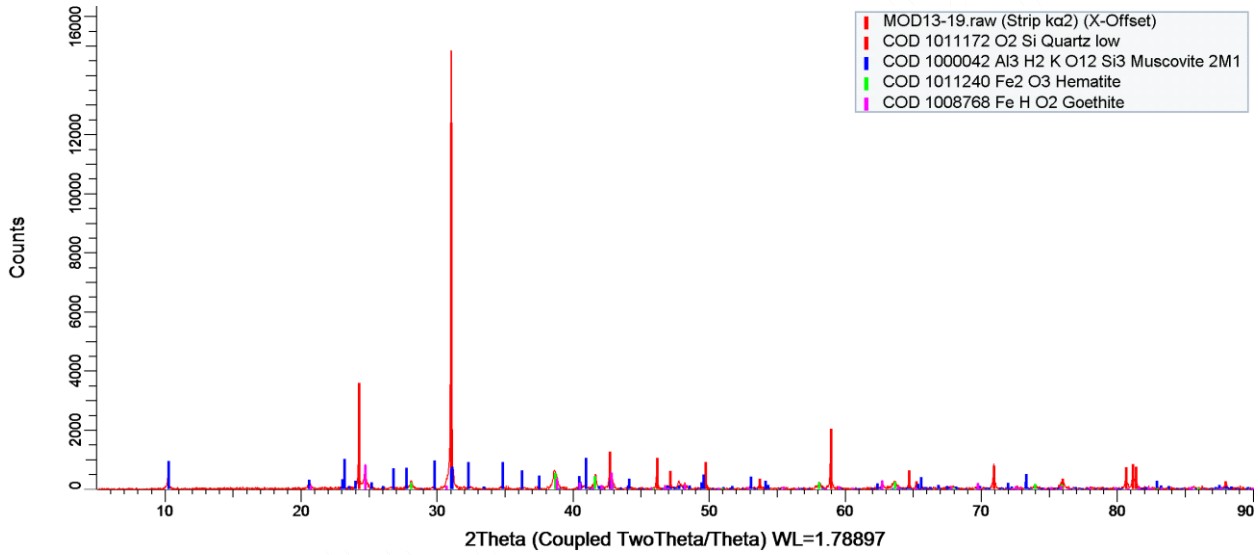

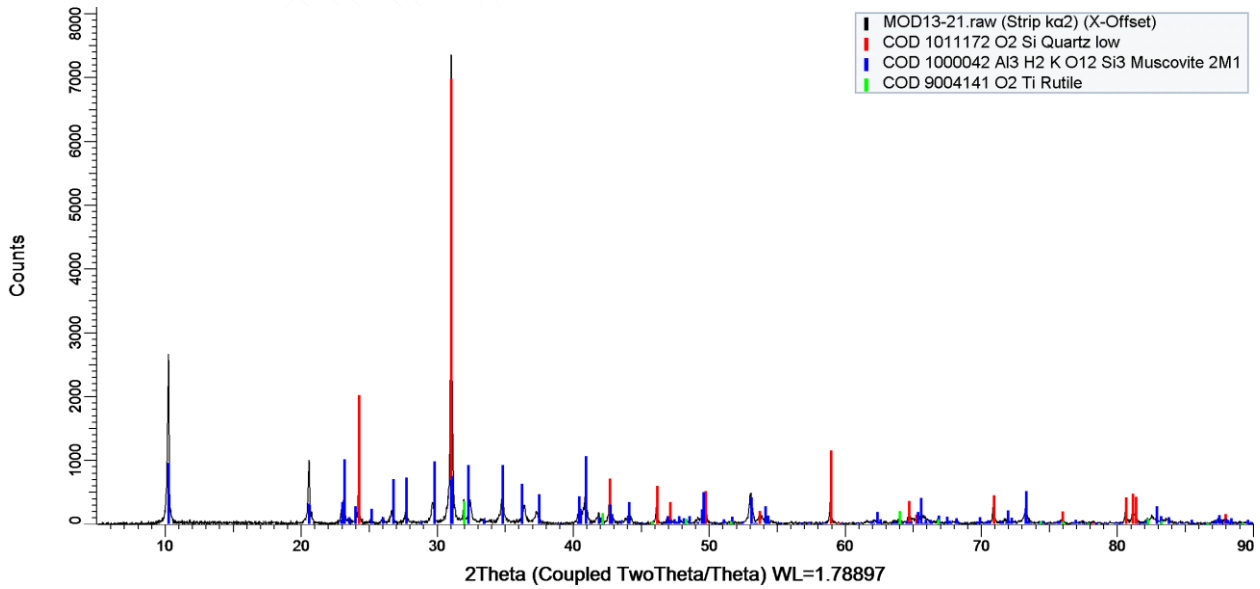

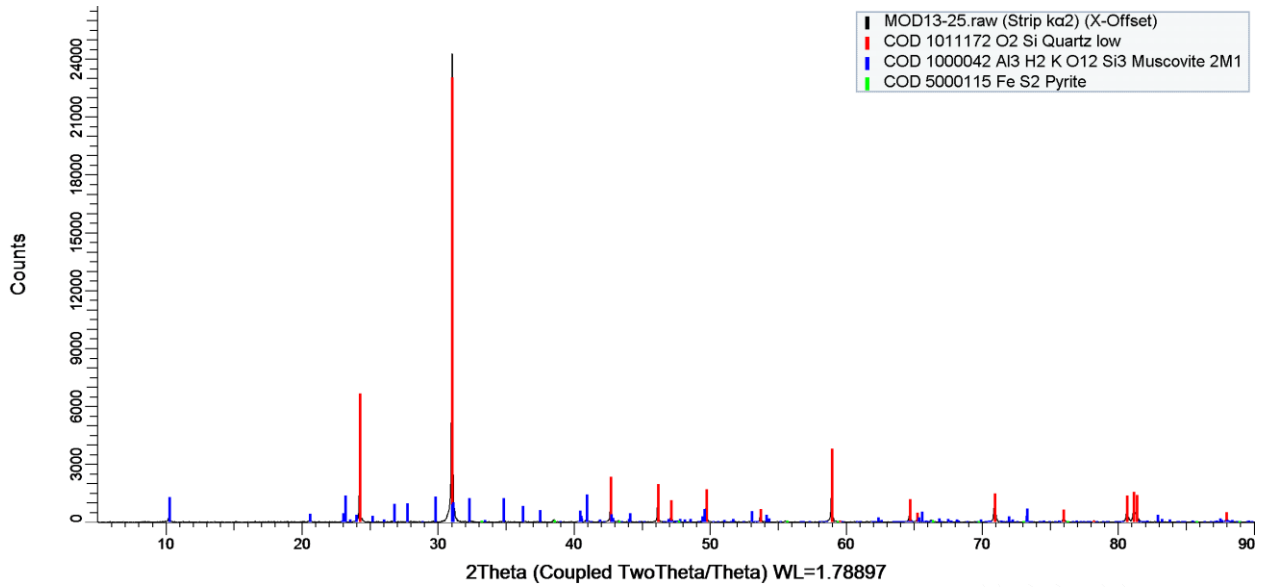
MOD13-25.raw (Strip kα2) (X-Offset)
COD 1011172 O2 Si Quartz low
COD 1000042 Al3 H2 K O12 Si3 Muscovite 2M1
COD 5000115 Fe S2 Pyrite
Counts
0
3000
6000
9000
12000
15000
18000
21000
24000
10
20
30
40
50
60
70
80
90
2Theta (Coupled TwoTheta/Theta) WL=1.78897

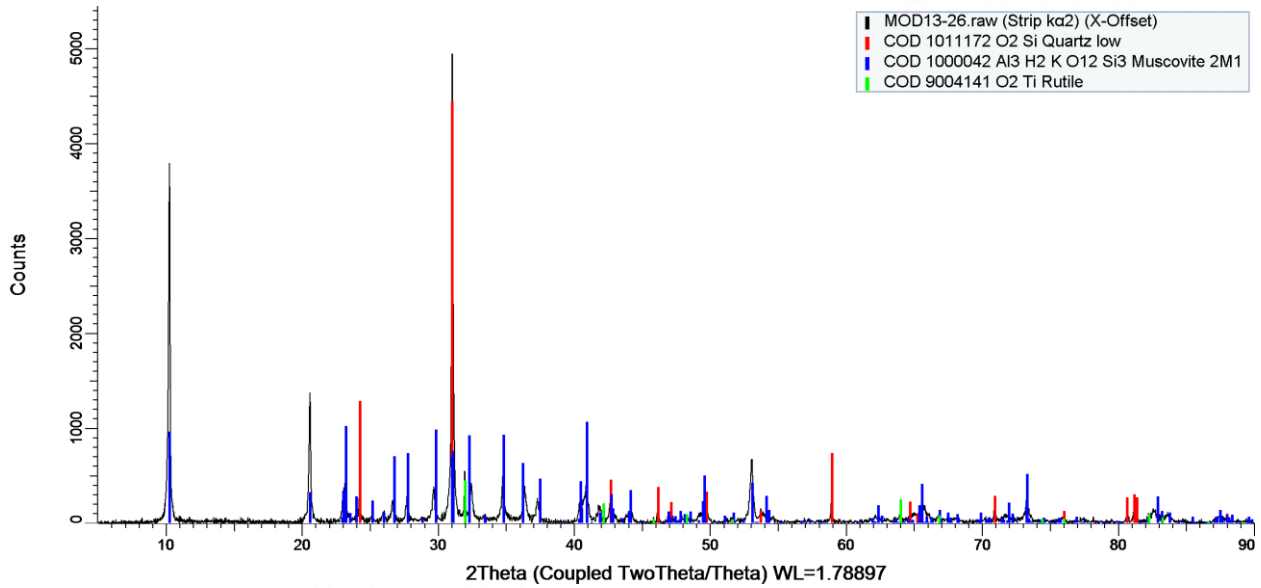
MOD13-26.raw (Strip kα2) (X-Offset)
COD 1011172 O2 Si Quartz low
COD 1000042 Al3 H2 K O12 Si3 Muscovite 2M1
COD 9004141 O2 Ti Rutile
Counts
0
1000
2000
3000
4000
5000
10
20
30
40
50
60
70
80
90
2Theta (Coupled TwoTheta/Theta) WL=1.78897

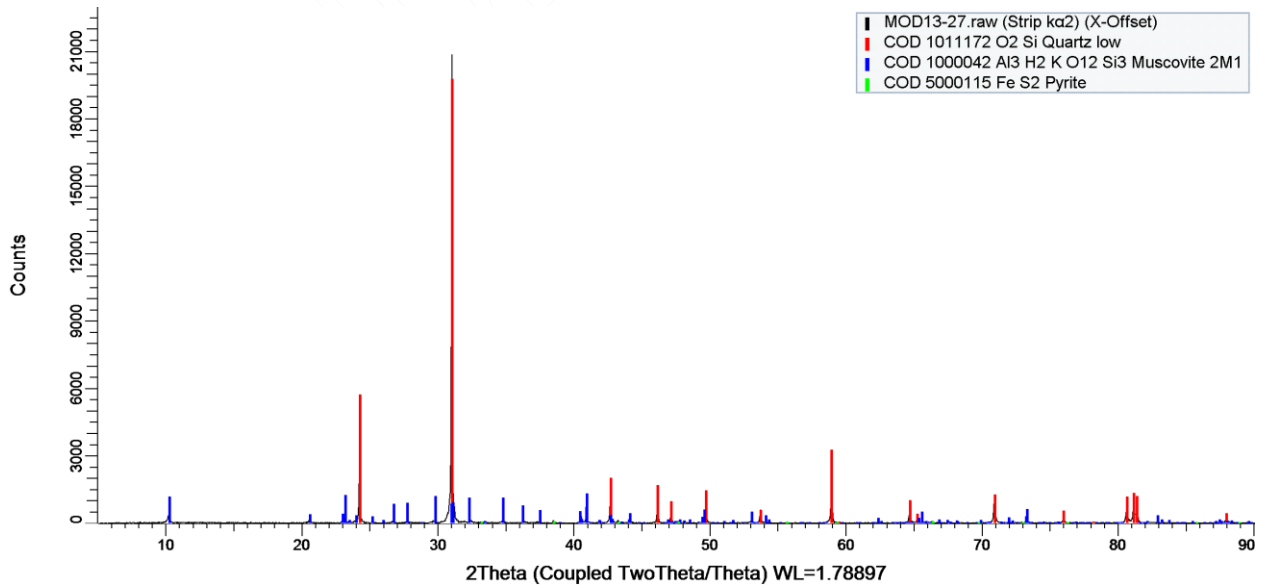
MOD13-27.raw (Strip kα2) (X-Offset)
COD 1011172 O2 Si Quartz low
COD 1000042 Al3 H2 K O12 Si3 Muscovite 2M1
COD 5000115 Fe S2 Pyrite
Counts
0
3000
6000
9000
12000
15000
18000
21000
10
20
30
40
50
60
70
80
90
2Theta (Coupled TwoTheta/Theta) WL=1.78897

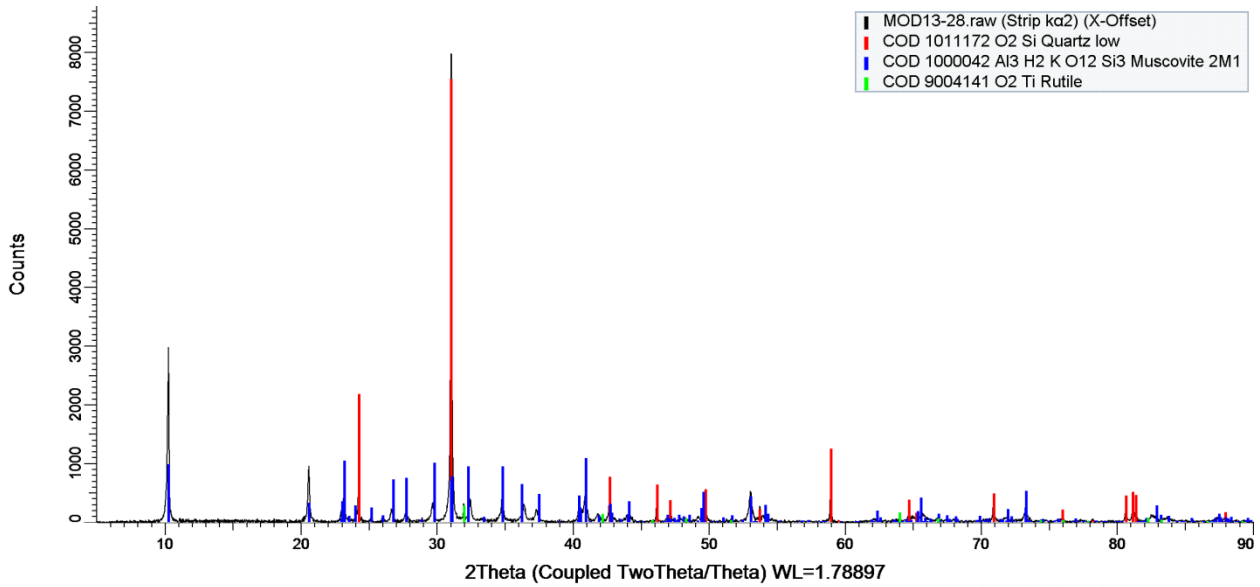
MOD13-28.raw (Strip kα2) (X-Offset)
COD 1011172 O2 Si Quartz low
COD 1000042 Al3 H2 K O12 Si3 Muscovite 2M1
COD 9004141 O2 Ti Rutile
Counts
0
1000
2000
3000
4000
5000
6000
7000
8000
10
20
30
40
50
60
70
80
90
2Theta (Coupled TwoTheta/Theta) WL=1.78897

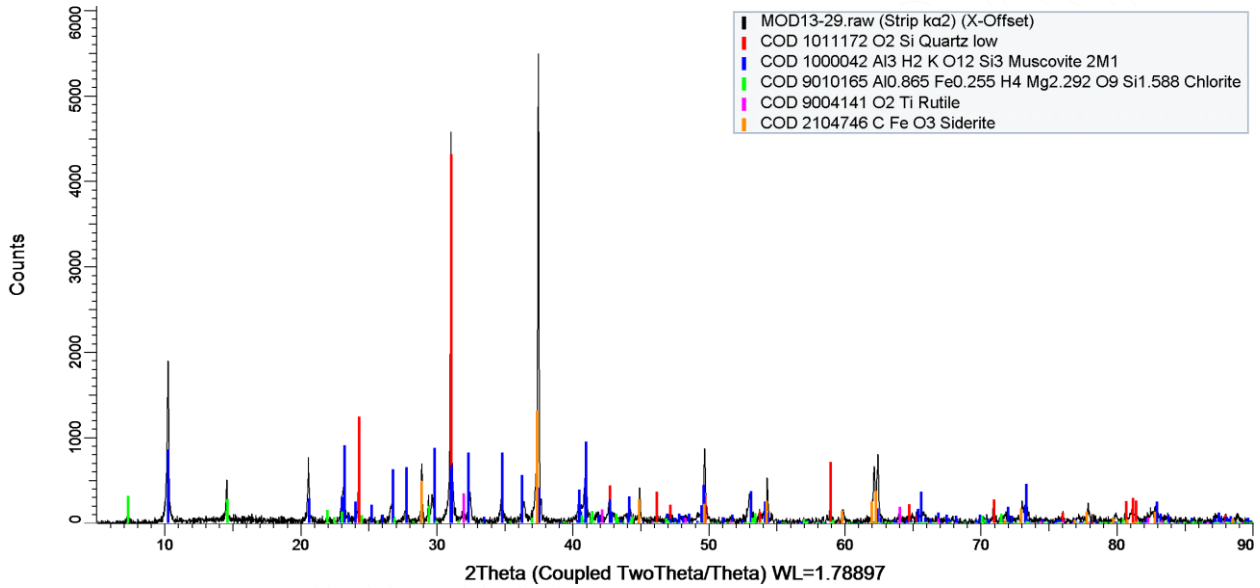
MOD13-29.raw (Strip kα2) (X-Offset)
COD 1011172 O2 Si Quartz low
COD 1000042 Al3 H2 K O12 Si3 Muscovite 2M1
COD 9010165 Al0.865 Fe0.255 H4 Mg2.292 O9 Si1.588 Chlorite
COD 9004141 O2 Ti Rutile
COD 2104746 C Fe O3 Siderite
Counts
0
1000
2000
3000
4000
5000
6000
10
20
30
40
50
60
70
80
90
2Theta (Coupled TwoTheta/Theta) WL=1.78897

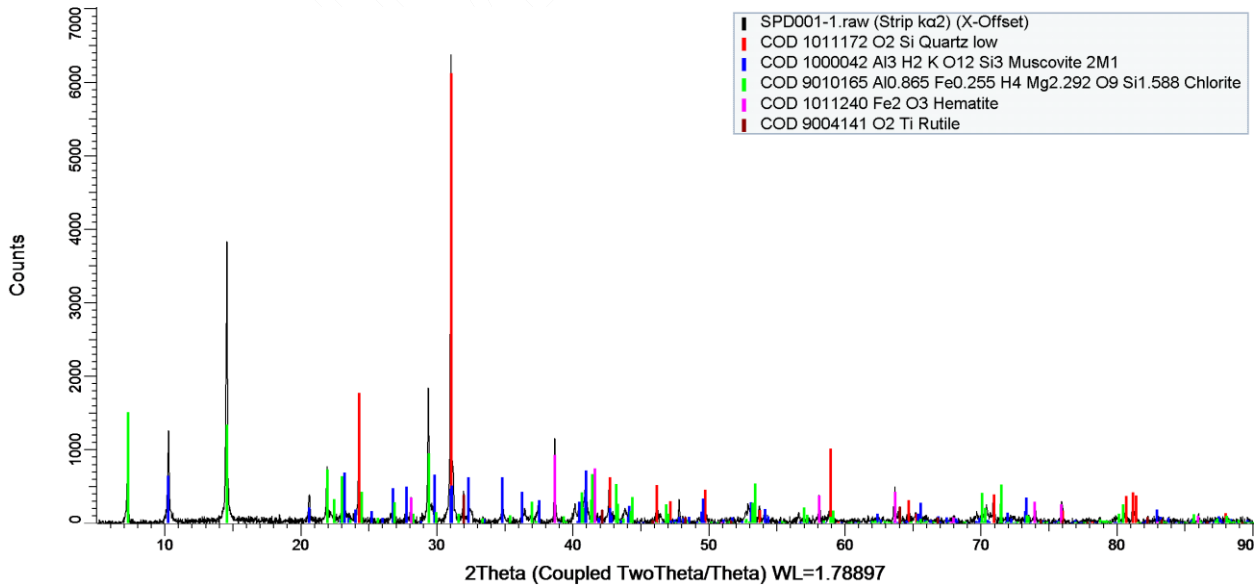
SPD001-1.raw (Strip kα2) (X-Offset)
COD 1011172 O2 Si Quartz low
COD 1000042 Al3 H2 K O12 Si3 Muscovite 2M1
COD 9010165 Al0.865 Fe0.255 H4 Mg2.292 O9 Si1.588 Chlorite
COD 1011240 Fe2 O3 Hematite
COD 9004141 O2 Ti Rutile
Counts
0
1000
2000
3000
4000
5000
6000
7000
10
20
30
40
50
60
70
80
90
2Theta (Coupled TwoTheta/Theta) WL=1.78897

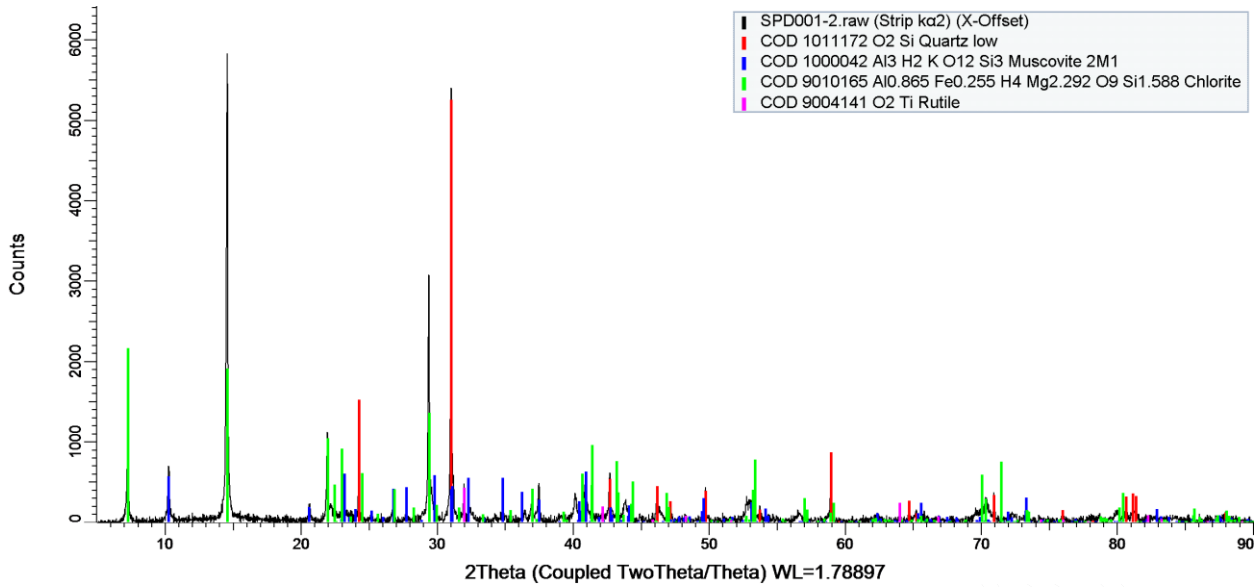
SPD001-2.raw (Strip kα2) (X-Offset)
COD 1011172 O2 Si Quartz low
COD 1000042 Al3 H2 K O12 Si3 Muscovite 2M1
COD 9010165 Al0.865 Fe0.255 H4 Mg2.292 O9 Si1.588 Chlorite
COD 9004141 O2 Ti Rutile
Counts
2Theta (Coupled TwoTheta/Theta) WL=1.78897

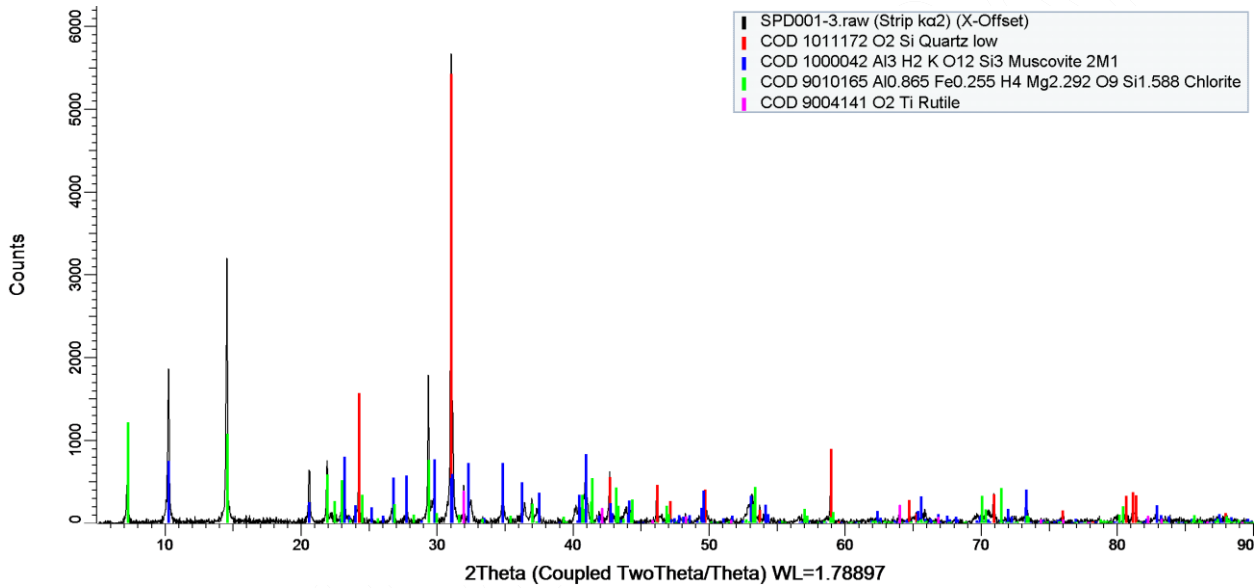
SPD001-3.raw (Strip kα2) (X-Offset)
COD 1011172 O2 Si Quartz low
COD 1000042 Al3 H2 K O12 Si3 Muscovite 2M1
COD 9010165 Al0.865 Fe0.255 H4 Mg2.292 O9 Si1.588 Chlorite
COD 9004141 O2 Ti Rutile
Counts
2Theta (Coupled TwoTheta/Theta) WL=1.78897

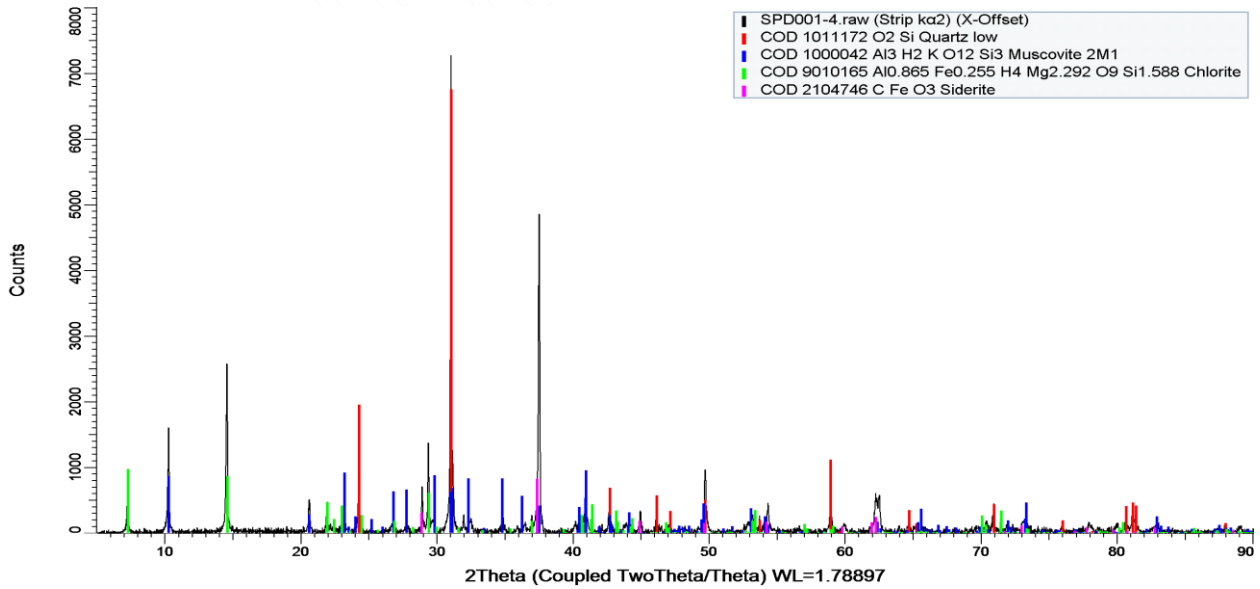
SPD001-4.raw (Strip kα2) (X-Offset)
COD 1011172 O2 Si Quartz low
COD 1000042 Al3 H2 K O12 Si3 Muscovite 2M1
COD 9010165 Al0.865 Fe0.255 H4 Mg2.292 O9 Si1.588 Chlorite
COD 2104746 C Fe O3 Siderite
Counts
2Theta (Coupled TwoTheta/Theta) WL=1.78897

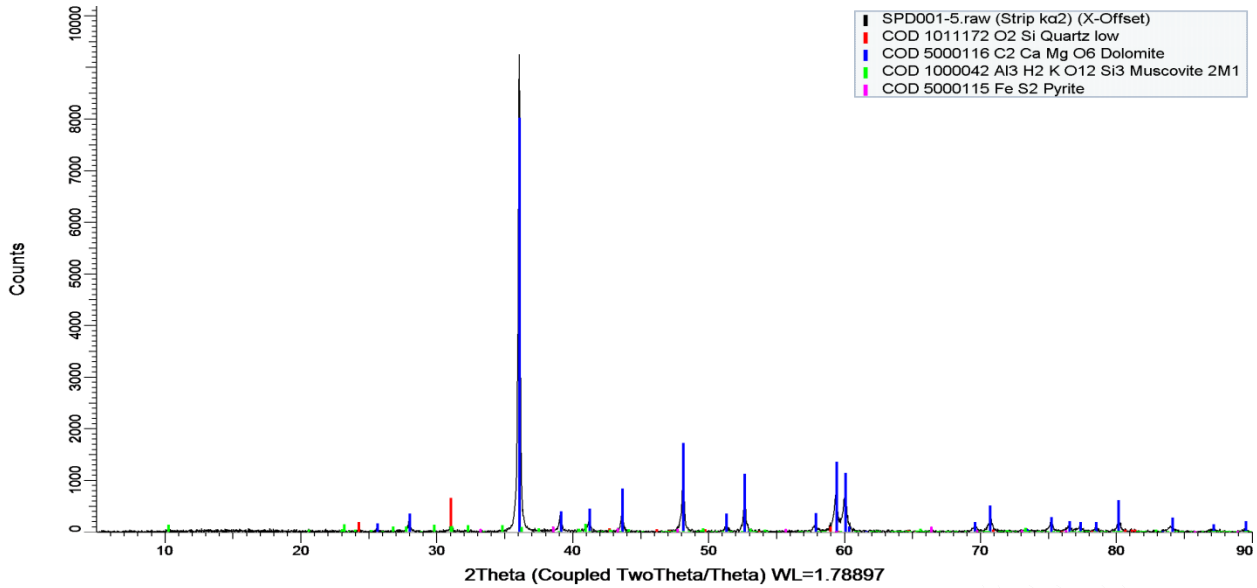
SPD001-5.raw (Strip kα2) (X-Offset)
COD 1011172 O2 Si Quartz low
COD 5000116 C2 Ca Mg O6 Dolomite
COD 1000042 Al3 H2 K O12 Si3 Muscovite 2M1
COD 5000115 Fe S2 Pyrite
Counts
2Theta (Coupled TwoTheta/Theta) WL=1.78897

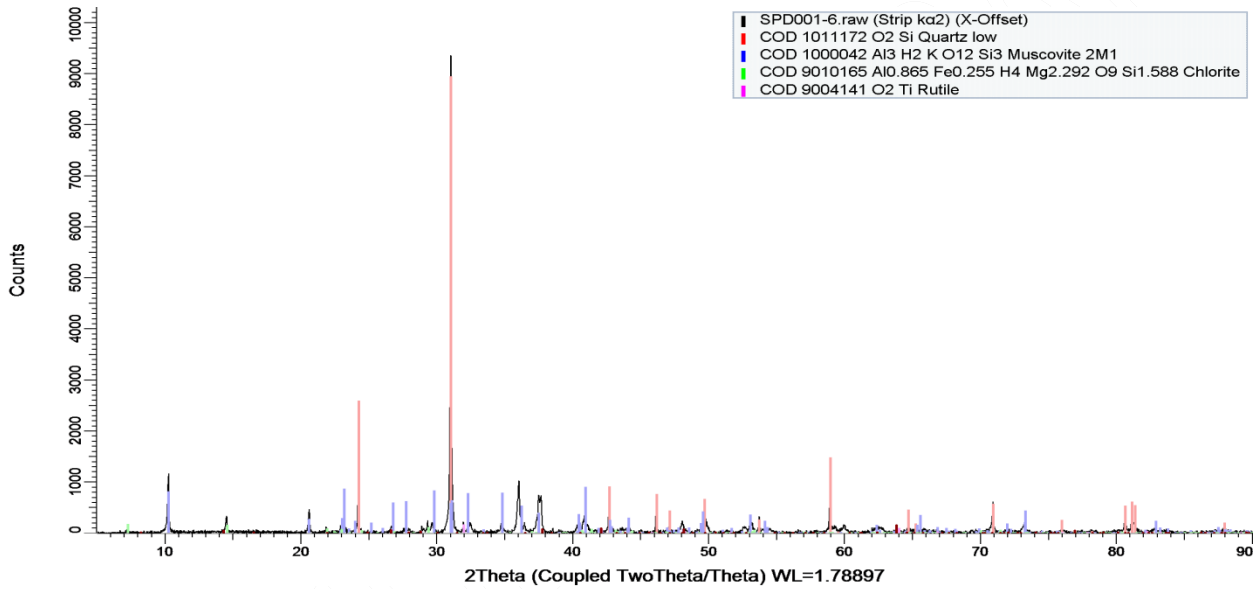
SPD001-6.raw (Strip kα2) (X-Offset)
COD 1011172 O2 Si Quartz low
COD 1000042 Al3 H2 K O12 Si3 Muscovite 2M1
COD 9010165 Al0.865 Fe0.255 H4 Mg2.292 O9 Si1.588 Chlorite
COD 9004141 O2 Ti Rutile
Counts
2Theta (Coupled TwoTheta/Theta) WL=1.78897

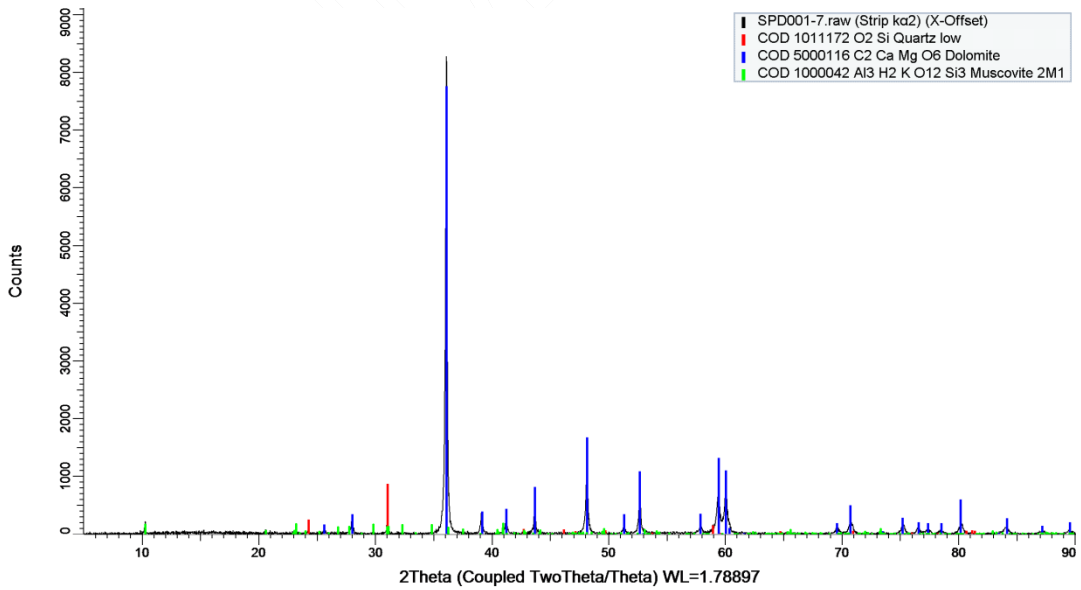
SPD001-7.raw (Strip kα2) (X-Offset)
COD 1011172 O2 Si Quartz low
COD 5000116 C2 Ca Mg O6 Dolomite
COD 1000042 Al3 H2 K O12 Si3 Muscovite 2M1
Counts
2Theta (Coupled TwoTheta/Theta) WL=1.78897

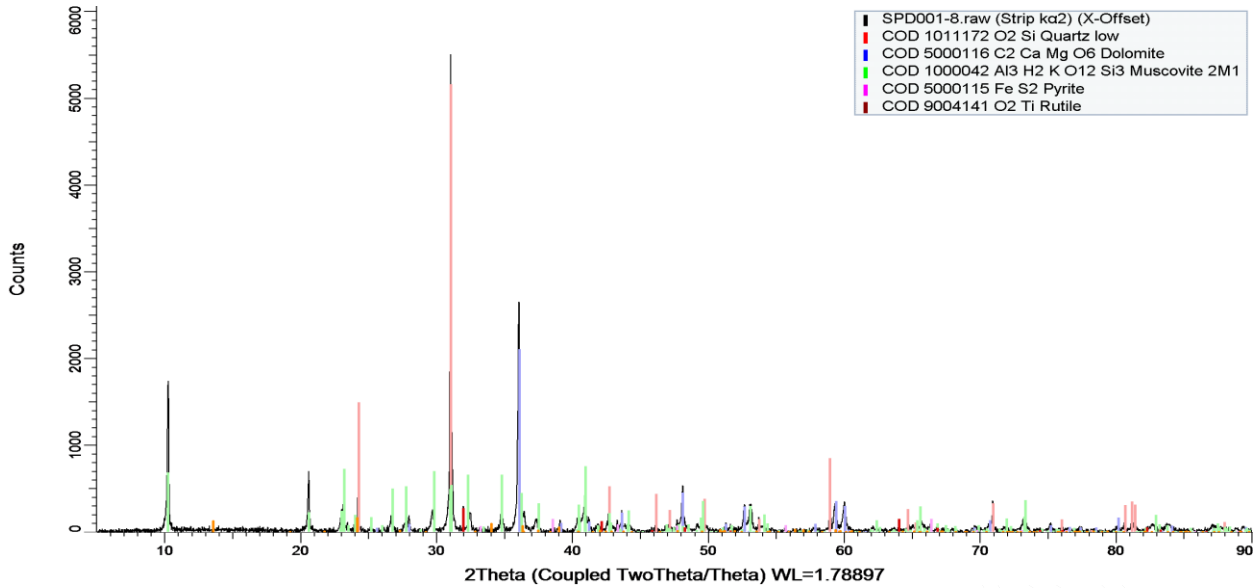
SPD001-8.raw (Strip kα2) (X-Offset)
COD 1011172 O2 Si Quartz low
COD 5000116 C2 Ca Mg O6 Dolomite
COD 1000042 Al3 H2 K O12 Si3 Muscovite 2M1
COD 5000115 Fe S2 Pyrite
COD 9004141 O2 Ti Rutile
Counts
2Theta (Coupled TwoTheta/Theta) WL=1.78897

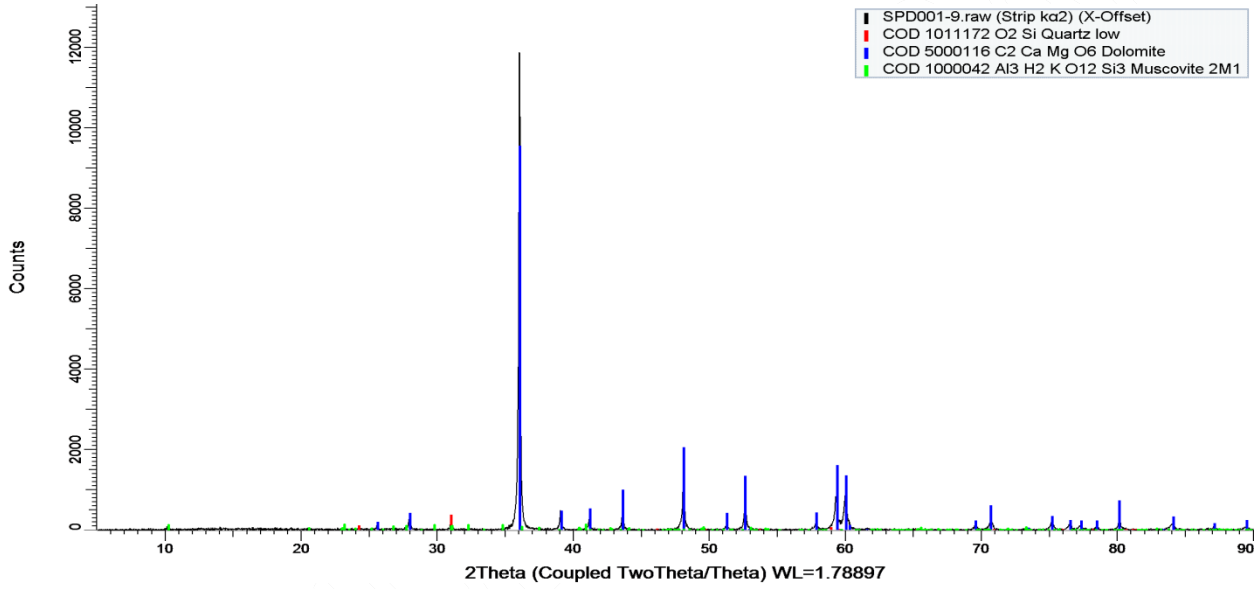
SPD001-9.raw (Strip kα2) (X-Offset)
COD 1011172 O2 Si Quartz low
COD 5000116 C2 Ca Mg O6 Dolomite
COD 1000042 Al3 H2 K O12 Si3 Muscovite 2M1
Counts
2Theta (Coupled TwoTheta/Theta) WL=1.78897

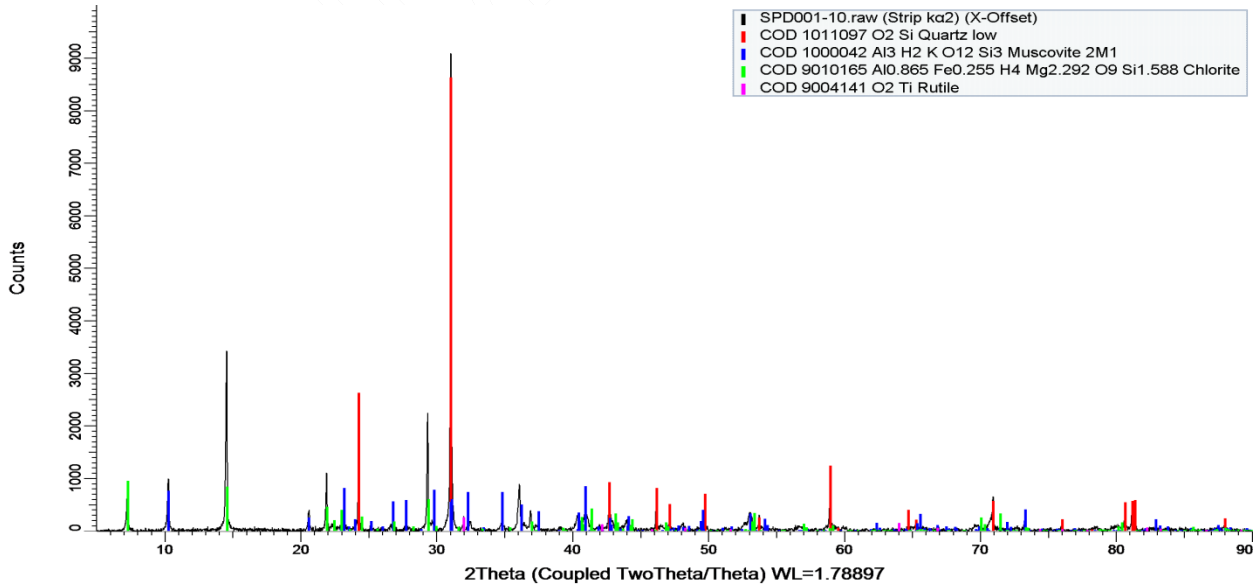
SPD001-10.raw (Strip kα2) (X-Offset)
COD 1011097 O2 Si Quartz low
COD 1000042 Al3 H2 K O12 Si3 Muscovite 2M1
COD 9010165 Al0.865 Fe0.255 H4 Mg2.292 O9 Si1.588 Chlorite
COD 9004141 O2 Ti Rutile
Counts
2Theta (Coupled TwoTheta/Theta) WL=1.78897

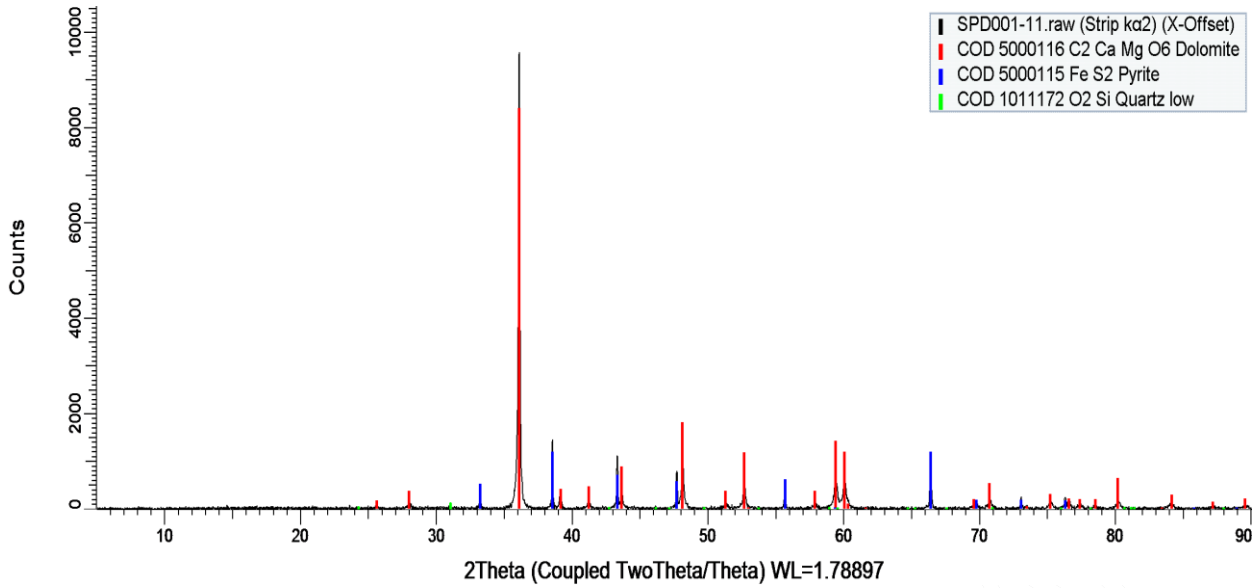
SPD001-11.raw (Strip kα2) (X-Offset)
COD 5000116 C2 Ca Mg O6 Dolomite
COD 5000115 Fe S2 Pyrite
COD 1011172 O2 Si Quartz low
Counts
2Theta (Coupled TwoTheta/Theta) WL=1.78897

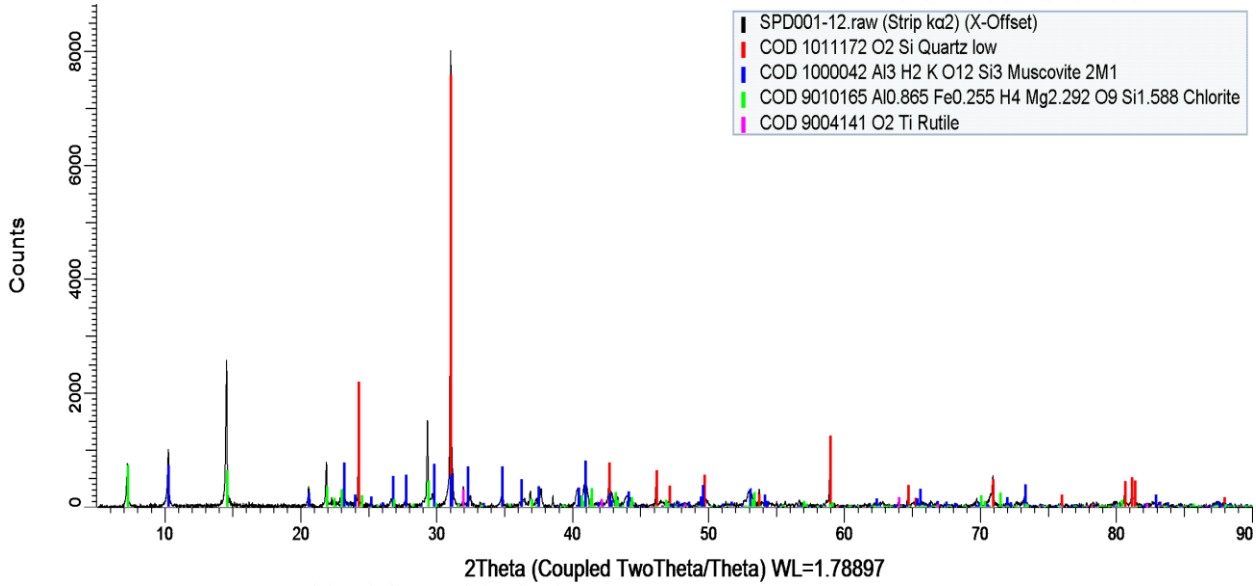
SPD001-12.raw (Strip kα2) (X-Offset)
COD 1011172 O2 Si Quartz low
COD 1000042 Al3 H2 K O12 Si3 Muscovite 2M1
COD 9010165 Al0.865 Fe0.255 H4 Mg2.292 O9 Si1.588 Chlorite
COD 9004141 O2 Ti Rutile
Counts
2Theta (Coupled TwoTheta/Theta) WL=1.78897

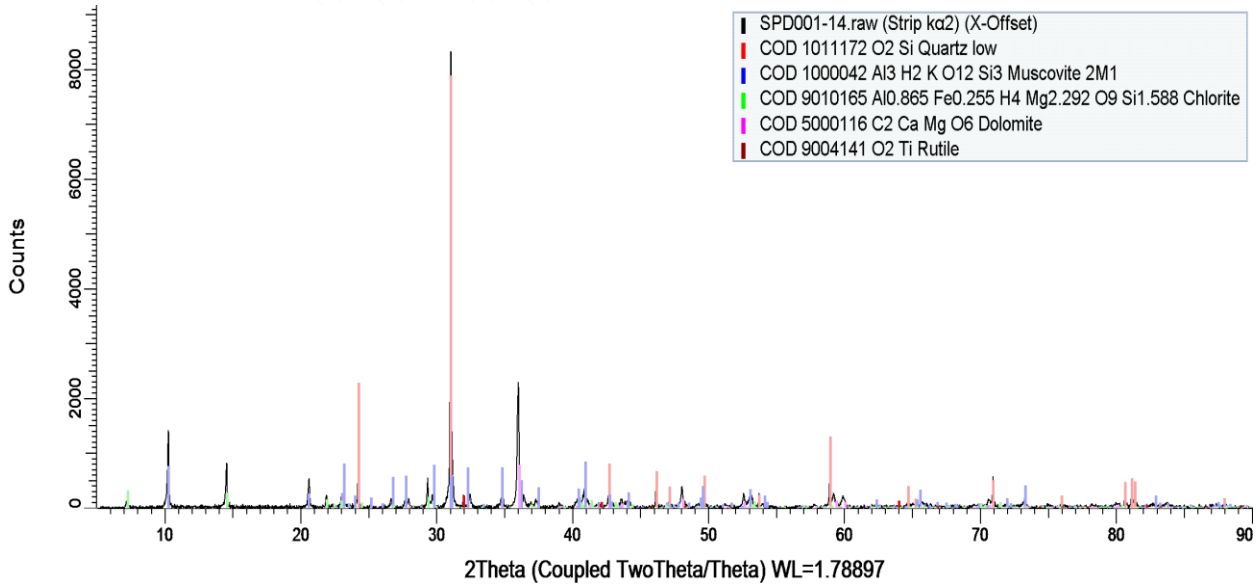
SPD001-14.raw (Strip kα2) (X-Offset)
COD 1011172 O2 Si Quartz low
COD 1000042 Al3 H2 K O12 Si3 Muscovite 2M1
COD 9010165 Al0.865 Fe0.255 H4 Mg2.292 O9 Si1.588 Chlorite
COD 5000116 C2 Ca Mg O6 Dolomite
COD 9004141 O2 Ti Rutile
Counts
2Theta (Coupled TwoTheta/Theta) WL=1.78897

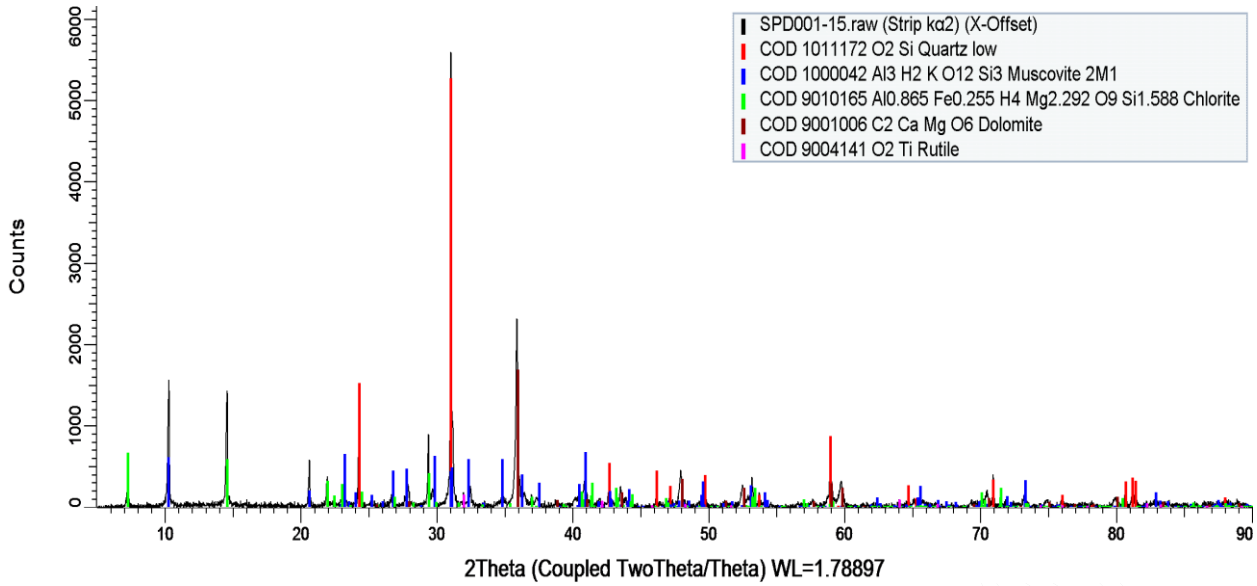
SPD001-15.raw (Strip kα2) (X-Offset)
COD 1011172 O2 Si Quartz low
COD 1000042 Al3 H2 K O12 Si3 Muscovite 2M1
COD 9010165 Al0.865 Fe0.255 H4 Mg2.292 O9 Si1.588 Chlorite
COD 9001006 C2 Ca Mg O6 Dolomite
COD 9004141 O2 Ti Rutile
Counts
2Theta (Coupled TwoTheta/Theta) WL=1.78897

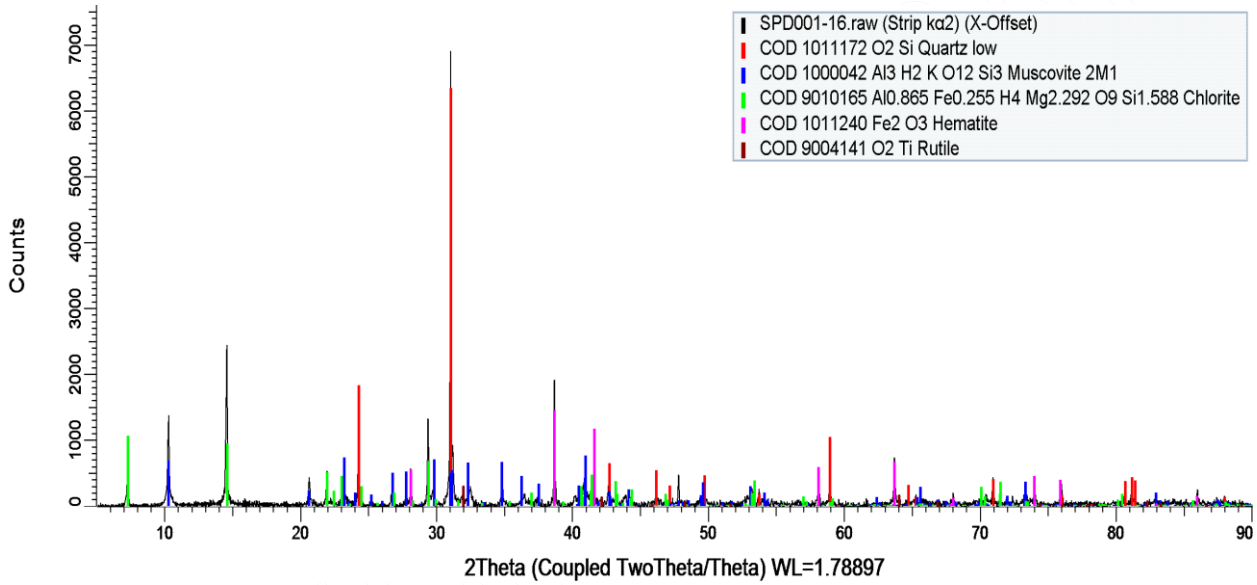
SPD001-16.raw (Strip kα2) (X-Offset)
COD 1011172 O2 Si Quartz low
COD 1000042 Al3 H2 K O12 Si3 Muscovite 2M1
COD 9010165 Al0.865 Fe0.255 H4 Mg2.292 O9 Si1.588 Chlorite
COD 1011240 Fe2 O3 Hematite
COD 9004141 O2 Ti Rutile
Counts
2Theta (Coupled TwoTheta/Theta) WL=1.78897

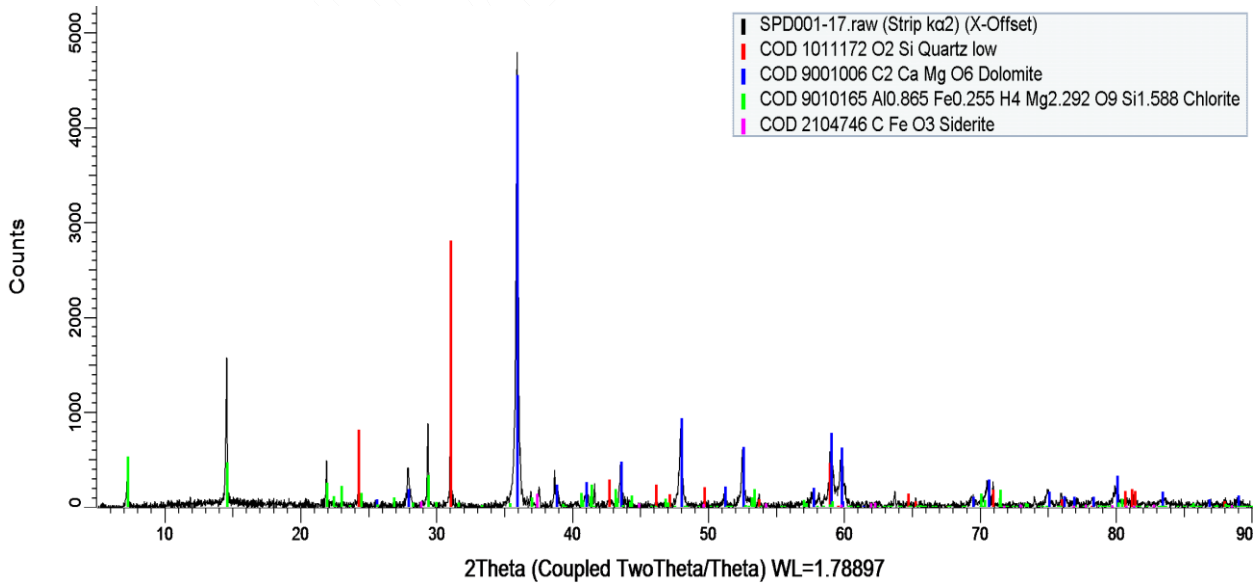
SPD001-17.raw (Strip kα2) (X-Offset)
COD 1011172 O2 Si Quartz low
COD 9001006 C2 Ca Mg O6 Dolomite
COD 9010165 Al0.865 Fe0.255 H4 Mg2.292 O9 Si1.588 Chlorite
COD 2104746 C Fe O3 Siderite
Counts
2Theta (Coupled TwoTheta/Theta) WL=1.78897

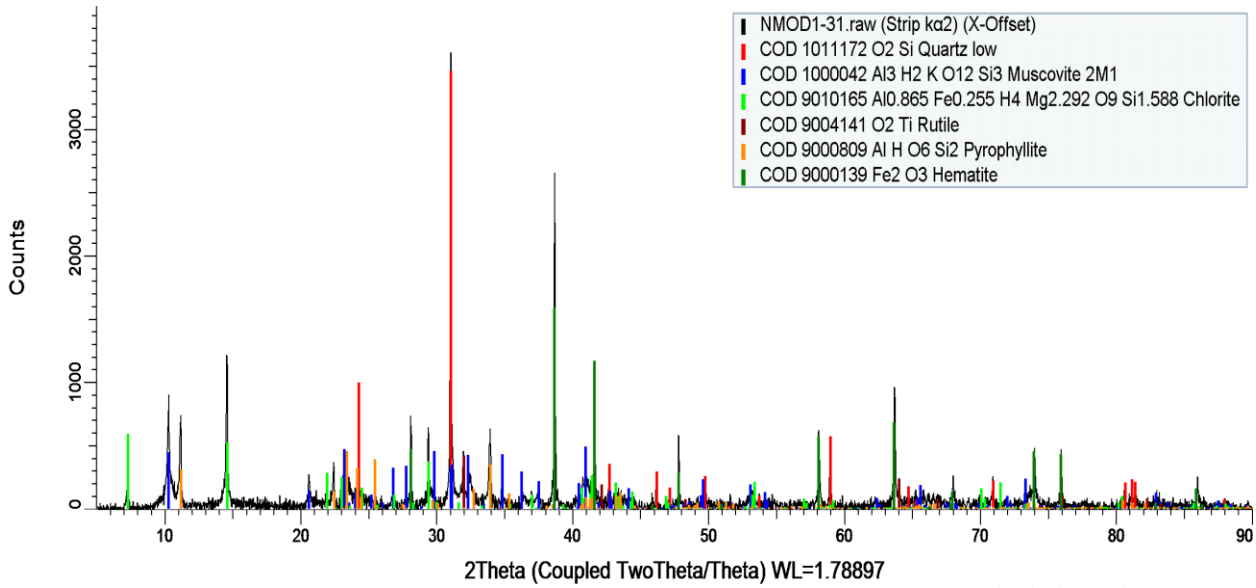
NMOD1-31.raw (Strip kα2) (X-Offset)
COD 1011172 O2 Si Quartz low
COD 1000042 Al3 H2 K O12 Si3 Muscovite 2M1
COD 9010165 Al0.865 Fe0.255 H4 Mg2.292 O9 Si1.588 Chlorite
COD 9004141 O2 Ti Rutile
COD 9000809 Al H O6 Si2 Pyrophyllite
COD 9000139 Fe2 O3 Hematite
Counts
0
1000
2000
3000
10
20
30
40
50
60
70
80
90
2Theta (Coupled TwoTheta/Theta) WL=1.78897

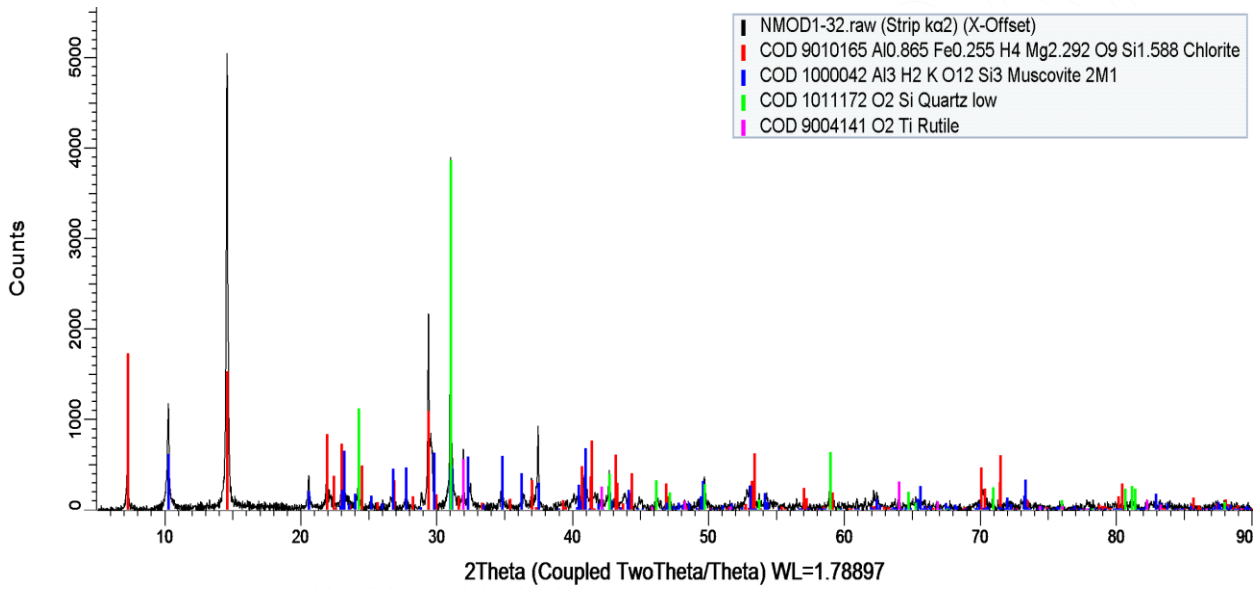
NMOD1-32.raw (Strip kα2) (X-Offset)
COD 9010165 Al0.865 Fe0.255 H4 Mg2.292 O9 Si1.588 Chlorite
COD 1000042 Al3 H2 K O12 Si3 Muscovite 2M1
COD 1011172 O2 Si Quartz low
COD 9004141 O2 Ti Rutile
Counts
0
1000
2000
3000
4000
5000
10
20
30
40
50
60
70
80
90
2Theta (Coupled TwoTheta/Theta) WL=1.78897

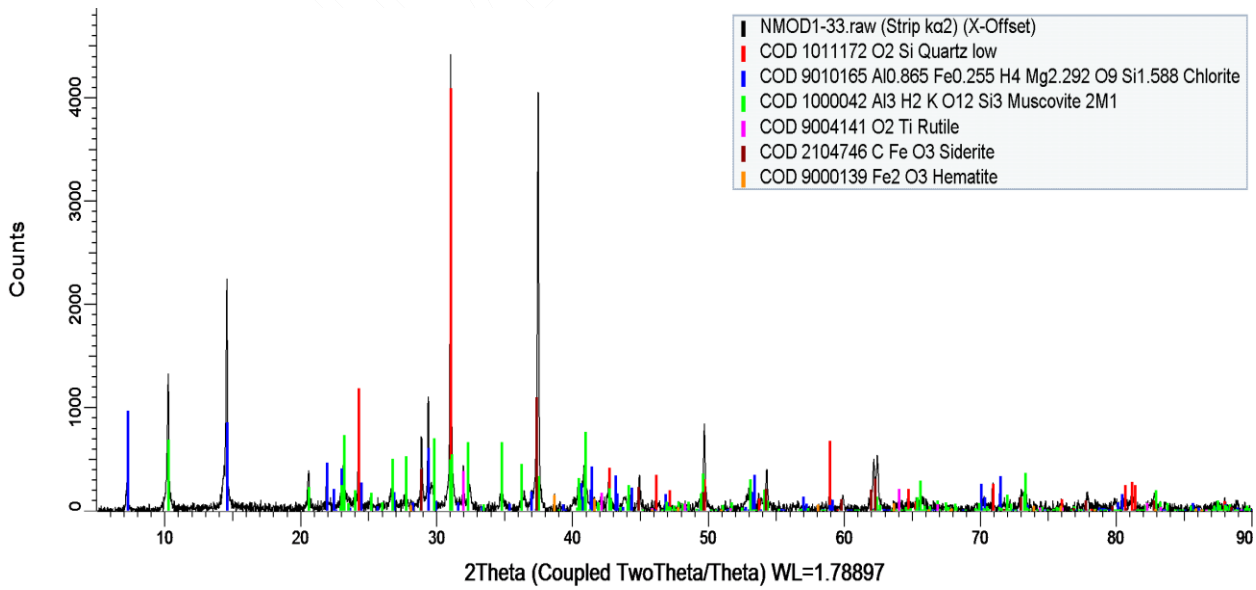
NMOD1-33.raw (Strip kα2) (X-Offset)
COD 1011172 O2 Si Quartz low
COD 9010165 Al0.865 Fe0.255 H4 Mg2.292 O9 Si1.588 Chlorite
COD 1000042 Al3 H2 K O12 Si3 Muscovite 2M1
COD 9004141 O2 Ti Rutile
COD 2104746 C Fe O3 Siderite
COD 9000139 Fe2 O3 Hematite
Counts
0
1000
2000
3000
4000
10
20
30
40
50
60
70
80
90
2Theta (Coupled TwoTheta/Theta) WL=1.78897

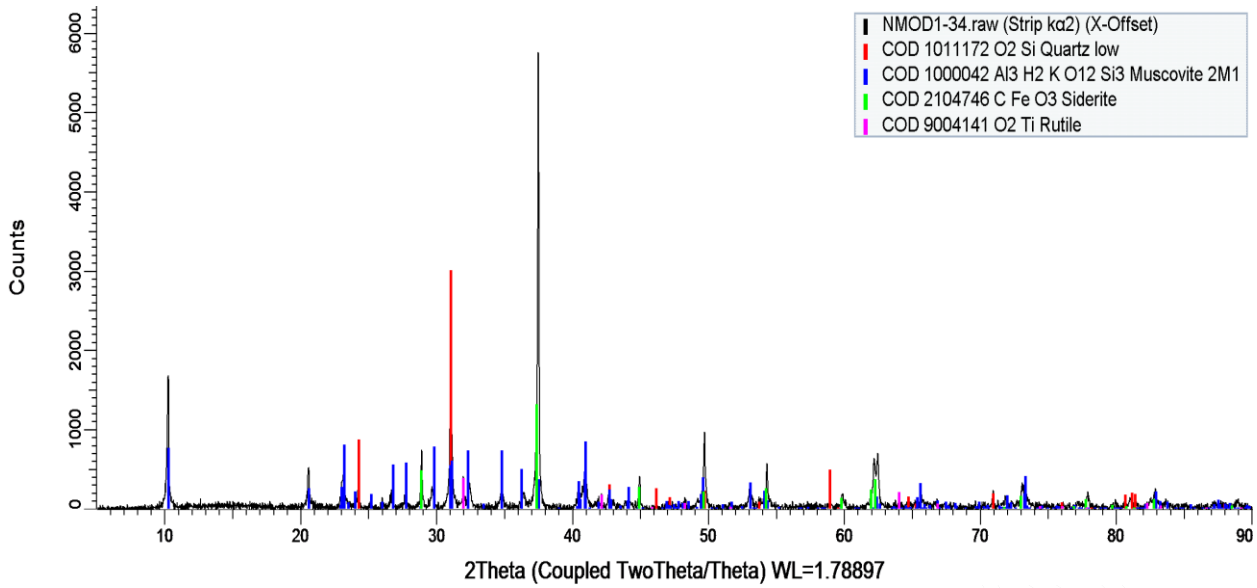
NMOD1-34.raw (Strip kα2) (X-Offset)
COD 1011172 O2 Si Quartz low
COD 1000042 Al3 H2 K O12 Si3 Muscovite 2M1
COD 2104746 C Fe O3 Siderite
COD 9004141 O2 Ti Rutile
Counts
2Theta (Coupled TwoTheta/Theta) WL=1.78897

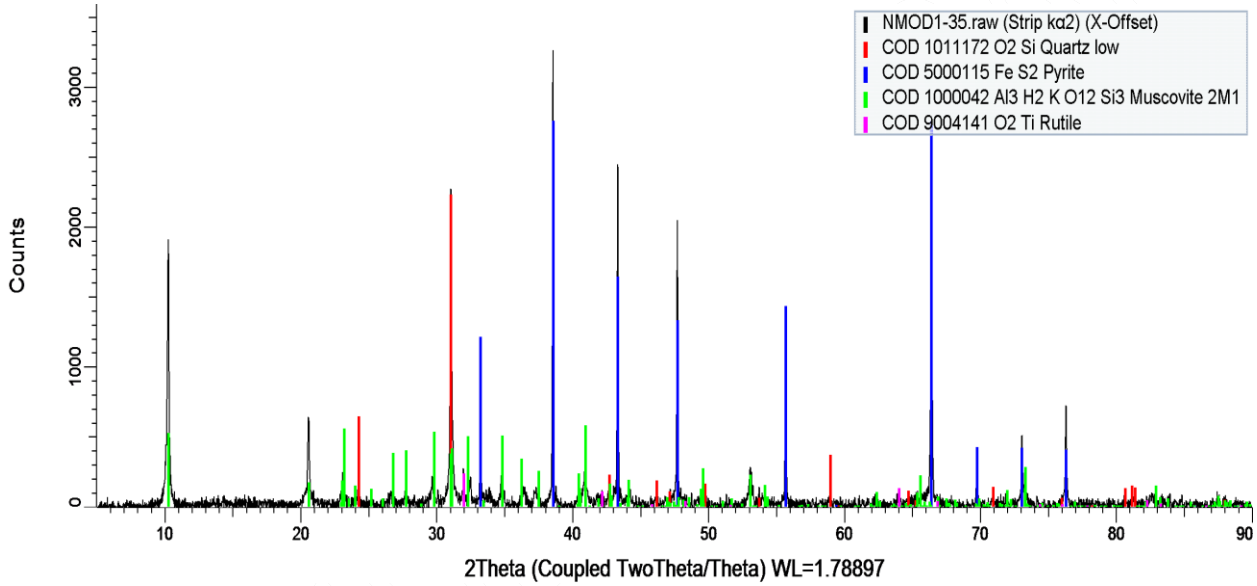
NMOD1-35.raw (Strip kα2) (X-Offset)
COD 1011172 O2 Si Quartz low
COD 5000115 Fe S2 Pyrite
COD 1000042 Al3 H2 K O12 Si3 Muscovite 2M1
COD 9004141 O2 Ti Rutile
Counts
2Theta (Coupled TwoTheta/Theta) WL=1.78897

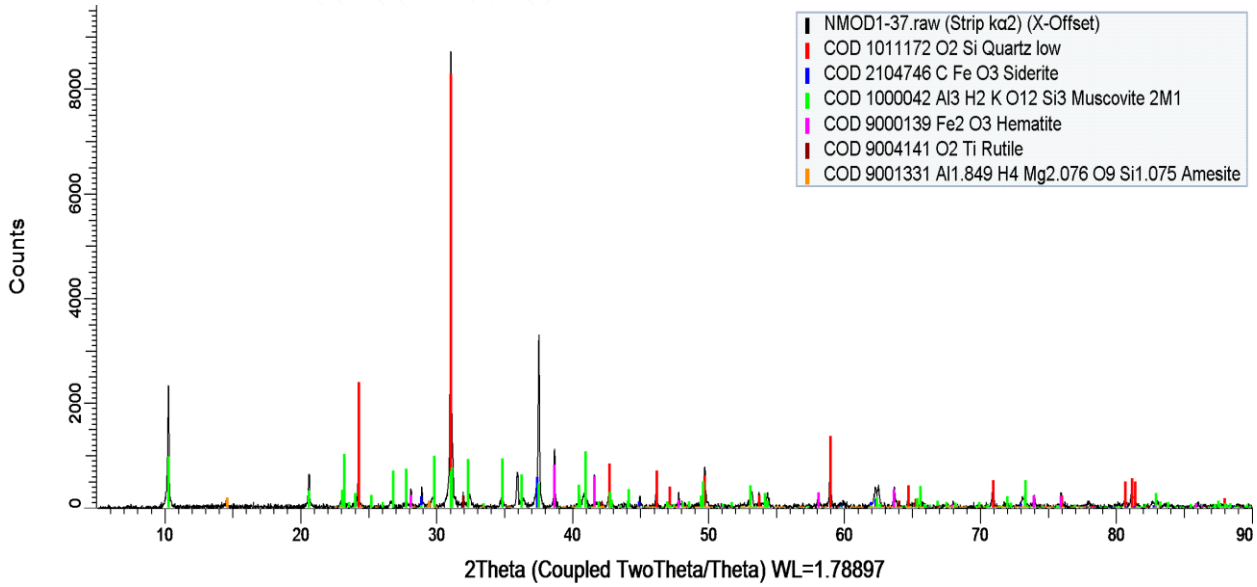
NMOD1-37.raw (Strip kα2) (X-Offset)
COD 1011172 O2 Si Quartz low
COD 2104746 C Fe O3 Siderite
COD 1000042 Al3 H2 K O12 Si3 Muscovite 2M1
COD 9000139 Fe2 O3 Hematite
COD 9004141 O2 Ti Rutile
COD 9001331 Al1.849 H4 Mg2.076 O9 Si1.075 Amesite
Counts
2Theta (Coupled TwoTheta/Theta) WL=1.78897

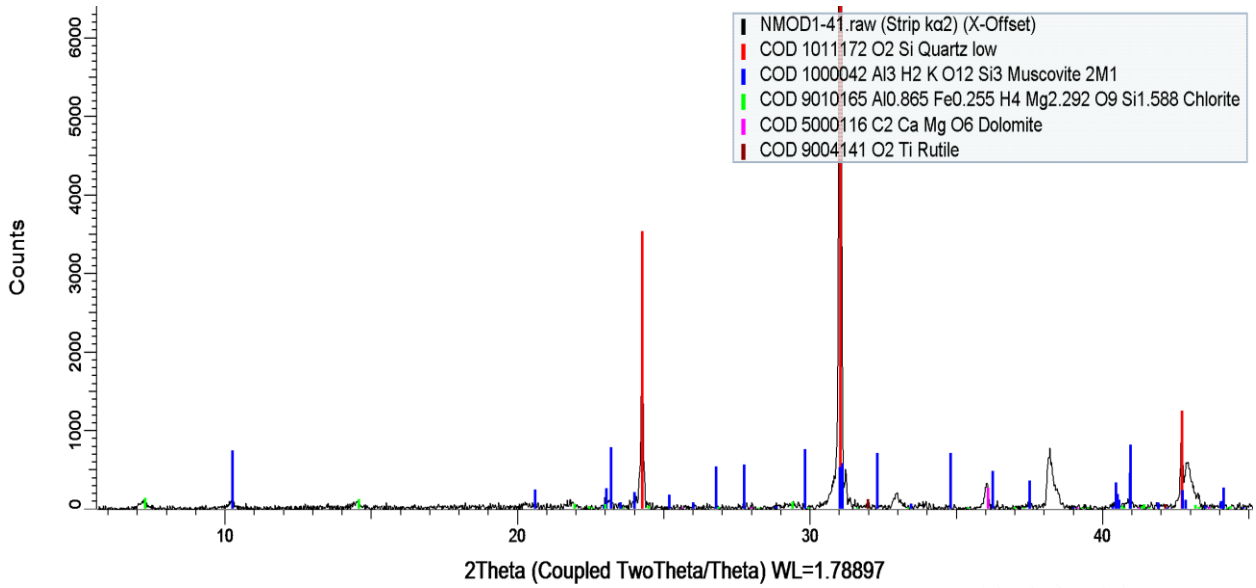
NMOD1-41.raw (Strip kα2) (X-Offset)
COD 1011172 O2 Si Quartz low
COD 1000042 Al3 H2 K O12 Si3 Muscovite 2M1
COD 9010165 Al0.865 Fe0.255 H4 Mg2.292 O9 Si1.588 Chlorite
COD 5000116 C2 Ca Mg O6 Dolomite
COD 9004141 O2 Ti Rutile
Counts
2Theta (Coupled TwoTheta/Theta) WL=1.78897

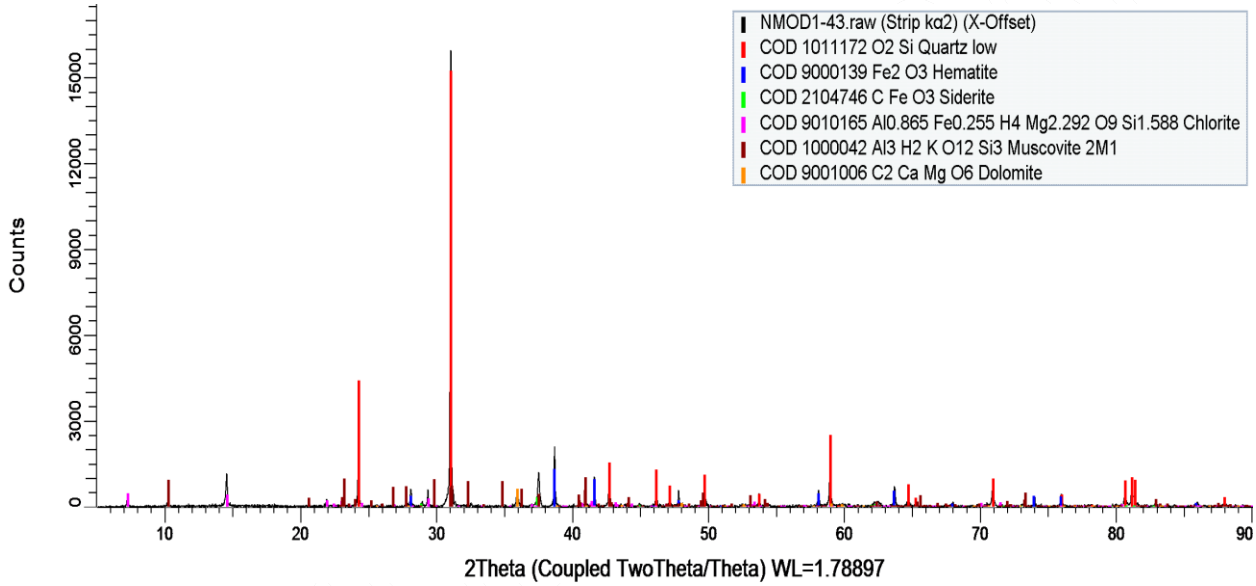
NMOD1-43.raw (Strip kα2) (X-Offset)
COD 1011172 O2 Si Quartz low
COD 9000139 Fe2 O3 Hematite
COD 2104746 C Fe O3 Siderite
COD 9010165 Al0.865 Fe0.255 H4 Mg2.292 O9 Si1.588 Chlorite
COD 1000042 Al3 H2 K O12 Si3 Muscovite 2M1
COD 9001006 C2 Ca Mg O6 Dolomite
Counts
2Theta (Coupled TwoTheta/Theta) WL=1.78897

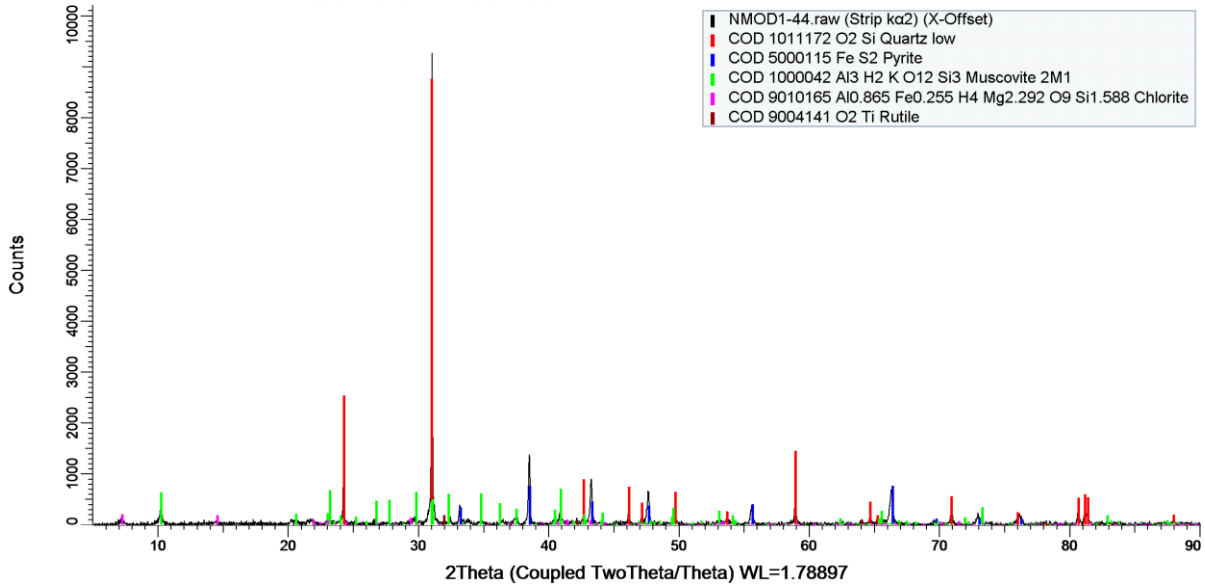
NMOD1-44.raw (Strip kα2) (X-Offset)
COD 1011172 O2 Si Quartz low
COD 5000115 Fe S2 Pyrite
COD 1000042 Al3 H2 K O12 Si3 Muscovite 2M1
COD 9010165 Al0.865 Fe0.255 H4 Mg2.292 O9 Si1.588 Chlorite
COD 9004141 O2 Ti Rutile
Counts
2Theta (Coupled TwoTheta/Theta) WL=1.78897

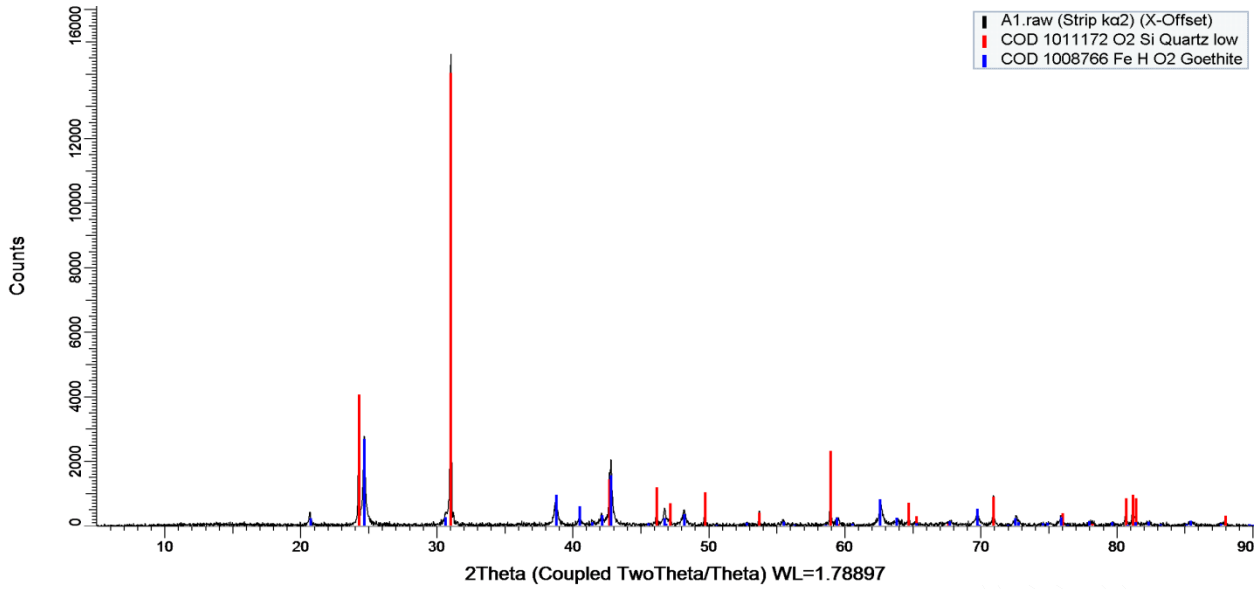
A1.raw (Strip kα2) (X-Offset)
COD 1011172 O2 Si Quartz low
COD 1008766 Fe H O2 Goethite
Counts
2Theta (Coupled TwoTheta/Theta) WL=1.78897

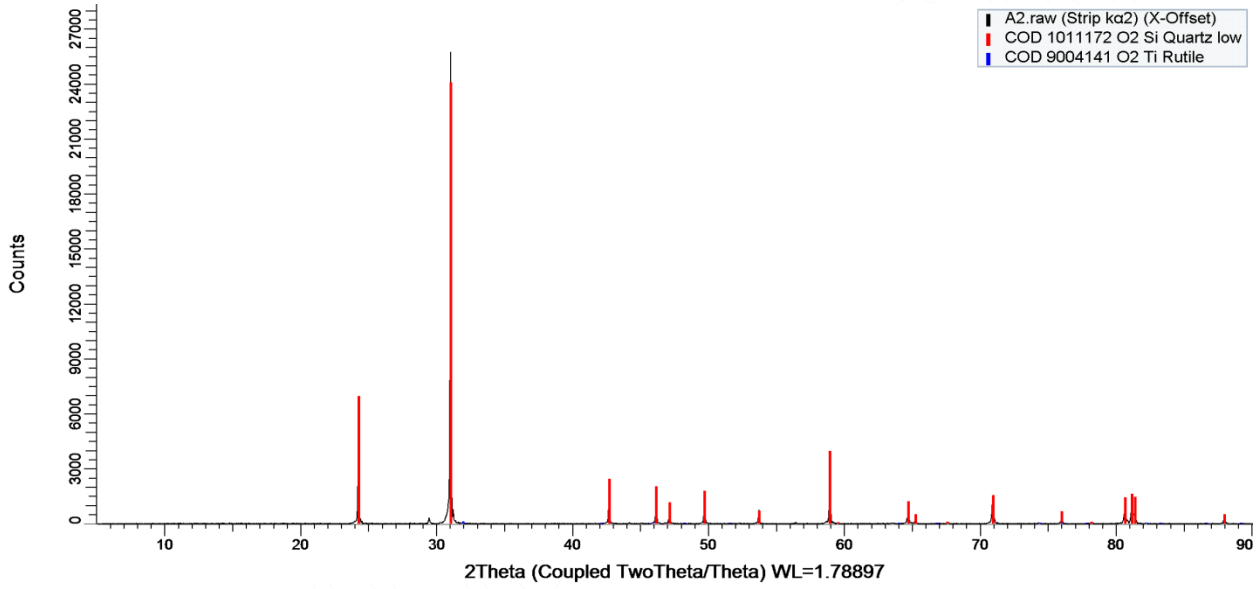
A2.raw (Strip kα2) (X-Offset)
COD 1011172 O2 Si Quartz low
COD 9004141 O2 Ti Rutile
Counts
2Theta (Coupled TwoTheta/Theta) WL=1.78897

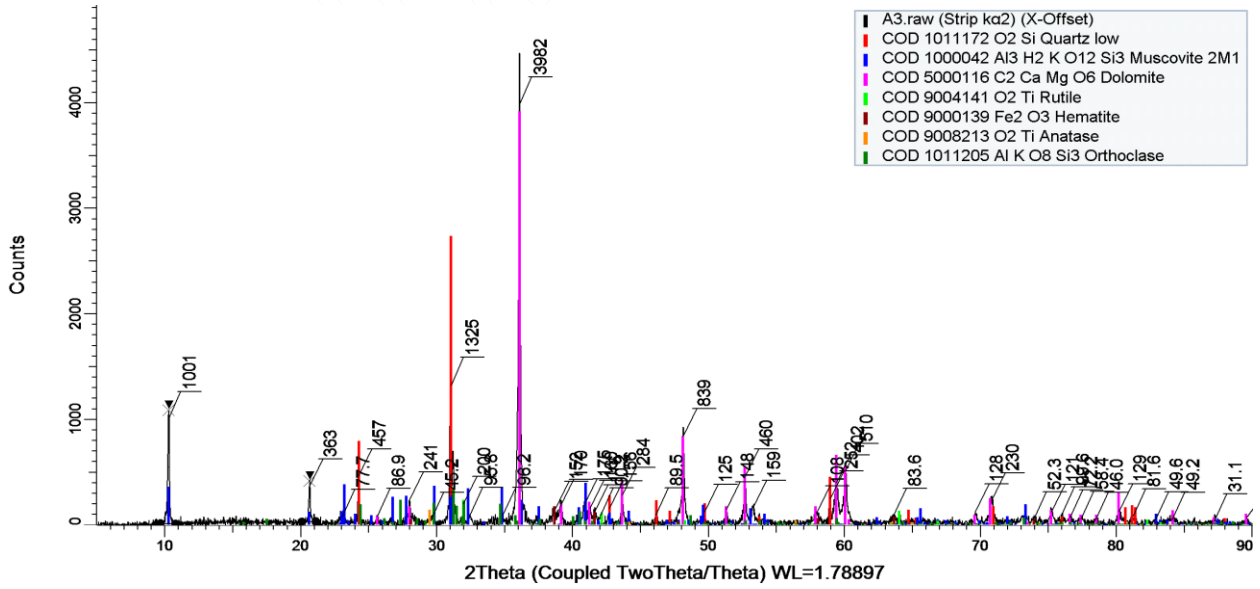
A3.raw (Strip kα2) (X-Offset)
COD 1011172 O2 Si Quartz low
COD 1000042 Al3 H2 K O12 Si3 Muscovite 2M1
COD 5000116 C2 Ca Mg O6 Dolomite
COD 9004141 O2 Ti Rutile
COD 9000139 Fe2 O3 Hematite
COD 9008213 O2 Ti Anatase
COD 1011205 Al K O8 Si3 Orthoclase
Counts
2Theta (Coupled TwoTheta/Theta) WL=1.78897

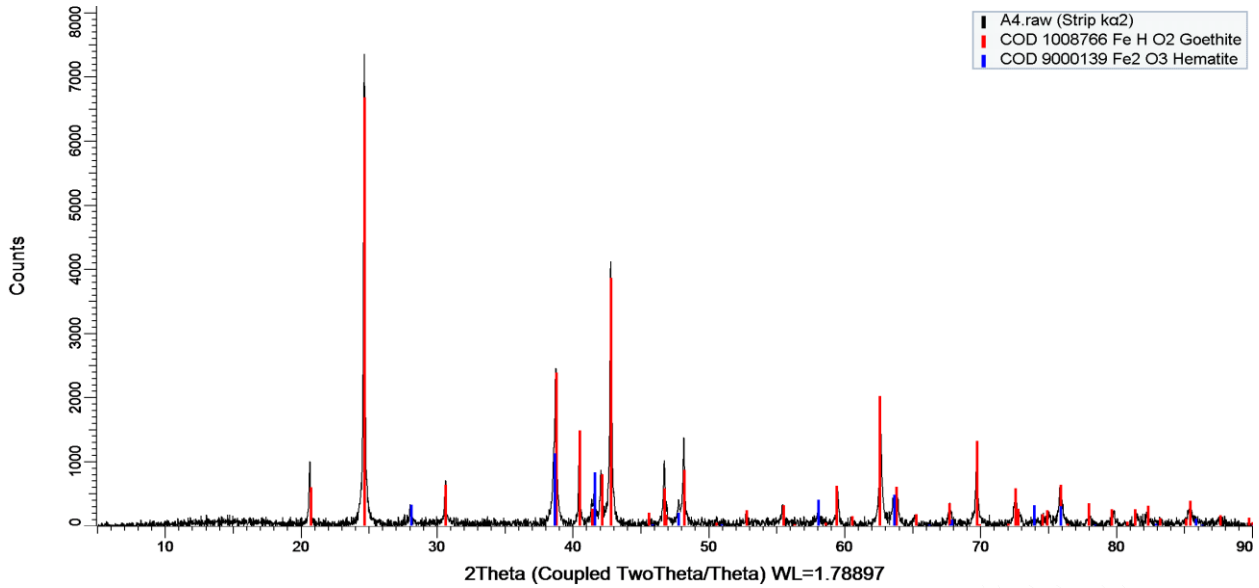
A4.raw (Strip kα2)
COD 1008766 Fe H O2 Goethite
COD 9000139 Fe2 O3 Hematite
Counts
2Theta (Coupled TwoTheta/Theta) WL=1.78897

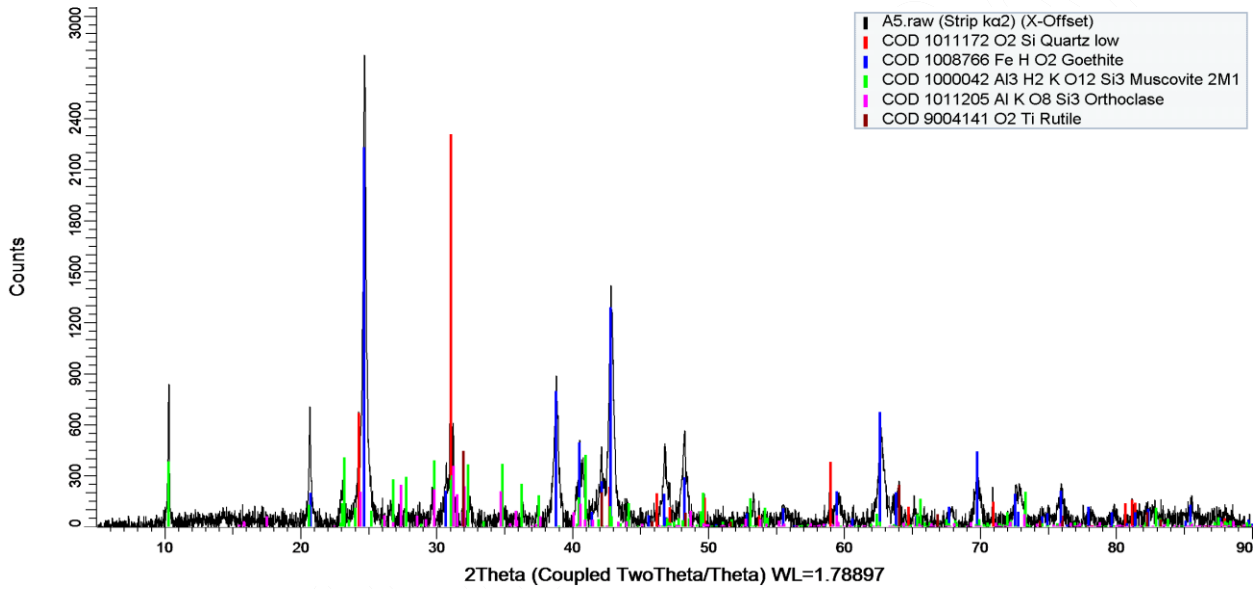
A5.raw (Strip kα2) (X-Offset)
COD 1011172 O2 Si Quartz low
COD 1008766 Fe H O2 Goethite
COD 1000042 Al3 H2 K O12 Si3 Muscovite 2M1
COD 1011205 Al K O8 Si3 Orthoclase
COD 9004141 O2 Ti Rutile
Counts
2Theta (Coupled TwoTheta/Theta) WL=1.78897

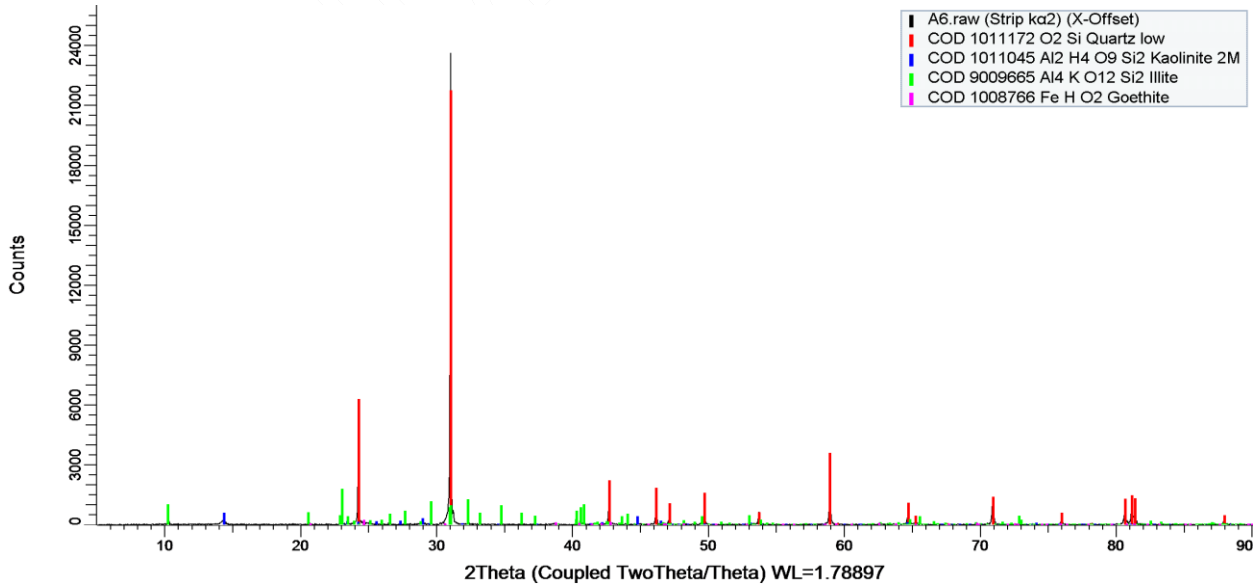
A6.raw (Strip kα2) (X-Offset)
COD 1011172 O2 Si Quartz low
COD 1011045 Al2 H4 O9 Si2 Kaolinite 2M
COD 9009665 Al4 K O12 Si2 Illite
COD 1008766 Fe H O2 Goethite
Counts
2Theta (Coupled TwoTheta/Theta) WL=1.78897

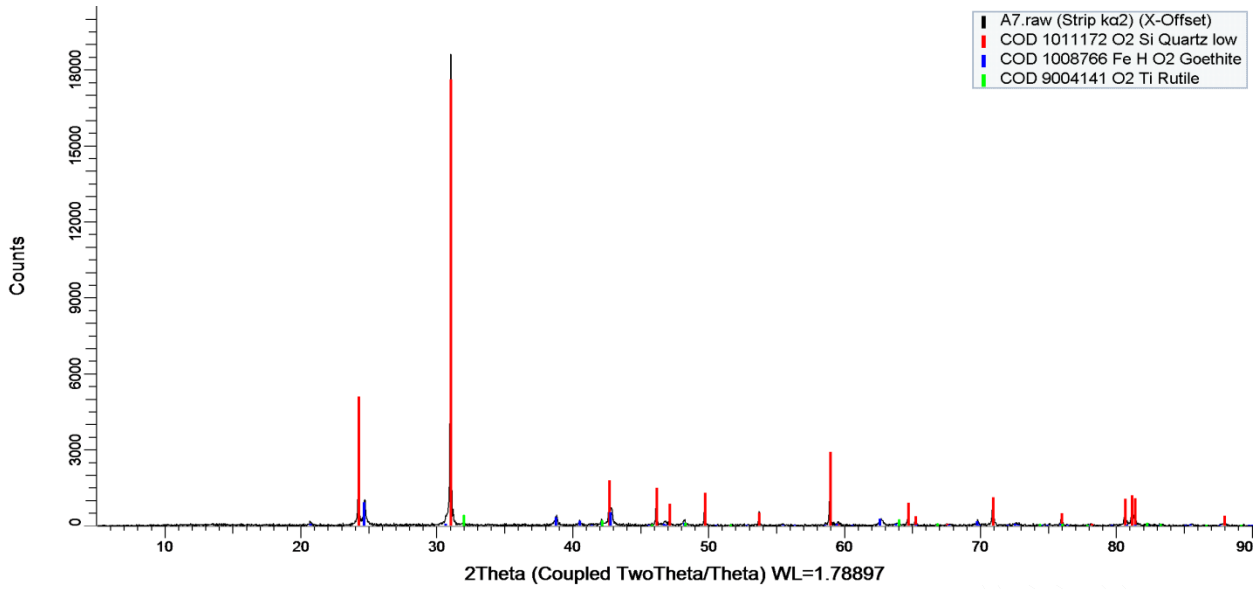
A7.raw (Strip kα2) (X-Offset)
COD 1011172 O2 Si Quartz low
COD 1008766 Fe H O2 Goethite
COD 9004141 O2 Ti Rutile
Counts
2Theta (Coupled TwoTheta/Theta) WL=1.78897

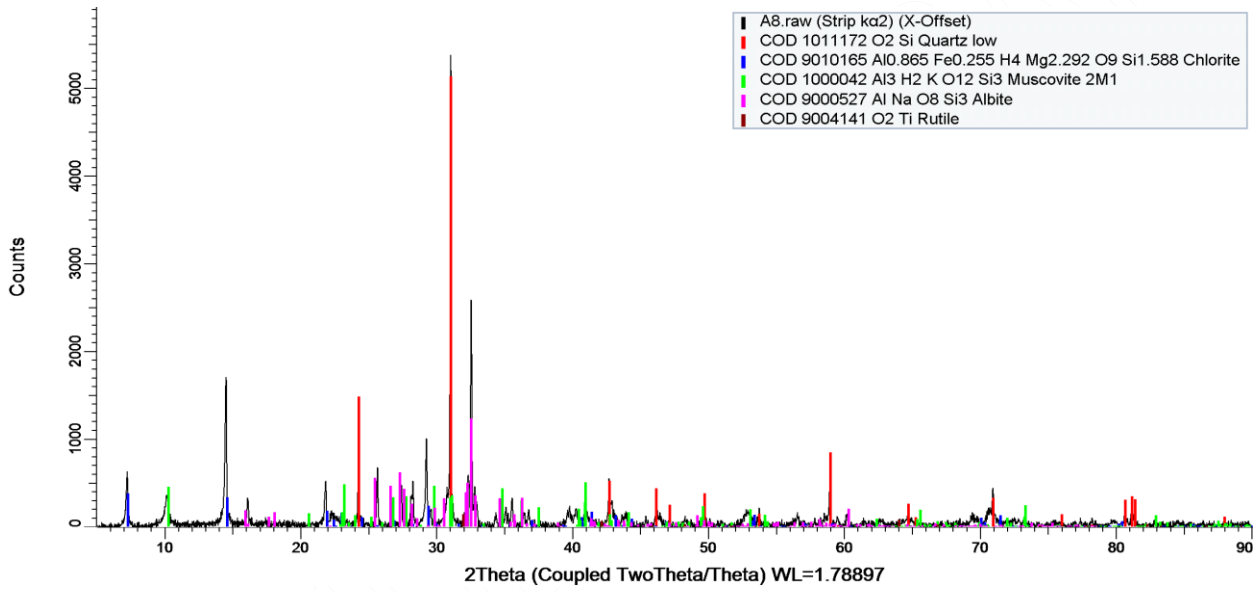
A8.raw (Strip kα2) (X-Offset)
COD 1011172 O2 Si Quartz low
COD 9010165 Al0.865 Fe0.255 H4 Mg2.292 O9 Si1.588 Chlorite
COD 1000042 Al3 H2 K O12 Si3 Muscovite 2M1
COD 9000527 Al Na O8 Si3 Albite
COD 9004141 O2 Ti Rutile
Counts
2Theta (Coupled TwoTheta/Theta) WL=1.78897

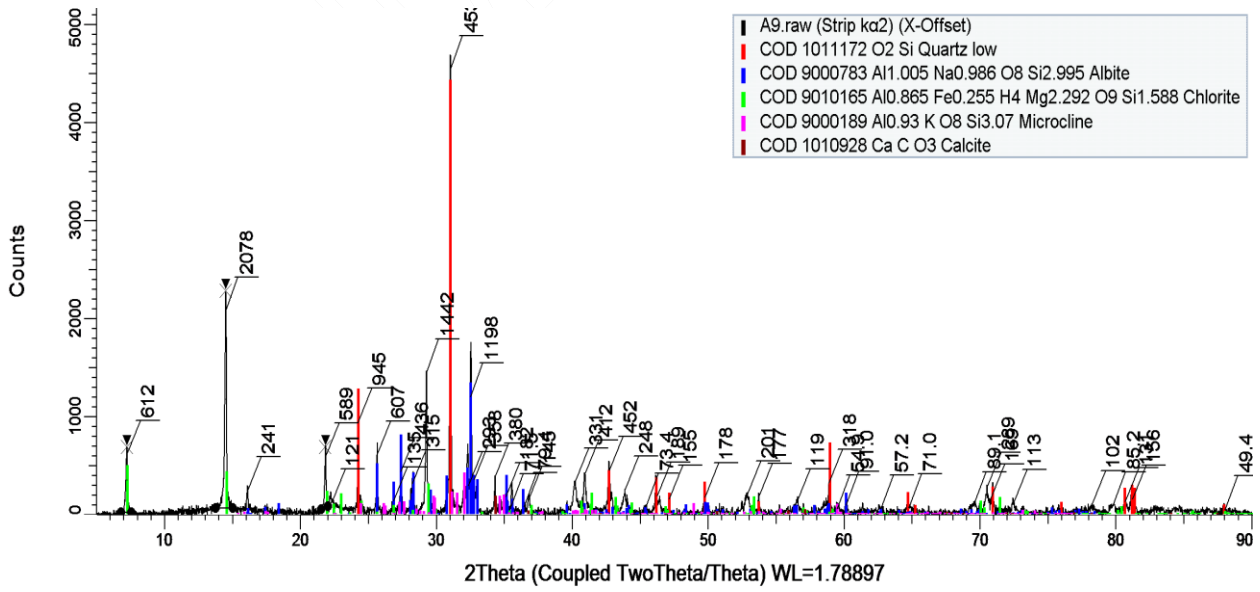
A9.raw (Strip kα2) (X-Offset)
COD 1011172 O2 Si Quartz low
COD 9000783 Al1.005 Na0.986 O8 Si2.995 Albite
COD 9010165 Al0.865 Fe0.255 H4 Mg2.292 O9 Si1.588 Chlorite
COD 9000189 Al0.93 K O8 Si3.07 Microcline
COD 1010928 Ca C O3 Calcite
Counts
2078
1442
1198
945
612
607
589
452
412
380
331
315
248
241
201
178
177
155
121
119
113
102
89.1
71.0
57.2
49.4
2Theta (Coupled TwoTheta/Theta) WL=1.78897

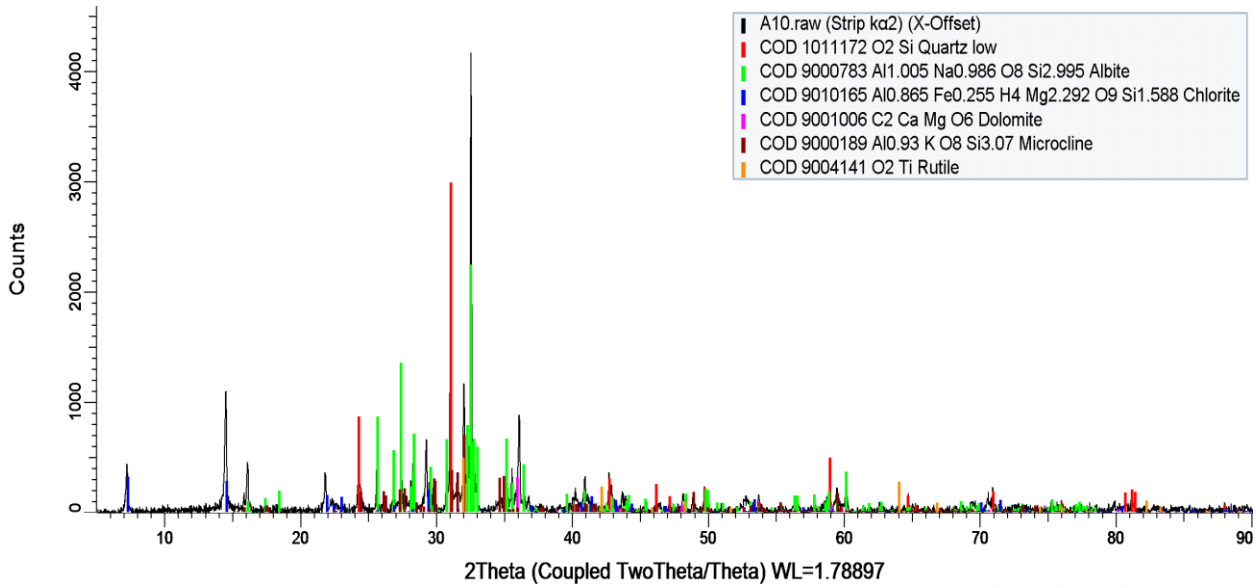
A10.raw (Strip kα2) (X-Offset)
COD 1011172 O2 Si Quartz low
COD 9000783 Al1.005 Na0.986 O8 Si2.995 Albite
COD 9010165 Al0.865 Fe0.255 H4 Mg2.292 O9 Si1.588 Chlorite
COD 9001006 C2 Ca Mg O6 Dolomite
COD 9000189 Al0.93 K O8 Si3.07 Microcline
COD 9004141 O2 Ti Rutile
Counts
2Theta (Coupled TwoTheta/Theta) WL=1.78897

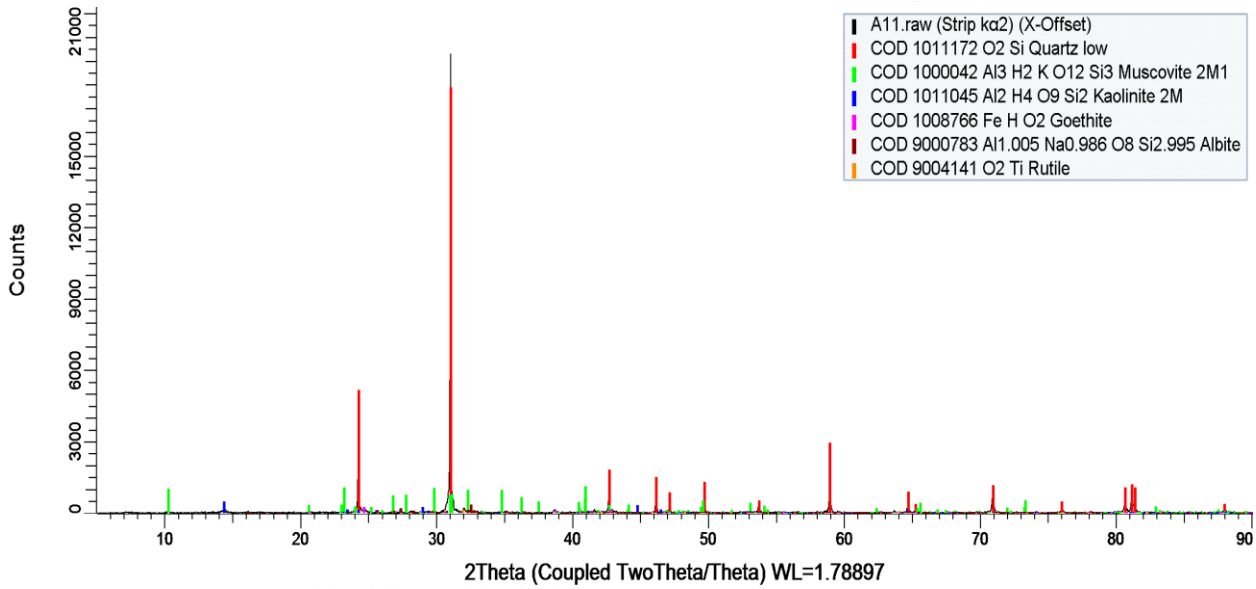
A11.raw (Strip kα2) (X-Offset)
COD 1011172 O2 Si Quartz low
COD 1000042 Al3 H2 K O12 Si3 Muscovite 2M1
COD 1011045 Al2 H4 O9 Si2 Kaolinite 2M
COD 1008766 Fe H O2 Goethite
COD 9000783 Al1.005 Na0.986 O8 Si2.995 Albite
COD 9004141 O2 Ti Rutile
Counts
2Theta (Coupled TwoTheta/Theta) WL=1.78897

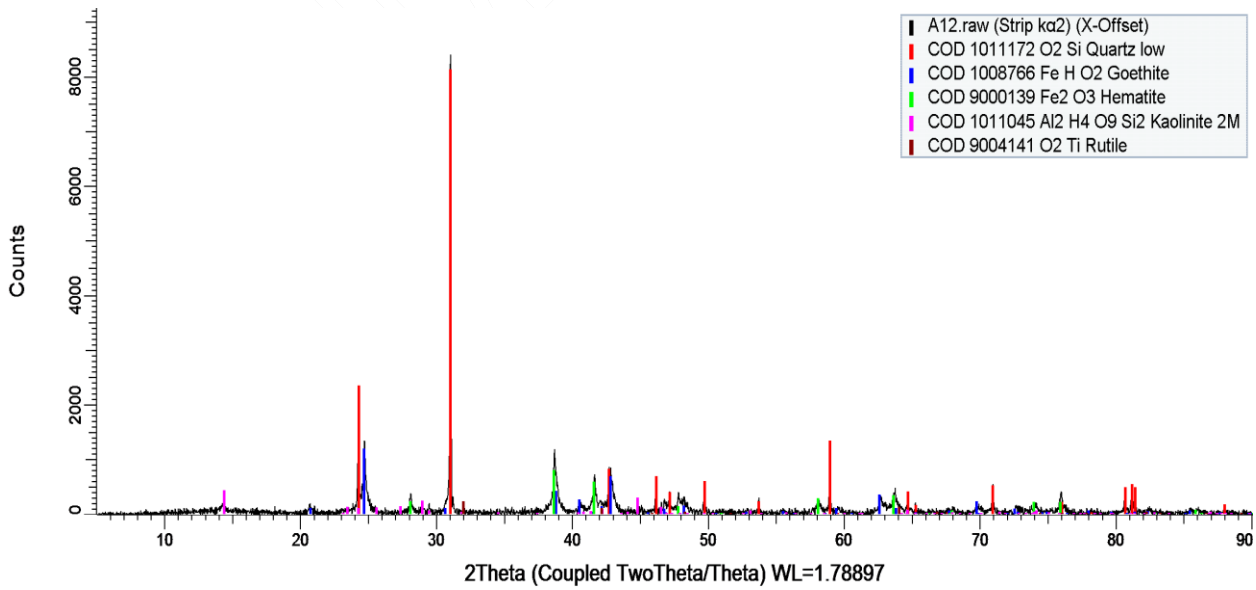
A12.raw (Strip kα2) (X-Offset)
COD 1011172 O2 Si Quartz low
COD 1008766 Fe H O2 Goethite
COD 9000139 Fe2 O3 Hematite
COD 1011045 Al2 H4 O9 Si2 Kaolinite 2M
COD 9004141 O2 Ti Rutile
Counts
2Theta (Coupled TwoTheta/Theta) WL=1.78897

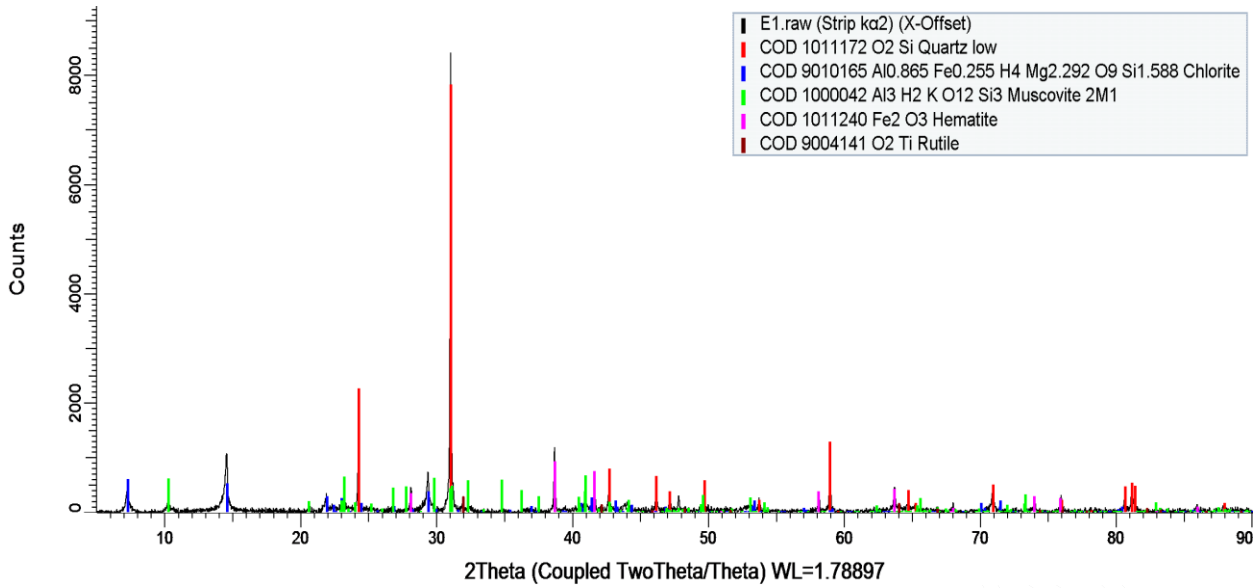
E1.raw (Strip kα2) (X-Offset)
COD 1011172 O2 Si Quartz low
COD 9010165 Al0.865 Fe0.255 H4 Mg2.292 O9 Si1.588 Chlorite
COD 1000042 Al3 H2 K O12 Si3 Muscovite 2M1
COD 1011240 Fe2 O3 Hematite
COD 9004141 O2 Ti Rutile
Counts
0
2000
4000
6000
8000
10
20
30
40
50
60
70
80
90
2Theta (Coupled TwoTheta/Theta) WL=1.78897

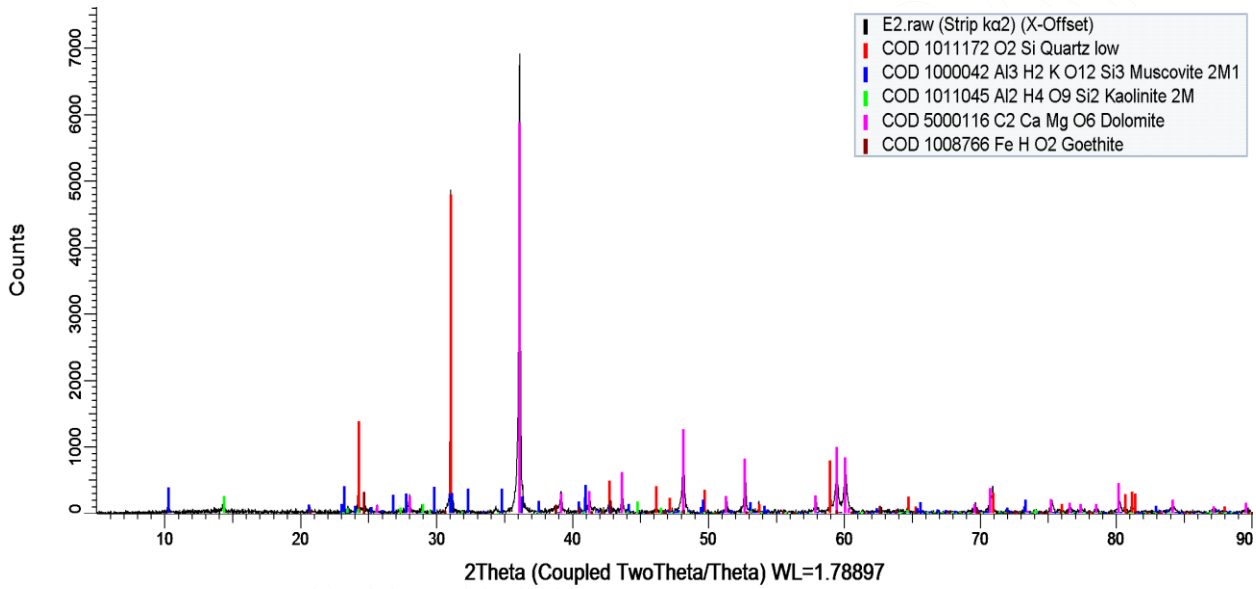
E2.raw (Strip kα2) (X-Offset)
COD 1011172 O2 Si Quartz low
COD 1000042 Al3 H2 K O12 Si3 Muscovite 2M1
COD 1011045 Al2 H4 O9 Si2 Kaolinite 2M
COD 5000116 C2 Ca Mg O6 Dolomite
COD 1008766 Fe H O2 Goethite
Counts
0
1000
2000
3000
4000
5000
6000
7000
10
20
30
40
50
60
70
80
90
2Theta (Coupled TwoTheta/Theta) WL=1.78897

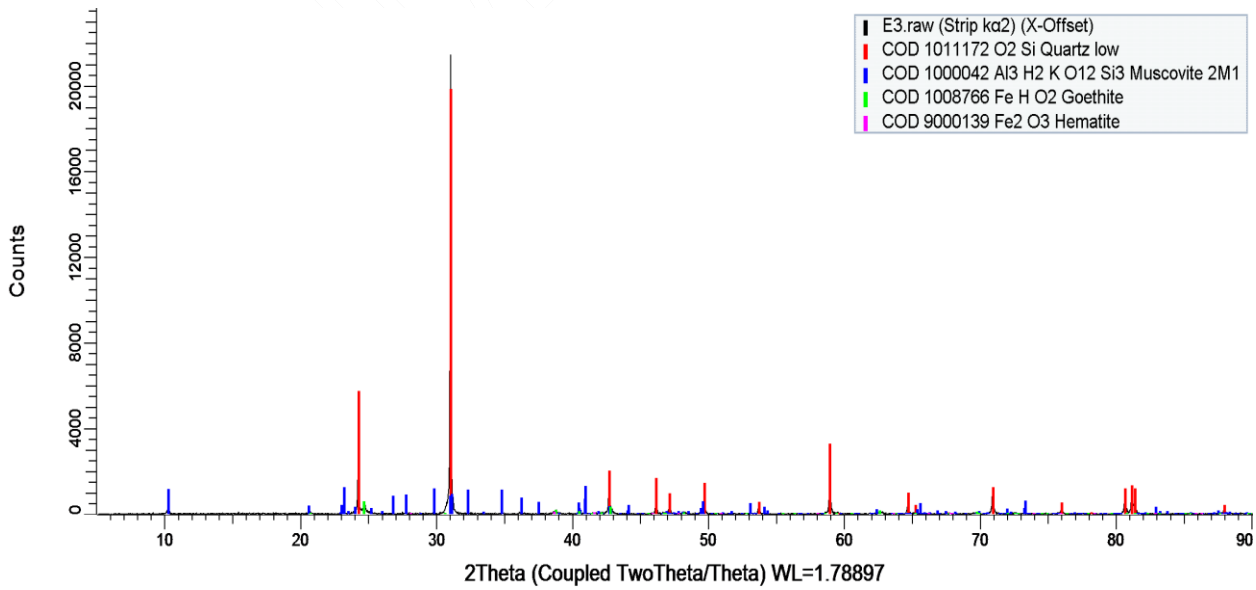
E3.raw (Strip kα2) (X-Offset)
COD 1011172 O2 Si Quartz low
COD 1000042 Al3 H2 K O12 Si3 Muscovite 2M1
COD 1008766 Fe H O2 Goethite
COD 9000139 Fe2 O3 Hematite
Counts
0
4000
8000
12000
16000
20000
10
20
30
40
50
60
70
80
90
2Theta (Coupled TwoTheta/Theta) WL=1.78897

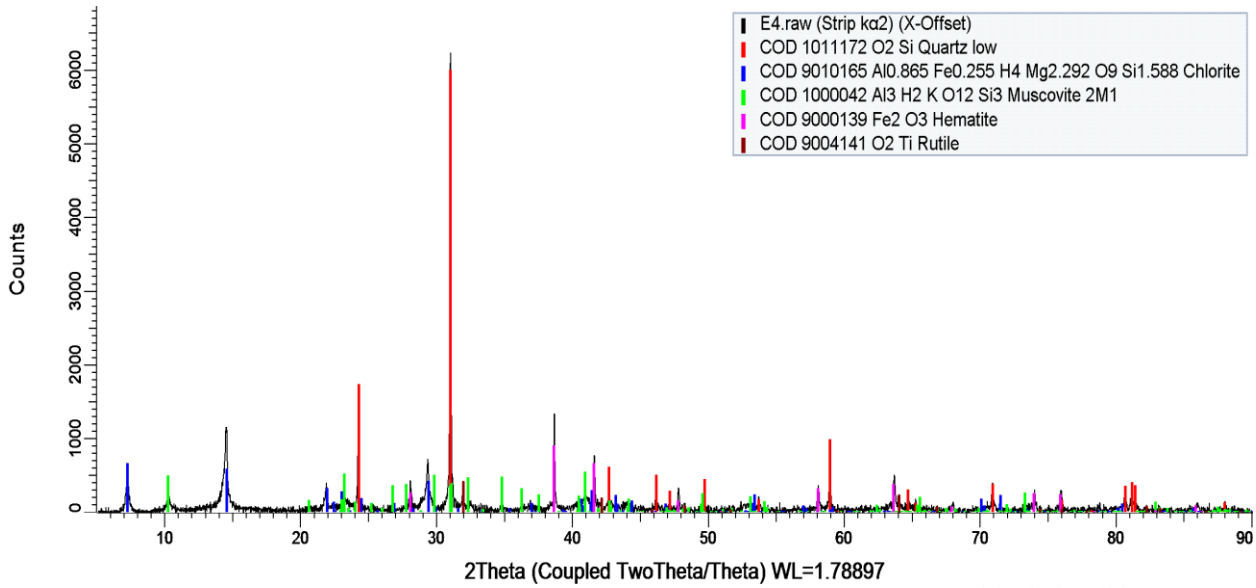
E4.raw (Strip kα2) (X-Offset)
COD 1011172 O2 Si Quartz low
COD 9010165 Al0.865 Fe0.255 H4 Mg2.292 O9 Si1.588 Chlorite
COD 1000042 Al3 H2 K O12 Si3 Muscovite 2M1
COD 9000139 Fe2 O3 Hematite
COD 9004141 O2 Ti Rutile
Counts
0
1000
2000
3000
4000
5000
6000
10
20
30
40
50
60
70
80
90
2Theta (Coupled TwoTheta/Theta) WL=1.78897

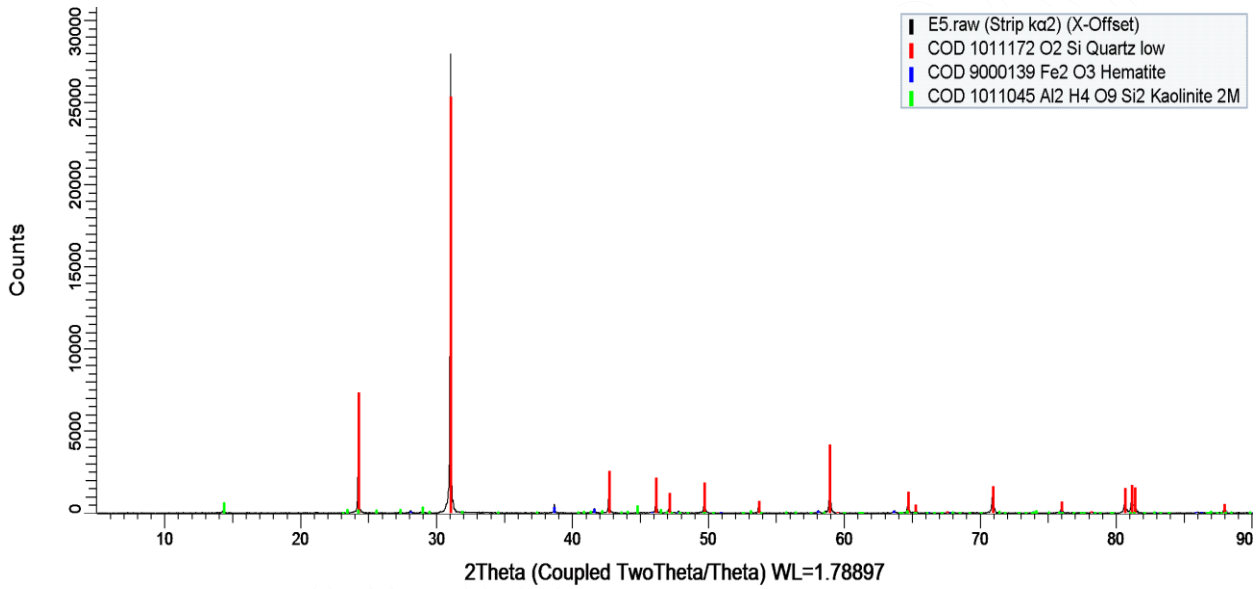
E5.raw (Strip kα2) (X-Offset)
COD 1011172 O2 Si Quartz low
COD 9000139 Fe2 O3 Hematite
COD 1011045 Al2 H4 O9 Si2 Kaolinite 2M
Counts
0
5000
10000
15000
20000
25000
30000
10
20
30
40
50
60
70
80
90
2Theta (Coupled TwoTheta/Theta) WL=1.78897

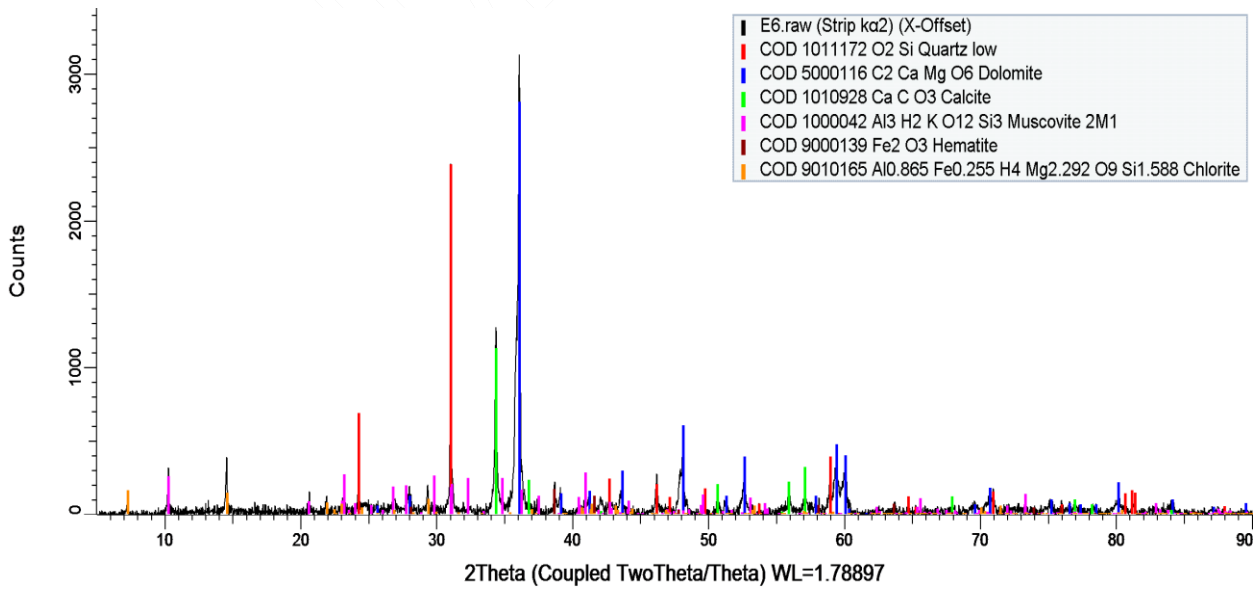
E6.raw (Strip kα2) (X-Offset)
COD 1011172 O2 Si Quartz low
COD 5000116 C2 Ca Mg O6 Dolomite
COD 1010928 Ca C O3 Calcite
COD 1000042 Al3 H2 K O12 Si3 Muscovite 2M1
COD 9000139 Fe2 O3 Hematite
COD 9010165 Al0.865 Fe0.255 H4 Mg2.292 O9 Si1.588 Chlorite
Counts
0
1000
2000
3000
10
20
30
40
50
60
70
80
90
2Theta (Coupled TwoTheta/Theta) WL=1.78897

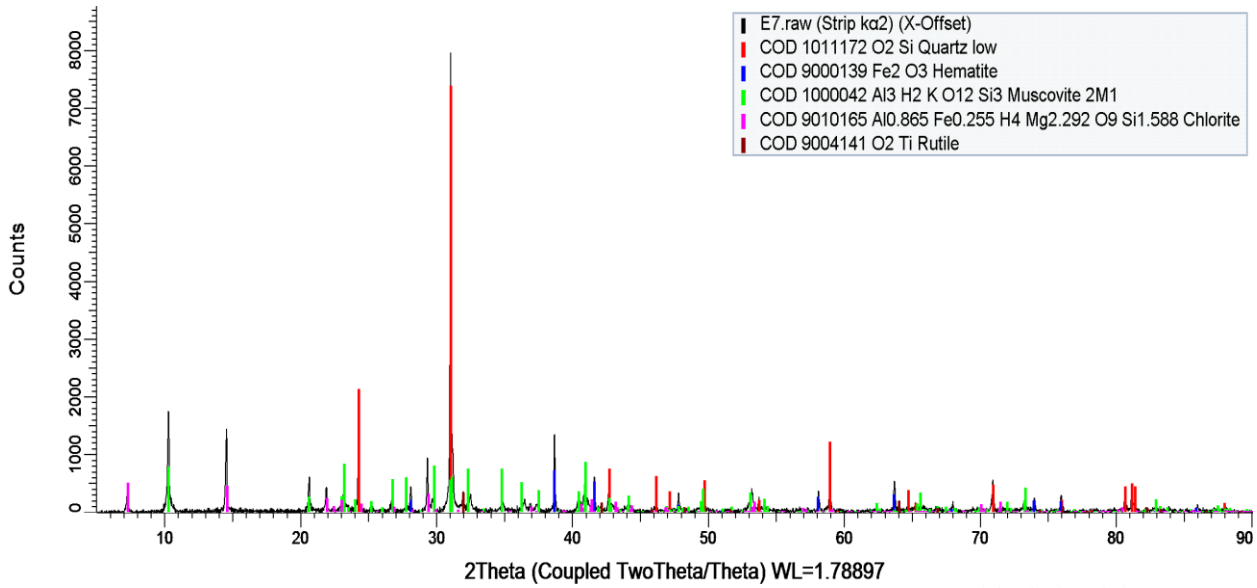
E7.raw (Strip kα2) (X-Offset)
COD 1011172 O2 Si Quartz low
COD 9000139 Fe2 O3 Hematite
COD 1000042 Al3 H2 K O12 Si3 Muscovite 2M1
COD 9010165 Al0.865 Fe0.255 H4 Mg2.292 O9 Si1.588 Chlorite
COD 9004141 O2 Ti Rutile
Counts
0
1000
2000
3000
4000
5000
6000
7000
8000
10
20
30
40
50
60
70
80
90
2Theta (Coupled TwoTheta/Theta) WL=1.78897

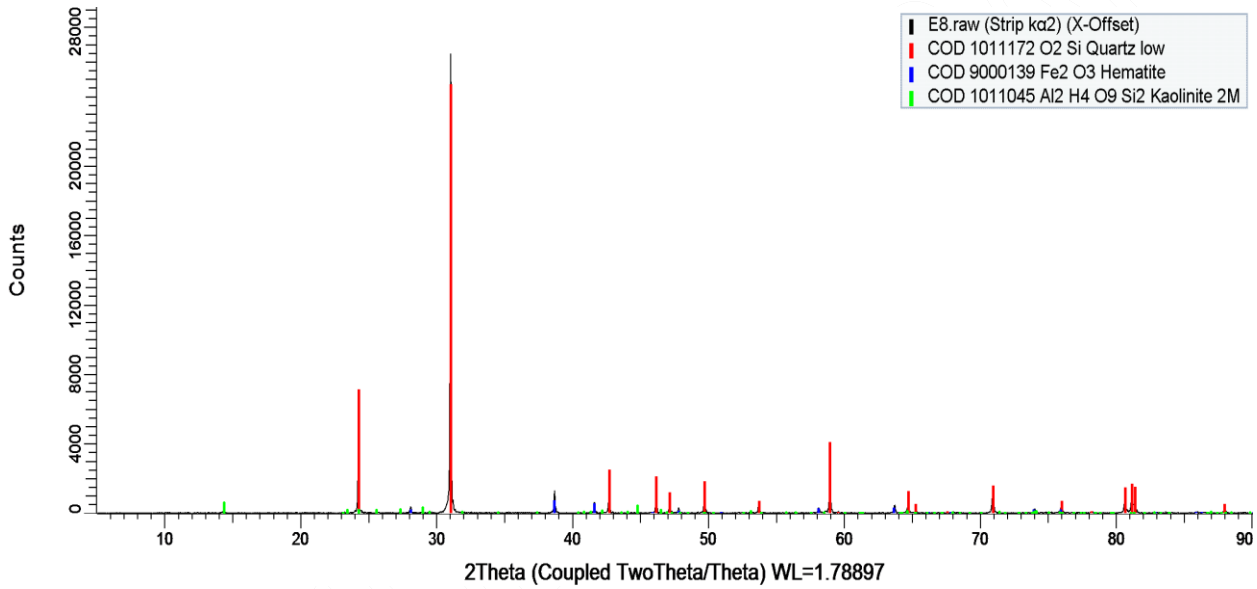
E8.raw (Strip kα2) (X-Offset)
COD 1011172 O2 Si Quartz low
COD 9000139 Fe2 O3 Hematite
COD 1011045 Al2 H4 O9 Si2 Kaolinite 2M
Counts
0
4000
8000
12000
16000
20000
28000
10
20
30
40
50
60
70
80
90
2Theta (Coupled TwoTheta/Theta) WL=1.78897

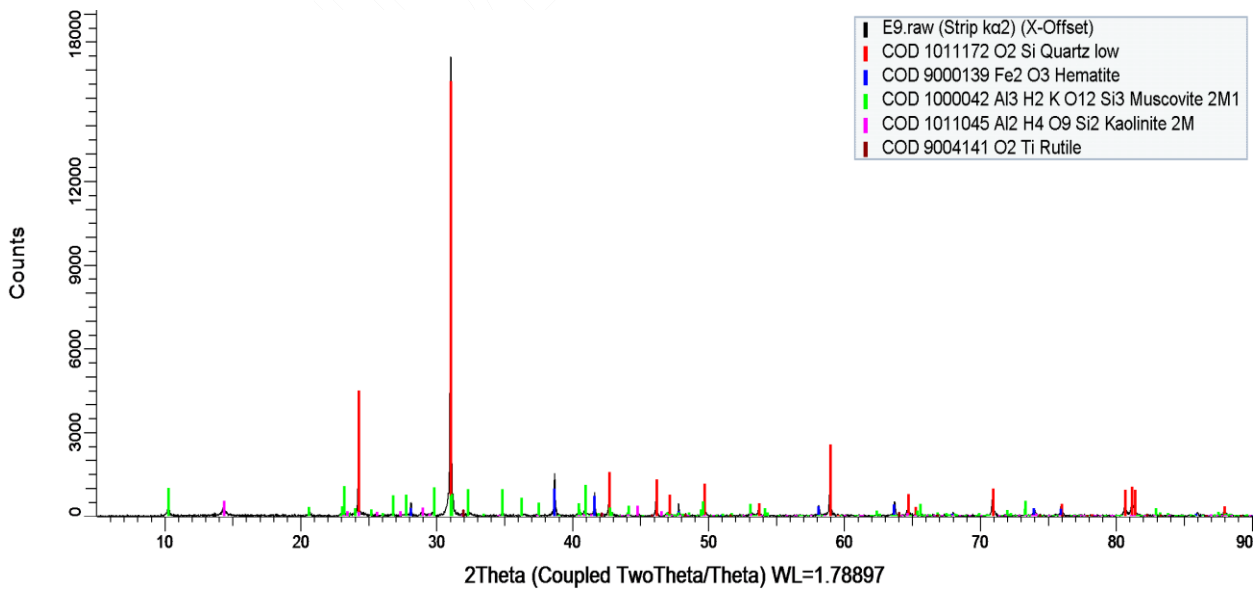
E9.raw (Strip kα2) (X-Offset)
COD 1011172 O2 Si Quartz low
COD 9000139 Fe2 O3 Hematite
COD 1000042 Al3 H2 K O12 Si3 Muscovite 2M1
COD 1011045 Al2 H4 O9 Si2 Kaolinite 2M
COD 9004141 O2 Ti Rutile
Counts
0
3000
6000
9000
12000
18000
10
20
30
40
50
60
70
80
90
2Theta (Coupled TwoTheta/Theta) WL=1.78897

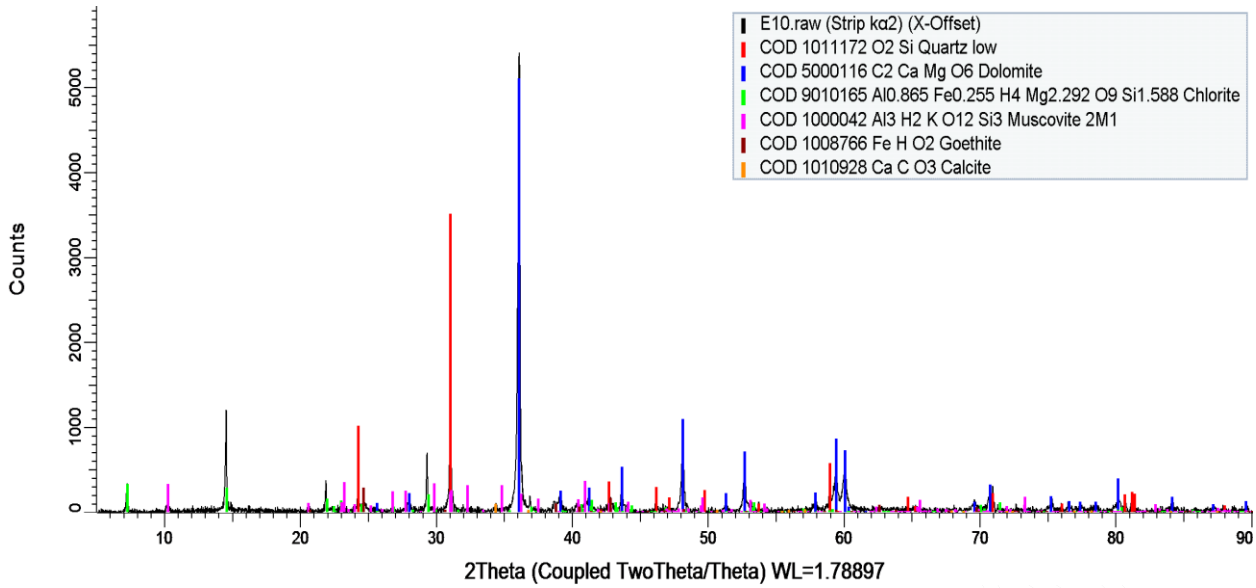
E10.raw (Strip kα2) (X-Offset)
COD 1011172 O2 Si Quartz low
COD 5000116 C2 Ca Mg O6 Dolomite
COD 9010165 Al0.865 Fe0.255 H4 Mg2.292 O9 Si1.588 Chlorite
COD 1000042 Al3 H2 K O12 Si3 Muscovite 2M1
COD 1008766 Fe H O2 Goethite
COD 1010928 Ca C O3 Calcite
Counts
0
1000
2000
3000
4000
5000
10
20
30
40
50
60
70
80
90
2Theta (Coupled TwoTheta/Theta) WL=1.78897

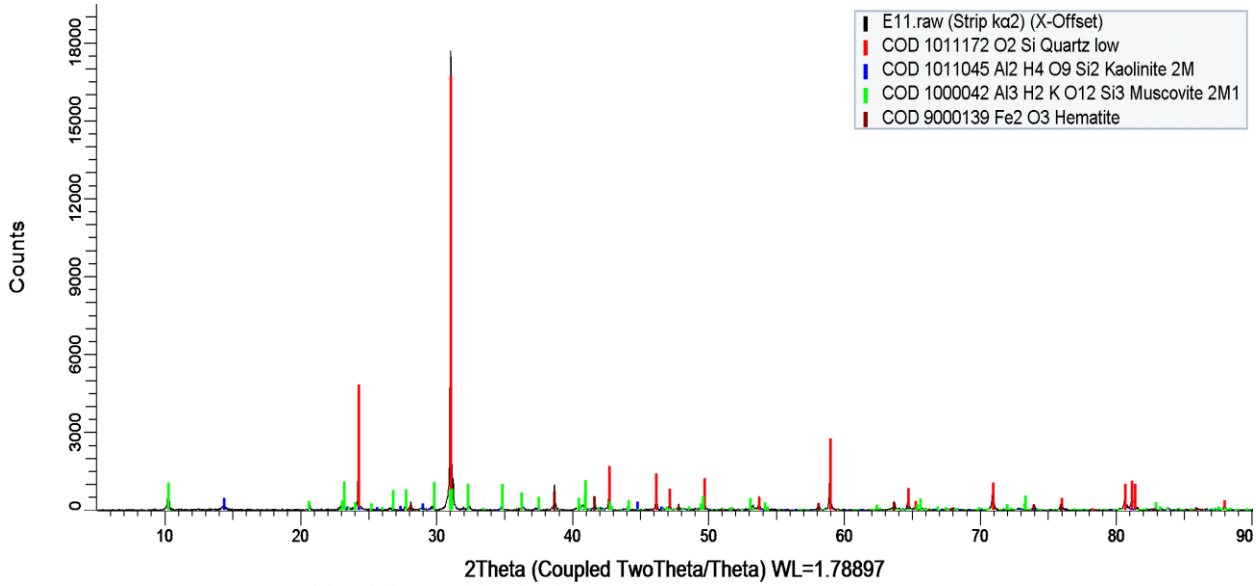
E11.raw (Strip kα2) (X-Offset)
COD 1011172 O2 Si Quartz low
COD 1011045 Al2 H4 O9 Si2 Kaolinite 2M
COD 1000042 Al3 H2 K O12 Si3 Muscovite 2M1
COD 9000139 Fe2 O3 Hematite
Counts
0
3000
6000
9000
12000
15000
18000
10
20
30
40
50
60
70
80
90
2Theta (Coupled TwoTheta/Theta) WL=1.78897

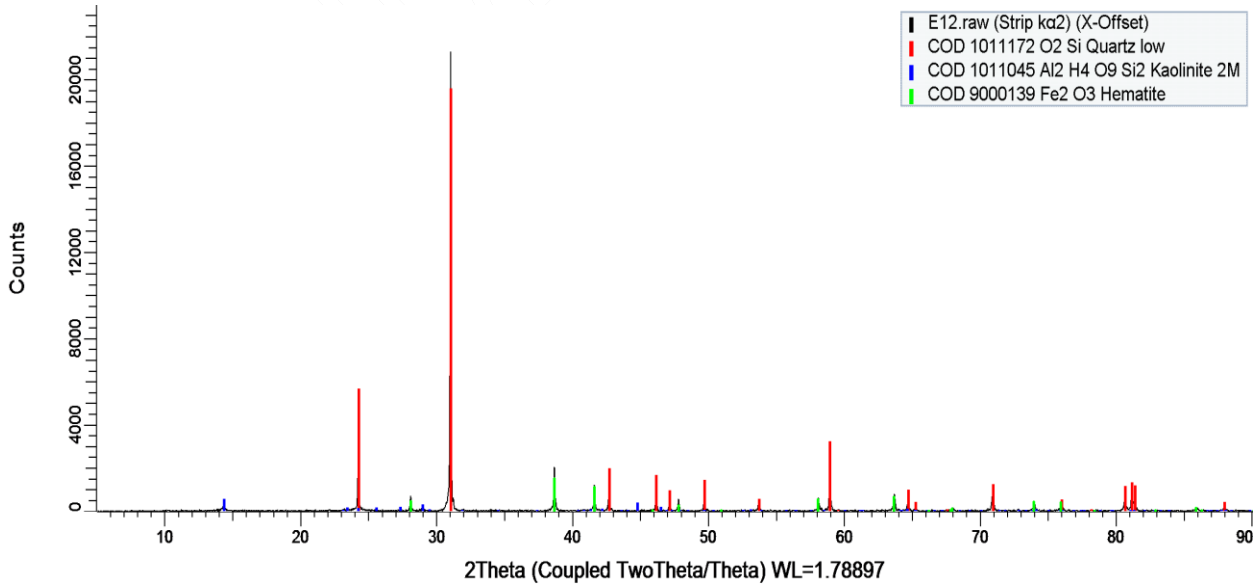
E12.raw (Strip kα2) (X-Offset)
COD 1011172 O2 Si Quartz low
COD 1011045 Al2 H4 O9 Si2 Kaolinite 2M
COD 9000139 Fe2 O3 Hematite
Counts
0
4000
8000
12000
16000
20000
10
20
30
40
50
60
70
80
90
2Theta (Coupled TwoTheta/Theta) WL=1.78897

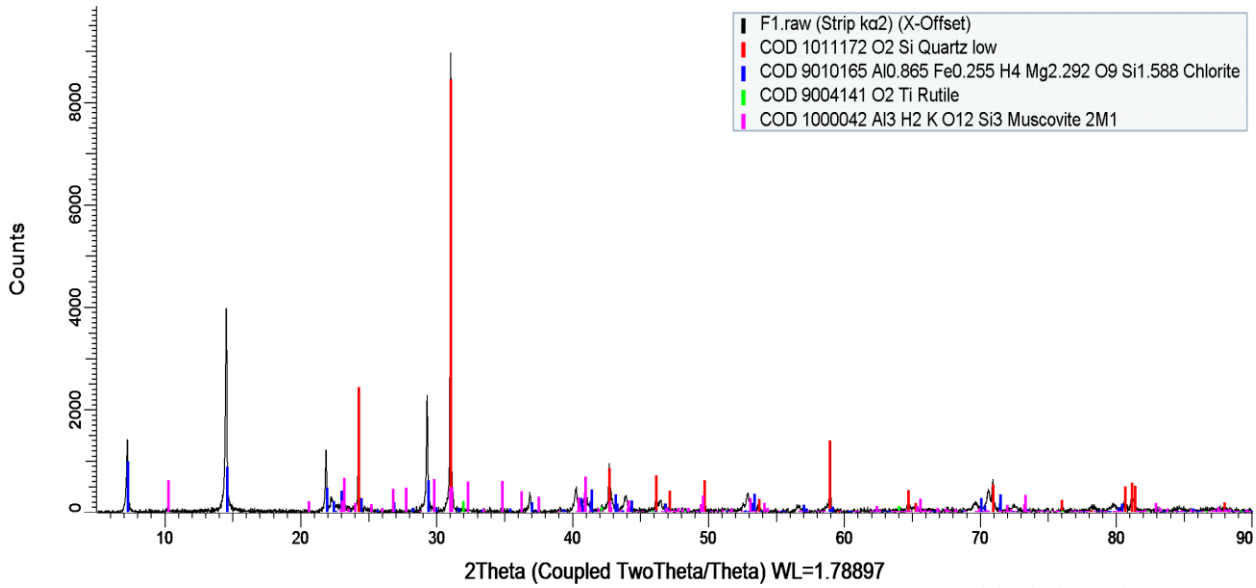
F1.raw (Strip kα2) (X-Offset)
COD 1011172 O2 Si Quartz low
COD 9010165 Al0.865 Fe0.255 H4 Mg2.292 O9 Si1.588 Chlorite
COD 9004141 O2 Ti Rutile
COD 1000042 Al3 H2 K O12 Si3 Muscovite 2M1
Counts
2Theta (Coupled TwoTheta/Theta) WL=1.78897

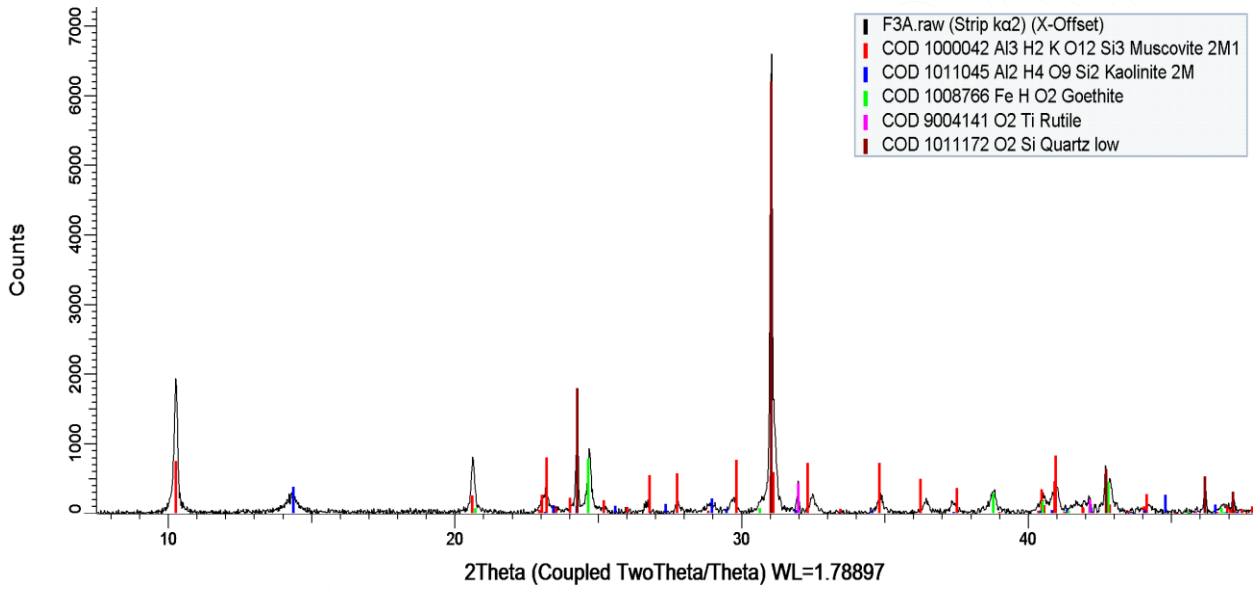
F3A.raw (Strip kα2) (X-Offset)
COD 1000042 Al3 H2 K O12 Si3 Muscovite 2M1
COD 1011045 Al2 H4 O9 Si2 Kaolinite 2M
COD 1008766 Fe H O2 Goethite
COD 9004141 O2 Ti Rutile
COD 1011172 O2 Si Quartz low
Counts
2Theta (Coupled TwoTheta/Theta) WL=1.78897

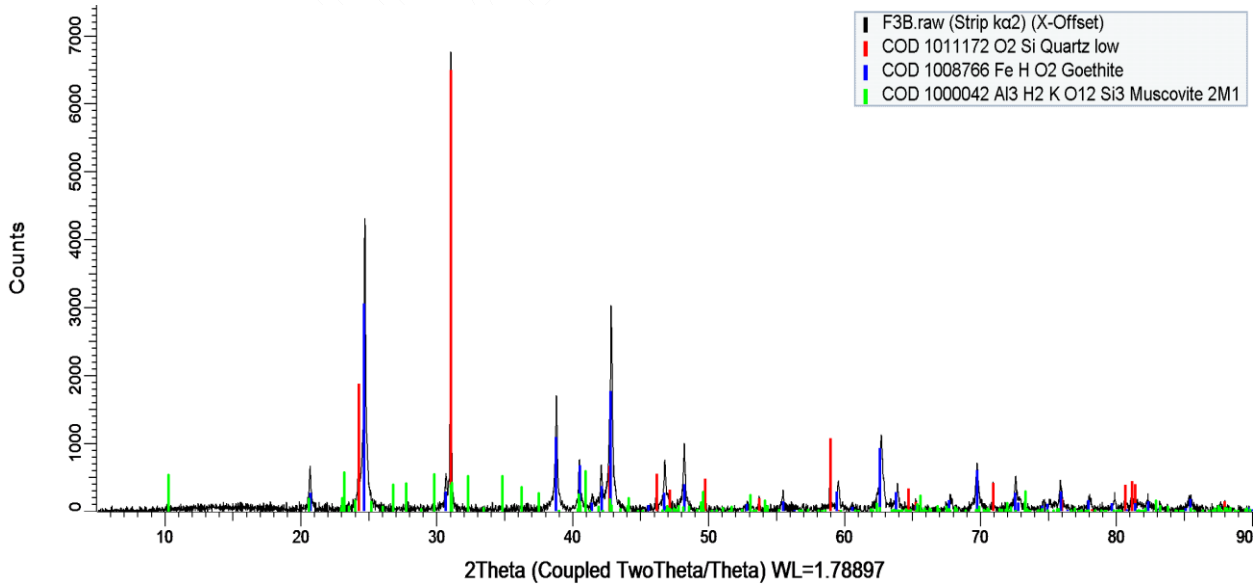
F3B.raw (Strip kα2) (X-Offset)
COD 1011172 O2 Si Quartz low
COD 1008766 Fe H O2 Goethite
COD 1000042 Al3 H2 K O12 Si3 Muscovite 2M1
Counts
2Theta (Coupled TwoTheta/Theta) WL=1.78897

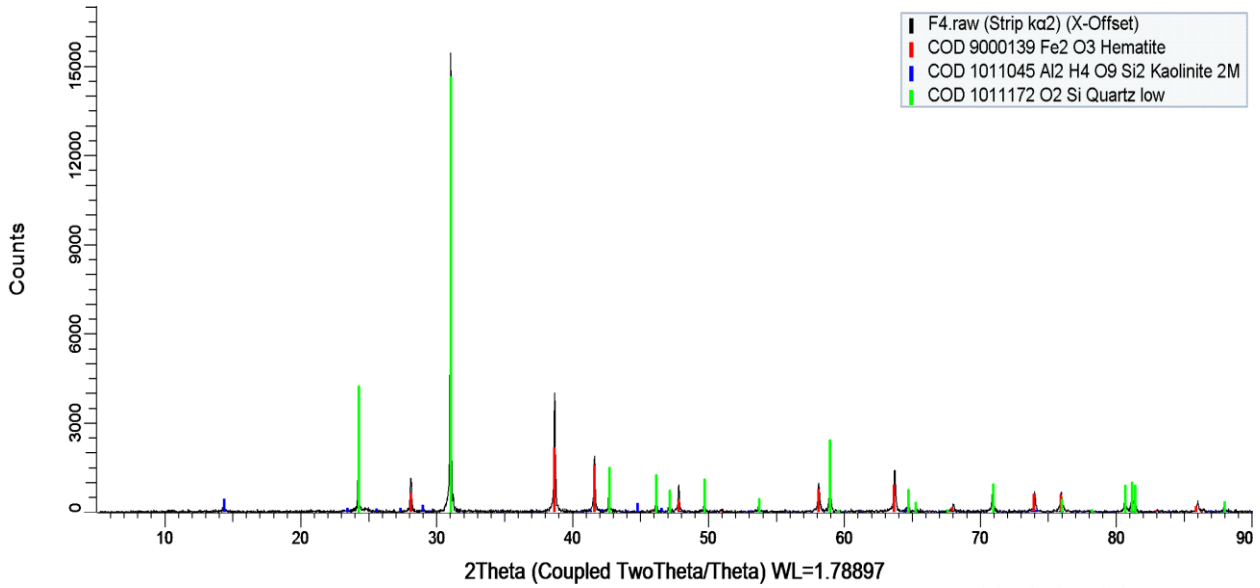
F4.raw (Strip kα2) (X-Offset)
COD 9000139 Fe2 O3 Hematite
COD 1011045 Al2 H4 O9 Si2 Kaolinite 2M
COD 1011172 O2 Si Quartz low
Counts
0
3000
6000
9000
12000
15000
10
20
30
40
50
60
70
80
90
2Theta (Coupled TwoTheta/Theta) WL=1.78897

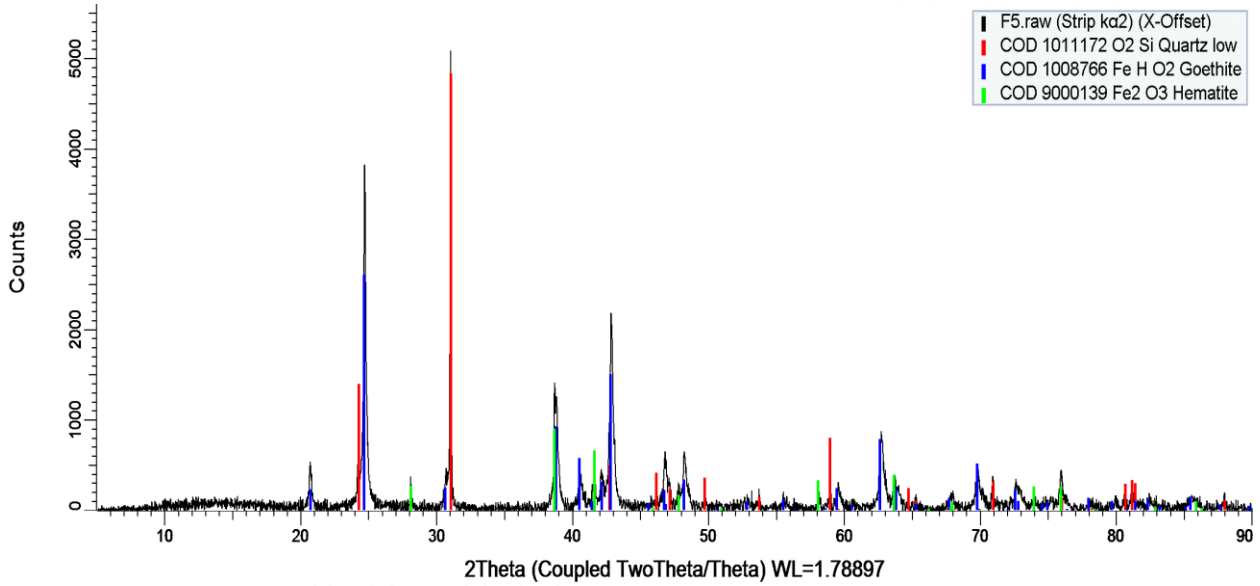
F5.raw (Strip kα2) (X-Offset)
COD 1011172 O2 Si Quartz low
COD 1008766 Fe H O2 Goethite
COD 9000139 Fe2 O3 Hematite
Counts
0
1000
2000
3000
4000
5000
10
20
30
40
50
60
70
80
90
2Theta (Coupled TwoTheta/Theta) WL=1.78897

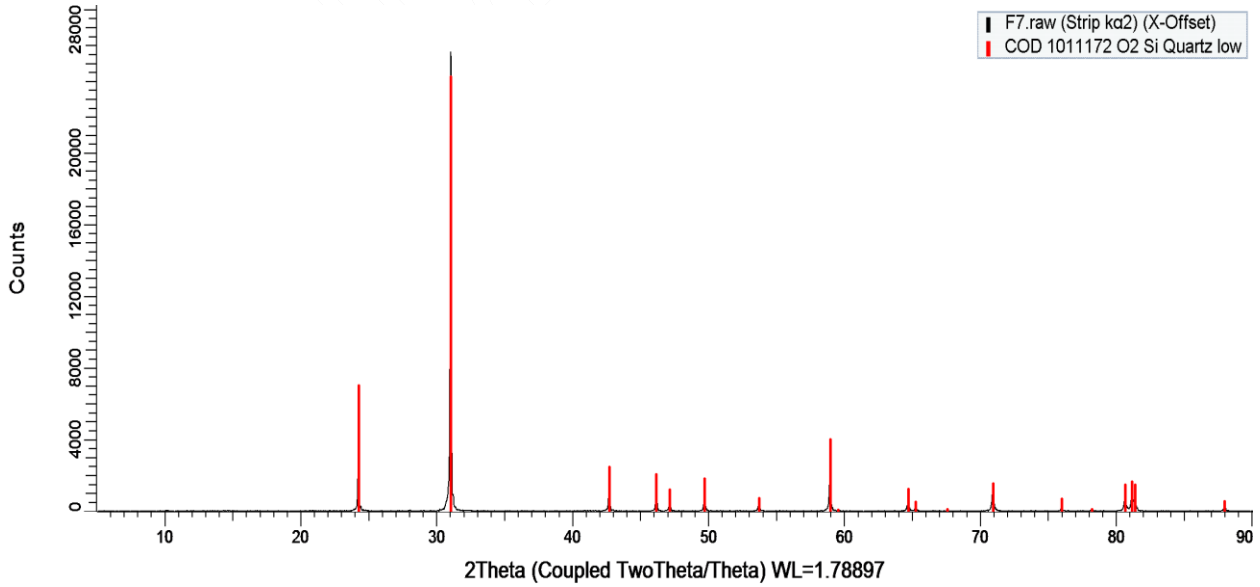
F7.raw (Strip kα2) (X-Offset)
COD 1011172 O2 Si Quartz low
Counts
0
4000
8000
12000
16000
20000
24000
28000
10
20
30
40
50
60
70
80
90
2Theta (Coupled TwoTheta/Theta) WL=1.78897

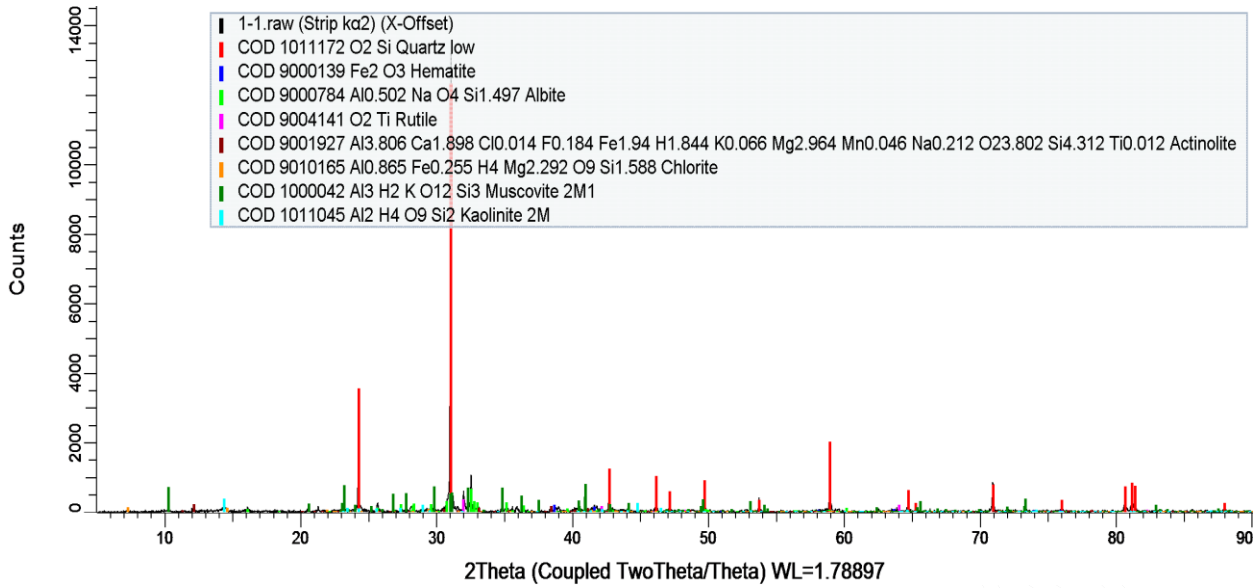
1-1.raw (Strip kα2) (X-Offset)
COD 1011172 O2 Si Quartz low
COD 9000139 Fe2 O3 Hematite
COD 9000784 Al0.502 Na O4 Si1.497 Albite
COD 9004141 O2 Ti Rutile
COD 9001927 Al3.806 Ca1.898 Cl0.014 F0.184 Fe1.94 H1.844 K0.066 Mg2.964 Mn0.046 Na0.212 O23.802 Si4.312 Ti0.012 Actinolite
COD 9010165 Al0.865 Fe0.255 H4 Mg2.292 O9 Si1.588 Chlorite
COD 1000042 Al3 H2 K O12 Si3 Muscovite 2M1
COD 1011045 Al2 H4 O9 Si2 Kaolinite 2M
Counts
2Theta (Coupled TwoTheta/Theta) WL=1.78897

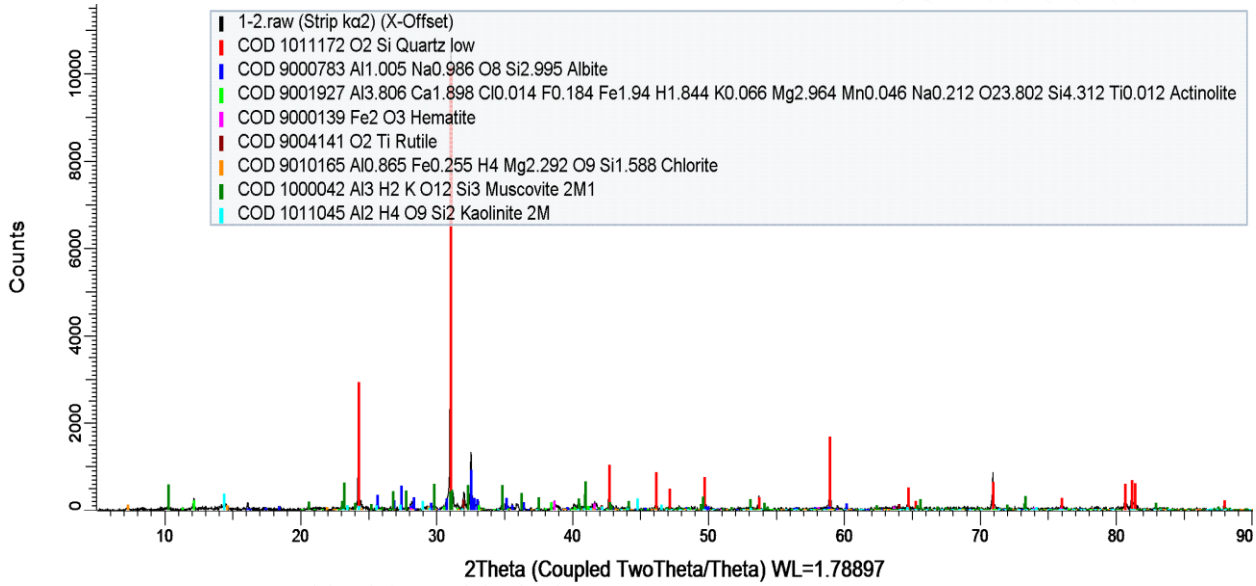
1-2.raw (Strip kα2) (X-Offset)
COD 1011172 O2 Si Quartz low
COD 9000783 Al1.005 Na0.986 O8 Si2.995 Albite
COD 9001927 Al3.806 Ca1.898 Cl0.014 F0.184 Fe1.94 H1.844 K0.066 Mg2.964 Mn0.046 Na0.212 O23.802 Si4.312 Ti0.012 Actinolite
COD 9000139 Fe2 O3 Hematite
COD 9004141 O2 Ti Rutile
COD 9010165 Al0.865 Fe0.255 H4 Mg2.292 O9 Si1.588 Chlorite
COD 1000042 Al3 H2 K O12 Si3 Muscovite 2M1
COD 1011045 Al2 H4 O9 Si2 Kaolinite 2M
Counts
2Theta (Coupled TwoTheta/Theta) WL=1.78897

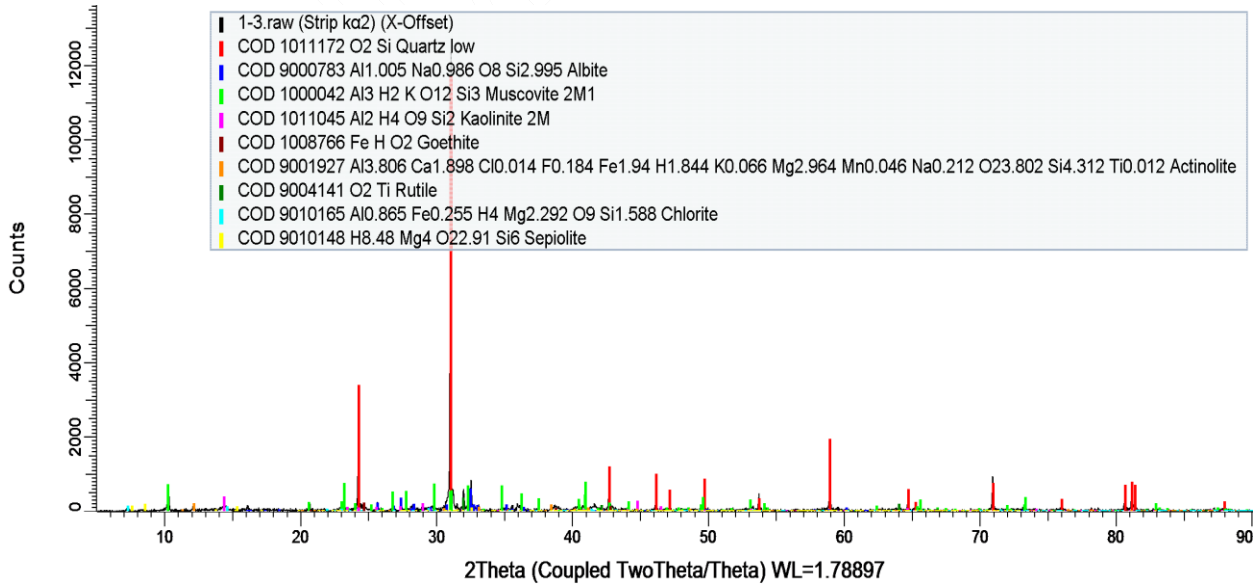
1-3.raw (Strip kα2) (X-Offset)
COD 1011172 O2 Si Quartz low
COD 9000783 Al1.005 Na0.986 O8 Si2.995 Albite
COD 1000042 Al3 H2 K O12 Si3 Muscovite 2M1
COD 1011045 Al2 H4 O9 Si2 Kaolinite 2M
COD 1008766 Fe H O2 Goethite
COD 9001927 Al3.806 Ca1.898 Cl0.014 F0.184 Fe1.94 H1.844 K0.066 Mg2.964 Mn0.046 Na0.212 O23.802 Si4.312 Ti0.012 Actinolite
COD 9004141 O2 Ti Rutile
COD 9010165 Al0.865 Fe0.255 H4 Mg2.292 O9 Si1.588 Chlorite
COD 9010148 H8.48 Mg4 O22.91 Si6 Sepiolite
Counts
2Theta (Coupled TwoTheta/Theta) WL=1.78897

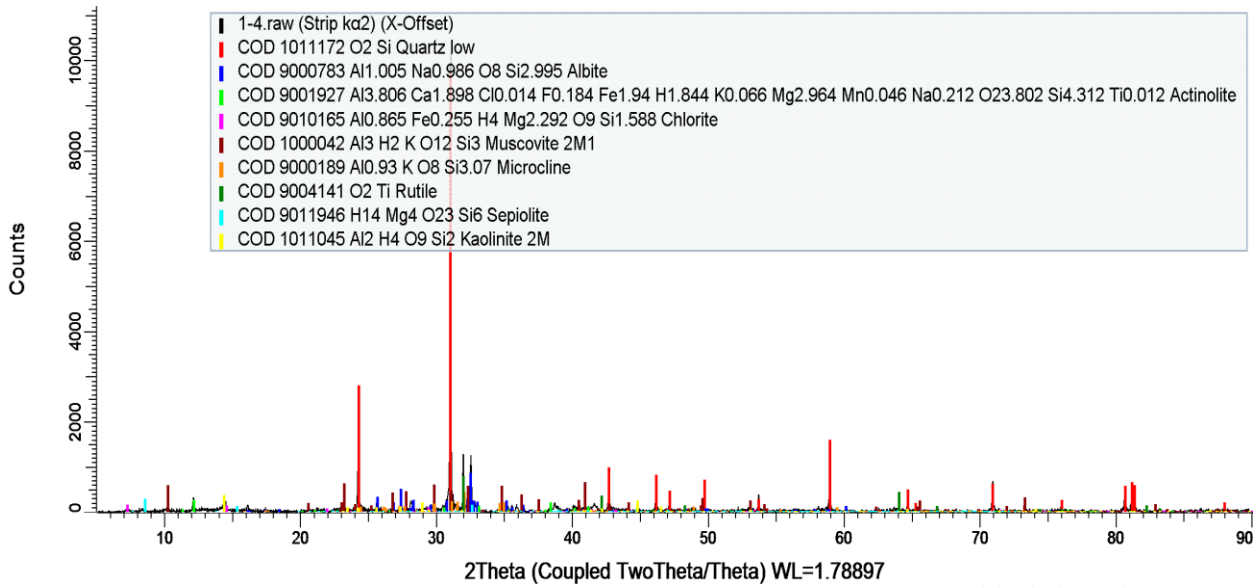
1-4.raw (Strip kα2) (X-Offset)
COD 1011172 O2 Si Quartz low
COD 9000783 Al1.005 Na0.986 O8 Si2.995 Albite
COD 9001927 Al3.806 Ca1.898 Cl0.014 F0.184 Fe1.94 H1.844 K0.066 Mg2.964 Mn0.046 Na0.212 O23.802 Si4.312 Ti0.012 Actinolite
COD 9010165 Al0.865 Fe0.255 H4 Mg2.292 O9 Si1.588 Chlorite
COD 1000042 Al3 H2 K O12 Si3 Muscovite 2M1
COD 9000189 Al0.93 K O8 Si3.07 Microcline
COD 9004141 O2 Ti Rutile
COD 9011946 H14 Mg4 O23 Si6 Sepiolite
COD 1011045 Al2 H4 O9 Si2 Kaolinite 2M
Counts
2Theta (Coupled TwoTheta/Theta) WL=1.78897

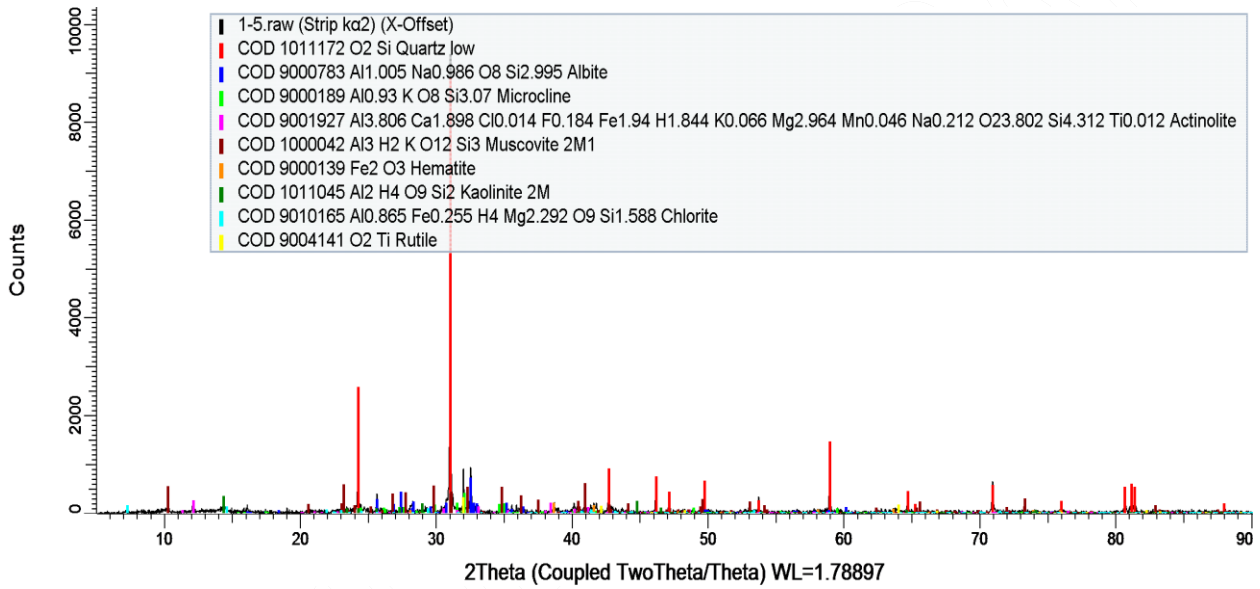
1-5.raw (Strip kα2) (X-Offset)
COD 1011172 O2 Si Quartz low
COD 9000783 Al1.005 Na0.986 O8 Si2.995 Albite
COD 9000189 Al0.93 K O8 Si3.07 Microcline
COD 9001927 Al3.806 Ca1.898 Cl0.014 F0.184 Fe1.94 H1.844 K0.066 Mg2.964 Mn0.046 Na0.212 O23.802 Si4.312 Ti0.012 Actinolite
COD 1000042 Al3 H2 K O12 Si3 Muscovite 2M1
COD 9000139 Fe2 O3 Hematite
COD 1011045 Al2 H4 O9 Si2 Kaolinite 2M
COD 9010165 Al0.865 Fe0.255 H4 Mg2.292 O9 Si1.588 Chlorite
COD 9004141 O2 Ti Rutile
Counts
2Theta (Coupled TwoTheta/Theta) WL=1.78897

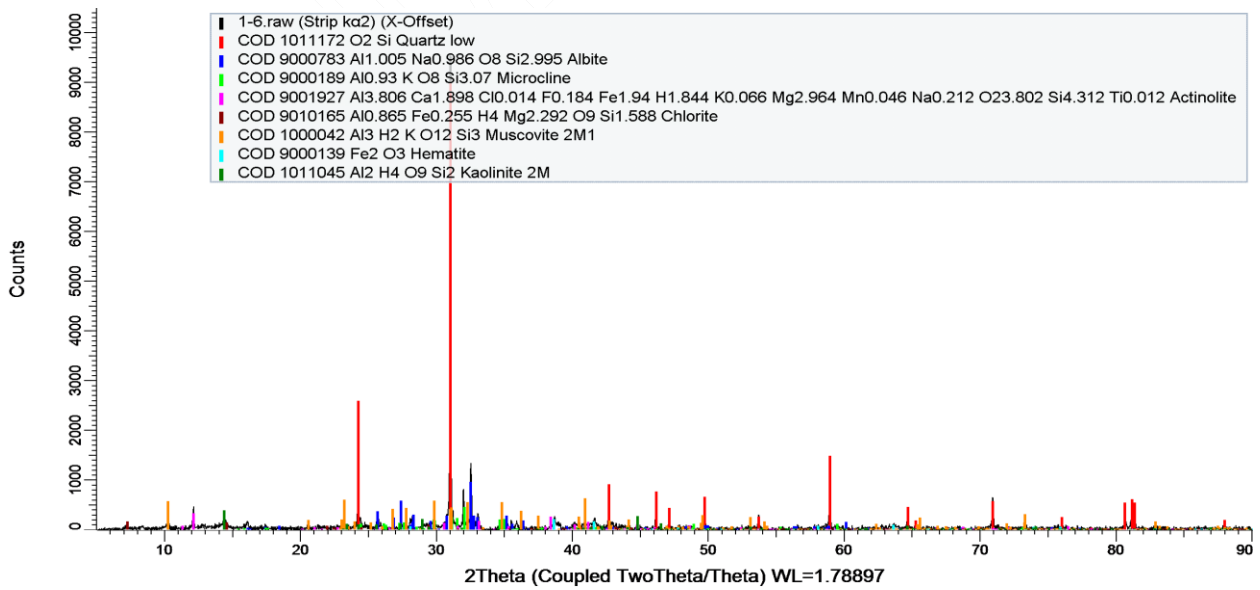
1-6.raw (Strip kα2) (X-Offset)
COD 1011172 O2 Si Quartz low
COD 9000783 Al1.005 Na0.986 O8 Si2.995 Albite
COD 9000189 Al0.93 K O8 Si3.07 Microcline
COD 9001927 Al3.806 Ca1.898 Cl0.014 F0.184 Fe1.94 H1.844 K0.066 Mg2.964 Mn0.046 Na0.212 O23.802 Si4.312 Ti0.012 Actinolite
COD 9010165 Al0.865 Fe0.255 H4 Mg2.292 O9 Si1.588 Chlorite
COD 1000042 Al3 H2 K O12 Si3 Muscovite 2M1
COD 9000139 Fe2 O3 Hematite
COD 1011045 Al2 H4 O9 Si2 Kaolinite 2M
Counts
2Theta (Coupled TwoTheta/Theta) WL=1.78897

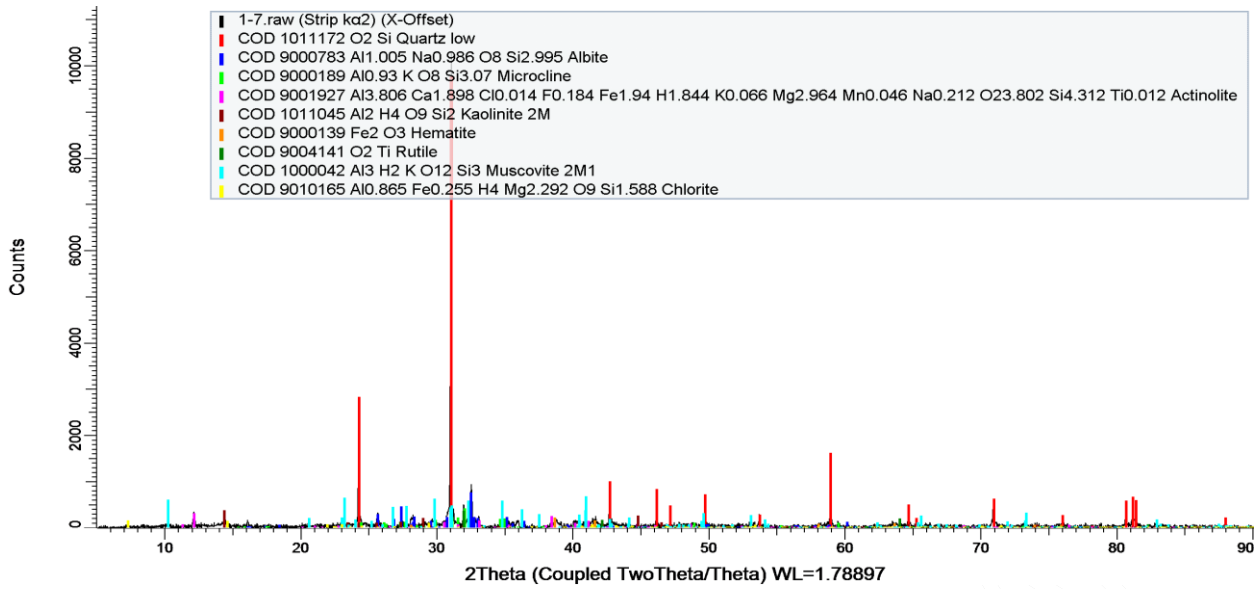
1-7.raw (Strip kα2) (X-Offset)
COD 1011172 O2 Si Quartz low
COD 9000783 Al1.005 Na0.986 O8 Si2.995 Albite
COD 9000189 Al0.93 K O8 Si3.07 Microcline
COD 9001927 Al3.806 Ca1.898 Cl0.014 F0.184 Fe1.94 H1.844 K0.066 Mg2.964 Mn0.046 Na0.212 O23.802 Si4.312 Ti0.012 Actinolite
COD 1011045 Al2 H4 O9 Si2 Kaolinite 2M
COD 9000139 Fe2 O3 Hematite
COD 9004141 O2 Ti Rutile
COD 1000042 Al3 H2 K O12 Si3 Muscovite 2M1
COD 9010165 Al0.865 Fe0.255 H4 Mg2.292 O9 Si1.588 Chlorite
Counts
2Theta (Coupled TwoTheta/Theta) WL=1.78897

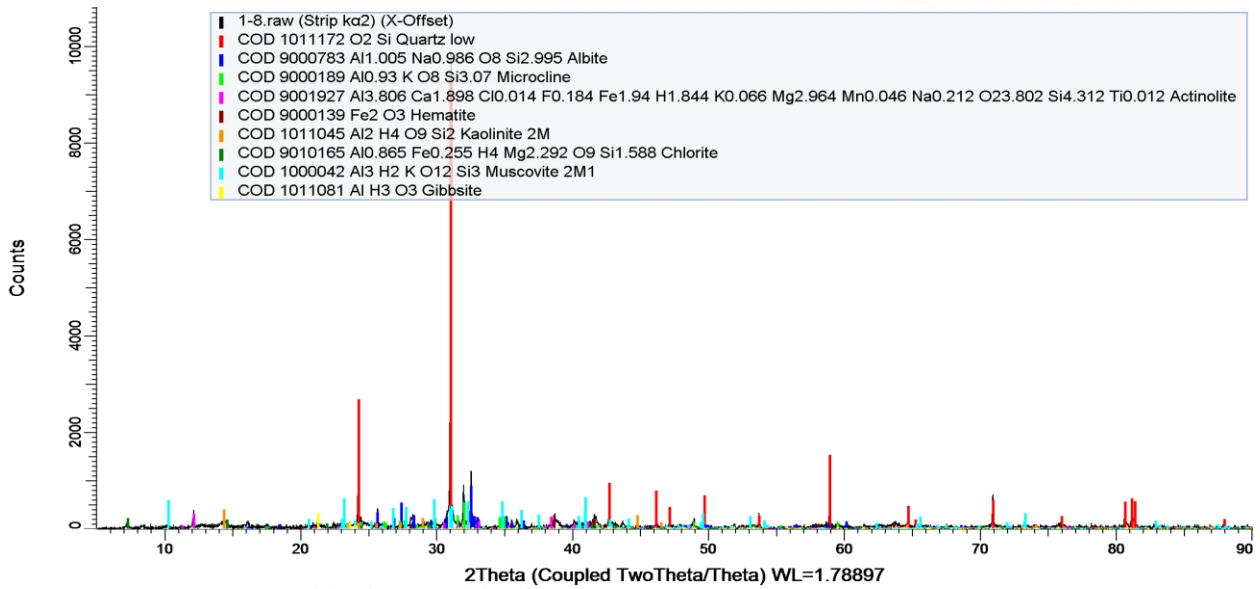
1-8.raw (Strip kα2) (X-Offset)
COD 1011172 O2 Si Quartz low
COD 9000783 Al1.005 Na0.986 O8 Si2.995 Albite
COD 9000189 Al0.93 K O8 Si3.07 Microcline
COD 9001927 Al3.806 Ca1.898 Cl0.014 F0.184 Fe1.94 H1.844 K0.066 Mg2.964 Mn0.046 Na0.212 O23.802 Si4.312 Ti0.012 Actinolite
COD 9000139 Fe2 O3 Hematite
COD 1011045 Al2 H4 O9 Si2 Kaolinite 2M
COD 9010165 Al0.865 Fe0.255 H4 Mg2.292 O9 Si1.588 Chlorite
COD 1000042 Al3 H2 K O12 Si3 Muscovite 2M1
COD 1011081 Al H3 O3 Gibbsite
Counts
2Theta (Coupled TwoTheta/Theta) WL=1.78897

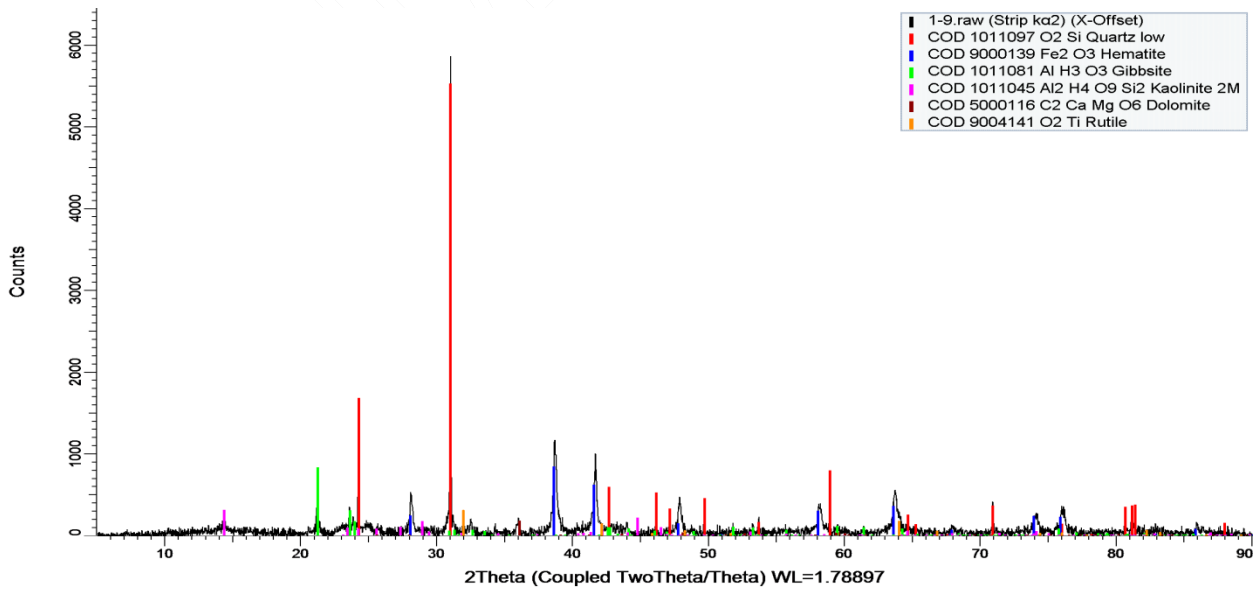
1-9.raw (Strip kα2) (X-Offset)
COD 1011097 O2 Si Quartz low
COD 9000139 Fe2 O3 Hematite
COD 1011081 Al H3 O3 Gibbsite
COD 1011045 Al2 H4 O9 Si2 Kaolinite 2M
COD 5000116 C2 Ca Mg O6 Dolomite
COD 9004141 O2 Ti Rutile
Counts
2Theta (Coupled TwoTheta/Theta) WL=1.78897

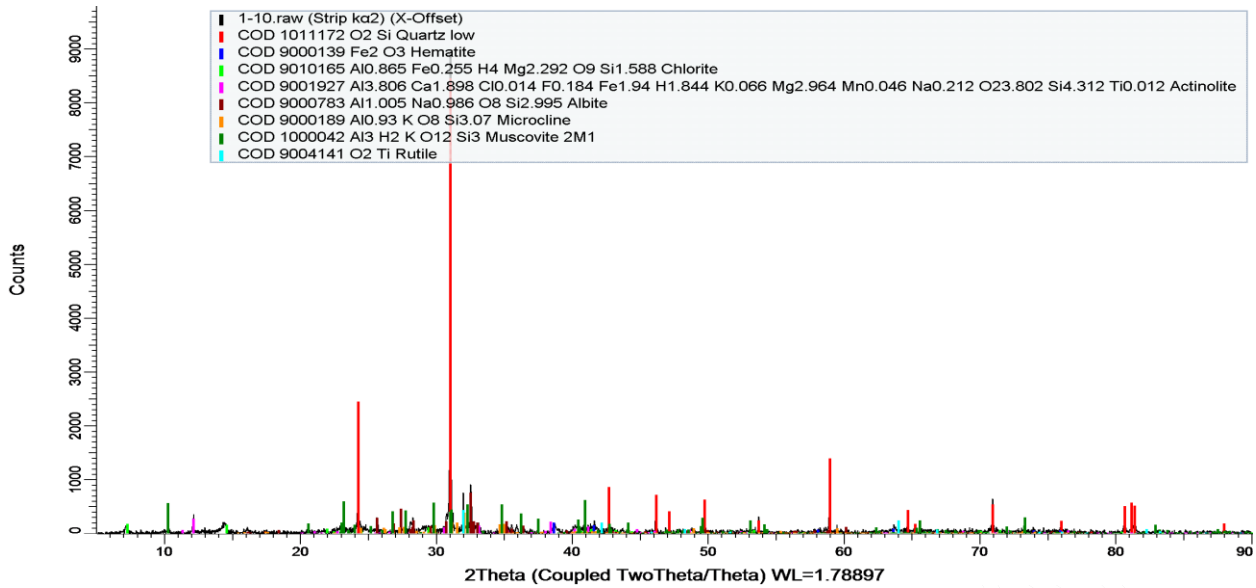
1-10.raw (Strip kα2) (X-Offset)
COD 1011172 O2 Si Quartz low
COD 9000139 Fe2 O3 Hematite
COD 9010165 Al0.865 Fe0.255 H4 Mg2.292 O9 Si1.588 Chlorite
COD 9001927 Al3.806 Ca1.898 Cl0.014 F0.184 Fe1.94 H1.844 K0.066 Mg2.964 Mn0.046 Na0.212 O23.802 Si4.312 Ti0.012 Actinolite
COD 9000783 Al1.005 Na0.986 O8 Si2.995 Albite
COD 9000189 Al0.93 K O8 Si3.07 Microcline
COD 1000042 Al3 H2 K O12 Si3 Muscovite 2M1
COD 9004141 O2 Ti Rutile
Counts
2Theta (Coupled TwoTheta/Theta) WL=1.78897

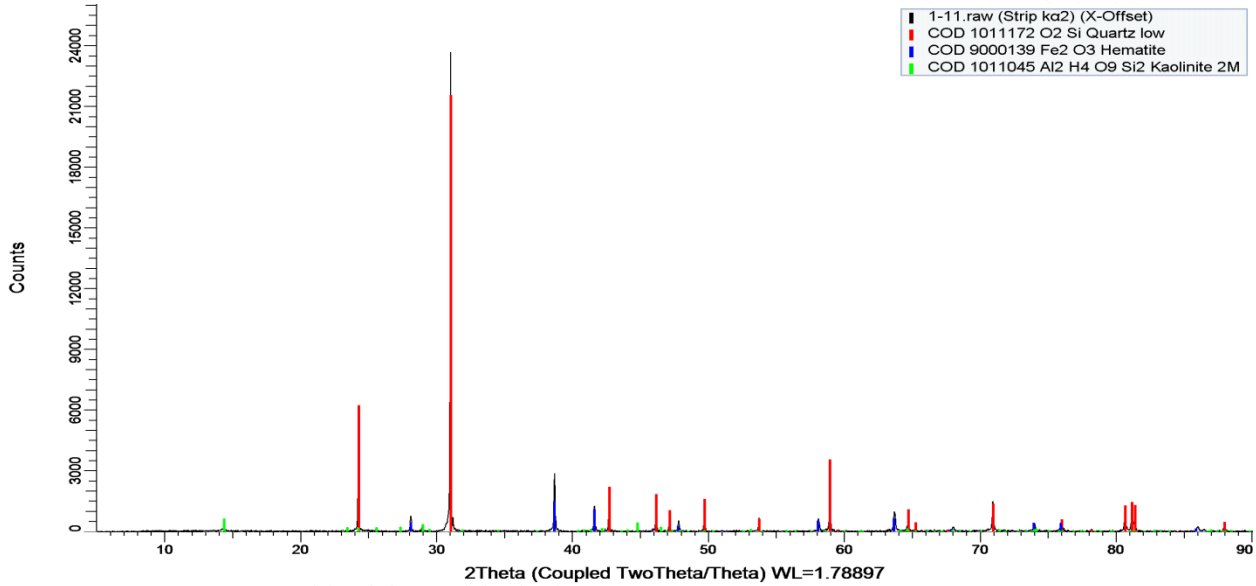
1-11.raw (Strip kα2) (X-Offset)
COD 1011172 O2 Si Quartz low
COD 9000139 Fe2 O3 Hematite
COD 1011045 Al2 H4 O9 Si2 Kaolinite 2M
Counts
2Theta (Coupled TwoTheta/Theta) WL=1.78897

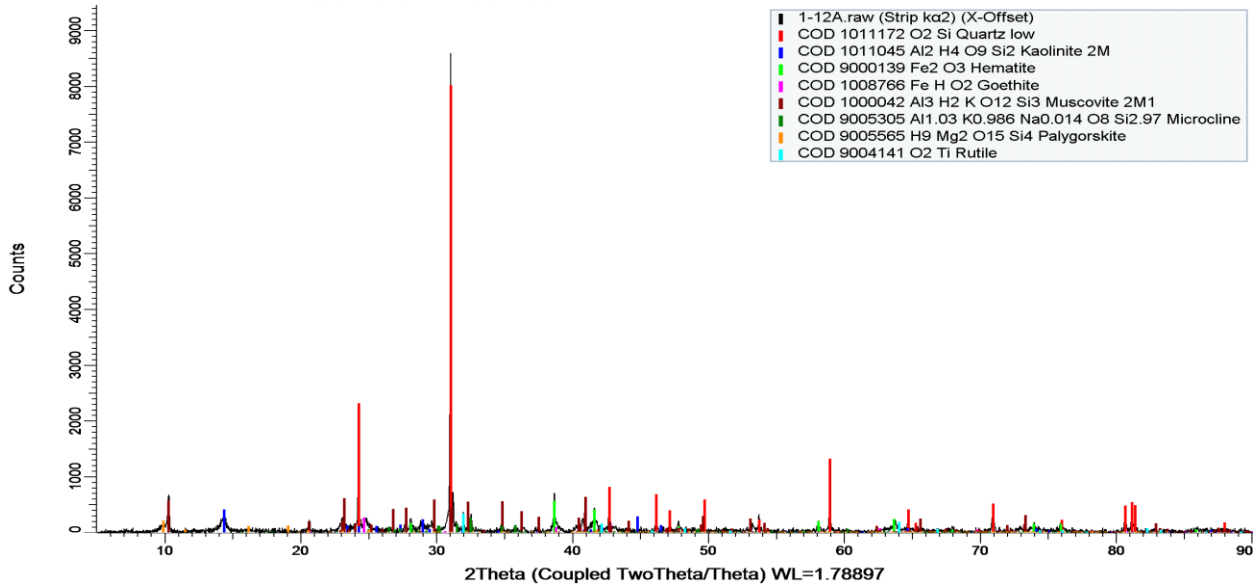
1-12A.raw (Strip kα2) (X-Offset)
COD 1011172 O2 Si Quartz low
COD 1011045 Al2 H4 O9 Si2 Kaolinite 2M
COD 9000139 Fe2 O3 Hematite
COD 1008766 Fe H O2 Goethite
COD 1000042 Al3 H2 K O12 Si3 Muscovite 2M1
COD 9005305 Al1.03 K0.986 Na0.014 O8 Si2.97 Microcline
COD 9005565 H9 Mg2 O15 Si4 Palygorskite
COD 9004141 O2 Ti Rutile
Counts
2Theta (Coupled TwoTheta/Theta) WL=1.78897

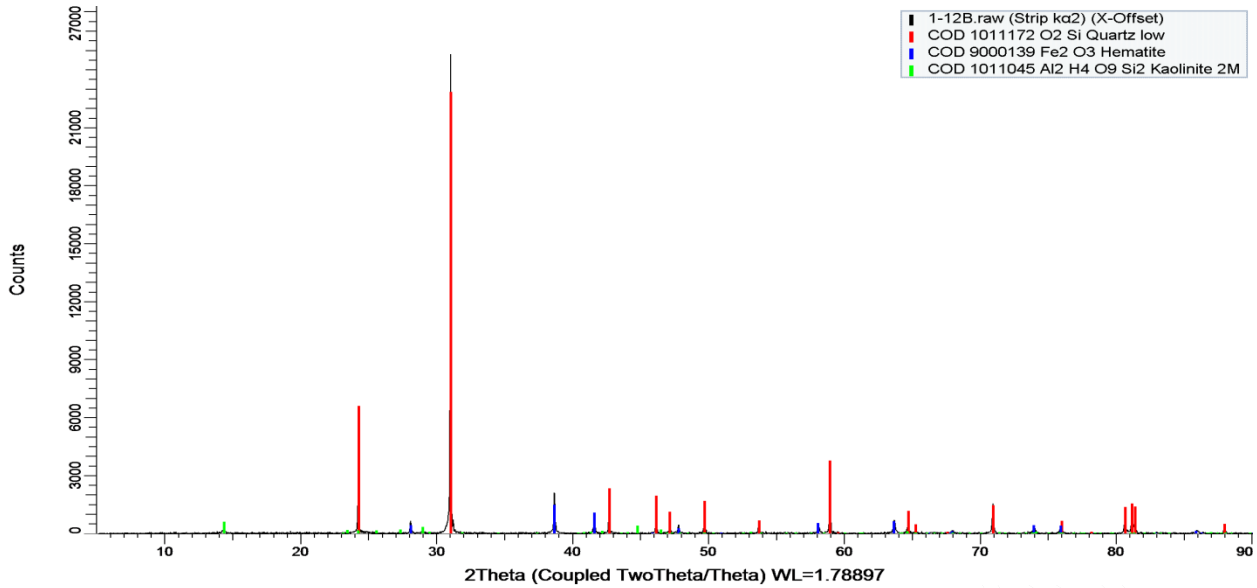
1-12B.raw (Strip kα2) (X-Offset)
COD 1011172 O2 Si Quartz low
COD 9000139 Fe2 O3 Hematite
COD 1011045 Al2 H4 O9 Si2 Kaolinite 2M
Counts
2Theta (Coupled TwoTheta/Theta) WL=1.78897

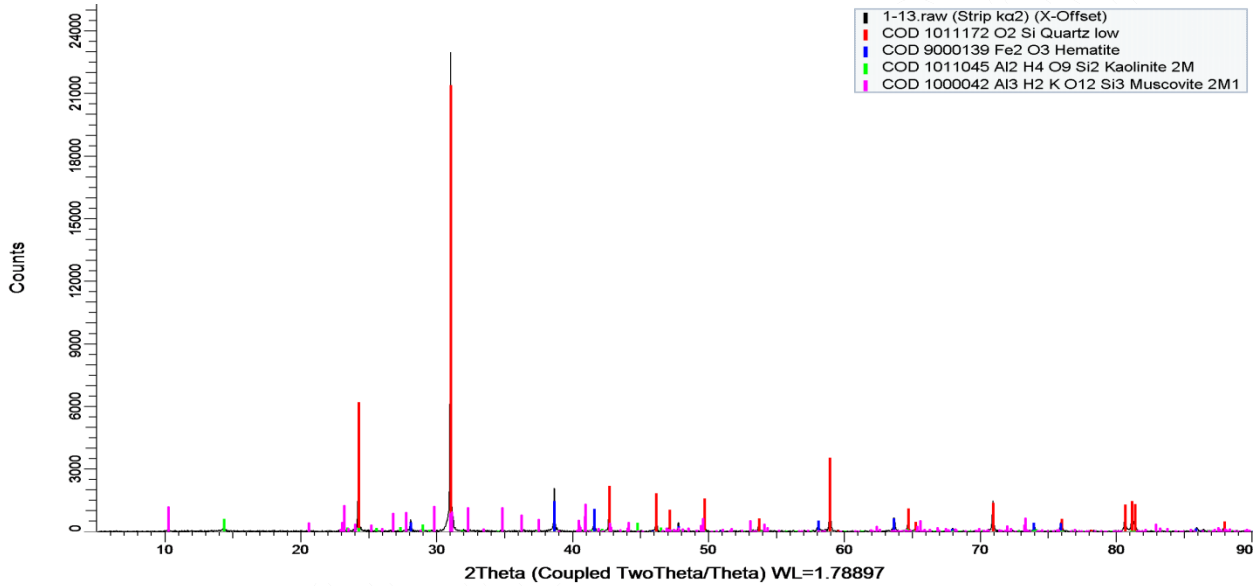
1-13.raw (Strip kα2) (X-Offset)
COD 1011172 O2 Si Quartz low
COD 9000139 Fe2 O3 Hematite
COD 1011045 Al2 H4 O9 Si2 Kaolinite 2M
COD 1000042 Al3 H2 K O12 Si3 Muscovite 2M1
Counts
2Theta (Coupled TwoTheta/Theta) WL=1.78897

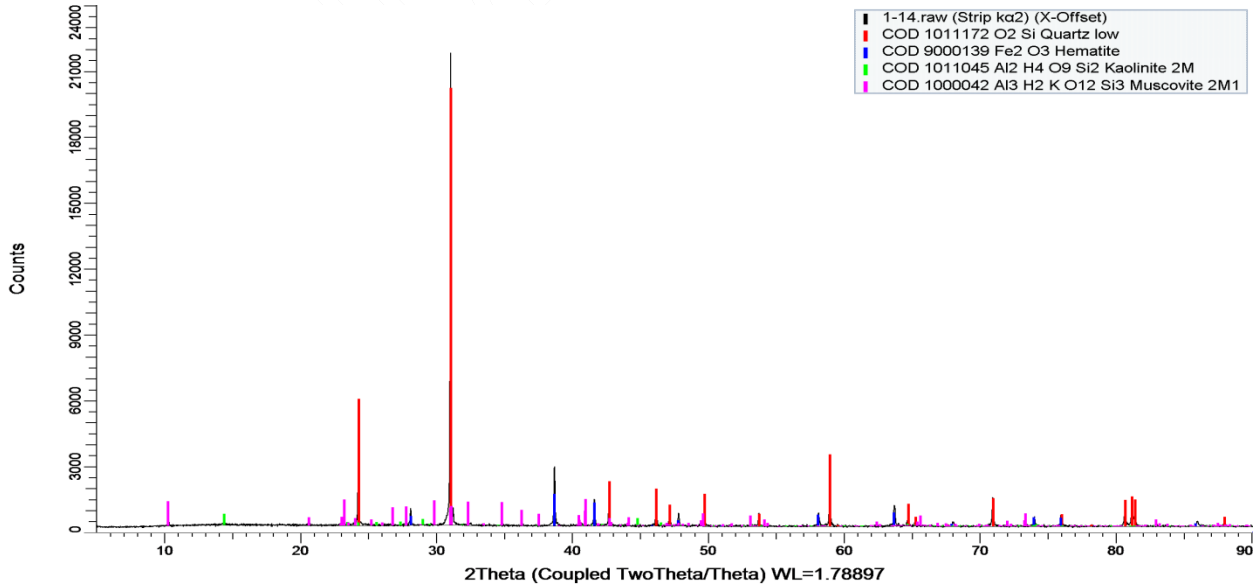
1-14.raw (Strip kα2) (X-Offset)
COD 1011172 O2 Si Quartz low
COD 9000139 Fe2 O3 Hematite
COD 1011045 Al2 H4 O9 Si2 Kaolinite 2M
COD 1000042 Al3 H2 K O12 Si3 Muscovite 2M1
Counts
2Theta (Coupled TwoTheta/Theta) WL=1.78897

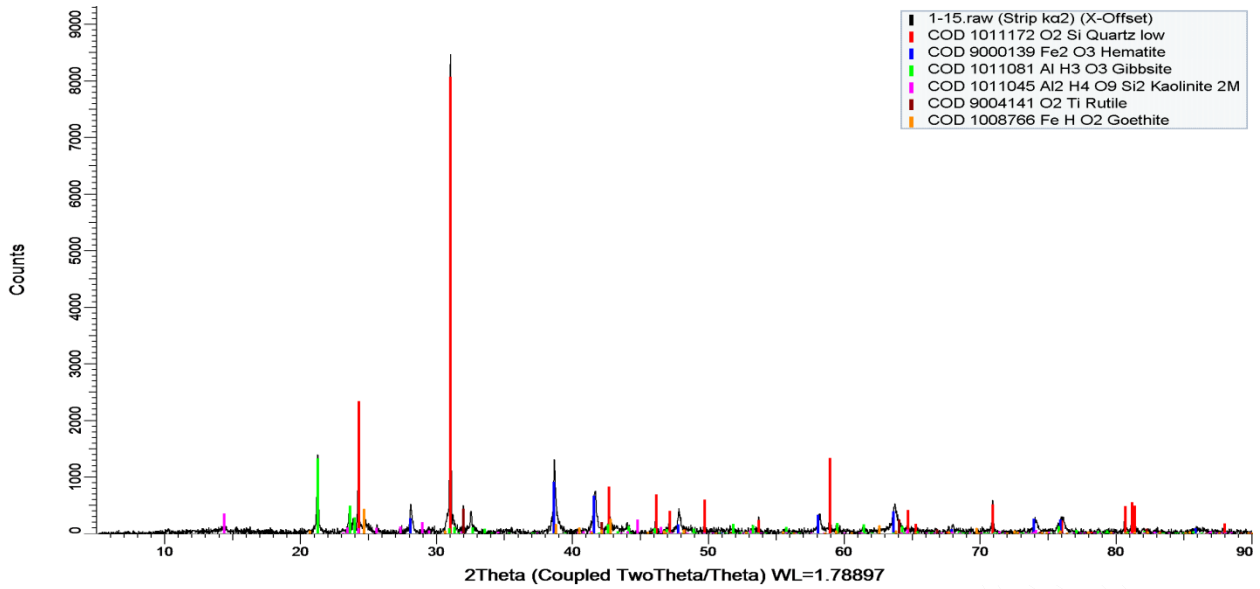
1-15.raw (Strip kα2) (X-Offset)
COD 1011172 O2 Si Quartz low
COD 9000139 Fe2 O3 Hematite
COD 1011081 Al H3 O3 Gibbsite
COD 1011045 Al2 H4 O9 Si2 Kaolinite 2M
COD 9004141 O2 Ti Rutile
COD 1008766 Fe H O2 Goethite
Counts
2Theta (Coupled TwoTheta/Theta) WL=1.78897

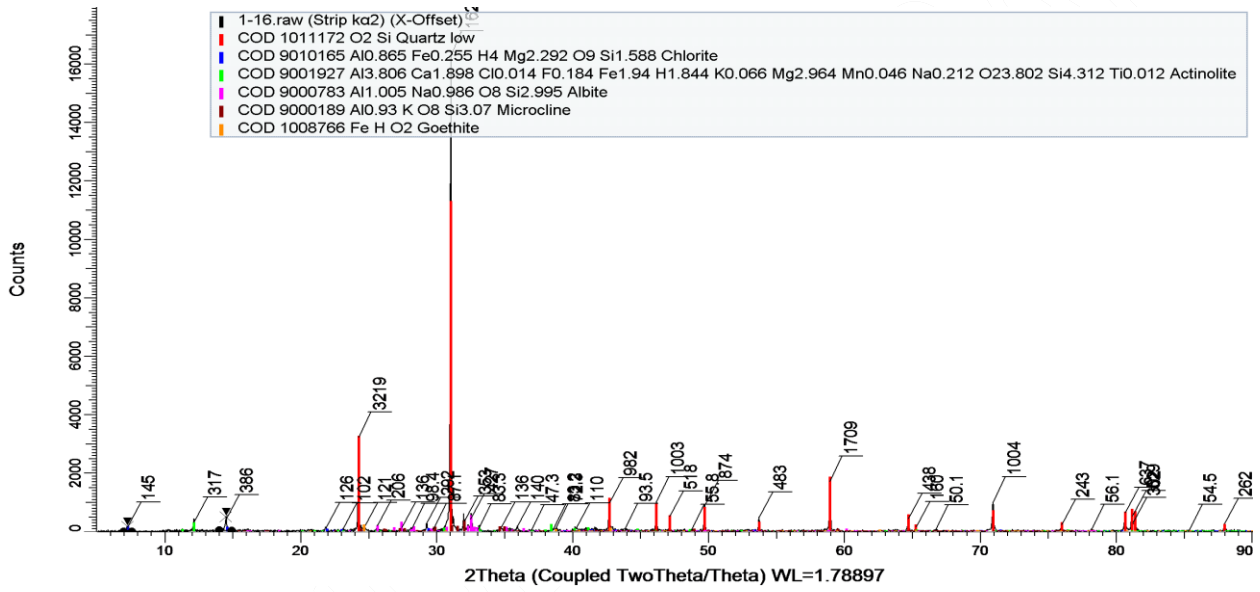
1-16.raw (Strip kα2) (X-Offset)
COD 1011172 O2 Si Quartz low
COD 9010165 Al0.865 Fe0.255 H4 Mg2.292 O9 Si1.588 Chlorite
COD 9001927 Al3.806 Ca1.898 Cl0.014 F0.184 Fe1.94 H1.844 K0.066 Mg2.964 Mn0.046 Na0.212 O23.802 Si4.312 Ti0.012 Actinolite
COD 9000783 Al1.005 Na0.986 O8 Si2.995 Albite
COD 9000189 Al0.93 K O8 Si3.07 Microcline
COD 1008766 Fe H O2 Goethite
Counts
2Theta (Coupled TwoTheta/Theta) WL=1.78897

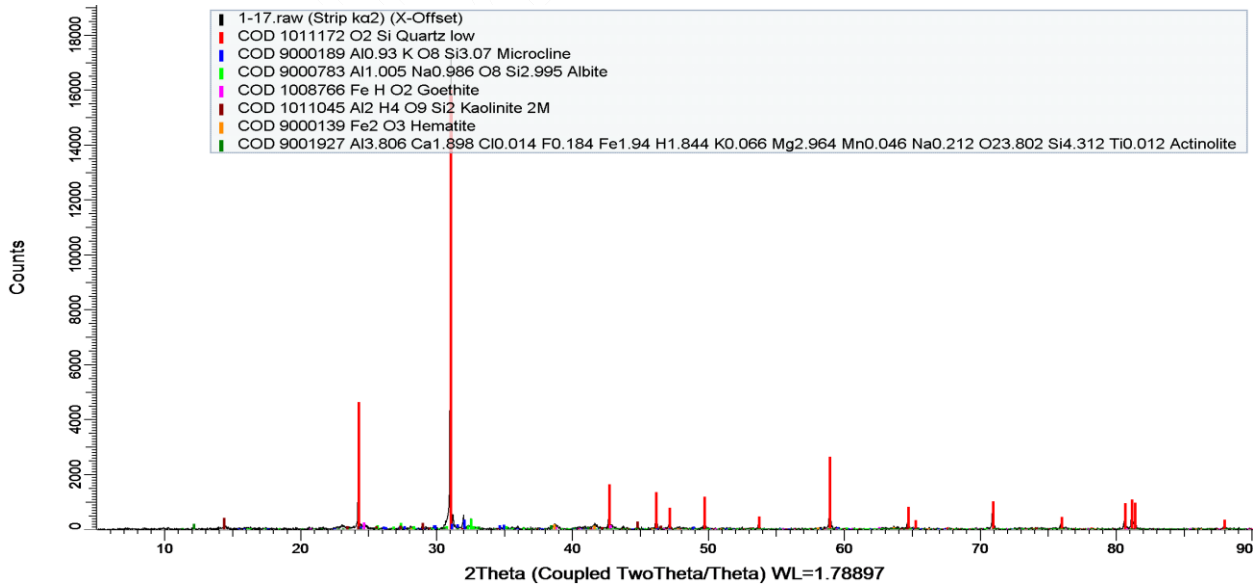
1-17.raw (Strip kα2) (X-Offset)
COD 1011172 O2 Si Quartz low
COD 9000189 Al0.93 K O8 Si3.07 Microcline
COD 9000783 Al1.005 Na0.986 O8 Si2.995 Albite
COD 1008766 Fe H O2 Goethite
COD 1011045 Al2 H4 O9 Si2 Kaolinite 2M
COD 9000139 Fe2 O3 Hematite
COD 9001927 Al3.806 Ca1.898 Cl0.014 F0.184 Fe1.94 H1.844 K0.066 Mg2.964 Mn0.046 Na0.212 O23.802 Si4.312 Ti0.012 Actinolite
Counts
2Theta (Coupled TwoTheta/Theta) WL=1.78897

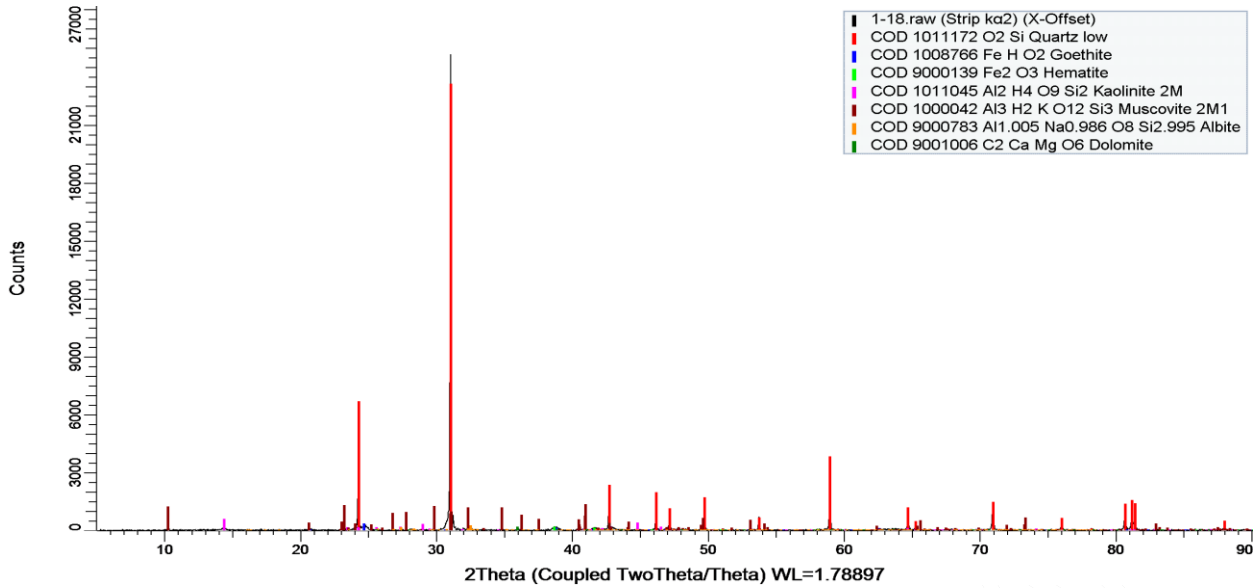
1-18.raw (Strip kα2) (X-Offset)
COD 1011172 O2 Si Quartz low
COD 1008766 Fe H O2 Goethite
COD 9000139 Fe2 O3 Hematite
COD 1011045 Al2 H4 O9 Si2 Kaolinite 2M
COD 1000042 Al3 H2 K O12 Si3 Muscovite 2M1
COD 9000783 Al1.005 Na0.986 O8 Si2.995 Albite
COD 9001006 C2 Ca Mg O6 Dolomite
Counts
2Theta (Coupled TwoTheta/Theta) WL=1.78897

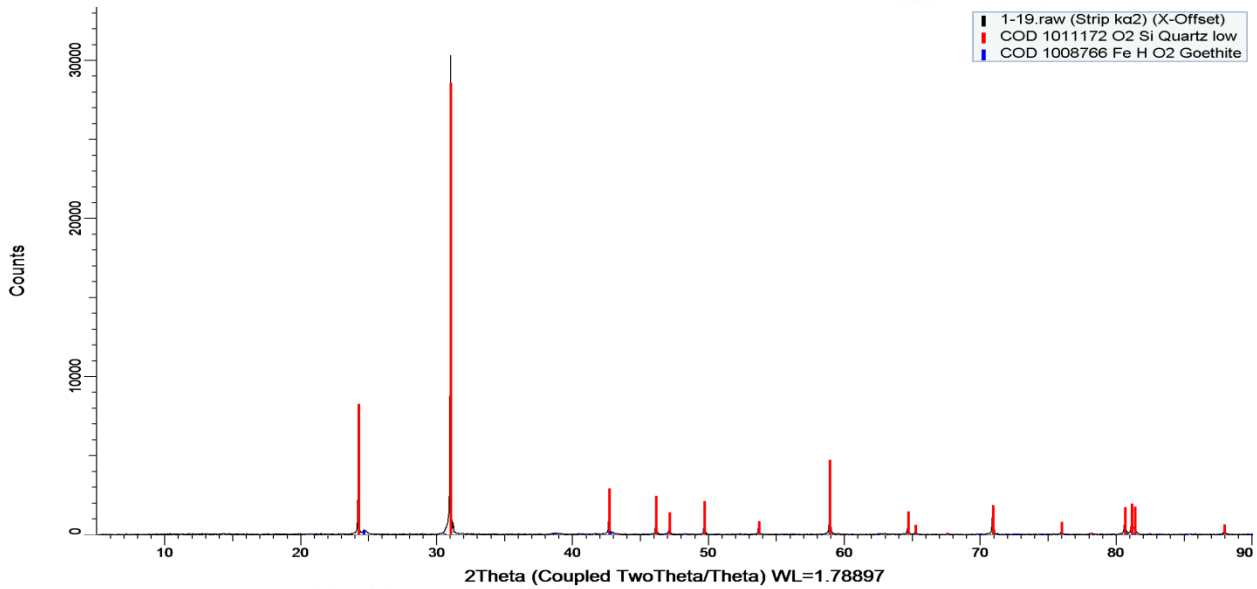
1-19.raw (Strip kα2) (X-Offset)
COD 1011172 O2 Si Quartz low
COD 1008766 Fe H O2 Goethite
Counts
2Theta (Coupled TwoTheta/Theta) WL=1.78897

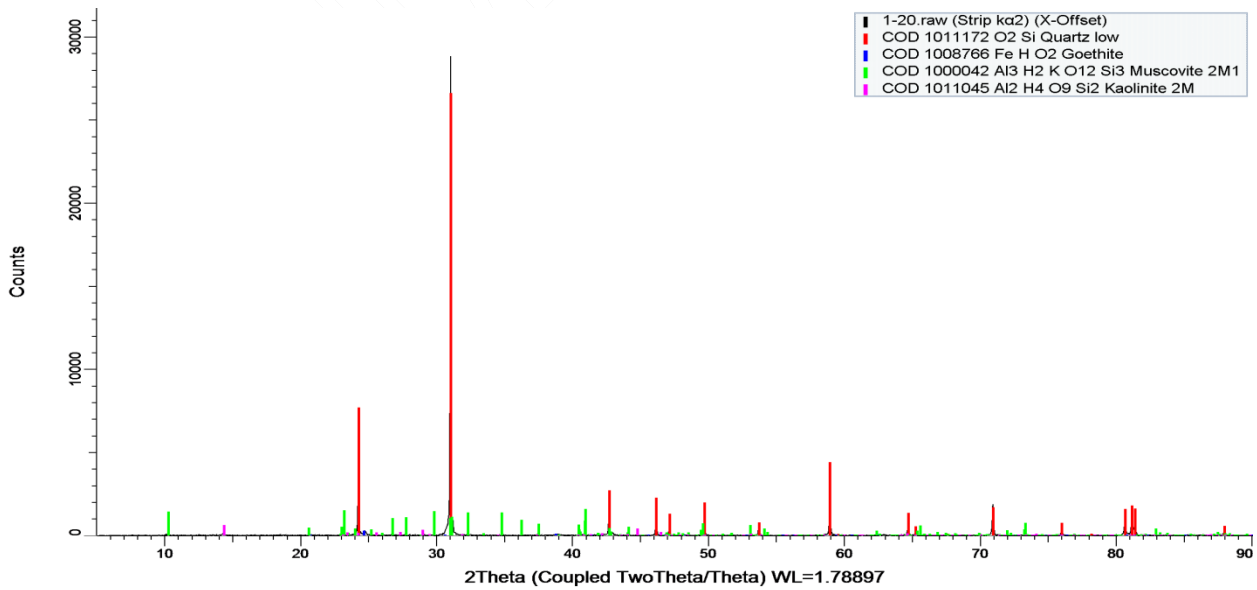
1-20.raw (Strip kα2) (X-Offset)
COD 1011172 O2 Si Quartz low
COD 1008766 Fe H O2 Goethite
COD 1000042 Al3 H2 K O12 Si3 Muscovite 2M1
COD 1011045 Al2 H4 O9 Si2 Kaolinite 2M
Counts
2Theta (Coupled TwoTheta/Theta) WL=1.78897

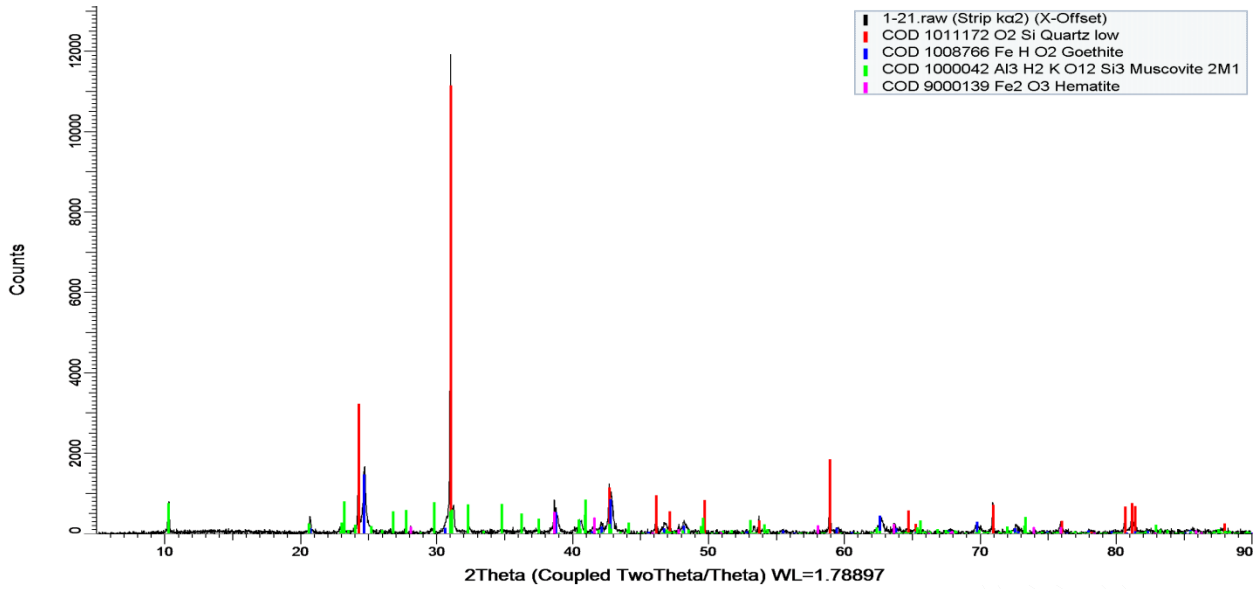
1-21.raw (Strip kα2) (X-Offset)
COD 1011172 O2 Si Quartz low
COD 1008766 Fe H O2 Goethite
COD 1000042 Al3 H2 K O12 Si3 Muscovite 2M1
COD 9000139 Fe2 O3 Hematite
Counts
2Theta (Coupled TwoTheta/Theta) WL=1.78897

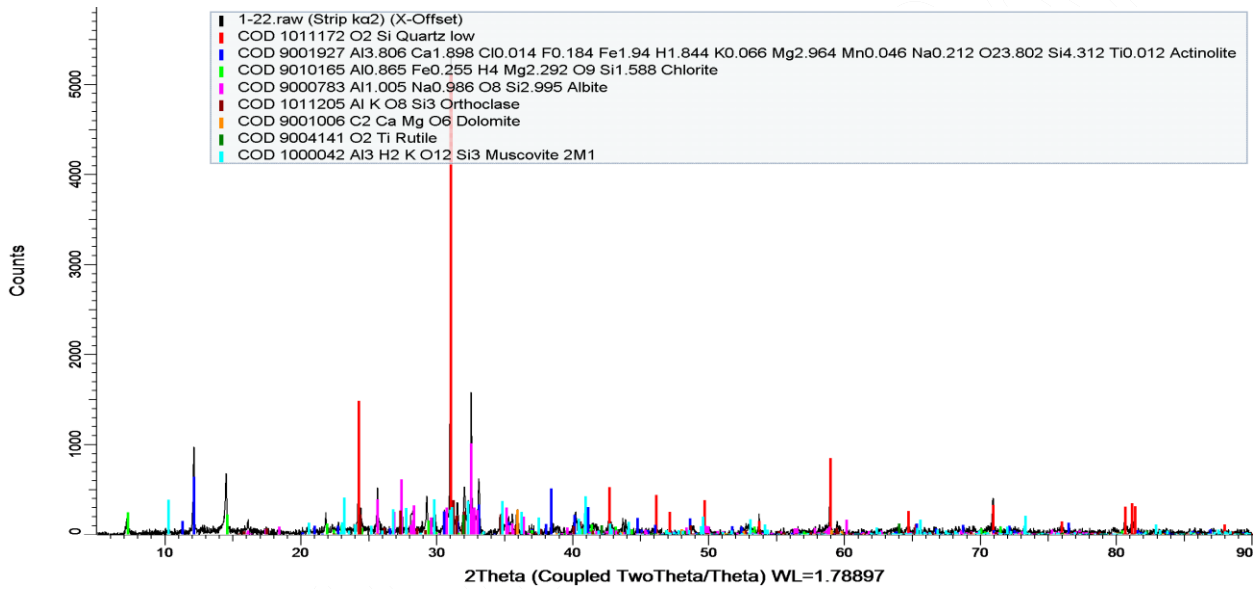
1-22.raw (Strip kα2) (X-Offset)
COD 1011172 O2 Si Quartz low
COD 9001927 Al3.806 Ca1.898 Cl0.014 F0.184 Fe1.94 H1.844 K0.066 Mg2.964 Mn0.046 Na0.212 O23.802 Si4.312 Ti0.012 Actinolite
COD 9010165 Al0.865 Fe0.255 H4 Mg2.292 O9 Si1.588 Chlorite
COD 9000783 Al1.005 Na0.986 O8 Si2.995 Albite
COD 1011205 Al K O8 Si3 Orthoclase
COD 9001006 C2 Ca Mg O6 Dolomite
COD 9004141 O2 Ti Rutile
COD 1000042 Al3 H2 K O12 Si3 Muscovite 2M1
Counts
2Theta (Coupled TwoTheta/Theta) WL=1.78897

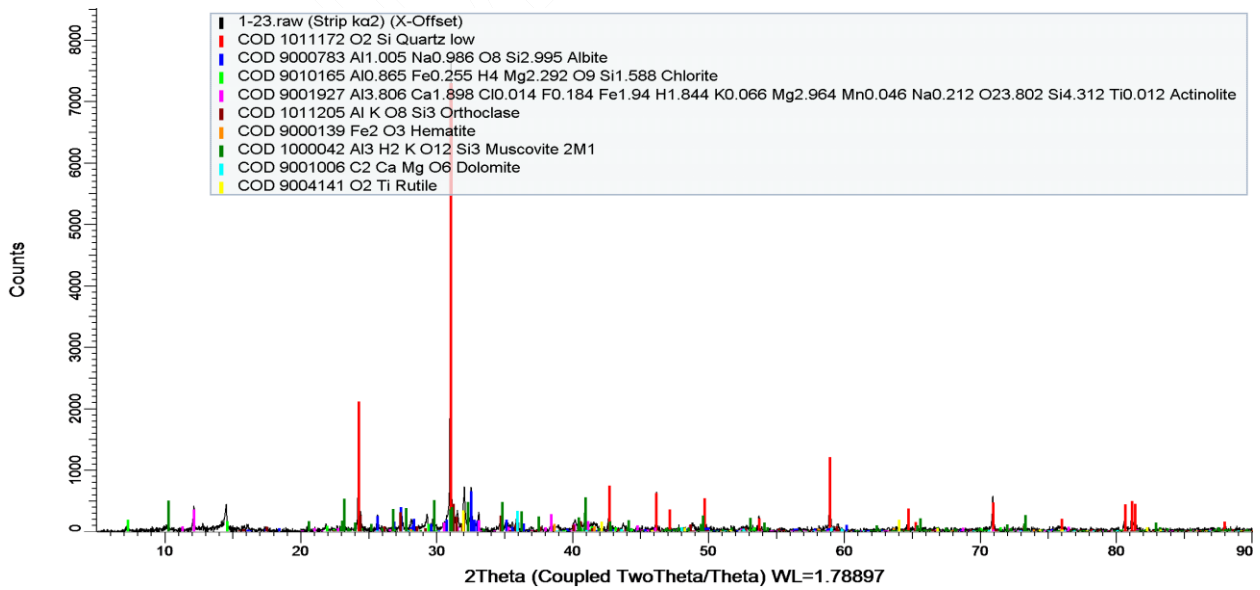
1-23.raw (Strip kα2) (X-Offset)
COD 1011172 O2 Si Quartz low
COD 9000783 Al1.005 Na0.986 O8 Si2.995 Albite
COD 9010165 Al0.865 Fe0.255 H4 Mg2.292 O9 Si1.588 Chlorite
COD 9001927 Al3.806 Ca1.898 Cl0.014 F0.184 Fe1.94 H1.844 K0.066 Mg2.964 Mn0.046 Na0.212 O23.802 Si4.312 Ti0.012 Actinolite
COD 1011205 Al K O8 Si3 Orthoclase
COD 9000139 Fe2 O3 Hematite
COD 1000042 Al3 H2 K O12 Si3 Muscovite 2M1
COD 9001006 C2 Ca Mg O6 Dolomite
COD 9004141 O2 Ti Rutile
Counts
2Theta (Coupled TwoTheta/Theta) WL=1.78897

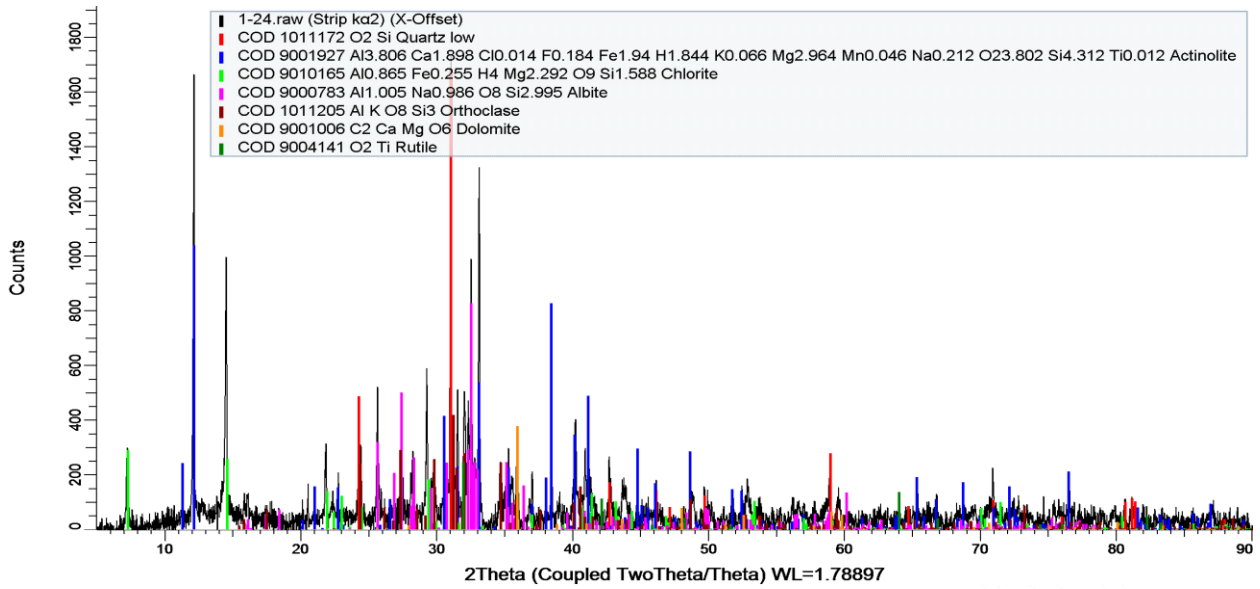
1-24.raw (Strip kα2) (X-Offset)
COD 1011172 O2 Si Quartz low
COD 9001927 Al3.806 Ca1.898 Cl0.014 F0.184 Fe1.94 H1.844 K0.066 Mg2.964 Mn0.046 Na0.212 O23.802 Si4.312 Ti0.012 Actinolite
COD 9010165 Al0.865 Fe0.255 H4 Mg2.292 O9 Si1.588 Chlorite
COD 9000783 Al1.005 Na0.986 O8 Si2.995 Albite
COD 1011205 Al K O8 Si3 Orthoclase
COD 9001006 C2 Ca Mg O6 Dolomite
COD 9004141 O2 Ti Rutile
Counts
2Theta (Coupled TwoTheta/Theta) WL=1.78897

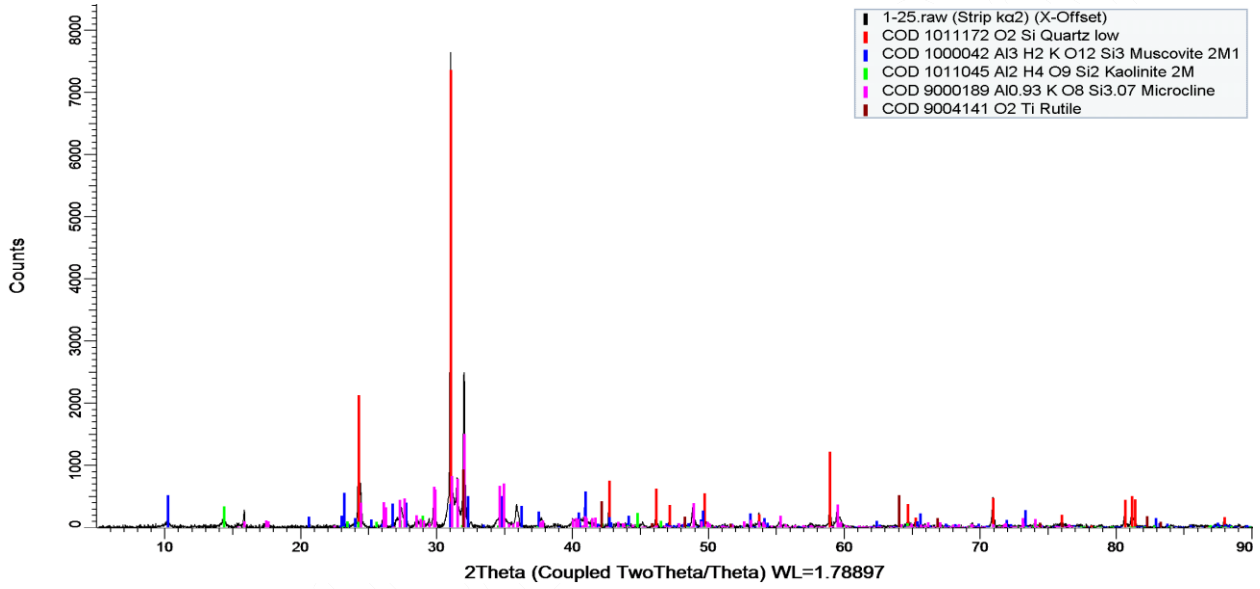
1-25.raw (Strip kα2) (X-Offset)
COD 1011172 O2 Si Quartz low
COD 1000042 Al3 H2 K O12 Si3 Muscovite 2M1
COD 1011045 Al2 H4 O9 Si2 Kaolinite 2M
COD 9000189 Al0.93 K O8 Si3.07 Microcline
COD 9004141 O2 Ti Rutile
Counts
2Theta (Coupled TwoTheta/Theta) WL=1.78897

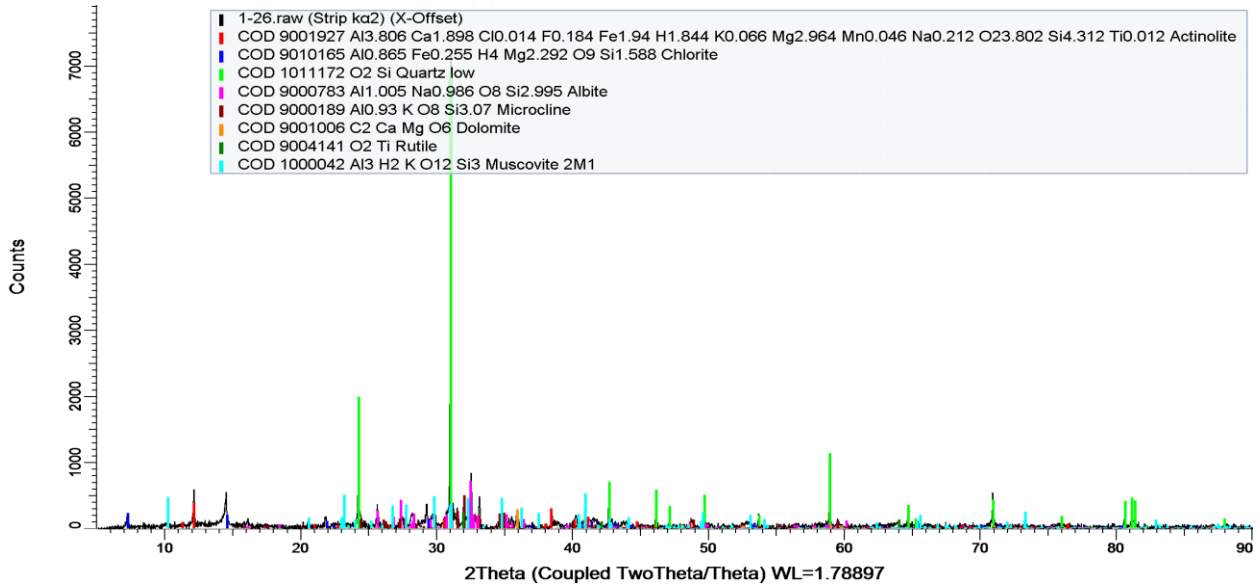
1-26.raw (Strip kα2) (X-Offset)
COD 9001927 Al3.806 Ca1.898 Cl0.014 F0.184 Fe1.94 H1.844 K0.066 Mg2.964 Mn0.046 Na0.212 O23.802 Si4.312 Ti0.012 Actinolite
COD 9010165 Al0.865 Fe0.255 H4 Mg2.292 O9 Si1.588 Chlorite
COD 1011172 O2 Si Quartz low
COD 9000783 Al1.005 Na0.986 O8 Si2.995 Albite
COD 9000189 Al0.93 K O8 Si3.07 Microcline
COD 9001006 C2 Ca Mg O6 Dolomite
COD 9004141 O2 Ti Rutile
COD 1000042 Al3 H2 K O12 Si3 Muscovite 2M1
Counts
2Theta (Coupled TwoTheta/Theta) WL=1.78897

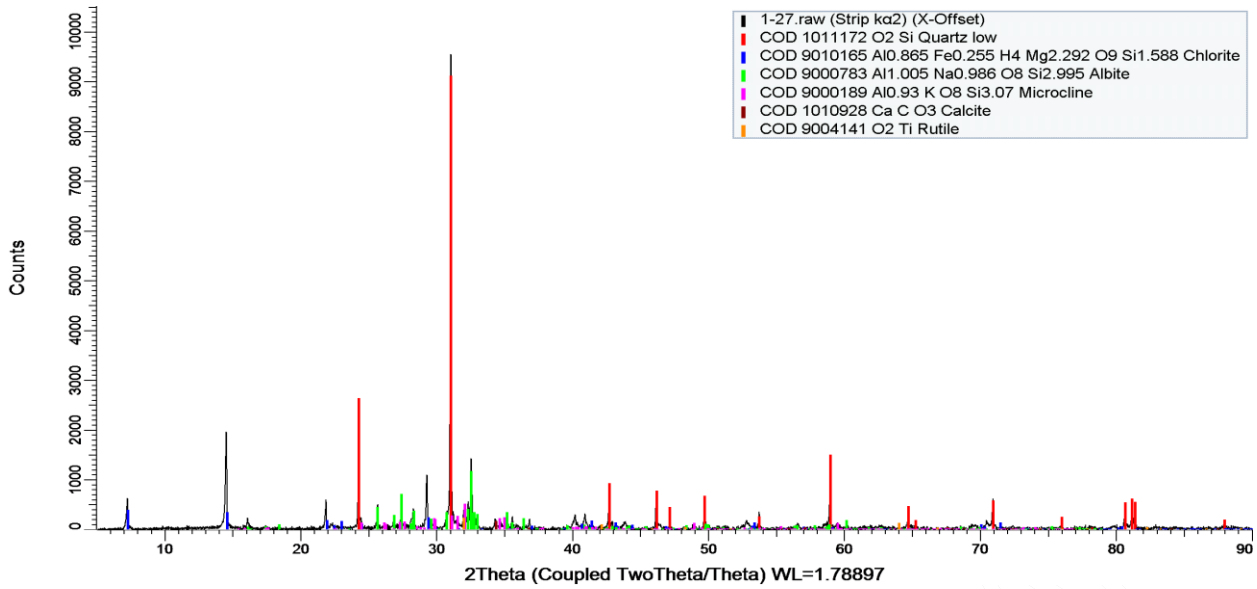
1-27.raw (Strip kα2) (X-Offset)
COD 1011172 O2 Si Quartz low
COD 9010165 Al0.865 Fe0.255 H4 Mg2.292 O9 Si1.588 Chlorite
COD 9000783 Al1.005 Na0.986 O8 Si2.995 Albite
COD 9000189 Al0.93 K O8 Si3.07 Microcline
COD 1010928 Ca C O3 Calcite
COD 9004141 O2 Ti Rutile
Counts
2Theta (Coupled TwoTheta/Theta) WL=1.78897

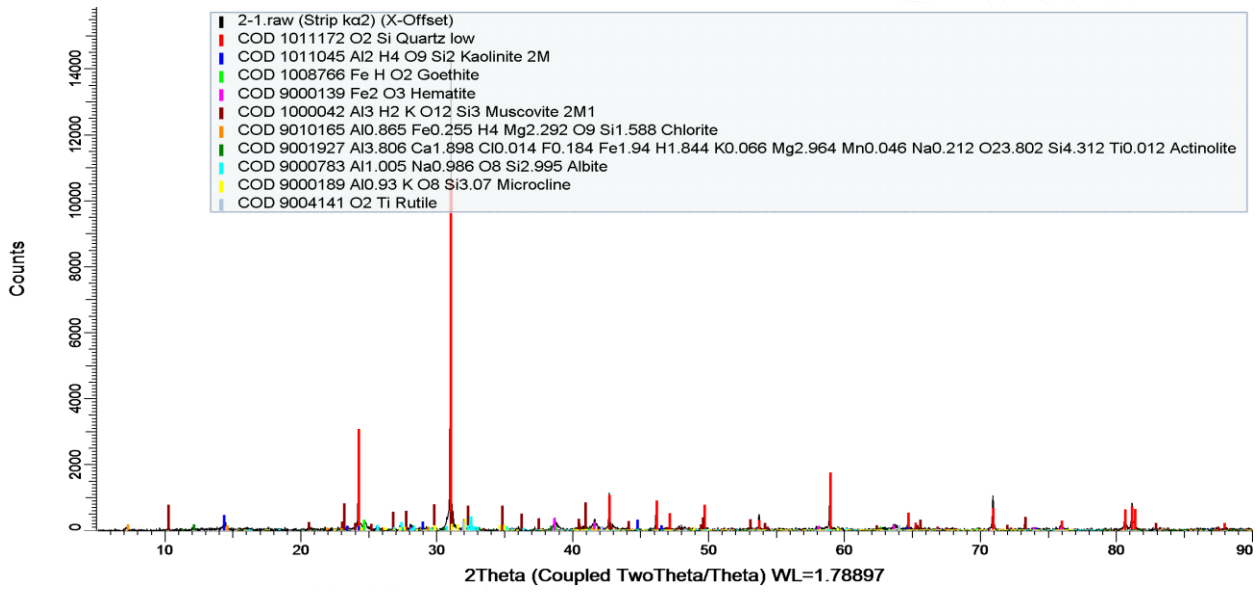
2-1.raw (Strip kα2) (X-Offset)
COD 1011172 O2 Si Quartz low
COD 1011045 Al2 H4 O9 Si2 Kaolinite 2M
COD 1008766 Fe H O2 Goethite
COD 9000139 Fe2 O3 Hematite
COD 1000042 Al3 H2 K O12 Si3 Muscovite 2M1
COD 9010165 Al0.865 Fe0.255 H4 Mg2.292 O9 Si1.588 Chlorite
COD 9001927 Al3.806 Ca1.898 Cl0.014 F0.184 Fe1.94 H1.844 K0.066 Mg2.964 Mn0.046 Na0.212 O23.802 Si4.312 Ti0.012 Actinolite
COD 9000783 Al1.005 Na0.986 O8 Si2.995 Albite
COD 9000189 Al0.93 K O8 Si3.07 Microcline
COD 9004141 O2 Ti Rutile
Counts
2Theta (Coupled TwoTheta/Theta) WL=1.78897

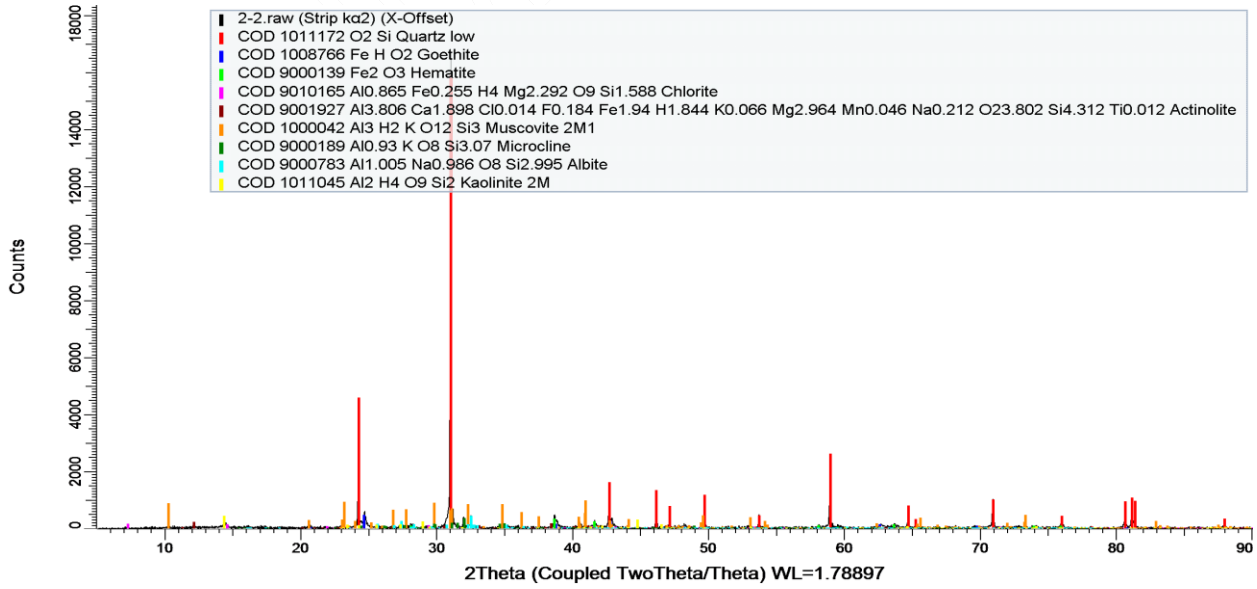
2-2.raw (Strip kα2) (X-Offset)
COD 1011172 O2 Si Quartz low
COD 1008766 Fe H O2 Goethite
COD 9000139 Fe2 O3 Hematite
COD 9010165 Al0.865 Fe0.255 H4 Mg2.292 O9 Si1.588 Chlorite
COD 9001927 Al3.806 Ca1.898 Cl0.014 F0.184 Fe1.94 H1.844 K0.066 Mg2.964 Mn0.046 Na0.212 O23.802 Si4.312 Ti0.012 Actinolite
COD 1000042 Al3 H2 K O12 Si3 Muscovite 2M1
COD 9000189 Al0.93 K O8 Si3.07 Microcline
COD 9000783 Al1.005 Na0.986 O8 Si2.995 Albite
COD 1011045 Al2 H4 O9 Si2 Kaolinite 2M
Counts
2Theta (Coupled TwoTheta/Theta) WL=1.78897

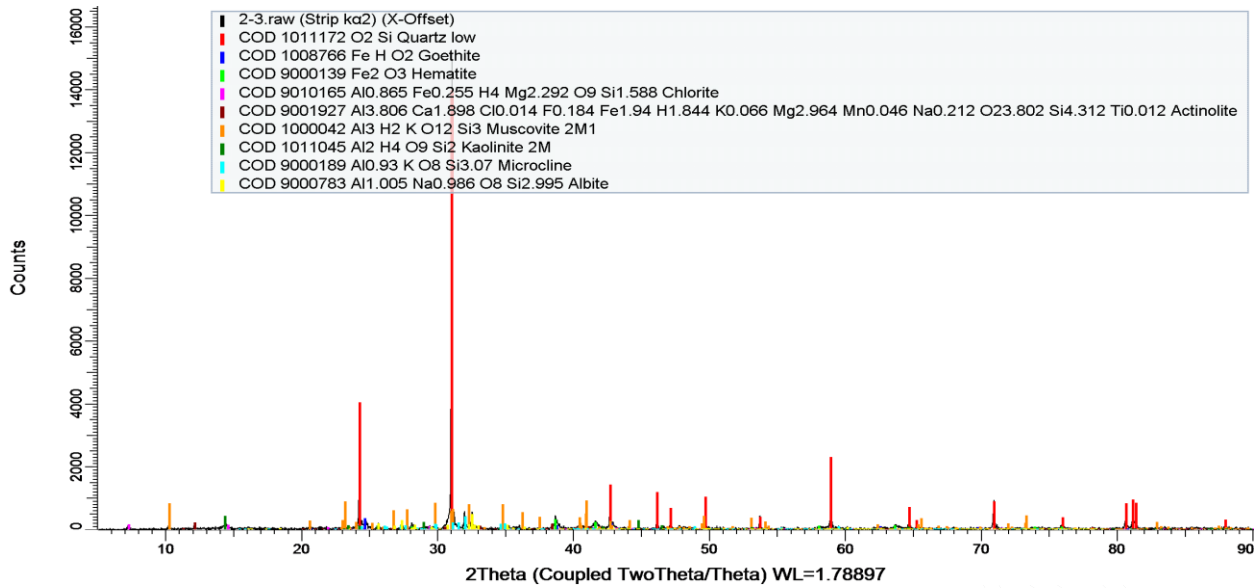
2-3.raw (Strip kα2) (X-Offset)
COD 1011172 O2 Si Quartz low
COD 1008766 Fe H O2 Goethite
COD 9000139 Fe2 O3 Hematite
COD 9010165 Al0.865 Fe0.255 H4 Mg2.292 O9 Si1.588 Chlorite
COD 9001927 Al3.806 Ca1.898 Cl0.014 F0.184 Fe1.94 H1.844 K0.066 Mg2.964 Mn0.046 Na0.212 O23.802 Si4.312 Ti0.012 Actinolite
COD 1000042 Al3 H2 K O12 Si3 Muscovite 2M1
COD 1011045 Al2 H4 O9 Si2 Kaolinite 2M
COD 9000189 Al0.93 K O8 Si3.07 Microcline
COD 9000783 Al1.005 Na0.986 O8 Si2.995 Albite
Counts
2Theta (Coupled TwoTheta/Theta) WL=1.78897

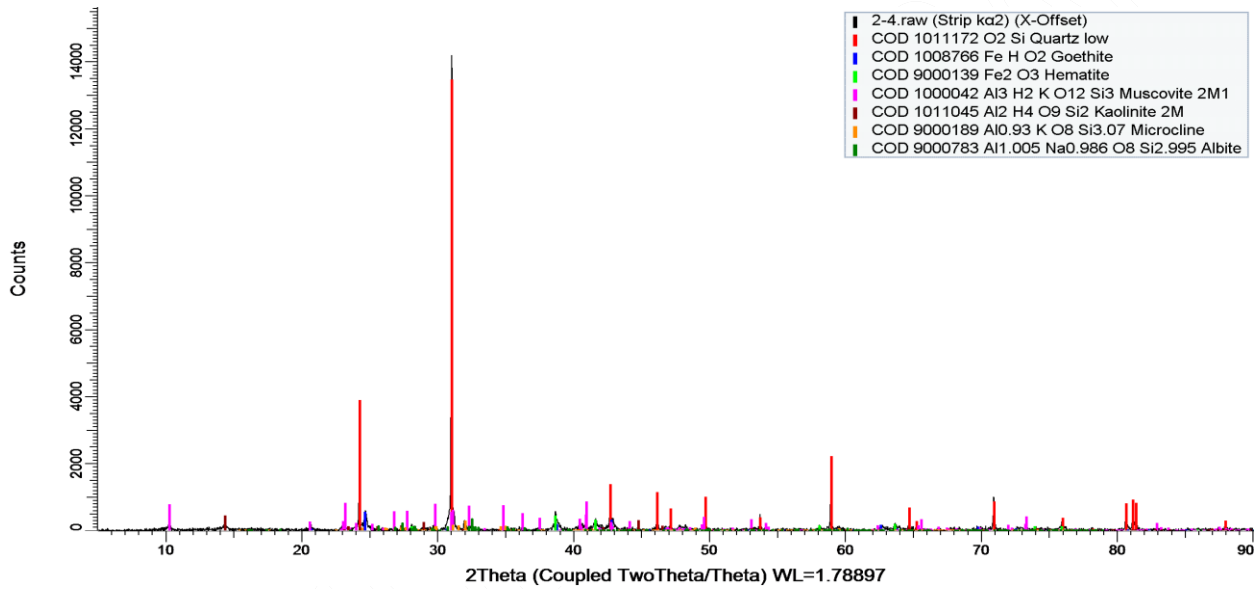
2-4.raw (Strip kα2) (X-Offset)
COD 1011172 O2 Si Quartz low
COD 1008766 Fe H O2 Goethite
COD 9000139 Fe2 O3 Hematite
COD 1000042 Al3 H2 K O12 Si3 Muscovite 2M1
COD 1011045 Al2 H4 O9 Si2 Kaolinite 2M
COD 9000189 Al0.93 K O8 Si3.07 Microcline
COD 9000783 Al1.005 Na0.986 O8 Si2.995 Albite
Counts
2Theta (Coupled TwoTheta/Theta) WL=1.78897

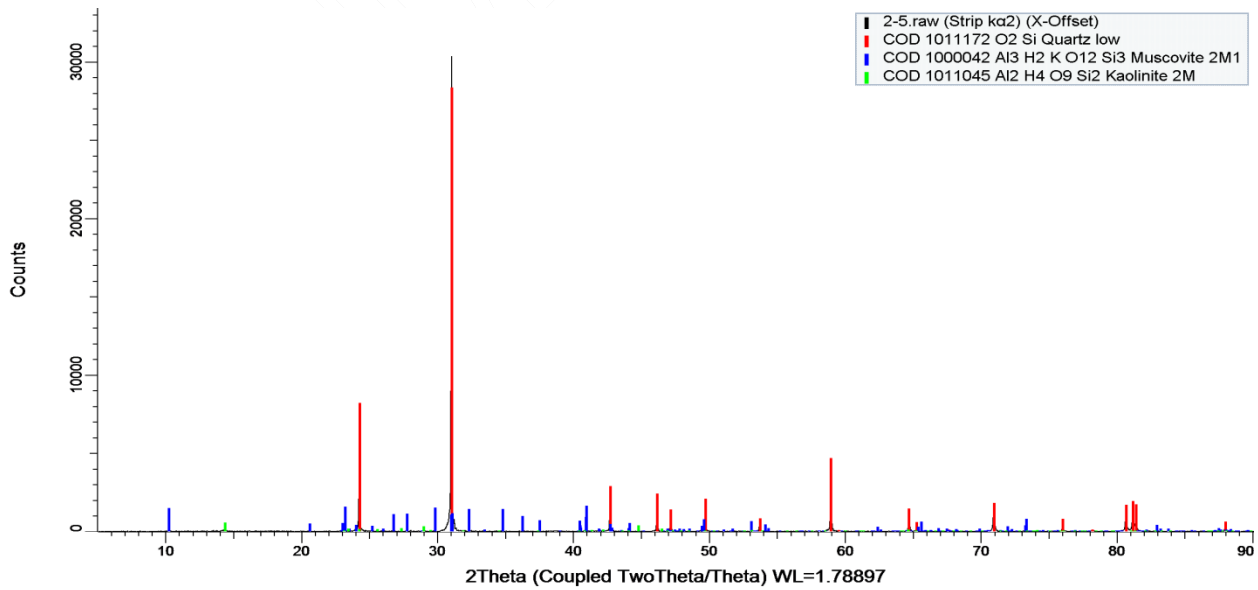
2-5.raw (Strip kα2) (X-Offset)
COD 1011172 O2 Si Quartz low
COD 1000042 Al3 H2 K O12 Si3 Muscovite 2M1
COD 1011045 Al2 H4 O9 Si2 Kaolinite 2M
Counts
2Theta (Coupled TwoTheta/Theta) WL=1.78897

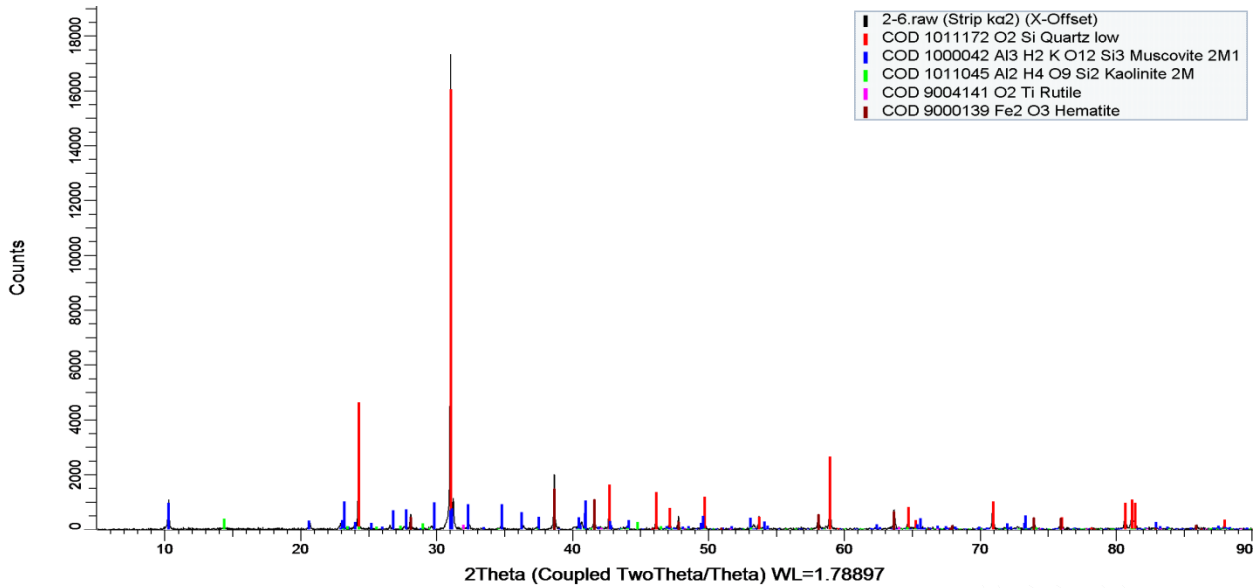
2-6.raw (Strip kα2) (X-Offset)
COD 1011172 O2 Si Quartz low
COD 1000042 Al3 H2 K O12 Si3 Muscovite 2M1
COD 1011045 Al2 H4 O9 Si2 Kaolinite 2M
COD 9004141 O2 Ti Rutile
COD 9000139 Fe2 O3 Hematite
Counts
2Theta (Coupled TwoTheta/Theta) WL=1.78897

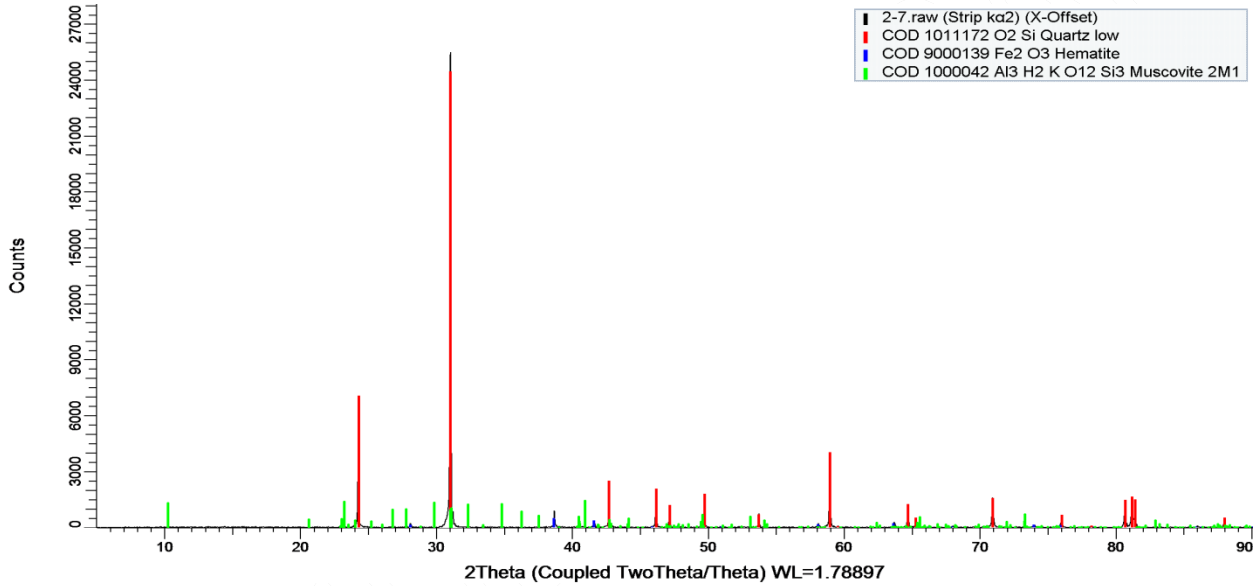
2-7.raw (Strip kα2) (X-Offset)
COD 1011172 O2 Si Quartz low
COD 9000139 Fe2 O3 Hematite
COD 1000042 Al3 H2 K O12 Si3 Muscovite 2M1
Counts
2Theta (Coupled TwoTheta/Theta) WL=1.78897

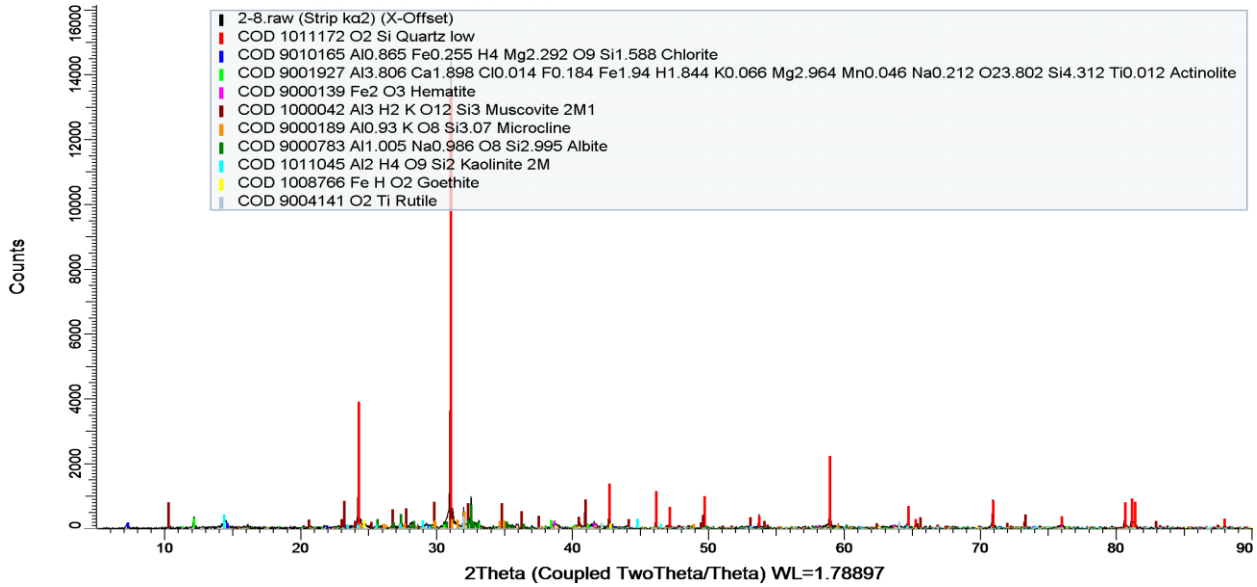
2-8.raw (Strip kα2) (X-Offset)
COD 1011172 O2 Si Quartz low
COD 9010165 Al0.865 Fe0.255 H4 Mg2.292 O9 Si1.588 Chlorite
COD 9001927 Al3.806 Ca1.898 Cl0.014 F0.184 Fe1.94 H1.844 K0.066 Mg2.964 Mn0.046 Na0.212 O23.802 Si4.312 Ti0.012 Actinolite
COD 9000139 Fe2 O3 Hematite
COD 1000042 Al3 H2 K O12 Si3 Muscovite 2M1
COD 9000189 Al0.93 K O8 Si3.07 Microcline
COD 9000783 Al1.005 Na0.986 O8 Si2.995 Albite
COD 1011045 Al2 H4 O9 Si2 Kaolinite 2M
COD 1008766 Fe H O2 Goethite
COD 9004141 O2 Ti Rutile
Counts
2Theta (Coupled TwoTheta/Theta) WL=1.78897

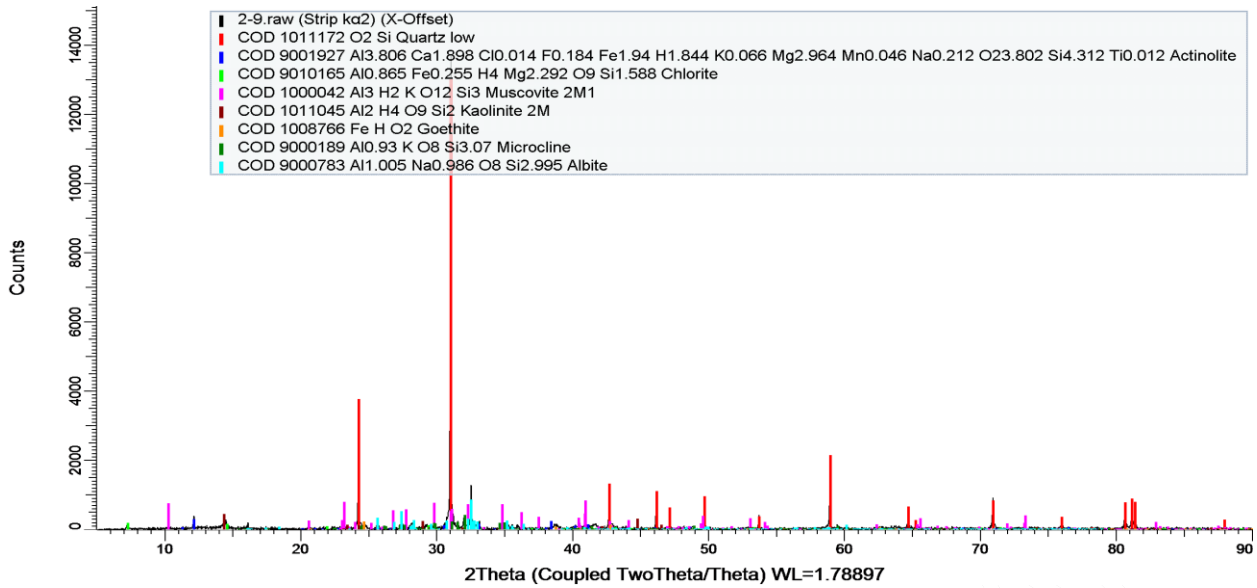
2-9.raw (Strip kα2) (X-Offset)
COD 1011172 O2 Si Quartz low
COD 9001927 Al3.806 Ca1.898 Cl0.014 F0.184 Fe1.94 H1.844 K0.066 Mg2.964 Mn0.046 Na0.212 O23.802 Si4.312 Ti0.012 Actinolite
COD 9010165 Al0.865 Fe0.255 H4 Mg2.292 O9 Si1.588 Chlorite
COD 1000042 Al3 H2 K O12 Si3 Muscovite 2M1
COD 1011045 Al2 H4 O9 Si2 Kaolinite 2M
COD 1008766 Fe H O2 Goethite
COD 9000189 Al0.93 K O8 Si3.07 Microcline
COD 9000783 Al1.005 Na0.986 O8 Si2.995 Albite
Counts
2Theta (Coupled TwoTheta/Theta) WL=1.78897

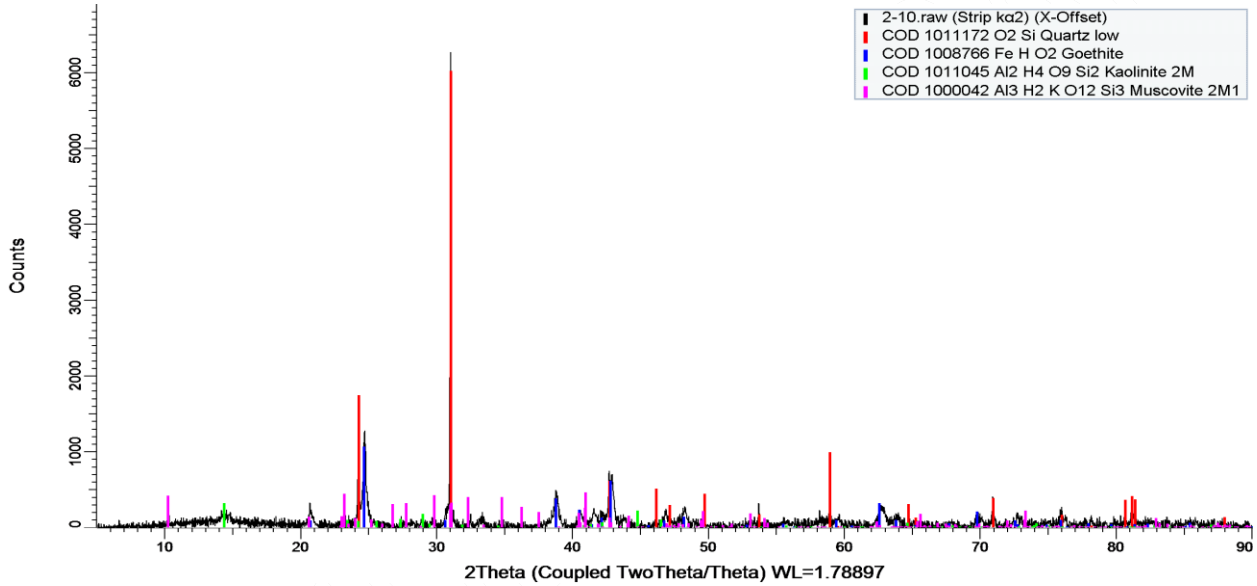
2-10.raw (Strip kα2) (X-Offset)
COD 1011172 O2 Si Quartz low
COD 1008766 Fe H O2 Goethite
COD 1011045 Al2 H4 O9 Si2 Kaolinite 2M
COD 1000042 Al3 H2 K O12 Si3 Muscovite 2M1
Counts
2Theta (Coupled TwoTheta/Theta) WL=1.78897

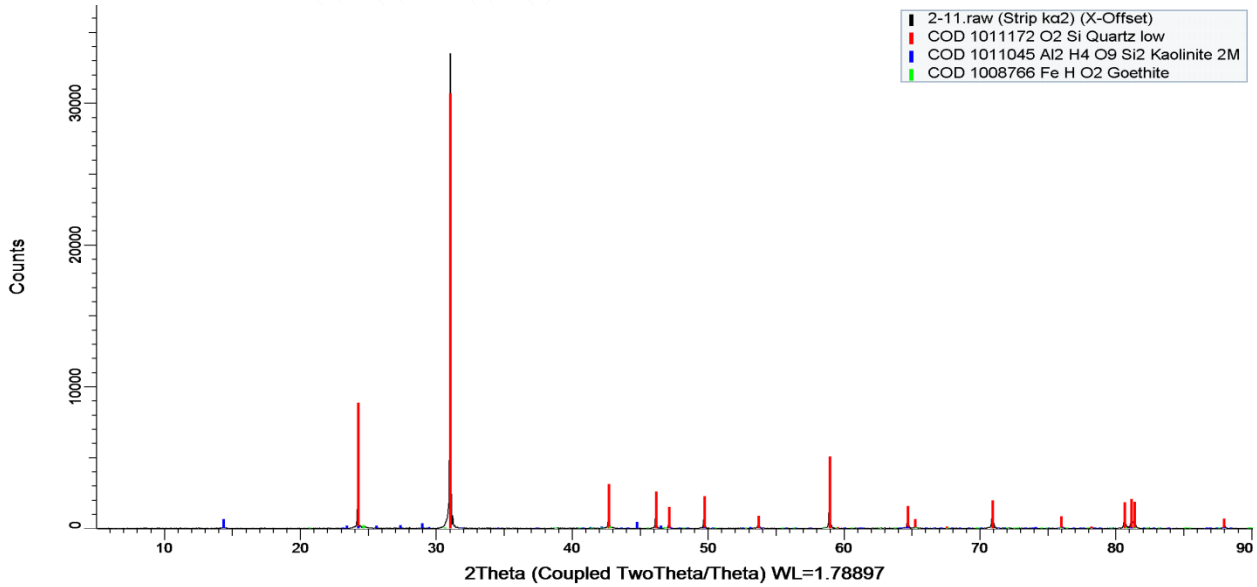
2-11.raw (Strip kα2) (X-Offset)
COD 1011172 O2 Si Quartz low
COD 1011045 Al2 H4 O9 Si2 Kaolinite 2M
COD 1008766 Fe H O2 Goethite
Counts
2Theta (Coupled TwoTheta/Theta) WL=1.78897

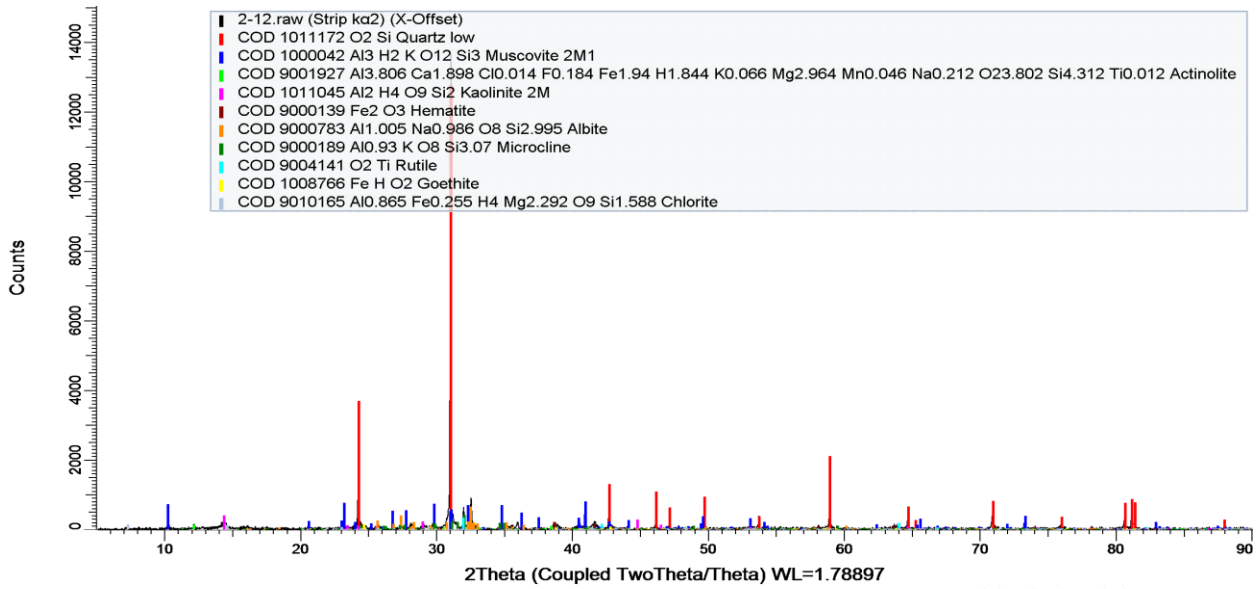
2-12.raw (Strip kα2) (X-Offset)
COD 1011172 O2 Si Quartz low
COD 1000042 Al3 H2 K O12 Si3 Muscovite 2M1
COD 9001927 Al3.806 Ca1.898 Cl0.014 F0.184 Fe1.94 H1.844 K0.066 Mg2.964 Mn0.046 Na0.212 O23.802 Si4.312 Ti0.012 Actinolite
COD 1011045 Al2 H4 O9 Si2 Kaolinite 2M
COD 9000139 Fe2 O3 Hematite
COD 9000783 Al1.005 Na0.986 O8 Si2.995 Albite
COD 9000189 Al0.93 K O8 Si3.07 Microcline
COD 9004141 O2 Ti Rutile
COD 1008766 Fe H O2 Goethite
COD 9010165 Al0.865 Fe0.255 H4 Mg2.292 O9 Si1.588 Chlorite
Counts
2Theta (Coupled TwoTheta/Theta) WL=1.78897

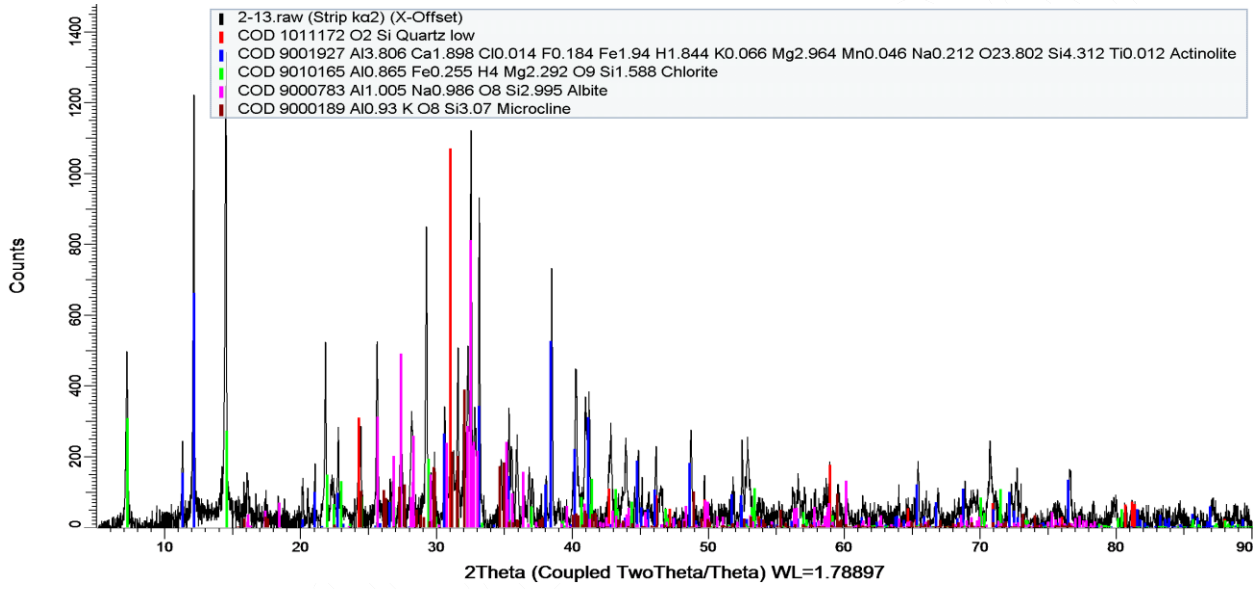
2-13.raw (Strip kα2) (X-Offset)
COD 1011172 O2 Si Quartz low
COD 9001927 Al3.806 Ca1.898 Cl0.014 F0.184 Fe1.94 H1.844 K0.066 Mg2.964 Mn0.046 Na0.212 O23.802 Si4.312 Ti0.012 Actinolite
COD 9010165 Al0.865 Fe0.255 H4 Mg2.292 O9 Si1.588 Chlorite
COD 9000783 Al1.005 Na0.986 O8 Si2.995 Albite
COD 9000189 Al0.93 K O8 Si3.07 Microcline
Counts
2Theta (Coupled TwoTheta/Theta) WL=1.78897

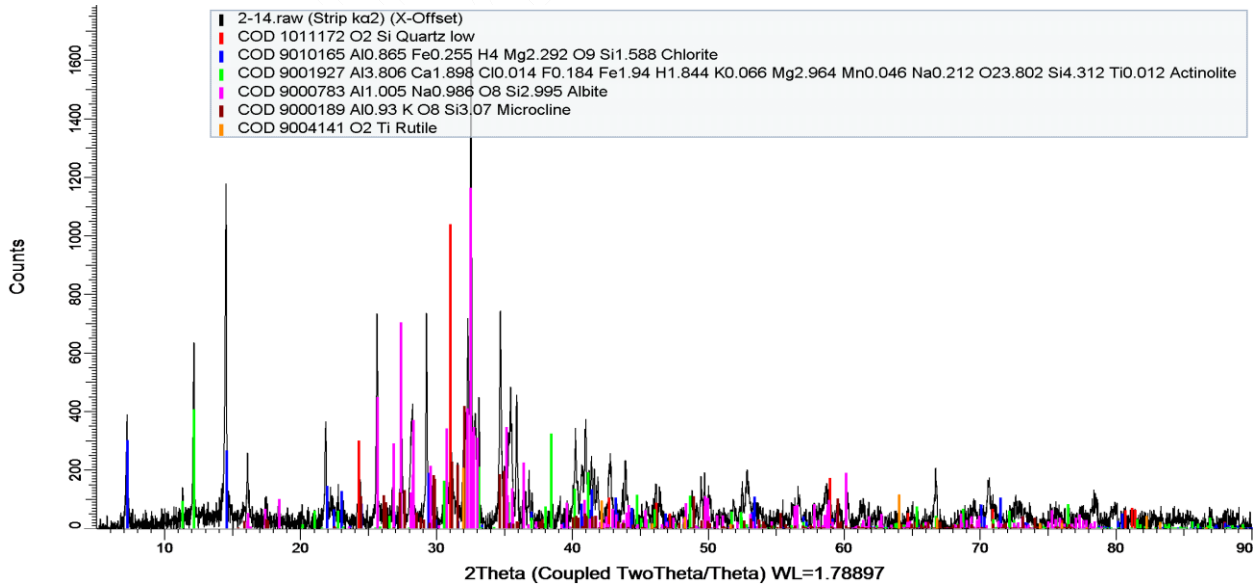
2-14.raw (Strip kα2) (X-Offset)
COD 1011172 O2 Si Quartz low
COD 9010165 Al0.865 Fe0.255 H4 Mg2.292 O9 Si1.588 Chlorite
COD 9001927 Al3.806 Ca1.898 Cl0.014 F0.184 Fe1.94 H1.844 K0.066 Mg2.964 Mn0.046 Na0.212 O23.802 Si4.312 Ti0.012 Actinolite
COD 9000783 Al1.005 Na0.986 O8 Si2.995 Albite
COD 9000189 Al0.93 K O8 Si3.07 Microcline
COD 9004141 O2 Ti Rutile
Counts
2Theta (Coupled TwoTheta/Theta) WL=1.78897

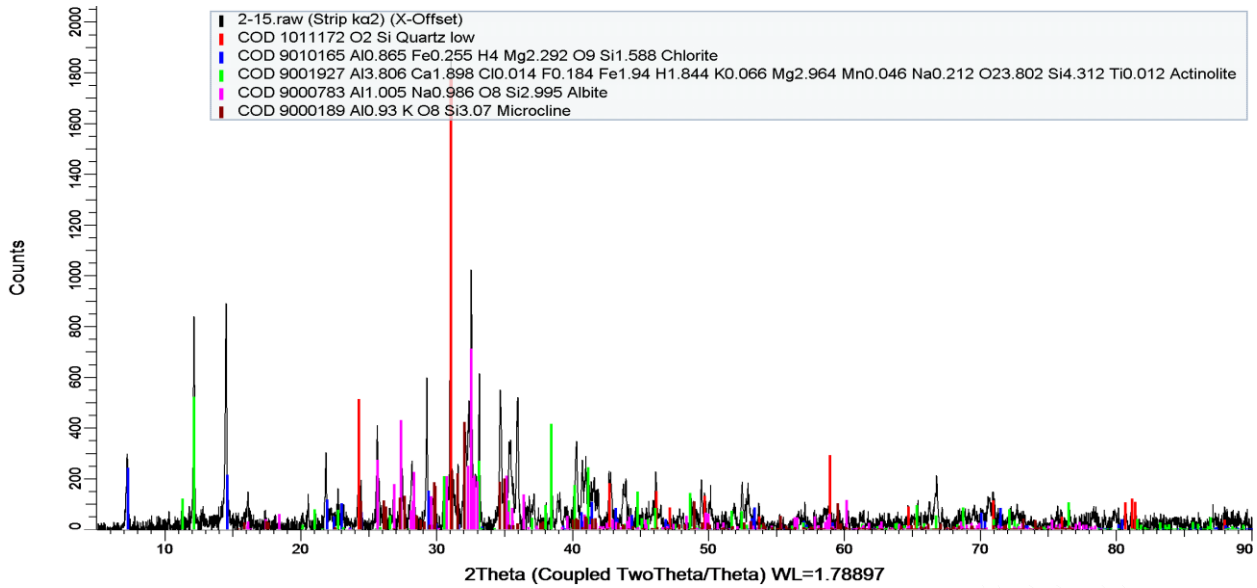

Drill core XRD Validation (Dickite and Pyrophyllite)

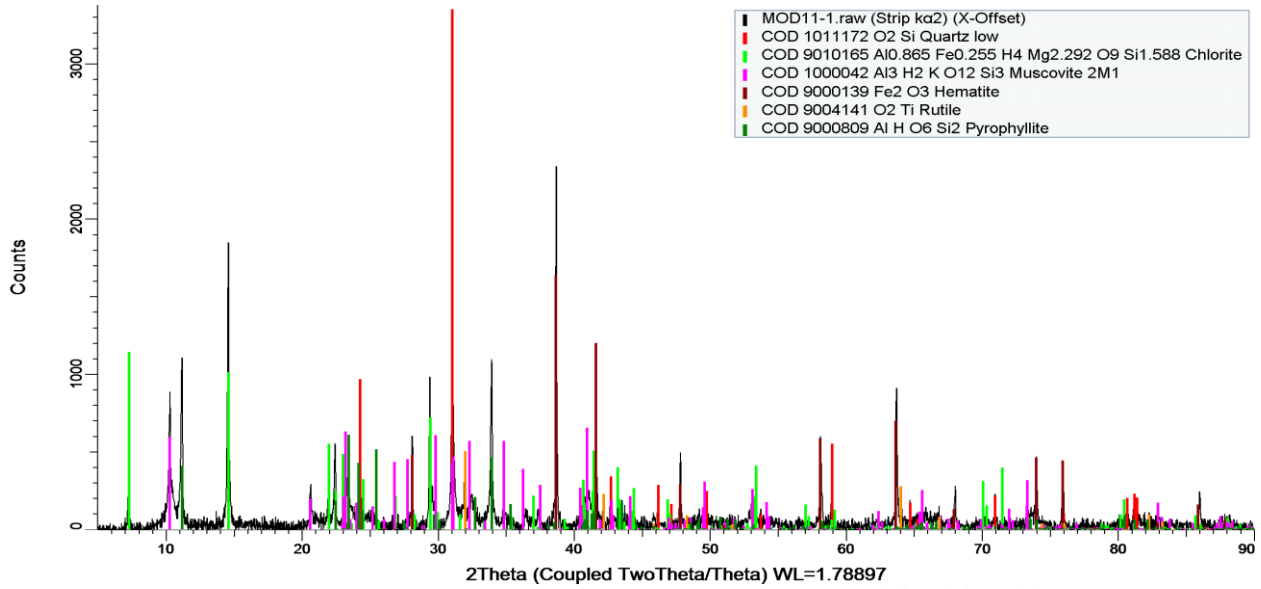

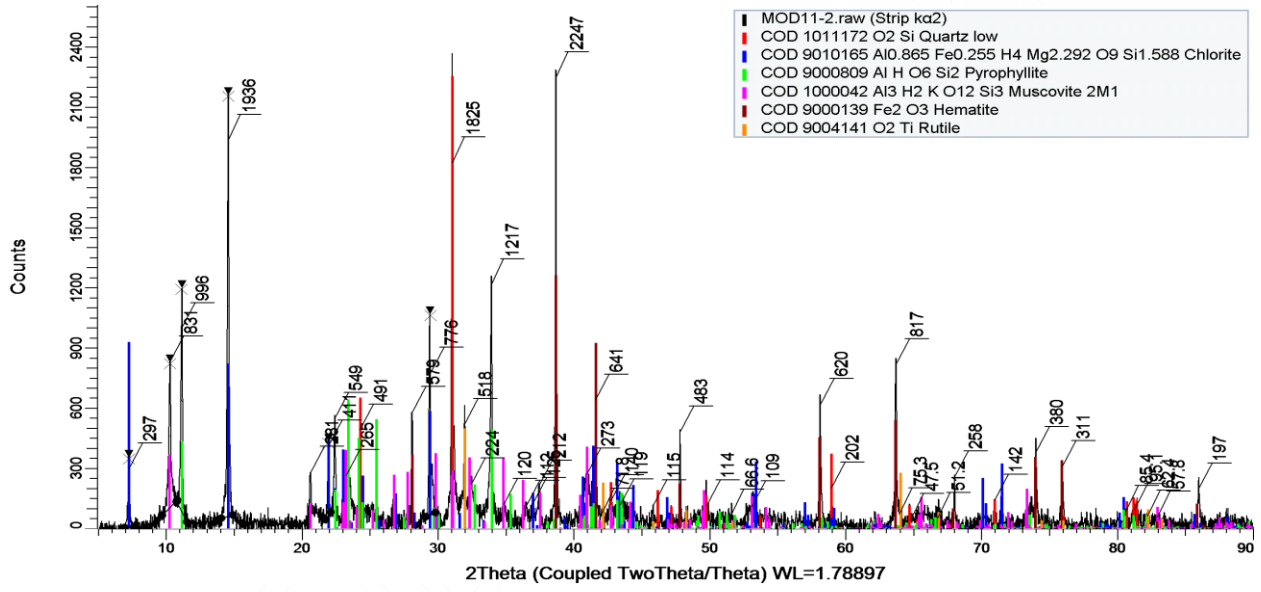

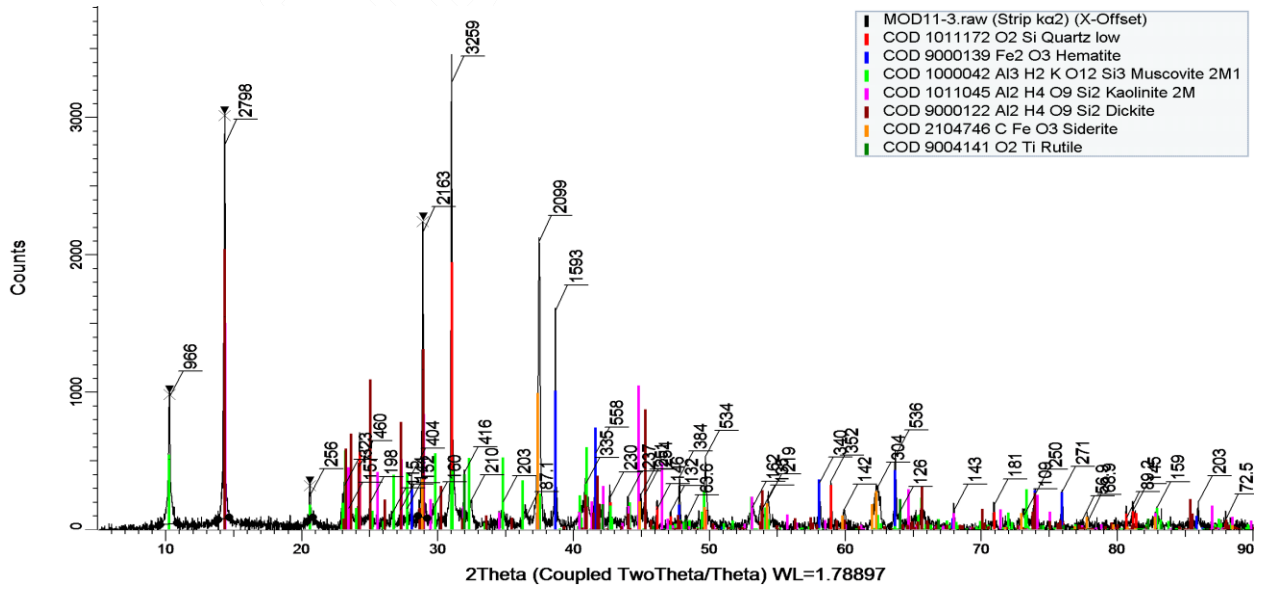

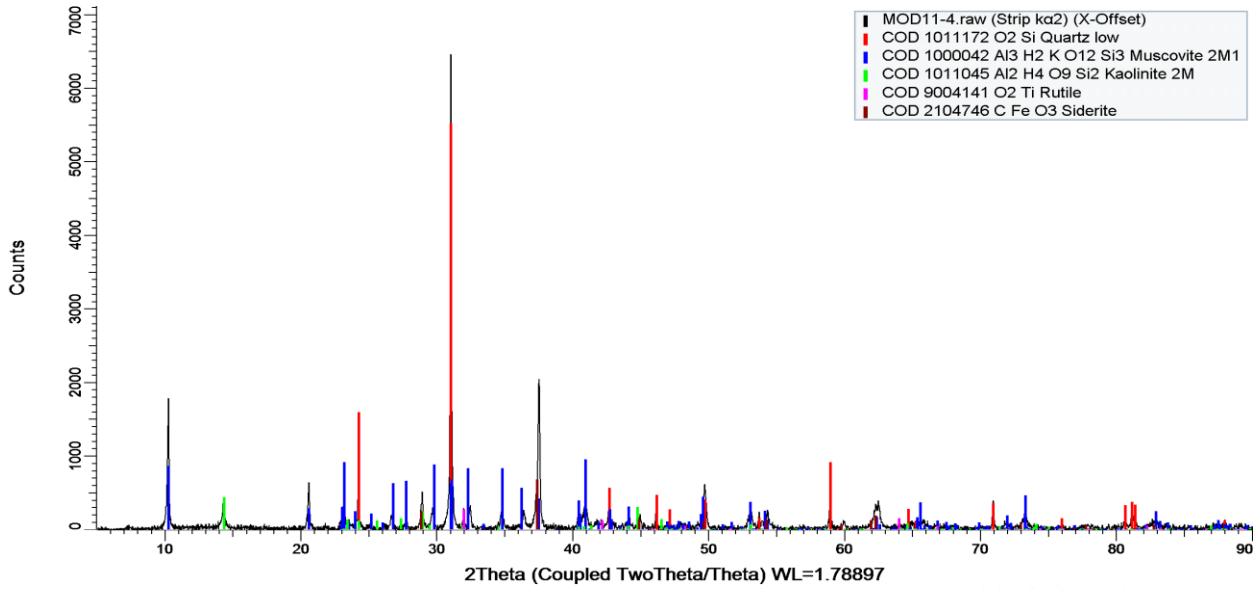
MOD11-4.raw (Strip kα2) (X-Offset)
COD 1011172 O2 Si Quartz low
COD 1000042 Al3 H2 K O12 Si3 Muscovite 2M1
COD 1011045 Al2 H4 O9 Si2 Kaolinite 2M
COD 9004141 O2 Ti Rutile
COD 2104746 C Fe O3 Siderite
Counts
2Theta (Coupled TwoTheta/Theta) WL=1.78897

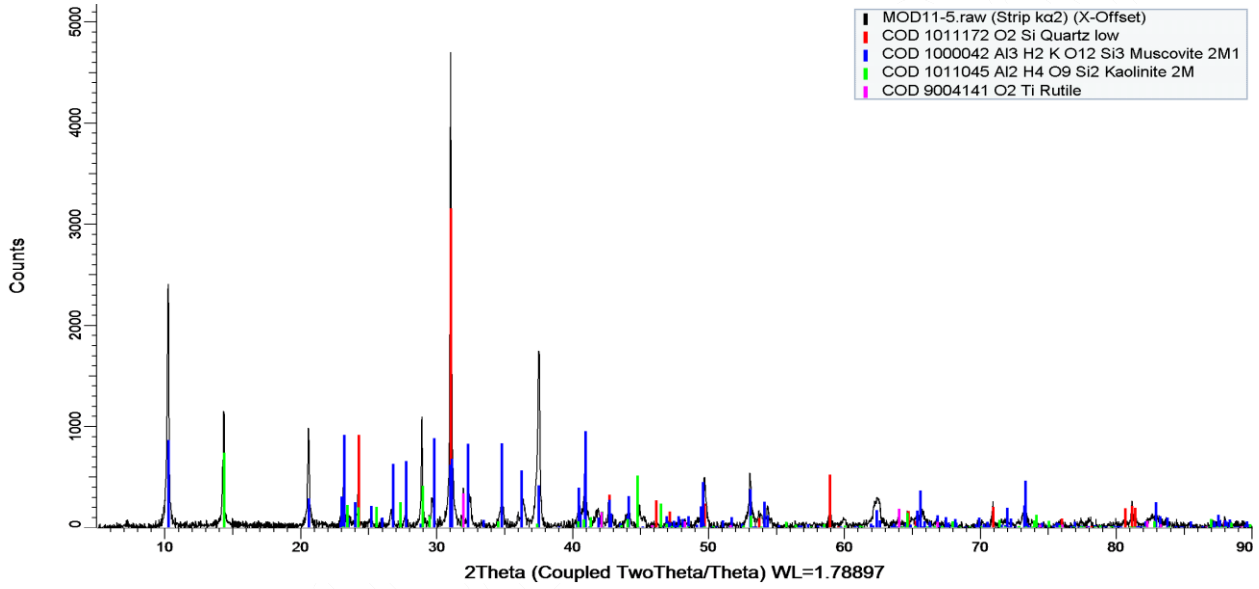
MOD11-5.raw (Strip kα2) (X-Offset)
COD 1011172 O2 Si Quartz low
COD 1000042 Al3 H2 K O12 Si3 Muscovite 2M1
COD 1011045 Al2 H4 O9 Si2 Kaolinite 2M
COD 9004141 O2 Ti Rutile
Counts
2Theta (Coupled TwoTheta/Theta) WL=1.78897

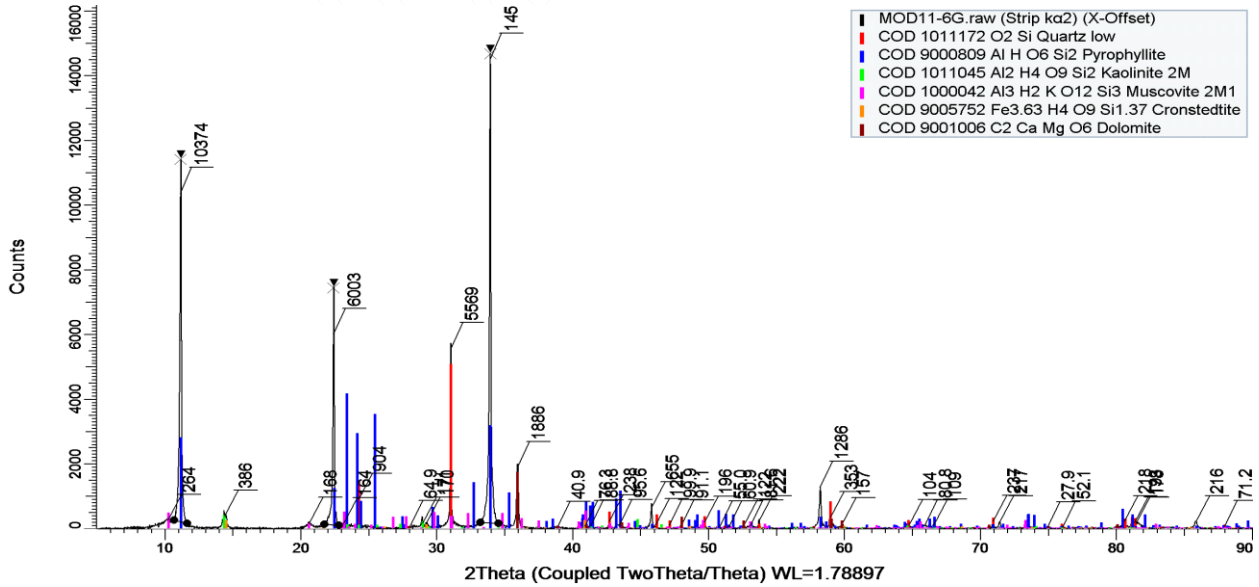
MOD11-6G.raw (Strip kα2) (X-Offset)
COD 1011172 O2 Si Quartz low
COD 9000809 Al H O6 Si2 Pyrophyllite
COD 1011045 Al2 H4 O9 Si2 Kaolinite 2M
COD 1000042 Al3 H2 K O12 Si3 Muscovite 2M1
COD 9005752 Fe3.63 H4 O9 Si1.37 Cronstedtite
COD 9001006 C2 Ca Mg O6 Dolomite
Counts
2Theta (Coupled TwoTheta/Theta) WL=1.78897

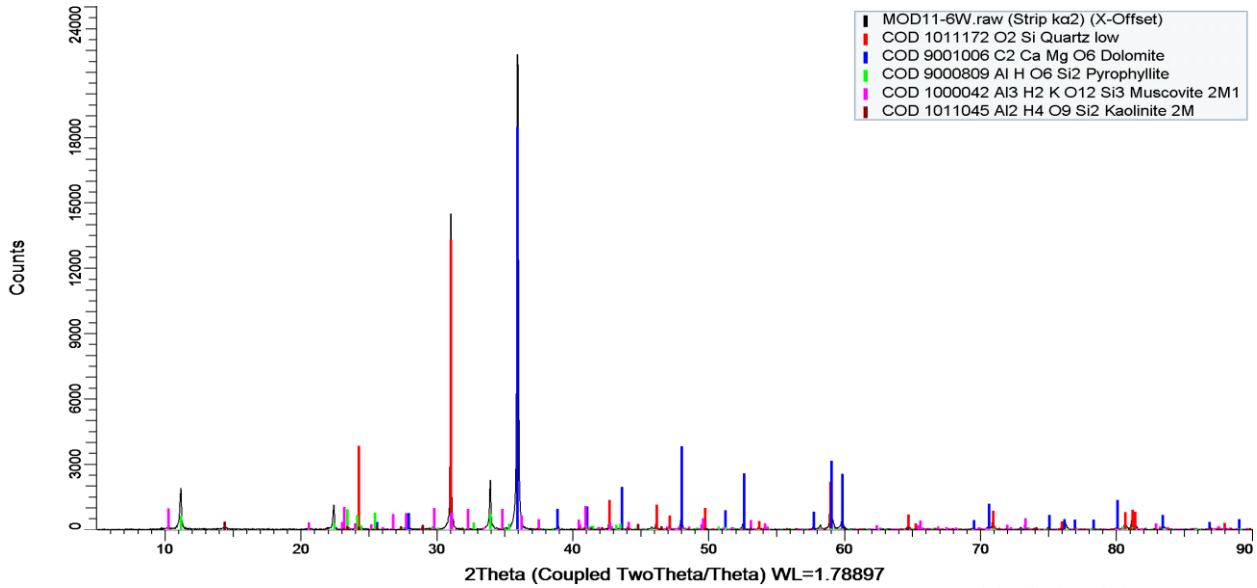
MOD11-6W.raw (Strip kα2) (X-Offset)
COD 1011172 O2 Si Quartz low
COD 9001006 C2 Ca Mg O6 Dolomite
COD 9000809 Al H O6 Si2 Pyrophyllite
COD 1000042 Al3 H2 K O12 Si3 Muscovite 2M1
COD 1011045 Al2 H4 O9 Si2 Kaolinite 2M
Counts
2Theta (Coupled TwoTheta/Theta) WL=1.78897

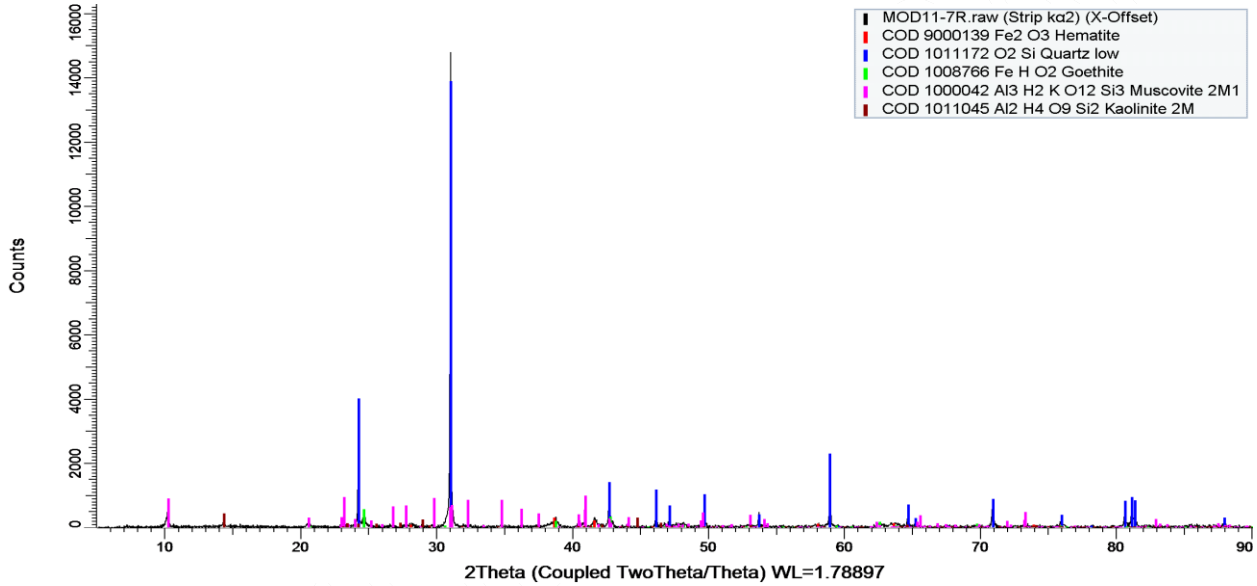
MOD11-7R.raw (Strip kα2) (X-Offset)
COD 9000139 Fe2 O3 Hematite
COD 1011172 O2 Si Quartz low
COD 1008766 Fe H O2 Goethite
COD 1000042 Al3 H2 K O12 Si3 Muscovite 2M1
COD 1011045 Al2 H4 O9 Si2 Kaolinite 2M
Counts
2Theta (Coupled TwoTheta/Theta) WL=1.78897

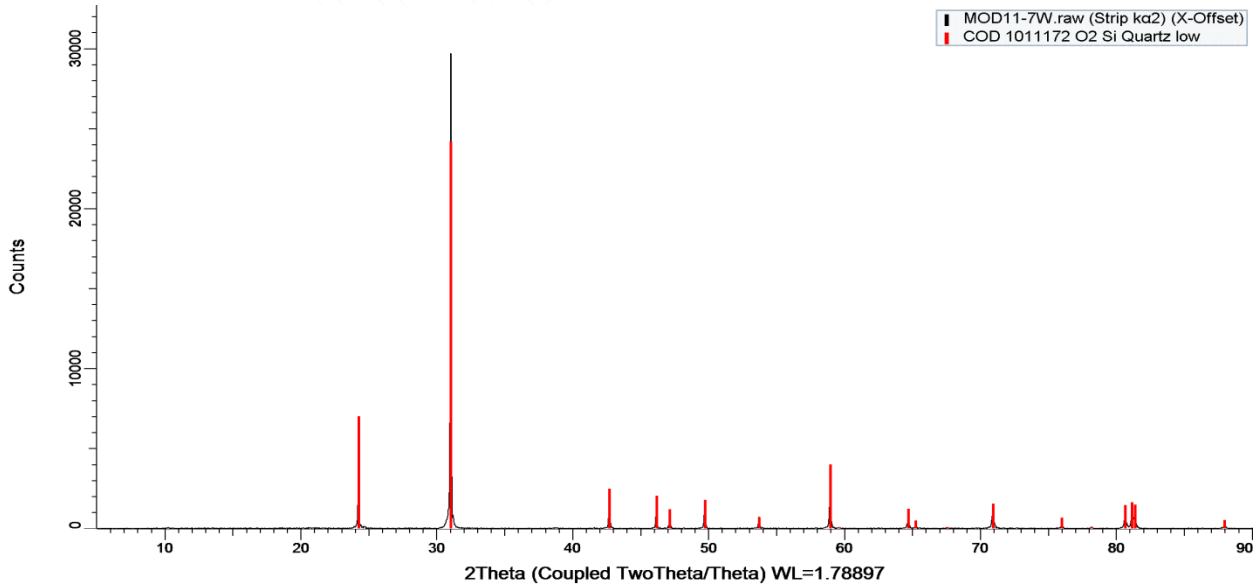
MOD11-7W.raw (Strip kα2) (X-Offset)
COD 1011172 O2 Si Quartz low
Counts
2Theta (Coupled TwoTheta/Theta) WL=1.78897

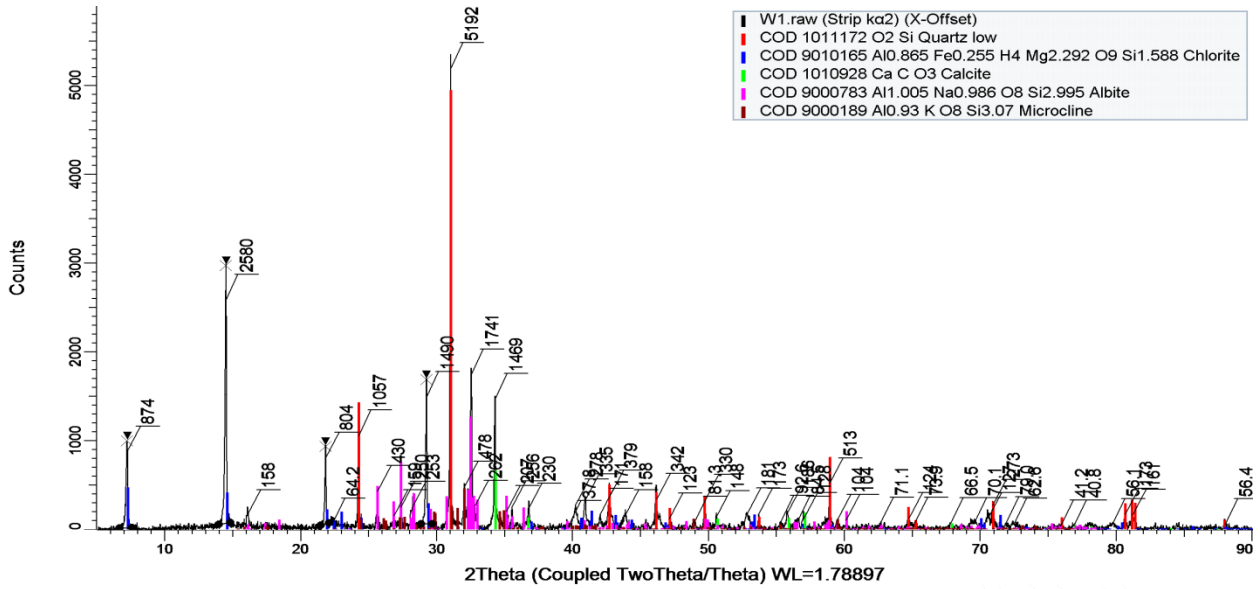
W1.raw (Strip kα2) (X-Offset)
COD 1011172 O2 Si Quartz low
COD 9010165 Al0.865 Fe0.255 H4 Mg2.292 O9 Si1.588 Chlorite
COD 1010928 Ca C O3 Calcite
COD 9000783 Al1.005 Na0.986 O8 Si2.995 Albite
COD 9000189 Al0.93 K O8 Si3.07 Microcline
Counts
2Theta (Coupled TwoTheta/Theta) WL=1.78897

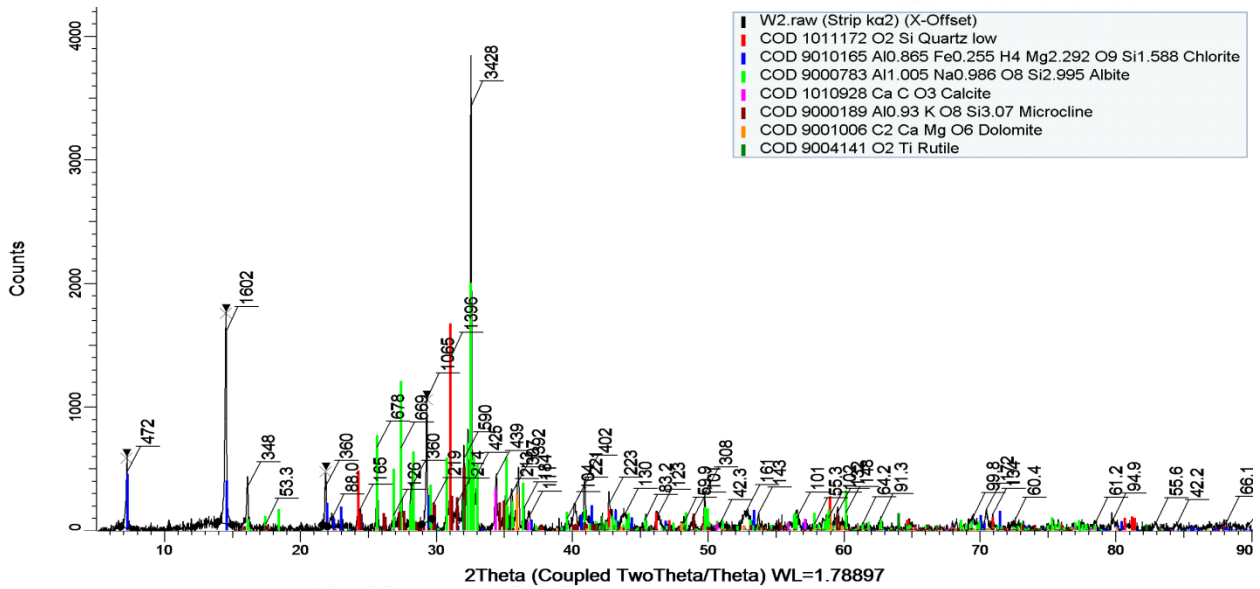
W2.raw (Strip kα2) (X-Offset)
COD 1011172 O2 Si Quartz low
COD 9010165 Al0.865 Fe0.255 H4 Mg2.292 O9 Si1.588 Chlorite
COD 9000783 Al1.005 Na0.986 O8 Si2.995 Albite
COD 1010928 Ca C O3 Calcite
COD 9000189 Al0.93 K O8 Si3.07 Microcline
COD 9001006 C2 Ca Mg O6 Dolomite
COD 9004141 O2 Ti Rutile
Counts
2Theta (Coupled TwoTheta/Theta) WL=1.78897

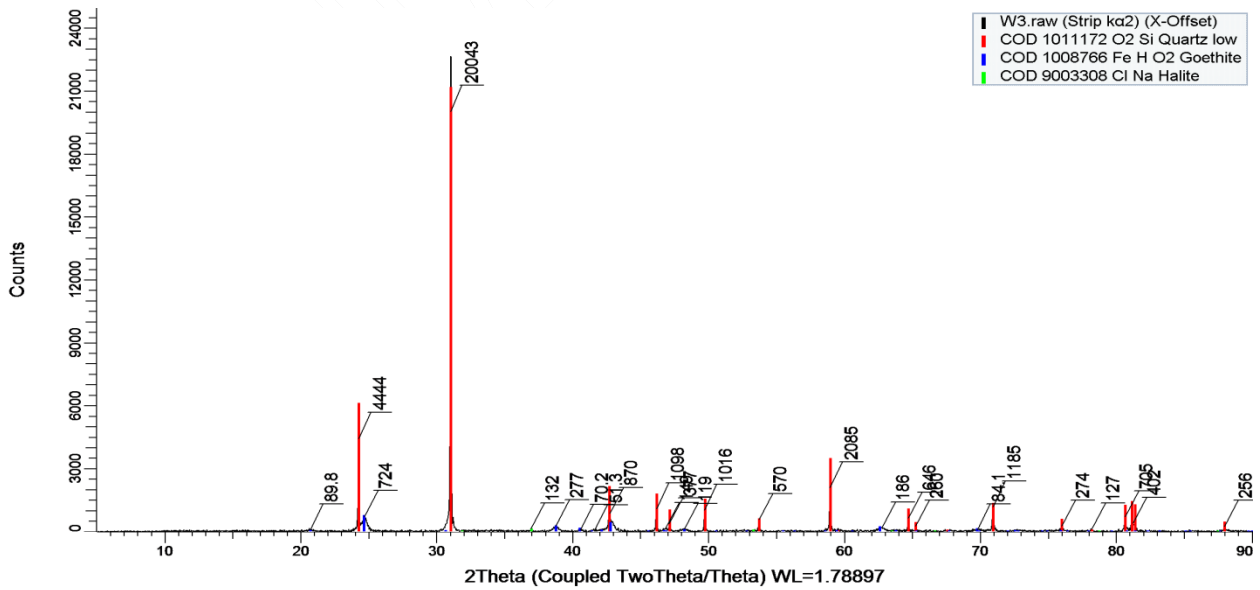
W3.raw (Strip kα2) (X-Offset)
COD 1011172 O2 Si Quartz low
COD 1008766 Fe H O2 Goethite
COD 9003308 Cl Na Halite
Counts
2Theta (Coupled TwoTheta/Theta) WL=1.78897

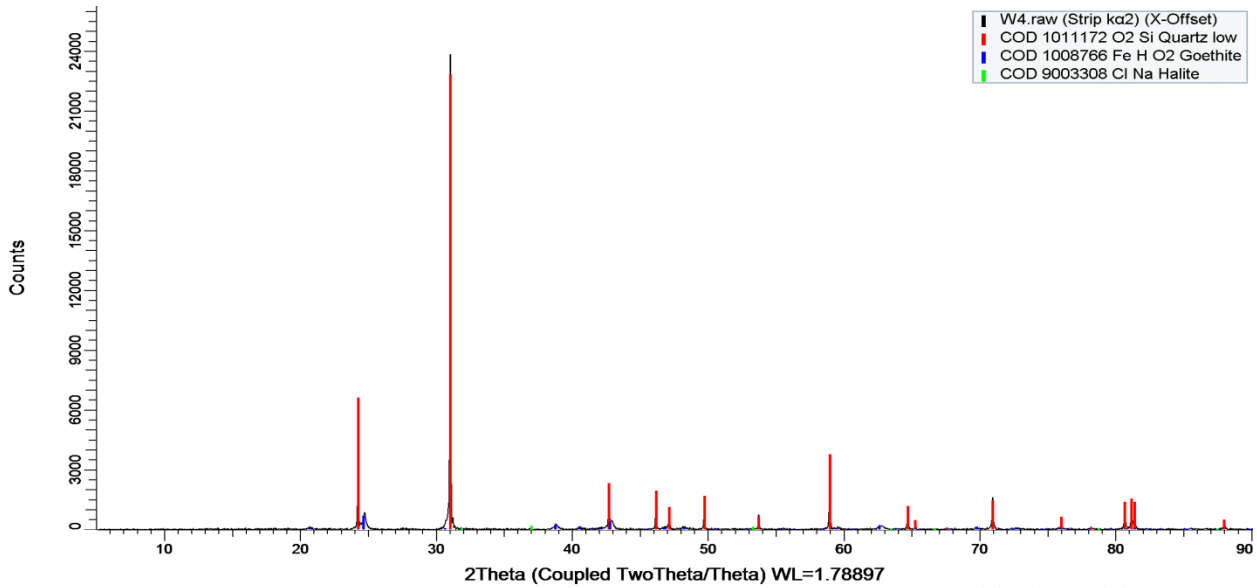
W4.raw (Strip kα2) (X-Offset)
COD 1011172 O2 Si Quartz low
COD 1008766 Fe H O2 Goethite
COD 9003308 Cl Na Halite
Counts
2Theta (Coupled TwoTheta/Theta) WL=1.78897

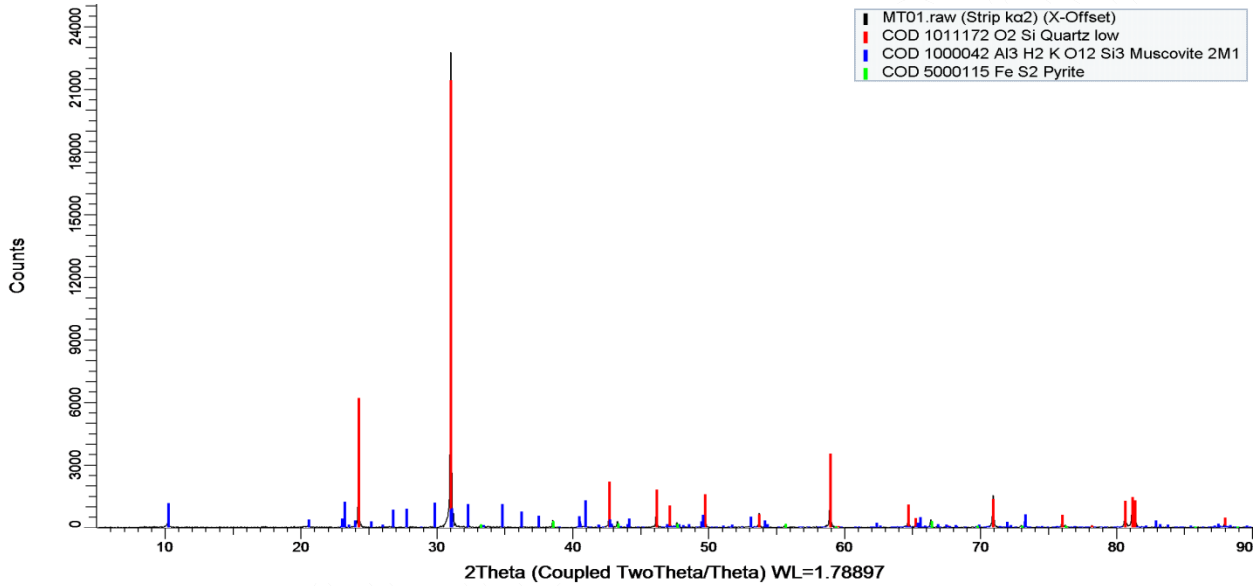
MT01.raw (Strip kα2) (X-Offset)
COD 1011172 O2 Si Quartz low
COD 1000042 Al3 H2 K O12 Si3 Muscovite 2M1
COD 5000115 Fe S2 Pyrite
Counts
2Theta (Coupled TwoTheta/Theta) WL=1.78897

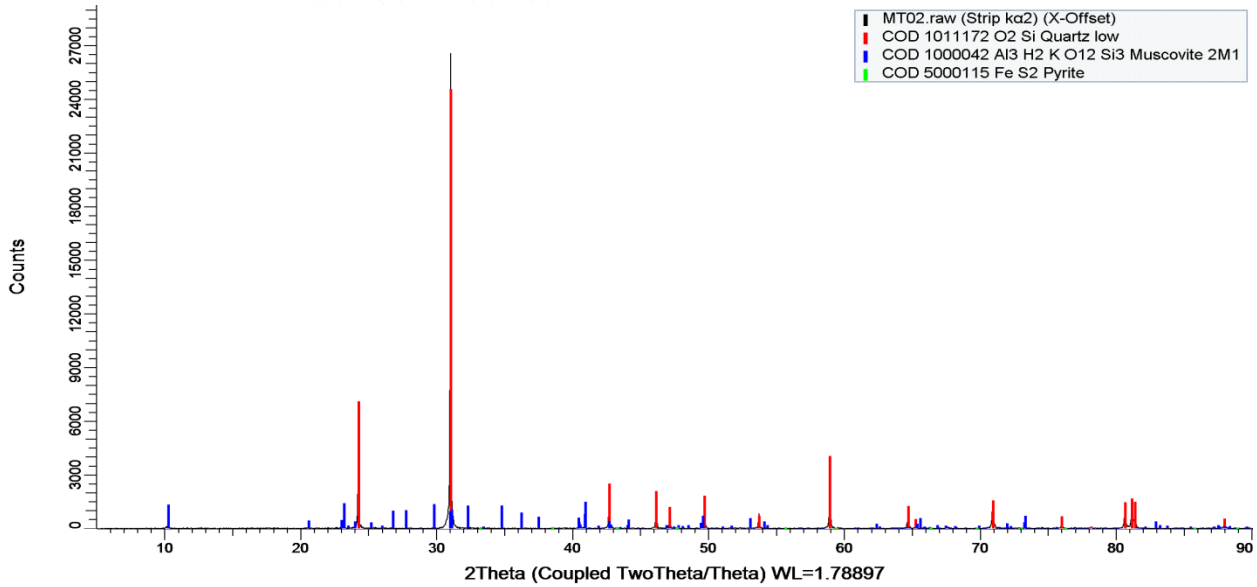
MT02.raw (Strip kα2) (X-Offset)
COD 1011172 O2 Si Quartz low
COD 1000042 Al3 H2 K O12 Si3 Muscovite 2M1
COD 5000115 Fe S2 Pyrite
Counts
2Theta (Coupled TwoTheta/Theta) WL=1.78897

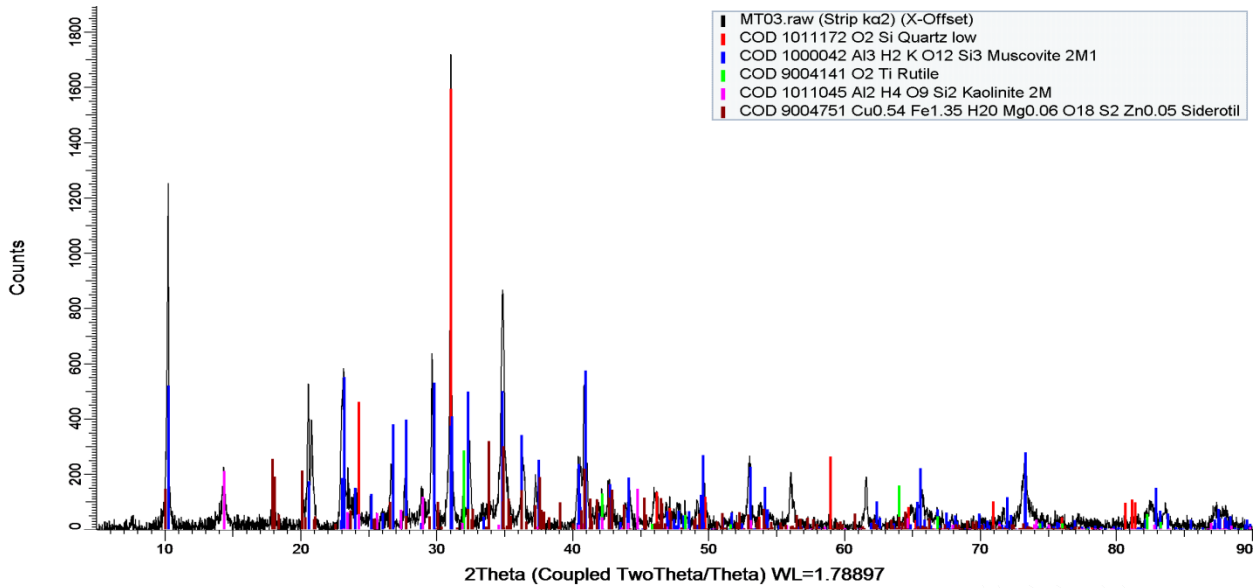
MT03.raw (Strip kα2) (X-Offset)
COD 1011172 O2 Si Quartz low
COD 1000042 Al3 H2 K O12 Si3 Muscovite 2M1
COD 9004141 O2 Ti Rutile
COD 1011045 Al2 H4 O9 Si2 Kaolinite 2M
COD 9004751 Cu0.54 Fe1.35 H20 Mg0.06 O18 S2 Zn0.05 Siderotil
Counts
2Theta (Coupled TwoTheta/Theta) WL=1.78897

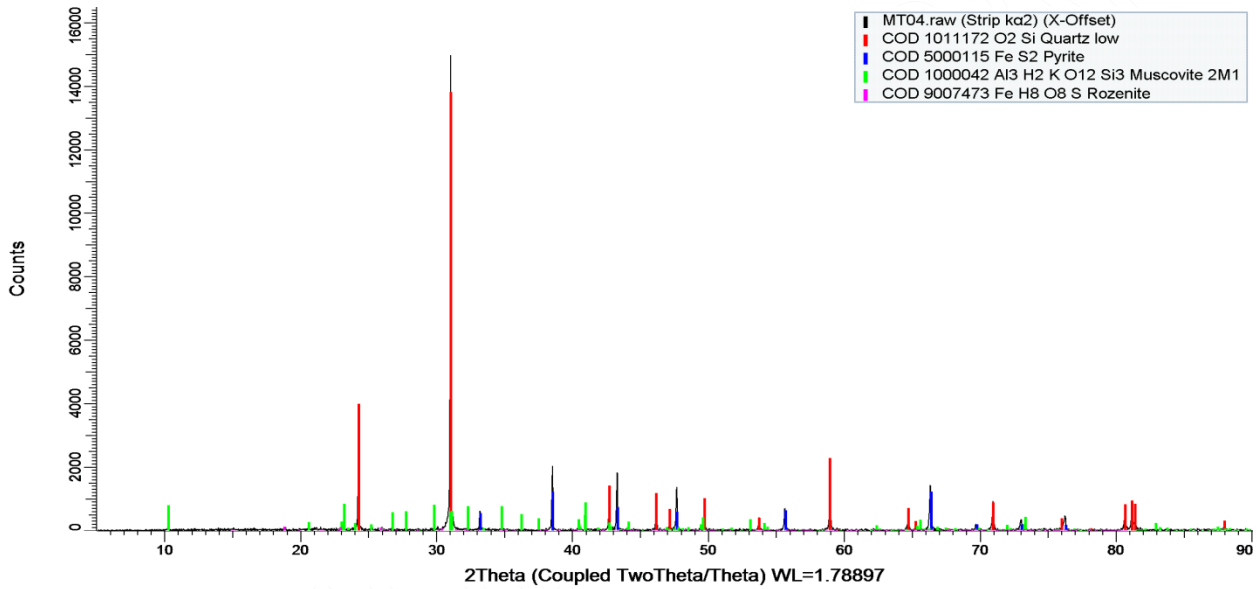
MT04.raw (Strip kα2) (X-Offset)
COD 1011172 O2 Si Quartz low
COD 5000115 Fe S2 Pyrite
COD 1000042 Al3 H2 K O12 Si3 Muscovite 2M1
COD 9007473 Fe H8 O8 S Rozenite
Counts
2Theta (Coupled TwoTheta/Theta) WL=1.78897

Appendix 5 GSWA regolith samples

Refer to the associated Excel (.xlsx) spreadsheet “Appendix 5_NF_Regolith_Geochemistry.xlsx” file for location and geochemistry assay data for selected GSWA regolith samples.

GSWANO	DLong	DLat	LITHNAME	SITENO	ORIGNAME	Total %	LOI_pct	Al2O3	CaO	Fe2O3	K2O	MgO	MnO	Na2O_pct	P2O5	S	SiO2	TiO2	Co_ppm	Cr_ppm	Cu_ppm	Ni_ppm
150806	117.90894	-23.25395	Alluvium	398944	RegGeoMap	100.16	4.67	4.85	0.29	48.34	1.09	0.54	0.1	0.38	0.17	-0.1	39.4	0.58	13	84	42	24
150805	117.82364	-23.25316	Alluvium	398943	RegGeoMap	98.11	5.25	6.73	-0.1	66.44	0.35	0.26	0.14	-0.1	0.11	-0.1	18.64	0.64	13	170	4	37
150803	117.86218	-23.3321	Alluvium	398941	RegGeoMap	99.09	5.2	4.75	-0.1	72.91	0.12	-0.1	-0.05	-0.1	0.19	-0.1	16.06	0.46	5	150	5	18
150802	117.94403	-23.3283	Alluvium	398940	RegGeoMap	100.01	5.5	5.77	-0.1	53.06	0.72	0.22	0.13	-0.1	0.19	-0.1	34.5	0.37	11	60	14	24
150801	117.97207	-23.39013	Alluvium	398939	RegGeoMap	98.62	3.84	11.07	-0.1	22.45	1.53	0.33	0.05	0.36	0.09	-0.1	58.11	1.14	19	98	76	42
150709	117.90235	-23.29657	Alluvium	398885	RegGeoMap	98.51	6.29	4.17	-0.1	72.09	0.30	0.2	0.27	-0.1	0.28	-0.1	15.1	0.26	21	94	39	30
150708	117.82962	-23.29333	Soil	398884	RegGeoMap	99.13	9.61	12.24	-0.1	49.91	0.21	0.1	0.2	-0.1	0.11	-0.1	26.58	0.62	13	70	36	35
150706	117.85404	-23.36126	Alluvium	398882	RegGeoMap	99.80	3.9	4.26	-0.1	59.20	0.29	0.14	0.07	-0.1	0.19	-0.1	31.73	0.47	6	230	41	26
150705	117.94964	-23.36446	Alluvium	398881	RegGeoMap	99.79	4.18	3.67	-0.1	62.85	0.27	0.12	0.07	-0.1	0.19	-0.1	28.51	0.38	6	220	36	24
150704	117.97677	-23.42785	Alluvium	398880	RegGeoMap	98.85	5.77	18.2	-0.1	27.42	2.00	0.32	0.1	0.79	0.13	-0.1	42.54	1.93	46	61	152	59
150703	117.90369	-23.42185	Alluvium	398879	RegGeoMap	99.73	6.14	12.85	0.17	24.65	2.26	1.15	0.14	0.39	0.14	-0.1	50.79	1.3	45	61	124	53
150615	117.87127	-23.24939	Alluvium	398828	RegGeoMap	100.12	5.57	3.71	0.21	61.25	0.59	0.42	0.12	0.21	0.24	-0.1	27.31	0.74	9	62	33	22
150612	117.89848	-23.33457	Alluvium	398825	RegGeoMap	99.60	5.43	5.61	0.43	49.37	0.86	0.96	0.18	0.75	0.16	-0.1	35.56	0.54	18	66	35	25
150611	117.98228	-23.31874	Soil	398824	RegGeoMap	99.44	6.91	11.3	-0.1	26.81	0.88	0.23	0.11	0.16	0.09	-0.1	52.24	1.06	11	180	40	32
150610	117.9313	-23.39632	Sheetwash	398823	RegGeoMap	99.54	3.71	11.9	-0.1	16.99	1.81	0.51	-0.05	0.45	-0.05	-0.1	63.53	1.09	32	63	72	49
150609	117.86377	-23.40061	Alluvium	398822	RegGeoMap	100.42	4.95	11.64	-0.1	22.91	1.82	0.76	0.2	0.37	0.13	-0.1	56.65	1.34	69	64	124	62
150606	117.86632	-23.47244	Alluvium	398819	RegGeoMap	99.68	4.52	10.02	-0.1	37.71	1.79	0.37	0.15	0.17	0.09	-0.1	43.69	1.52	32	160	93	42
150605	117.94608	-23.48227	Alluvium	398818	RegGeoMap	99.53	6.53	13.67	0.13	15.55	2.61	0.56	-0.05	0.44	0.07	-0.1	58.92	1.35	33	79	116	46
150513	117.94301	-23.28299	Alluvium	398764	RegGeoMap	98.03	4.88	5.53	-0.1	55.28	0.32	0.26	0.05	-0.1	0.14	-0.1	31.45	0.57	7	78	40	14
150512	117.86004	-23.29051	Sheetwash	398763	RegGeoMap	98.50	7.26	9.39	0.15	30.05	0.67	0.25	0.07	0.14	0.1	-0.1	49.84	0.83	14	110	28	30
150509	117.89911	-23.36095	Alluvium	398760	RegGeoMap	98.36	4.78	4.91	-0.1	59.62	0.17	0.11	0.06	-0.1	0.19	-0.1	28.47	0.5	7	260	34	26
150508	117.98455	-23.36607	Alluvium	398759	RegGeoMap	97.97	4.42	5.83	0.2	39.29	0.45	0.35	0.08	0.12	0.13	-0.1	46.77	0.58	12	250	43	33
150507	117.9378	-23.43147	Alluvium	398758	RegGeoMap	99.05	5.09	16.84	-0.1	28.72	1.96	0.57	0.07	0.69	0.1	-0.1	43.81	1.55	36	66	115	58
150506	117.85233	-23.44141	Sheetwash	398757	RegGeoMap	98.58	4.92	15.44	0.13	22.89	2.81	0.53	0.05	0.41	0.1	-0.1	50.01	1.54	28	72	118	40
150500	117.89977	-23.39861	Alluvium	398751	RegGeoMap	98.75	3.37	10	-0.1	16.46	2.40	0.55	-0.05	-0.1	-0.05	-0.1	65.5	1.02	14	74	57	29
150496	117.89653	-23.47069	Alluvium	398747	RegGeoMap	99.26	5	12.61	-0.1	24.70	2.23	0.52	0.07	0.22	0.07	-0.1	52.82	1.37	30	97	106	42
150495	117.98532	-23.47128	Alluvium	398746	RegGeoMap	99.65	4.34	13.94	-0.1	21.38	1.87	0.46	0.08	0.68	0.14	-0.1	55.52	1.59	29	58	144	50
150044	117.44214	-23.2248	Sheetwash	398294	RegGeoMap	98.39	4.29	2.78	2.25	21.22	0.30	0.38	0.24	-0.1	-0.05	-0.1	67.07	0.26	16	63	30	35
150043	117.35502	-23.21464	Sheetwash	398293	RegGeoMap	98.38	7.61	9.62	2.11	19.67	0.84	2.8	0.18	0.66	0.1	-0.1	53.88	1.16	31	67	75	54
150042	117.27274	-23.22746	Alluvium	398292	RegGeoMap	98.06	3.83	10.89	-0.1	7.38	1.97	0.8	0.15	0.29	-0.05	-0.1	72.62	0.53	16	69	33	57
150041	117.19601	-23.21708	Alluvium	398291	RegGeoMap	98.23	3.83	6.29	1.25	12.17	0.91	1.29	0.1	0.27	0.07	-0.1	71.72	0.58	19	98	45	61
150037	117.16198	-23.14416	Alluvium	398287	RegGeoMap	99.19	1.66	2.67	0.35	7.69	0.23	0.33	0.06	-0.1	-0.05	-0.1	86.31	0.29	9	63	24	28
150036	117.24382	-23.1554	Alluvium	398286	RegGeoMap	100.09	5.66	12.23	1.21	22.70	1.46	2.08	0.16	0.51	0.15	-0.1	52.82	1.36	38	223	96	101
150035	117.31764	-23.15087	Alluvium	398285	RegGeoMap	100.23	7.49	11.24	6.34	13.41	0.51	10.88	0.2	1.09	0.16	-0.1	47.06	2.1	61	1083	57	424
150034	117.38958	-23.14466	Sheetwash	398284	RegGeoMap	100.60	8.06	13.23	2.5	11.51	1.24	3.47	0.15	0.88	0.07	-0.1	58.6	1.14	40	96	63	92
150030	117.26146	-23.07704	Alluvium	398280	RegGeoMap	100.59	7.56	12.73	4.9	13.80	0.82	6.69	0.2	1.55	0.14	-0.1	51.13	1.32	42	257	72	113
150029	117.19551	-23.08093	Alluvium	398279	RegGeoMap	99.02	3.24	8.94	-0.1	12.86	2.10	0.4	-0.05	0.12	0.09	-0.1	70.97	0.7	14	75	44	30
150019	117.54649	-23.28371	Alluvium	398269	RegGeoMap	97.85	1.79	6.42	-0.1	5.18	1.70	0.7	0.07	0.4	-0.05	-0.1	81.71	0.28	9	27	21	25
150012	117.51164	-23.21962	Alluvium	398262	RegGeoMap	99.91	3.96	5.4	-0.1	63.46	0.25	0.2	0.13	-0.1	0.17	-0.1	25.9	0.89	8	145	26	32
149947	117.39201	-23.28925	Alluvium	398197	RegGeoMap	99.82	1.78	4.7	0.11	7.28	0.88	0.53	0.08	0.42	-0.05	-0.1	84.07	0.27	8	38	20	23
149946	117.47575	-23.28528	Alluvium	398196	RegGeoMap	99.88	4.84	7.97	2.78	27.19	0.77	2.09	0.14	0.65	0.12	-0.1	52.7	0.88	23	86	45	59
149945	117.47641	-23.21973	Alluvium	398195	RegGeoMap	99.81	3.1	3.51	-0.1	64.08	0.15	0.13	0.13	-0.1	0.15	-0.1	28.43	0.58	6	62	24	15
149944	117.3991	-23.22579	Alluvium	398194	RegGeoMap	100.12	2.28	8.88	0.15	4.89	2.44	1.05	0.1	0.76	-0.05	-0.1	79.48	0.39	12	28	21	34
149943	117.31871	-23.21698	Alluvium	398193	RegGeoMap	99.84	1.2	3.96	-0.1	4.20	0.83	0.45	0.06	0.39	-0.05	-0.1	88.93	0.22	8	25	17	24
149942	117.23563	-23.22362	Alluvium	398192	RegGeoMap	99.81	4.54	8.18	4.31	13.57	0.65	4.95	0.19	0.82	0.14	-0.1	61.65	1.06	36	809	51	190

GSWANO	DLong	DLat	LITHNAME	SITENO	ORIGNAME	Total %	LOI_pct	Al2O3	CaO	Fe2O3	K2O	MgO	MnO	Na2O_pct	P2O5	S	SiO2	TiO2	Co_ppm	Cr_ppm	Cu_ppm	Ni_ppm
149937	117.18867	-23.14655	Alluvium	398187	RegGeoMap	99.21	4.4	5.75	2.78	12.53	0.48	1.2	0.15	0.37	0.09	-0.1	71.03	0.68	16	115	47	54
149936	117.27111	-23.14872	Alluvium	398186	RegGeoMap	99.34	5.18	12.67	1.55	17.79	2.10	1.64	0.32	0.57	0.14	-0.1	56.16	1.47	38	170	113	102
149935	117.34912	-23.15179	Alluvium	398185	RegGeoMap	100.10	7.39	11.71	5.92	12.19	0.73	7.98	0.53	0.96	0.15	-0.1	51.4	1.39	47	572	60	222
149934	117.42337	-23.14663	Alluvium	398184	RegGeoMap	100.65	6.8	13.98	3.98	10.66	1.32	5.64	0.13	1.35	0.09	-0.1	55.89	1.06	41	74	60	107
149930	117.22275	-23.07628	Alluvium	398180	RegGeoMap	100.30	6.06	12.65	6.07	12.89	0.62	7.3	0.22	1.2	0.15	-0.1	52.01	1.38	68	543	71	201
149929	117.16483	-23.08217	Alluvium	398179	RegGeoMap	98.90	3.82	7.29	1.15	8.62	1.79	0.79	0.13	-0.1	0.08	-0.1	75.15	0.43	22	49	29	43
149921	117.54578	-23.31942	Alluvium	398171	RegGeoMap	98.32	1.63	5.54	0.1	3.85	1.19	0.72	0.1	0.37	-0.05	-0.1	84.88	0.24	10	26	18	34
149914	117.54084	-23.25581	Sheetwash	398164	RegGeoMap	100.25	9.77	7.83	0.78	24.60	0.88	3.11	0.12	1.17	0.09	0.31	50.19	0.94	22	130	36	45
149913	117.51685	-23.17711	Alluvium	398163	RegGeoMap	98.17	6.03	6.12	0.85	49.65	0.38	1.13	0.34	0.11	0.14	-0.1	33.01	0.66	30	245	65	88
149849	117.43446	-23.29849	Alluvium	398099	RegGeoMap	99.95	3.2	3.99	0.63	42.80	0.38	0.67	0.19	0.18	0.11	-0.1	47.54	0.51	13	103	37	33
149848	117.46967	-23.25564	Alluvium	398098	RegGeoMap	99.42	3.17	3.2	0.33	55.86	0.20	0.26	0.17	-0.1	0.13	-0.1	36.06	0.39	8	90	34	22
149847	117.39597	-23.25568	Alluvium	398097	RegGeoMap	98.26	1.1	3.4	-0.1	3.91	0.83	0.42	0.08	0.23	-0.05	-0.1	88.53	0.16	11	15	26	26
149846	117.32817	-23.26394	Alluvium	398096	RegGeoMap	99.25	3.74	14.93	0.19	7.20	3.29	1.33	0.11	0.3	-0.05	-0.1	67.91	0.55	15	70	26	55
149840	117.20131	-23.19656	Alluvium	398090	RegGeoMap	99.28	5.12	7.58	2.22	5.02	1.54	2.34	0.29	0.6	-0.05	-0.1	74.53	0.34	18	38	26	44
149839	117.27611	-23.18303	Alluvium	398089	RegGeoMap	99.47	1.5	1.9	0.35	3.64	0.15	0.23	0.07	-0.1	-0.05	-0.1	91.84	0.19	8	32	14	19
149838	117.34084	-23.17964	Sheetwash	398088	RegGeoMap	99.40	10.06	9.15	3.58	28.59	0.84	2.99	0.24	0.21	0.14	-0.1	42.92	0.93	28	183	52	93
149837	117.42501	-23.18564	Alluvium	398087	RegGeoMap	99.24	7.2	8.15	0.11	55.04	0.26	0.19	0.05	0.11	0.22	-0.1	27.1	1.06	9	191	24	32
149834	117.31148	-23.10799	Alluvium	398084	RegGeoMap	100.47	6.7	11.85	5.95	14.83	0.53	8.17	0.22	1.22	0.14	-0.1	49.81	1.3	63	805	169	293
149833	117.22906	-23.10614	Alluvium	398083	RegGeoMap	99.95	5.6	12.14	4.29	15.12	0.88	3.87	0.19	0.75	0.12	-0.1	55.77	1.47	39	306	71	142
149832	117.16349	-23.10645	Alluvium	398082	RegGeoMap	99.27	2.98	5.62	0.73	10.11	1.21	0.52	0.15	-0.1	-0.05	-0.1	77.95	0.4	13	51	29	29
149828	117.16047	-23.04112	Alluvium	398079	RegGeoMap	100.49	4.11	13.25	0.19	18.72	2.91	0.62	0.11	0.23	0.07	-0.1	58.91	1.62	43	99	96	53
149814	117.51235	-23.2562	Sheetwash	398065	RegGeoMap	100.26	4.32	6.49	3.07	13.55	0.87	2.68	0.12	0.55	0.09	-0.1	67.99	0.78	21	91	38	74
149746	117.43687	-23.25203	Alluvium	397997	RegGeoMap	99.61	2.04	7.94	0.13	6.21	1.70	0.74	0.08	0.45	-0.05	-0.1	80.26	0.36	10	48	24	38
149745	117.35166	-23.26043	Alluvium	397996	RegGeoMap	99.05	3.06	12.96	0.13	6.67	3.01	1.36	0.13	0.51	-0.05	-0.1	70.98	0.54	17	73	26	53
149744	117.28548	-23.25487	Alluvium	397995	RegGeoMap	99.31	2.93	10.95	-0.1	7.63	2.17	0.6	0.17	0.2	-0.05	-0.1	74.6	0.46	25	74	40	61
149739	117.15502	-23.18354	Alluvium	397990	RegGeoMap	98.59	3.21	12.29	0.12	7.11	2.62	1.07	0.11	0.55	-0.05	-0.1	71.28	0.53	14	71	26	51
149738	117.23371	-23.18751	Soil	397989	RegGeoMap	99.17	5.23	5.85	0.6	6.79	0.85	2.57	0.1	0.86	-0.05	-0.1	76.27	0.35	6	90	21	24
149737	117.31004	-23.18974	Alluvium	397988	RegGeoMap	99.03	1.44	2.47	0.1	4.08	0.27	0.19	-0.05	-0.1	-0.05	-0.1	90.74	0.19	3	47	12	14
149736	117.39182	-23.19302	Alluvium	397987	RegGeoMap	100.83	4.68	4.38	1.07	78.47	0.16	0.44	0.07	-0.1	0.21	-0.1	11.01	0.69	5	135	31	32
149735	117.48333	-23.18074	Alluvium	397986	RegGeoMap	100.72	6.8	8.9	-0.1	55.59	0.13	0.35	0.2	-0.1	0.21	-0.1	27.75	1.24	16	127	32	30
149732	117.27191	-23.10365	Alluvium	397983	RegGeoMap	100.60	7.31	14.67	3.07	15.36	1.48	4.92	0.19	0.94	0.09	-0.1	51.45	1.37	48	191	132	122
149731	117.19651	-23.10037	Alluvium	397982	RegGeoMap	99.47	4.6	11.12	4.77	14.82	0.92	3.94	0.17	0.82	0.13	-0.1	57.21	1.22	38	289	71	135
149726	117.20342	-23.04339	Alluvium	397977	RegGeoMap	100.73	4.91	13.03	4.47	16.68	1.12	4.08	0.21	0.93	0.15	-0.1	53.67	1.73	50	240	77	113
149719	117.50368	-23.28757	Alluvium	397970	RegGeoMap	100.16	6.89	11.79	2.81	12.78	1.16	2.72	0.14	0.82	0.07	-0.1	60.09	1.14	31	101	61	83

GSWANO	DLong	DLat	LITHNAME	SITENO	ORIGNAME	Total	Ag	Ars	Au	Ba	Be	Bi	Cd	Ce	Cl	F	Ga	Ind	La	Li	Mo	Nb	Pb (ppm)	Pd	Pt	Rb	Sb	Sc	Se	Sn	Sr	Ta	Te	Th	U	V	W	Y	Zn	Zr
150806	117.90894	-23.25395	Alluvium	398944	RegGeoMap	100.16	-0.1	11	-0.001	167	2	-0.5	-1	19.6			9	-0.1	12.8	5	1	5.9	11	4	2	56.8	2.2	8	2.4	1	29	3		4	0.7	143	2	15	40	55
150805	117.82364	-23.25316	Alluvium	398943	RegGeoMap	98.11	-0.1	81	-0.001	93	1	0.6	-1	20			23	0.2	11.7	4	3	17.2	24	-1	-1	18.8	4.6	11	2.9	3	9	-2		13.5	2.4	221	2	10	38	101
150803	117.86218	-23.3321	Alluvium	398941	RegGeoMap	99.09	-0.1	25	-0.001	63	2	-0.5	-1	20			15	0.1	15	-3	1	9.2	10	-1	-1	9.9	2.4	9	1.3	1	11	-2		8.8	1.5	210	2	10	16	98
150802	117.94403	-23.3283	Alluvium	398940	RegGeoMap	100.01	-0.1	24	0.003	135	2	-0.5	-1	37			17	-0.1	18	-3	-1	12.5	9	1	2	24.2	2.9	10	-0.5	2	12	-2		8.9	2.4	129	2	20	31	105
150801	117.97207	-23.39013	Alluvium	398939	RegGeoMap	98.62	-0.1	13	-0.001	218	1	-0.5	-1	40			20	0.1	21	21	-1	13.8	11	-1	2	55.2	2.7	20	-0.5	2	34	-2		9.2	2.1	241	-1	13	68	119
150709	117.90235	-23.29657	Alluvium	398885	RegGeoMap	98.51	-0.1	20	-0.001	188	3	-0.5	-1	34			9	-0.1	16.1	-3	2	6.3	9	-1	-1	13.2	2.7	10	0.6	-1	19	-2		6.7	1.5	136	2	17	24	56
150708	117.82962	-23.29333	Soil	398884	RegGeoMap	99.13	-0.1	43	-0.001	305	2	0.5	-1	107			17	-0.1	18.8	13	4	21.7	34	3	3	16.8	2.3	11	1.8	3	16	-2		12.1	1.9	146	2	15	19	142
150706	117.85404	-23.36126	Alluvium	398882	RegGeoMap	99.80	-0.1	20	-0.001	87	2	0.5	-1	28			13	0.1	18.7	-3	2	8.5	14	-1	-1	11.5	3.6	11	0.7	2	13	-2		9.8	1.5	242	2	14	31	77
150705	117.94964	-23.36446	Alluvium	398881	RegGeoMap	99.79	-0.1	22	-0.001	77	2	-0.5	-1	19.6			11	-0.1	11.3	-3	2	7.1	13	-1	-1	12.4	2.9	9	1.3	1	10	-2		9	1.4	201	2	10	22	67
150704	117.97677	-23.42785	Alluvium	398880	RegGeoMap	98.85	-0.1	21	0.001	218	2	-0.5	-1	61			32	0.2	31	50	2	13.1	41	-1	-1	60.1	6.9	34	-0.5	2	54	-2		10.1	2.7	321	-1	19	142	149
150703	117.90369	-23.42185	Alluvium	398879	RegGeoMap	99.73	-0.1	23	0.004	331	2	-0.5	-1	54			22	-0.1	24	18	2	9	13	-1	2	66.8	2.6	28	-0.5	1	36	-2		8	2.6	251	-1	16	113	127
150615	117.87127	-23.24939	Alluvium	398828	RegGeoMap	100.12	-0.1	12	-0.001	153	2	-0.5	-1	29			12	-0.1	12.6	4	1	11.1	13	-1	-1	40.3	0.9	7	1.1	1	27	-2		5.2	1.1	158	2	19	30	59
150612	117.89848	-23.33457	Alluvium	398825	RegGeoMap	99.60	-0.1	13	-0.001	229	2	-0.5	-1	28			10	-0.1	12.6	6	1	8.3	10	-1	-1	37.5	2	13	0.8	-1	28	-2		5.1	1.4	182	1	24	46	59
150611	117.98228	-23.31874	Soil	398824	RegGeoMap	99.44	-0.1	15	-0.001	203	1	-0.5	-1	39			17	0.1	17.1	11	1	16.1	16	4	1	52.3	1.1	14	0.6	2	24	-2		11.7	2	190	1	16	44	307
150610	117.9313	-23.39632	Sheetwash	398823	RegGeoMap	99.54	-0.1	13	-0.001	210	1	-0.5	-1	44			28	0.1	23.6	31	1	12.7	12	1	2	67.5	2.1	29	-0.5	2	41	-2		6.7	1.8	241	-1	16	67	153
150609	117.86377	-23.40061	Alluvium	398822	RegGeoMap	100.42	-0.1	27	-0.001	312	2	-0.5	-1	59			33	0.1	23.4	26	2	14.3	23	1	3	64.5	4.3	31	1.2	2	44	-2		7.3	2.3	359	-1	21	108	176
150606	117.86632	-23.47244	Alluvium	398819	RegGeoMap	99.68	-0.1	130	0.006	262	2	0.8	-1	52			43	0.2	24.3	13	2	18.8	41	-1	1	65.6	14.1	20	1.6	3	27	-2		19.8	2.6	476	2	18	98	215
150605	117.94608	-23.48227	Alluvium	398818	RegGeoMap	99.53	0.1	8	-0.001	475	2	-0.5	-1	63			29	0.1	28.8	23	1	15.3	14	-1	-1	96.5	1.8	24	-0.5	2	44	-2		7.8	2	248	-1	20	91	207
150513	117.94301	-23.28299	Alluvium	398764	RegGeoMap	98.03	-0.1	11	-0.001	86	1	-0.5	-1	18.7			17	-0.1	11.8	4	3	11.7	11	1	-1	27.4	1.4	6	0.8	2	10	-2		5.6	0.8	107	1	10	11	98
150512	117.86004	-23.29051	Sheetwash	398763	RegGeoMap	98.50	0.1	21	-0.001	179	1	-0.5	-1	41			21	-0.1	21	15	3	19.5	20	-1	-1	48.7	1.5	11	2.7	2	24	-2		11.2	1.4	149	2	15	29	207
150509	117.89911	-23.36095	Alluvium	398760	RegGeoMap	98.36	-0.1	19	-0.001	71	1	0.7	-1	19			16	-0.1	12.3	3	3	9.6	15	-1	-1	12.5	2.6	11	1.7	1	9	-2		7.2	0.9	261	1	9	33	91
150508	117.98455	-23.36607	Alluvium	398759	RegGeoMap	97.97	-0.1	16	-0.001	159	1	-0.5	-1	37			18	0.1	19	7	2	10.4	18	-1	2	22.3	1.9	12	1.5	1	21	-2		9.1	1.2	280	-1	15	43	121
150507	117.9378	-23.43147	Alluvium	398758	RegGeoMap	99.05	-0.1	15	-0.001	218	2	0.5	-1	59			32	0.1	30	50	2	16.8	12	1	2	71.6	2.6	30	0.7	2	59	-2		8.8	2.2	339	2	13	116	148
150506	117.85233	-23.44141	Sheetwash	398757	RegGeoMap	98.58	0.2	20	-0.001	229	1	0.5	-1	61			32	0.2	31	23	5	19.7	18	1	2	93.1	4.2	25	0.7	2	42	-2		11.4	2.1	303	1	13	107	152
150500	117.89977	-23.39861	Alluvium	398751	RegGeoMap	98.75	-0.1	6	-0.001	465	1	-0.5	-1	58			19	-0.1	27	8	-1	9.9	9	3	2	75.2	1.4	15	-0.5	1	28	-2		7	1.7	185	-1	16	40	141
150496	117.89653	-23.47069	Alluvium	398747	RegGeoMap	99.26	0.2	28	0.003	336	1	-0.5	-1	60			27	0.1	24	20	-1	17	15	3	2	73.7	4.5	21	0.5	2	27	-2		8.7	1.7	300	-1	13	82	146
150495	117.98532	-23.47128	Alluvium	398746	RegGeoMap	99.65	0.1	9	-0.001	268	1	0.5	-1	63			29	0.1	33	35	2	20	8	2	2	73.9	1.5	20	0.6	2	57	-2		8.1	1.9	325	1	14	105	127
150044	117.44214	-23.2248	Sheetwash	398294	RegGeoMap	98.39	-0.1	32	-0.001	285	1	-0.5	-1	45			10	-0.1	26	6	3	5.9	71	-1	1	12	4.4	6	-0.5	1	24	-2		6.6	1.4	160	1	12	77	58
150043	117.35502	-23.21464	Sheetwash	398293	RegGeoMap	98.38	-0.1	17	0.001	261	2	-0.5	-1	42			18	-0.1	25	21	1	14	18	1	1	42	2.7	21	0.5	2	69	-2		7.7	1.9	301	1	20	48	143
150042	117.27274	-23.22746	Alluvium	398292	RegGeoMap	98.06	-0.1	8	0.001	324	2	0.5	-1	50			14	-0.1	16	30	1	12	20	-1	-1	108	3.2	10	-0.5	3	27	-2		11.8	2.2	97	2	5	53	137
150041	117.19601	-23.21708	Alluvium	398291	RegGeoMap	98.23	-0.1	37	0.001	242	1	-0.5	-1	34			12	-0.1	18	10	2	7.1	25	-1	-1	42	4.9	12	-0.5	2	43	-2		7.4	2.1	152	-1	10	96	93
150037	117.16198	-23.14416	Alluvium	398287	RegGeoMap	99.19	-0.1	21	-0.001	91	-1	-0.5	-1	19			6	-0.1	8.3	6	1	3	12	-1	-1	9.6	2.8	5	-0.5	-1	19	-2		3.6	0.8	90	-1	5	43	60
150036	117.24382	-23.1554	Alluvium	398286	RegGeoMap	100.09	-0.1	34	0.001	440	2	-0.5	-1	50			21	-0.1	27	17	1	10	17	-1	2	56	5	25	0.8	2	48	-2		7.6	2	291	1	19	128	175
150035	117.31764	-23.15087	Alluvium	398285	RegGeoMap	100.23	0.2	6	0.001	184	-1	-0.5	-1	32			17	-0.1	16	11	-1	18	5	3	3	19	0.6	21	-0.5	2	122	-2		3	0.9	247	-1	25	84	163
150034	117.38958	-23.14466	Sheetwash	398284	RegGeoMap	100.60	-0.1	9	-0.001	355	2	-0.5	-1	59			18	-0.1	18	20	1	18	13	-1	1	53	1.4	19	-0.5	2	100	-2		8.9	2.3	233	1	17	92	262
150030	117.26146	-23.07704	Alluvium	398280	RegGeoMap	100.59	-0.1	5	0.001	224	-1	-0.5	-1	33			17	-0.1	13	17	-1	11	10	5	4	31	1	19	0.7	1	82	-2		3.1	0.8	204	-1	21	131	125
150029	117.19551	-23.08093	Alluvium	398279	RegGeoMap	99.02	-0.1	11	-0.001	193	1	-0.5	-1	39			16	-0.1	20	7	1	9.1	10	-1	1	72	1.5	10	-0.5	2	22	-2		7.7	2.2	110	-1	11	39	118
150019	117.54649	-23.28371	Alluvium	398269	RegGeoMap	97.85	-0.1	10	-0.001	378	1	0.6	-1	35			9	-0.1	15	12	1	7.3	13	-1	-1	85	1.9	5	0.6	1	32	-2		9.5	1.7	43	1	7	31	96
150012	117.51164	-23.21962	Alluvium	398262	RegGeoMap	99.91	-0.1	17	-0.001	134	1	0.8	-1	41			15	-0.1	22	4	1	7.2	16	-1	1	10	4.5	13	1.5	1	22	-2		7.2	2.2	260	1	13	12	74
149947	117.39201	-23.28925	Alluvium	398197	RegGeoMap	99.82	-0.1	6	-0.001	188	-1	-0.5	-1	25			8	-0.1	19	11	-1	3.4	21	-1	-1	43	1.5	5	-0.5	4	24	-2		8.1	1.6	52	-1	8	31	65
149946	117.47575	-23.28528	Alluvium	398196	RegGeoMap	99.88	-0.1	16	0.001	219	1	-0.5	-1	26			14	-0.1	19	10	1	7.4	13	1	1	30	1.5	14	0.7	2	55	-2		6	1.6	195	1	18	86	97
149945	117.47641	-23.21973	Alluvium	398195	RegGeoMap	99.81	-0.1	27	-0.001	111	1	-0.5	-1	26			12	-0.1	16	-3	2	9.9	16	-1	-1	4.1	3.5	9	1.3	1	17	-2		7.9	2	217	3	11	27	83
149944	117.3991	-23.22579	Alluvium	398194	RegGeoMap	100.12	-0.1	5	-0.001	478	2	-0.5	-1	48			12	-0.1	26	18	-1	6.4	32	1	-1	104	1	7	-0.5	2	50	2		15.8	2.5	54	1	11	44	122
149943	117.31871	-23.21698	Alluvium	398193	RegGeoMap	99.84	-0.1	5	-0.001	191	1	-0.5	-1	20			7	-0.1	15	9	-1	5.5	16	-1	-1	43	1.5	3	-0.5	1	21	-2		7.4	1.6	29	1	6	26	56
149942	117.23563	-23.22362	Alluvium	398192	RegGeoMap	99.81	-0.1	8	0.001	264	-1	-0.5	-1	29			14	-0.1	17	11	-1	4.2	13	1	2	24	1.3	15	-0.5	1	80	2		4	1.2	102	-1	20	102	101
149937	117.18867	-23.14655	Alluvium	398187	RegGeoMap	99.21	-0.1	30	-0.001	241	1	-0.5	-1	26			14	-0.1	15	8	-1	7.3	20	-1	-1	22	3.1	9	1	1	72	-2		7.3	1.5	169	-1	15	67	90
149936	117.27111	-23.14872	Alluvium	398186	RegGeoMap	99.34	0.2	39	-0.001	361	2	-0.5	-1	54			26	-0.1	26	16	1	13	20	-1	2	65	7.3	24	1.3	2	61	-2		6.5	2.6	289	-1	21	121	161
149935	117.34912	-23.15179	Alluvium	398185	RegGeoMap	100.10	0.3	10	-0.001	233	-1	-0.5	-1	32			19	-0.1	16	17	-1	15	12	2	3	23	1	19	1.1	1	91	-2		3.6	1	224	-1	25	110	136
149934	117.42337	-23.14663	Alluvium	398184	RegGeoMap	100.65	0.3	8	-0.001	385	1	-0.5	-1	41			23	-0.1	21	22	1	18	13	-1	-1	44	0.5	25	1.3	2	80	2		8.5	2	184	1	30	97	164
149930	117.22275	-23.07628	Alluvium	398180	RegGeoMap	100.30	0.2	11	-0.001	222	-1	-0.5	-1	38			27	0.1	18	13	-1	15	12	2	5	26	1.4	25	1.3	2	129	-2		4.2	1	248	-1	34	115	144
149929	117.16483	-23.08217	Alluvium	398179	RegGeoMap	98.90	0.1	58	-0.001	241	2	-0.5	-1	44			16	-0.1	26	11	2	12	22	-1	-1	72	4	7	0.5	2	25	-2		11.9	3.2	110	2	16	82	84
149921	117.54578	-23.31942	Alluvium	398171	RegGeoMap	98.32	-0.1	4	-0.001	255	1	-0.5	-1	33			9	-0.1	18	18	-1	7.1	18	-1	-1	60	1	4	-0.5	1	23	-2		9.2	1.7	45	1	8	44	61
149914	117.54084	-23.25581	Sheetwash	398164	RegGeoMap	100.25	-0.1	19	0.002	725	1	-0.5	-1	45			20	-0.1	24	11	4	12	28	-1	-1	39	2.3	12	1.6	2	74	-2		8.5	2.1	219	1	18	69	155
149913	117.51685	-23.17711	Alluvium	398163	RegGeoMap	98.17	-0.1	51	-0.001	182	2	-0.5	-1	41			22	0.1	20	8	2	11	28	3	4	19	5.8	15	1.4	2	21	-2		7.9	1.7	313	2	19	167	80
149849	117.43446	-23.29849	Alluvium	398099	RegGeoMap	99.95	-0.1	26	-0.001	196	-1	-0.5	-1	35			15	-0.1	20	6	2	8.4	22	-1	1	19	2.5	9	1	1	26	-2		6.9	2.2	206	1	13	30	73
149848	117.46967	-23.25564	Alluvium	398098	RegGeoMap	99.42	-0.1	29	-0.001	164	1	-0.5	-1	36			16	-0.1	20	3	2	8.5	24	-1	-1	11	3.5	8	1.3	1	20	-2		7.4	1.9	196	2	12	18	59
149847	117.39597	-23.25568	Alluvium	398097	RegGeoMap	98.26	-0.1	13	-0.001	208	-1	-0.5	-1	29			7	-0.1	17	10	1	5.6	46	-1	-1	39	2.5	3	-0.5	-1	20	-2		6.4	2	31	-1	8	54	47
149846	117.32817	-23.26394	Alluvium	398096	RegGeoMap	99.25	0.2	11	-0.001	435	2	0.7	-1	75			21	-0.1	44	42	-1	19	23	-1	-1	168	3.2	13	-0.5	3	37	2		15.5	2.8	99	3	10	93	109
149840	117.20131	-23.19656	Alluvium	398090	RegGeoMap	99.28	0.1	8	-0.001	348	1	0.6	-1	55			14	-0.1	28	24	1	8.4	30	-1	-1	75	3.7	7	-0.5	2	79	-2		10.7	2.6	63	1	7	54	81
149839	117.27611	-23.18303	Alluvium	398089	RegGeoMap	99.47	-0.1	16	-0.001	123	-1	-0.5	-1	15			4	-0.1	5.9	6	1	2.9	12	-1	-1	9.7	2.4	2	-0.5	-1	10	-2		1.7	0.6	42	-1	4	21	32
149838	117.34084	-23.17964	Sheetwash	398088	RegGeoMap	99.40	0.2	29	-0.001	255	1	-0.5	-1	68			19	-0.1	39	16	2	12	24	3	2	39	2.3	16	0.8	2	56	-2		7.8	1.5	267	1	23	71	113
149837	117.42501	-23.18564	Alluvium	398087	RegGeoMap	99.24	0.2	21	0.001	70	1	-0.5	-1	29			17	0.1	18	6	2	12	12	-1	-1	14	5.3	20	2	2	18	-2		6.6	1.3	333	2	13	11	106
149834	117.31148	-23.10799	Alluvium	398084	RegGeoMap	100.47	0.3	12	-0.001	190	-1	-0.5	-1	39			19	0.1	19	14	1	14	31	6	5	20	2.4	23	0.5	10	109	-2		2.7	0.8	256	-1	25	145	111
149833	117.22906	-23.10614	Alluvium	398083	RegGeoMap	99.95	0.2	15	-0.001	236	1	-0.5	-1	44			19	0.1	23	15	2	11	15	2	3	34	2.4	22	0.5	2	116	-2		4.6	1.2	279	-1	25	123	137
149832	117.16349	-23.10645	Alluvium	398082	RegGeoMap	99.27	0.1	45	0.001	380	1	-0.5	-1	36			12	-0.1	24	8	4	9.1	19	-1	-1	47	3.5	7	0.6	2	24	-2		10.8	2.5	122	2	13	52	88

			LITHNAME	SITENO	ORIGNAME	Total	Ag	Ars	Au	Ba	Be	Bi	Cd	Ce	Cl	F	Ga	Ind	La	Li	Mo	Nb	Pb (ppm)	Pd	Pt	Rb	Sb	Sc	Se	Sn	Sr	Ta	Te	Th	U	V	W	Y	Zn	Zr
149828	117.16047	-23.04112	Alluvium	398079	RegGeoMap	100.49	0.3	9	-0.001	286	1	-0.5	-1	58			22	0.1	28	9	2	30	11	1	1	77	3.5	18	0.8	2	34	-2		8.6	2.1	293	2	20	85	179
149814	117.51235	-23.2562	Sheetwash	398065	RegGeoMap	100.26	0.1	8	-0.001	244	-1	-0.5	-1	31			11	-0.1	13	8	-1	5.7	9	-1	-1	26	0.8	11	-0.5	-1	63	-2		4.2	1.2	160	-1	14	66	72
149746	117.43687	-23.25203	Alluvium	397997	RegGeoMap	99.61	-0.1	3	-0.001	295	1	-0.5	-1	35			10	-0.1	15	16	-1	9.1	13	-1	-1	97	1.1	7	-0.5	2	29	-2		10.9	1.9	66	1	9	32	96
149745	117.35166	-23.26043	Alluvium	397996	RegGeoMap	99.05	-0.1	6	-0.001	470	3	0.7	-1	70			19	-0.1	38	33	-1	13	23	-1	-1	157	2.4	11	-0.5	4	36	-2		18.2	2.7	87	2	11	66	110
149744	117.28548	-23.25487	Alluvium	397995	RegGeoMap	99.31	-0.1	5	-0.001	357	2	0.7	-1	70			17	-0.1	31	27	-1	11	23	-1	-1	116	2.6	10	-0.5	4	28	-2		15.7	3.3	81	2	11	57	95
149739	117.15502	-23.18354	Alluvium	397990	RegGeoMap	98.59	-0.1	8	-0.001	383	2	0.6	-1	63			18	-0.1	38	30	-1	17	19	-1	-1	145	3.1	9	-0.5	4	37	-2		16.8	2.8	79	3	8	58	119
149738	117.23371	-23.18751	Soil	397989	RegGeoMap	99.17	-0.1	32	0.002	366	-1	-0.5	-1	38			11	-0.1	17	8	1	7	25	-1	-1	37	6.7	7	-0.5	2	40	-2		10.6	2.3	87	1	7	35	73
149737	117.31004	-23.18974	Alluvium	397988	RegGeoMap	99.03	-0.1	7	-0.001	59	-1	-0.5	-1	17			4	-0.1	13	7	-1	3.7	18	-1	-1	12	2.8	3	-0.5	-1	6	-2		3.8	0.6	47	-1	4	8	32
149736	117.39182	-23.19302	Alluvium	397987	RegGeoMap	100.83	-0.1	29	-0.001	96	2	-0.5	-1	30			15	-0.1	18	4	-1	8.6	15	-1	-1	6.1	11	14	1.4	2	28	-2		7.8	1.8	216	2	13	7	77
149735	117.48333	-23.18074	Alluvium	397986	RegGeoMap	100.72	-0.1	17	-0.001	146	1	-0.5	-1	22			19	-0.1	12	6	-1	7.6	9	-1	-1	5.7	3.1	22	2.2	2	14	-2		6.2	1.5	265	1	12	10	82
149732	117.27191	-23.10365	Alluvium	397983	RegGeoMap	100.60	0.1	19	-0.001	362	1	-0.5	-1	46			22	0.3	24	27	-1	15	32	4	5	54	3.7	27	0.6	3	66	-2		6	1.5	225	-1	24	361	171
149731	117.19651	-23.10037	Alluvium	397982	RegGeoMap	99.47	-0.1	22	-0.001	245	1	-0.5	-1	41			22	0.1	24	15	-1	11	12	2	3	34	2.6	22	-0.5	2	131	-2		5.3	1.3	233	-1	23	113	142
149726	117.20342	-23.04339	Alluvium	397977	RegGeoMap	100.73	-0.1	14	-0.001	229	1	-0.5	-1	44			25	0.1	20	16	-1	14	13	2	3	34	2.1	27	-0.5	2	134	-2		5.1	1.4	264	-1	28	107	168
149719	117.50368	-23.28757	Alluvium	397970	RegGeoMap	100.16	0.1	12	0.001	269	1	-0.5	-1	37			19	-0.1	20	18	-1	15	16	3	2	47	1.2	16	-0.5	2	75	-2		8.5	2	193	1	19	103	128

Appendix 6 Tornado mapping

MOD13_28 (127.80–127.85 m)

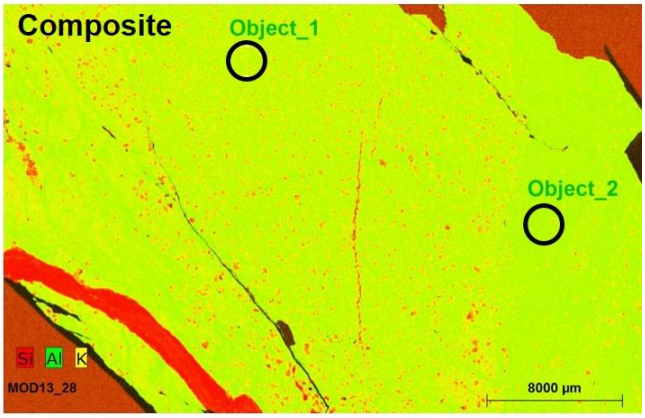

Element	Obj1	Obj2
Si	56.3	50.2
Al	21.3	24.1
K	18.8	20.9
Ti	2.86	3.97
Fe	0.71	0.85

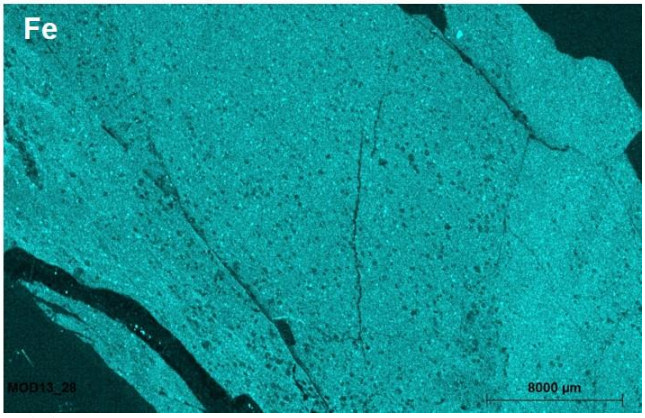

MOD13_29 (139.20–139.27 m)

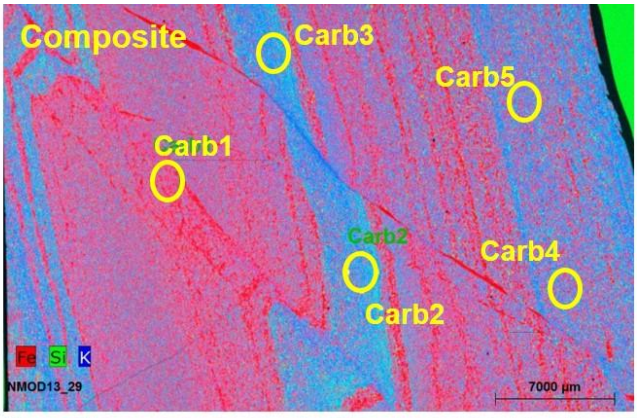

Element	Carb1	Carb2	Carb3	Carb4	Carb5
Fe	35.1	9.53	8.03	17.7	18.4
Si	34.5	48.0	48.0	46.1	45.0
Al	20.9	22.0	22.8	23.2	23.5
K	6.73	16.4	16.8	9.23	9.32
Ti	2.24	4.08	4.37	3.79	3.85
Mg	0.61				

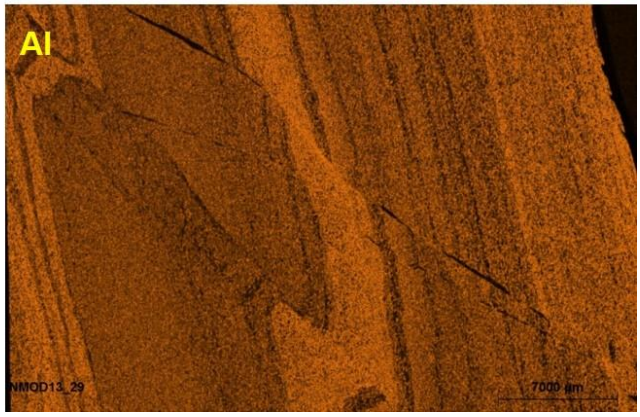

NMOD1_36 (270.0–270.35)

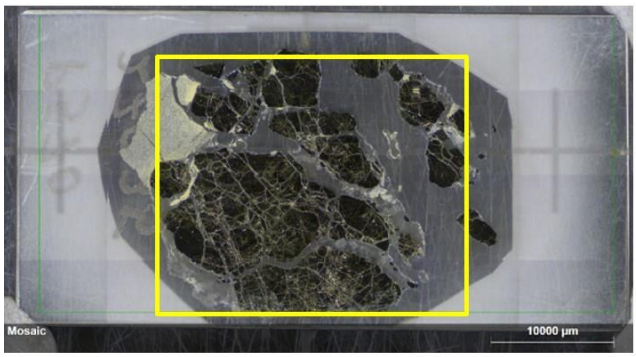

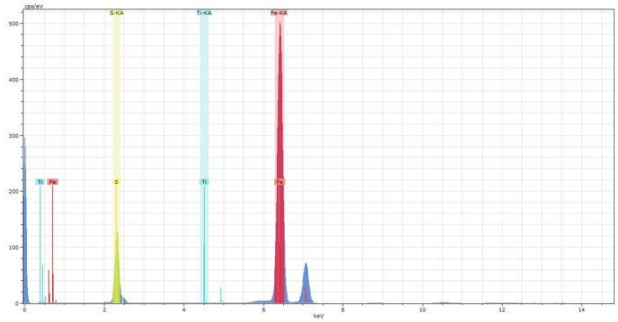

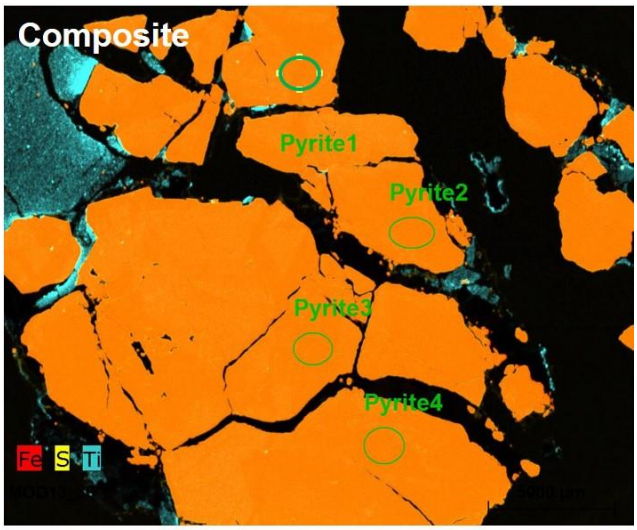

Element	Py1	Py2	Py3	Py4
Fe	46.4	46.2	51.3	51.8
S	53.6	53.8	48.7	48.2

NMOD1_41 (362.64–362.76)

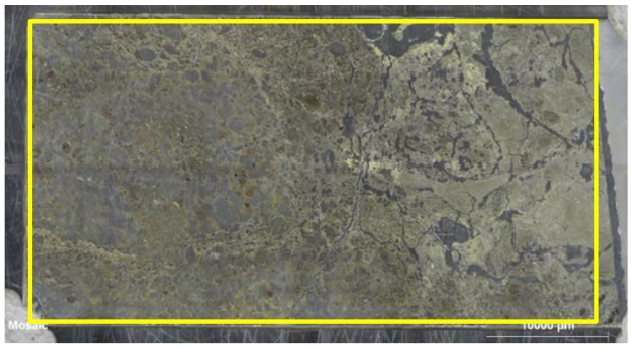

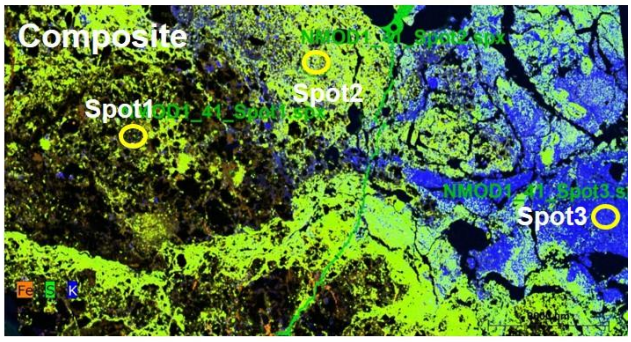

Element	Spot1	Spot2	Spot3
Si	66.0	41.3	41.1
Ca	8.79		2.61
S	6.29	23.6	4.82
Al	5.67	8.87	24.5
Fe	5.62	18.0	5.09
P	3.77		
Ti	1.80	1.20	4.30
K	1.53	5.55	17.6
As	0.50	1.49	

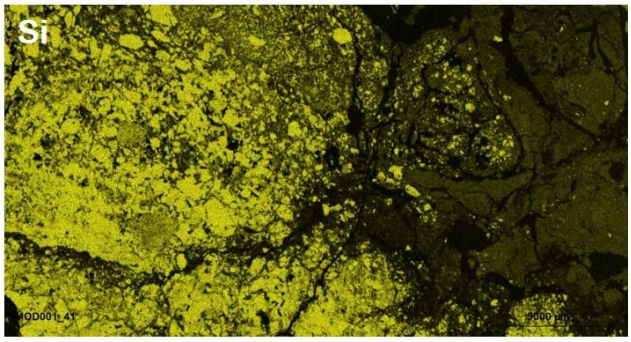

NMOD1_43 (438.10–438.29)

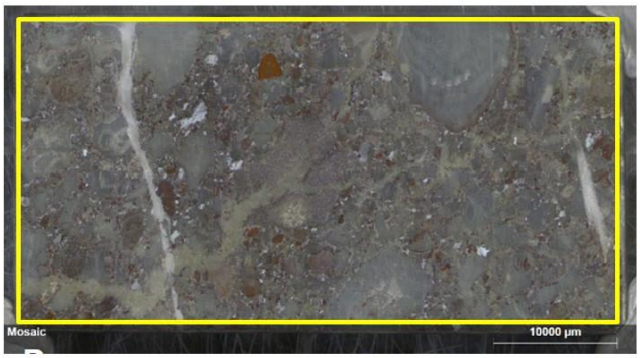

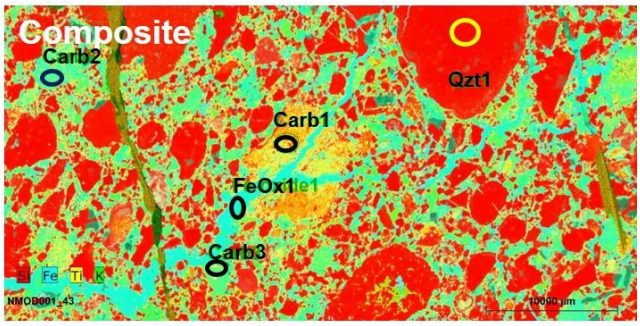

Element	Carb1	Carb2	Carb3	FeOx1	Qzt1
Si	76.0	17.2	1.21	1.49	100
Fe	13.5	51.8	38.0	85.6	
Ca	7.31	17.1	45.5	1.64	
Ti	3.18	1.33	1.88		
Mg		7.46	12.8	10.65	
Al		5.14			
Mn				0.62	
Sc			0.55		

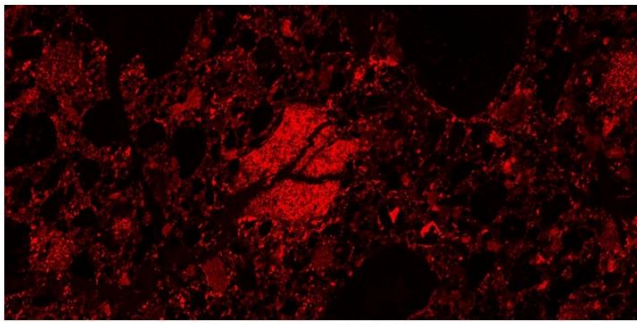

SPD001_7 (386.00–386.25)

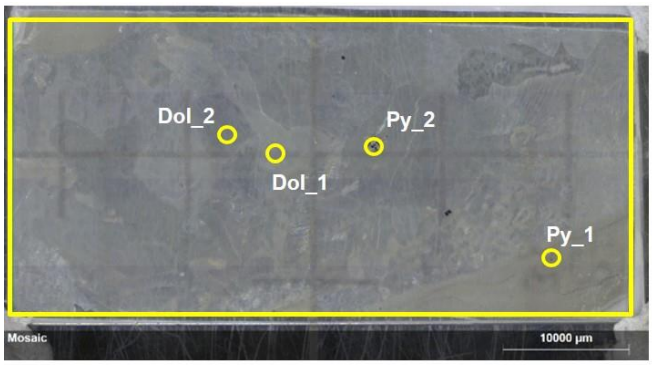

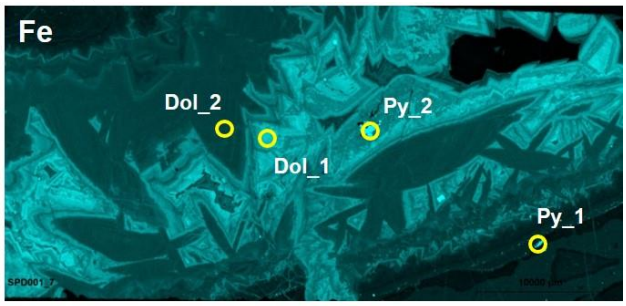

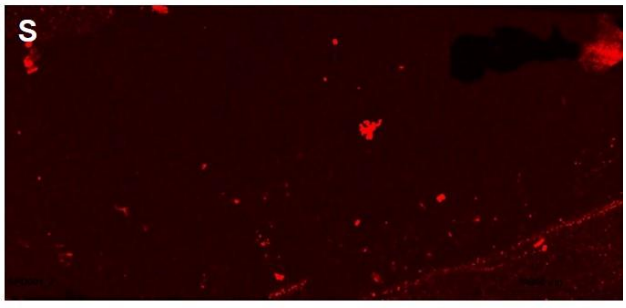

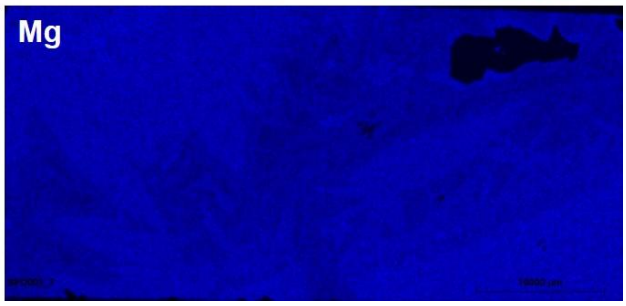

Element	Dol_1	Dol_2	Py_1	Py_2
Ca	56.3	63.9	6.55	6.27
Fe	22.7	7.56	47.0	44.2
Mg	20.3	28.0		
Mn	0.72	0.57		
S			46.4	49.6

SPD001_13 (445.68-445.82)

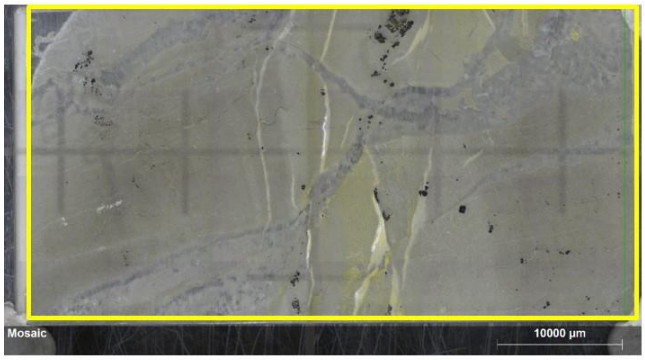

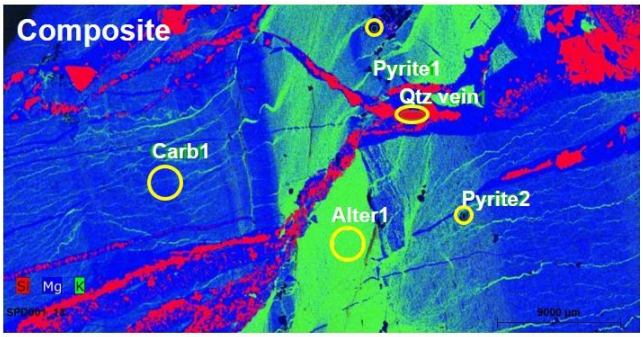

Element	Alter1	Carb1
Si	38.8	5.80
Al	28.7	4.58
K	22.9	2.55
Ti	5.59	0.57
Ca	2.43	55.2
Fe	0.92	10.5
Mg	0.69	20.0
Mn		0.67
P		0.06
Ni		0.04
S		0.00

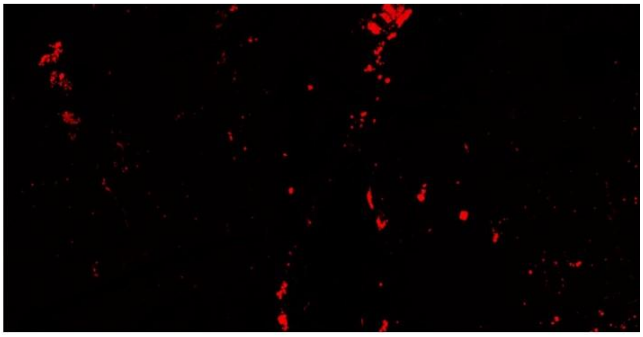

Mt Olympus sample: MT02 (Mt Olympus pit: surface)

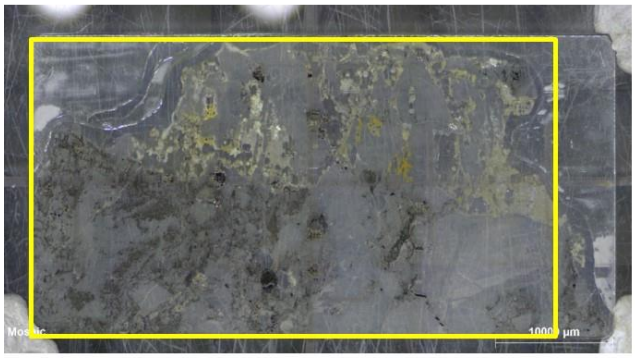

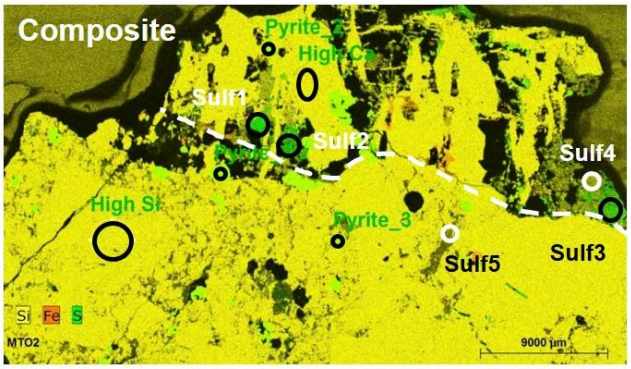

Element	Py1	Py2	Py3	Sulf1	Sulf2	Sulf3	Sulf4	Sulf5
S	52.0	52.3	51.6	34.5	28.5	31.1	6.77	4.49
Fe	43.2	44.2	42.6	2.02	1.47	4.86	2.10	3.96
Si	2.96	2.23	3.02	4.12	24.49	11.19	74.9	44.0
As	1.81	1.32	1.21					
Al			0.94	30.2	19.3	24.6		23.0
K			0.67	25.7	20.6	18.8	2.03	18.9
Ca				3.42	5.62	9.42	14.2	4.23
Ti								1.36

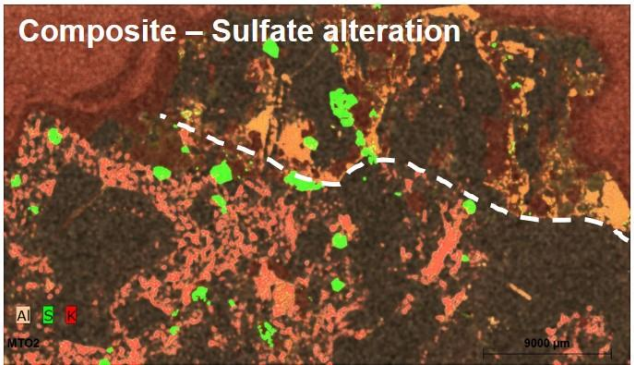

Appendix 7 Drill core logs

Refer to the associated Power Point file (Appendix &_TSA Drill Core Logs_Final.pptx), which provides TSA summary logs for all of the EIS and Sipa Resources drill holes examined in this work.

Appendix 7: Drill core logs

TSA summary logs for EIS and Sipa Resources drill holes examined

GSWA- CSIRO

18.12.2015

www.csiro.au

MOD4 (max Au 33 ppm)

Mineralized interval: ferruginous fine-grain conglomerate with jarosite. Reflectance >20%

Chipped quartz vein with grey/white sulphates

Mineralized interval: sheared siltstone/shale with grey and white sulphates

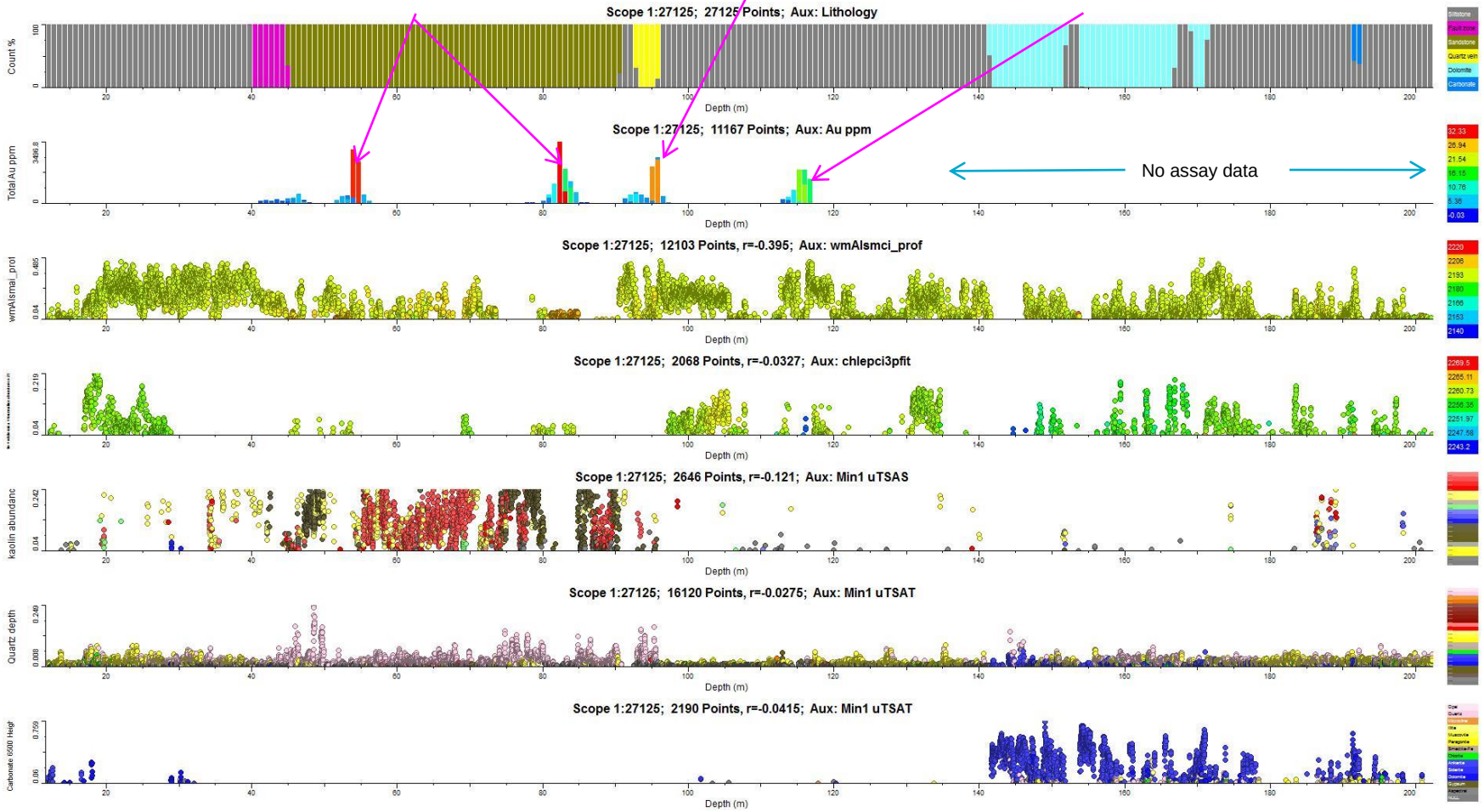

MOD4

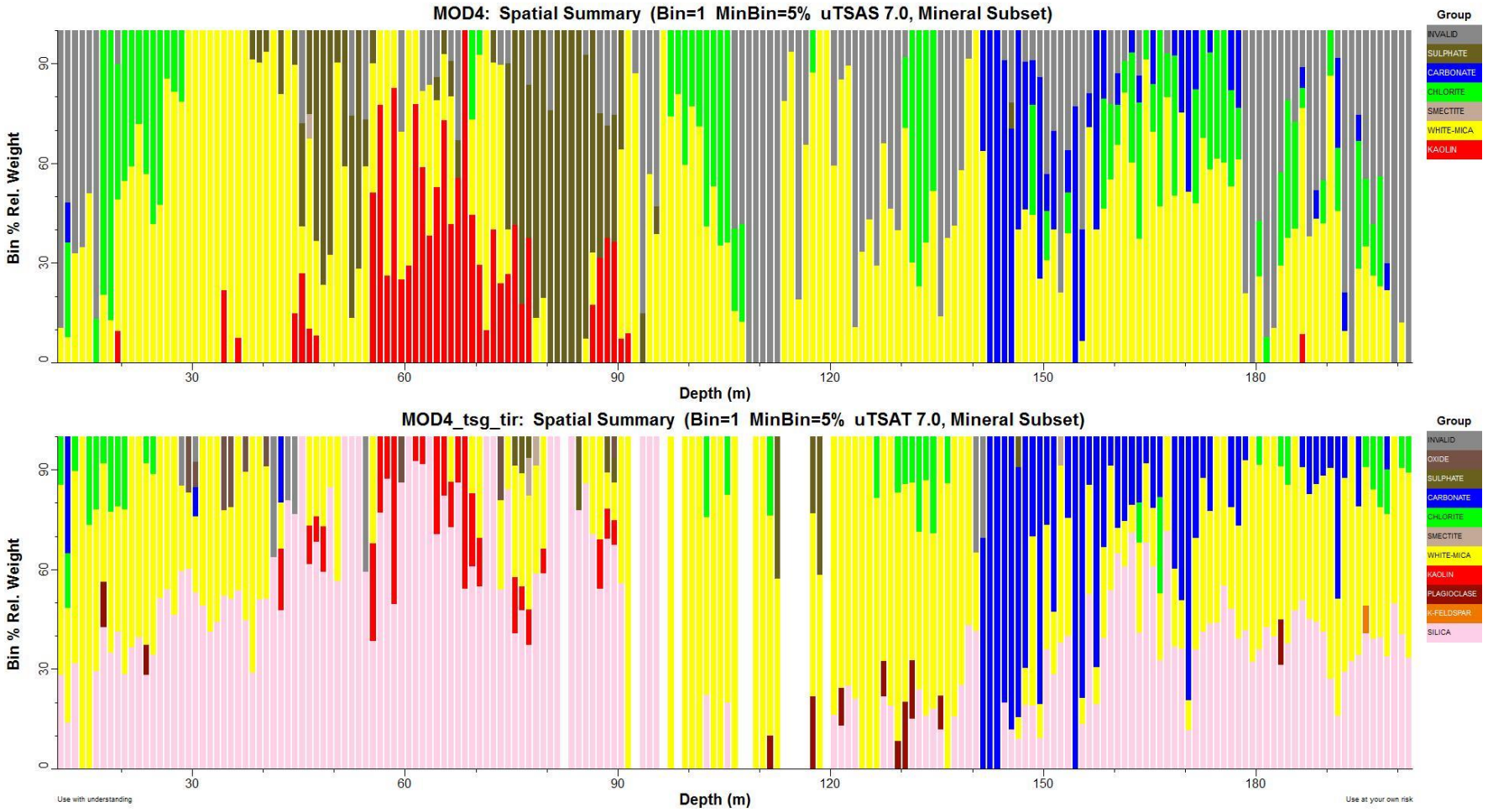
MOD4: Spatial Summary (Bin=1 MinBin=5% uTSAS 7.0, Mineral Subset)
Group
INVALID
SULPHATE
CARBONATE
CHLORITE
SMECTITE
WHITE-MICA
KAOLIN
Bin % Rel. Weight
0
30
60
90
30
60
90
120
150
180
Depth (m)
MOD4_tsg_tir: Spatial Summary (Bin=1 MinBin=5% uTSAT 7.0, Mineral Subset)
Group
INVALID
OXIDE
SULPHATE
CARBONATE
CHLORITE
SMECTITE
WHITE-MICA
KAOLIN
PLAGIOCLASE
K-FELDSPAR
SILICA
Bin % Rel. Weight
0
30
60
90
30
60
90
120
150
180
Depth (m)
Use with understanding
Use at your own risk

MOD5 (max Au 17 ppm)

- TSA shows jarosite for chlorite script
- Higher kaolin abundance

Different lithology to MOD12 and MOD13: conglomerates and sandstone
Only last siltstone unit correlates with MOD12 lithology at 140 m

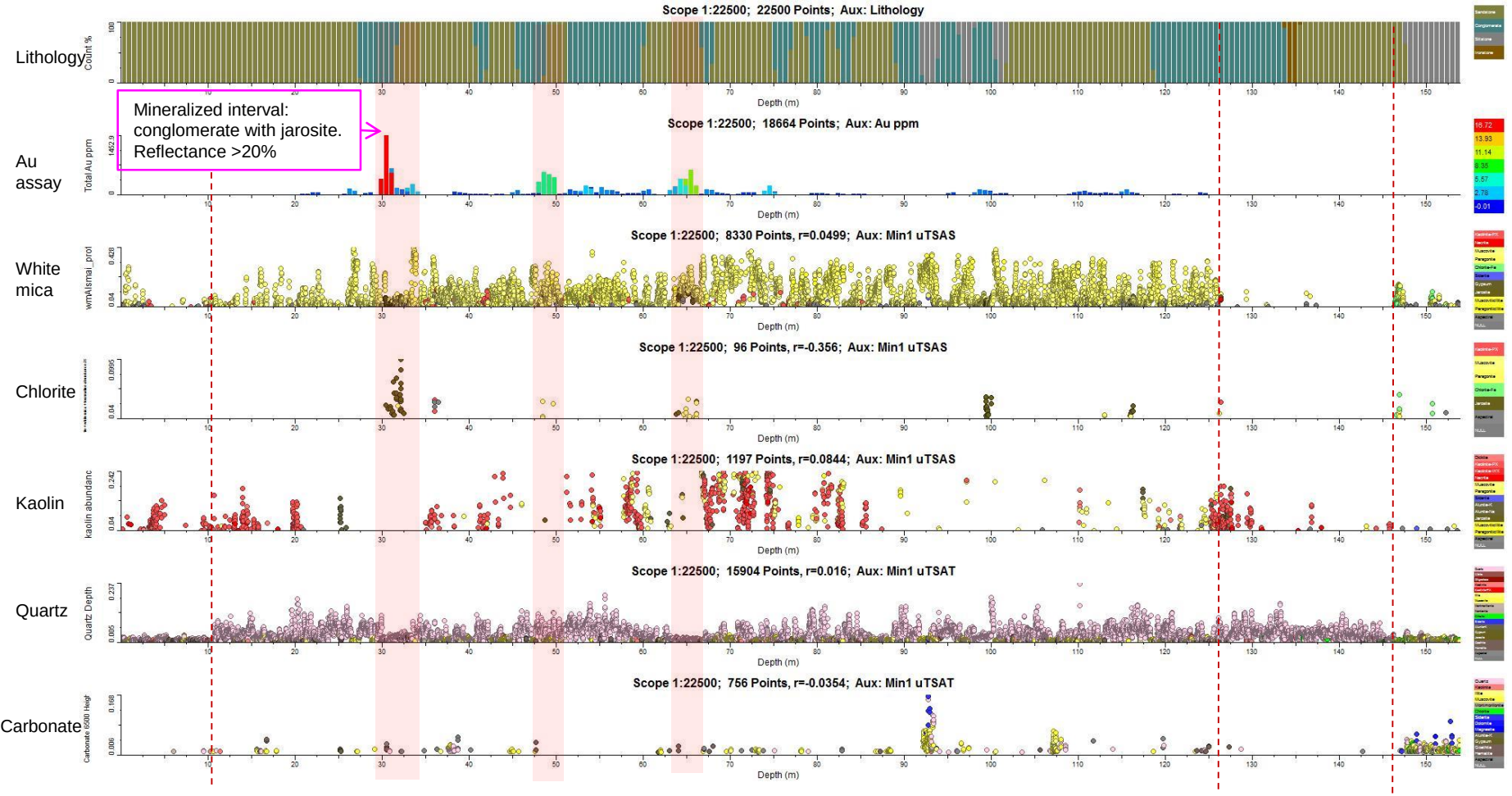

MOD5

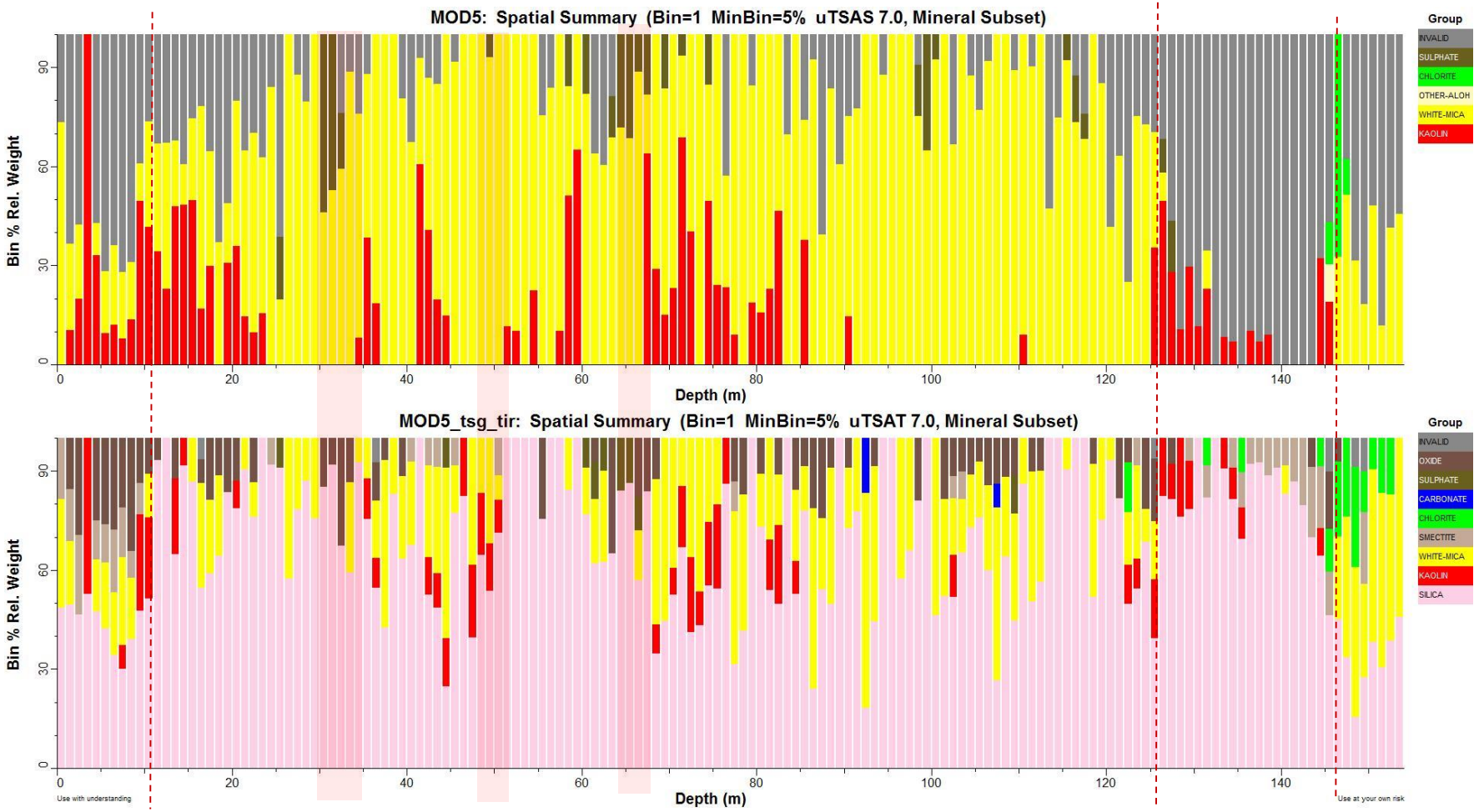
MOD5: Spatial Summary (Bin=1 MinBin=5% uTSAS 7.0, Mineral Subset)
Group
INVALID
SULPHATE
CHLORITE
OTHER-ALOH
WHITE-MICA
KAOLIN
Bin % Rel. Weight
Depth (m)
MOD5_tsg_tir: Spatial Summary (Bin=1 MinBin=5% uTSAT 7.0, Mineral Subset)
Group
INVALID
OXIDE
SULPHATE
CARBONATE
CHLORITE
SMECTITE
WHITE-MICA
KAOLIN
SILICA
Bin % Rel. Weight
Depth (m)
Use with understanding
Use at your own risk

MOD 6 (max Au 16 ppm)

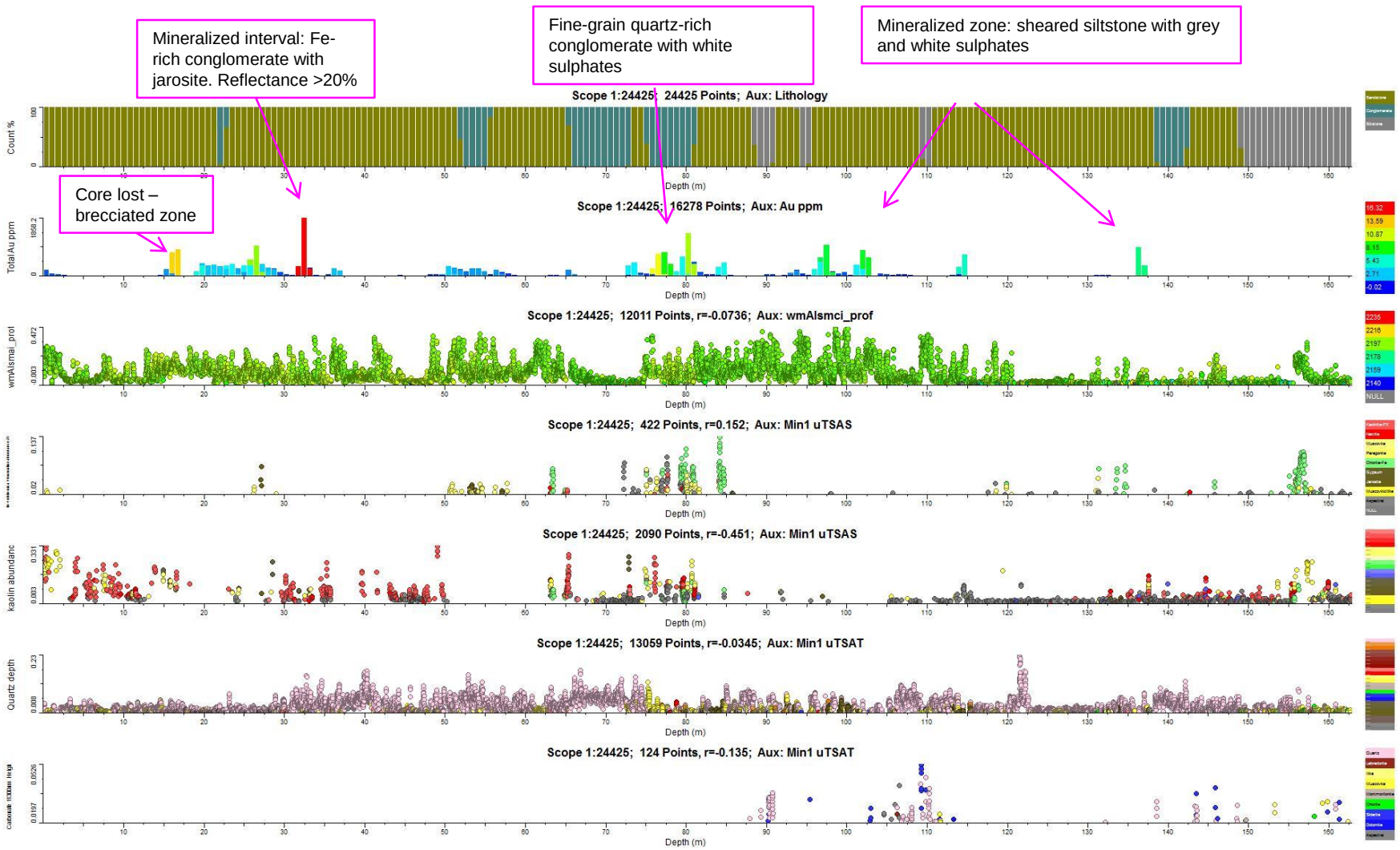

MOD 6

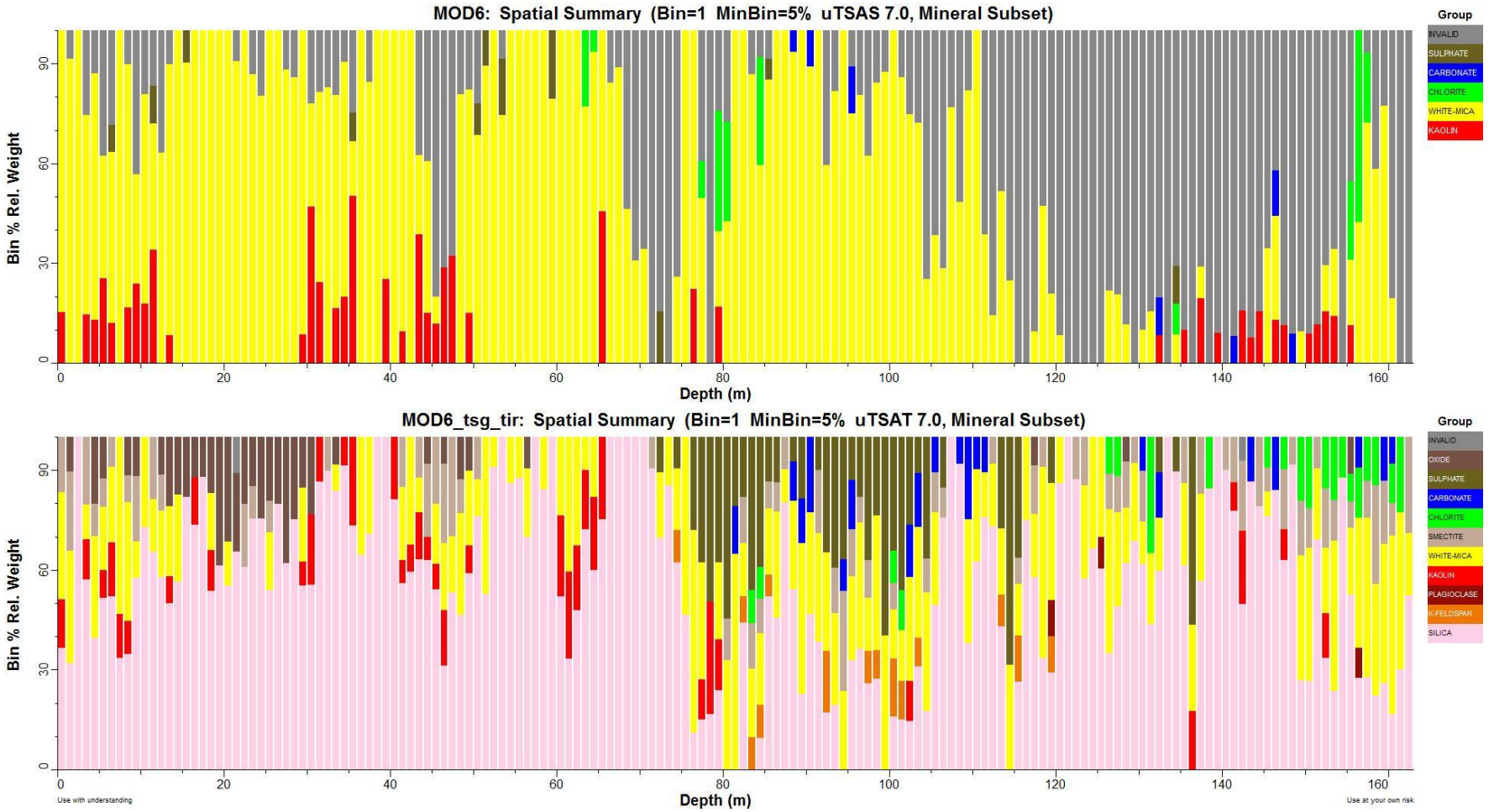
MOD6: Spatial Summary (Bin=1 MinBin=5% uTSAS 7.0, Mineral Subset)
Group
INVALID
SULPHATE
CARBONATE
CHLORITE
WHITE-MICA
KAOLIN
Bin % Rel. Weight
0
30
60
90
0
20
40
60
80
100
120
140
160
Depth (m)
MOD6_tsg_tir: Spatial Summary (Bin=1 MinBin=5% uTSAT 7.0, Mineral Subset)
Group
INVALID
OXIDE
SULPHATE
CARBONATE
CHLORITE
SMECTITE
WHITE-MICA
KAOLIN
PLAGIOCLASE
K-FELDSPAR
SILICA
Bin % Rel. Weight
Use with understanding
Use at your own risk
Depth (m)

MOD7 (max Au 32 ppm)

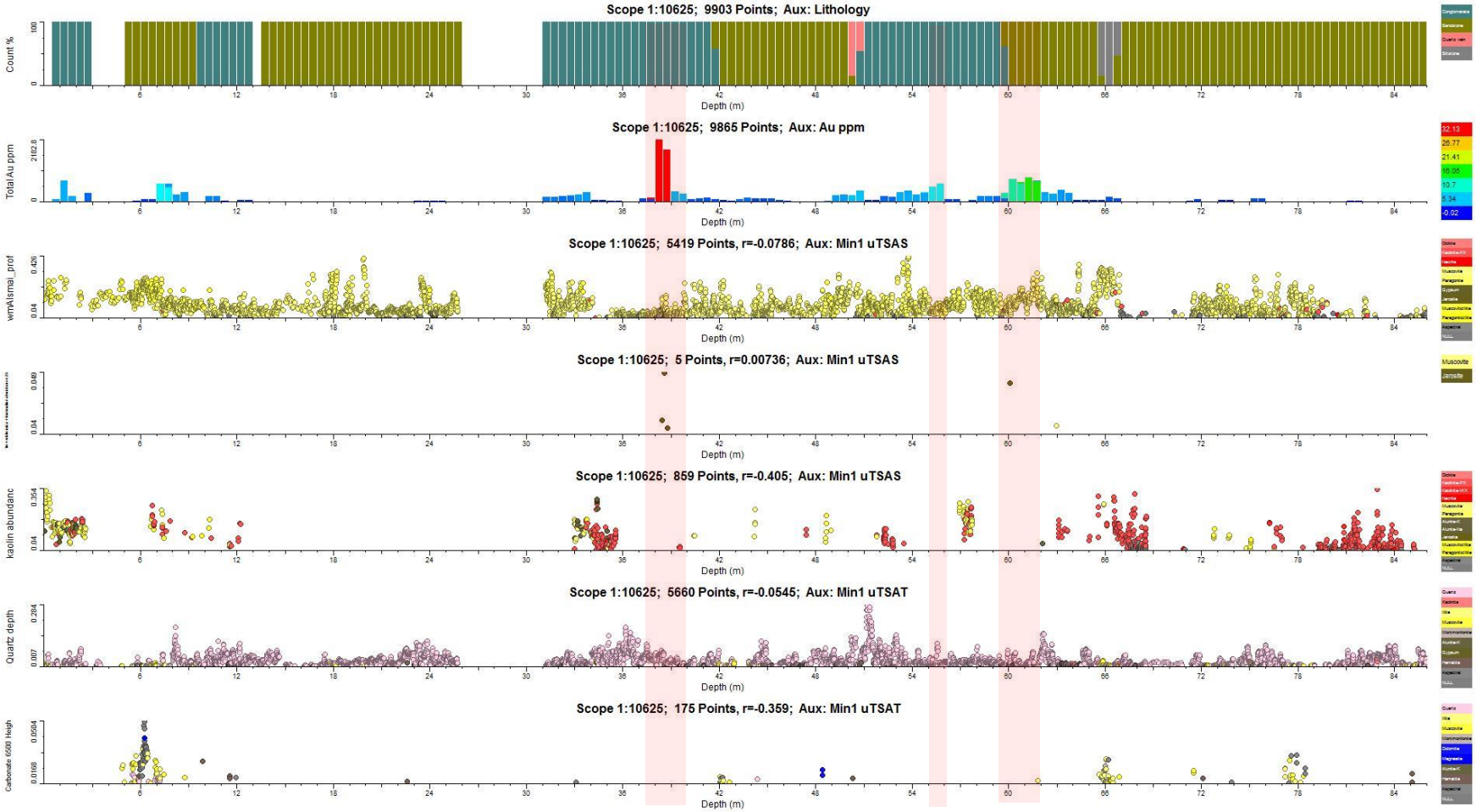

MOD7

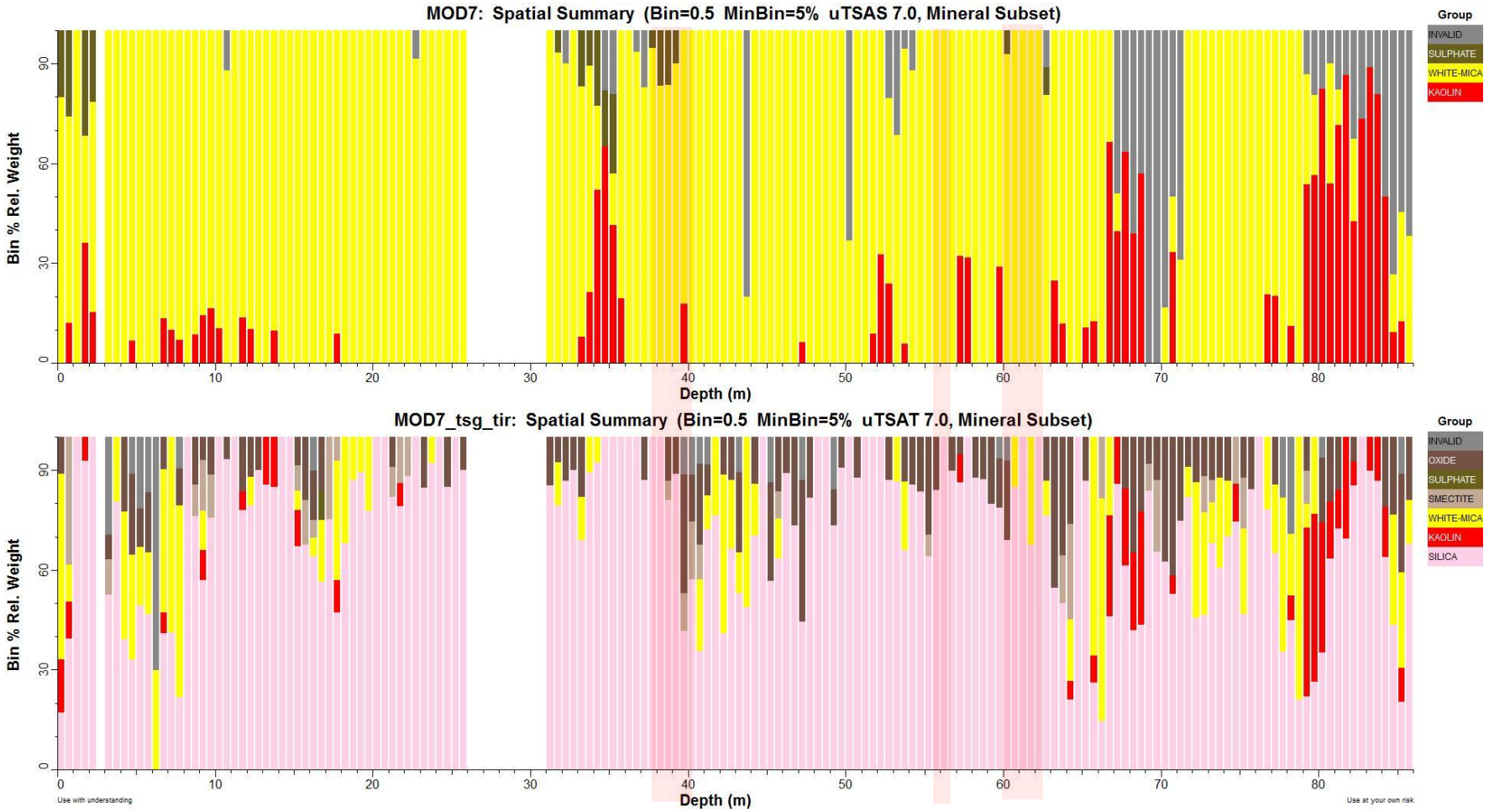
MOD7: Spatial Summary (Bin=0.5 MinBin=5% uTSAS 7.0, Mineral Subset)
Group
INVALID
SULPHATE
WHITE-MICA
KAOLIN
Bin % Rel. Weight
0
30
60
90
0
10
20
30
40
50
60
70
80
Depth (m)
MOD7_tsg_tir: Spatial Summary (Bin=0.5 MinBin=5% uTSAT 7.0, Mineral Subset)
Group
INVALID
OXIDE
SULPHATE
SMECTITE
WHITE-MICA
KAOLIN
SILICA
Bin % Rel. Weight
0
30
60
90
0
10
20
30
40
50
60
70
80
Depth (m)
Use with understanding
Use at your own risk

MOD8 (max Au 13 ppm)

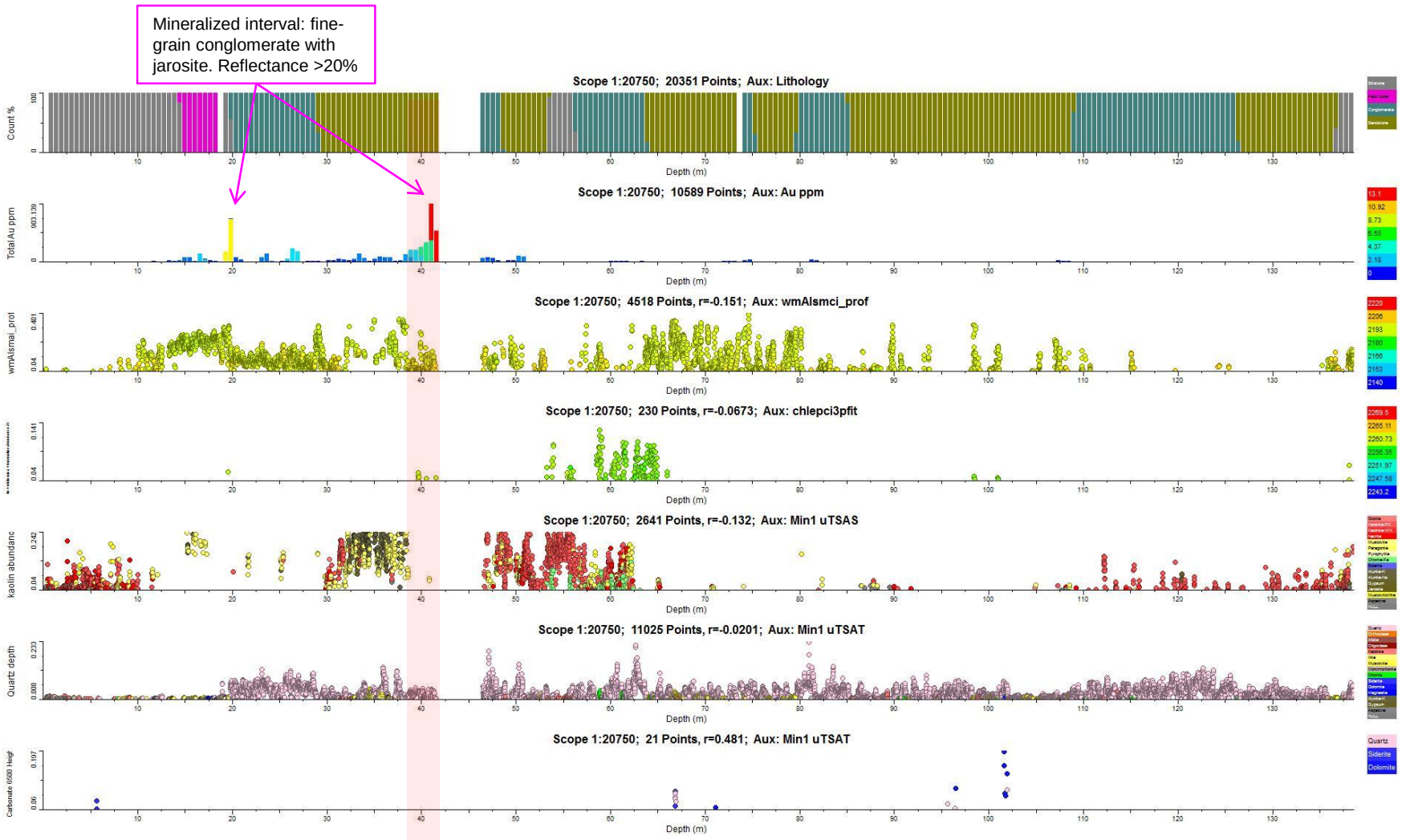

MOD8

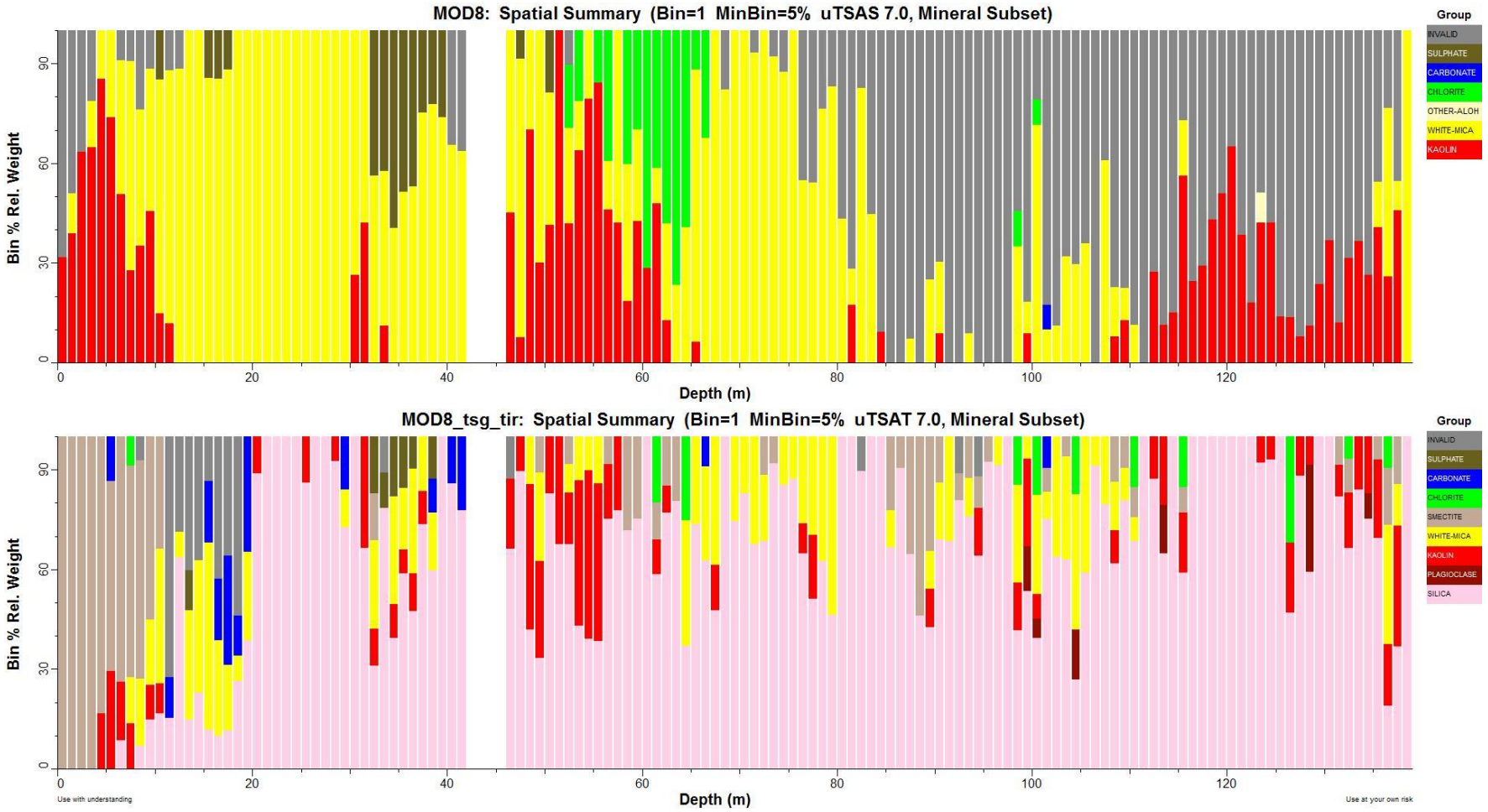
MOD8: Spatial Summary (Bin=1 MinBin=5% uTSAS 7.0, Mineral Subset)
Group
INVALID
SULPHATE
CARBONATE
CHLORITE
OTHER-ALOH
WHITE-MICA
KAOLIN
Bin % Rel. Weight
0
30
60
90
0
20
40
60
80
100
120
Depth (m)
MOD8_tsg_tir: Spatial Summary (Bin=1 MinBin=5% uTSAT 7.0, Mineral Subset)
Group
INVALID
SULPHATE
CARBONATE
CHLORITE
SMECTITE
WHITE-MICA
KAOLIN
PLAGIOCLASE
SILICA
Bin % Rel. Weight
0
30
60
90
0
20
40
60
80
100
120
Depth (m)
Use with understanding
Use at your own risk

MOD12 (max Au 5 ppm)

Mineralized zone: sheared siltstone with grey and white sulphates.

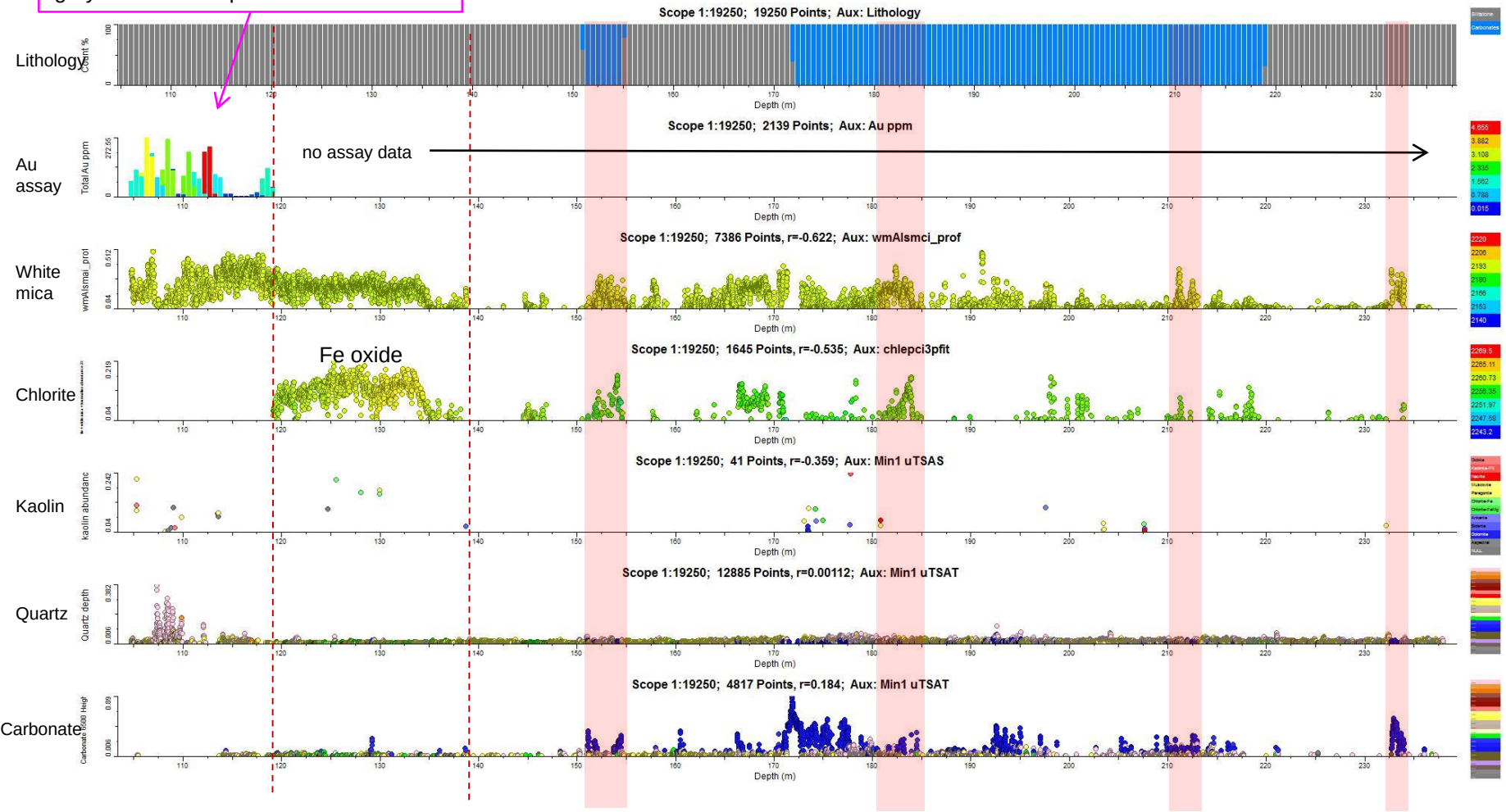

MOD12

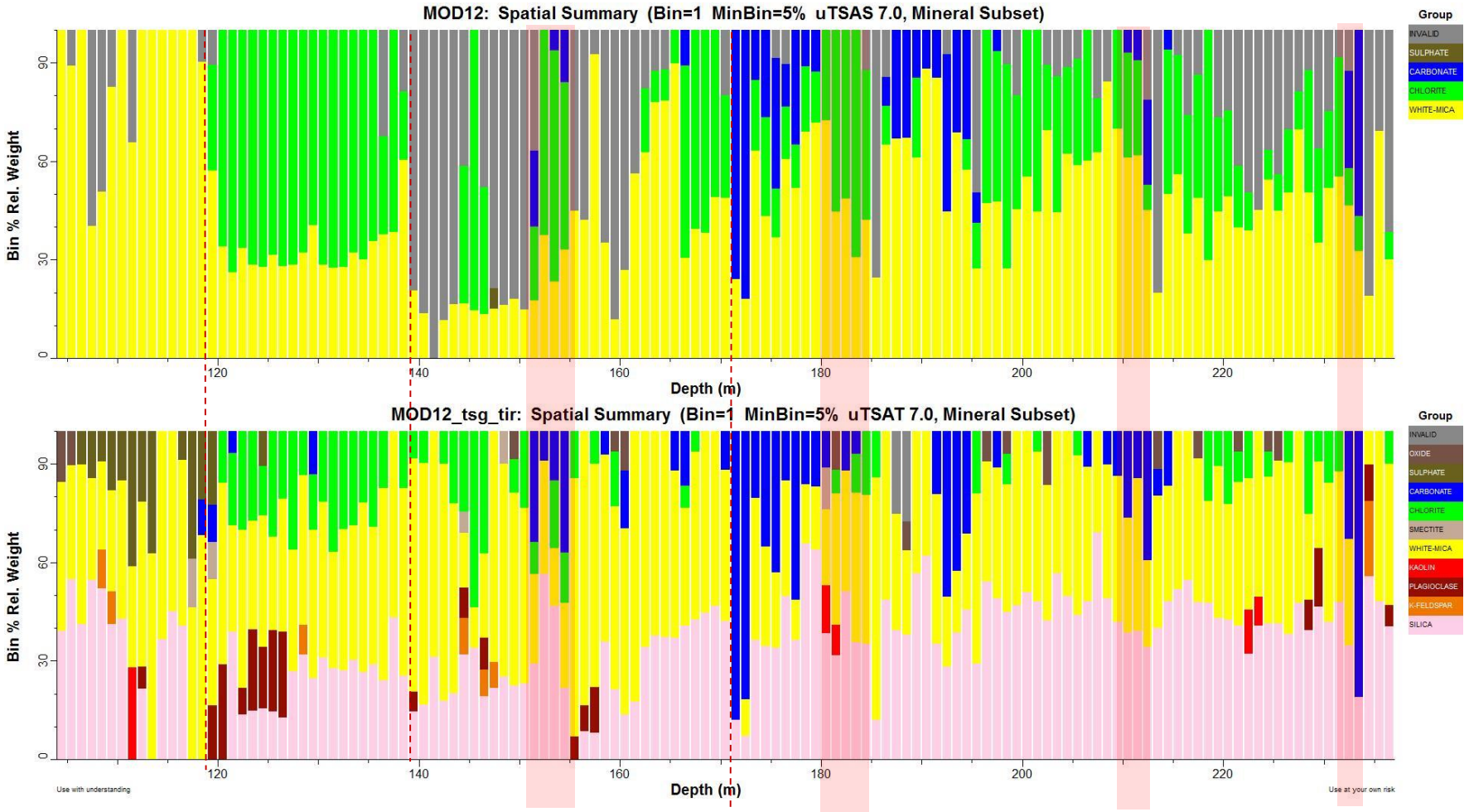
MOD12: Spatial Summary (Bin=1 MinBin=5% uTSAS 7.0, Mineral Subset)
Group
INVALID
SULPHATE
CARBONATE
CHLORITE
WHITE-MICA
Bin % Rel. Weight
0
30
60
90
120
140
160
180
200
220
Depth (m)
MOD12_tsg_tir: Spatial Summary (Bin=1 MinBin=5% uTSAT 7.0, Mineral Subset)
Group
INVALID
OXIDE
SULPHATE
CARBONATE
CHLORITE
SMECTITE
WHITE-MICA
KAOLIN
PLAGIOCLASE
K-FELDSPAR
SILICA
Bin % Rel. Weight
0
30
60
90
120
140
160
180
200
220
Depth (m)
Use with understanding
Use at your own risk

MOD13 (max Au 124 ppm)

- Lack of chlorite, only at 140 m
- No kaolin minerals by TSA
- Carbonate script maps more samples
- Only muscovite presents

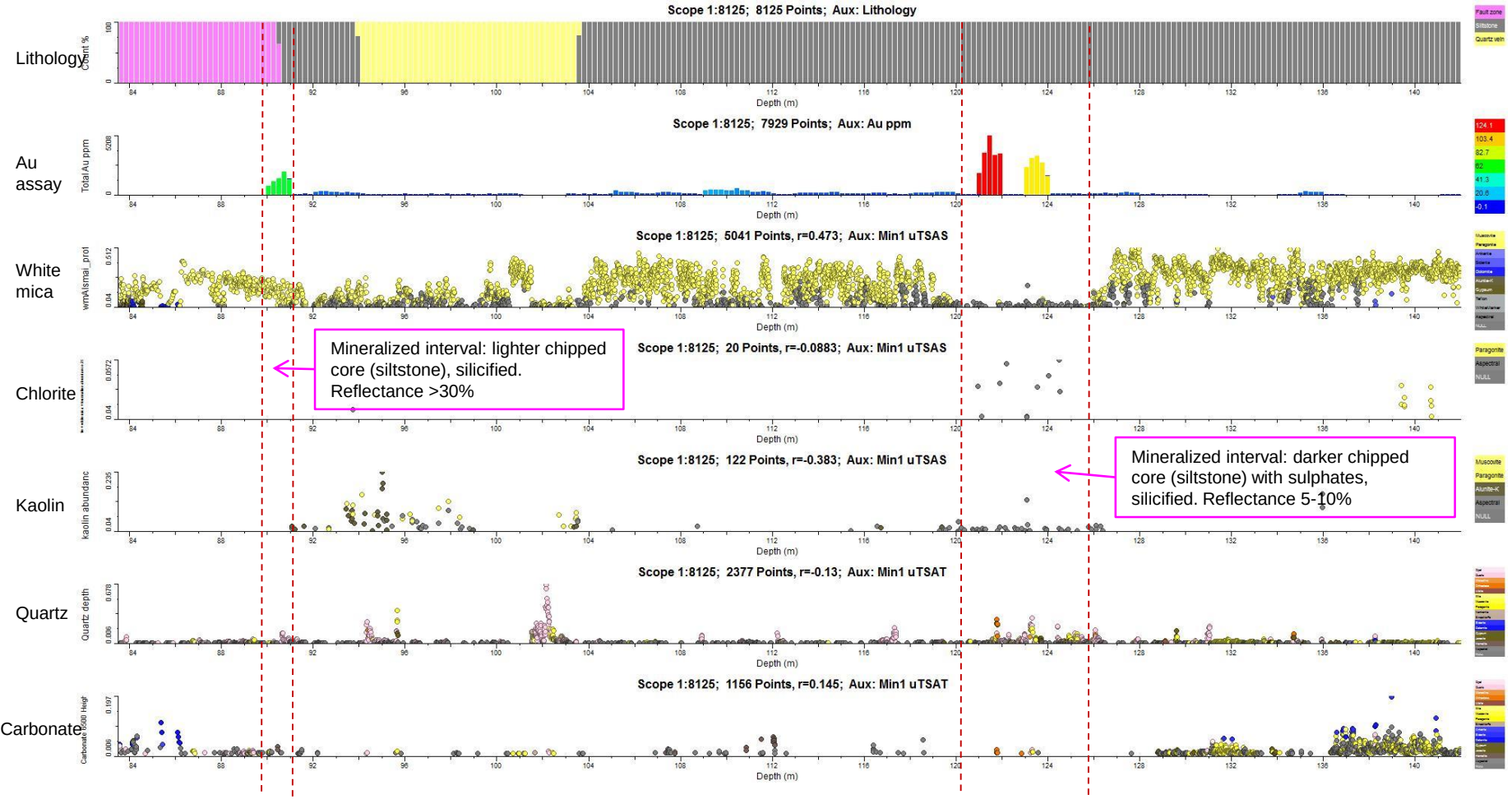

MOD13

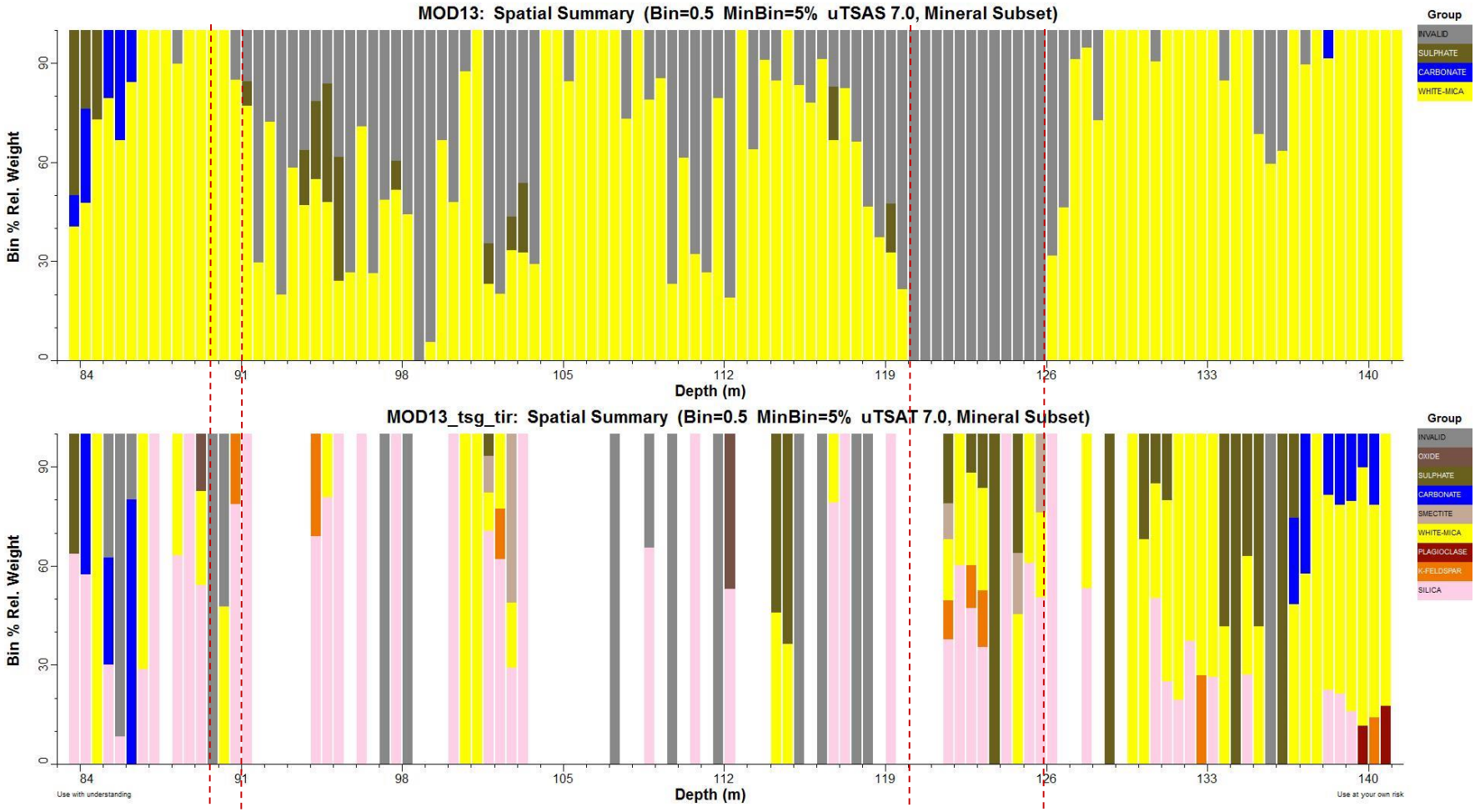
MOD13: Spatial Summary (Bin=0.5 MinBin=5% uTSAS 7.0, Mineral Subset)
Group
INVALID
SULPHATE
CARBONATE
WHITE-MICA
Bin % Rel. Weight
0
30
60
90
84
91
98
105
112
119
126
133
140
Depth (m)
MOD13_tsg_tir: Spatial Summary (Bin=0.5 MinBin=5% uTSAT 7.0, Mineral Subset)
Group
INVALID
OXIDE
SULPHATE
CARBONATE
SMECTITE
WHITE-MICA
PLAGIOCLASE
K-FELDSPAR
SILICA
Bin % Rel. Weight
Use with understanding
Use at your own risk

MOD14 (max Au 11 ppm)

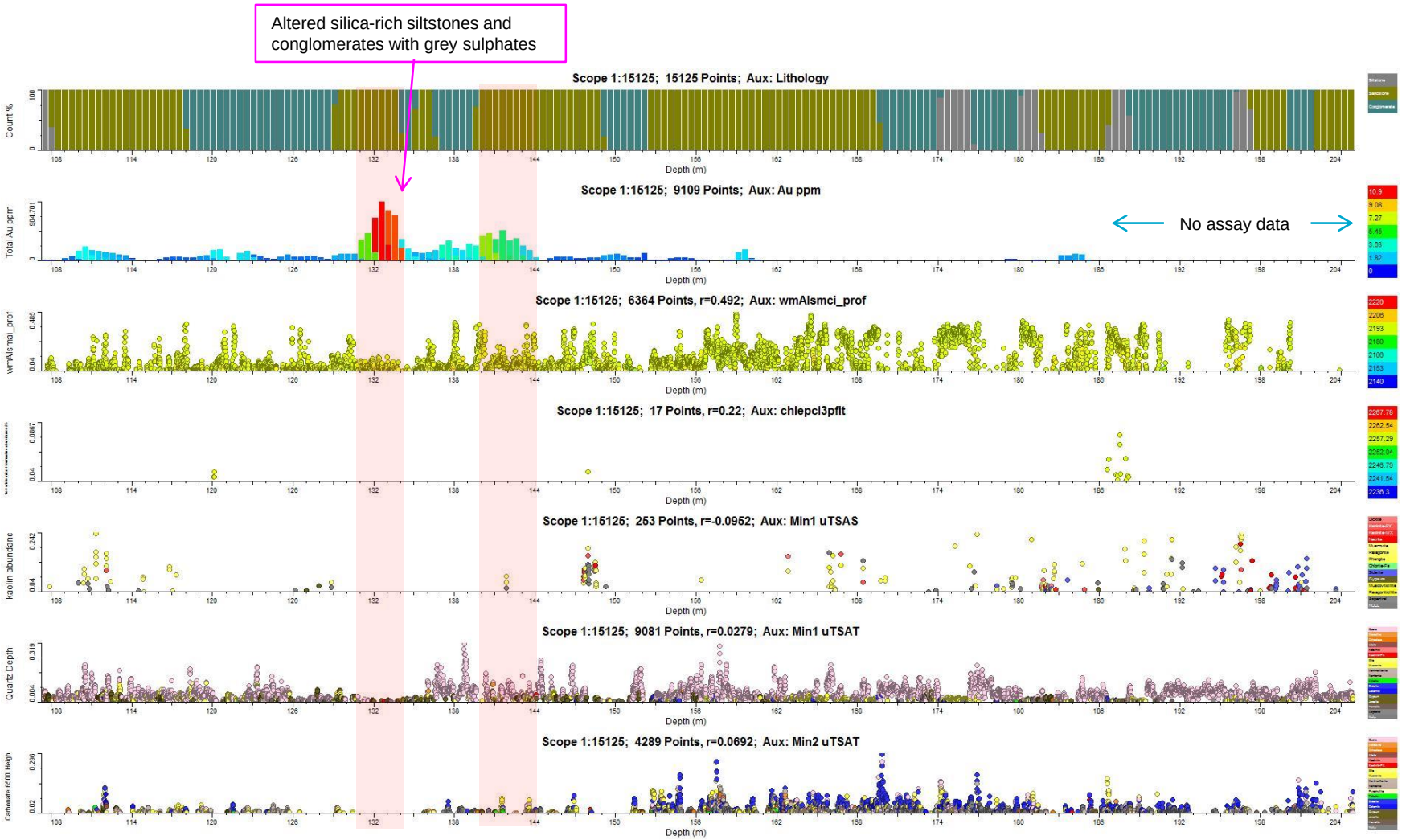

MOD14

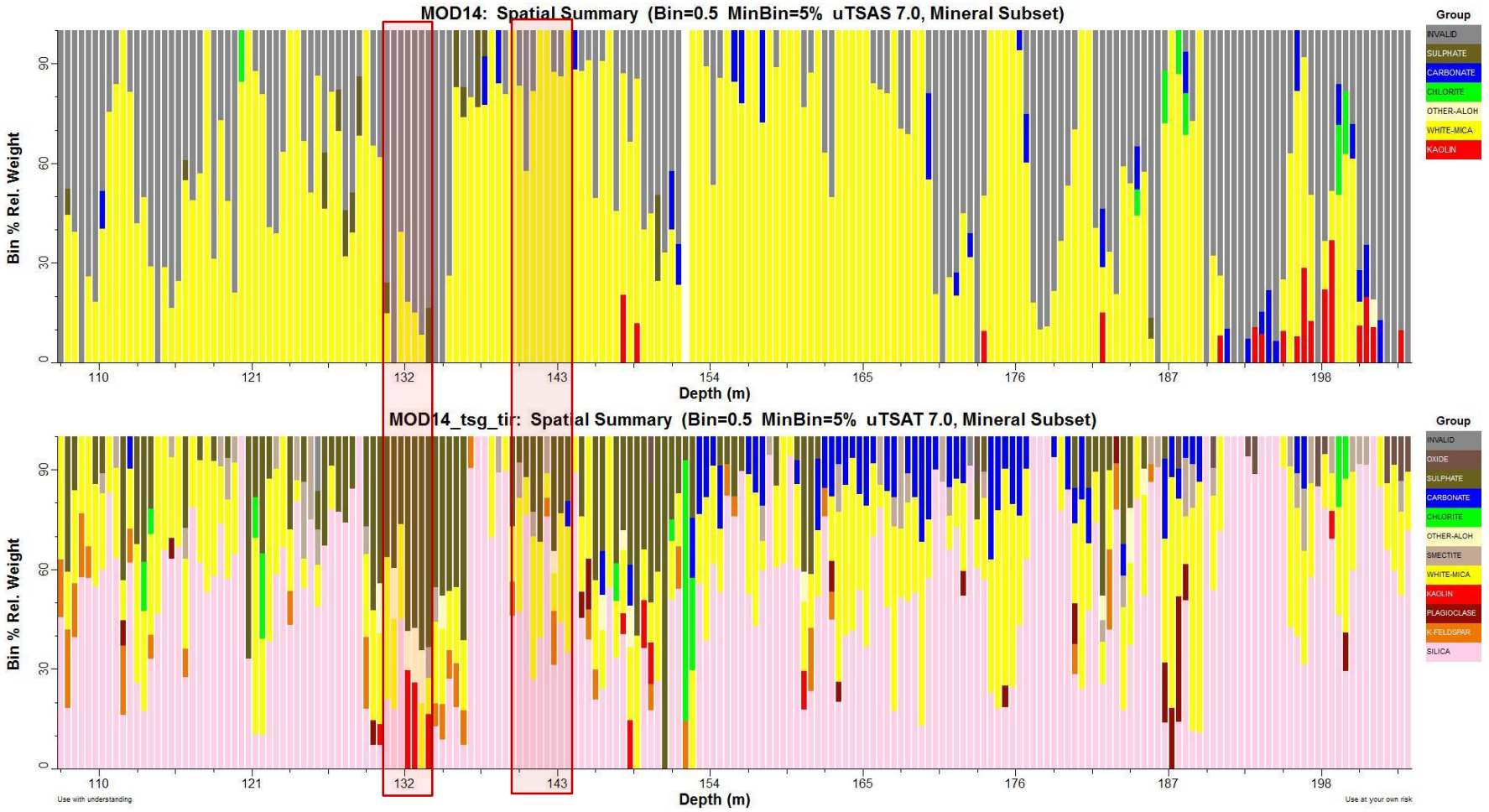
MOD14: Spatial Summary (Bin=0.5 MinBin=5% uTSAS 7.0, Mineral Subset)
Group
INVALID
SULPHATE
CARBONATE
CHLORITE
OTHER-ALOH
WHITE-MICA
KAOLIN
Bin % Rel. Weight
0
30
60
90
110
121
132
143
154
165
176
187
198
Depth (m)
MOD14_tsg_tir: Spatial Summary (Bin=0.5 MinBin=5% uTSAT 7.0, Mineral Subset)
Group
INVALID
OXIDE
SULPHATE
CARBONATE
CHLORITE
OTHER-ALOH
SMECTITE
WHITE-MICA
KAOLIN
PLAGIOCLASE
K-FELDSPAR
SILICA
Bin % Rel. Weight
Depth (m)
Use with understanding
Use at your own risk

Summary for high-grade mineralization in the oxidized zone

- Down to about 140 m
- Max Au 17-32 ppm at 30-38 m, 60 ppm at 90 m up to 124 ppm at 121-124 m
- In hematite-rich conglomerate and siltstone
- Broad muscovite alteration
- No or low chlorite
- Sulphates (TSA picks up jarosite and alunites)
- More or less (MOD 13) kaolin
- Lack of carbonates
- Broad quartz abundance (conglomerates and sandstone)

MOD3 (max Au 1.3 ppm)

Same mineralized zone as per MOD12: sheared siltstone/shale with grey and white sulphates.

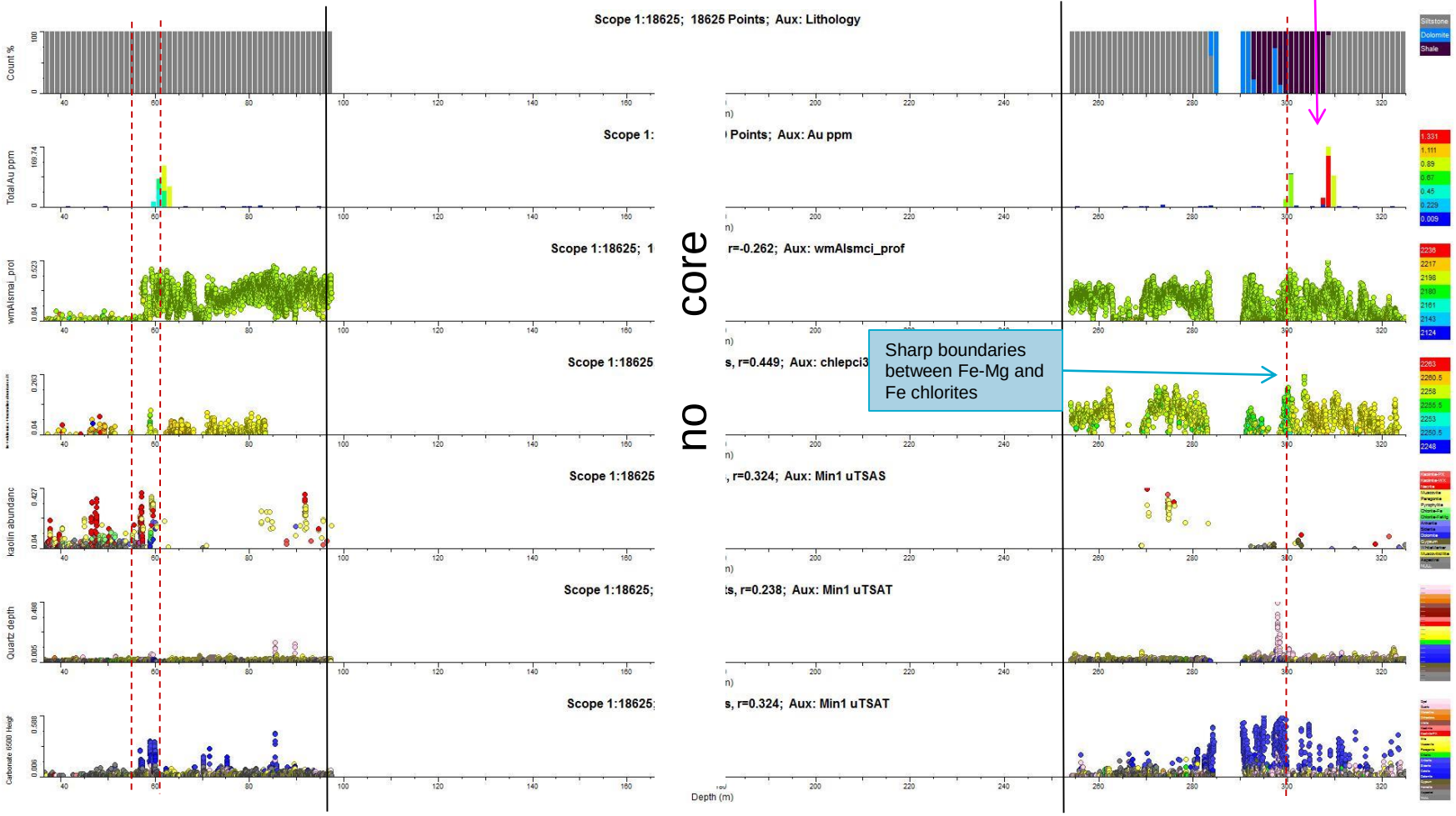

MOD3

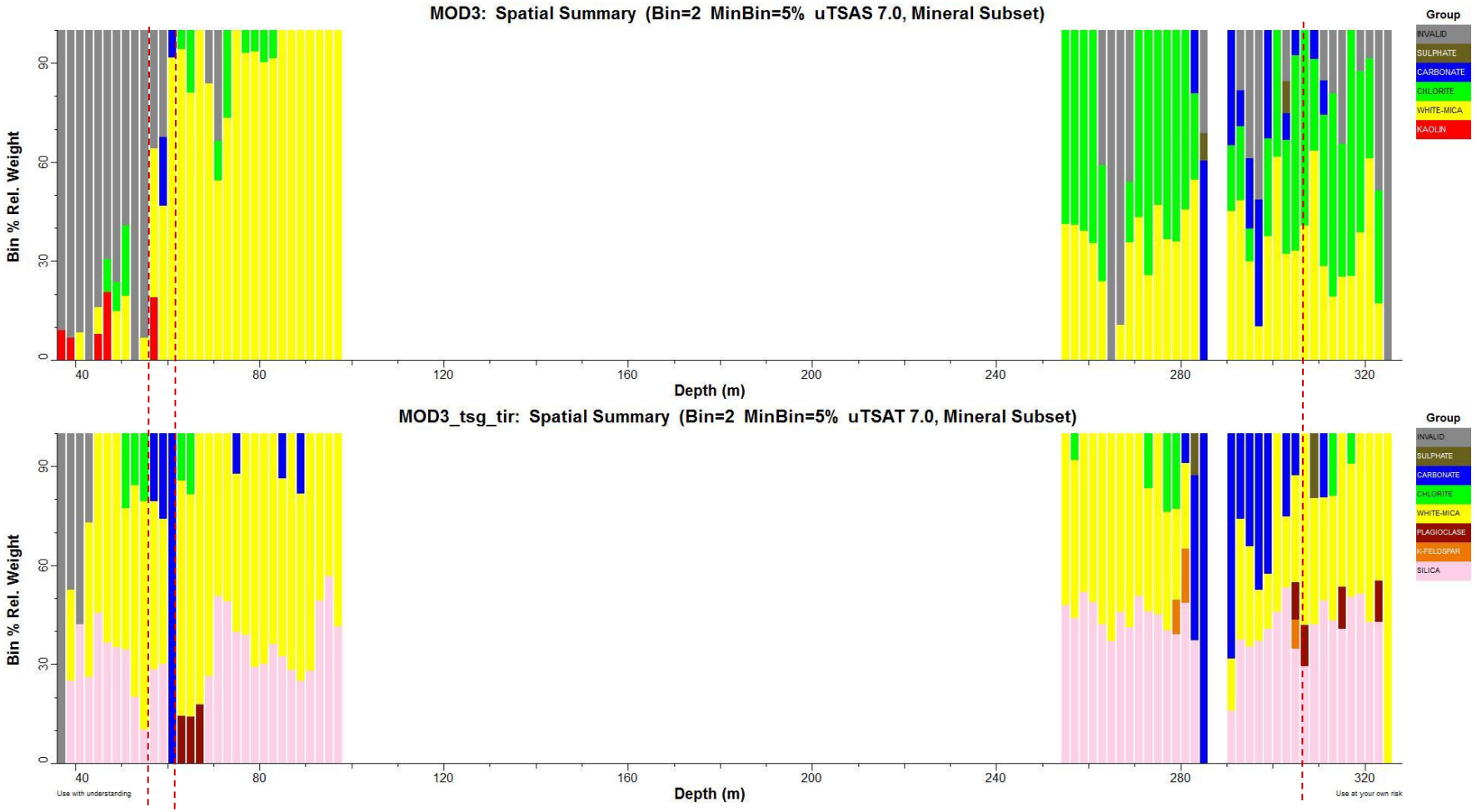
MOD3: Spatial Summary (Bin=2 MinBin=5% uTSAS 7.0, Mineral Subset)
Group
INVALID
SULPHATE
CARBONATE
CHLORITE
WHITE-MICA
KAOLIN
Bin % Rel. Weight
0
30
60
90
40
80
120
160
200
240
280
320
Depth (m)
MOD3_tsg_tir: Spatial Summary (Bin=2 MinBin=5% uTSAT 7.0, Mineral Subset)
Group
INVALID
SULPHATE
CARBONATE
CHLORITE
WHITE-MICA
PLAGIOCLASE
K-FELDSPAR
SILICA
Bin % Rel. Weight
Use with understanding
Use at your own risk
Depth (m)

MOD11 (max Au 13 ppm)

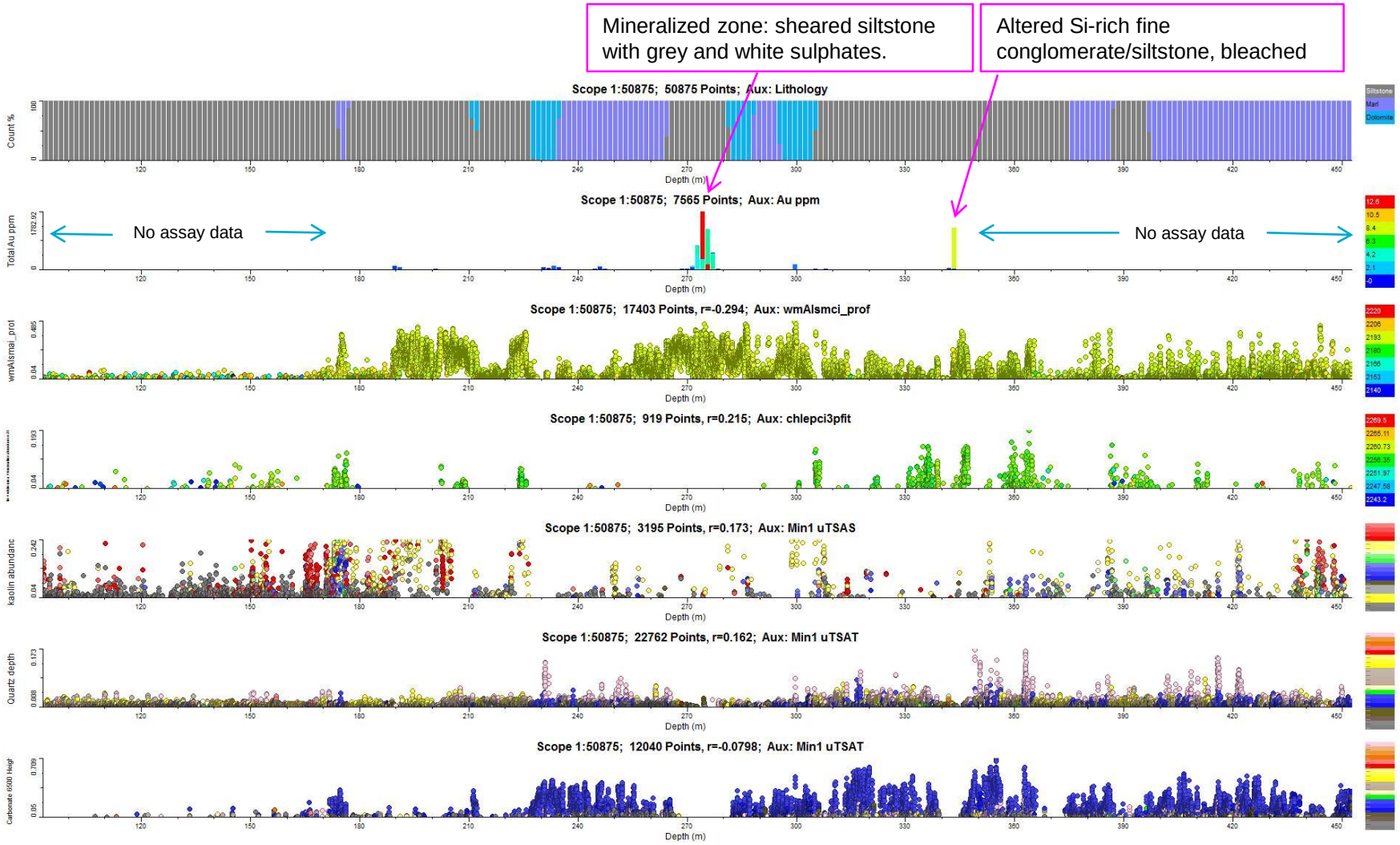

MOD11

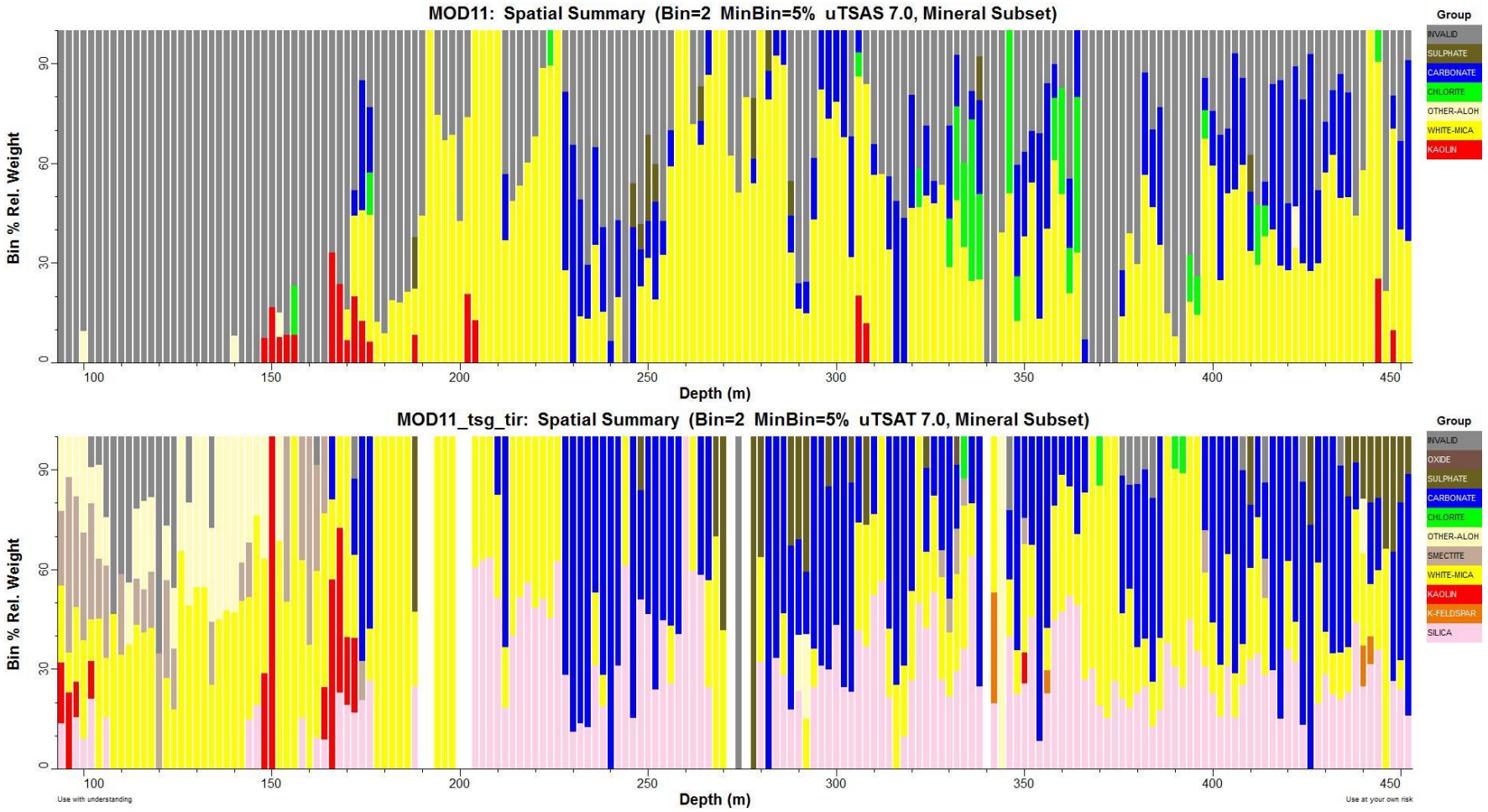
MOD11: Spatial Summary (Bin=2 MinBin=5% uTSAS 7.0, Mineral Subset)
Group
INVALID
SULPHATE
CARBONATE
CHLORITE
OTHER-ALOH
WHITE-MICA
KAOLIN
Bin % Rel. Weight
0
30
60
90
100
150
200
250
300
350
400
450
Depth (m)
MOD11_tsg_tir: Spatial Summary (Bin=2 MinBin=5% uTSAT 7.0, Mineral Subset)
Group
INVALID
OXIDE
SULPHATE
CARBONATE
CHLORITE
OTHER-ALOH
SMECTITE
WHITE-MICA
KAOLIN
K-FELDSPAR
SILICA
Bin % Rel. Weight
0
30
60
90
100
150
200
250
300
350
400
450
Depth (m)
Use with understanding
Use at your own risk

MTO90 (Au max 23 ppm)

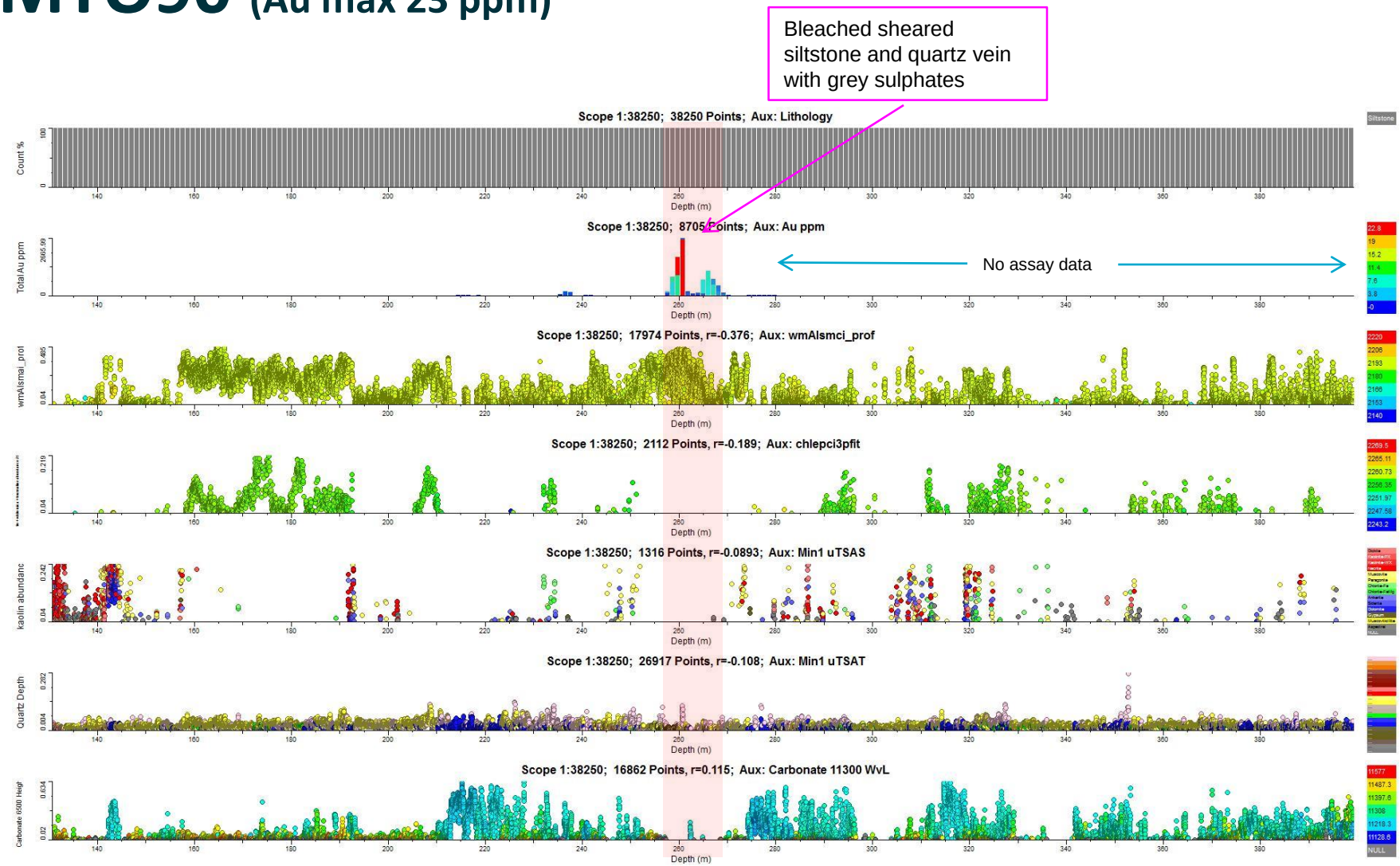

MTO90 Au mineralization

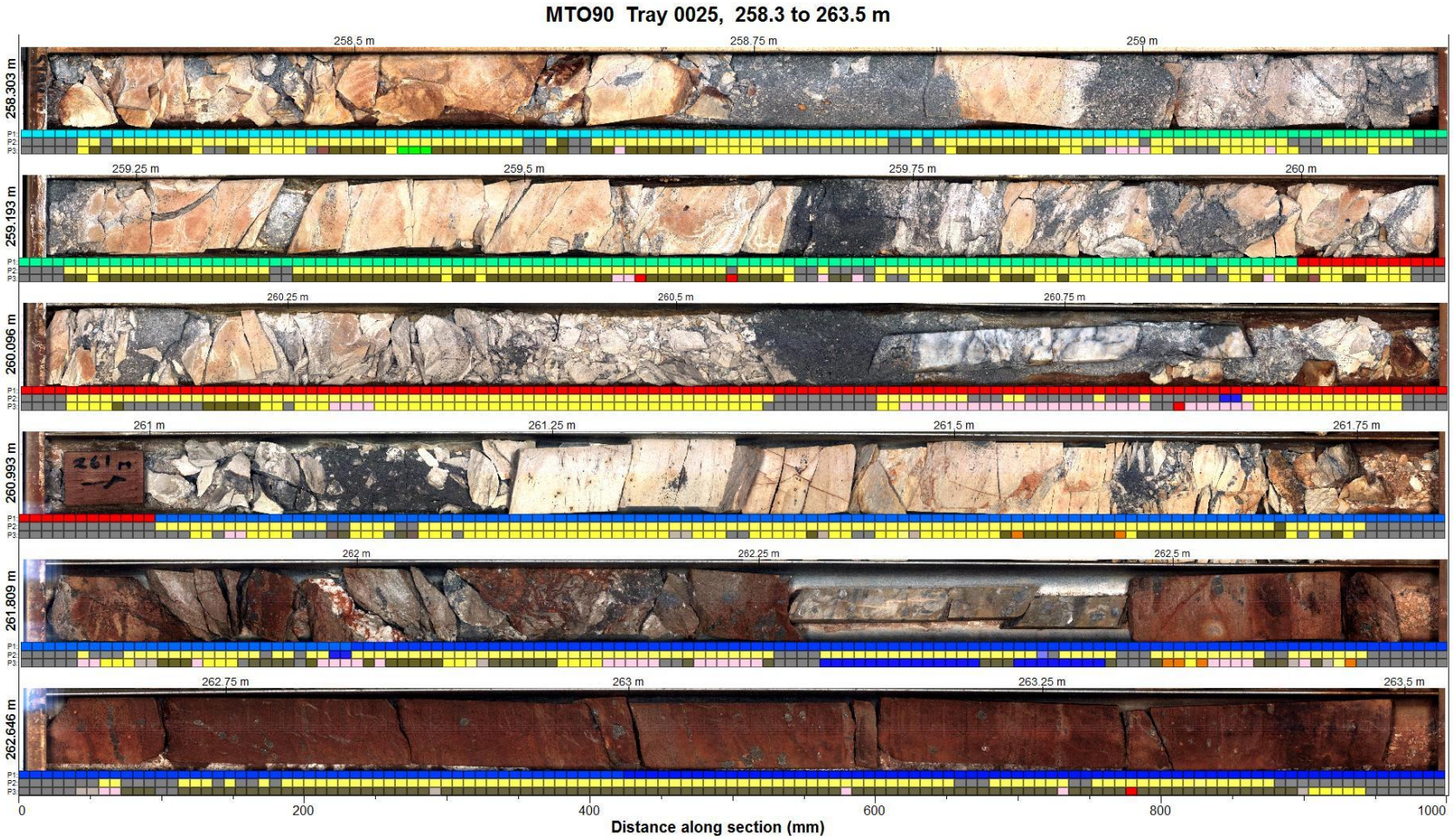

MTO90

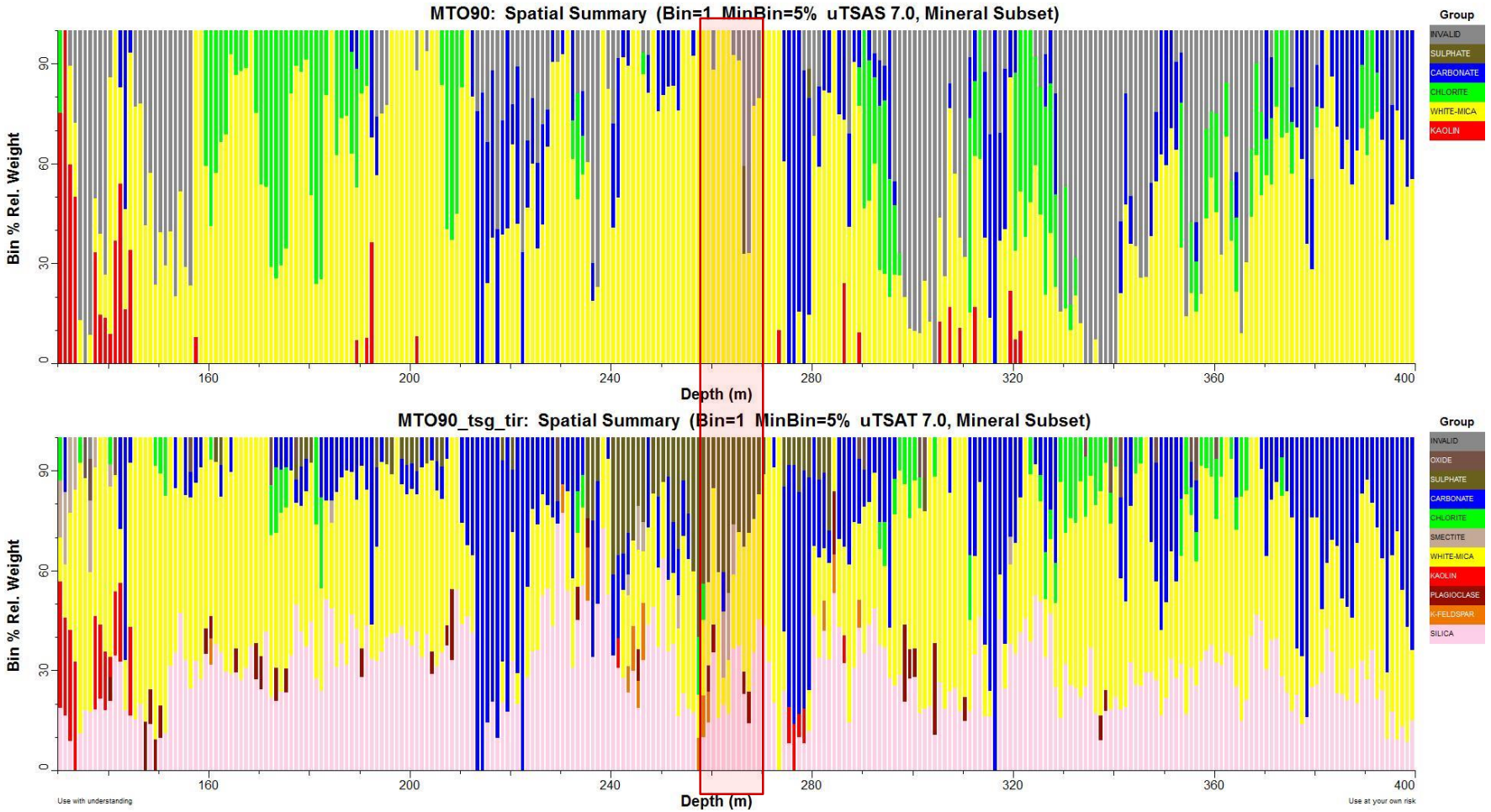
MTO90: Spatial Summary (Bin=1 MinBin=5% uTSAS 7.0, Mineral Subset)
Group
INVALID
SULPHATE
CARBONATE
CHLORITE
WHITE-MICA
KAOLIN
Bin % Rel. Weight
0
30
60
90
160
200
240
280
320
360
400
Depth (m)
MTO90_tsg_tir: Spatial Summary (Bin=1 MinBin=5% uTSAT 7.0, Mineral Subset)
Group
INVALID
OXIDE
SULPHATE
CARBONATE
CHLORITE
SMECTITE
WHITE-MICA
KAOLIN
PLAGIOCLASE
K-FELDSPAR
SILICA
Bin % Rel. Weight
0
30
60
90
160
200
240
280
320
360
400
Depth (m)
Use with understanding
Use at your own risk

NMOD001 (max Au 4 ppm)

NMOD001 Au mineralization

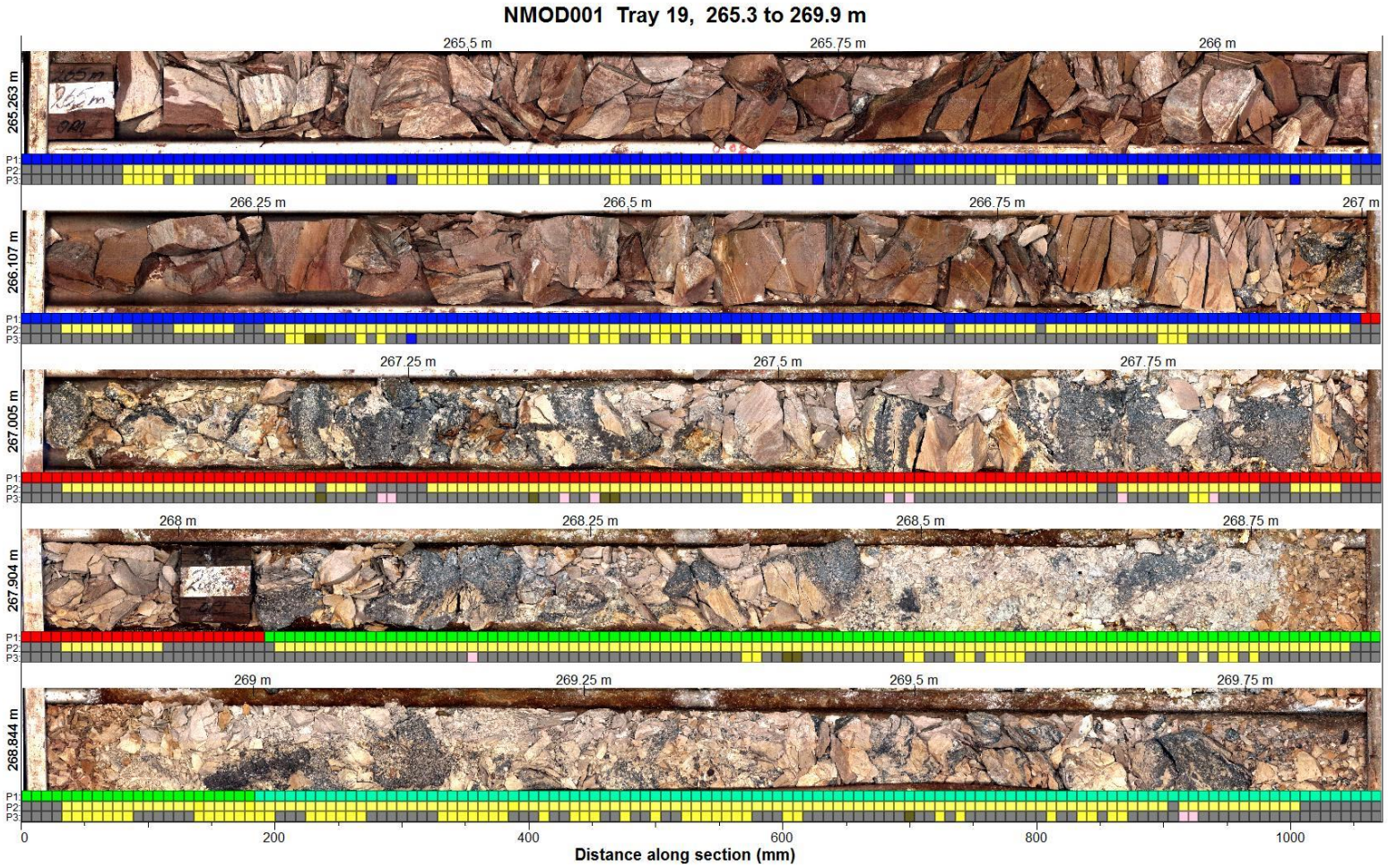

NMOD001

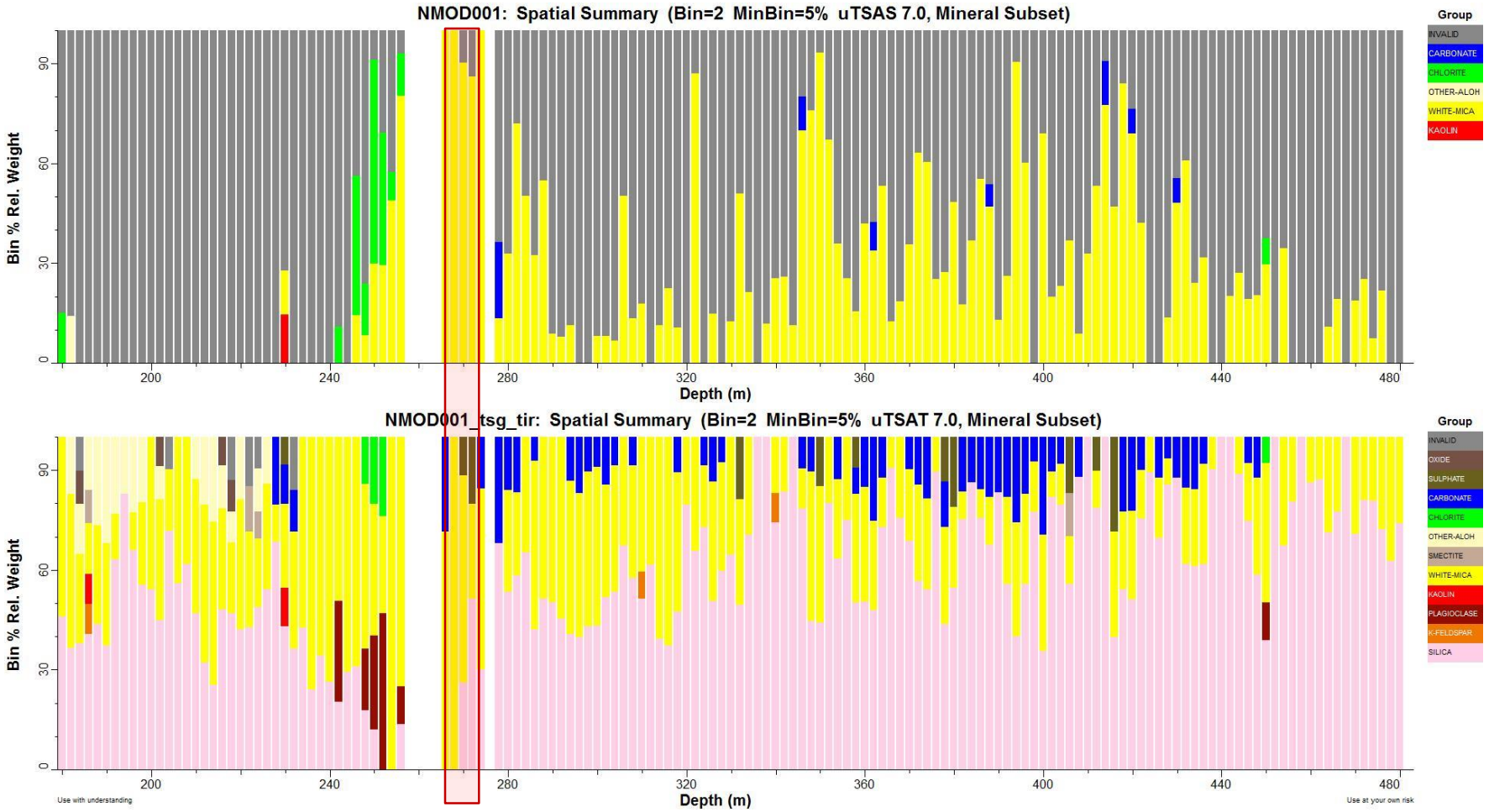
NMOD001: Spatial Summary (Bin=2 MinBin=5% uTSAS 7.0, Mineral Subset)
Group
INVALID
CARBONATE
CHLORITE
OTHER-ALOH
WHITE-MICA
KAOLIN
Bin % Rel. Weight
0
30
60
90
200
240
280
320
360
400
440
480
Depth (m)
NMOD001_tsg_tir: Spatial Summary (Bin=2 MinBin=5% uTSAT 7.0, Mineral Subset)
Group
INVALID
OXIDE
SULPHATE
CARBONATE
CHLORITE
OTHER-ALOH
SMECTITE
WHITE-MICA
KAOLIN
PLAGIOCLASE
K-FELDSPAR
SILICA
Bin % Rel. Weight
0
30
60
90
200
240
280
320
360
400
440
480
Use with understanding
Depth (m)
Use at your own risk

NMOD002 max Au 4 ppm

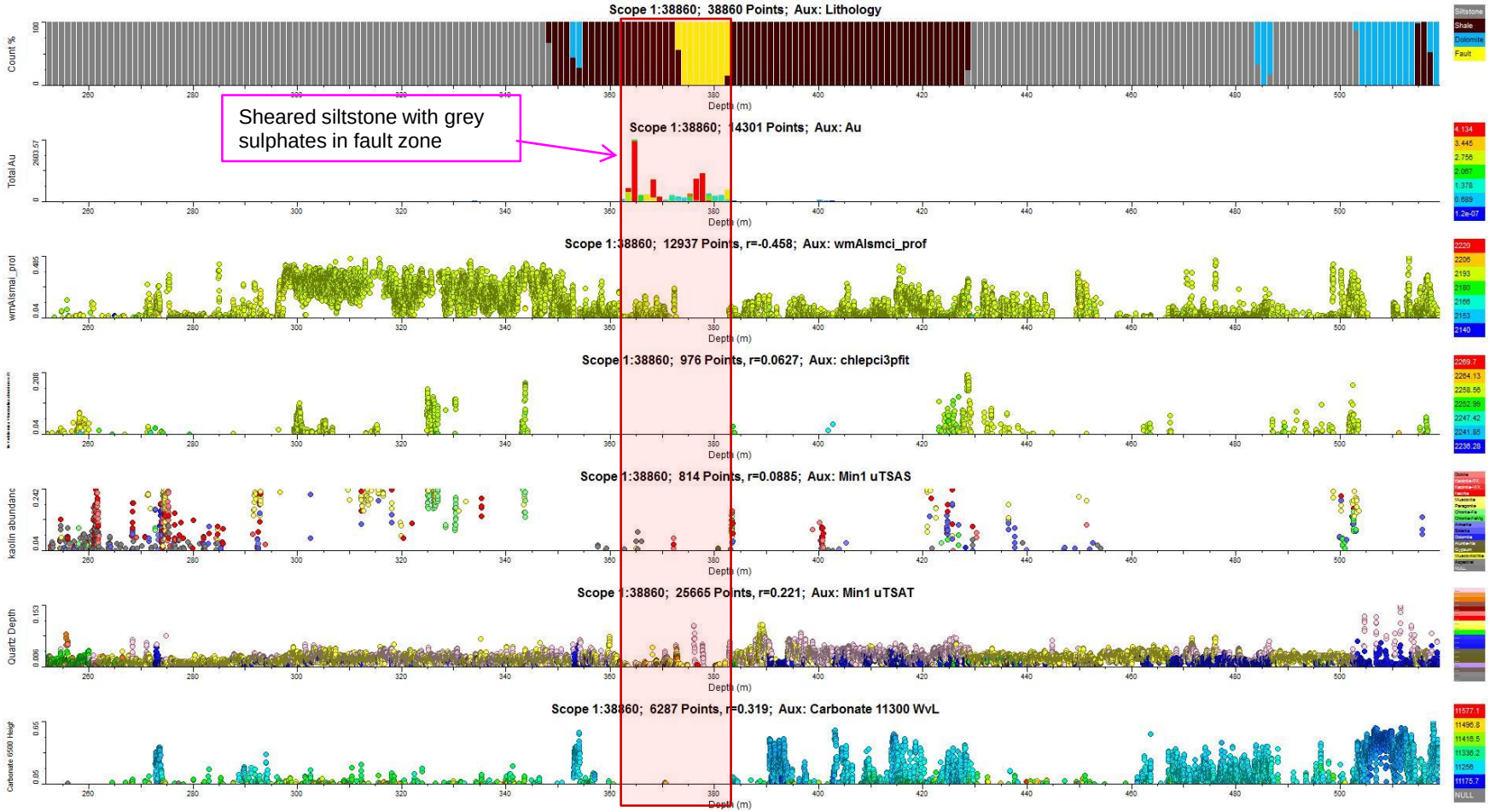

NMOD002 Au mineralization

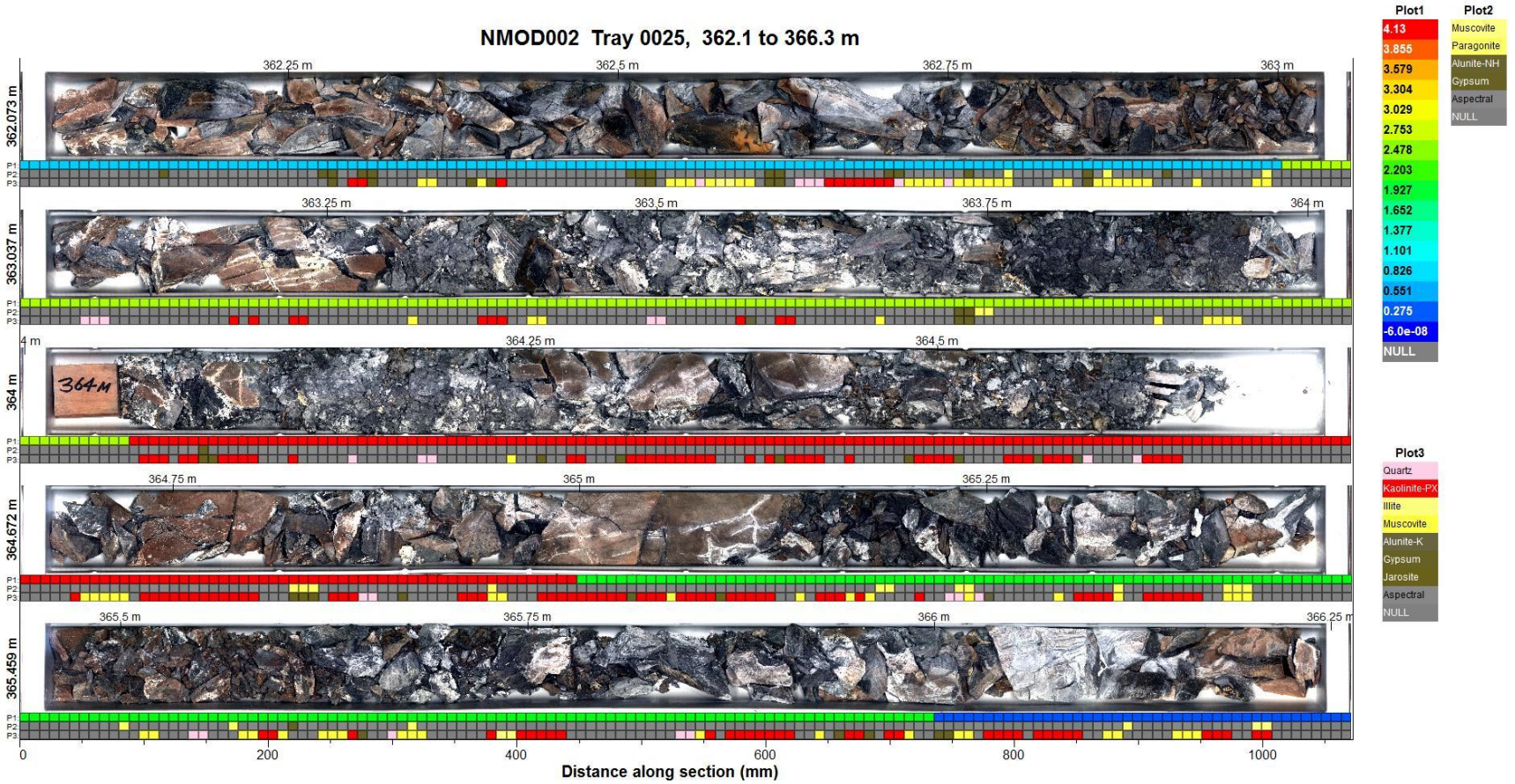

NMOD002

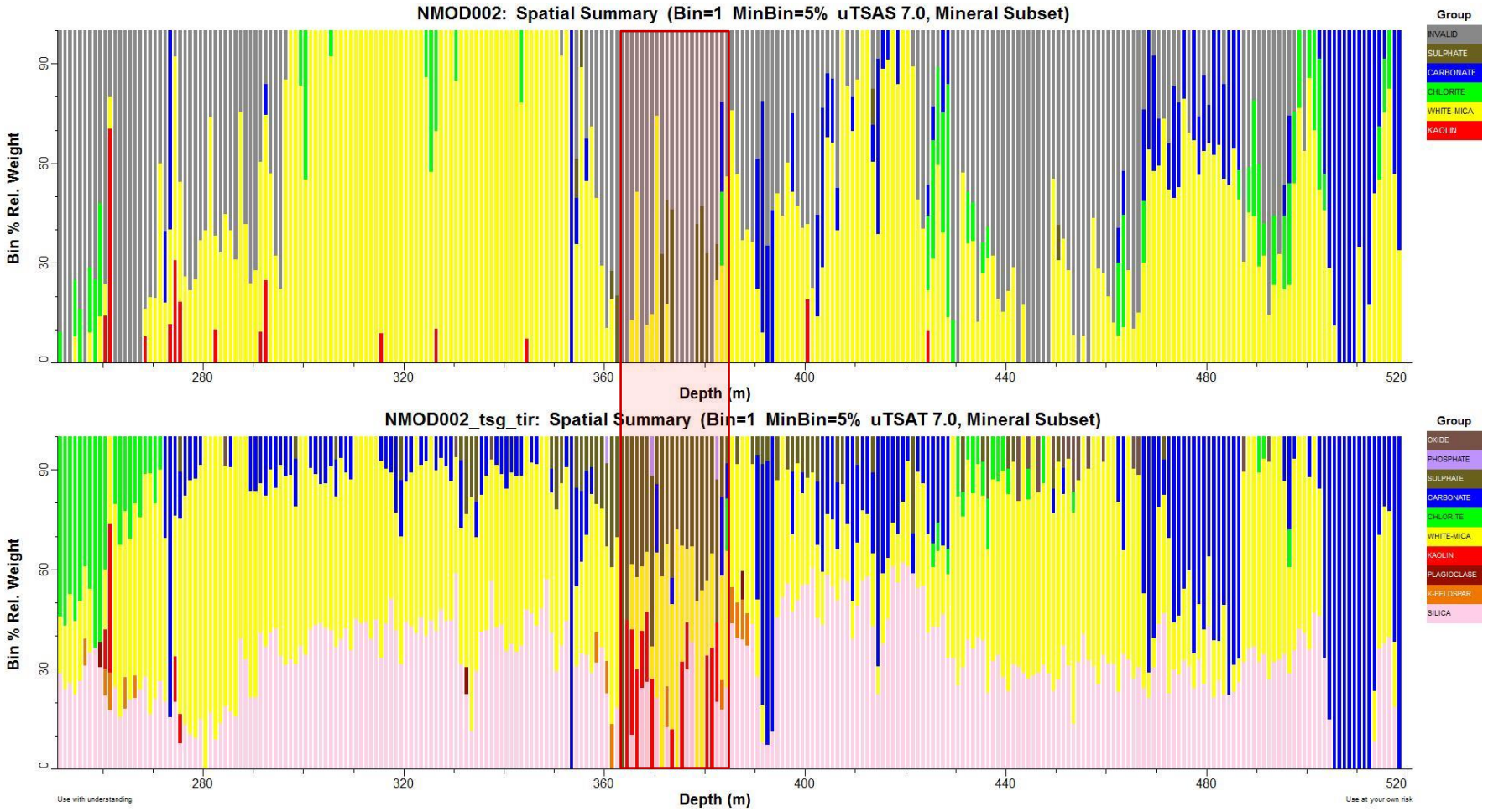
NMOD002: Spatial Summary (Bin=1 MinBin=5% uTSAS 7.0, Mineral Subset)
Group
INVALID
SULPHATE
CARBONATE
CHLORITE
WHITE-MICA
KAOLIN
Bin % Rel. Weight
0
30
60
90
280
320
360
400
440
480
520
Depth (m)
NMOD002_tsg_tir: Spatial Summary (Bin=1 MinBin=5% uTSAT 7.0, Mineral Subset)
Group
OXIDE
PHOSPHATE
SULPHATE
CARBONATE
CHLORITE
WHITE-MICA
KAOLIN
PLAGIOCLASE
K-FELDSPAR
SILICA
Bin % Rel. Weight
Depth (m)
Use with understanding
Use at your own risk

NMOD005 max Au 5 ppm

NMOD005 Au mineralization

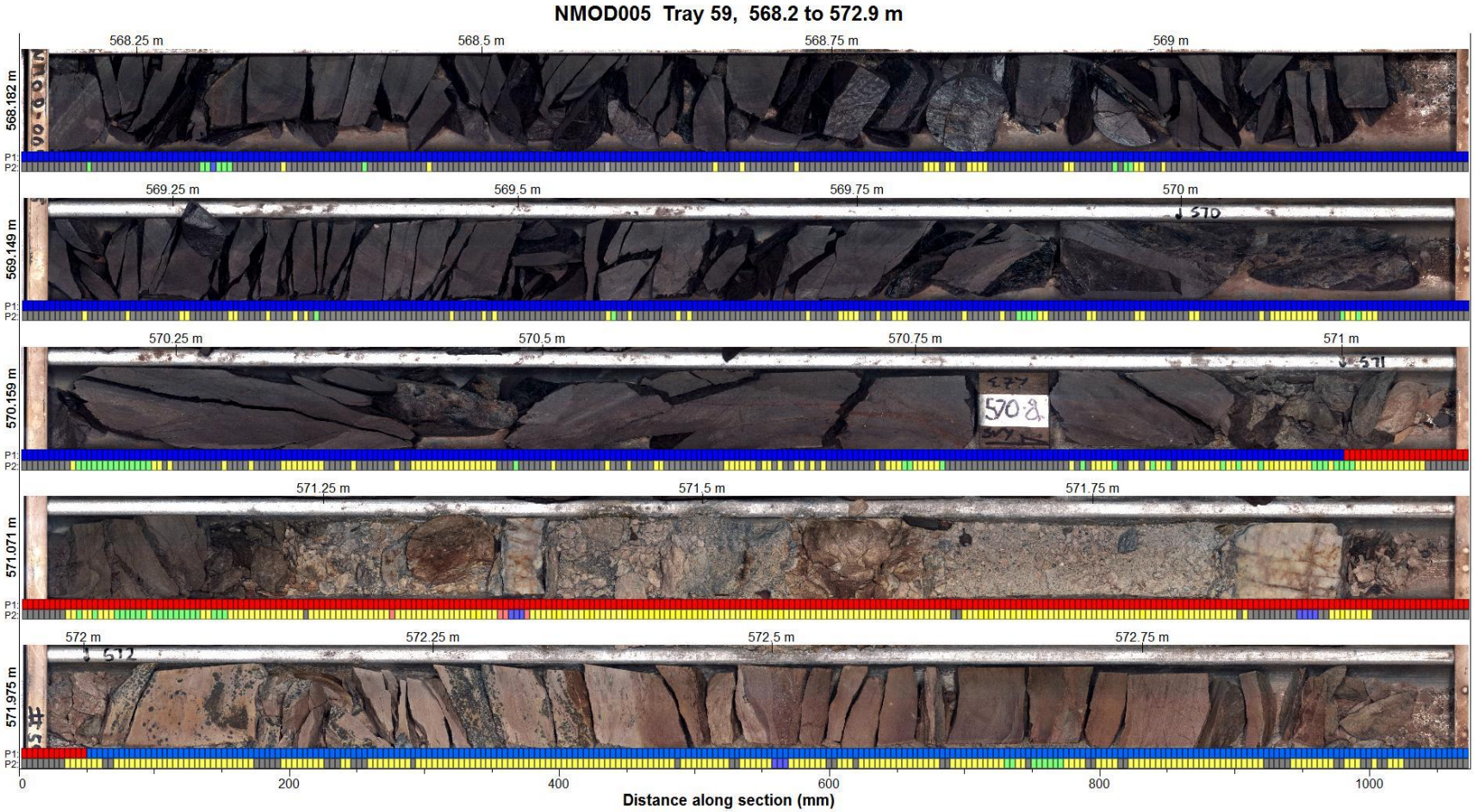

NMOD005

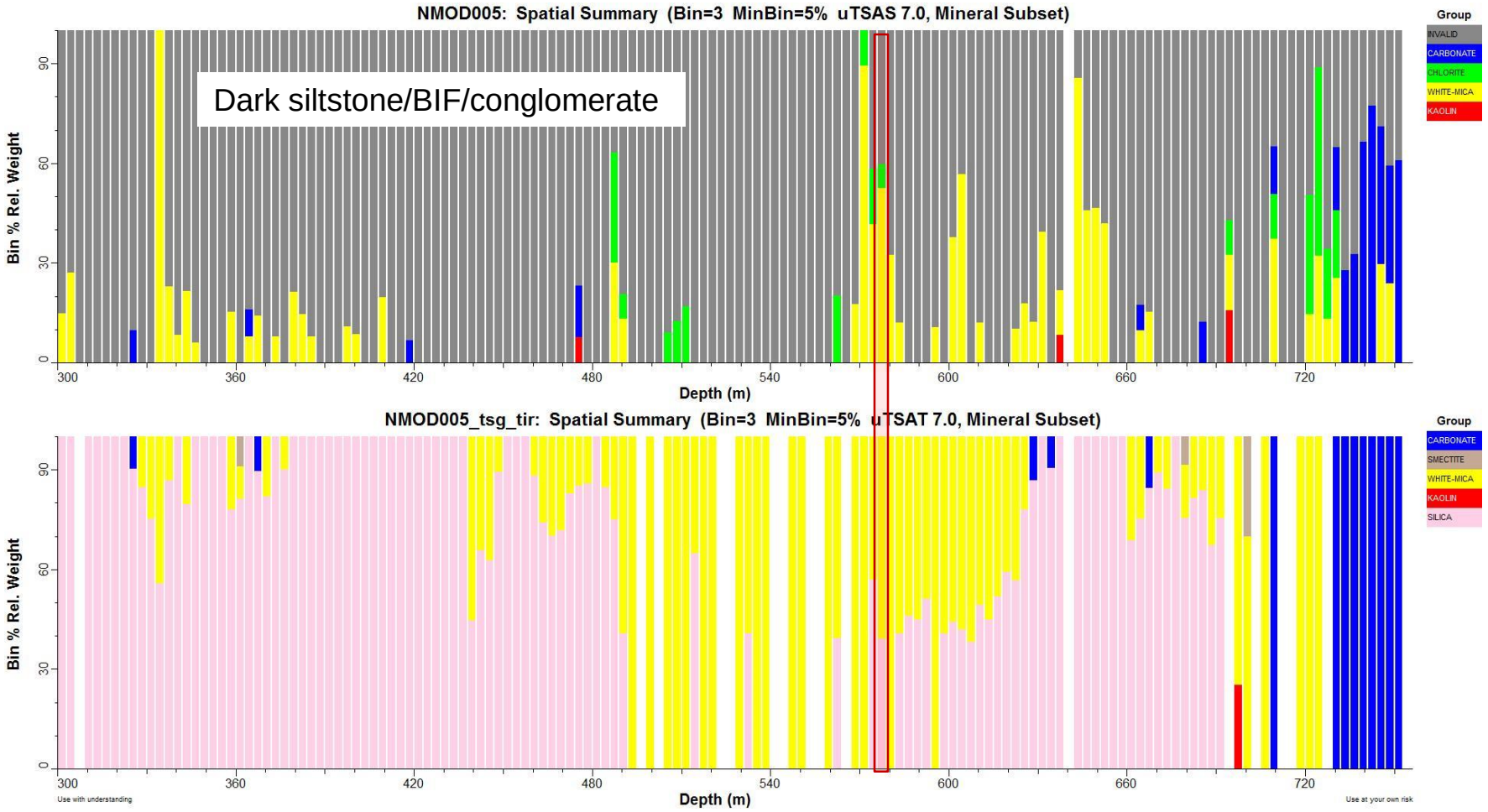
NMOD005: Spatial Summary (Bin=3 MinBin=5% uTSAS 7.0, Mineral Subset)
Dark siltstone/BIF/conglomerate
Group
INVALID
CARBONATE
CHLORITE
WHITE-MICA
KAOLIN
Bin % Rel. Weight
0
30
60
90
300
360
420
480
540
600
660
720
Depth (m)
NMOD005_tsg_tir: Spatial Summary (Bin=3 MinBin=5% uTSAT 7.0, Mineral Subset)
Group
CARBONATE
SMECTITE
WHITE-MICA
KAOLIN
SILICA
Bin % Rel. Weight
Depth (m)
Use with understanding
Use at your own risk

Summary for primary oxidized low-grade mineralization

- Depth down from 140 m (570 m for NMOD005)
- Max Au 23 ppm at MTO90, average – a few ppm
- In sheared bleached Si-rich siltstones, fault zones
- Abundant Fe-rich carbonate
- Patchy chlorite, proximal Fe-rich chlorite
- Sulphates – jarosite or gypsum (by TSA)
- Abundant kaolin (by scripts)

AMODD0026 max Au 36 ppm

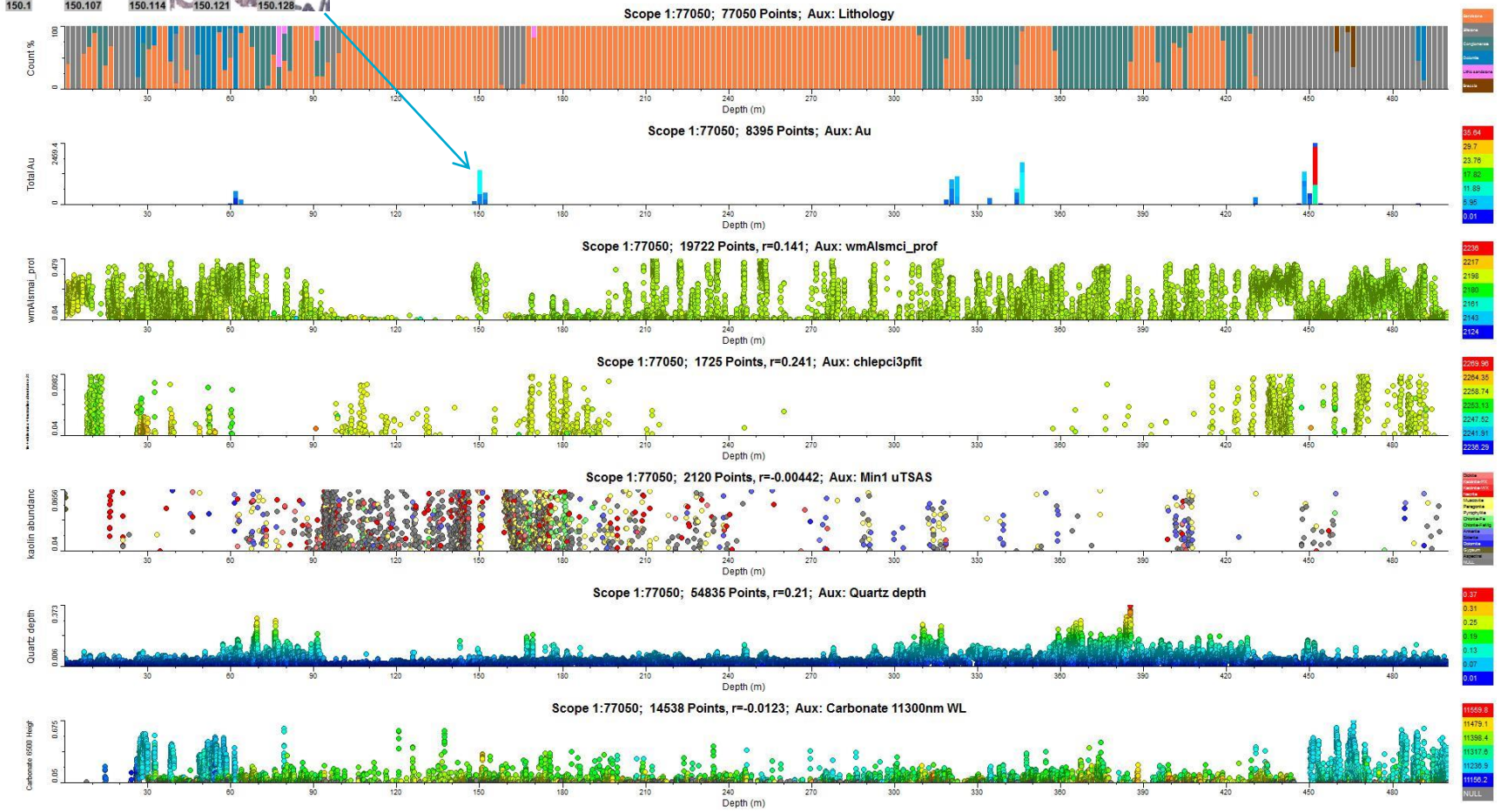

AMODD0026 EIS Northern Star drilling

Fresh primary mineralization (36 ppm) in brecciated quartz with lenses and veins of massive pyrite

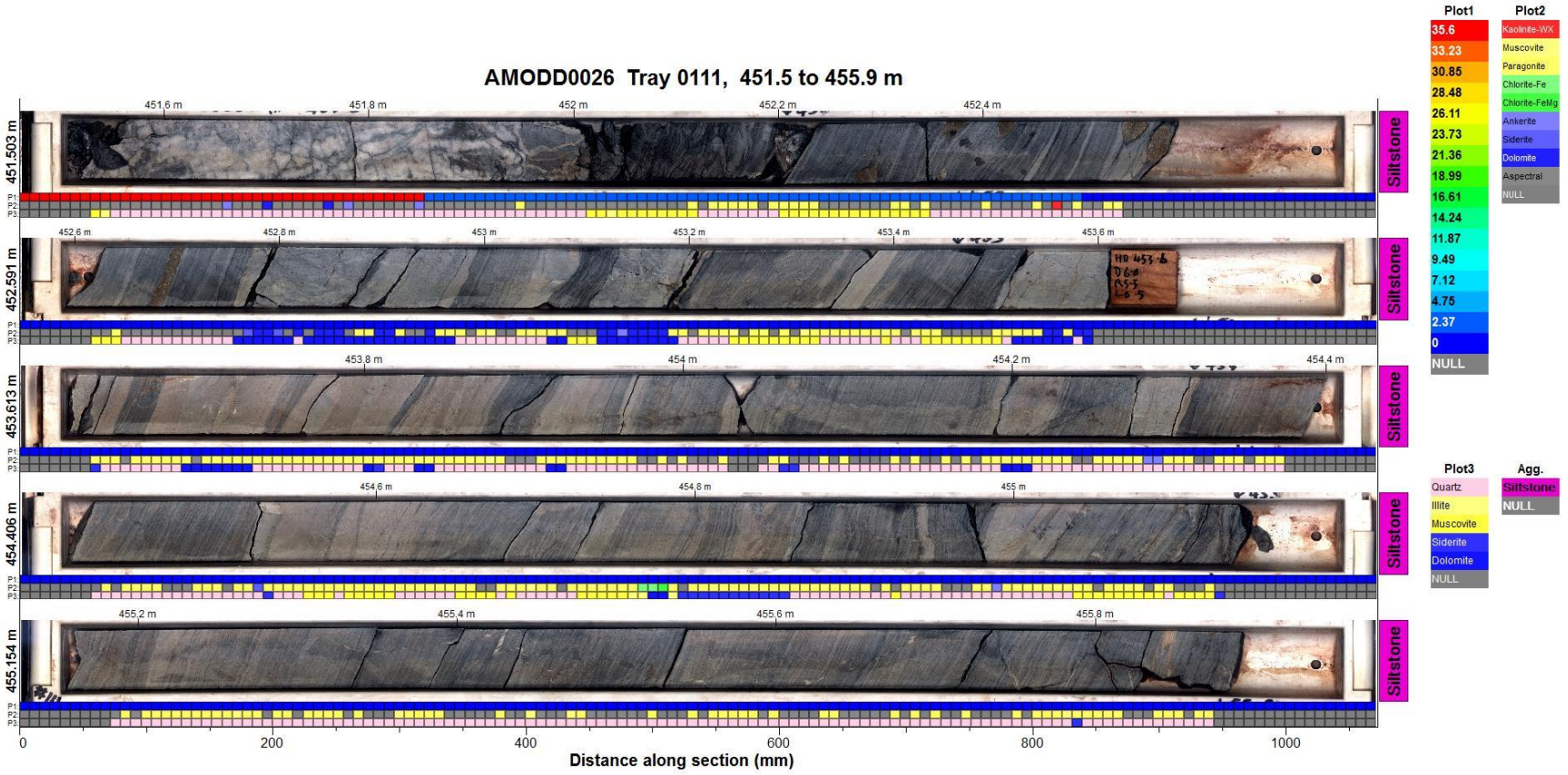

AMODD0026

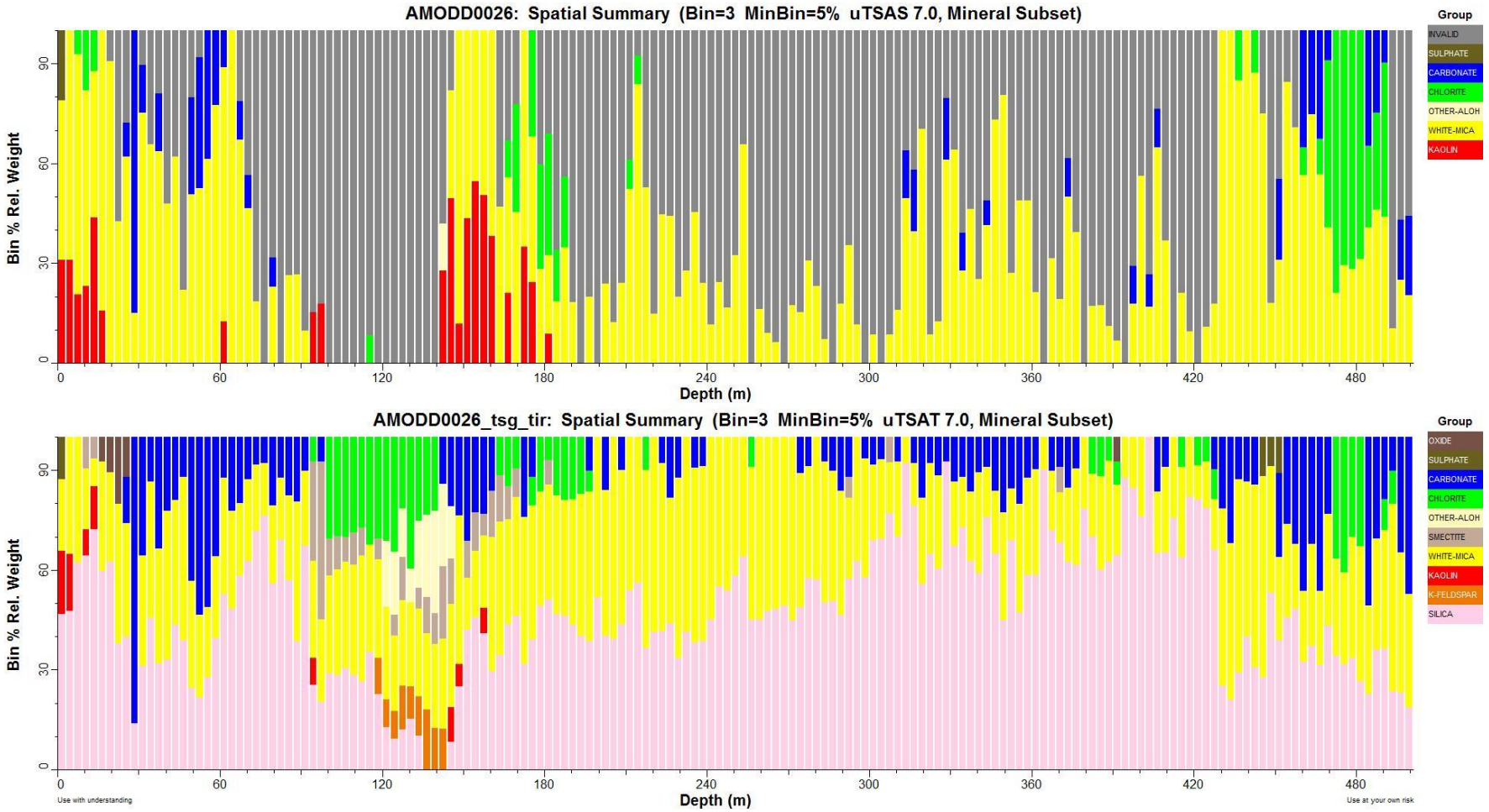
AMODD0026: Spatial Summary (Bin=3 MinBin=5% uTSAS 7.0, Mineral Subset)
Group
INVALID
SULPHATE
CARBONATE
CHLORITE
OTHER-ALOH
WHITE-MICA
KAOLIN
Bin % Rel. Weight
0
30
60
90
0
60
120
180
240
300
360
420
480
Depth (m)
AMODD0026_tsg_tir: Spatial Summary (Bin=3 MinBin=5% uTSAT 7.0, Mineral Subset)
Group
OXIDE
SULPHATE
CARBONATE
CHLORITE
OTHER-ALOH
SMECTITE
WHITE-MICA
KAOLIN
K-FELDSPAR
SILICA
Bin % Rel. Weight
Use with understanding
Use at your own risk
Depth (m)

AMODD0026 – primary mineralization

- At depth of 62 m (3.5 ppm), 150 m (9.1 ppm), and 450 m (36 ppm) gold locate in quartz-pyrite brecciated veins within sandstone and siltstone units
- At depth of 322 m (5 ppm) gold is associated with hematite-rich sandstone (BIF?)
- At depth of 345 m (10 ppm) gold is associated with coarse-grain brecciated sandstone and graphite
- No sulphates

AMODD0028 max Au 20 ppm

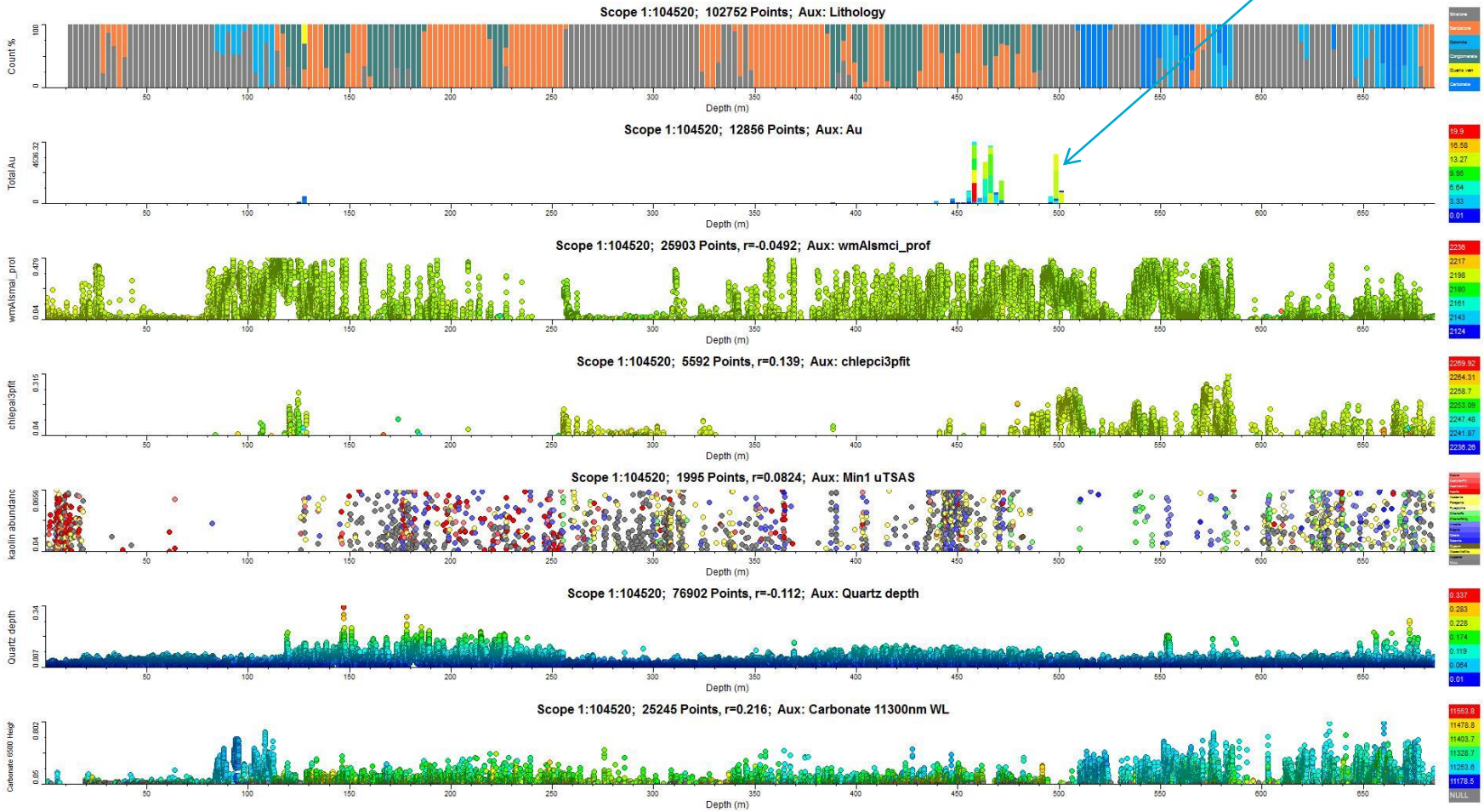

AMODD0028 EIS Northern Star drilling

Primary mineralization (20 ppm) in bleached sand- and siltstones with massive pyrite, no quartz veins

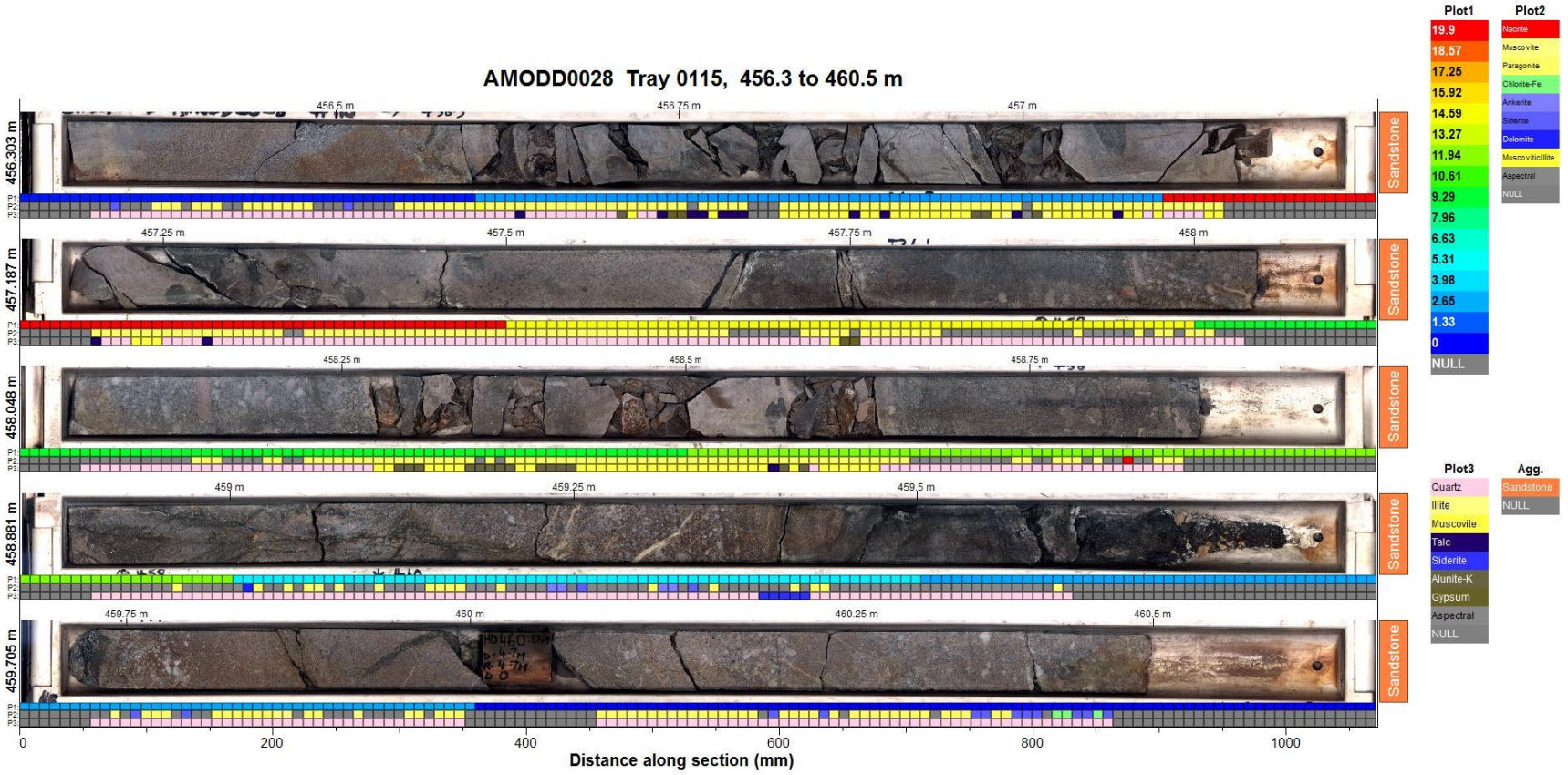

AMODD0028

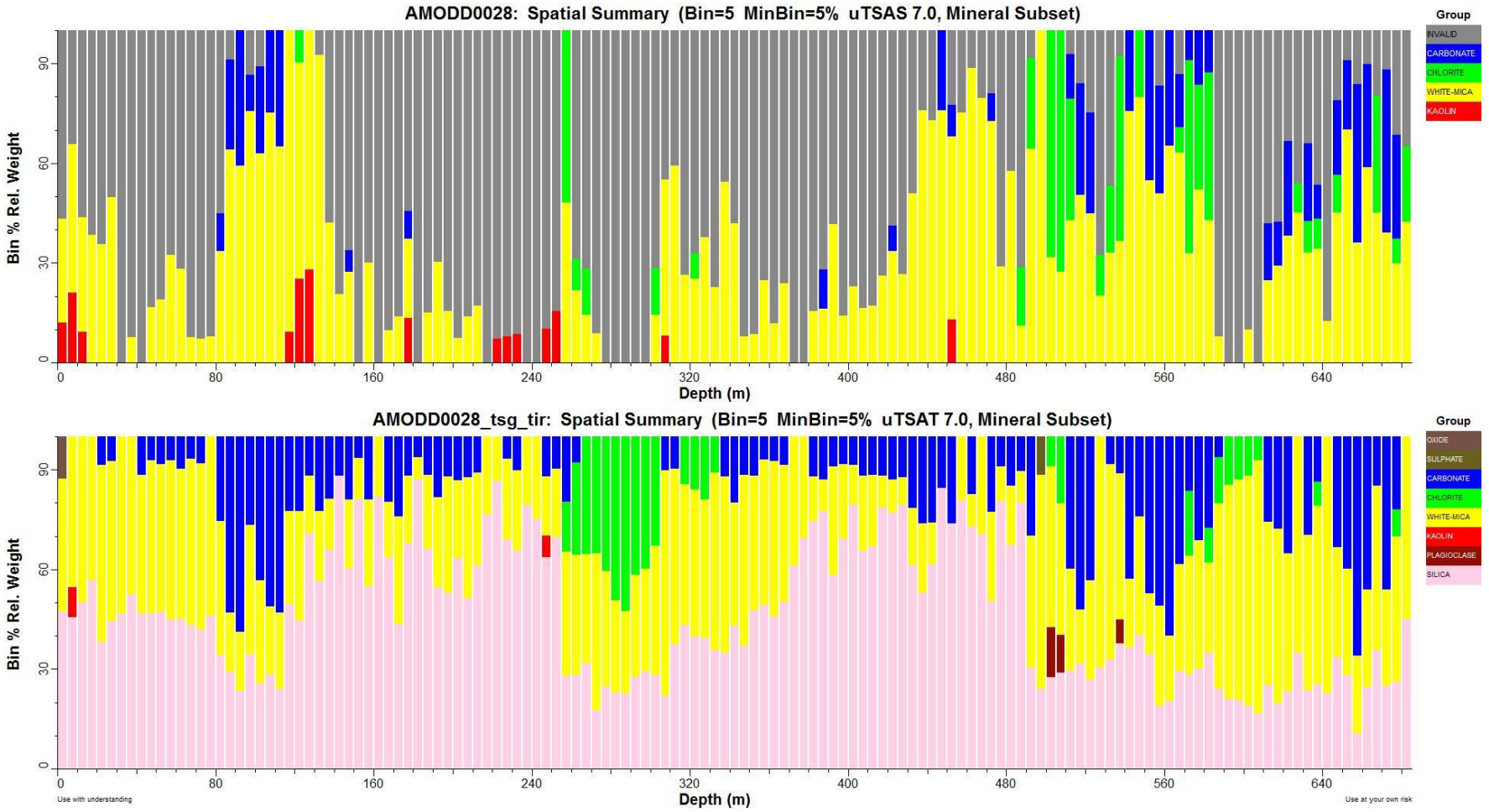
AMODD0028: Spatial Summary (Bin=5 MinBin=5% uTSAS 7.0, Mineral Subset)
Group
INVALID
CARBONATE
CHLORITE
WHITE-MICA
KAOLIN
Bin % Rel. Weight
0
30
60
90
0
80
160
240
320
400
480
560
640
Depth (m)
AMODD0028_tsg_tir: Spatial Summary (Bin=5 MinBin=5% uTSAT 7.0, Mineral Subset)
Group
OXIDE
SULPHATE
CARBONATE
CHLORITE
WHITE-MICA
KAOLIN
PLAGIOCLASE
SILICA
Bin % Rel. Weight
0
30
60
90
0
80
160
240
320
400
480
560
640
Depth (m)
Use with understanding
Use at your own risk

AMODD0028 – primary mineralization

- At depth of 457 m (20 ppm) and 500 m (14 ppm) gold locate in bleached sandstones/siltstones with pyrite blobs and conglomerates
- No sulphates
- No quartz veins

MDO3 max Au 3 ppm

MD03

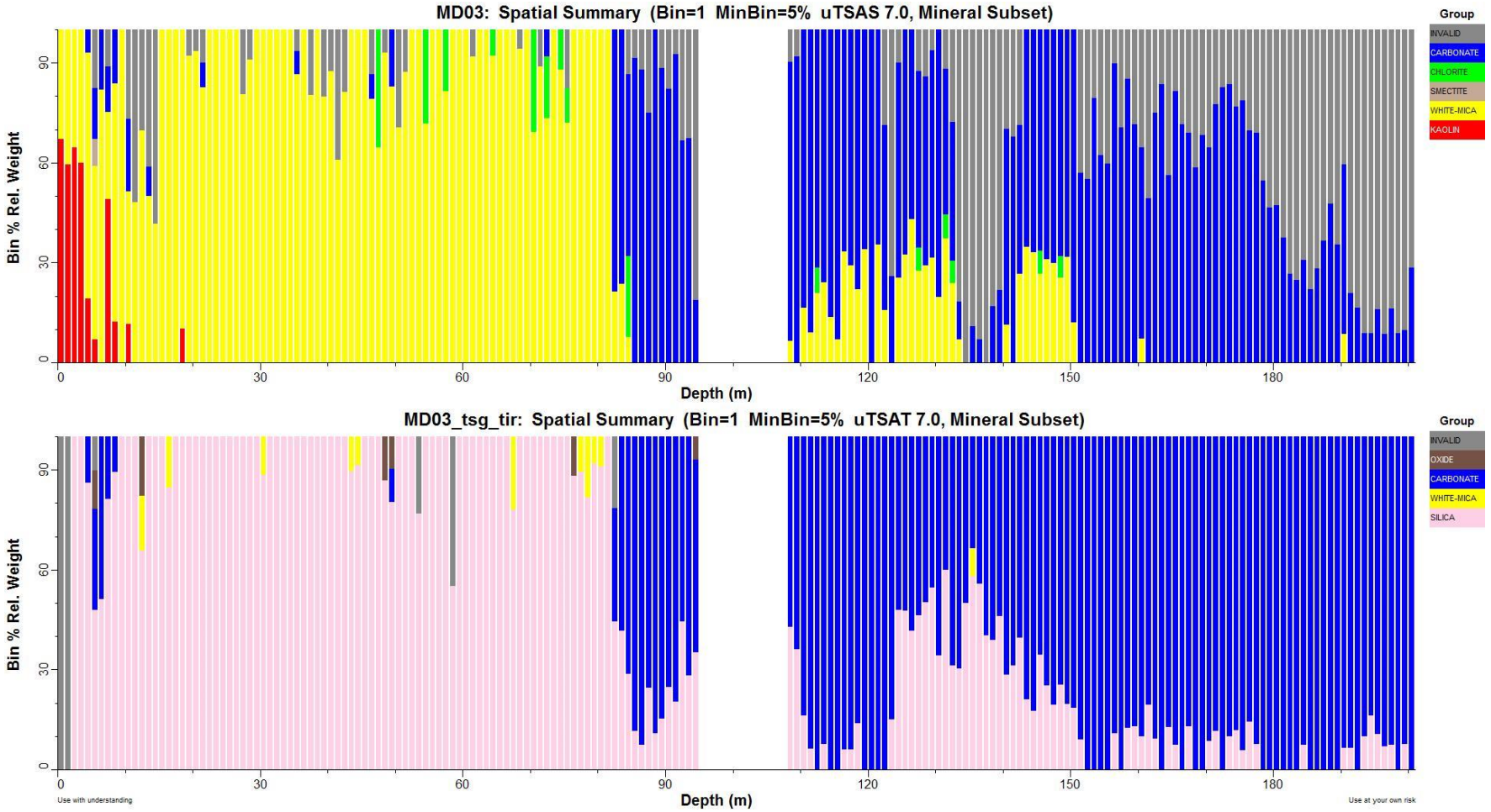
MD03: Spatial Summary (Bin=1 MinBin=5% uTSAS 7.0, Mineral Subset)
Group
INVALID
CARBONATE
CHLORITE
SMECTITE
WHITE-MICA
KAOLIN
Bin % Rel. Weight
0
30
60
90
0
30
60
90
120
150
180
Depth (m)
MD03_tsg_tir: Spatial Summary (Bin=1 MinBin=5% uTSAT 7.0, Mineral Subset)
Group
INVALID
OXIDE
CARBONATE
WHITE-MICA
SILICA
Bin % Rel. Weight
Use with understanding
Use at your own risk

NMOD004 max Au 2 ppm

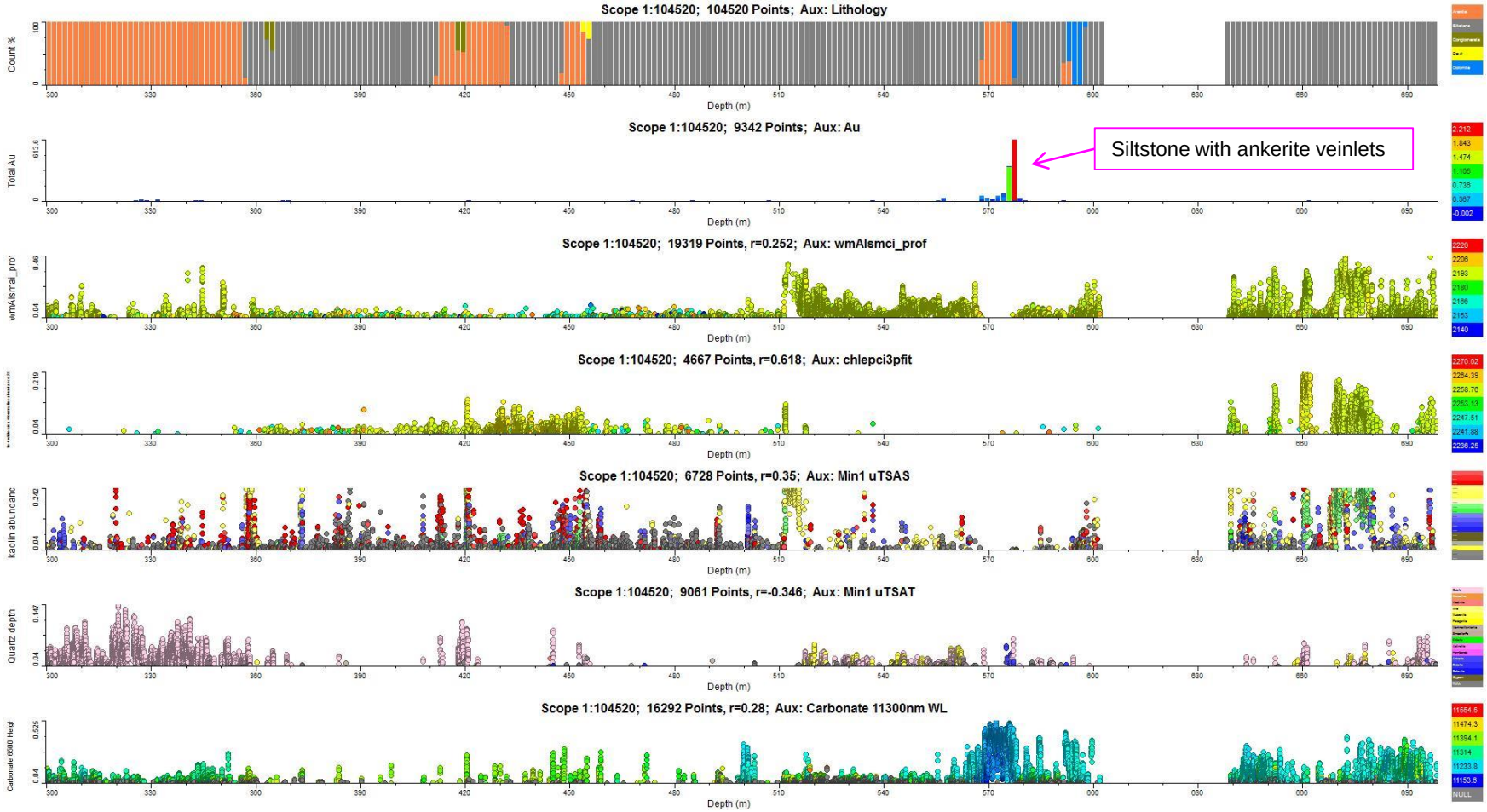

NMOD004

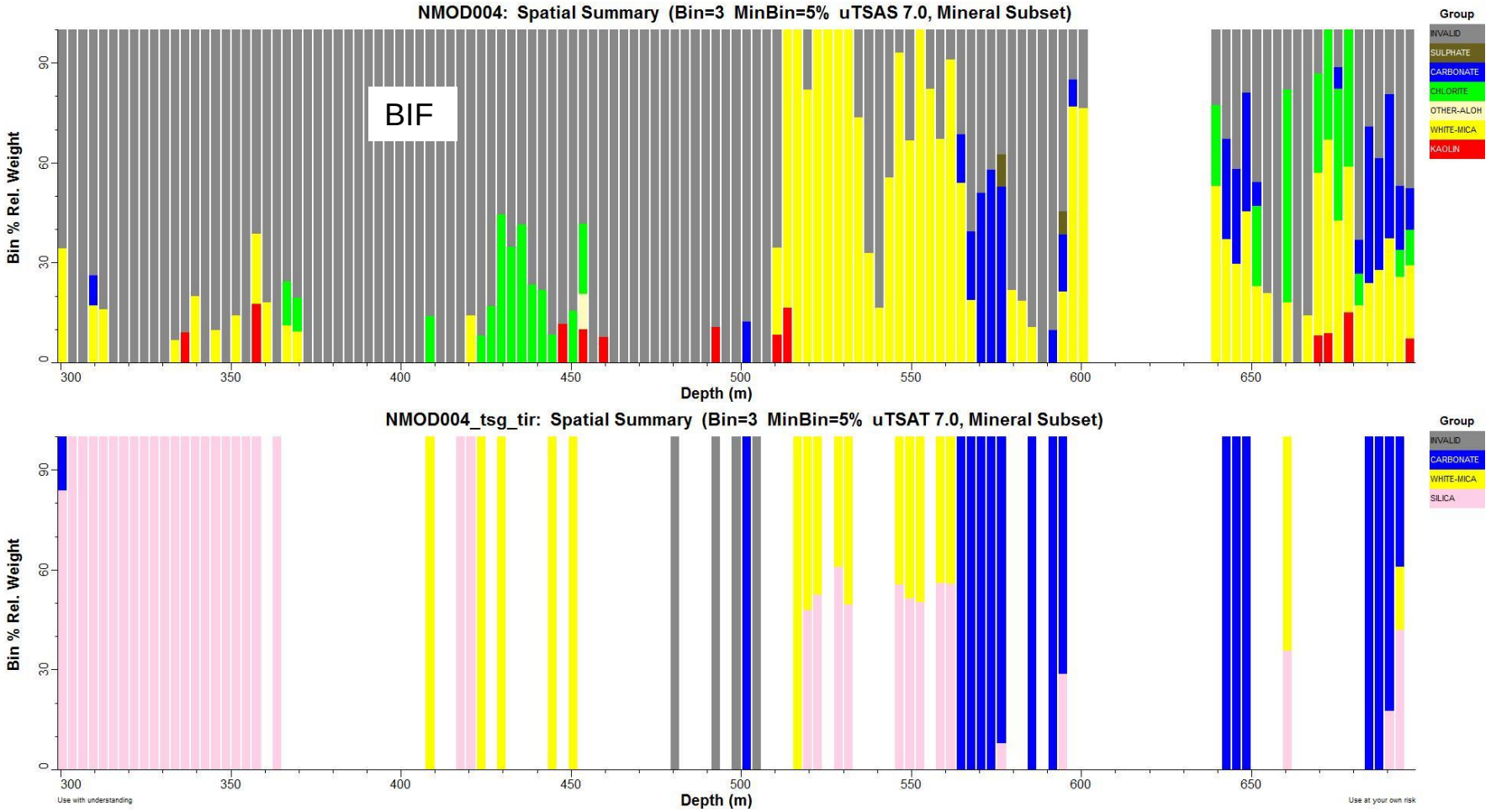
NMOD004: Spatial Summary (Bin=3 MinBin=5% uTSAS 7.0, Mineral Subset)
BIF
Group
INVALID
SULPHATE
CARBONATE
CHLORITE
OTHER-ALOH
WHITE-MICA
KAOLIN
Bin % Rel. Weight
Depth (m)
NMOD004_tsg_tir: Spatial Summary (Bin=3 MinBin=5% uTSAT 7.0, Mineral Subset)
Group
INVALID
CARBONATE
WHITE-MICA
SILICA
Bin % Rel. Weight
Depth (m)
Use with understanding
Use at your own risk

SPD001 max Au < 1 ppm

SPD001

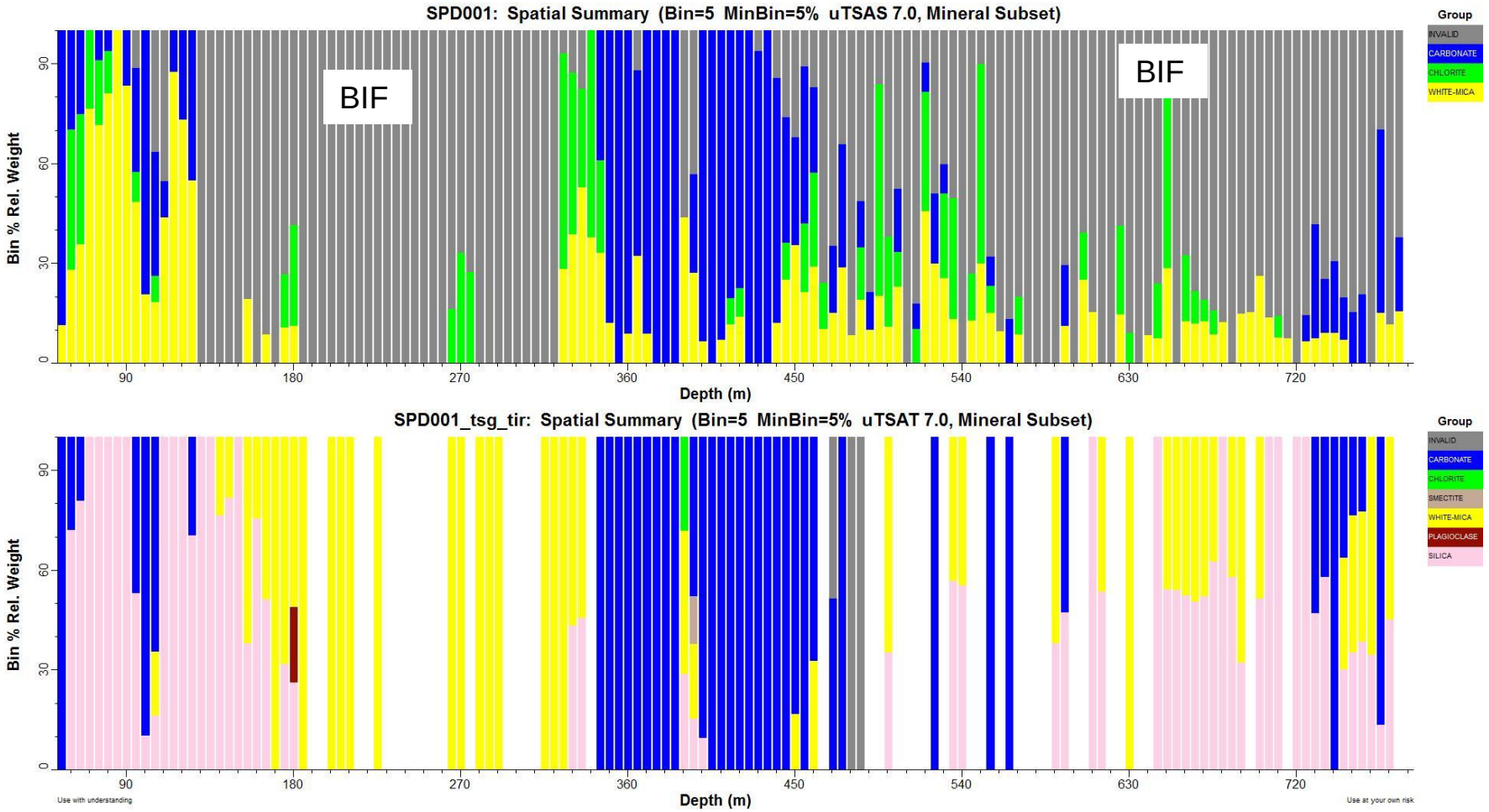
SPD001: Spatial Summary (Bin=5 MinBin=5% uTSAS 7.0, Mineral Subset)
BIF
BIF
Group
INVALID
CARBONATE
CHLORITE
WHITE-MICA
Bin % Rel. Weight
0
30
60
90
90
180
270
360
450
540
630
720
Depth (m)
SPD001_tsg_tir: Spatial Summary (Bin=5 MinBin=5% uTSAT 7.0, Mineral Subset)
Group
INVALID
CARBONATE
CHLORITE
SMECTITE
WHITE-MICA
PLAGIOCLASE
SILICA
Bin % Rel. Weight
0
30
60
90
90
180
270
360
450
540
630
720
Depth (m)
Use with understanding
Use at your own risk

AWD003 max Au < 1 ppm

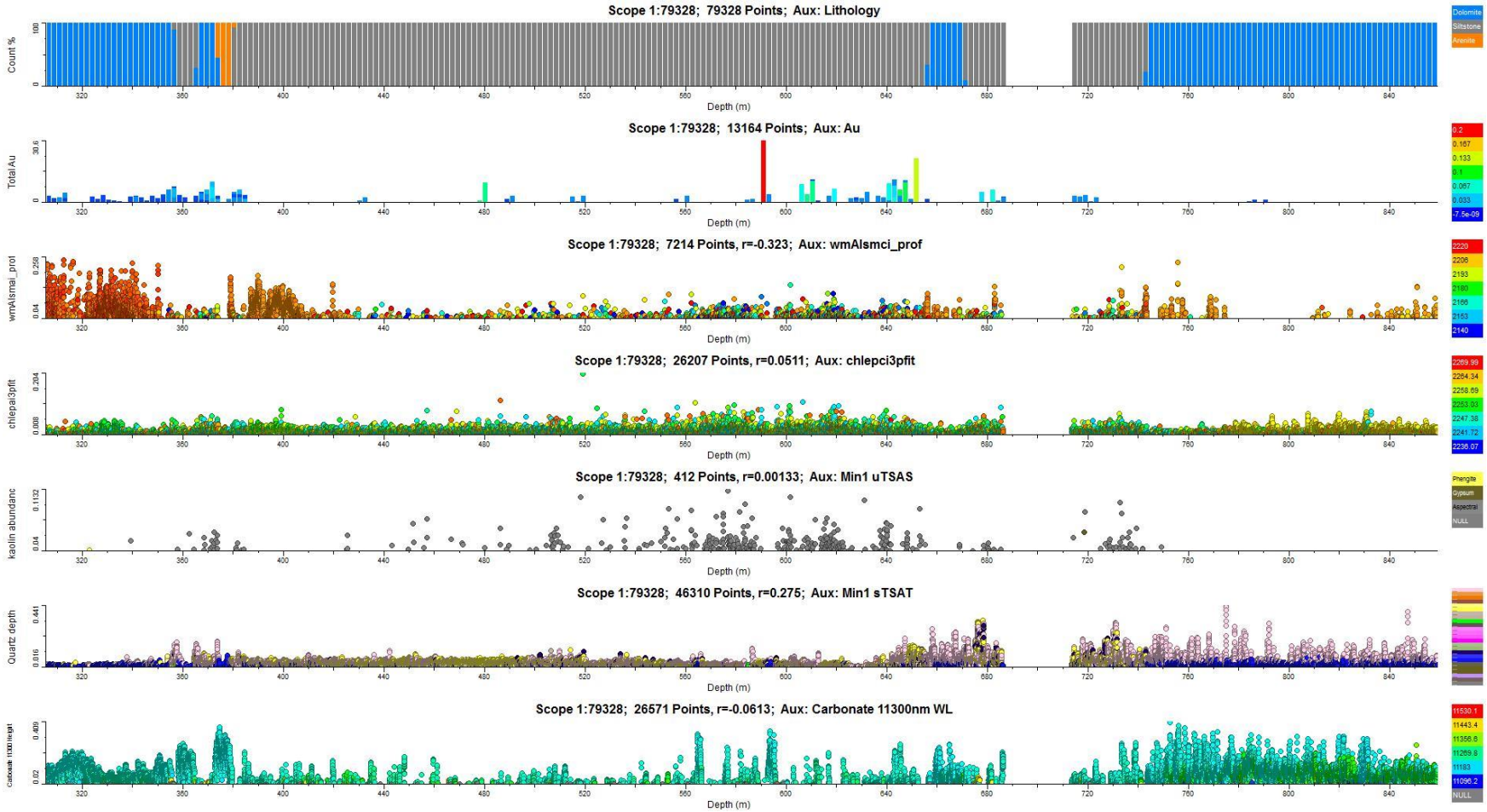

AWD003

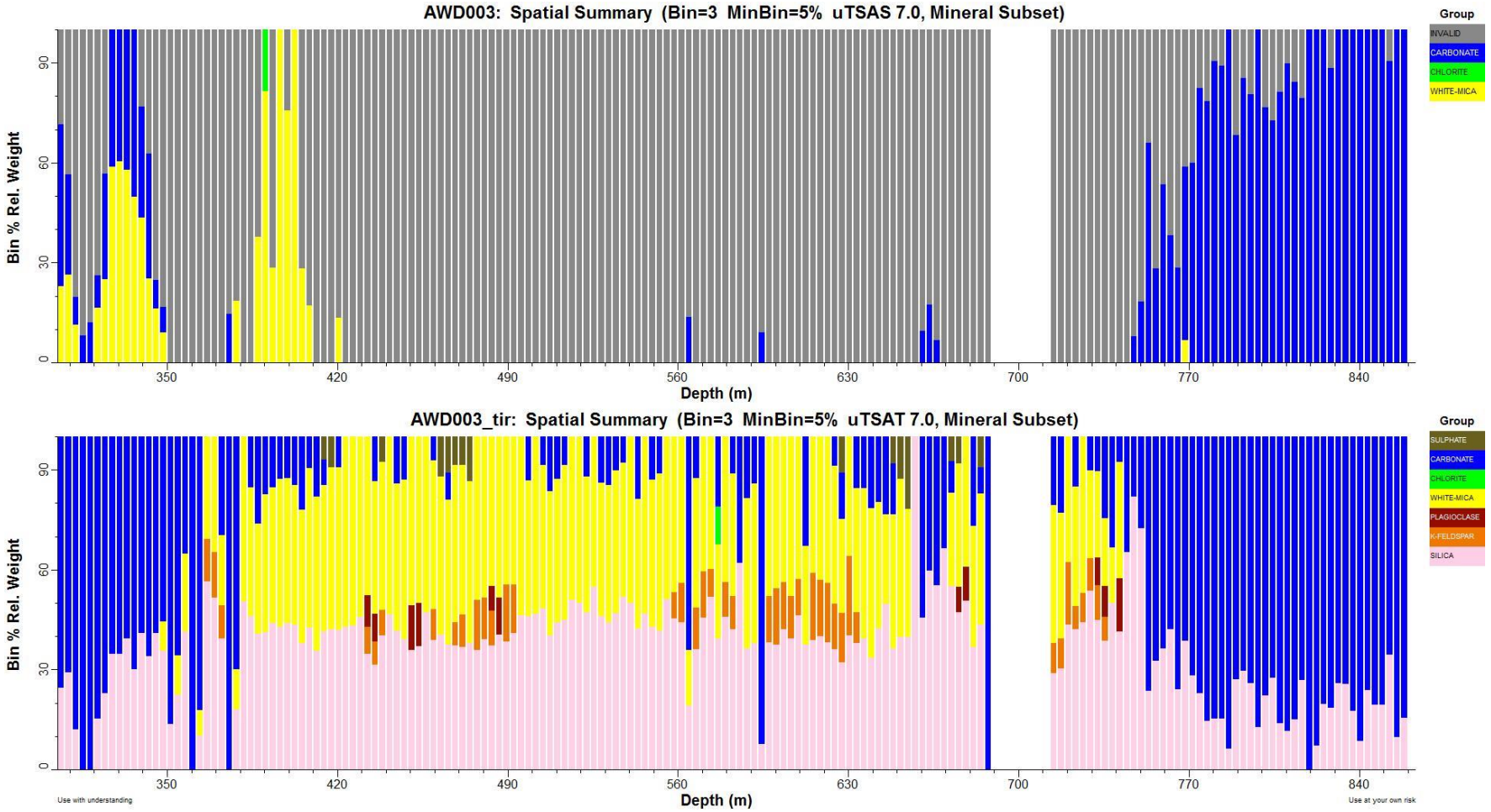
AWD003: Spatial Summary (Bin=3 MinBin=5% uTSAS 7.0, Mineral Subset)
Group
INVALID
CARBONATE
CHLORITE
WHITE-MICA
Bin % Rel. Weight
0
30
60
90
350
420
490
560
630
700
770
840
Depth (m)
AWD003_tir: Spatial Summary (Bin=3 MinBin=5% uTSAT 7.0, Mineral Subset)
Group
SULPHATE
CARBONATE
CHLORITE
WHITE-MICA
PLAGIOCLASE
K-FELDSPAR
SILICA
Bin % Rel. Weight
0
30
60
90
350
420
490
560
630
700
770
840
Depth (m)
Use with understanding
Use at your own risk

EDD005 max Au < 1 ppm

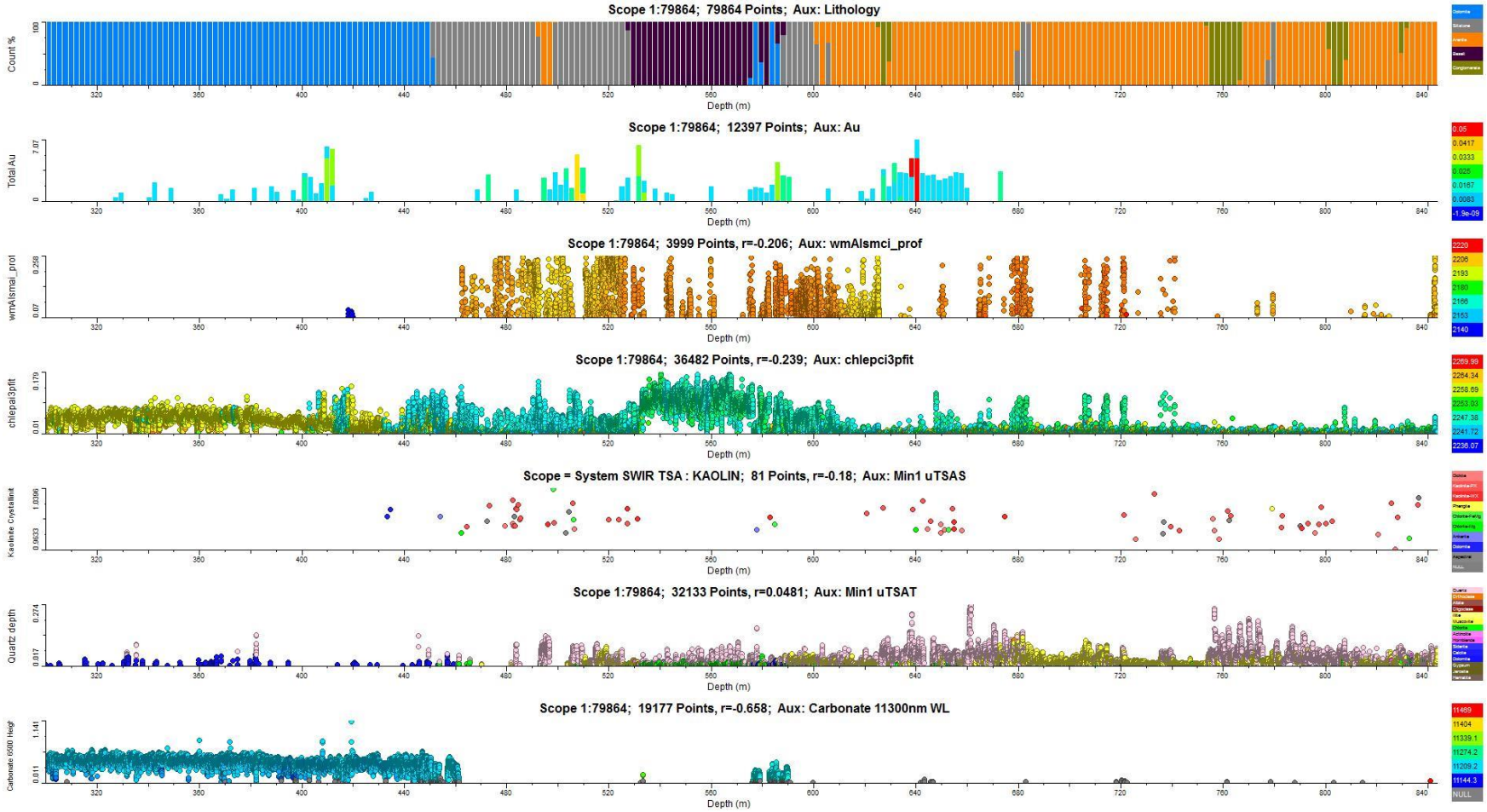

EDD005

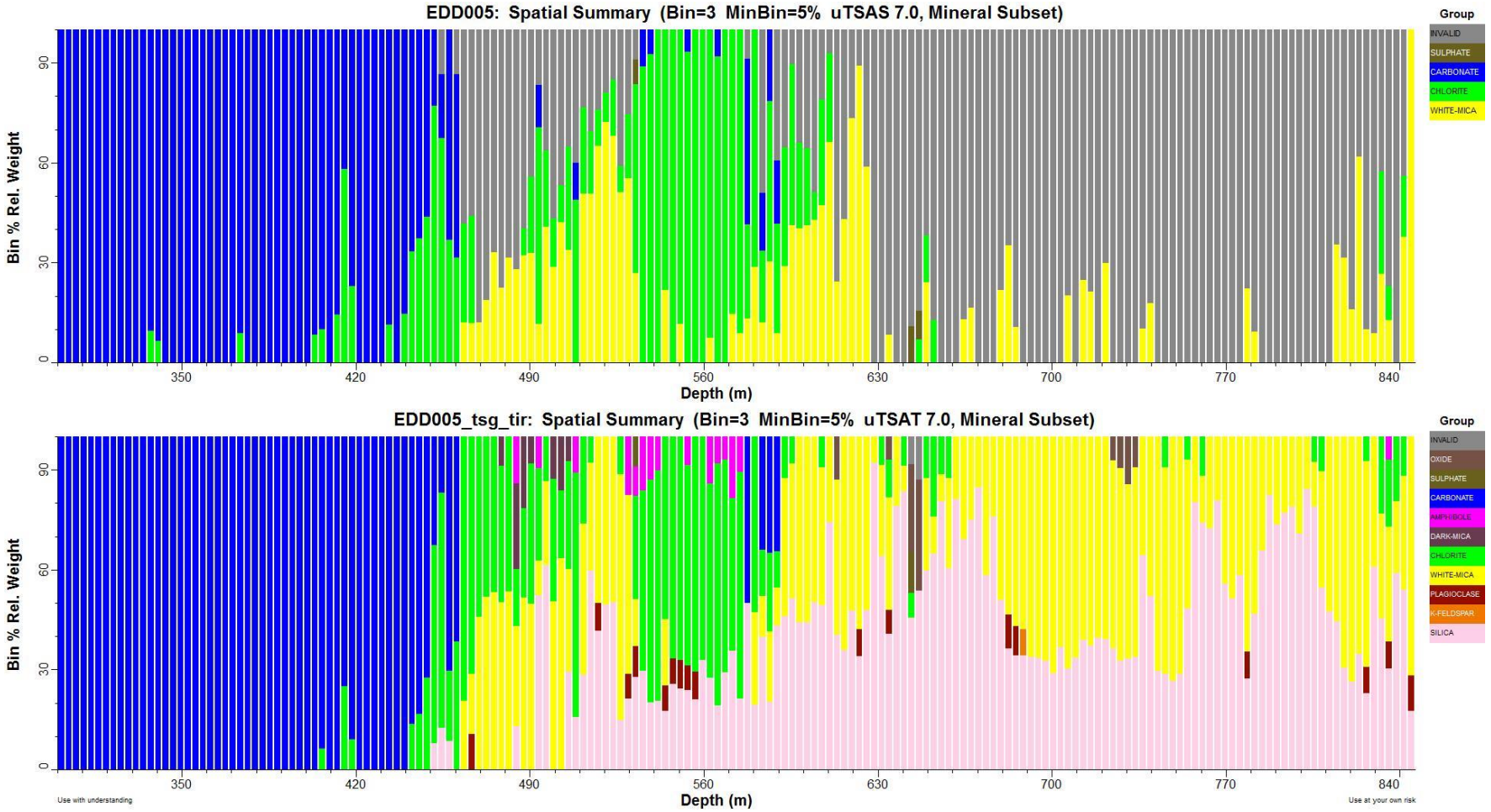
EDD005: Spatial Summary (Bin=3 MinBin=5% uTSAS 7.0, Mineral Subset)
Group
INVALID
SULPHATE
CARBONATE
CHLORITE
WHITE-MICA
Bin % Rel. Weight
0
30
60
90
350
420
490
560
630
700
770
840
Depth (m)
EDD005_tsg_tir: Spatial Summary (Bin=3 MinBin=5% uTSAT 7.0, Mineral Subset)
Group
INVALID
OXIDE
SULPHATE
CARBONATE
AMPHIBOLE
DARK-MICA
CHLORITE
WHITE-MICA
PLAGIOCLASE
K-FELDSPAR
SILICA
Bin % Rel. Weight
0
30
60
90
350
420
490
560
630
700
770
840
Depth (m)
Use with understanding
Use at your own risk

NMD001 max Au < 1 ppm

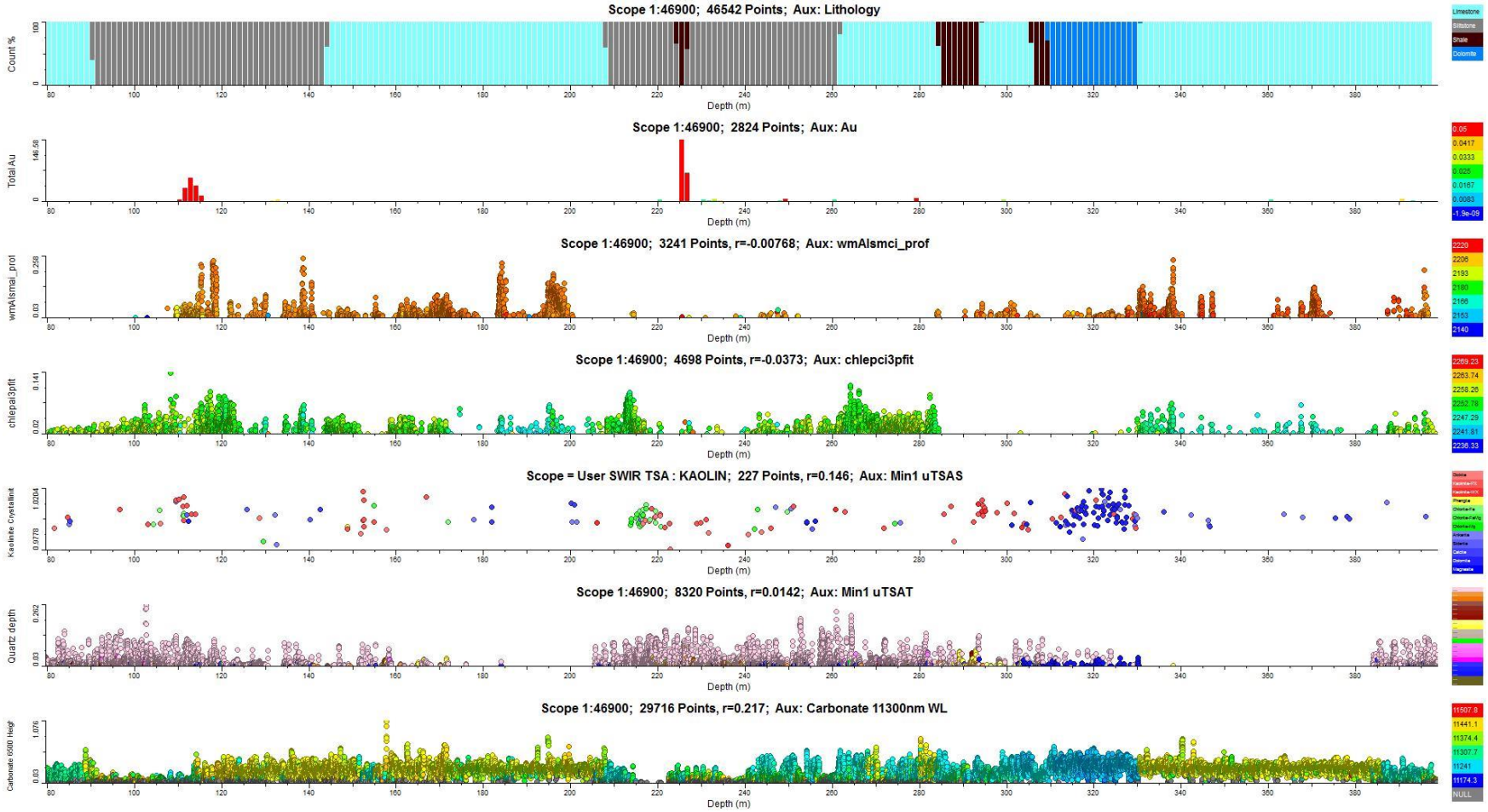

NMD001

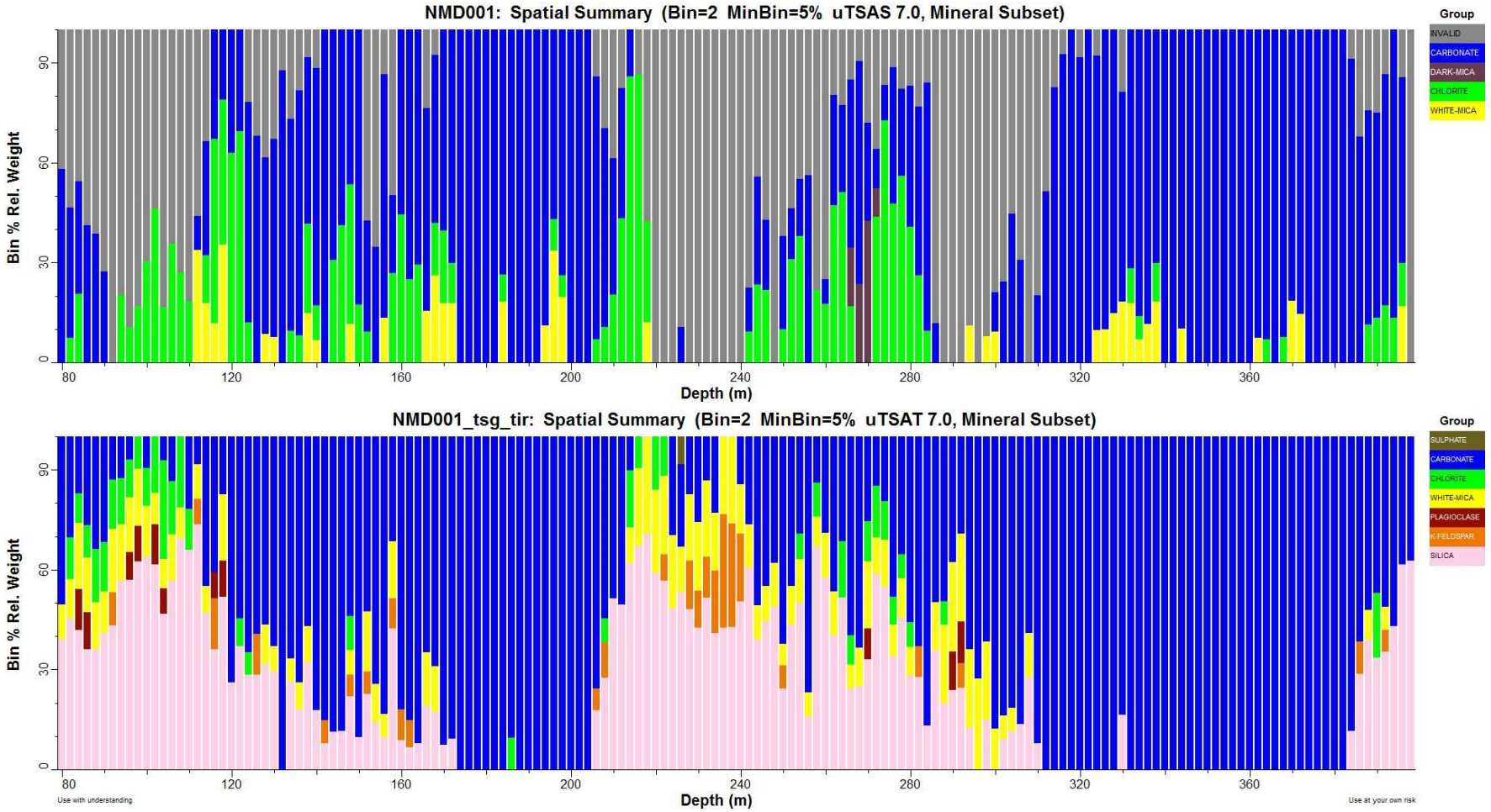
NMD001: Spatial Summary (Bin=2 MinBin=5% uTSAS 7.0, Mineral Subset)
Group
INVALID
CARBONATE
DARK-MICA
CHLORITE
WHITE-MICA
Bin % Rel. Weight
0
30
60
90
80
120
160
200
240
280
320
360
Depth (m)
NMD001_tsg_tir: Spatial Summary (Bin=2 MinBin=5% uTSAT 7.0, Mineral Subset)
Group
SULPHATE
CARBONATE
CHLORITE
WHITE-MICA
PLAGIOCLASE
K-FELDSPAR
SILICA
Bin % Rel. Weight
0
30
60
90
80
120
160
200
240
280
320
360
Depth (m)
Use with understanding
Use at your own risk

ID001 max Au < 1 ppm

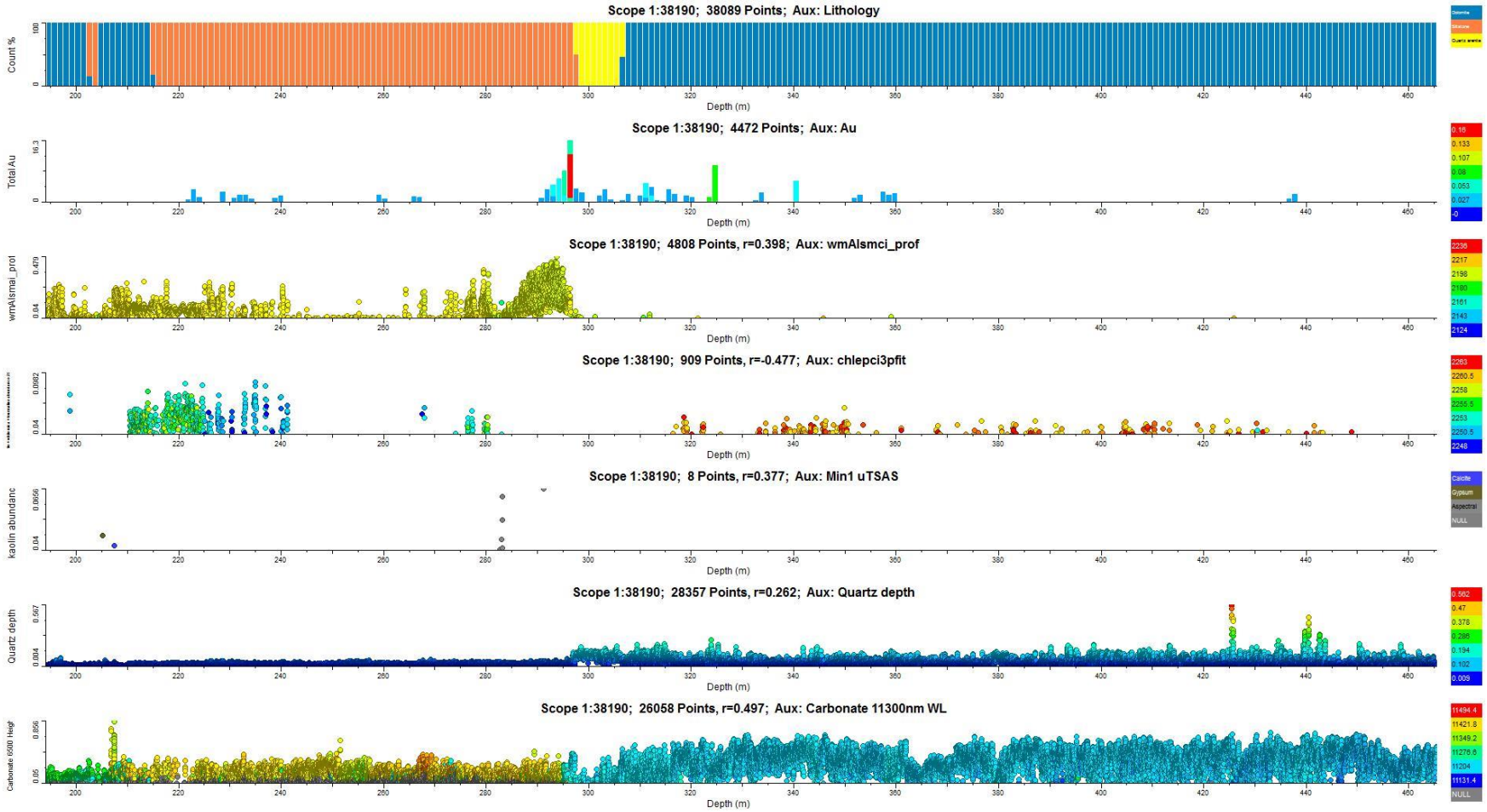

ID001

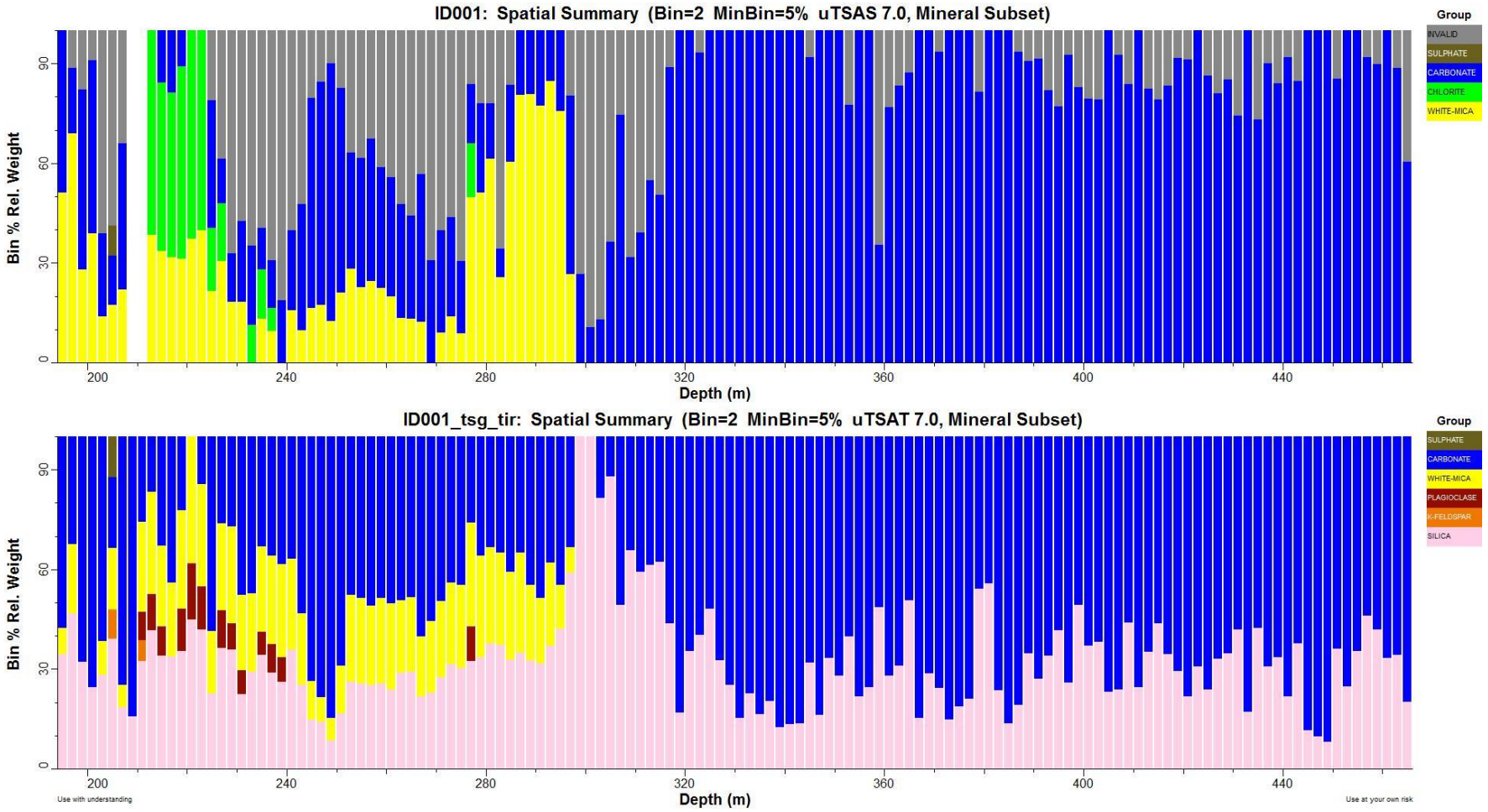
ID001: Spatial Summary (Bin=2 MinBin=5% uTSAS 7.0, Mineral Subset)
Group
INVALID
SULPHATE
CARBONATE
CHLORITE
WHITE-MICA
Bin % Rel. Weight
0
30
60
90
200
240
280
320
360
400
440
Depth (m)
ID001_tsg_tir: Spatial Summary (Bin=2 MinBin=5% uTSAT 7.0, Mineral Subset)
Group
SULPHATE
CARBONATE
WHITE-MICA
PLAGIOCLASE
K-FELDSPAR
SILICA
Bin % Rel. Weight
0
30
60
90
200
240
280
320
360
400
440
Depth (m)
Use with understanding
Use at your own risk

LD004 max Au 2 ppm in weathering zone and max Au > 1 ppm in dolomites

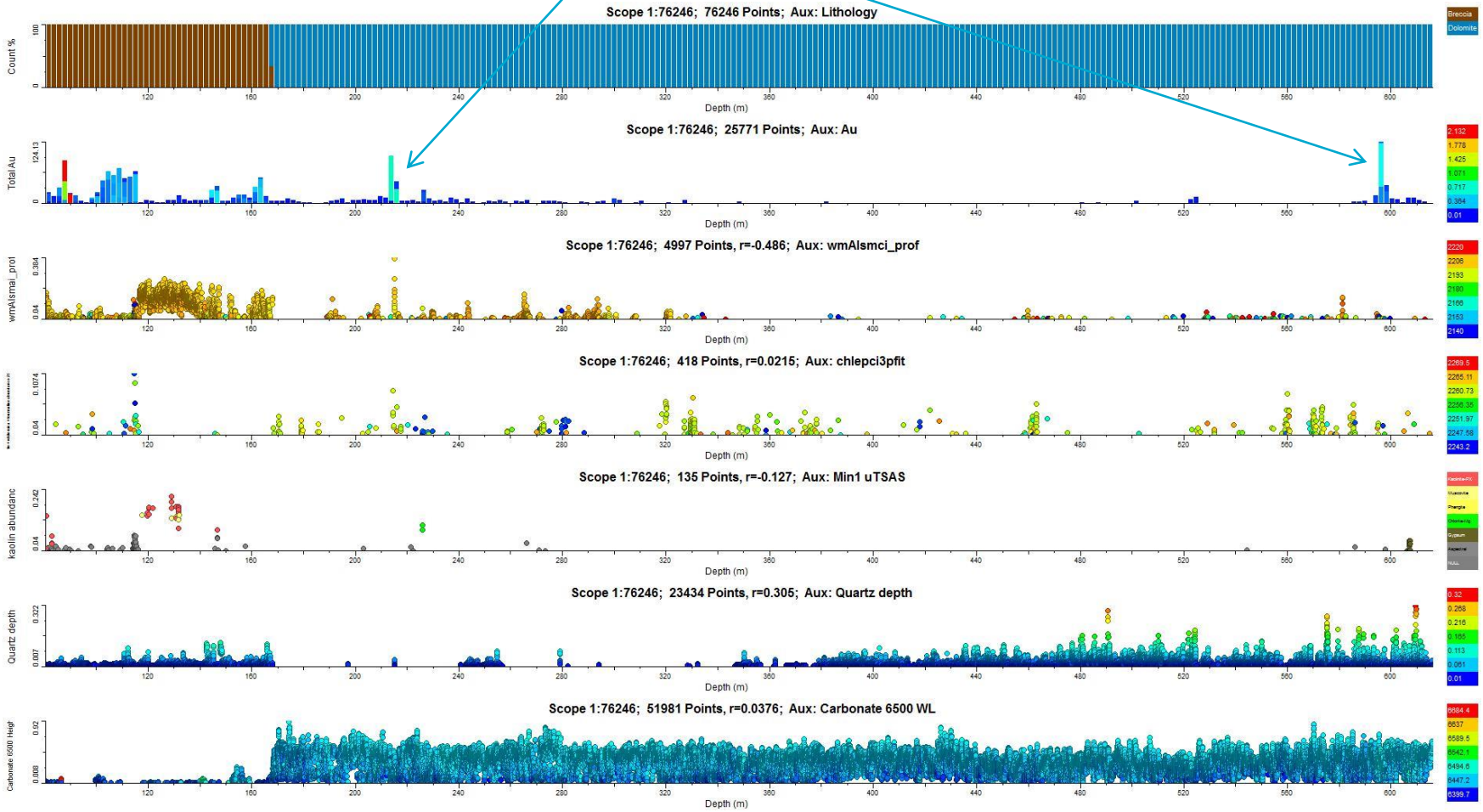

LD004

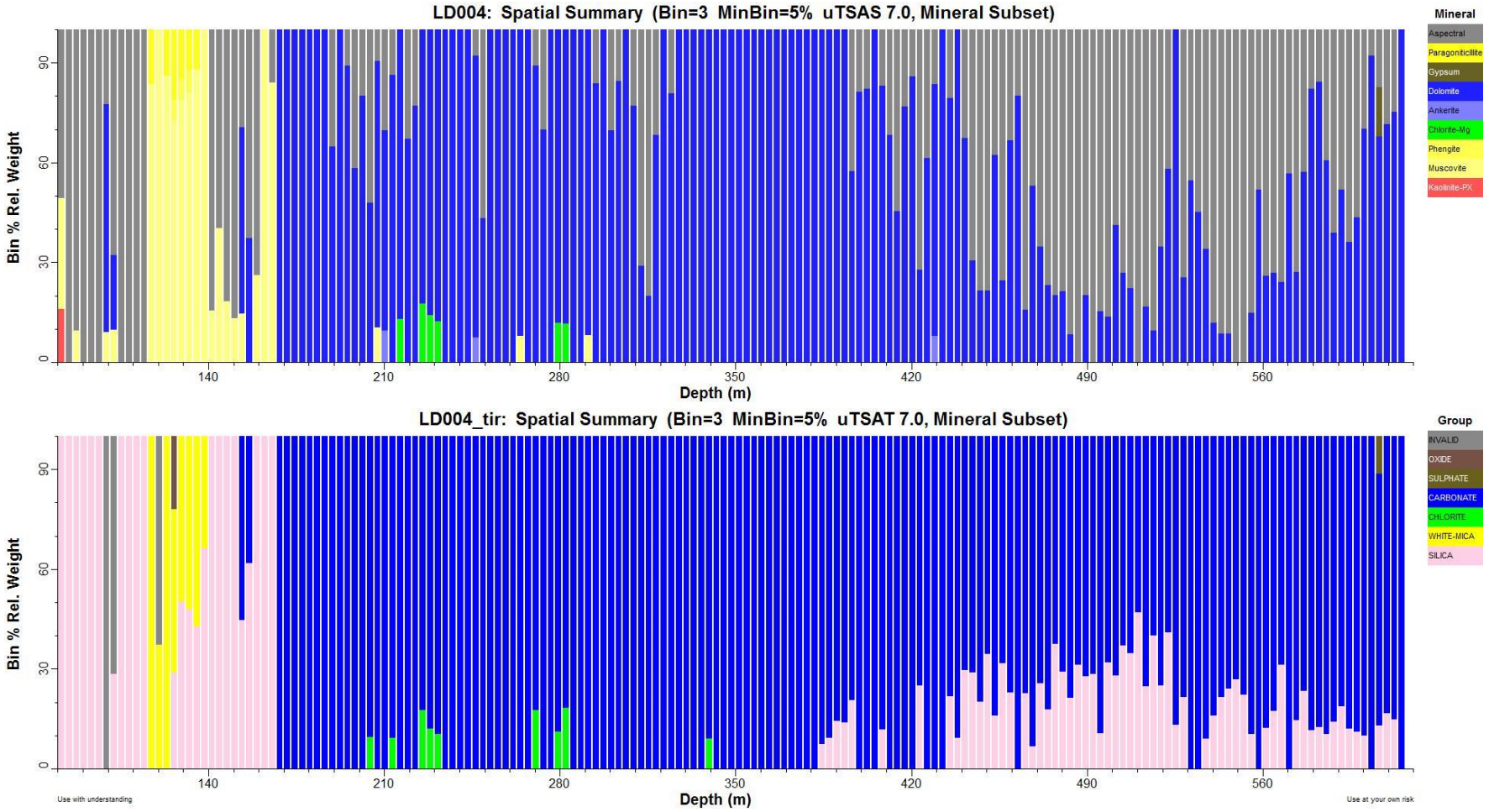
LD004: Spatial Summary (Bin=3 MinBin=5% uTSAS 7.0, Mineral Subset)
Mineral
Aspectral
Paragonitic/Illite
Gypsum
Dolomite
Ankerite
Chlorite-Mg
Phengite
Muscovite
Kaolinite-PX
Bin % Rel. Weight
0
30
60
90
140
210
280
350
420
490
560
Depth (m)
LD004_tir: Spatial Summary (Bin=3 MinBin=5% uTSAT 7.0, Mineral Subset)
Group
INVALID
OXIDE
SULPHATE
CARBONATE
CHLORITE
WHITE-MICA
SILICA
Bin % Rel. Weight
0
30
60
90
140
210
280
350
420
490
560
Depth (m)
Use with understanding
Use at your own risk

Summary for distal low-grade mineralization

- Depth 80-860 m
- Max Au 2 ppm at NMOD004 in siltstones with carbonate veinlets and 3 ppm at MDO3 in hematite-rich fault zone
- BIF unit and fault zone (Mount Olympus holes NMOD004, SPD001 and MDO3)
- Amphiboles in basalt (EDD005)
- Abundant carbonate **or** Fe-Mg chlorite

Sulphate and clay mineralogy derived from scalars and TSA

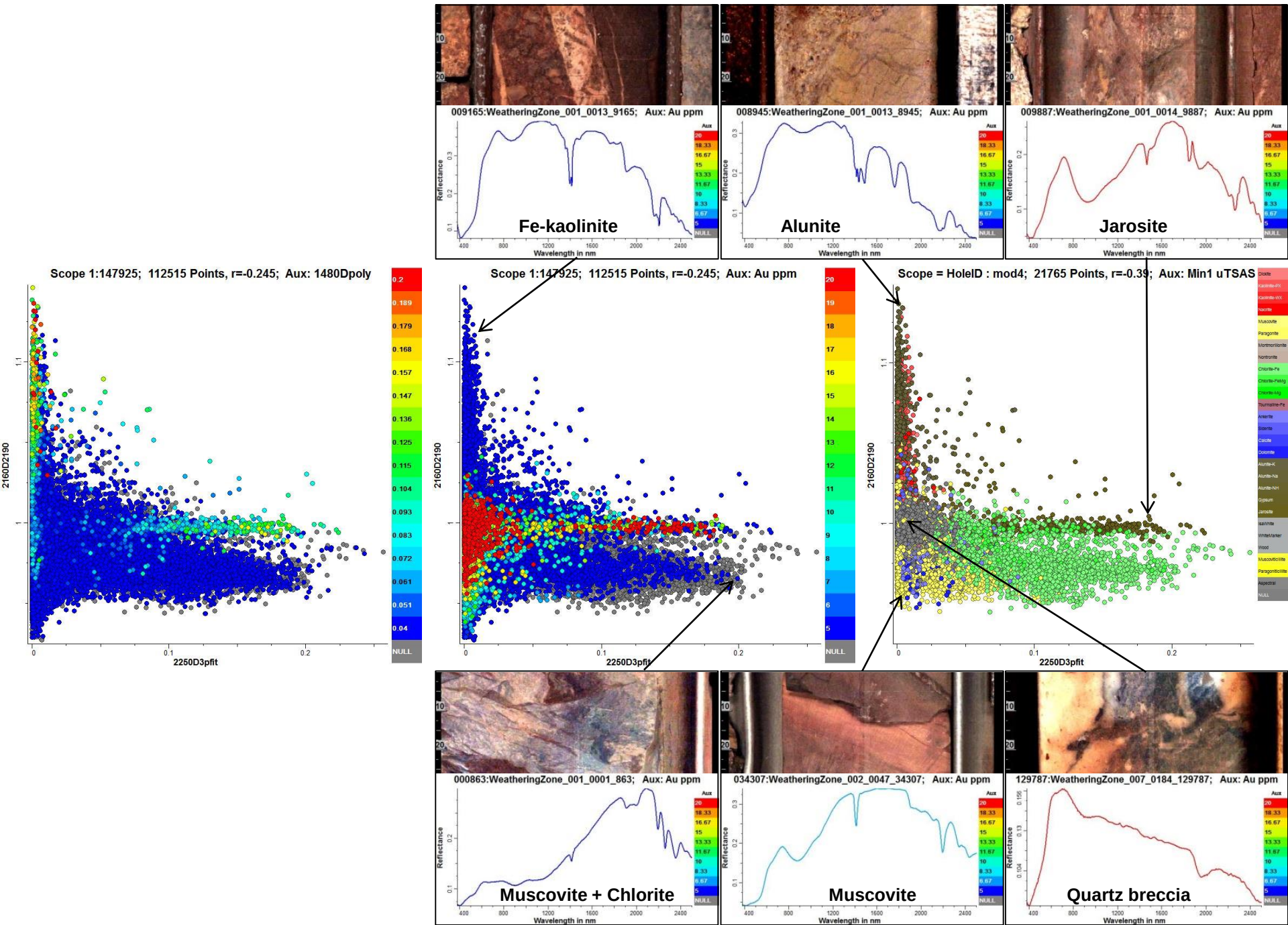
009165:WeatheringZone_001_0013_9165; Aux: Au ppm
Fe-kaolinite
008945:WeatheringZone_001_0013_8945; Aux: Au ppm
Alunite
009887:WeatheringZone_001_0014_9887; Aux: Au ppm
Jarosite
Scope 1:147925; 112515 Points, r=-0.245; Aux: 1480Dpoly
Scope 1:147925; 112515 Points, r=-0.245; Aux: Au ppm
Scope = HoleID : mod4; 21765 Points, r=-0.39; Aux: Min1 uTSAS
2160D2190
2250D3pfit
Reflectance
Wavelength in nm
000863:WeatheringZone_001_0001_863; Aux: Au ppm
Muscovite + Chlorite
034307:WeatheringZone_002_0047_34307; Aux: Au ppm
Muscovite
129787:WeatheringZone_007_0184_129787; Aux: Au ppm
Quartz breccia

Sulphates

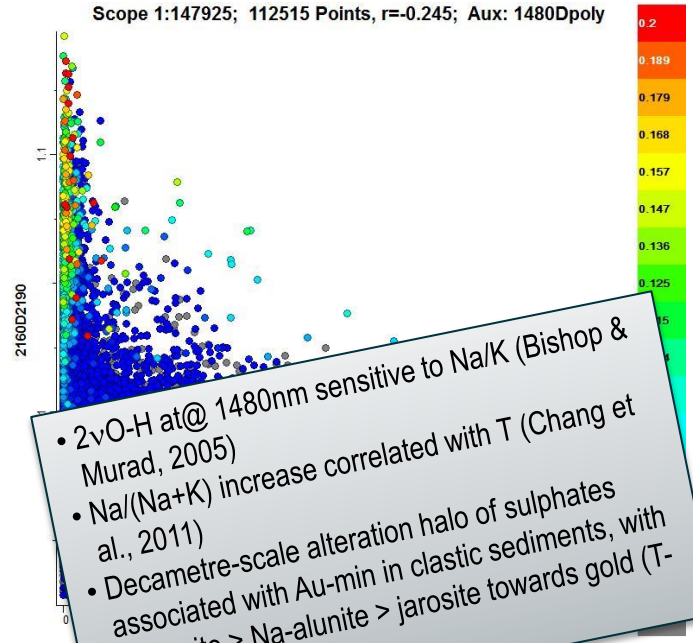

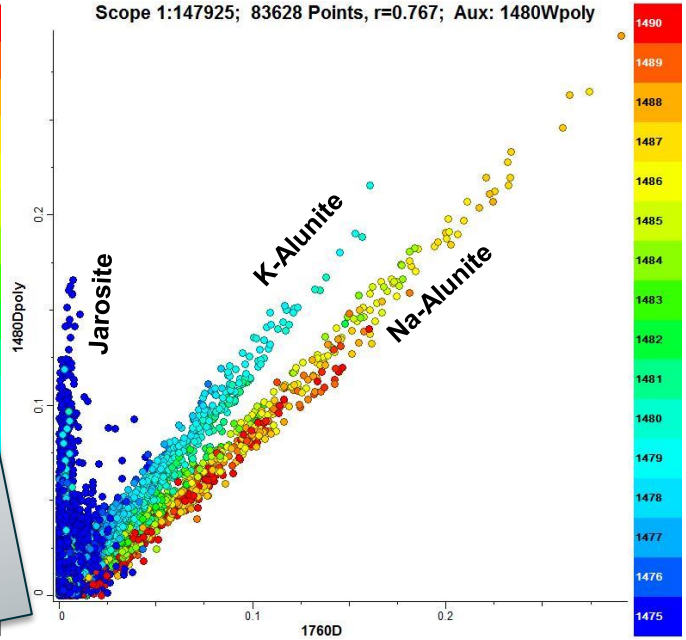

- 2νO-H at@ 1480nm sensitive to Na/K (Bishop & Murad, 2005)
- Na/(Na+K) increase correlated with T (Chang et al., 2011)
- Decametre-scale alteration halo of sulphates associated with Au-min in clastic sediments, with K-alunite > Na-alunite > jarosite towards gold (T-increase?!?)?!

~1480nm
$2\nu(O\text{-}H),\ \nu+2\delta(H_2O)$

1760nm
$\nu+\delta(O\text{-}H)$

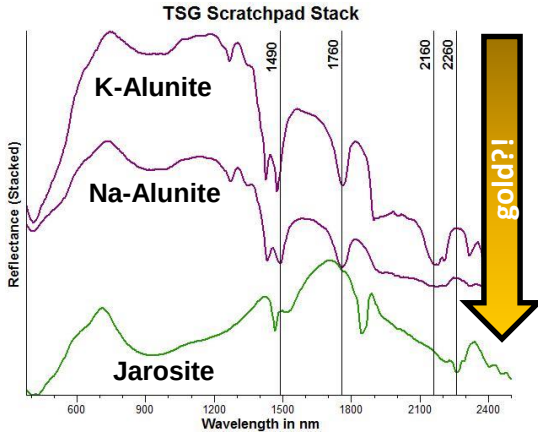

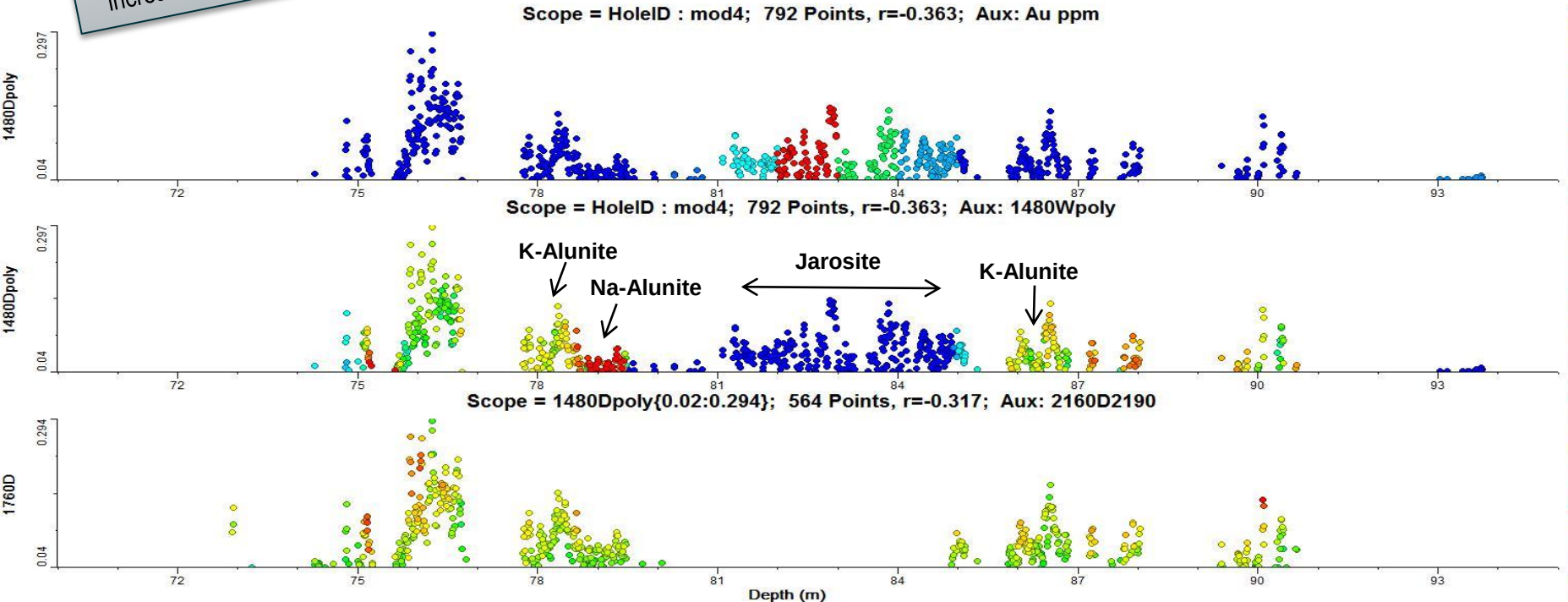

Appendix 8 AEM flight line profiles, Electric Dingo Area

AEM inversion processing was only conducted for flight lines Fid36, FID37, FID39 (Electric Dingo area) and for FID59 and FID60 (Mt Olympus area) as described in the main text. Initial AEM results are presented below for flight lines in the Electric Dingo Area (refer to the main report for a more detailed discussion).

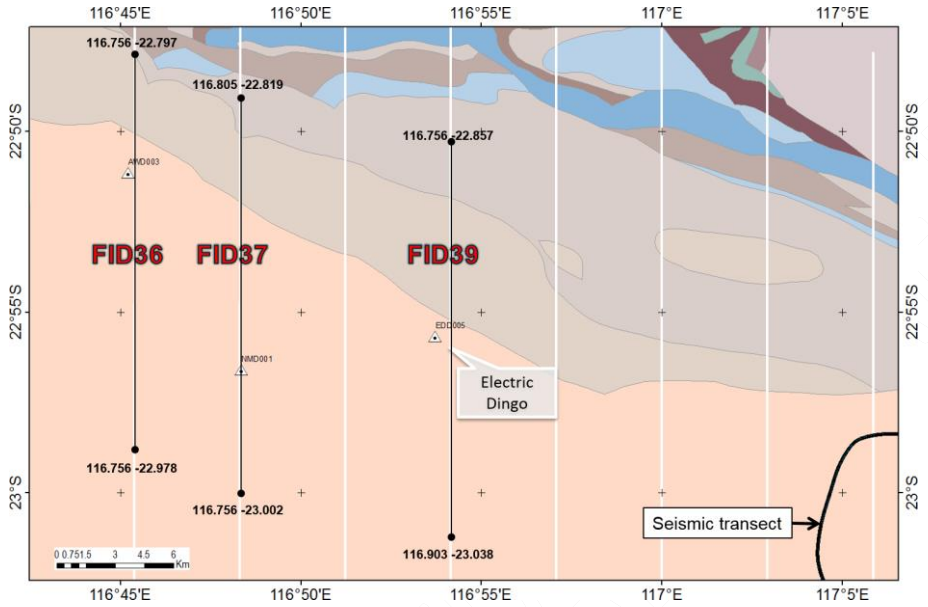

Location of the processed AEM TEMPEST flight lines in the Electric Dingo area.

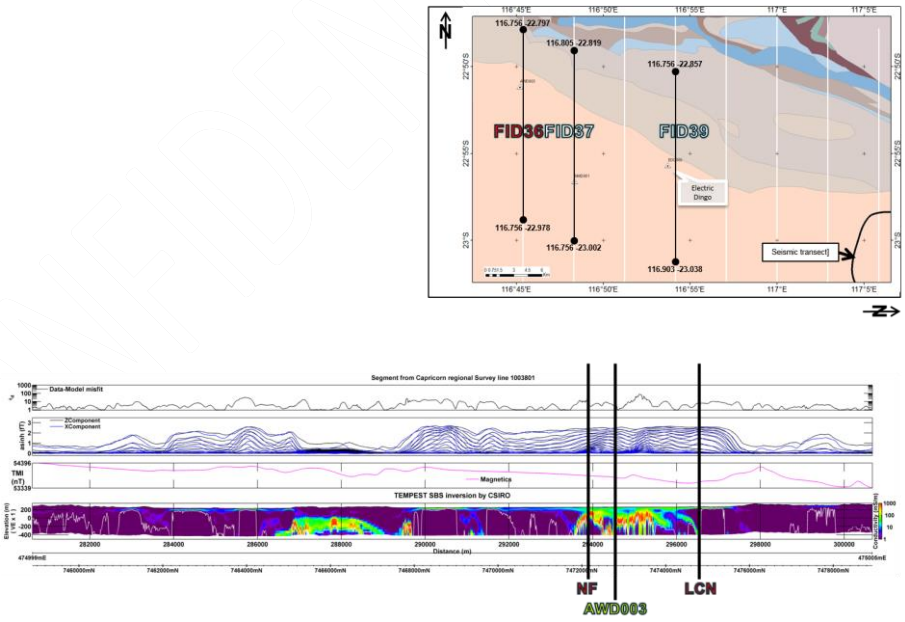

AEM processing for flight line FID36.

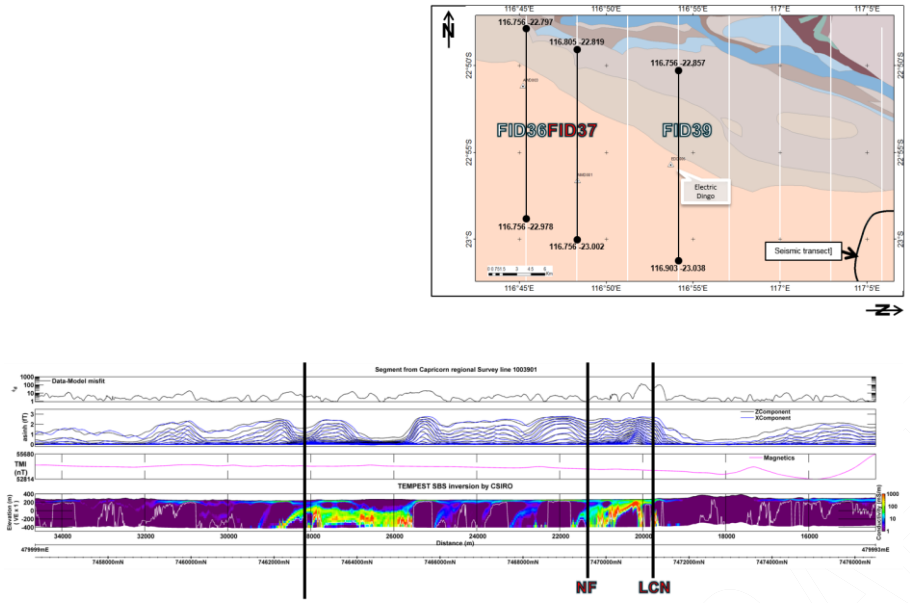

AEM processing for flight line FID37.

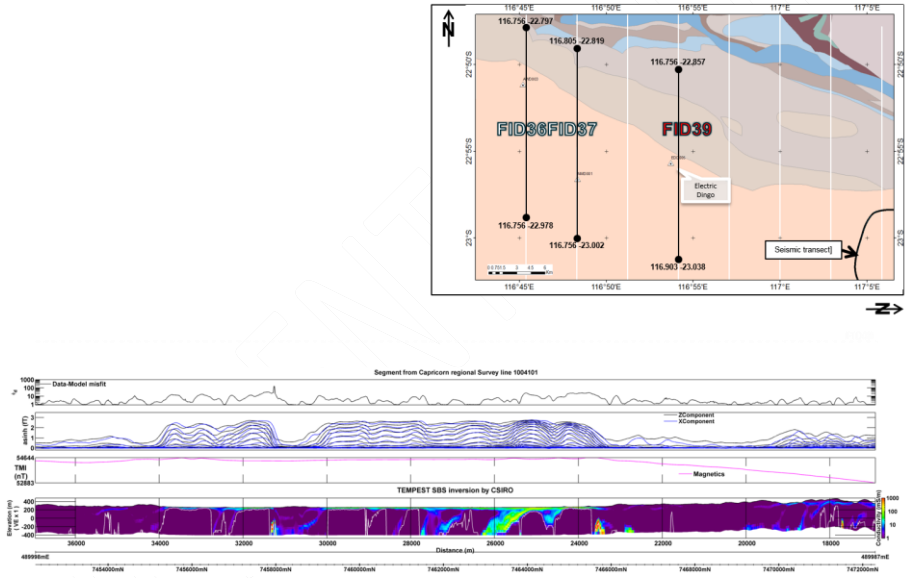

AEM processing for flight line FID39.

Appendix 9 Regolith geochemistry and related data

This data is held within the associated Regolith Geochemistry TSG files and relevant data exported from TSG as Excel (.xlsx) files. A summary description of the files is given below:

- TSG file with ASD spectra of regolith geochemical samples collected from the Mt Olympus area, including Easting/Northing and imported geochem (GSWA_RegolithSamples_MtOlympus_ASD.tsg/.ini/.bip)
- TSG file of the ASD spectra downsampled to ASTER multispectral resolution (GSWA_RegolithSamples_MtOlympus_ASTER.tsg/.ini/.bip)
- Xls files exported from the respective TSG files containing selected TSA and batch script scalars as well as geochem (GSWA_RegolithSamples_MtOlympus_ASTERtsgexport.xlsx; GSWA_RegolithSamples_MtOlympus_ASDtsgexport.xlsx)

CONTACT US

t 1300 363 400
+61 3 9545 2176
e enquiries@csiro.au
w www.csiro.au

YOUR CSIRO

Australia is founding its future on science and innovation. Its national science agency, CSIRO, is a powerhouse of ideas, technologies and skills for building prosperity, growth, health and sustainability. It serves governments, industries, business and communities across the nation.

FOR FURTHER INFORMATION

Mineral Resources
Martin Wells
t +61 8 6436 8812
e martin.wells@csiro.au
w www.csiro.au/

Mineral Resources
Carsten Laukamp
t +61 8 6436 8754
e carsten.laukamp@csiro.au
w http://c3dmm.csiro.au/

CONTACT US

t 1300 363 400
+61 3 9545 2176
e enquiries@csiro.au
w www.csiro.au

YOUR CSIRO

Australia is founding its future on science and innovation. Its national science agency, CSIRO, is a powerhouse of ideas, technologies and skills for building prosperity, growth, health and sustainability. It serves governments, industries, business and communities across the nation.

FOR FURTHER INFORMATION

Mineral Resources
Martin Wells
t +61 8 6436 8812
e martin.wells@csiro.au
w www.csiro.au/

Mineral Resources
Carsten Laukamp
t +61 8 6436 8754
e carsten.laukamp@csiro.au
w http://c3dmm.csiro.au/

The Nanjilgardy Fault is a major northwest-trending deep-seated structure that defines a corridor potentially highly prospective for gold mineralization in the northern margin of the Ashburton Basin (Capricorn Orogen, Western Australia). Four gold mineralization types and associated alteration patterns were identified at the Mt Olympus deposit using HyLogger-3 mineralogical data. Hydrothermal alteration phases identified along the Nanjilgardy Fault and at the Mt Olympus deposit were Na/K-alunite, kaolinite, dickite, pyrophyllite, white mica and chlorite. HyLogging-3 data at the mineral group level were verified by XRD analyses. A 3D model was created of the gold distribution and associated alteration within and around Mt Olympus. Mineralogical variations associated with large and small-scale structures were investigated using remotely sensed AEM and ASTER data.

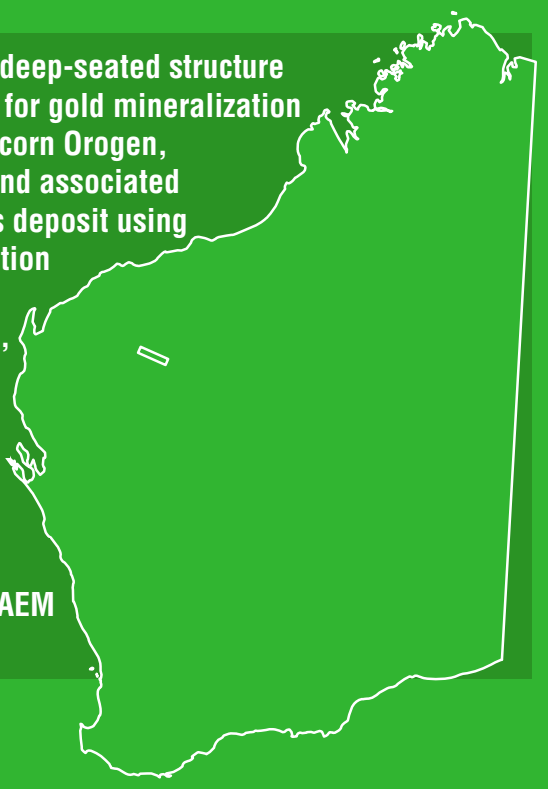

Further details of geological products and maps produced by the Geological Survey of Western Australia are available from:

Information Centre
Department of Mines and Petroleum
100 Plain Street
EAST PERTH WA 6004
Phone: (08) 9222 3459 Fax: (08) 9222 3444

www.dmp.wa.gov.au/GSWApublications

WELLS et al.

INTEGRATED SPECTRAL MAPPING OF PRECIOUS AND BASE METAL RELATED MINERAL FOOTPRINTS, NANJILGARDY FAULT, WESTERN AUSTRALIA

REPORT 156